The Finite-Difference Modelling of Earthquake Motions
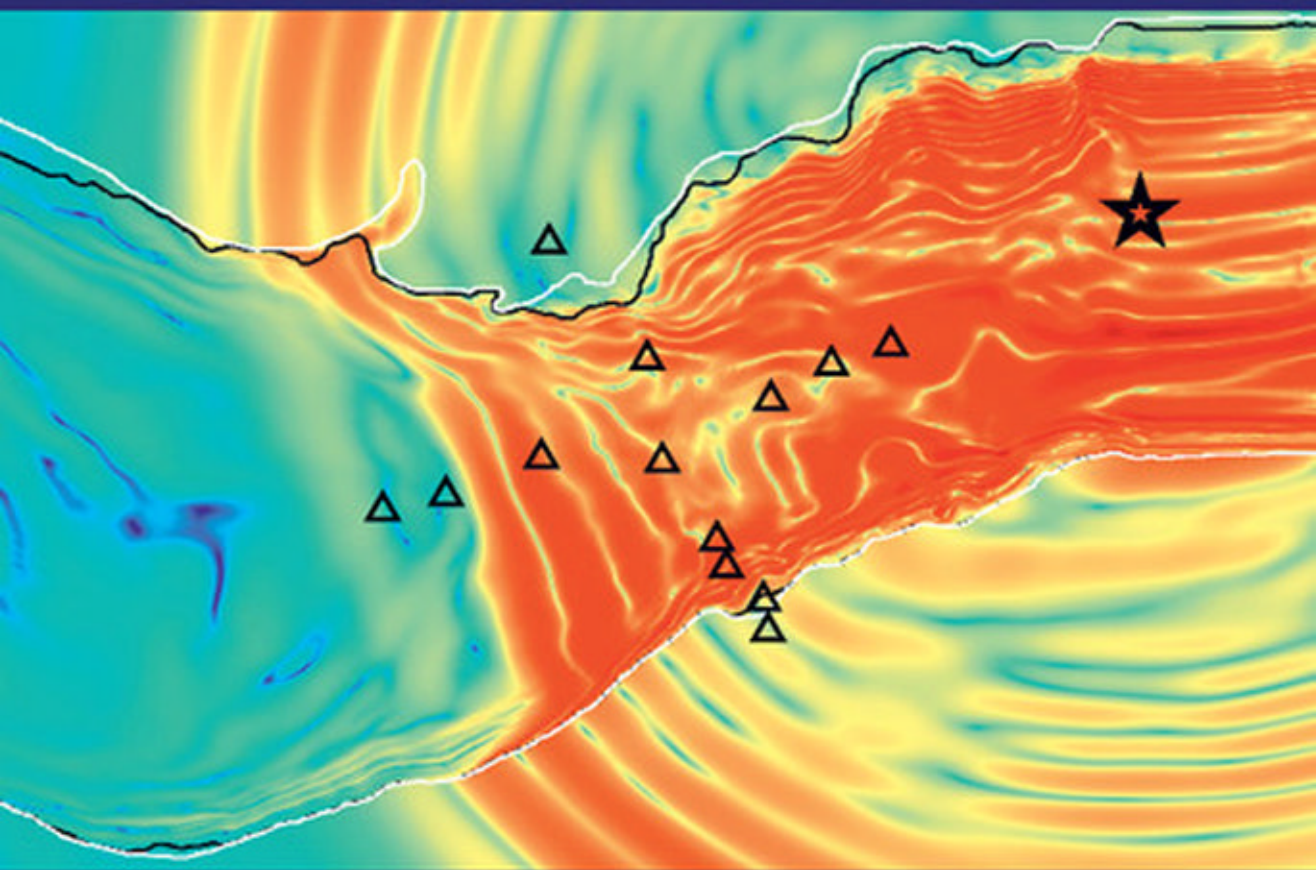
Waves and Ruptures

Peter Moczo

Jozef Kristek

Martin Gális

THE FINITE-DIFFERENCE MODELLING OF EARTHQUAKE MOTIONS
Waves and Ruptures

Numerical simulation is an irreplaceable tool in earthquake ground motion research. Among all the numerical methods in seismology, the finite-difference (FD) technique is the most widely used, providing the best balance of accuracy and computational efficiency. Now, for the first time, this book offers a comprehensive introduction to this method and its applications to earthquake motion.

Using a systematic tutorial approach, the book requires only an undergraduate degree-level mathematical background and provides a user-friendly explanation of the relevant theory. It explains FD schemes for solving wave equations and elastodynamic equations of motion in heterogeneous media, and provides an introduction to the rheology of viscoelastic and elastoplastic media. It also presents an advanced FD time-domain method for efficient numerical simulations of earthquake ground motion in realistic complex models of local surface sedimentary structures, which are often responsible for anomalous earthquake motion and site effects in earthquakes.

Accompanied by a suite of online resources to help put the theory into practice, this is a vital resource for professionals and academic researchers using numerical seismological techniques, and for graduate students in earthquake seismology, computational and numerical modelling, and applied mathematics.

PETER MOCZO is a professor of physics and Chair of the Department of Astronomy, Physics of the Earth, and Meteorology at Comenius University, Bratislava. He is the main author of several monographs and extended articles on the finite-difference method (including the seminal *Acta Physica Slovaca* article that partly forms the basis of this book). Professor Moczo is a member of the Learned Society of the Slovak Academy of Sciences, and his awards include the Prize of the Slovak Academy of Sciences for Infrastructure, the Silver Medal of the Faculty of Mathematics, Physics and Informatics of Comenius University, and the Dionyz Stur Medal of the Slovak Academy of Sciences for Achievements in Natural Sciences.

Along with his two co-authors, Professor Moczo is a leading member of the (informal) NuQuake research group, studying numerical modelling of seismic wave propagation and earthquake motion, at Comenius University and the Slovak Academy of Sciences in Bratislava. As part of this group, all three authors were major contributors to the elaboration of the finite-difference method and hybrid finite-difference–finite-element method.

JOZEF KRISTEK is an associate professor of physics at the Department of Astronomy, Physics of the Earth, and Meteorology at Comenius University, Bratislava. His research, as part of the NuQuake group, focuses on the development of numerical-modelling methods for seismic wave propagation and earthquake motion in structurally complex media, and Dr Kristek has been awarded the Prize of the Slovak Academy of Sciences for Infrastructure and the Dean's Prize for Science for his work in this area.

MARTIN GÁLIS is a post-doctoral researcher at the King Abdullah University of Science and Technology (KAUST), Saudi Arabia. Dr Gális' research also focuses on the development of numerical-modelling methods for seismic wave propagation and earthquake motion in structurally complex media. He has also been awarded the Prize of the Slovak Academy of Sciences for Infrastructure.

The present volume is part of an informal series of books, all of which originated from review articles published in *Acta Physica Slovaca*. The journal can be accessed for free at www.physics.sk/aps.

Vladimir Buzek, editor of the journal

THE FINITE-DIFFERENCE MODELLING OF EARTHQUAKE MOTIONS

Waves and Ruptures

PETER MOCZO

Comenius University, Bratislava
and
Slovak Academy of Sciences, Bratislava

JOZEF KRISTEK

Comenius University, Bratislava
and
Slovak Academy of Sciences, Bratislava

MARTIN GALIS

King Abdullah University of Science and Technology, Saudi Arabia

with contributions by
MIRIAM KRISTEKOVA, EMMANUEL CHALJUB,
MARTIN KÄSER, PETER KLIN AND
CHRISTIAN PELTIES

To Janulka, Mirka and Fibi

Contents

Acknowledgements

We are very grateful to all who directly or indirectly helped us to write this book.

Over recent years, we had several friendly informal suggestions to write a book on finite-difference modelling, but we finally decided to do so after physicist Vladimír Bužek, a chief editor of our *Acta Physica Slovaca* volume in 2007, suggested the book to Cambridge University Press, and Jean Virieux encouraged us to accept the challenge and evaluated our proposal. We thank both Vladimír and Jean for their vision, advice and encouragement.

We also thank three anonymous reviewers for constructive and helpful reviews of the book proposal.

We are grateful to Emmanuel Chaljub for contributing the section on the spectral-element method, Peter Klin for the section on the Fourier pseudo-spectral method, Martin Käser and Christian Pelties for the section on the arbitrarily high-order-derivative–discontinuous Galerkin method, and Miriam Kristekova for the section on the time–frequency misfit criteria. We also thank Emmanuel Chaljub and Florent De Martin for their SEM simulations, and Miriam Kristekova for calculating time–frequency goodness-of-fit criteria. We thank Rafael Abreu for collaboration on stability analysis.

We specially thank our students Aneta Richterová, Svetlana Stripajová, Zuzana Margočová and Filip Kubina. Aneta helped us to elaborate the section on the elastoplastic continuum. Aneta, Svetlana and Zuzana carefully and critically read the whole manuscript, corrected misprints and mistakes, and suggested several improvements to make the text more student-friendly. Filip critically read the first half of Chapter 7.

We greatly appreciate the kind and constructive help of colleagues who found time in their intense schedules to critically read parts of the manuscript and made suggestions that helped us to improve the book: Steve Day, Jean-Paul Ampuero, Pierre-Yves Bard, Emmanuel Chaljub, Wei Zhang, Eric Dunham, Rafael Abreu, Florent De Martin, Martin Mai, Fabian Bonilla, Leila Etemadsaeed and Anders Petersson.

Over the years of elaboration of our finite-difference modelling we enjoyed discussions and learned much from Jean Virieux, Michel Bouchon, Pierre-Yves Bard, Steve Day, Emmanuel Chaljub, Ralph Archuleta, Robert Geller, Johan Robertsson, Jacobo Bielak, Martin Käser, Jean-Paul Ampuero, Heiner Igel, Andreas Fichtner, Robert Graves, Arben Pitarka, Wei Zhang, Rafael Abreu, Zhenguo Zhang, Leo Eisner, Richard Liska and other colleagues. All that we learned helped us to create the concept and contents of the book.

Selected symbols

Abbreviations

AFDA	adjusted finite-difference approximation technique
CG	conventional grid
D	displacement formulation (does not apply to abbreviations 2D or 3D)
DS	displacement–stress formulation
DVS	displacement–velocity–stress formulation
DRP	dispersion-relation-preserving
EQ	partial differential equation
FD	finite-difference
FDEQ	finite-difference equation
FDM	finite-difference method
FDTD	finite-difference time-domain method
FE	finite-element
FEM	finite-element method
GMB-EK	generalized Maxwell body (Emmerich and Korn 1987)
GZB	generalized Zener body
l.h.s.	left hand side (of equation)
PML	perfectly matched layer
r.h.s.	right hand side (of equation)
SEM	spectral-element method
SG	staggered grid
PSG	partly-staggered grid
TSN	traction-at-split-node
VS	velocity–stress formulation

Mathematical notation

$D_x^a \circ D_x^b \equiv D_x^{ab}$	convolution of operators
$\mathcal{F}, \mathcal{F}^{-1}$	direct and inverse Fourier transforms

$x(t) * y(t)$	convolution of functions
$\dfrac{d^j}{d\xi^j}$	j-th total derivative with respect to ξ
$\dfrac{\partial^j}{\partial\xi^j}$	j-th partial derivative with respect to ξ
$\varphi_{i,j}$	concise notation of spatial partial derivative
$\dot{\varphi}$	concise notation of temporal partial derivative

Greek symbols

α	P-wave speed and attenuation coefficient (Subsection 3.3.5)
$\tilde{\alpha}$	grid P-wave velocity
β	S-wave speed
$\tilde{\beta}$	grid S-wave velocity
$\delta(t)$	Dirac delta function
δ_{ij}	Kronecker delta
δM	modulus defect (relaxation of modulus)
Δ	time step
$\Delta x,\ \Delta y,\ \Delta z$	grid spacings
$\varepsilon,\ \varepsilon_{ij}$	1D strain, strain tensor
$\vec{\varepsilon}$	strain vector
ε_{kji}	Levi-Civita symbol
$\zeta_l(t)$	anelastic function for velocity–stress formulation
$\zeta(\omega),\ \zeta_{ij}^{p}(\omega)$	auxiliary functions for 1D and 3D PML
$\theta(\omega),\ \theta_{i}^{p}(\omega)$	auxiliary functions for 1D and 3D PML
κ	bulk modulus
λ	Lamé constant or wavelength
μ	shear modulus (Lamé constant)
μ_f	coefficient of friction
$\mu_s,\ \mu_d$	static and dynamic coefficients of friction
$\xi_l(t)$	anelastic function for displacement formulation
ρ	density
ρ_I^A	effective grid density
$\sigma,\ \sigma_{ij}$	1D stress, stress tensor
$\vec{\sigma}$	stress vector
$\tau_0,\ \tau_n$	initial and normal tractions
$\tau_d,\ \tau_s$	dynamic and static frictional shear tractions
$\varphi_{I,K,L}^{m},\ \Phi_{I,K,L}^{m}$	exact and approximate values of function φ at a grid point $(x_I,\ y_K,\ z_L,\ t_m)$
ω	angular frequency
$\tilde{\omega}$	grid angular frequency

ω_l	characteristic (relaxation) frequency
Ω^{ref}	reference element

Latin symbols

c	phase velocity
c_{ijkl}	tensor of elastic constants
D_c	characteristic (critical) slip-weakening distance
$D_x^{(1-2)}, D_x^{(1-4)}$	operators for the 2nd-order and 4th-order approximations of the 1st x-derivative
D_x^F, D_x^B	forward and backward approximations of the 1st derivative
h	grid spacing in the uniform grid
I, K, L	spatial grid-point indices
m	time-level index
M_0	scalar seismic moment
$\vec{n}, n_j$	normal vector
$O(h^n)$	order of a remainder in Taylor series
p	stability ratio
Q	quality factor
r	V_P / V_S ratio
$\vec{s}$	slip
$\dot{\vec{s}}$	slip rate (slip velocity)
S	surface (Section 2.2)
	frictional strength / fault friction (Sections 4.1, 14.1, 17.1)
	fault surface (Section 4.2)
	stability factor (Courant number) (Chapter 7)
	strength parameter (Section 14.3)
t	time
t_m	time at time level m
T	period
$T_{I\pm1/2}^m$	discrete approximation of stress
$TXX, TYY, TZZ, TXY,$ TYZ, TZX	discrete grid values of the stress-tensor components
$\vec{u}, u_i, u_x, u_y, u_z$	displacement
U_I^m	discrete approximation of displacement
UX, UY	discrete grid values of the displacement-vector components
$\tilde{v}$	grid phase velocity
$\tilde{v}_G$	grid group velocity
$\tilde{v}_U$	grid phase velocity of the unstable wave
$\vec{v}, v_i, v_x, v_y, v_z$	particle velocity

V_I^m	discrete approximation of the particle velocity
VX, VY, VZ	discrete grid values of the particle velocity
V_P, V_S	P-wave speed, S-wave speed
$Y_l, Y_l^\kappa, Y_l^\mu, Y_l^\alpha, Y_l^\beta, Y_l^\lambda$	anelastic coefficients
(x_I, y_K, z_L)	spatial grid-point coordinates

1

Introduction

A tectonic earthquake is a unique, interesting and challenging natural phenomenon. At the same time the earthquake can cause death and huge material losses. The Emilia-Romagna, Italy (moment magnitude $M_w = 5.9$, May 20, 2012), Tohoku-Oki, Japan ($M_w = 9.0$, March 3, 2011), Christchurch, New Zealand ($M_w = 6.3$, February 22, 2011), Chile ($M_w = 8.8$, February 27, 2010), Port-au-Prince, Haiti ($M_w = 7.0$, January 12, 2010), L'Aquila, Italy ($M_w = 6.3$, April 6, 2009), Sichuan, China ($M_w = 7.9$, May 12, 2008), Pisco, Peru ($M_w = 8.0$, August 15, 2007), Kashmir, Pakistan ($M_w = 7.6$, October 8, 2005), Sumatra, Indonesia ($M_w = 9.1$, December 26, 2004), Bam, Iran ($M_w = 6.6$, December 26, 2003), Gujarat, India ($M_w = 7.7$, January 26, 2001), Izmit, Turkey ($M_w = 7.6$, August 17, 1999), Kobe, Japan ($M_w = 6.8$, January 17, 1995), and Northridge, California ($M_w = 6.7$, January 17, 1994) earthquakes are well-known examples of tragic and catastrophic events of the past two decades. Three of them belong to the largest earthquakes ever recorded. Some of them, however, indicate a troubling and important fact: an earthquake that kills and causes large material damage is not necessarily a big event in terms of released energy. The M_w 6.7 Northridge 1994 and M_w 6.8 Kobe 1995 earthquakes caused, at the time, unprecedented record economic losses in the USA and Japan, respectively, although they released (in the form of seismic waves) roughly 3000 times less energy than the M_w 9.0 Tohoku-Oki 2011 earthquake. In the long-term average, there are approximately 13 earthquakes in the magnitude range [7, 7.9] and 120 in the magnitude range [6, 6.9] per year. Any earthquake of this size can become a tragic and damaging event if it hits a densely populated area.

Apparently surprisingly, a significant part of the world's population lives in earthquake-prone areas: large populated areas are close to active seismogenic faults, and, moreover, large cities are often located at the surface of sediment-filled basins and valleys. The reasons why large human settlements developed in such areas relate to the geology, hydrology, climate and geography of the areas and regions. Both aspects of the locations of large cities, that is, being close to seismogenic faults and atop sediments, have strong impacts on the earthquake hazard and consequently also earthquake risk. Being close to a seismogenic fault obviously poses an earthquake threat. Also being atop a sediment-filled basin or valley can considerably increase the earthquake hazard. This is because seismic wave interference and resonant phenomena in sediment-filled basins and valleys can produce anomalously large

earthquake motion at the Earth's surface and lead to so-called 'site effects': characteristics of the earthquake vibratory motion of the Earth's surface can attain locally anomalous values – e.g., amplitudes can be considerably amplified in the time or frequency domain, and strong motion can be significantly prolonged. The anomalous values can occur at frequencies at which buildings, constructions and industrial facilities can be damaged or destroyed. The greatest damage to buildings and constructions is often due to mutual resonance between the local geological and artificial structures. The September 19, 1985 Mexico quake is one of the best examples of the damaging potential of such effects. The epicentre was on the Pacific coast; however, the earthquake caused major damage in Ciudad de México – more than 350 km away from the epicentre. A major part of the Mexican capital sits on unconsolidated lake sediments and artificial land or, in other words, atop a very soft sedimentary basin. The interference and resonant phenomena in sediments led to disastrous effects. Hundreds of buildings were completely destroyed, hundreds partially collapsed or were seriously damaged. At least 10 000 people died.

In the worldwide long-term average, the number of earthquakes will not decrease. On the other hand, the density of population will increase in many areas. In industrialized nations the technological complexity of the populated areas will increase. This could bring more vulnerability to earthquakes if building codes are not either at the state-of-the-art level or actually enforced. In developing countries the increasing population means great and growing earthquake risk. Even relatively weak earthquakes will be capable of causing tremendous human losses and damage, and consequently significantly affect the economy of the region or the entire country.

Two natural scientific tasks for seismologists are, therefore, earthquake prediction and prediction of ground motion during future earthquakes at a site of interest. These tasks are also primary scientific responsibilities of seismologists towards society.

Seismologists still cannot predict the time, place and size of future earthquakes. Even more interestingly, we still do not know whether such prediction is possible in principle and will be possible technically. This is because we still do not have answers to important questions regarding the processes of the long-term preparation and nucleation of earthquakes. We still do not know enough about seismogenic faults and the Earth's interior at depths where earthquakes are being prepared. This is mainly because we cannot simply install sensors and instruments at those depths and places. In other words, a classical direct controlled physical experiment aiming to measure these processes is impossible – at least from an economic viewpoint at present. Direct measurements are practically restricted to the Earth's surface, and almost all information about the rupture process and structure of the Earth's interior is encoded in instrument records of earth motion (seismograms) during earthquakes. Consequently, our knowledge of the earthquake source and the Earth's interior has to be confronted with the seismograms.

Hereby, we come to the role of theoretical and numerical-modelling methods. They are irreplaceable tools in earthquake research – in investigating preparation and nucleation of earthquakes, the rupture process on the fault, radiation of seismic waves, seismic wave propagation in the Earth's interior, and earthquake motion of the Earth's surface.

No matter whether seismologists can or cannot timely predict earthquake occurrence, they must predict earthquake ground motion during potential future earthquakes in densely populated areas and sites of special importance, e.g., sites of nuclear power plants, big dams and key industrial facilities. Even if the timely prediction of earthquake occurrence were physically possible and technically feasible, seismologists must predict what can or will happen during a future earthquake. This is vital for land-use planning, designing new buildings and reinforcing existing ones. It is also extremely important for undertaking actions that could help mitigate losses during future earthquakes.

Prediction of the earthquake ground motion for a given area or site might be based on an empirical approach if sufficient earthquake recordings at the site or physically relevant for the site were available. In most cases, however, there is a severe lack of data. Consequently, it is the theory and numerical simulations that have to be applied.

Although we still need to better understand processes in the Earth and considerably better know the Earth's interior and seismogenic faults, the present state of our knowledge and the capabilities of modern seismic arrays impose stringent requirements on the theoretical and computational models. For example, considering computational models of surface local geological structures, it is necessary to include nonplanar interfaces between layers – possibly with large contrasts in values of material parameters, gradients in P-wave and S-wave speeds, density and quality factors inside layers, P-wave to S-wave speed ratio possibly as large as 5 and more in the soft surface sediments, and often also free-surface topography. In particular, the rheology of the medium has to allow for realistic broad-band attenuation. Realistic strong ground motion simulations should also account for the possibility of nonlinear behaviour in soft soils.

There are no exact (analytical) solutions for such realistic models. Only approximate computational methods are able to account for the geometrical and rheological complexity of the sufficiently realistic models. The most important aspects of all methods are accuracy and computational efficiency (in terms of computer memory and time). These two aspects are in most cases contradictory. It is, however, the reasonable balance between the accuracy and computational efficiency in the case of complex realistic structures that makes the numerical-modelling methods and, more specifically, so-called domain (in the spatial sense) numerical methods dominant among all approximate methods.

A variety of domain numerical methods have been developed in application to earthquake motion during the past few decades. The best known are the (time-domain) finite-difference, finite-element, Fourier pseudo-spectral, spectral-element and discontinuous Galerkin methods. Both theoretical analyses and numerical experience show that none of these methods can be chosen as the universally best (in terms of accuracy and computational efficiency) method for all important problems in earthquake research, that is, for all medium-wavefield configurations. Each method has its advantages and disadvantages, which often depend on the particular application.

Moreover, recent experience from two international comparative numerical exercises for the Grenoble valley, France, and the Mygdonian basin near Thessaloniki, Greece (ESG 2006 and E2VP, respectively), show that at least two different but comparably accurate

methods should be used in order to obtain a reliable numerical prediction of earthquake ground motion for a site of interest.

Two decades of 3D earthquake motion modelling, mainly in California, the SCEC comparative exercises, ESG 2006 and E2VP confirmed that, despite development of alternative and new methods, the FD time-domain method has an important and, without hesitation and exaggeration, irreplaceable position and role among recent time-domain numerical-modelling methods in earthquake research.

It is important to say that the term 'finite-difference method'(FDM) in the numerical modelling of earthquake motion may represent one out of a large number of various FD schemes and codes. The schemes may considerably differ from each other in several methodological aspects. Consequently, the schemes and the numerical results obtained by different schemes may differ considerably in accuracy and computational efficiency.

The most advanced FD schemes can be more than competitive, for many important configurations, with other modern methods: at the same level of accuracy they can be computationally more efficient. For some configurations, other methods can be more appropriate.

More than four decades of development of the FDM in application to seismic wave propagation and earthquake motion, and the present state of FD theory suggest that there is room for further improvements, and that the future will bring even more accurate, efficient and competitive schemes for geometrically and rheologically complex realistic problem configurations.

In this book we focus on the FDM as applied to modelling earthquake motion and earthquake ground motion prediction. Obviously, the included material also reflects our contributions to the methodology of FD modelling. Due to the chosen focus and limited extent, we do not cover all aspects of FD modelling. At the same time, we believe that the book brings material that will be found useful by those who are not familiar with the method (students, professionals, researchers) and also those who develop and apply numerical modelling in their earthquake research or investigations of elastic wave propagation in complex media (e.g., oil exploration, shallow geophysics, machine-induced vibrations).

Part I

Mathematical-physical model

2

Basic mathematical-physical model

In this chapter we briefly present the basics of the mathematical-physical model necessary for the explanations and elaborations in the following chapters. For more detailed expositions of the theory of earthquakes, seismic wave propagation and earthquake ground motion we refer to some of the recent monographs and fundamental textbooks. For a general introduction to seismology – Aki and Richards (2002), Pujol (2003), Shearer (2009), Stein and Wysession (2003), Lay and Wallace (1995), Kennett (2001), Beroza and Kanamori (2009), Dziewonski and Romanowicz (2009); for earthquake sources – Kostrov and Das (2005), Scholz (2002), Ohnaka (2013); for theory of seismic wave propagation – Ben-Menahem and Singh (2000) and Carcione (2007); for global seismic wave propagation – Dahlen and Tromp (1998); for full waveform modelling and inversion – Fichtner (2011); for geotechnical earthquake engineering – Kramer (1996); and for waves and vibrations in soils caused by earthquakes, traffic, shocks and construction works – Semblat and Pecker (2009).

2.1 Medium

In order to reasonably numerically simulate seismic wave propagation and earthquake motion in the Earth we need an adequate model of the medium inside a target domain (volume) of the Earth. We should clearly distinguish geological models, physical models and discrete (or grid) models.

In general, a physical model of a medium is described by 3D distributions of all material parameters that determine seismic wave propagation and earthquake motion. Being focused on seismic and earthquake motion in near-surface local structures, in most cases the real material can be modelled as a heterogeneous linear viscoelastic isotropic continuum. Models of the medium may comprise both spatially smooth and discontinuous variations of material parameters. The model has to properly account for attenuation due to anelasticity of the Earth's real material. A perfectly elastic medium or oversimplified description of attenuation is not sufficient. A reasonable rheological viscoelastic model is necessary in order to account for the realistic dependence of attenuation on frequency and its spatial variations.

So far, the least addressed aspect in numerical modelling of earthquake motion in near-surface local structures is the (an)isotropy of the real material. We know, in general, that there are true isotropic materials and true anisotropic materials. The question is, what can be seen in seismic records? For example, anisotropy of the Earth's upper mantle is clearly observed in seismic records, and numerical modelling of seismic waves at the regional and global scales has to assume inherent physical anisotropy. We are not in such a situation in numerical modelling of earthquake motion in near-surface local structures.

Although the real medium and its physical model may consist of truly isotropic materials, the mathematical-physical and grid representations of wave propagation in such a medium may be anisotropic. We may speak, for instance, of an equivalent anisotropic medium in the case of a low-frequency approximation (wavelengths much larger than the characteristic size of heterogeneity) for wave propagation in heterogeneous isotropic media (Backus 1962, Helbig 1984).

The usual physical model of the medium is specified by 3D spatial distributions of the P-wave and S-wave speeds (V_P or α, and V_S or β, respectively) at some frequency, density (ρ), and P-wave and S-wave quality factors as functions of frequency ($Q_P(\omega)$ and $Q_S(\omega)$, respectively).

Soft sediments near the free surface may behave in a nonlinear fashion. The stress–strain relation is not linear but nonlinear hysteretic. In the simplest (but still tremendously demanding) case the medium has to be represented by a rheological elastoplastic model. This poses a major complication for 3D modelling of earthquake motion. At present, reasonable 3D numerical modelling with possibly nonlinear behaviour of part of the whole model is still a challenge for numerical modellers.

Plastic deformation in the close vicinity of a rupturing fault is another example of nonlinear behaviour that is not trivial to model numerically.

2.2 Governing equation: equation of motion

Consider a material volume V of continuum with surface S. Material parameters are continuous functions of spatial coordinates inside V. Consider an arbitrary volume Ω with surface S^Ω inside volume V. Let $\vec{n}^\Omega$ be a normal vector to surface S^Ω pointing from the interior of volume Ω outward. Let $\vec{f}(x_k, t)$ be the density of the body force acting in volume Ω and $\vec{T}^\Omega(x_k, t)$ the traction acting at surface S^Ω. Here $x_k; k \in \{1, 2, 3\}$ are Cartesian coordinates and t is time. The configuration is shown in Fig. 2.1. Let $\vec{u}\,(u_1, u_2, u_3)$ or, in an alternative notation, $\vec{u}\,(u_x, u_y, u_z)$, be the displacement vector. Let ε_{ij} be the strain tensor,

$$\varepsilon_{ij} = \frac{1}{2}\left(\frac{\partial u_i}{\partial x_j} + \frac{\partial u_j}{\partial x_i}\right); \quad i, j \in \{1, 2, 3\} \tag{2.1}$$

and σ_{ij} the stress tensor. We briefly introduce the basic forms of the equations of motion for the considered configuration.
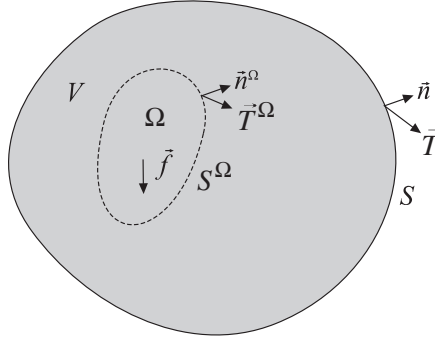
Figure 2.1 Material volume V of a smooth continuum bounded by surface S. External traction $\vec{T}$ acts at surface S, body force $\vec{f}$ acts in volume V. Volume Ω with surface S^Ω is a testing volume considered in the derivation of the equation of motion.

In the following formulations, the traction vector appears explicitly, which means the possible imposition of the Neumann boundary condition on a surface. The possible application of the Dirichlet boundary condition (prescribed displacement) does not explicitly appear in the formulations.

2.2.1 Strong form

An application of Newton's second law to volume Ω gives

$$\frac{d}{dt} \int_\Omega \rho \frac{\partial u_i}{\partial t} dV = \int_{S^\Omega} T_i^\Omega dS + \int_\Omega f_i dV \tag{2.2}$$

Throughout the text dV and dS will be used for volume and surface elements, respectively. Because Ω and S^Ω move with particles, the particle mass ρdV does not change with time. The equation can be written as

$$\int_\Omega \rho \frac{\partial^2 u_i}{\partial t^2} dV = \int_{S^\Omega} T_i^\Omega dS + \int_\Omega f_i dV \tag{2.3}$$

At surface S^Ω, traction T_i^Ω is related to the stress tensor σ_{ij}:

$$T_i^\Omega = \sigma_{ij} n_j^\Omega \tag{2.4}$$

In Eq. (2.4) and hereafter we assume the Einstein summation convention for repeated indices. Assuming continuity of the stress tensor throughout volume Ω, Gauss's divergence theorem can be applied to the surface integral:

$$\int_{S^\Omega} T_i^\Omega dS = \int_{S^\Omega} \sigma_{ij} n_j^\Omega dS = \int_\Omega \frac{\partial \sigma_{ij}}{\partial x_j} dV \tag{2.5}$$

Equation (2.3) can be then written as

$$\int_{\Omega} \left(\rho \frac{\partial^2 u_i}{\partial t^2} - \frac{\partial \sigma_{ij}}{\partial x_j} - f_i \right) dV = 0 \tag{2.6}$$

Equation (2.6) is valid for any volume Ω inside V. Assume that the integrand is greater than 0 at some point inside V. Because the integrand is continuous throughout V, it is possible to find such a volume Ω (containing that point) for which the integrand is greater than 0. This, however, would be in contradiction with Eq. (2.6). Consequently,

$$\rho \frac{\partial^2 u_i}{\partial t^2} - \frac{\partial \sigma_{ij}}{\partial x_j} - f_i = 0 \tag{2.7}$$

everywhere in V. Equation (2.7) together with the boundary condition at surface S,

$$T_i = \sigma_{ij} n_j \tag{2.8}$$

represent a strong formulation for the considered problem. The formulation requires continuity of displacement and its first spatial and temporal derivatives.

2.2.2 Weak form

Alternatively to the application of Newton's second law to the material volume V we can apply the principle of virtual work. Consider a fixed state of continuum at some time and its virtual (arbitrary, infinitesimal) deformation. Let δu_i be the corresponding virtual displacement. Then the virtual deformation is characterized by the virtual strain tensor $\delta \varepsilon_{ij}$:

$$\delta \varepsilon_{ij} = \frac{1}{2} \left(\frac{\partial}{\partial x_j} \delta u_i + \frac{\partial}{\partial x_i} \delta u_j \right) \tag{2.9}$$

Because the virtual displacements are assumed in a fixed state of continuum, they do not affect displacements and accelerations of continuum particles in this state. The principle states that during virtual deformation the work done by external forces has to be equal to the sum of the increment of energy of deformation and the work of inertial forces:

$$\int_S T_i \delta u_i dS + \int_V f_i \delta u_i dV = \int_V \sigma_{ij} \delta \varepsilon_{ij} dV + \int_V \rho \frac{\partial^2 u_i}{\partial t^2} \delta u_i dV \tag{2.10}$$

Functions δu_i are arbitrary; they are equivalent to weight functions. Therefore, we replace δu_i by w_i in Eqs. (2.9) and (2.10). Then, due to symmetry of the stress tensor,

$$\sigma_{ij} \delta \varepsilon_{ij} = \frac{1}{2} \left(\sigma_{ij} \frac{\partial w_i}{\partial x_j} + \sigma_{ij} \frac{\partial w_j}{\partial x_i} \right) = \sigma_{ij} \frac{\partial w_i}{\partial x_j} \tag{2.11}$$

Equation (2.10) can be written as

$$\int_V \left(\rho \frac{\partial^2 u_i}{\partial t^2} - f_i \right) w_i dV + \int_V \sigma_{ij} \frac{\partial w_i}{\partial x_j} dV = \int_S T_i w_i dS \tag{2.12}$$

Equation (2.12) is called the weak form of the equation of motion. This is because the requirement of continuity of displacement and its first spatial derivatives in the strong form is replaced here by a weaker requirement of continuity of displacement and the weight functions.

2.2.3 Integral strong form

Integration by parts of the last term on the left hand side (l.h.s.) of Eq. (2.12) yields

$$\int_V \left(\rho \frac{\partial^2 u_i}{\partial t^2} - f_i \right) w_i \, dV + \int_V \frac{\partial}{\partial x_j} \left(\sigma_{ij} w_i \right) dV - \int_V \frac{\partial \sigma_{ij}}{\partial x_j} w_i \, dV = \int_S T_i w_i \, dS \quad (2.13)$$

and, using Gauss's divergence theorem,

$$\int_V \left(\rho \frac{\partial^2 u_i}{\partial t^2} - f_i \right) w_i \, dV + \int_S \sigma_{ij} n_j w_i \, dS - \int_V \frac{\partial \sigma_{ij}}{\partial x_j} w_i \, dV = \int_S T_i w_i \, dS \quad (2.14)$$

Assembling the volume and surface integrals together gives

$$\int_V \left(\rho \frac{\partial^2 u_i}{\partial t^2} - \frac{\partial \sigma_{ij}}{\partial x_j} - f_i \right) w_i \, dV = \int_S \left(T_i - \sigma_{ij} n_j \right) w_i \, dS \quad (2.15)$$

In Eq. (2.15) we can specify the boundary condition for traction at surface S by specifying values of T_i. We can call Eq. (2.15) the integral strong form of the equation of motion (we adopted this term based on our personal communication with Robert J. Geller). While being integral, the form requires continuity of the first derivative of displacement. These two features clearly distinguish it from the (differential) strong form and the integral weak form.

2.2.4 Concluding remark

In principle, any of the three forms can be the basis for discretization aiming in an FD scheme. Most of the developed FD schemes are based on the differential strong form – likely due to its apparent relative simplicity. Depending on the problem configuration, one of the two other forms may be found more suitable. The weak form is the basis for the traditional FEM, the more recent spectral-element method and the discontinuous Galerkin method. These methods will be briefly characterized in Chapter 5.

2.3 Constitutive law: stress–strain relation

In order to solve the equation of motion we need a constitutive law that specifies the relation between the stress and strain tensors, and consequently also the relation between the stress tensor and displacement vector. We will consider three types of continuum – linear elastic, linear viscoelastic and nonlinear elastoplastic. The linear elastic continuum is the simplest type of continuum. It is useful for a simple introduction of many important concepts and approaches but is incapable of accounting for attenuation of seismic waves

and motion. Realistic attenuation can be reasonably accounted for by the viscoelastic medium. Eventually we also describe the simplest elastoplastic continuum in order to account for the hysteretic stress–strain relation in surface soft sediments. Rheological models of a continuum will be addressed in detail in Chapter 3. Here we concisely present the fundamental relations for the elastic and viscoelastic continua.

2.3.1 Elastic continuum

Cauchy's generalization of the original Hooke's law in tensor form reads

$$\sigma_{ij} = c_{ijkl}\varepsilon_{kl} \tag{2.16}$$

where c_{ijkl} is a tensor of elastic constants (they are constant with respect to the strain-tensor components, not necessarily with respect to spatial position). Equation (2.16) assumes that each stress-tensor component is a linear combination of all components of the strain tensor. Symmetry of the stress tensor and application of the first law of thermodynamics imply symmetries

$$c_{ijkl} = c_{jikl}, \quad c_{ijkl} = c_{klji} \tag{2.17}$$

respectively. They yield additional symmetry

$$c_{ijkl} = c_{jilk} \tag{2.18}$$

Symmetries (2.17) and (2.18) reduce from 81 down to 21 the number of independent elastic constants that describe the most general anisotropic medium. The situation dramatically simplifies in the case of an isotropic medium. The stress–strain relation of an isotropic elastic medium is described by two independent elastic constants. The stress–strain relation can be written in the form

$$\sigma_{ij} = \kappa\varepsilon_{kk}\delta_{ij} + 2\mu\left(\varepsilon_{ij} - \tfrac{1}{3}\varepsilon_{kk}\delta_{ij}\right) \tag{2.19}$$

where κ and μ are bulk and shear moduli, respectively, and

$$\delta_{ij} = 1; \quad i = j \qquad \delta_{ij} = 0; \quad i \neq j \tag{2.20}$$

defines the Kronecker delta. Equation (2.19) corresponds to decomposition of the stress tensor into dilatational and deviatoric components. Alternatively, using

$$\kappa = \lambda + \tfrac{2}{3}\mu \tag{2.21}$$

the stress–strain relation can be written using Lamé constants λ and μ in the form

$$\sigma_{ij} = \lambda\varepsilon_{kk}\delta_{ij} + 2\mu\varepsilon_{ij} \tag{2.22}$$

or as

$$\sigma_{ij} = \lambda\frac{\partial u_k}{\partial x_k}\delta_{ij} + \mu\left(\frac{\partial u_i}{\partial x_j} + \frac{\partial u_j}{\partial x_i}\right) \tag{2.23}$$

2.3.2 Viscoelastic continuum

The stress–strain relation in a viscoelastic medium can be defined as

$$\sigma_{ij}(t) = \int_{-\infty}^{t} \psi_{ijkl}(t-\tau) \frac{\partial \varepsilon_{kl}(\tau)}{\partial \tau} d\tau \tag{2.24}$$

where ψ_{ijkl} is a tensor of relaxation functions describing the behaviour of the material. An alternative form of the stress–strain relation is

$$\varepsilon_{ij}(t) = \int_{-\infty}^{t} \chi_{ijkl}(t-\tau) \frac{\partial \sigma_{kl}(\tau)}{\partial \tau} d\tau \tag{2.25}$$

where χ_{ijkl} is a tensor of creep functions.

For an isotropic medium the stress–strain relation can be written as

$$\begin{aligned}
\sigma_{ij}(t) = \delta_{kl} \int_{-\infty}^{t} \psi_{ijkl}^{\kappa}(t-\tau) \frac{\partial \varepsilon_{kk}(\tau)}{\partial \tau} d\tau \\
+ 2 \int_{-\infty}^{t} \psi_{ijkl}^{\mu}(t-\tau) \left[\frac{\partial \varepsilon_{kl}(\tau)}{\partial \tau} - \frac{1}{3} \frac{\partial \varepsilon_{kk}(\tau)}{\partial \tau} \delta_{kl} \right] d\tau
\end{aligned} \tag{2.26}$$

where ψ_{ijkl}^{κ} and ψ_{ijkl}^{μ} are relaxation functions for the bulk and shear moduli, respectively. Alternatively, using the time-dependent moduli, the stress–strain relation is

$$\begin{aligned}
\sigma_{ij}(t) = \delta_{ij} \int_{-\infty}^{t} \kappa(t-\tau) \varepsilon_{kk}(\tau) d\tau \\
+ 2 \int_{-\infty}^{t} \mu(t-\tau) \left[\varepsilon_{ij}(\tau) - \frac{1}{3} \varepsilon_{kk}(\tau) \delta_{ij} \right] d\tau
\end{aligned} \tag{2.27}$$

Analogously to the case of the elastic continuum, the latter relations can be expressed also for Lamé constants λ and μ.

It is obvious from Eqs (2.24), (2.26) and (2.27) that the stress–strain relations in a viscoelastic medium mean a considerable complication compared to an elastic medium: stress at each spatial position and each time is determined not only by the strain at the same time but by the entire history of the strain or strain rate at that spatial position. The approach to avoiding this substantial computational difficulty as well as rheological models of the viscoelastic continuum capable of accounting for realistic attenuation will be explained in detail in Chapter 3.

2.4 Strong-form formulations of equations

Having found the equation of motion and constitutive law, we can now mention alternative formulations in terms of which a field quantity is considered as an unknown function. Here we restrict discussion to the strong formulation for an elastic and isotropic medium. We can easily obtain four alternative formulations. Each of them can be the basis for a specific FD scheme.

Formally, it is easy to write down also formulations for a viscoelastic continuum – the stress–strain relations for an elastic continuum would simply be replaced by those for a viscoelastic one. We will address this later in detail.

2.4.1 Displacement–stress formulation

In the displacement–stress formulation both displacement vector and stress tensor are treated explicitly as unknown variables:

$$\rho \frac{\partial^2 u_i}{\partial t^2} = \frac{\partial \sigma_{ij}}{\partial x_j} + f_i$$

$$\sigma_{ij} = \kappa \varepsilon_{kk} \delta_{ij} + 2\mu \left(\varepsilon_{ij} - \tfrac{1}{3} \varepsilon_{kk} \delta_{ij} \right)$$

(2.28)

2.4.2 Displacement formulation

Substitution of Hooke's law for the stress tensor in the equation of motion yields

$$\rho \frac{\partial^2 u_i}{\partial t^2} = \frac{\partial}{\partial x_i} \left[\left(\kappa - \tfrac{2}{3}\mu \right) \frac{\partial u_k}{\partial x_k} \right] + \frac{\partial}{\partial x_j} \left(\mu \frac{\partial u_i}{\partial x_j} \right) + \frac{\partial}{\partial x_j} \left(\mu \frac{\partial u_j}{\partial x_i} \right) + f_i \quad (2.29)$$

The displacement vector is the only unknown variable.

2.4.3 Displacement–velocity–stress formulation

Considering particle velocity v_i we can treat explicitly displacement, particle velocity and stress as unknown variables:

$$\rho \frac{\partial v_i}{\partial t} = \frac{\partial \sigma_{ij}}{\partial x_j} + f_i, \quad v_i = \frac{\partial u_i}{\partial t}$$

$$\sigma_{ij} = \kappa \varepsilon_{kk} \delta_{ij} + 2\mu \left(\varepsilon_{ij} - \tfrac{1}{3} \varepsilon_{kk} \delta_{ij} \right)$$

(2.30)

2.4.4 Velocity–stress formulation

The equation of motion and the stress–strain relation differentiated with respect to time in which the particle-velocity vector appears instead of the displacement vector give the velocity–stress formulation:

$$\rho \frac{\partial v_i}{\partial t} = \frac{\partial \sigma_{ij}}{\partial x_j} + f_i$$

$$\frac{\partial \sigma_{ij}}{\partial t} = \kappa \frac{\partial \varepsilon_{kk}}{\partial t} \delta_{ij} + 2\mu \left(\frac{\partial \varepsilon_{ij}}{\partial t} - \frac{1}{3} \frac{\partial \varepsilon_{kk}}{\partial t} \delta_{ij} \right)$$

(2.31)

where

$$\frac{\partial \varepsilon_{ij}}{\partial t} = \frac{1}{2}\left(\frac{\partial v_i}{\partial x_j} + \frac{\partial v_j}{\partial x_i}\right) \tag{2.32}$$

This formulation is the one most used as a basis for FD schemes.

It may be advantageous to write the hyperbolic system of nine equations (2.31) in a concise matrix form:

$$\frac{\partial \tilde{Q}_p}{\partial t} + A_{pq}\frac{\partial \tilde{Q}_q}{\partial x} + B_{pq}\frac{\partial \tilde{Q}_q}{\partial y} + C_{pq}\frac{\partial \tilde{Q}_q}{\partial z} = 0; \quad p, q \in \{1, \ldots, 9\} \tag{2.33}$$

$$\tilde{Q} = \left(\sigma_{xx}, \sigma_{yy}, \sigma_{zz}, \sigma_{xy}, \sigma_{yz}, \sigma_{xz}, v_x, v_y, v_z\right)^T \tag{2.34}$$

$$A = \begin{pmatrix} 0 & 0 & 0 & 0 & 0 & 0 & -(\lambda+2\mu) & 0 & 0 \\ 0 & 0 & 0 & 0 & 0 & 0 & -\lambda & 0 & 0 \\ 0 & 0 & 0 & 0 & 0 & 0 & -\lambda & 0 & 0 \\ 0 & 0 & 0 & 0 & 0 & 0 & 0 & -\mu & 0 \\ 0 & 0 & 0 & 0 & 0 & 0 & 0 & 0 & 0 \\ 0 & 0 & 0 & 0 & 0 & 0 & 0 & 0 & -\mu \\ -b & 0 & 0 & 0 & 0 & 0 & 0 & 0 & 0 \\ 0 & 0 & 0 & -b & 0 & 0 & 0 & 0 & 0 \\ 0 & 0 & 0 & 0 & 0 & -b & 0 & 0 & 0 \end{pmatrix} \tag{2.35}$$

$$B = \begin{pmatrix} 0 & 0 & 0 & 0 & 0 & 0 & 0 & -\lambda & 0 \\ 0 & 0 & 0 & 0 & 0 & 0 & 0 & -(\lambda+2\mu) & 0 \\ 0 & 0 & 0 & 0 & 0 & 0 & 0 & -\lambda & 0 \\ 0 & 0 & 0 & 0 & 0 & 0 & -\mu & 0 & 0 \\ 0 & 0 & 0 & 0 & 0 & 0 & 0 & 0 & -\mu \\ 0 & 0 & 0 & 0 & 0 & 0 & 0 & 0 & 0 \\ 0 & 0 & 0 & -b & 0 & 0 & 0 & 0 & 0 \\ 0 & -b & 0 & 0 & 0 & 0 & 0 & 0 & 0 \\ 0 & 0 & 0 & 0 & -b & 0 & 0 & 0 & 0 \end{pmatrix} \tag{2.36}$$

$$C = \begin{pmatrix} 0 & 0 & 0 & 0 & 0 & 0 & 0 & 0 & -\lambda \\ 0 & 0 & 0 & 0 & 0 & 0 & 0 & 0 & -\lambda \\ 0 & 0 & 0 & 0 & 0 & 0 & 0 & 0 & -(\lambda+2\mu) \\ 0 & 0 & 0 & 0 & 0 & 0 & 0 & 0 & 0 \\ 0 & 0 & 0 & 0 & 0 & 0 & 0 & -\mu & 0 \\ 0 & 0 & 0 & 0 & 0 & 0 & -\mu & 0 & 0 \\ 0 & 0 & 0 & 0 & 0 & -b & 0 & 0 & 0 \\ 0 & 0 & 0 & 0 & -b & 0 & 0 & 0 & 0 \\ 0 & 0 & -b & 0 & 0 & 0 & 0 & 0 & 0 \end{pmatrix} \tag{2.37}$$

Here

$$b = 1/\rho \tag{2.38}$$

2.5 Boundary conditions

Away from a rupturing fault, the two most important boundary conditions relate to the Earth's free surface and internal material discontinuities (interfaces). The rupturing fault will be addressed in Subsection 4.1.1.

2.5.1 Free surface

In the numerical modelling of seismic wave propagation and earthquake motion in the Earth it is sufficient, in most applications, to replace air above the Earth's surface by vacuum. Consequently, the Earth's real surface, that is the real air/solid or air/water interface, can be considered a traction-free surface. The traction-free surface is usually more briefly called the free surface.

Consider surface S with normal vector $\vec{n}$. Let $\vec{T}(\vec{n})$ be the traction vector at surface S corresponding to the normal vector $\vec{n}$. Then the traction-free condition at surface S is

$$\vec{T}(\vec{n}) = 0 \tag{2.39}$$

or, equivalently,

$$\sigma_{ij} n_j = 0 \tag{2.40}$$

If surface S is planar and perpendicular to the z-axis, the normal vector is $\vec{n} = (0, 0, -1)$ and the traction-free condition implies

$$\sigma_{iz} = 0; \quad i \in \{x, y, z\} \tag{2.41}$$

2.5.2 Welded material interface

The boundary conditions on the welded material interface are continuity of displacement and continuity of traction. Let Σ be a smooth material interface with a unit normal vector $\vec{n}$ pointing, say, from Σ^- to Σ^+. Then,

$$u_i|_{\Sigma^+} = u_i|_{\Sigma^-} \tag{2.42}$$

and

$$\sigma_{ij} n_j \big|_{\Sigma^+} = \sigma_{ij} n_j \big|_{\Sigma^-} \tag{2.43}$$

express continuity of displacement and traction at Σ, respectively. These conditions have to be incorporated in the mathematical-physical model if the medium includes a material discontinuity that can be considered a welded interface.

For strong, weak, integral strong and discontinuous strong formulations for a canonical problem with a smooth material interface see Moczo *et al.* (2007a).

2.6 Initial conditions

It is usually assumed that the medium at an initial time is at rest. In the case of the displacement–stress and displacement formulations, Eqs. (2.28) and (2.29), we therefore assume the same conditions: $u_i(t = 0, x_j) = 0$ and $\frac{\partial^2 u_i}{\partial t^2}(t = 0, x_j) = 0$. In the case of the displacement–velocity–stress formulation, Eq. (2.30), we assume $u_i(t = 0, x_j) = 0$ and $v_i(t = 0, x_j) = 0$, and, in the case of the velocity–stress formulation, Eq. (2.31), $v_i(t = 0, x_j) = 0$ and $\sigma_{ij}(t = 0, x_k) = 0$. In all cases $f_i(t = 0, x_j) = 0$.

The case of a dynamically rupturing fault is addressed in the next section.

2.7 Wavefield source (wavefield excitation)

Earthquake motion is due to spontaneous rupture on a fault. In general, seismic waves, seismic motion and seismic noise can be generated by numerous natural and artificial sources. Depending on the problem configuration and purpose of the numerical modelling we can consider a point source, a finite-size rupturing fault, or incidence of a plane wave.

A point double-couple or moment-tensor source localized in the computational domain can be adequate in the case of small local or near-regional earthquakes. Although a point displacement discontinuity (slip, dislocation) is assumed at the source, mathematically the source can be represented through the body-force term in the equation of motion for the continuous medium. The point source is described by its position, focal mechanism and source–time function for displacement or particle velocity.

A finite-size rupturing fault can be modelled kinematically or dynamically. In the kinematic model we assume a space–time distribution of point sources on the fault. Each point source is defined a priori and it does not change during the numerical simulation. Its time window, source–time function and focal mechanism are determined in order to mimic rupture propagation on the fault. It is obvious that in the kinematic model there is no causal interaction between the rupturing fault and generated seismic motion. The kinematic model is used for its relative mathematical-physical and implementation simplicity.

In a dynamic model, assuming an initial traction and material parameters of the fault, the nucleation, propagation and arrest of the rupture are controlled by the friction law. The friction law relates the total traction to slip or slip rate at the same point of the fault. The rupture causally interacts with the medium in seismic motion.

Incidence of a plane wave is sometime considered for specific purposes and investigations of transfer properties of local near-surface structures. In general it is possible to consider 'injecting' an analytical source solution in the computational domain.

3

Rheological models of a continuum

We consider mechanical models representing specific types of behaviour of real materials under applications of stress. Such models are also called rheological models. We use them in order to quantitatively describe two important phenomena: the intrinsic attenuation of seismic waves due to anelasticity of the Earth's real material, and the nonlinear hysteretic stress–strain relation in very soft surface sediments in the case of large stress and strain during so-called strong ground motion.

Attenuation in the Earth Observations, e.g., McDonal *et al.* (1958), Liu *et al.* (1976), Spencer (1981), Murphy (1982), have shown that the internal friction (a measure of attenuation) in the Earth is nearly constant over the seismic frequency range (from seismic body waves to the Earth's free oscillations, that is, for periods from approximately 0.01 s up to 1 hour). This is a consequence of the fact that the Earth's material is composed of different minerals and the attenuation in each of them is contributed to by several processes. Liu *et al.* (1976) showed that a distribution of relaxation mechanisms (standard linear solids or Zener bodies) can yield a reasonable approximation of the quality factor Q (Q^{-1} being the measure of internal friction) which satisfies seismic observations.

Conversion of the convolutory stress–strain relation into a differential form Whereas the stress–strain relation in a viscoelastic medium has a simple form in the frequency domain, stress being a product of the complex viscoelastic modulus $M(\omega)$ and strain $\varepsilon(\omega)$, $\sigma(\omega) = M(\omega)\varepsilon(\omega)$, it takes the form of the convolutory integral in the time domain. This means that for updating stress at each time and each spatial position it is necessary to know (and store) the entire history of strain and evaluate the convolutory integral. This would pose a major problem in the time-domain numerical methods. If, however, $M(\omega)$ is a rational function of frequency, the inverse Fourier transform of $M(\omega)\varepsilon(\omega)$ yields the nth-order differential equation for $\sigma(t)$, which can be numerically solved much more easily than the convolution integral. Day and Minster (1984) did not assume that, in general, the viscoelastic modulus is a rational function. Therefore, they approximated a general viscoelastic modulus by an nth-order rational function and determined its coefficients by the Padé approximant method. They obtained n ordinary differential equations for n additional internal variables, which replace the convolution integral. The sum of the internal variables

multiplied by the unrelaxed modulus gives an additional viscoelastic term to the elastic stress. The work of Day and Minster not only developed one particular approach but, in fact, indirectly suggested the future evolution – direct use of the rheological models whose $M(\omega)$ is a rational function.

Generalized Maxwell body and generalized Zener body Emmerich and Korn (1987) realized that an acceptable relaxation function corresponds to the rheology of what they defined as the generalized Maxwell body – n Maxwell bodies and one Hooke element (elastic spring) connected in parallel; see Fig. 3.7. (Note that the generalized Maxwell body in the literature on rheology is usually defined without the additional single spring. Therefore, we denote the model considered by Emmerich and Korn by GMB-EK.) Because the viscoelastic modulus of the GMB-EK has the form of a rational function, Emmerich and Korn (1987) obtained similar differential equations as Day and Minster (1984). In order to fit an arbitrary $Q(\omega)$ law they chose the relaxation frequencies logarithmically equidistant over a desired frequency range and used the least-square method to determine the weight factors of the relaxation mechanisms (classical Maxwell bodies). Independently, Carcione *et al*. (1988a, b), in accordance with the approach by Liu *et al*. (1976), assumed the generalized Zener body (GZB) – n Zener bodies, connected in parallel; see Fig. 3.7. Carcione *et al*. developed a theory for the GZB and introduced the term 'memory variables' for the additional variables obtained.

After the important articles by Emmerich and Korn (1987) and Carcione *et al*. (1988a, b) different authors decided either for the GMB-EK or for the GZB. The GMB-EK formulas were used by Emmerich (1992), Fäh (1992), Moczo and Bard (1993), and in many other studies. Moczo *et al*. (1997) implemented the approach also in the finite-element method (FEM) and hybrid finite-difference–finite-element (FD–FE) method. In the mentioned articles, one memory variable was defined for one displacement component. (Later Xu and McMechan (1995) introduced the term 'composite memory variables'. The composite memory variables, however, did not differ from the variables used from the very beginning in the above articles.) Robertsson *et al*. (1994) implemented the memory variables based on the GZB rheology into the staggered-grid velocity–stress FD scheme. Blanch *et al*. (1995) suggested an approximate single-parameter method, the τ-method, to approximate the constant $Q(\omega)$ law. Blanch and Robertsson (1997) implemented the GZB rheology in their scheme based on a modified Lax–Wendroff correction. Xu and McMechan (1998) used simulated annealing for determining the best combination of relaxation mechanisms to approximate the desired $Q(\omega)$ law. (There was a missing factor in the relaxation functions in the two latter articles; see Subsection 3.3.7.)

Relation between GMB-EK and GZB There appear to have been few or no comments by the authors using the GZB on the rheology of the GMB-EK and the corresponding algorithms, and vice versa. Thus, two parallel sets of publications and algorithms were developed over the years. Therefore, Moczo and Kristek (2005) analyzed both rheologies and showed that they are equivalent.

Coarse spatial distribution of memory variables The memory variables and material
coefficients describing attenuation in a medium considerably increase the number of quan-
tities that have to be stored. Zeng (1996) and independently Day (1998) realized that it is
not necessary to spatially sample the anelastic quantities as finely as the elastic quantities.
Therefore, they suggested a coarse spatial distribution of memory variables (in Day's ter-
minology – coarse graining of memory variables). Day's (1998) analysis of the problem is
remarkable. Day and Bradley (2001) extended the coarse-grain memory variable approach
proposed by Day (1998) to anelastic wave propagation in three dimensions. They imple-
mented the coarse-grain memory variables in the 4th-order velocity–stress staggered-grid
FD scheme. Graves and Day (2003) analyzed the stability and accuracy of the scheme with
coarse spatial sampling and defined the effective modulus and the quality factor necessary
to achieve sufficient accuracy. Liu and Archuleta (2006) developed an efficient and accurate
approach for determining parameters of the GMB-EK/GZB based on simulated annealing.
The approach is well applicable to the coarse-grain memory variables.

 The memory variables introduced by Day and Minster (1984), Emmerich and Korn
(1987), Carcione *et al.* (1988a,b) and Robertsson *et al.* (1994) and considered by Day
(1998), Day and Bradley (2001), Graves and Day (2003) and Liu and Archuleta (2006) are
material dependent. In the case of the coarse spatial distribution it is necessary to interpolate
the missing variables at a grid position. The missing variables are obtained by averaging
of memory variables in the neighbouring positions. Consequently, such spatial averaging
introduces an additional and artificial averaging of the material parameters. However, there
is no reason for such an additional averaging. The problem can be circumvented by using
the material-independent anelastic functions introduced by Kristek and Moczo (2003).
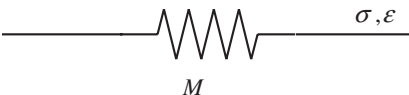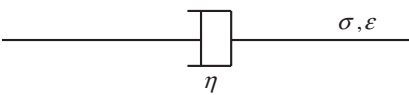
3.1 Basic rheological models

We first briefly describe three fundamental and extreme rheological models. Then we
describe and analyze such combinations of these models as allow for quantitative descrip-
tion of realistic attenuation and hysteresis. For simplicity of explanation we restrict the
discussion to 1D models. In this chapter we will not explicitly indicate that both material
parameters and functional variables (stress, strain, anelastic functions) are functions of a
spatial coordinate. We will explicitly distinguish just functional dependence on time or
frequency because this is the essential aspect of the exposition in this chapter.

3.1.1 Hooke elastic solid

The Hooke elastic solid (H) represented by an ideally elastic weightless spring is a mechan-
ical model for the behaviour of a perfectly elastic (lossless) solid material in which stress
is a linear function of strain. The only material parameter is a time-independent elastic
modulus M [Pa]. The stress–strain relations in the time and frequency domains are given
in Table 3.1. Recall that we indicate explicitly only functional dependence on time or
frequency although both material parameters and stress and strain are also functions of a
spatial coordinate. Stress at a given time depends only on the deformation at the same time

Table 3.1 *Stress–strain relations for Hooke solid and Newton liquid*

Model	Stress-strain relation	
	Time domain	Frequency domain
Hooke elastic solid (spring) σ,ε M	$\sigma(t) = M\,\varepsilon(t)$	$\sigma(\omega) = M\,\varepsilon(\omega)$
Newton viscous liquid (dashpot) σ,ε η	$\sigma(t) = \eta\dfrac{\partial}{\partial t}\varepsilon(t)$	$\sigma(\omega) = i\,\omega\eta\,\varepsilon(\omega)$
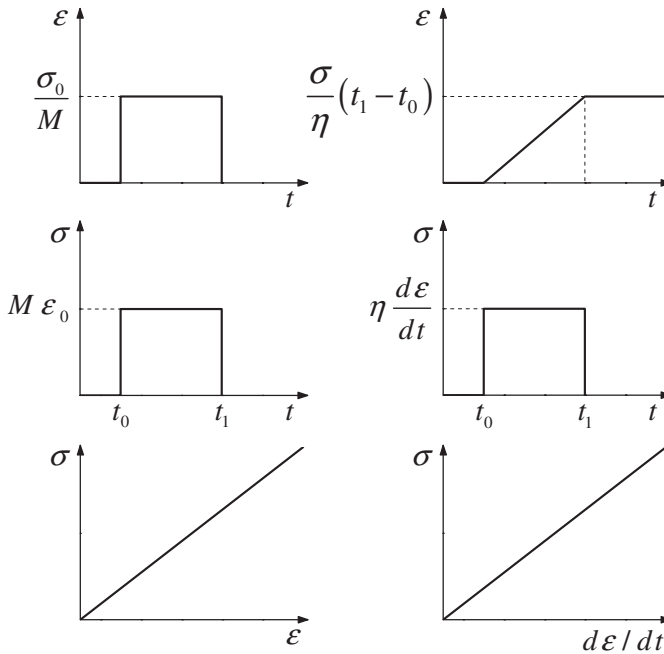
Figure 3.1 Upper and middle panels: Behaviour of a Hooke solid (left) and a Newton liquid (right) upon application of a step in stress at time t_0 and its removal at time t_1. Lower panel: Stress–strain and stress–strain rate diagrams.

(a Hooke solid does not have memory). Application of a stress yields an instantaneous strain. Removal of the stress yields instantaneous and total removal of the strain. In other words, a Hooke solid can completely recover because the elastic energy does not dissipate. The behaviour of a Hooke solid is illustrated in Fig. 3.1.
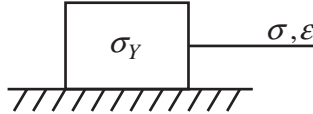
Figure 3.2 Saint-Venant body.

3.1.2 Newton viscous liquid

The Newton viscous liquid (N) is a mechanical model for the behaviour of a linearly viscous liquid in which stress is a linear function of the strain rate. It is represented by a dashpot consisting of a cylinder filled with a viscous liquid, and a piston with holes through which the liquid can flow. The only material parameter is a time-independent (Newtonian) viscosity η [Pa s]. The stress–strain relations are given in Table 3.1. Upon application of a step in stress, strain starts linearly to increase. The accumulated strain completely remains after removal of the stress (a Newton liquid has extreme memory). We can also say that the dashpot is not capable of recovering because all the elastic energy has dissipated. The behaviour of a Newton viscous liquid is illustrated in Fig. 3.1.

3.1.3 Saint-Venant plastic solid
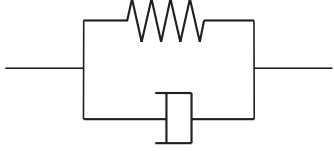
Whereas at small strain and stress below some critical value a real material exhibits, in general, linear viscoelastic behaviour, it fails if the stress reaches a critical value – a yield stress. Failure of a material can result in discontinuous deformation, fracture, or continuous deformation, plastic flow. In the case of plastic flow, with increasing strain the stress can increase (so-called strain hardening), decrease (strain softening) or remain constant (ideal or pure plasticity). We consider here the third case.

The Saint-Venant body (StV) is a mechanical model for the behaviour of an ideal or pure plastic material. It is represented by a block on a rough base (Fig. 3.2). Note that, in general, the static friction between a block and a base defines a yield stress σ_Y. When the applied stress reaches the value of the static friction, the block starts sliding and in a short time the frictional stress decreases to a smaller value corresponding to a dynamic friction. In the definition of a Saint-Venant body the static and dynamic friction levels are not distinguished. Thus, if the applied stress is smaller than the yield stress σ_Y, the Saint-Venant body behaves as a rigid solid. If the block starts sliding and the loading stress does not decrease below σ_Y, the strain increases (at a constant $\sigma = \sigma_Y$) to a value that depends only on the time duration of the stress application. If the loading stress decreases below σ_Y, the sliding stops and the accumulated strain remains.

Clearly, a Saint-Venant body alone can approximate plastic behaviour but it cannot approximate behaviour before the loading stress reaches σ_Y and after (the plastic episode) the stress decreases below σ_Y.

Considering the configuration in Fig. 3.2, we can distinguish two possible directions of stress application and the consequent sliding – to the right and to the left. Choosing, say, the x -axis and stress positive to the right, we can distinguish two values of the yield stress: σ_Y and $-\sigma_Y$. We will come back to the plastic behaviour in Section 3.4.

Table 3.2 *Time-domain and frequency-domain rules for combining rheological models*

Connection		Stress σ	Strain ε
In series		Equal	Additive
In parallel		Additive	Equal

3.2 Combined rheological models

It is obvious that each of the three fundamental models has extremely simple behaviour that approximates only one particular aspect of the behaviour of real materials. A Hooke solid cannot dissipate elastic energy, a Newton liquid and a Saint-Venant body have no elasticity. Reasonable combinations of the three fundamental models are necessary for approximating the behaviour of real materials.

For combining the fundamental models (hereafter also called elements) we need unambiguous rules. Consider two elements, of different or the same type, in a connection. It is reasonable to assume that in some situations both elements are exposed to the same loading stress while they can respond with different strains. On the other hand, in some other situations they have to be exposed to different loading stresses in order to share the same strain. Both situations can be unambiguously described by simple rules for connecting elements in series and in parallel. They are given in Table 3.2.

3.3 Viscoelastic continuum and its rheological models

First we introduce concepts and relations that will be used in the next sections.

Fourier transform Hereafter we will use the symbol $\mathcal{F}$ for the direct and $\mathcal{F}^{-1}$ for the inverse Fourier transforms:

$$\mathcal{F}\{\xi(t)\} = \xi(\omega) = \int_{-\infty}^{\infty} \xi(t) \exp(-i\omega t)\, dt$$

$$\mathcal{F}^{-1}\{\xi(\omega)\} = \xi(t) = \frac{1}{2\pi} \int_{-\infty}^{\infty} \xi(\omega) \exp(i\omega t)\, d\omega$$

(3.1)

Convolution Consider a linear causal system. Let $i_S(t)$ be an input (input signal) to the system and $r(t)$ the system's response to the input (say, output signal). Assume that the

system is invariable with respect to time: if input $i_S(t)$ yields response $r(t)$, then input $i_S(t - \tau)$ yields $r(t - \tau)$. Then,

$$r(t) = \int_{-\infty}^{t} \mathcal{H}(t - \tau) i_S(\tau) d\tau \qquad (3.2)$$

where $\mathcal{H}(t)$ is the impulse response of the system, that is, the response of the system to the Dirac delta function $\delta(t)$ as an input. $\mathcal{H}(t)$ characterizes transfer properties of the system in the time domain. In other words, response $r(t)$ is given by convolution of input $i_S(t)$ and impulse response $\mathcal{H}(t)$. Application of the Fourier transform to Eq. (3.2) gives

$$r(\omega) = \mathcal{H}(\omega) i_S(\omega) \qquad (3.3)$$

where $\mathcal{H}(\omega) = \mathcal{F}\{\mathcal{H}(t)\}$ is the transfer function in the frequency domain.

The integral in Eq. (3.2) is called a convolutory integral. It is obvious that the response at time t depends on the entire signal $i_S(t)$, or, in other words, on the entire history of quantity i_S. Therefore, the integral in Eq. (3.2) is also called a hereditary integral.

3.3.1 Stress–strain and strain–stress relations in a viscoelastic continuum

3.3.1.1 Preliminary considerations

A Hooke solid, described by the stress–strain relation (Table 3.1)

$$\sigma(t) = M\varepsilon(t) \qquad (3.4)$$

has elasticity but no memory and, consequently, is incapable of dissipating energy. We can formally 'add memory' by generalizing the simple relation (3.4) to the convolutory relation

$$\sigma(t) = \int_{-\infty}^{t} M(t - \tau) \varepsilon(\tau) d\tau \qquad (3.5)$$

Note that the time-dependent modulus $M(t)$ does not contradict the model invariability with respect to time – as assumed in the previous section. $M(t)$ behaves in the same way no matter when the Dirac delta function $\delta(t)$ in strain is applied. Application of the Fourier transform gives

$$\sigma(\omega) = M(\omega)\varepsilon(\omega) \qquad (3.6)$$

with

$$\sigma(\omega) = \mathcal{F}\{\sigma(t)\}, \quad M(\omega) = \mathcal{F}\{M(t)\}, \quad \varepsilon(\omega) = \mathcal{F}\{\varepsilon(t)\} \qquad (3.7)$$

We can see that the assumption of a complex and frequency-dependent modulus, and thus assumption of relation (3.6), would be exactly the most natural generalization of the stress–strain relation of a Hooke solid in the frequency domain (Table 3.1).

We can further consider some function $\psi(t)$

$$\frac{\partial}{\partial t}\psi(t) = M(t) \qquad (3.8)$$

Then, due to a property of convolution, Eq. (3.5) can be written as

$$\sigma(t) = \int_{-\infty}^{t} \frac{\partial}{\partial t}\psi(t - \tau) \varepsilon(\tau) d\tau = \int_{-\infty}^{t} \psi(t - \tau) \frac{\partial}{\partial \tau}\varepsilon(\tau) d\tau \qquad (3.9)$$

Comparing Eq. (3.9) with the relation in Table 3.1 for a Newton liquid we can see that formally the generalization of perfect elasticity, Eq. (3.5), can also be viewed as a generalization of pure viscosity.

3.3.1.2 General theory in 1D

For a linear isotropic viscoelastic medium the stress–strain relation can be expressed by Eq. (3.9), which can be considered a form of Boltzmann's superposition and causality principle. Function $\psi(t)$ is the stress relaxation function. With reference to Eq. (3.2), $\psi(t)$ is a stress response to a Dirac delta function in the strain rate or, equivalently, to a Heaviside unit step in the strain. Stress relaxation means a decrease of stress. Considering Eq. (3.5) or (3.8), $M(t)$ is the stress response to a Dirac delta function in strain. Application of the Fourier transform to Eq. (3.8) yields

$$\mathcal{F}\left\{\frac{\partial}{\partial t}\psi(t)\right\} = M(\omega) \quad \text{and} \quad \psi(\omega) = \frac{M(\omega)}{i\omega} \tag{3.10}$$

and application of the inverse Fourier transform to the latter equation gives

$$\psi(t) = \mathcal{F}^{-1}\left\{\frac{M(\omega)}{i\omega}\right\} \tag{3.11}$$

$M(\omega)$ is, in general, a complex frequency-dependent viscoelastic modulus, and Eq. (3.11) is an important relation between the relaxation function and viscoelastic modulus.

Because $\psi(t)$ is the stress response to a Heaviside unit step in strain, we can consider

$$\psi(t) = \tilde{\psi}(t)H(t); \quad H(t) = 0; \quad t < 0, \quad H(t) = 1; \quad t \geq 0 \tag{3.12}$$

Here and hereafter in this chapter, the Heaviside function, $H(t)$, is equal to 1 for zero argument. Equivalently, $\tilde{\psi}(t) = \psi(t); t \geq 0$. Then,

$$\frac{\partial \psi}{\partial t} = \frac{\partial \tilde{\psi}}{\partial t}H(t) + \tilde{\psi}(t)\delta(t) \tag{3.13}$$

and, according to the first of Eqs. (3.10),

$$M(\omega) = \int_{-\infty}^{\infty} \left[\frac{\partial \tilde{\psi}}{\partial t}H(t) + \tilde{\psi}(t)\delta(t)\right] \exp(-i\omega t)dt$$

$$= \psi(0) + \int_0^{\infty} \frac{\partial \psi}{\partial t} \exp(-i\omega t)dt$$

$$= \psi(0) + \int_0^{\infty} \frac{\partial}{\partial t}[\psi(t) - \psi(\infty)] \exp(-i\omega t)dt$$

$$= \psi(0) + \{[\psi(t) - \psi(\infty)] \exp(-i\omega t)\}|_0^{\infty} - \int_0^{\infty} [\psi(t) - \psi(\infty)] \frac{d}{dt} \exp(-i\omega t)dt$$

$$= \psi(0) - [\psi(0) - \psi(\infty)] - \int_0^{\infty} [\psi(t) - \psi(\infty)] \frac{d}{dt} \exp(-i\omega t)dt$$

$$= \psi(\infty) + i\omega \int_0^{\infty} [\psi(t) - \psi(\infty)] \exp(-i\omega t)dt \tag{3.14}$$

Thus,

$$M(\omega) = \psi(\infty) + i\omega \int_0^\infty [\psi(t) - \psi(\infty)] \exp(-i\omega t) dt \qquad (3.15)$$

and, consequently,

$$M(\omega = 0) = \psi(t \to \infty) \qquad (3.16)$$

Alternatively to Eq. (3.14) we can consider

$$M(\omega) = \int_{-\infty}^\infty \left[\frac{\partial \tilde{\psi}}{\partial t} H(t) + \tilde{\psi}(t)\delta(t) \right] \exp(-i\omega t) dt$$

$$= \psi(0) + \int_0^\infty \frac{\partial \psi}{\partial t} \exp(-i\omega t) dt$$

$$= \psi(0) + \left[\frac{\partial \psi}{\partial t} \frac{\exp(-i\omega t)}{-i\omega} \right]_0^\infty - \int_0^\infty \frac{\partial^2 \psi}{\partial t^2} \frac{\exp(-i\omega t)}{-i\omega} dt \qquad (3.17)$$

Then,

$$\lim_{\omega \to \infty} M(\omega) = \psi(0) + \lim_{\omega \to \infty} \left\{ \left[\frac{\partial \psi}{\partial t} \frac{\exp(-i\omega t)}{-i\omega} \right]_0^\infty - \int_0^\infty \frac{\partial^2 \psi}{\partial t^2} \frac{\exp(-i\omega t)}{-i\omega} dt \right\}$$

$$= \psi(0) \qquad (3.18)$$

and

$$M(\omega \to \infty) = \psi(t = 0) \qquad (3.19)$$

Recall that $\psi(t)$ is a stress response to a Heaviside unit step in strain. Relation (3.19) means that an instantaneous stress response to a Heaviside unit step in strain is equal to $M(\omega \to \infty)$. Relation (3.16) means that the stress eventually relaxes to a value equal to $M(\omega = 0)$. Therefore, it is reasonable to introduce the unrelaxed modulus M_U:

$$M_U = \lim_{t \to 0} \psi(t) = \lim_{\omega \to \infty} M(\omega) \qquad (3.20)$$

relaxed modulus M_R:

$$M_R = \lim_{t \to \infty} \psi(t) = \lim_{\omega \to 0} M(\omega) \qquad (3.21)$$

and modulus defect or relaxation of modulus δM:

$$\delta M = M_U - M_R \qquad (3.22)$$

Alternatively to the stress–strain relation (3.9), it is possible to characterize the behaviour of a viscoelastic medium using the strain–stress relation:

$$\varepsilon(t) = \int_{-\infty}^t \chi(t - \tau) \frac{\partial}{\partial \tau} \sigma(\tau) d\tau \qquad (3.23)$$

where $\chi(t)$ is the creep function – a strain response to a Dirac delta function in the stress rate or, equivalently, to a Heaviside unit step in the stress. Creep means an increase of strain.

In analogy to relations (3.5), (3.8), (3.10), (3.11) and (3.20)–(3.22) there are relations

$$\varepsilon(t) = \int_{-\infty}^{t} C(t-\tau)\,\sigma(\tau)d\tau$$

$$\frac{\partial}{\partial t}\chi(t) = C(t)$$

$$\mathcal{F}\left\{\frac{\partial}{\partial t}\chi(t)\right\} = C(\omega) \quad \text{and} \quad \chi(\omega) = \frac{C(\omega)}{i\omega}$$

$$\chi(t) = \mathcal{F}^{-1}\left\{\frac{C(\omega)}{i\omega}\right\} \tag{3.24}$$

$$C_U = \lim_{t\to 0}\chi(t) = \lim_{\omega\to\infty}C(\omega)$$

$$C_R = \lim_{t\to\infty}\chi(t) = \lim_{\omega\to 0}C(\omega)$$

$$\delta C = C_R - C_U$$

where C means compliance and is equal to $1/M$.

3.3.2 Maxwell and Kelvin–Voigt bodies

The two simplest possible viscoelastic rheological models are the Maxwell body (spring and dashpot connected in series) and the Kelvin–Voigt body (spring and dashpot connected in parallel). For a detailed analysis of the two models we refer to Moczo *et al*. (2007a) or other monographic texts. Here we restrict our discussion to essential aspects relevant to the possibility of using these models for incorporating attenuation. Figure 3.3 shows the strain response of the two models to a step in stress, that is, creep. It is obvious that each of the two models has a problem preventing its application for incorporating realistic attenuation. A Maxwell body is capable of instantaneous elastic strain but fails to fully recover – it cannot remove strain accumulated in the dashpot. In other words, a particle of such a viscoelastic continuum would be unable to return to the original equilibrium position. A Kelvin–Voigt model can fully recover but is incapable of an instantaneous nonzero strain response upon application of a step in stress.

3.3.3 Zener body (standard linear solid)

The incapability of a Kelvin–Voigt body to instantaneously respond with nonzero strain upon application of a step in stress naturally suggests connecting the Kelvin–Voigt model in series with a spring. The additional spring can respond instantaneously with nonzero strain. We can denote such a model as H-s-KV.
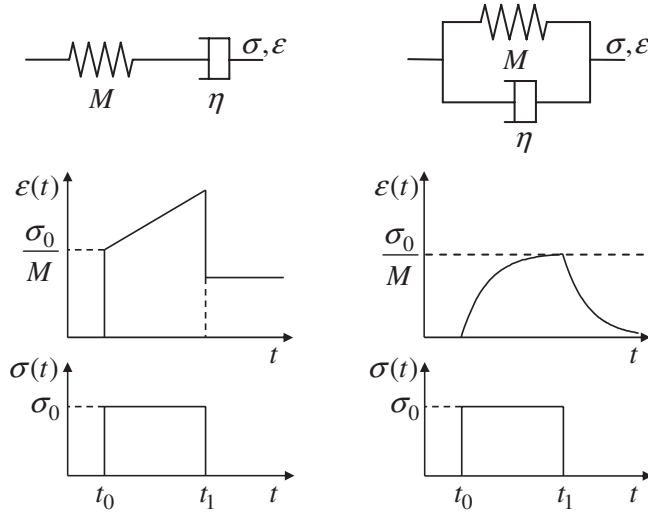
Figure 3.3 Behaviour of a Maxwell body (left) and a Kelvin–Voigt body (right) upon application of a step in stress at time t_0 and its removal at time t_1.
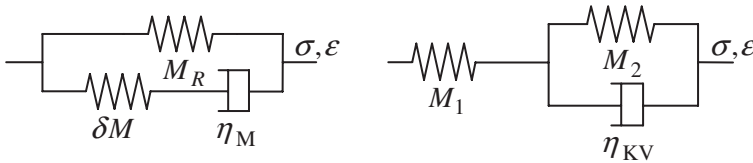
Figure 3.4 Two alternative models of a Zener body (standard linear solid). Left: spring connected in parallel with Maxwell model. Right: spring connected in series with Kelvin–Voigt model.

On the other hand, the incapability of a Maxwell body to remove accumulated strain is due to the absence of a spring connected in parallel with the dashpot. This suggests connecting a Maxwell body in parallel with a spring. We can denote this model as H-p-M. Both configurations are shown in Fig. 3.4.

Hooke solid connected in parallel with Maxwell body: H-p-M It is easier to see the meaning of the elastic moduli in H-p-M. At the time of application of the unit step in strain an instantaneous stress, i.e., unrelaxed stress M_U, will be given by the sum of the moduli of the springs. At the same time, the strain of the dashpot will start to grow from zero. The growth of the strain will gradually release the stress of the spring connected in series with the dashpot. In the limit, the relaxed stress, M_R, will be only in the spring connected in parallel with the Maxwell body. Because $M_U = M_R + \delta M$, M_R is the modulus of the spring connected in parallel with the Maxwell body and δM is the modulus of the spring in the Maxwell body.

In the following, subscripts H and M will indicate quantities related to the Hooke and Maxwell models. Application of the frequency-domain rules (Table 3.2) to model H-p-M yields

$$\sigma(\omega) = \sigma_H(\omega) + \sigma_M(\omega), \quad \varepsilon(\omega) = \varepsilon_H(\omega) = \varepsilon_M(\omega) \tag{3.25}$$

where

$$\sigma_H(\omega) = M_R \, \varepsilon(\omega) \tag{3.26}$$

and $\sigma_M(\omega)$ is obtained from application of the rules to the Maxwell model:

$$\varepsilon(\omega) = \frac{\sigma_M(\omega)}{\delta M} + \frac{\sigma_M(\omega)}{i\omega\eta_M}$$

$$\sigma_M(\omega) = \left(\frac{i\omega\eta_M \delta M}{\delta M + i\omega\eta_M} \right) \varepsilon(\omega) \tag{3.27}$$

Substitution of $\sigma_H(\omega)$ and $\sigma_M(\omega)$ in Eq. (3.25) yields

$$\sigma(\omega) = M_R \varepsilon(\omega) + \frac{i\omega\eta_M \delta M}{\delta M + i\omega\eta_M} \varepsilon(\omega)$$

$$= M_R \frac{1 + i\omega \dfrac{\eta_M}{\delta M} \dfrac{M_U}{M_R}}{1 + i\omega \dfrac{\eta_M}{\delta M}} \varepsilon(\omega) \tag{3.28}$$

Denoting

$$\tau_\sigma \equiv \frac{\eta_M}{\delta M}, \quad \tau_\varepsilon \equiv \frac{\eta_M}{\delta M} \frac{M_U}{M_R} \tag{3.29}$$

the stress–strain relation in the frequency domain and the viscoelastic modulus are

$$\sigma(\omega) = M(\omega)\varepsilon(\omega); \quad M(\omega) = M_R \frac{1 + i\omega\tau_\varepsilon}{1 + i\omega\tau_\sigma} \tag{3.30}$$

Using Eq. (3.11)

$$\psi(t) = \mathcal{F}^{-1} \left\{ M_R \left[\frac{-i}{\omega} + \frac{i\tau_\varepsilon}{i - \tau_\sigma\omega} - \frac{i\tau_\sigma}{i - \tau_\sigma\omega} \right] \right\}$$

$$= M_R \left[1 + \left(\frac{\tau_\varepsilon}{\tau_\sigma} - 1 \right) \exp\left(-\frac{t}{\tau_\sigma} \right) \right] H(t) \tag{3.31}$$

It is also easy to obtain the creep function:

$$\chi(t) = \frac{1}{M_R} \left[1 - \frac{\tau_\sigma}{\tau_\varepsilon} \left(\frac{\tau_\varepsilon}{\tau_\sigma} - 1 \right) \exp\left(-\frac{t}{\tau_\varepsilon} \right) \right] H(t) \tag{3.32}$$

Noting that

$$\frac{\tau_\varepsilon}{\tau_\sigma} = \frac{M_U}{M_R} > 1 \tag{3.33}$$

it is clear from relations (3.31) and (3.32) that τ_σ and τ_ε have the meanings of characteristic stress-relaxation time and characteristic creep time, respectively.

Hooke solid connected in series with Kelvin–Voigt body: H-s-KV Application of the frequency-domain rules (Table 3.2) to model H-s-KV yields

$$\sigma(\omega) = \sigma_H(\omega) = \sigma_{KV}(\omega), \quad \varepsilon(\omega) = \varepsilon_H(\omega) + \varepsilon_{KV}(\omega) \tag{3.34}$$

where

$$\varepsilon_H(\omega) = \frac{\sigma(\omega)}{M_1} \tag{3.35}$$

Application of the rules to the Kelvin–Voigt model gives

$$\sigma(\omega) = M_2 \varepsilon_{KV}(\omega) + i\omega\eta_{KV}\varepsilon_{KV}(\omega) \tag{3.36}$$

Then,

$$\varepsilon(\omega) = \left(\frac{1}{M_1} + \frac{1}{M_2 + i\omega\eta_{KV}} \right) \sigma(\omega) \tag{3.37}$$

$$\sigma(\omega) = \frac{M_1 M_2 + i\omega\eta_{KV} M_1}{M_1 + M_2 + i\omega\eta_{KV}} \varepsilon(\omega) \tag{3.38}$$

and

$$\sigma(\omega) = M(\omega)\varepsilon(\omega), \quad M(\omega) = \frac{M_1 M_2}{M_1 + M_2} \frac{1 + i\omega \dfrac{\eta_{KV}}{M_2}}{1 + i\omega \dfrac{\eta_{KV}}{M_1 + M_2}} \tag{3.39}$$

The unrelaxed and relaxed moduli are

$$\lim_{\omega \to \infty} M(\omega) = M_1, \quad \lim_{\omega \to 0} M(\omega) = \frac{M_1 M_2}{M_1 + M_2} \tag{3.40}$$

The relations between moduli M_1 and M_2 in H-s-KV and moduli M_R and δM in H-p-M are

$$M_R = \frac{M_1 M_2}{M_1 + M_2}, \quad \delta M = \frac{M_1^2}{M_1 + M_2} \tag{3.41}$$

The behaviour of a Zener body is illustrated in Fig. 3.5.

Viscosities η_{KV} and η_M of the H-s-KV and H-p-M, respectively, are related by

$$\eta_{KV} = \eta_M \left(\frac{M_U}{\delta M} \right)^2 \tag{3.42}$$

Note that for a given set of M_R, δM and η_M in H-p-M it would be impossible to find moduli M_1 and M_2 if we assumed $\eta_{KV} = \eta_M$.
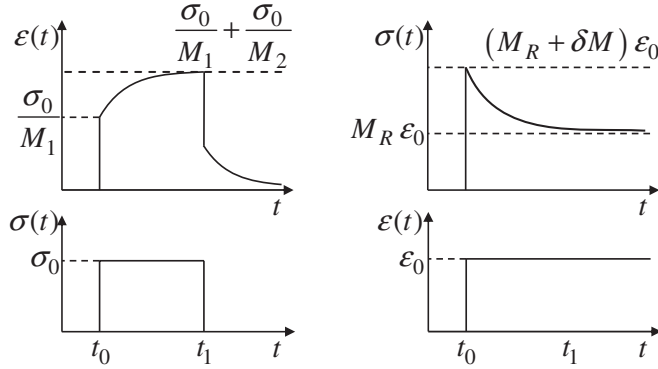
Figure 3.5 Behaviour of a Zener body. Left: strain upon application of step in stress at time t_0 and its removal at time t_1. Right: stress response upon application of step in strain.

3.3.4 Phase velocity in elastic and viscoelastic continua

Phase velocity in a perfectly elastic medium Consider a harmonic wave propagating in the positive *x*-direction:

$$u = \exp\left[i\left(\omega t - kx\right)\right] \tag{3.43}$$

The requirement of $\omega t - kx = \omega\left(t + \Delta t\right) - k\left(x + \Delta x\right)$ implies

$$\frac{\Delta x}{\Delta t} = \frac{\omega}{k} \tag{3.44}$$

and the phase velocity c:

$$c = \frac{\omega}{k} \tag{3.45}$$

The 1D equation of motion and Hooke's law in the elastic homogeneous medium are

$$\rho\frac{\partial^2 u}{\partial t^2} = \frac{\partial \sigma}{\partial x}, \quad \sigma = M\frac{\partial u}{\partial x} \tag{3.46}$$

or

$$\frac{\partial^2 u}{\partial t^2} = \frac{M}{\rho}\frac{\partial^2 u}{\partial x^2} \tag{3.47}$$

where M is a real constant elastic modulus. Assuming u is given by Eq. (3.43), Eq. (3.47) implies

$$(i\omega)^2 u = \frac{M}{\rho}(-ik)^2 u \tag{3.48}$$

$$\left(\frac{\omega}{k}\right)^2 = \frac{M}{\rho} \tag{3.49}$$

The phase velocity is

$$c = \frac{\omega}{k} = \left(\frac{M}{\rho}\right)^{\frac{1}{2}} \tag{3.50}$$

Phase velocity in a viscoelastic medium The 1D equation of motion and Hooke's law in the viscoelastic medium are

$$\rho \frac{\partial^2 u}{\partial t^2} = \frac{\partial \sigma}{\partial x}, \quad \sigma = M(t) * \frac{\partial u}{\partial x} \tag{3.51}$$

or

$$\rho \frac{\partial^2 u}{\partial t^2} = M(t) * \frac{\partial^2 u}{\partial x^2} \tag{3.52}$$

where the asterisk indicates the convolution. Application of the Fourier transform to Eq. (3.52) gives

$$(i\omega)^2 \mathcal{F}\{u\} = \frac{M(\omega)}{\rho} \frac{\partial^2}{\partial x^2} \mathcal{F}\{u\} \tag{3.53}$$

where $M(\omega)$ is, in general, the complex frequency-dependent viscoelastic modulus. In order to distinguish the wavenumber in the viscoelastic medium from that in the elastic medium, we denote it by K. Then, for any wave (the harmonic wave being a special case),

$$u(t, x) = \tilde{u}(t) \exp(-iKx) \tag{3.54}$$

we obtain

$$\frac{\partial^2}{\partial x^2} \mathcal{F}\{u\} = -K^2 \mathcal{F}\{u\} \tag{3.55}$$

Equation (3.53) implies

$$-\omega^2 = \frac{M(\omega)}{\rho}(-K^2) \tag{3.56}$$

and

$$\frac{K}{\omega} = \sqrt{\frac{\rho}{M(\omega)}} \tag{3.57}$$

Assuming real ω, Eq. (3.57) implies that K may be complex:

$$K = K_{\text{real}} + i K_{\text{imag}} \tag{3.58}$$

Generalization of the wave in Eq. (3.43) with the complex wavenumber K gives

$$u = \exp(K_{\text{imag}}x) \exp[i(\omega t - K_{\text{real}}x)] \tag{3.59}$$

In analogy with Eqs. (3.43) and (3.45), the real phase velocity is

$$c = \frac{\omega}{K_{\text{real}}} \tag{3.60}$$

Considering (3.57) and (3.60) we obtain

$$\frac{1}{c} = \frac{K_{\text{real}}}{\omega} = \left(\sqrt{\frac{\rho}{M(\omega)}} \right)_{\text{real}} \tag{3.61}$$

Consequently, we can use the symbol of real k instead of K_{real},

$$k \equiv K_{\text{real}} \tag{3.62}$$

and write

$$K = k + i K_{\text{imag}} \tag{3.63}$$

We can also define a complex velocity $V = V_{\text{real}} + i V_{\text{imag}}$ as

$$V \equiv \sqrt{\frac{M(\omega)}{\rho}} \tag{3.64}$$

Using Eqs. (3.57), (3.63) and (3.64),

$$k = \omega \frac{V_{\text{real}}}{|V|^2}, \quad K_{\text{imag}} = -\omega \frac{V_{\text{imag}}}{|V|^2} \tag{3.65}$$

Considering $M = M_{\text{real}} + i M_{\text{imag}}$ we obtain

$$\frac{M_{\text{real}}}{\rho} = V_{\text{real}}^2 - V_{\text{imag}}^2, \quad \frac{M_{\text{imag}}}{\rho} = 2 V_{\text{real}} V_{\text{imag}} \tag{3.66}$$

We easily find the relation between the complex velocity V and the real phase velocity c using Eqs. (3.61) and (3.65):

$$c = \frac{|V|^2}{V_{\text{real}}} = \frac{V_{\text{real}}^2 + V_{\text{imag}}^2}{V_{\text{real}}} \tag{3.67}$$

3.3.5 Measure of dissipation and attenuation in a viscoelastic continuum

Whereas a Hooke perfectly elastic solid does not dissipate elastic (or strain) energy at all, a Newton viscous liquid dissipates the energy completely but has no elasticity. A Zener body, properly combining a Hooke solid and a Newton liquid, is capable of both an elastic response and energy dissipation. A Hooke solid is characterized by a real elastic frequency-independent modulus, a Zener body by a complex frequency-dependent viscoelastic modulus. Therefore, one may intuitively guess that the ratio between the imaginary and real parts of the viscoelastic modulus, $M_{\text{imag}}/M_{\text{real}}$, might be related to some measure of dissipation. Indeed, O'Connell and Budiansky (1978) suggested using this ratio as a measure of dissipation in a viscoelastic medium. Correspondingly, they suggested a definition of the quality parameter Q of the medium (a term borrowed from electric circuit theory) as

$$Q(\omega) = \frac{M_{\text{real}}}{M_{\text{imag}}} \tag{3.68}$$

In seismology, Q is commonly termed a quality factor. O'Connell and Budiansky (1978) showed that Q is related to the energy dissipated per oscillation cycle assuming harmonic loading in a unit volume of the continuum:

$$\frac{1}{Q(\omega)} = \frac{1}{4\pi} \frac{E_{\text{dissipated}}}{E_{\text{average}}} \tag{3.69}$$

Here $E_{\text{dissipated}}$ is the dissipated energy and E_{average} is the average elastic energy stored during one cycle of loading.

Note that the ratio of the imaginary and real parts of the viscoelastic modulus was used as a loss parameter previously by White (1965) in his book on seismic waves.

Anelastic dissipation causes attenuation of free oscillations in time or spatial attenuation of a propagating wave.

Recall wave (3.59) with k used instead of K_{real}:

$$u = \exp(K_{\text{imag}} x) \exp[i(\omega t - kx)] \tag{3.70}$$

Assume that u has its peak value at x_P. Consider a fixed time t and evaluate the ratio of the u values at $x_P + \lambda$ and x_P, where λ is the wavelength:

$$\frac{u(x_P + \lambda, t)}{u(x_P, t)} = \exp(K_{\text{imag}} \lambda) \exp(-ik\lambda) = \exp(K_{\text{imag}} \lambda) \tag{3.71}$$

The latter equality is due to $k\lambda = 2\pi$. It is clear that K_{imag} has to be negative if the amplitude decays with distance. Indeed, the attenuation coefficient $\alpha > 0$ is defined as

$$\alpha = -K_{\text{imag}} \tag{3.72}$$

and thus,

$$\frac{u(x_P + \lambda, t)}{u(x_P, t)} = \exp(-\alpha\lambda) \tag{3.73}$$

The spatial Q is defined by relation

$$\exp(-\alpha\lambda) = \exp\left(-\frac{\pi}{Q_{\text{spatial}}}\right) \tag{3.74}$$

Hence,

$$Q_{\text{spatial}} = \frac{\pi}{\alpha\lambda} = \frac{k}{2\alpha} \tag{3.75}$$

Using Eqs. (3.65) and (3.72) we obtain

$$Q_{\text{spatial}} = \frac{V_{\text{real}}}{2V_{\text{imag}}} \tag{3.76}$$

Compare Q_{spatial} with Q defined by Eq. (3.68). Using Eq. (3.66),

$$Q = \frac{M_{\text{real}}}{M_{\text{imag}}} = \frac{V_{\text{real}}^2 - V_{\text{imag}}^2}{2V_{\text{real}} V_{\text{imag}}} = \frac{V_{\text{real}}}{2V_{\text{imag}}} - \frac{V_{\text{imag}}}{2V_{\text{real}}} \tag{3.77}$$

Using Eq. (3.76) we obtain

$$Q = Q_{\text{spatial}} - \frac{1}{4 Q_{\text{spatial}}} \tag{3.78}$$

Assuming $Q_{\text{spatial}} \gg 1$ we have $Q \approx Q_{\text{spatial}}$. Consider, e.g., $Q_{\text{spatial}} = 10$. Then $Q = 9.975$. For $Q_{\text{spatial}} = 5$ there is $Q = 4.95$. These are small differences that can be neglected in most numerical applications.

For more details we refer to the article by O'Connell and Budiansky (1978) and, for example, books by Aki and Richards (2002), and Pujol (2003).

3.3.6 Attenuation in a Zener body

The viscoelastic modulus given by Eq. (3.30) can be written as

$$M(\omega) = M_R \frac{1 + \omega^2 \tau_\sigma \tau_\varepsilon + i \omega (\tau_\varepsilon - \tau_\sigma)}{1 + \omega^2 \tau_\sigma^2} \tag{3.79}$$

Equation (3.79) implies

$$\frac{1}{Q(\omega)} = \frac{M_{\text{imag}}(\omega)}{M_{\text{real}}(\omega)} = \frac{\omega (\tau_\varepsilon - \tau_\sigma)}{1 + \omega^2 \tau_\sigma \tau_\varepsilon} \tag{3.80}$$

$Q^{-1}(\omega)$ has its maximum at frequency

$$\omega_{\text{m}} = \frac{1}{\sqrt{\tau_\sigma \tau_\varepsilon}} = \frac{\delta M}{\eta} \sqrt{\frac{M_R}{M_U}} \tag{3.81}$$

$Q^{-1}(\omega)$ is illustrated in Fig. 3.6. It is clear from the figure that one Zener body cannot approximate, for instance, constant or almost constant $Q(\omega)$. A superposition of several Zener bodies whose peaks are properly distributed over a desired frequency range might provide a reasonable approximation.

3.3.7 Generalized Zener body (GZB)

A generalized Zener body (GZB) is a parallel connection of n Zener bodies. Consider each of them to be of the H-p-M type (Fig. 3.7). The relaxed modulus M_{Rl}, modulus defect δM_l and viscosity η_l characterize each l-th Zener body. We denote by M_l, M_{Ul}, $\tau_{\sigma l}$ and $\tau_{\varepsilon l}$ the viscoelastic modulus, unrelaxed modulus, characteristic stress-relaxation time and characteristic creep time of the l-th Zener body, respectively. Denoting stress and strain of the l-th Zener body by $\sigma_l(\omega)$ and $\varepsilon_l(\omega)$, application of the frequency-domain rules for combined models yields

$$\sigma(\omega) = \sum_{l=1}^{n} \sigma_l(\omega), \quad \varepsilon(\omega) = \varepsilon_l(\omega); \quad l = 1, 2, \ldots, n \tag{3.82}$$
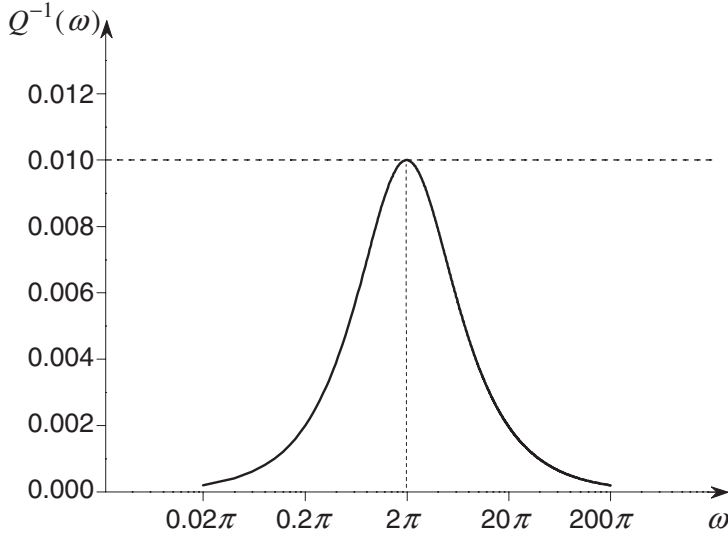
Figure 3.6 Example of $Q^{-1}(\omega)$ of Zener body.

Using Eq. (3.30),

$$\sigma_l(\omega) = M_l(\omega)\varepsilon(\omega); \quad M_l(\omega) = M_{Rl}\frac{1 + i\omega\tau_{\varepsilon l}}{1 + i\omega\tau_{\sigma l}} \tag{3.83}$$

with

$$\tau_{\sigma l} = \frac{\eta_l}{\delta M_l}, \quad \tau_{\varepsilon l} = \frac{\eta_l}{\delta M_l}\frac{M_{Ul}}{M_{Rl}} \tag{3.84}$$

we obtain

$$\sigma(\omega) = M(\omega)\varepsilon(\omega), \quad M(\omega) = \sum_{l=1}^{n} M_{Rl}\frac{1 + i\omega\tau_{\varepsilon l}}{1 + i\omega\tau_{\sigma l}} \tag{3.85}$$

The relaxed and unrelaxed moduli are

$$M_R = \lim_{\omega \to 0} M(\omega) = \sum_{l=1}^{n} M_{Rl} \tag{3.86}$$

and, using Eq. (3.33),

$$M_U = \lim_{\omega \to \infty} M(\omega) = \sum_{l=1}^{n} M_{Rl}\frac{\tau_{\varepsilon l}}{\tau_{\sigma l}} = \sum_{l=1}^{n} M_{Ul}$$

$$= \sum_{l=1}^{n} (M_{Rl} + \delta M_l) = M_R + \delta M \tag{3.87}$$

where δM is the modulus defect (relaxation of modulus):

$$\delta M = \sum_{l=1}^{n} \delta M_l \tag{3.88}$$

As expected, upon application of a unit step in strain, the instantaneous elastic response, quantified by the unrelaxed modulus M_U, is due to the superposition of all the springs in
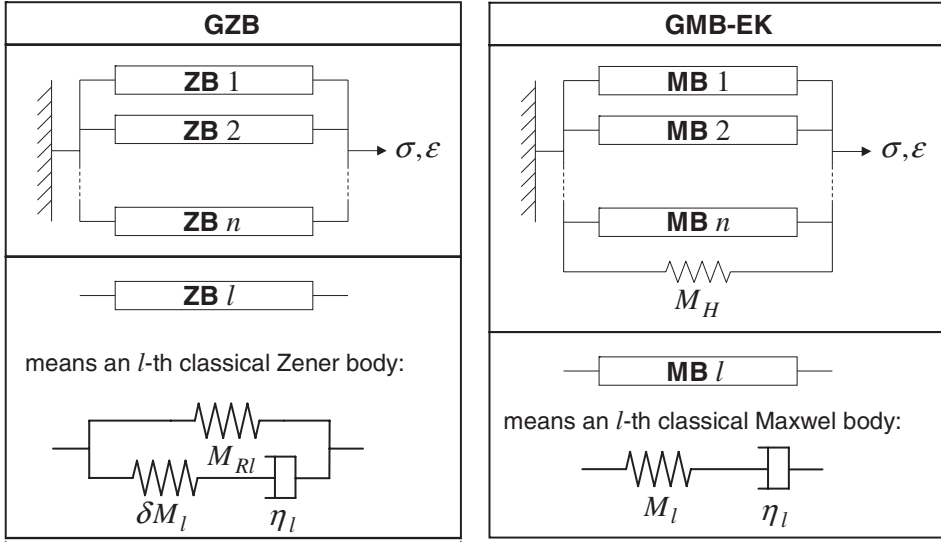
Figure 3.7 Left: generalized Zener body. Each single Zener body is of the H-p-M type. Right: generalized Maxwell body as defined by Emmerich and Korn (1987).

the model. Under a constant unit strain the model eventually relaxes down to the stress of the superposition of all the springs connected in parallel with Maxwell bodies.

Using Eq. (3.11) we easily obtain the relaxation function:

$$\psi(t) = \left\{ \sum_{l=1}^{n} M_{Rl} \left[1 + \left(\frac{\tau_{\varepsilon l}}{\tau_{\sigma l}} - 1 \right) \exp \left(-\frac{t}{\tau_{\sigma l}} \right) \right] \right\} H(t) \tag{3.89}$$

Assuming simplification (Carcione 2001, 2007; we will comment on this later)

$$M_{Rl} = \frac{1}{n} M_R \tag{3.90}$$

we obtain

$$M(\omega) = \frac{M_R}{n} \sum_{l=1}^{n} \frac{1 + i\omega\tau_{\varepsilon l}}{1 + i\omega\tau_{\sigma l}} \tag{3.91}$$

$$\psi(t) = M_R \left[1 + \frac{1}{n} \sum_{l=1}^{n} \left(\frac{\tau_{\varepsilon l}}{\tau_{\sigma l}} - 1 \right) \exp \left(-\frac{t}{\tau_{\sigma l}} \right) \right] H(t) \tag{3.92}$$

Formulas (3.90) and (3.91) were presented by Carcione (2001, 2007). Most, if not all, articles dealing with the incorporation of the attenuation based on GZB, starting from Liu *et al*. (1976), had the same error – the missing factor $1/n$ in the viscoelastic modulus and relaxation function ($1/L$ in most of the papers, L being the number of Zener bodies).

The attenuation corresponding to $M(\omega)$ given by Eq. (3.85) is quantified by

$$\frac{1}{Q(\omega)} = \frac{M_{\text{imag}}(\omega)}{M_{\text{real}}(\omega)} = \frac{\sum_{l=1}^{n} M_{Rl} \dfrac{\omega\,(\tau_{\varepsilon l} - \tau_{\sigma l})}{1 + \omega^2 \tau_{\sigma l}^2}}{\sum_{l=1}^{n} M_{Rl} \dfrac{1 + \omega^2 \tau_{\varepsilon l}\tau_{\sigma l}}{1 + \omega^2 \tau_{\sigma l}^2}} \tag{3.93}$$

from which a simplified version due to (3.90) is obtained immediately.

Before we quantitatively illustrate the attenuation in the GZB model we look at an alternative model published by Emmerich and Korn (1987).

3.3.8 Generalized Maxwell body (GMB-EK)

The model published by Emmerich and Korn (1987) is shown in Fig. 3.7. Note that often in the literature on rheology the generalized Maxwell body is defined as n Maxwell bodies connected in parallel, that is, without the additional spring. The additional spring here, however, makes that significant difference. Therefore, we use the abbreviation GMB-EK instead of just GMB.

The l-th Maxwell body is characterized by elastic modulus M_l and viscosity η_l. The additional Hooke spring is characterized by elastic modulus M_H. Subscript l will indicate the l-th Maxwell body whereas subscript H will indicate the additional spring. Application of the rules in the frequency domain yields

$$\sigma(\omega) = \sigma_H(\omega) + \sum_{l=1}^{n} \sigma_l(\omega), \quad \varepsilon(\omega) = \varepsilon_H(\omega) = \varepsilon_l(\omega); \quad l = 1, 2, \ldots, n \tag{3.94}$$

where

$$\sigma_H(\omega) = M_H \varepsilon(\omega) \tag{3.95}$$

$$\varepsilon(\omega) = \varepsilon_l(\omega) = \frac{\sigma_l(\omega)}{M_l} + \frac{\sigma_l(\omega)}{i\omega\eta_l} \tag{3.96}$$

The latter equation implies

$$\sigma_l(\omega) = \frac{i\eta_l M_l \omega}{M_l + i\eta_l \omega}\varepsilon(\omega) \tag{3.97}$$

Define a characteristic (relaxation) frequency

$$\omega_l \equiv \frac{M_l}{\eta_l} \tag{3.98}$$

Then,

$$\sigma(\omega) = M(\omega)\varepsilon(\omega), \quad M(\omega) = M_H + \sum_{l=1}^{n} \frac{i M_l \omega}{\omega_l + i\omega} \tag{3.99}$$

The relaxed and unrelaxed moduli are

$$M_U = \lim_{\omega \to \infty} M(\omega) = M_{\mathrm{H}} + \sum_{l=1}^{n} M_l$$

$$M_R = \lim_{\omega \to 0} M(\omega) = M_{\mathrm{H}} \tag{3.100}$$

Because $M_U = M_R + \delta M$,

$$\delta M = \sum_{l=1}^{n} M_l \tag{3.101}$$

and M_l has the meaning of δM_l. As expected, upon application of a unit step in strain, the instantaneous elastic response, quantified by the unrelaxed modulus M_U, is due to superposition of all springs in the model. Under a constant unit strain the model eventually relaxes down to the stress of the additional spring, that is, M_{H}. Compare this with the analogous statement regarding the GZB model after Eq. (3.87): the additional spring in the GMB model plays the same role as all the springs connected in parallel with Maxwell bodies in individual Zener bodies together.

Using Eq. (3.11), the second of Eqs. (3.99) and Eq. (3.100) we obtain the relaxation function

$$\psi(t) = \left[M_R + \sum_{l=1}^{n} M_l e^{-\omega_l t} \right] H(t) \tag{3.102}$$

The viscoelastic modulus and relaxation function can also be expressed using the unrelaxed modulus. In the second of Eqs. (3.99) we replace M_{H} by difference $M_U - \delta M$, then δM using Eq. (3.101), and obtain

$$M(\omega) = M_U - \sum_{l=1}^{n} \frac{M_l \omega_l}{\omega_l + i\omega} \tag{3.103}$$

Similarly we modify Eq. (3.102):

$$\psi(t) = \left[M_U - \sum_{l=1}^{n} M_l \left(1 - e^{-\omega_l t} \right) \right] H(t) \tag{3.104}$$

The attenuation corresponding to $M(\omega)$ given by Eq. (3.103) is quantified by

$$\frac{1}{Q(\omega)} = \frac{M_{\mathrm{imag}}(\omega)}{M_{\mathrm{real}}(\omega)} = \frac{\sum_{l=1}^{n} \dfrac{M_l \omega_l \omega}{\omega_l^2 + \omega^2}}{M_U - \sum_{l=1}^{n} \dfrac{M_l \omega_l^2}{\omega_l^2 + \omega^2}} \tag{3.105}$$

Before we continue with the attenuation we compare the GZB and GMB-EK models.

3.3.9 Equivalence of GZB and GMB-EK

The viscoelastic modulus of GZB is usually presented in the literature in the form of Eq. (3.85), or in the simplified form of Eq. (3.91). Consider, however, expressions for the

Table 3.3 *Equivalence of GZB and GMB-EK*

	GZB	GMB-EK
$M(\omega)$	$\sum_{l=1}^{n} M_{Rl} + \sum_{l=1}^{n} \dfrac{i\,\eta_l\,\delta M_l\,\omega}{\delta M_l + i\,\eta_l\,\omega}$	$M_{\mathrm{H}} + \sum_{l=1}^{n} \dfrac{i\,\eta_l\,M_l\,\omega}{M_l + i\,\eta_l\,\omega}$
M_U	$\sum_{l=1}^{n} M_{Rl} + \sum_{l=1}^{n} \delta M_l$	$M_{\mathrm{H}} + \sum_{l=1}^{n} M_l$
M_R	$\sum_{l=1}^{n} M_{Rl}$	M_{H}
δM	$\sum_{l=1}^{n} \delta M_l$	$\sum_{l=1}^{n} M_l$
$M(\omega)$ using expression for M_R	$M_R + \sum_{l=1}^{n} \dfrac{i\,\eta_l\,\delta M_l\,\omega}{\delta M_l + i\,\eta_l\,\omega}$	$M_{\mathrm{R}} + \sum_{l=1}^{n} \dfrac{i\,\eta_l\,M_l\,\omega}{M_l + i\,\eta_l\,\omega}$
Consideration		
Assume η_l the same in GZB and GMB-EK, and $\delta M_l = M_l$. Then all M_{Rl}-springs in GZB can be replaced by one spring with $M_{\mathrm{H}} = \Sigma_{l=1}^{n} M_{Rl}$ connected in parallel with a parallel connection of Maxwell bodies that would remain after removal of the M_{Rl}-springs.		
Conclusion		
GZB and GMB-EK are equivalent		

moduli with the parameters of springs and dashpots characterizing both models (Fig. 3.7): for GZB using Eq. (3.28), for GMB-EK using (3.99). Both are given in Table 3.3, which concisely compares rheologies of both models and shows their equivalence. The equivalence was shown by Moczo and Kristek (2005). The equivalence could be similarly shown also if we assumed GZB to be composed of H-s-KV.

Because GZB and GMB-EK are equivalent we can further continue with any of them. GMB-EK has a smaller number of elements and its structure is simpler compared to GZB. Consequently, relations for GMB-EK are also slightly simpler compared to those for GZB. Moreover, description of GMB-EK uses one type of characteristic frequency whereas description of GZB uses two characteristic times. The equivalence also implies that there is no need for simplification (3.90).

3.3.10 Anelastic functions (memory variables)

Recall relations (3.5)–(3.11). The general form of the stress–strain relation in the frequency domain in the viscoelastic continuum is

$$\sigma(\omega) = M(\omega)\varepsilon(\omega) \tag{3.106}$$

Having relations for the viscoelastic modulus and measure of attenuation, $1/Q(\omega)$, we are ready to finalize the incorporation of attenuation in the frequency domain: according to the so-called correspondence principle in the linear theory of viscoelasticity, real frequency-independent moduli are simply replaced by complex frequency-dependent moduli. Thus, what remains is to find a way to determine the parameters of GMB-EK /GZB in order to fit or approximate the measured or desired $Q(\omega)$.

However, aiming to incorporate realistic attenuation in the time domain, we have to recall the stress–strain relation in the time domain:

$$\sigma(t) = \int_{-\infty}^{t} M(t - \tau)\varepsilon(\tau)d\tau \qquad (3.107)$$

with

$$M(t) = \mathcal{F}^{-1}\{M(\omega)\} \quad \text{or} \quad M(t) = \frac{\partial}{\partial t}\psi(t) \qquad (3.108)$$

Although we are ready to determine $M(t)$, we still have a problem: with relation (3.107) we need the entire history of strain in order to determine stress at time t at each spatial position. Moreover, we have to evaluate the convolutory integral at each time. This is, in practice, intractable or at least very inefficient – anticipating, for instance, no fewer than 10^6–10^8 spatial grid points and 10^3–10^4 time levels to be calculated in the grid methods. A reasonable solution of the problem is to introduce anelastic functions (also memory variables, new variables or internal variables).

Recall the relaxation function for GMB-EK, Eq. (3.104):

$$\psi(t) = \left[M_U - \sum_{l=1}^{n} M_l \left(1 - e^{-\omega_l t}\right)\right] H(t) \qquad (3.109)$$

Then,

$$M(t) = -\sum_{l=1}^{n} M_l \omega_l e^{-\omega_l t} H(t) + \left[M_U - \sum_{l=1}^{n} M_l \left(1 - e^{-\omega_l t}\right)\right] \delta(t) \qquad (3.110)$$

Substituting the r.h.s. for $M(t)$ in Eq. (3.107) yields

$$\sigma(t) = -\int_{-\infty}^{t} \sum_{l=1}^{n} M_l \omega_l e^{-\omega_l(t-\tau)} H(t - \tau)\varepsilon(\tau)d\tau$$

$$+ \int_{-\infty}^{t} M_U \delta(t - \tau)\varepsilon(\tau)d\tau$$

$$- \int_{-\infty}^{t} \sum_{l=1}^{n} M_l \left[1 - e^{-\omega_l(t-\tau)}\right]\delta(t - \tau)\varepsilon(\tau)d\tau \qquad (3.111)$$

and

$$\sigma(t) = M_U \varepsilon(t) - \sum_{l=1}^{n} M_l \omega_l \int_{-\infty}^{t} e^{-\omega_l(t-\tau)}\varepsilon(\tau)d\tau \qquad (3.112)$$

Now it is possible to replace the convolution integral by anelastic functions. Whereas Day and Minster (1984), Emmerich and Korn (1987) and Carcione *et al.* (1988a,b) defined the anelastic functions (additional internal variables, memory variables) as dependent also on the material properties, for an important reason that will be explained later, Kristek and Moczo (2003) defined their anelastic functions as independent of the material properties. Here we follow Kristek and Moczo (2003). Defining anelastic functions

$$\zeta_l(t) = \omega_l \int_{-\infty}^{t} e^{-\omega_l(t-\tau)}\varepsilon(\tau)d\tau, \quad l = 1, \ldots, n \qquad (3.113)$$

we rewrite the latter stress–strain relation as

$$\sigma(t) = M_U \varepsilon(t) - \sum_{l=1}^{n} M_l \zeta_l(t) \tag{3.114}$$

The stress–strain relation is now simple to evaluate if we know the anelastic functions. Differentiate Eq. (3.113) with respect to time:

$$\frac{\partial}{\partial t}\zeta_l(t) = \omega_l \left[-\omega_l \int_{-\infty}^{t} e^{-\omega_l(t-\tau)} \varepsilon(\tau) d\tau + \varepsilon(t) \right] \tag{3.115}$$

The first term in the brackets is equal to $-\zeta_l(t)$ and consequently

$$\frac{\partial}{\partial t}\zeta_l(t) + \omega_l \zeta_l(t) = \omega_l \varepsilon(t), \quad l = 1, \ldots, n \tag{3.116}$$

Equations (3.114) and (3.116) together represent the time-domain stress–strain relations for the viscoelastic continuum with GMB-EK/GZB rheology. The need to know the entire history of strain at each spatial position and evaluate the convolutory integral at each time is replaced by using additional functional variables that can be obtained by solving the additional differential equations (3.116).

Having the relation for stress is sufficient for the displacement–stress formulation and for developing the displacement formulation. We should also consider the velocity–stress formulation.

Temporal differentiation of Eqs. (3.114) and (3.116) gives

$$\frac{\partial}{\partial t}\sigma(t) = M_U \frac{\partial}{\partial t}\varepsilon(t) - \sum_{l=1}^{n} M_l \xi_l(t) \tag{3.117}$$

$$\frac{\partial}{\partial t}\xi_l(t) + \omega_l \xi_l(t) = \omega_l \frac{\partial}{\partial t}\varepsilon(t), \quad l = 1, \ldots, n \tag{3.118}$$

with

$$\xi_l(t) = \frac{\partial}{\partial t}\zeta_l(t), \quad l = 1, \ldots, n \tag{3.119}$$

Equations (3.112), (3.114) and (3.117) clearly decompose the whole stress into elastic and anelastic parts. The elastic part is proportional to the unrelaxed modulus M_U that corresponds to the elastic modulus in a perfectly elastic continuum. The anelastic part is determined by moduli M_l and anelastic functions $\zeta_l(t)$. We need to know how to find parameters of GMB-EK/GZB in order to fit or approximate the measured or desired $Q(\omega)$.

As mentioned in the introduction to this chapter, for many years two parallel sets of publications and algorithms were developed for the GMB-EK or GZB models. We show here equations equivalent to those presented by Robertsson *et al.* (1994) for GZB. Using Eqs. (3.89), (3.8), (3.5), (3.86) and (3.87) we can obtain the stress–strain relation

$$\frac{\partial}{\partial t}\sigma(t) = M_U \frac{\partial}{\partial t}\varepsilon(t) - \sum_{l=1}^{n} r_l(t) \tag{3.120}$$

and relaxation functions

$$r_l(t) = \frac{M_{Rl}}{\tau_{\sigma l}} \left(1 - \frac{\tau_{\varepsilon l}}{\tau_{\sigma l}}\right) \int_{-\infty}^{t} \frac{\partial}{\partial t} \varepsilon(\tau) \exp\left[-(t - \tau)/\tau_{\sigma l}\right] d\tau, \quad l = 1, \ldots, n \quad (3.121)$$

$$\dot{r}_l(t) + \frac{1}{\tau_{\sigma l}} r_l(t) = \frac{M_{Rl}}{\tau_{\sigma l}} \left(1 - \frac{\tau_{\varepsilon l}}{\tau_{\sigma l}}\right) \frac{\partial}{\partial t} \varepsilon(t), \quad l = 1, \ldots, n \quad (3.122)$$

3.3.11 Anelastic coefficients and unrelaxed modulus

We can define anelastic coefficients

$$Y_l = \frac{M_l}{M_U}; \quad l = 1, \ldots, n \quad (3.123)$$

(Do not mix these up with the lower-case $y_l = M_l/M_R$; $l = 1, \ldots, n$, used by Emmerich and Korn, 1987.) The stress–strain relations (3.114) and (3.117) become

$$\sigma(t) = M_U \left[\varepsilon(t) - \sum_{l=1}^{n} Y_l \zeta_l(t)\right] \quad (3.124)$$

$$\frac{\partial}{\partial t} \sigma(t) = M_U \left[\frac{\partial}{\partial t} \varepsilon(t) - \sum_{l=1}^{n} Y_l \xi_l(t)\right] \quad (3.125)$$

and Eqs. (3.116) and (3.118) remain unchanged. The viscoelastic and relaxed moduli are

$$M(\omega) = M_U \left[1 - \sum_{l=1}^{n} Y_l \frac{\omega_l}{\omega_l + i\omega}\right] \quad (3.126)$$

$$M_R = M_U \left(1 - \sum_{l=1}^{n} Y_l\right) \quad (3.127)$$

Note that $M_U \sum_{l=1}^{n} Y_l$ represents the modulus defect (or relaxation of modulus).

The attenuation corresponding to $M(\omega)$ given by Eq. (3.126) is quantified by

$$\frac{1}{Q(\omega)} = \frac{M_{\text{imag}}(\omega)}{M_{\text{real}}(\omega)} = \frac{\sum_{l=1}^{n} Y_l \dfrac{\omega_l \omega}{\omega_l^2 + \omega^2}}{1 - \sum_{l=1}^{n} Y_l \dfrac{\omega_l^2}{\omega_l^2 + \omega^2}} \quad (3.128)$$

The equation can be rewritten as

$$Q^{-1}(\omega) = \sum_{l=1}^{n} \frac{\omega_l \omega + \omega_l^2 Q^{-1}(\omega)}{\omega_l^2 + \omega^2} Y_l \quad (3.129)$$

Assume that values of $Q(\omega)$ in a frequency range of interest are known – they are measured or estimated. We can choose the number and values of the characteristic frequencies ω_l in order to reasonably cover the frequency range of interest. (Frequencies ω_l are the same for the whole computational domain.) Considering, for instance, Q values at frequencies $\tilde{\omega}_k$, a system of equations (3.129), one equation for each $Q(\tilde{\omega}_k)$, is obtained. The system can be

solved for the anelastic coefficients Y_l using the least-square method if number of frequencies $\tilde{\omega}_k$ is larger than number of frequencies ω_l.

Emmerich and Korn (1987) demonstrated that a sufficiently accurate approximation to nearly constant $Q(\omega)$ is obtained if frequencies ω_l cover the frequency range of interest logarithmically equidistantly. One possibility is to consider Q values at $2n - 1$ frequencies $\tilde{\omega}_k$, and $\omega_1 = \tilde{\omega}_1, \omega_2 = \tilde{\omega}_3, \ldots, \omega_n = \tilde{\omega}_{2n-1}$. Emmerich and Korn (1987) showed that $n = 3$ is sufficient for the frequency range $[\omega_{\min}, 100\omega_{\min}]$. A simple possible choice is $\tilde{\omega}_1 = \omega_{\min}$. A more detailed discussion of the frequency range and its sampling by frequencies $\tilde{\omega}_k$ can be found in the article by Graves and Day (2003; Eqs. 13 and 14). For an efficient and accurate determination of the parameters of the GMB-EK see Liu and Archuleta (2006).

If the phase velocity at a certain reference frequency ω_{ref}, that is $c\left(\omega_{ref}\right)$, is known from measurements, the unrelaxed modulus M_U can be determined from the value of $c\left(\omega_{ref}\right)$ and the viscoelastic modulus. Recall that

$$\frac{1}{c(\omega)} = \mathrm{Re}\left\{\left(\frac{M(\omega)}{\rho}\right)^{-1/2}\right\} \tag{3.130}$$

From Eqs. (3.126) and (3.130) we obtain (Moczo *et al.* 1997)

$$M_U = \rho c^2\left(\omega_{ref}\right)\frac{R + \Theta_1}{2R^2} \tag{3.131}$$

where

$$R = \left(\Theta_1^2 + \Theta_2^2\right)^{1/2},$$

$$\Theta_1 = 1 - \sum_{l=1}^{n} Y_l \frac{\omega_l^2}{\omega_l^2 + \omega_{ref}^2}, \quad \Theta_2 = \sum_{l=1}^{n} Y_l \frac{\omega_l \omega_{ref}}{\omega_l^2 + \omega_{ref}^2} \tag{3.132}$$

If we know $Q(\omega)$ and $c(\omega_{ref})$ from measurements, and if we assume viscoelastic rheology of GMB-EK/GZB, we can determine the parameters of the viscoelastic stress–strain relation using Eqs. (3.129) and (3.131) for a chosen set of frequencies ω_l reasonably covering the frequency range of interest.

3.3.12 *Attenuation and phase velocity in GMB-EK/GZB continuum*

In Fig. 3.8 we illustrate the attenuation and phase velocity for S waves, $Q^{-1}(\omega)$ and $c(\omega)$, obtained using the GMB-EK/GZB rheology assuming the exact constant $Q(\omega) = 20$ and the exact phase velocity $c(\omega_{ref}) = 200$ m/s specified at the reference frequency $\omega_{ref} = 2\pi 1$. Three relaxation frequencies are assumed: $\omega_1 = 2\pi 0.04, \omega_2 = 2\pi 0.4, \omega_3 = 2\pi 4$ in order to sufficiently accurately approximate the attenuation in the frequency range $[0.04, 4]$ Hz. This approximation was used in the modelling of seismic motion in the sedimentary Mygdonian basin near Thessaloniki, Greece, in the E2VP (EuroSeistest Verification and Validation Project; see also Chapter 19).
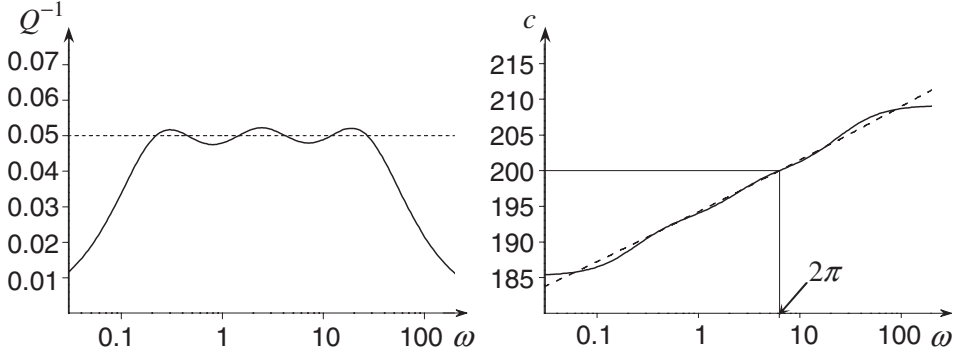
Figure 3.8 Left: $Q^{-1}(\omega)$ exact (dashed) and approximated (solid). The approximation is obtained for three relaxation frequencies $\omega_1 = 2\pi 0.04$, $\omega_2 = 2\pi 0.4$, $\omega_3 = 2\pi 4$ and constant $Q(\omega) = 20$. Right: $c(\omega)$ exact (dashed) and approximated (solid) for $c(\omega_{ref}) = 200$ m/s; $\omega_{ref} = 2\pi 1$.

3.3.13 Stress–strain relation in 3D

So far we have considered the 1D problem for simplicity. In the 3D elastic continuum, two independent elastic moduli are always necessary in order to describe both P- and S-wave propagation. Recall the stress–strain relation for a perfectly elastic isotropic continuum, Hooke's law, in the form of Eq. (2.19):

$$\sigma_{ij} = \kappa \varepsilon_{kk} \delta_{ij} + 2\mu \left(\varepsilon_{ij} - \tfrac{1}{3} \varepsilon_{kk} \delta_{ij} \right) \tag{3.133}$$

If we assume a viscoelastic medium in 3D with the rheology of GMB-EK/GZB instead of the perfectly elastic medium described by Eq. (3.133), we need two independent GMB-EK/GZB bodies: one for the bulk modulus κ and one for the shear modulus μ. Consequently, the stress–strain relation in 3D is

$$\begin{aligned} \sigma_{ij} = {}& \kappa \varepsilon_{kk} \delta_{ij} + 2\mu \left(\varepsilon_{ij} - \tfrac{1}{3} \varepsilon_{kk} \delta_{ij} \right) \\ & - \sum_{l=1}^{n} \left[Y_l^{\kappa} \kappa \zeta_l^{kk} \delta_{ij} + 2 Y_l^{\mu} \mu \left(\zeta_l^{ij} - \tfrac{1}{3} \zeta_l^{kk} \delta_{ij} \right) \right] \end{aligned} \tag{3.134}$$

The anelastic functions are solutions of the differential equations

$$\frac{\partial}{\partial t} \zeta_l^{ij}(t) + \omega_l \zeta_l^{ij}(t) = \omega_l \varepsilon_{ij}(t), \quad l = 1, \dots, n \tag{3.135}$$

The equal-index summation convention applies to spatial index k but does not apply to subscript l. For n characteristic frequencies ω_l we have n anelastic coefficients Y_l^{κ}, and n anelastic coefficients Y_l^{μ}. For each of six independent strain-tensor components ε_{ij} we have n material-independent anelastic functions ζ_l^{ij}. Thus, compared to the perfectly elastic medium we need $8n$ more quantities – $2n$ anelastic coefficients (material parameters) and $6n$ anelastic functions (additional functional variables).

In the case of the velocity–stress formulation, Eqs. (3.134) and (3.135) are replaced by

$$\frac{\partial}{\partial t}\sigma_{ij} = \kappa \frac{\partial}{\partial t}\varepsilon_{kk}\delta_{ij} + 2\mu\left(\frac{\partial}{\partial t}\varepsilon_{ij} - \frac{1}{3}\frac{\partial}{\partial t}\varepsilon_{kk}\delta_{ij}\right)$$
$$- \sum_{l=1}^{n}\left[Y_l^{\kappa}\kappa\xi_l^{kk}\delta_{ij} + 2Y_l^{\mu}\mu\left(\xi_l^{ij} - \frac{1}{3}\xi_l^{kk}\delta_{ij}\right)\right] \tag{3.136}$$

$$\frac{\partial}{\partial t}\xi_l^{ij}(t) + \omega_l\xi_l^{ij}(t) = \omega_l\frac{\partial}{\partial t}\varepsilon_{ij}(t), \quad l = 1,\ldots,n \tag{3.137}$$

Assume that we know the quality factors for P and S waves, that is $Q_\alpha(\omega)$ and $Q_\beta(\omega)$. Here α and β are the P-wave and S-wave speeds, respectively:

$$\alpha = \left[\left(\kappa + \frac{4}{3}\mu\right)/\rho\right]^{1/2}, \quad \beta = [\mu/\rho]^{1/2} \tag{3.138}$$

The anelastic functions corresponding to $Q_\alpha(\omega)$ and $Q_\beta(\omega)$ are Y_l^{α} and Y_l^{β}. They are obtained by solving the system of equations

$$Q_\gamma^{-1}(\tilde{\omega}_k) = \sum_{l=1}^{n}\frac{\omega_l\tilde{\omega}_k + \omega_l^2 Q_\gamma^{-1}(\tilde{\omega}_k)}{\omega_l^2 + \tilde{\omega}_k^2}Y_l^{\gamma}; \quad k = 1,\ldots,2n-1; \quad \gamma \in \{\alpha,\beta\} \tag{3.139}$$

using the least-square method. The anelastic coefficients Y_l^{κ} and Y_l^{μ} are obtained from

$$Y_l^{\kappa} = \left(\alpha^2 Y_l^{\alpha} - \frac{4}{3}\beta^2 Y_l^{\beta}\right)\Big/\left(\alpha^2 - \frac{4}{3}\beta^2\right), \quad Y_l^{\mu} = Y_l^{\beta}, \quad l = 1,\ldots,n \tag{3.140}$$

In the case of using moduli λ and μ instead of κ and μ we have

$$\frac{\partial}{\partial t}\sigma_{ij} = \lambda\frac{\partial}{\partial t}\varepsilon_{kk}\delta_{ij} + 2\mu\frac{\partial}{\partial t}\varepsilon_{ij}$$
$$- \sum_{l=1}^{n}\left[Y_l^{\lambda}\lambda\xi_l^{kk}\delta_{ij} + 2Y_l^{\mu}\mu\xi_l^{ij}\right] \tag{3.141}$$

instead of Eq. (3.136). The anelastic coefficients Y_l^{λ} are obtained from

$$Y_l^{\lambda} = \left(\alpha^2 Y_l^{\alpha} - 2\beta^2 Y_l^{\beta}\right)\Big/\left(\alpha^2 - 2\beta^2\right), \quad l = 1,\ldots,n \tag{3.142}$$

Given the theory presented, we are now ready to address implementation of viscoelastic rheology in the FD schemes.

3.4 Elastoplastic continuum

Figure 3.9 shows hysteresis loops reconstructed by Kausel and Assimaki (2002) from the strain time histories for the 1995 Kobe earthquake record using Masing's concept (see Subsection 3.4.2). The hysteresis loops very clearly illustrate the strong nonlinear effects induced in the surface soil during the earthquake.

The basic terms of the hysteresis loop, that is the backbone curve, loading, unloading and reversal point, are illustrated in Fig. 3.10. Note that strain appears on the horizontal axis
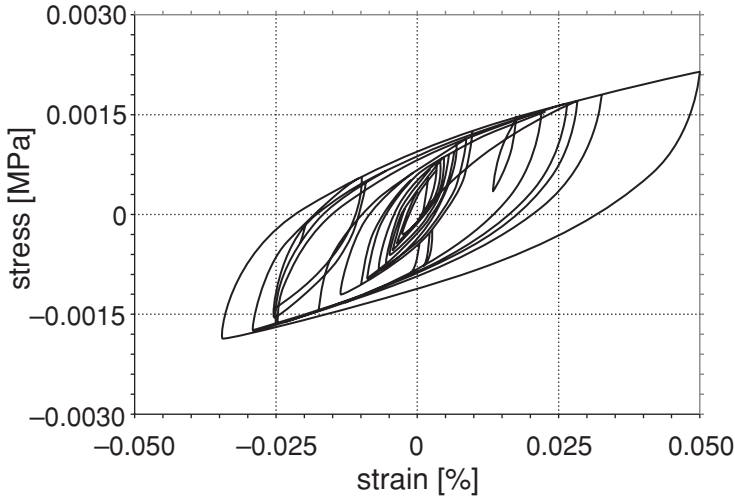
Figure 3.9 The hysteresis loops obtained by Kausel and Assimaki (2002) from the strain time histories for the 1995 Kobe earthquake record. The stress values are scaled by the low-strain elastic shear modulus and the strain values are scaled to the maximum strain of 0.05.
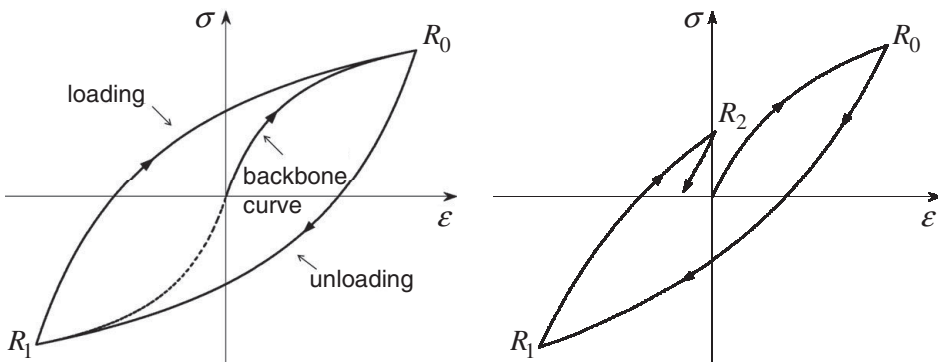
Figure 3.10 Left: a symmetric hysteresis loop corresponding to symmetric loading and unloading. Right: an asymmetric loop due to asymmetric loading and unloading.

and stress on the vertical axis. This corresponds to the fact that in the numerical simulation stress is calculated from strain.

3.4.1 Simplest elastoplastic bodies

Analogously with the viscoelastic models, the simplest models combining elastic and plastic behaviour can be obtained by serial or parallel connection of a Hooke solid (we will also use the term 'spring' or symbol H) and a Saint-Venant body (StV). The rules
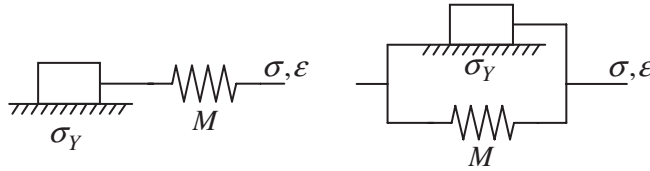
Figure 3.11 Left: H-s-StV – serial connection of a Hooke solid (spring) and a Saint-Venant body. Right: H-p-StV – parallel connection of a Hooke solid and a Saint-Venant body.
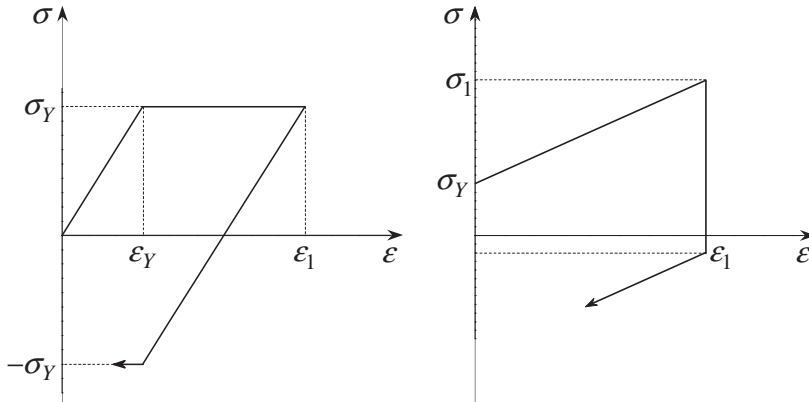
Figure 3.12 Left: stress–strain diagram of H-s-StV. Right: stress–strain diagram of H-p-StV.

for combining rheological models in Section 3.2 are also assumed for the elastoplastic models.

Serial connection of a Hooke solid and a Saint-Venant body: H-s-StV The rheological model is shown in Fig. 3.11(left). Stresses are equal, strains are additive:

$$\sigma = \sigma_{\mathrm{H}} = \sigma_{\mathrm{StV}}, \quad \varepsilon = \varepsilon_{\mathrm{H}} + \varepsilon_{\mathrm{StV}} \tag{3.143}$$

Consider, for instance, pulling to the right. The following development is illustrated by the stress–strain diagram in Fig. 3.12(left). If the applied stress is smaller than the yield stress σ_Y of StV, only the spring deforms (extends) – strain linearly increases with stress. When the applied stress reaches a value of σ_Y, StV starts deforming (moving to the right) and the spring stops deforming. If the loading stress does not decrease below σ_Y, the strain increases (at a constant $\sigma = \sigma_Y$) to a value that depends only on the time duration of the stress application and the strain of the spring is equal to ε_Y. With the spring inactive, the strain of StV increases until the value of the applied stress starts decreasing. We denote the total strain reached by ε_1. As soon as the applied stress starts decreasing, StV stops deforming (its strain is $\varepsilon_1 - \varepsilon_Y$) and the spring is activated. With StV inactive, the strain of the spring linearly decreases. Consequently, the total strain also decreases linearly. When the stress decreases down to zero, the spring has no stress and no strain. The total strain is

equal to the strain of StV, that is, $\varepsilon_1 - \varepsilon_Y$. If the stress further decreases, the spring starts shrinking. When the stress reaches a value of $-\sigma_Y$, StV starts deforming – moving to the left. At the same time, the spring stops deforming because StV is active at the constant stress $-\sigma_Y$. It is obvious that in H-s-StV the episodes of active spring (linear segments of the stress–strain diagram) may alternate with episodes of active StV (horizontal segments). It is also clear that H-s-StV does not exhibit plastic strain hardening. In this aspect it does not differ from StV itself, which is a mechanical model for the behaviour of an ideal or pure plastic material (see Subsection 3.1.3).

Parallel connection of Hooke solid and Saint-Venant body: H-p-StV The rheological model is shown in Fig. 3.11(right). Stresses are additive, strains are equal:

$$\sigma = \sigma_H + \sigma_{StV}, \quad \varepsilon = \varepsilon_H = \varepsilon_{StV} \tag{3.144}$$

Consider again pulling to the right. The following development is illustrated by the stress–strain diagram in Fig. 3.12(right). Because the strain at H, the strain at StV and the total strain are equal at any time, the body is inactive until the stress at StV reaches the yield stress σ_Y. After the stress reaches a value of σ_Y, both H and StV start deforming simultaneously. The deformation is controlled by H. Because StV can deform at the constant stress σ_Y, the strain is proportional to the difference $\sigma - \sigma_Y$ acting at H. (Note that because both H and StV are active simultaneously, H-p-StV exhibits plastic strain hardening.) Assume that after some time the stress reaches a value of σ_1. The corresponding strain is $(\sigma_1 - \sigma_Y)/M$, the stress at H is $\sigma_1 - \sigma_Y$, and the stress at StV is σ_Y. Assume that at this moment the stress starts decreasing. This instantaneously stops deformation of both H and StV. The decrease of the total stress reduces stress only at StV because at inactive H neither strain nor stress can change. Consequently, both bodies will remain inactive until stress at StV reaches the yield value of $-\sigma_Y$. The total stress at that moment is $\sigma_1 - 2\sigma_Y$. Note that during the episode with both bodies inactive the strain was constant although the stress was decreasing. As soon as both bodies are activated, the strain linearly decreases with decreasing stress. It is obvious that in H-p-StV the episodes with both bodies active (linear segments of the stress–strain diagram) may alternate with episodes with both bodies inactive (vertical segments in the stress–strain diagram).

Partial conclusion We can see the consequence and drawback of the serial connection of H and StV: after the applied stress reaches the value of the yield stress, strain increases at this stress until the applied stress starts decreasing. In other words, the model is not capable of plastic strain hardening. The consequence and drawback of the parallel connection of H and StV is that the model behaves as a rigid solid before the applied stress reaches the yield stress. The main advantage of the parallel connection is that both H and StV are active at the same time.

An indirect indication from the behaviour of both connections is to combine the serial and parallel connections. There are several possibilities. For example, if we connect H-p-StV in series with a spring, we add the capability of an instantaneous elastic response to the behaviour of H-p-StV. As a consequence, we remove the vertical segments in the

stress–strain diagram. Such a connection is used in the sophisticated and flexible model developed by Iwan (1967).

3.4.2 Iwan elastoplastic model for hysteretic stress–strain behaviour

3.4.2.1 Preliminary considerations

Serial connection of springs Consider first $N + 1$ springs connected in series. Let M_k be the elastic modulus of the k-th spring. Obviously, application of stress to a body consisting of springs connected in series instantaneously and simultaneously activates all the springs. Consider some reference state of stress and strain at some time:

$$\sigma^r = \sigma^r_{\mathrm{H},k}, \quad \varepsilon^r = \sum_{k=0}^{N} \varepsilon^r_{\mathrm{H},k} = \sum_{k=0}^{N} \frac{\sigma^r}{M_k} \tag{3.145}$$

At some later time, due to an increment $\Delta\sigma$ in stress, the stress and strain are

$$\sigma = \sigma^r + \Delta\sigma$$

$$\varepsilon = \varepsilon^r + \Delta\varepsilon = \varepsilon^r + \sum_{k=0}^{N} \frac{\Delta\sigma}{M_k} = \varepsilon^r + (\sigma - \sigma^r) \sum_{k=0}^{N} \frac{1}{M_k} \tag{3.146}$$

Serial connection of the H-p-StV bodies Consider now $N + 1$ H-p-StV bodies connected in series. Let M_k be an elastic modulus of the k-th spring and $\sigma_{Y,k}$ a yield stress of the k-th StV. Without loss of generality consider

$$\sigma_{Y,0} < \sigma_{Y,1} < \cdots < \sigma_{Y,N} \tag{3.147}$$

At each $(\mathrm{H}–\mathrm{p}–\mathrm{StV})_k$ at any time,

$$\sigma_k = \sigma_{\mathrm{H},k} + \sigma_{\mathrm{StV},k} = \sigma, \quad \varepsilon_k = \varepsilon_{\mathrm{H},k} = \varepsilon_{\mathrm{StV},k} \tag{3.148}$$

In general, we are interested in cyclic variation of the applied stress: not only the size but also the direction of the stress varies. The applied stress can reverse (change its direction) at any time. The application of stress in the positive direction may be called loading, the application of stress in the negative direction may be called unloading (see Fig. 3.10, left). A point at which the stress changes direction is a reversal point. Note that at each reversal point all elements of the model are deactivated. A curve connecting two successive reversal points is called a branch.

Contrary to the body consisting of springs connected in series, application of stress to a serial connection of several H-p-StV bodies does not necessarily activate one or more H–p–StV bodies. $(\mathrm{H}–\mathrm{p}–\mathrm{StV})_k$ is activated in the positive direction when $\sigma_{\mathrm{StV},k} = \sigma_{Y,k}$ and in the negative direction when $\sigma_{\mathrm{StV},k} = -\sigma_{Y,k}$. The total stress at which $(\mathrm{H}–\mathrm{p}–\mathrm{StV})_k$ is activated may be called the activating stress. It follows from the first of Eqs. (3.148) that the activating stresses for the two directions can be defined as

$$\vec{\sigma}_k^A \equiv \sigma_{\mathrm{H},k} + \sigma_{Y,k}, \quad \overleftarrow{\sigma}_k^A \equiv \sigma_{\mathrm{H},k} - \sigma_{Y,k} \tag{3.149}$$

Note that the orientation of the arrow indicates the direction of the applied stress.
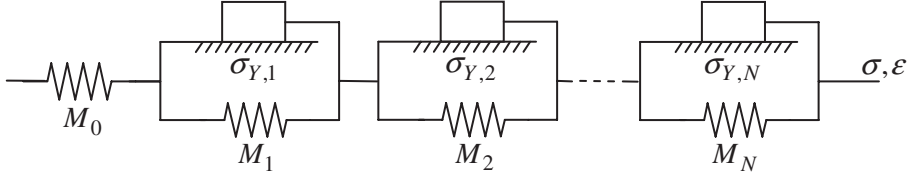
Figure 3.13 Iwan elastoplastic model.

Consider some state of stress and strain as a reversal point, and denote it by $[\sigma^R, \varepsilon^R]$. The first of Eqs. (3.148) and Eqs. (3.149) imply

$$\vec{\sigma}_k^A = \sigma^R - \sigma_{\text{StV},k}^R + \sigma_{Y,k}, \quad \overleftarrow{\sigma}_k^A = \sigma^R - \sigma_{\text{StV},k}^R - \sigma_{Y,k} \tag{3.150}$$

where the upper index R indicates the reversal point.

3.4.2.2 Iwan model

Assume that $\sigma_{Y,0} = 0$ in the above serial connection of the H-p-StV bodies. In other words, (H–p–StV)$_0$ reduces to a spring H$_0$. Consequently, we have a single spring H$_0$ connected in series with the serial connection of (H–p–StV)$_k$; $k = 1, \ldots, N$. This is the Iwan model (Fig. 3.13). The reduction of (H–p–StV)$_0$ to a single spring incorporates the capability of an elastic response.

Consider an initial state with $\sigma = 0$ and $\varepsilon = 0$. The following development is illustrated in Fig. 3.14. Assume application of stress σ in the positive direction (to the right) and

$$\sigma_{Y,K_0} \leq \sigma < \sigma_{Y,K_0+1} \tag{3.151}$$

This means that K_0 H-p-StV bodies are activated. H$_0$ and each of (H–p–StV)$_k$; $k = 1, \ldots, K_0$ contribute to the total strain proportionally to the difference $\sigma - \sigma_{Y,k}$ and inversely proportionally to M_k:

$$\varepsilon = \sum_{k=0}^{K_0} \frac{\sigma - \sigma_{Y,k}}{M_k} \tag{3.152}$$

Note that for conciseness we formally included also the zero-valued $\sigma_{Y,0}$.

Assume reversal at the state characterized by Eqs. (3.151) and (3.152), and denote the stress and strain at that state by σ^{R_0} and ε^{R_0}:

$$\varepsilon^{R_0} = \sum_{k=0}^{K_0} \frac{\sigma^{R_0} - \sigma_{Y,k}}{M_k} \tag{3.153}$$

(The stress–strain curve connecting the initial state $[\sigma = 0, \varepsilon = 0]$ with the reversal point $[\sigma^{R_0}, \varepsilon^{R_0}]$ is part of the backbone curve.)

We have to realize now that the next reversal of the stress may occur even before any of the H-p-StV bodies are activated during unloading. It may also happen that only some of the H-p-StV bodies activated during loading are activated during the unloading. For all possible developments we need to find the activating stresses in both directions.
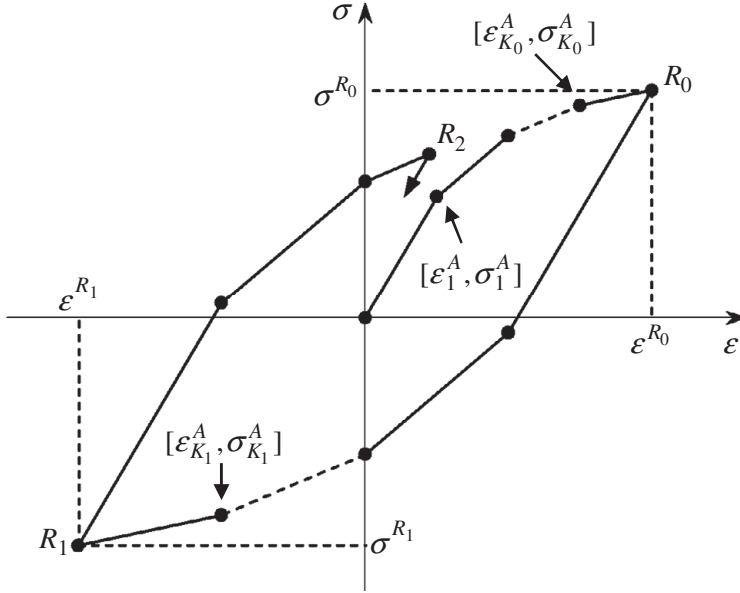
Figure 3.14 Development of stress σ and strain ε in the Iwan elastoplastic model. $[\vec{\varepsilon}_l^A, \vec{\sigma}_l^A]$ denotes the strain–stress point at which the l-th H–p–StV activates. R_j denotes the j-th reversal point.

At the time of reversal, $\sigma_{Y,K_0} \leq \sigma^{R_0} < \sigma_{Y,K_0+1}$ and

$$\sigma_{\text{StV},k}^{R_0} = \sigma_{Y,k}; \quad k = 0, \ldots, K_0, \quad \sigma_{\text{StV},k}^{R_0} = \sigma^{R_0}; \quad k = K_0 + 1, \ldots, N \quad (3.154)$$

Using Eqs. (3.154) and (3.150) we obtain activating stresses after the reversal point $\left[\sigma^{R_0}, \varepsilon^{R_0}\right]$:

$$\overset{\leftarrow}{\sigma}_k^A = \sigma^{R_0} - 2\sigma_{Y,k}, \quad \overset{\rightarrow}{\sigma}_k^A = \sigma^{R_0}; \quad k = 0, \ldots, K_0$$

$$\overset{\leftarrow}{\sigma}_k^A = -\sigma_{Y,k}, \quad \overset{\rightarrow}{\sigma}_k^A = \sigma_{Y,k}; \quad k = K_0 + 1, \ldots, N \quad (3.155)$$

Assume that after the change of stress direction at the reversal point $[\sigma^{R_0}, \varepsilon^{R_0}]$, the stress activates K_1 bodies and the model reaches a state characterized by values $[\sigma, \varepsilon]$. It follows from Eqs. (3.151) and (3.155) that

$$\overset{\leftarrow}{\sigma}_{K_1+1}^A < \sigma \leq \overset{\leftarrow}{\sigma}_{K_1}^A \quad (3.156)$$

The total strain is then

$$\varepsilon = \varepsilon^{R_0} + \Delta\varepsilon = \varepsilon^{R_0} + \sum_{k=0}^{K_1} \frac{\sigma - \overset{\leftarrow}{\sigma}_k^A}{M_k} \quad (3.157)$$

because the increment $\Delta\varepsilon$ in the total strain is a sum of increments of strains at all activated springs.

Consider now the state reached as a reversal point $[\sigma^{R_1}, \varepsilon^{R_1}]$:

$$\varepsilon^{R_1} = \varepsilon^{R_0} + \sum_{k=0}^{K_1} \frac{\sigma^{R_1} - \overleftarrow{\sigma}_k^A}{M_k} \tag{3.158}$$

As mentioned before, at the reversal point all elements of the model are deactivated. Therefore, we need to find activating stresses after the reversal point R_1. Recalling Eqs. (3.150) and distinguishing two possible cases we obtain

$$K_1 < K_0$$

$$k = 0, \ldots, K_1 \qquad : \quad \sigma_{\text{StV},k}^{R_1} = -\sigma_{Y,k}$$
$$\overrightarrow{\sigma}_k^A = \sigma^{R_1} + 2\sigma_{Y,k}, \ \ \overleftarrow{\sigma}_k^A = \sigma^{R_1}$$

$$k = K_1 + 1, \ldots, K_0 \ : \quad \sigma_{\text{StV},k}^{R_1} = \sigma_{Y,k} - (\sigma^{R_0} - \sigma^{R_1})$$
$$\overrightarrow{\sigma}_k^A = \sigma^{R_0}, \ \ \overleftarrow{\sigma}_k^A = \sigma^{R_0} - 2\sigma_{Y,k} \tag{3.159}$$

$$k = K_0 + 1, \ldots, N \quad : \quad \sigma_{\text{StV},k}^{R_1} = \sigma^{R_1}$$
$$\overrightarrow{\sigma}_k^A = \sigma_{Y,k}, \ \ \overleftarrow{\sigma}_k^A = -\sigma_{Y,k}$$

$$K_1 \geq K_0$$

$$k = 0, \ldots, K_0 \qquad : \quad \sigma_{\text{StV},k}^{R_1} = -\sigma_{Y,k}$$
$$\overrightarrow{\sigma}_k^A = \sigma^{R_1} + 2\sigma_{Y,k}, \quad \overleftarrow{\sigma}_k^A = \sigma^{R_1}$$

$$k = K_0 + 1, \ldots, K_1 \ : \quad \sigma_{\text{StV},k}^{R_1} = -\sigma_{Y,k}$$
$$\overrightarrow{\sigma}_k^A = \sigma^{R_1} + 2\sigma_{Y,k}, \quad \overleftarrow{\sigma}_k^A = \sigma^{R_1} \tag{3.160}$$

$$k = K_1 + 1, \ldots, N \quad : \quad \sigma_{\text{StV},k}^{R_1} = \sigma^{R_1}$$
$$\overrightarrow{\sigma}_k^A = \sigma_{Y,k}, \quad \overleftarrow{\sigma}_k^A = -\sigma_{Y,k}$$

Compare now the activating stresses after the reversal point R_1 with those after point R_0. We can see different activating stresses only for those H-p-StV that were activated between R_0 and R_1. (Note that it was not necessary to calculate activating stresses for H-p-StV not activated between R_0 and R_1.)

Assume that after the change of stress direction at the reversal point $[\sigma^{R_1}, \varepsilon^{R_1}]$, the stress activates K_2 bodies and the model reaches a state characterized by values $[\sigma, \varepsilon]$ and

$$\overrightarrow{\sigma}_{K_2}^A \leq \sigma < \overrightarrow{\sigma}_{K_2+1}^A \tag{3.161}$$

The total strain is then

$$\varepsilon = \varepsilon^{R_1} + \Delta\varepsilon = \varepsilon^{R_1} + \sum_{k=0}^{K_2} \frac{\sigma - \overrightarrow{\sigma}_k^A}{M_k} \tag{3.162}$$

We have shown the calculation of strain for the first loading along the backbone curve, the first unloading, and the second loading. It would be easy to continue if the state reached becomes a reversal point.

Table 3.4 *Calculation of activating stresses at reversal points and strain at any state of the system*

Original activating stresses at the initial state $\left[\, \sigma = 0,\, \varepsilon = 0 \,\right]$	
$\vec{\sigma}_k^A = \sigma_{Y,k}\quad,\quad \bar{\sigma}_k^A = -\sigma_{Y,k}\qquad$ for $\quad k = 0,...,N$	
Calculation of the activating stresses	
at reversal from loading to unloading	at reversal from unloading to loading
if $\ \vec{\sigma}_{K_j}^A \ \leq \sigma^{R_j} < \vec{\sigma}_{K_j+1}^A$	if $\ \bar{\sigma}_{K_j+1}^A < \sigma^{R_j} \leq \bar{\sigma}_{K_j}^A$
then	then
for $\ k = 0,...,K_j$	for $\ k = 0,...,K_j$
$\ddot{\sigma}_k^A = \sigma^{R_j} - 2\,\sigma_{Y,k}\quad,\quad \vec{\sigma}_k^A = \sigma^{R_j}$	$\vec{\sigma}_k^A = \sigma^{R_j} + 2\,\sigma_{Y,k}\quad,\quad \vec{\sigma}_k^A = \sigma^{R_j}$
For $\ k = K_j+1,...,N$ the activating stresses remain unchanged. Note that even values of $\ j\ $ (including 0) correspond to loading and odd values of $\ j\ $ correspond to unloading.	
Calculation of strain	
during unloading	during loading
$\varepsilon = \varepsilon^{R_j} + \displaystyle\sum_{k=0}^{K_{j+1}} \frac{\sigma - \bar{\sigma}_k^A}{M_k}$	$\varepsilon = \varepsilon^{R_j} + \displaystyle\sum_{k=0}^{K_{j+1}} \frac{\sigma - \vec{\sigma}_k^A}{M_k}$

General algorithm for calculating strain from stress The analysis performed leads to a general conclusion. Assume the initial state $[\sigma = 0,\, \varepsilon = 0]$ and original activating stresses (model's yield stresses) $\vec{\sigma}_k^A = \sigma_{Y,k},\, \bar{\sigma}_k^A = -\sigma_{Y,k}$. An activating stress for (H–p–StV)$_k$ changes at the reversal point R_j only if (H–p–StV)$_k$ is activated between R_{j-1} and R_j. Calculation of the activating stresses at the reversal points and calculation of the strain at any state of the system is summarized in Table 3.4.

Note an interesting point: considering formally the initial state as a reversal point and $\sigma_{Y,k}$ as the activating stresses we obtain Eq. (3.152).

General algorithm for calculating stress from strain Contrary to the previous paragraph, where we calculated strain from stress, in solving the equation of motion using a numerical scheme we need to update stress from strain at each time level. Therefore, we also summarize the corresponding algorithm.

Consider Eq. (3.162) and $\sigma = \vec{\sigma}_l^A$, $K_2 = l$, and calculate strain for $l = 0, \ldots, K_1$:

$$\vec{\varepsilon}_l^A = \varepsilon^{R_1} + \sum_{k=0}^{l} \frac{\vec{\sigma}_l^A - \vec{\sigma}_k^A}{M_k} \tag{3.163}$$

We denoted the total strain as $\vec{\varepsilon}_l^A$ for a simple reason: Eq. (3.163) gives the total strain in the Iwan model when (H–p–StV)$_l$ is activated between the reversal points R_1 and R_2. Therefore, we may speak about the activating strain. At the reversal point R_1 it is sufficient to update the activating strains only at those H–p–StV that were activated during unloading

Table 3.5 *Calculation of activating strains at reversal points and stress at any state of the system*

Original activating stresses at the initial state $\left[\, \sigma = 0,\, \varepsilon = 0 \,\right]$
$\vec{\sigma}_k^A = \sigma_{Y,k}$, $\bar{\sigma}_k^A = -\sigma_{Y,k}$ for $k = 0,...,N$
Calculation of the activating strains at the initial state $\left[\, \sigma = 0,\, \varepsilon = 0 \,\right]$
$\vec{\varepsilon}_l^A = \sum_{k=0}^{l} \dfrac{\sigma_{Y,l} - \sigma_{Y,k}}{M_k}$, $\bar{\varepsilon}_l^A = \sum_{k=0}^{l} \dfrac{(-\sigma_{Y,l}) - (-\sigma_{Y,k})}{M_k}$ for $l = 0,...,N$

Calculation of the activating stresses and strains

at reversal from loading to unloading	at reversal from unloading to loading
if $\vec{\varepsilon}_{K_j}^A \leq \varepsilon^{R_j} < \vec{\varepsilon}_{K_j+1}^A$ then	if $\bar{\varepsilon}_{K_j+1}^A < \varepsilon^{R_j} \leq \bar{\varepsilon}_{K_j}^A$ then
for $l = 0,...,K_j$	for $l = 0,...,K_j$
$\vec{\sigma}_l^A = \sigma^{R_j}$, $\bar{\sigma}_l^A = \sigma^{R_j} - 2\sigma_{Y,l}$	$\vec{\sigma}_l^A = \sigma^{R_j} + 2\sigma_{Y,l}$, $\bar{\sigma}_l^A = \sigma^{R_j}$
$\vec{\varepsilon}_l^A = \varepsilon^{R_j} + \sum_{k=0}^{l} \dfrac{\vec{\sigma}_l^A - \vec{\sigma}_k^A}{M_k}$	$\bar{\varepsilon}_l^A = \varepsilon^{R_j} + \sum_{k=0}^{l} \dfrac{\bar{\sigma}_l^A - \bar{\sigma}_k^A}{M_k}$

For $k = K_j + 1,...,N$ the activating stresses and strains remain unchanged.

Note that even values of j (including 0) correspond to loading and odd values of j correspond to unloading.

Calculation of stress

during unloading	during loading
if $\bar{\varepsilon}_{K_{j+1}+1}^A < \varepsilon \leq \bar{\varepsilon}_{K_{j+1}}^A$	if $\vec{\varepsilon}_{K_{j+1}}^A \leq \varepsilon < \vec{\varepsilon}_{K_{j+1}+1}^A$
$\sigma = \bar{\sigma}_{K_{j+1}}^A + \dfrac{\varepsilon - \bar{\varepsilon}_{K_{j+1}}^A}{\sum_{k=0}^{K_{j+1}} \dfrac{1}{M_k}}$	$\sigma = \vec{\sigma}_{K_{j+1}}^A + \dfrac{\varepsilon - \vec{\varepsilon}_{K_{j+1}}^A}{\sum_{k=0}^{K_{j+1}} \dfrac{1}{M_k}}$

between R_0 and R_1. (This is analogous to updating activating stresses at the reversal point.) Consider now a condition analogous to condition (3.161):

$$\vec{\varepsilon}_{K_2}^A \leq \varepsilon < \vec{\varepsilon}_{K_2+1}^A \tag{3.164}$$

The total strain in the Iwan model between states $\left[\vec{\varepsilon}_{K_2}^A, \vec{\sigma}_{K_2}^A\right]$ and $\left[\vec{\varepsilon}_{K_2+1}^A, \vec{\sigma}_{K_2+1}^A\right]$ is the same as the strain of K_2 springs connected in series. Consider therefore the second of Eqs. (3.146) and $\left[\varepsilon^r = \vec{\varepsilon}_{K_2}^A, \sigma^r = \vec{\sigma}_{K_2}^A\right]$. Then, assuming condition (3.164), we obtain

$$\sigma = \vec{\sigma}_{K_2}^A + \frac{\varepsilon - \vec{\varepsilon}_{K_2}^A}{\sum_{k=0}^{K_2} \frac{1}{M_k}} \tag{3.165}$$

for the loading stress. Analogously, we could continue with further reversal points and for unloading: Table 3.5 summarizes the relations for calculation of the activating strains and the total stress.

3.4.2.3 Iwan model and Masing rules

The hysteretic relation between stress and strain can also be modelled using several empirical rules. Two first rules were formulated by Masing (1926):
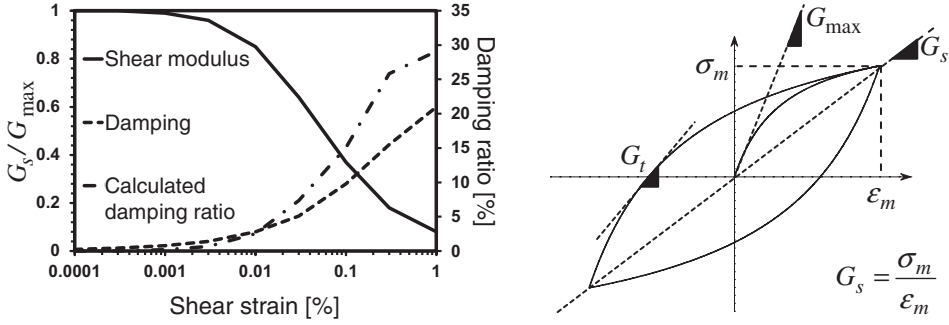
Figure 3.15 Left: modulus reduction curve, calculated and measured damping ratio. Right: secant shear modulus G_s, tangential shear modulus G_t and the elastic modulus $G_{\max}$.

(1) For initial loading, the stress–strain curve follows the backbone curve $\sigma = F_{bb}(\varepsilon)$.

(2) If stress reversal occurs at a point defined by $(\varepsilon^R, \sigma^R)$, the stress–strain curve follows a path given by $\frac{1}{2}(\sigma - \sigma^R) = F_{bb}(\frac{1}{2}(\varepsilon - \varepsilon^R))$. In other words, the unloading and loading curves have the same shape as the backbone curve (with the origin shifted to the reversal point) enlarged by a factor of two.

The two Masing rules are sufficient in the case of cyclic loading between two fixed limits. However, their application in the case of irregular loads gives a curve that is different from the experimentally found curve. Therefore, two more rules were formulated (e.g., Kramer 1996):

(3) If the unloading or reloading curve exceeds the maximum past strain and intersects the backbone curve, it follows the backbone curve until the next stress reversal.

(4) If an unloading or reloading curve crosses an unloading or reloading curve from the previous cycle, the stress–strain curve follows that of the previous cycle.

The four rules are called the extended Masing rules. It is worth noting that the Iwan model is consistent with all four rules, although the third and fourth rules were formulated after Iwan's (1967) article.

3.4.2.4 Determination of parameters for Iwan model

As shown previously, $(H\text{–}p\text{–}StV)_k$ is activated when the loading stress reaches a value of $\sigma_{Y,k}$. Activation of the spring with elastic modulus M_k changes the slope of the stress–strain curve. This means that the shear modulus of the Iwan model changes (it decreases). The tangential shear modulus is defined (Joyner and Chen 1975) as

$$G_t = \frac{\sigma_{Y,k+1} - \sigma_{Y,k}}{\varepsilon_{Y,k+1} - \varepsilon_{Y,k}} = \left(\sum_{i=0}^{k} \frac{1}{M_i} \right)^{-1} \tag{3.166}$$

In practice, the decrease of the shear modulus is characterized by the modulus reduction curve (Fig. 3.15, left) that shows normalized secant shear modulus $G_s/G_{\max}$ as a function of

strain. G_{max} is the elastic modulus and the secant modulus is illustrated in Fig. 3.15(right). Assume, for instance, that the true modulus reduction curve is reasonably piece-wise linearly approximated by a set of $[\varepsilon_i, (G_s/G_{max})_i]$ measured points. Then, see Fig. 3.15,

$$\sigma_{Y,i} = G_s \varepsilon_{Y,i} = (G_s/G_{max})_i \, G_{max} \varepsilon_{Y,i} \tag{3.167}$$

Having determined all yield stresses and corresponding strains, we can iteratively use relation (3.166) to calculate the elastic moduli M_i.

3.4.2.5 Note on damping

Damping, the ratio of the dissipated energy and the maximum strain energy stored in the system, see Eq. (3.69), is an inherent property of the Iwan model (beyond the first elastic part of the backbone curve). For a given strain ε_m the dissipated energy is equal to area of the symmetrical hysteresis loop – see Fig. 3.15(right). The Iwan model has no damping at low strains but its value at high strains could be larger than the measured damping. The first problem can be solved by including linear viscoelasticity, the second problem by changing loading/unloading paths according to specified damping values, as proposed by Muravskii (2005).

The Iwan model, as described in this chapter, is applicable in the case of intermediate strains. If possible, in order to check the validity of the procedure, it is recommended to check the damping corresponding to the maximum strain computed during wave propagation.

3.4.2.6 Concluding remark

In the section on the elastoplastic continuum we introduced only the basics of the nonlinear hysteretic behaviour of soft soil at moderate and large strains. The possibility of hysteretic behaviour considerably complicates numerical prediction of earthquake motion. If the computational domain includes a part with possibly nonlinear behaviour, the numerical scheme should be capable of accounting for such behaviour in order to produce realistic predictions. At present, this is still a nontrivial task for 3D numerical modelling.

We finish this section by mentioning two impressive studies. Gélis and Bonilla (2012) considered elastic, viscoelastic, elastoplastic and viscoelastoplastic rheologies, and investigated the influence of rheology on seismic motion. They concluded that numerical simulations should couple both viscoelasticity (to account for energy dissipation at small strains) and nonlinearity (to account for hysteretic energy dissipation and shear modulus degradation at higher strains) in order to obtain realistic results. Gélis and Bonilla also investigated the effect of the input motion on the development of nonlinear behaviour. For modelling and numerical implementation of nonlinear hysteretic behaviour we also refer to the comprehensive article by Assimaki *et al*. (2008). Both articles refer to other recent studies of nonlinear behaviour.

4

Earthquake source

In this chapter we will focus on seismic radiation as emitted from a rupturing fault in the Earth. On a large scale, due to tectonic loading the stress in the fault area increases until the yield stress of the rock material is reached at some point in the fault zone. Reaching yield stress leads to nonelastic deformation and to release of deformation energy. This increases stress in the vicinity of the point. Reaching the yield stress at the neighbouring points may consequently lead to a chain reaction – rupture propagation. When the rupture propagates fast enough and in a nonsteady way it radiates seismic waves which then propagate away from the fault. Note that seismic waves are radiated only if the rupture propagation speed is a significant fraction of the S-wave speed; slow ruptures do not radiate. Note also that subshear steady-state slip pulses do not radiate, except at their starting and stopping points; radiation from subshear ruptures requires nonsteady slip. Rupture propagates on the fault as long as the stress changes associated with the propagating rupture are large enough for the stress at points in front of the crack tip to reach the yield stress.

The earthquake fault is usually considered a frictional contact. Therefore, friction is the most important physical phenomenon during rupture nucleation and propagation. However, there are many other physical processes that have an impact on the effective friction, e.g., thermal pressurization of pore fluids, flash heating and melting of the material in the fault zone, nonelastic deformation (plasticity, crack formation, gouge formation), as summarized by Bizzarri (2010) and Bizzarri and Cocco (2005), for example. It has been shown that heterogeneous friction parameters (e.g., Ampuero *et al*. 2006, Liu and Lapusta 2008, Tinti *et al*. 2005, 2009), geometrical complexity (e.g., Oglesby and Day 2001, Oglesby *et al*. 2008, Oglesby and Mai 2012) and fault roughness (Dunham *et al*. 2011) may also significantly impact the rupture behaviour. Rupture propagation on faults at the contact of two different materials, the so-called bi-material faults, has also been intensively studied (e.g., Andrews and Ben-Zion 1997, Harris and Day 1997, Ben-Zion and Andrews 1998, Ranjith and Rice 2001, Rubin and Ampuero 2007, Ampuero and Ben-Zion 2008).

We can use a dynamic or kinematic model of the earthquake source. These models differ mainly in how they respect the physics. The temporal and spatial evolution of the slip rate in the dynamic model is calculated by solving an equation of motion together with the friction law, and possibly other physical laws (in order to explicitly include, for instance, pore pressure or temperature). Consequently, the interaction between rupture and wavefield
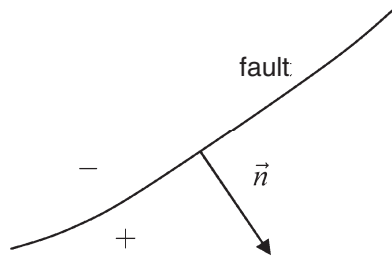
Figure 4.1 Fault surface and the normal vector $\vec{n}$.

is implicitly included. Therefore, we can consider the resulting slip-rate functions in the dynamic model to be physically consistent. On the other hand, the kinematic model is described by the temporal and spatial evolution of the slip rate. The slip-rate evolution is prescribed a priori and is not interacting with the stress changes induced by the rupture propagation. Therefore, the kinematic model may be inconsistent with known friction laws (this depends on how the slip-rate evolution was obtained). It is to be noted, however, that large uncertainties remain about the physics of fault friction at natural scales. In the next sections we will describe the models in more detail.

In order to use a source model in a numerical simulation we need to know values of the model parameters. The parameter set will be different for different types of source model but, in general, the parameters should be estimated from the observations. Different approaches are used to derive parameters of the point, finite-fault kinematic and dynamic source models from observations, although some of these parameters are poorly constrained (e.g., Ide 2009, Guatteri and Spudich 2000). However, this represents a very wide topic (which does not fit into the content of this book) and we refer the reader to, e.g., Dziewonski *et al.* (1981), Sipkin (1982), Langston *et al.* (1982), Olson and Apsel (1982), Hartzell and Heaton (1983), Peyrat *et al.* (2001), Liu and Archuleta (2004), Monelli *et al.* (2009), Festa and Zollo (2012), Di Carli *et al.* (2010).

4.1 Dynamic model of an earthquake source

In many seismological problems an earthquake fault may be represented by a surface embedded in a heterogeneous elastic or viscoelastic pre-stressed medium. Nonzero initial stress is due to tectonic loading and residual stress after previous earthquakes on the fault. An earthquake source itself may be modelled as spontaneous rupture propagation along the fault. The rupture generates seismic waves, which then propagate from the fault into the embedding medium. Inside the rupture, displacement and particle-velocity vectors are discontinuous across the fault. At the same time, traction is continuous. Let $\vec{n}(\vec{x})$ be a unit normal vector to the fault surface pointing from the '−' to the '+' side of the surface (Fig. 4.1).

Then slip, that is, discontinuity in displacement vector across the fault, can be defined as

$$\vec{s}(\vec{x}, t) \equiv \vec{u}(\vec{x}^+, t) - \vec{u}(\vec{x}^-, t) \tag{4.1}$$

Its time derivative, a slip rate, that is, discontinuity in the particle-velocity vector across the fault is then

$$\dot{\vec{s}}(\vec{x}, t) \equiv \vec{v}(\vec{x}^+, t) - \vec{v}(\vec{x}^-, t) \tag{4.2}$$

For slip and slip rate we use the notation of Day and his colleagues (e.g., Day and Ely 2002, Day *et al*. 2005, Dalguer and Day 2006, 2007).

The total traction on the fault can be divided into two parts:

$$\vec{T}(\vec{n}; \vec{x}, t) = \vec{T}^0(\vec{n}; \vec{x}) + \Delta\vec{T}(\vec{n}; \vec{x}, t) \tag{4.3}$$

$\Delta\vec{T}(\vec{n}; \vec{x}, t)$ is the traction change due to rupture propagation. $\vec{T}^0(\vec{n}; \vec{x})$ is the initial traction, that is, the state of tectonic traction on the fault at the time when rupture nucleates. The time it takes rupture to propagate over the fault depends on the size of the fault and consequently on the size of the earthquake. This time is much shorter than the time scale at which we can observe changes in the tectonic stress. Therefore, the changes in the tectonic stress during rupture will be negligible, and we can assume that the tectonic load is entirely accounted for by the initial traction. The friction determines the total traction inside the rupture:

$$\vec{T} = \vec{T}^f \tag{4.4}$$

where $\vec{T}^f$ is the frictional traction. The equation represents a fault constitutive law. The frictional traction is determined by a friction law. As we already indicated in the introduction to this chapter, friction may be a function of many different physical quantities, e.g., slip path, slip rate, state variable, temperature and effective normal stress. Two simple friction laws are shown in Subsection 4.1.2. Given the initial traction and material parameters of the fault, it is the friction law that controls nucleation, propagation and healing (arrest) of the rupture.

4.1.1 Boundary conditions for dynamic shear faulting

Consider only shear faulting. This means that there is no opening of the fault and no interpenetrating of the fault materials. Define frictional strength or fault friction as

$$S \equiv \mu_f \left| \vec{T}_n \right| \tag{4.5}$$

where μ_f is the time-dependent coefficient of friction and $\vec{T}_n$ is the fault-normal component of traction on the fault.

Assume a locked fault. If, at a point of the fault surface, loading is smaller than the frictional strength, the fault remains locked and the slip rate remains zero at the point. If the loading exceeds the frictional strength, slip occurs. The shear traction then varies following the friction law and eventually falls to the dynamic frictional level. Note that this illustrative description is valid only for slip-weakening friction. For example, in the case of

rate-and-state friction, the shear traction is always equal to the frictional strength and the fault is always slipping.

Let subscripts *sh* and *n* denote the shear and normal components with respect to the fault surface. The boundary conditions on the fault can be formulated as follows (Day 1982, Day *et al.* 2005).

Shear faulting

$$\vec{s}_n = 0, \quad \dot{\vec{s}}_n = 0, \quad \vec{s}_{sh} \neq 0, \quad \dot{\vec{s}}_{sh} \neq 0 \tag{4.6}$$

Shear traction bounded by the frictional strength

$$\left| \vec{T}_{sh} \right| \leq S \tag{4.7}$$

Colinearity of the shear traction and slip rate

$$\vec{T}_{sh}(\vec{n}) = S \frac{\dot{\vec{s}}_{sh}}{\left| \dot{\vec{s}}_{sh} \right|} \tag{4.8}$$

The slip is opposed by the friction. The fact that the frictional traction opposes the slip is consistent with the colinearity requirement because (1) we consider vector $\vec{n}$ to be oriented in the direction from the '−' to the '+' side of the fault (that is, $\vec{T}(\vec{n})$ characterizes traction with which the '+' side acts on the '−' side of the fault), (2) we consider slip as the relative motion of the '+' side with respect to the '−' side of the fault. Thus $\vec{T}(\vec{n})$ and slip have the same direction. If slip was defined as the relative motion of the '−' side with respect to the '+' side of the fault, the requirement of the antiparallelism with the '−' sign on the r.h.s. of Eq. (4.8) would be consistent with frictional traction opposing the relative motion of the fault faces.

4.1.2 Friction law

When a rupture front reaches a point of the fault and slip starts at that point (that is, the two originally neighbouring points, one at the '−' and the other at the '+' side of the fault, start slipping), the total traction varies according to a constitutive law that relates stress change and frictional behaviour, and eventually falls to the dynamic frictional level. If the variation in traction is gradual (not instantaneous), the traction at the point reaches the dynamic frictional level during a finite time. During this finite time, points of the fault in front of the considered point may start slipping. Thus, the process of traction degradation obviously occurs within a finite zone behind the so-called crack tip (the rupture frontmost point). This zone is termed the cohesive (also breakdown or process) zone. The friction law determines processes and phenomena in the cohesive zone.

Following Bizzarri and Cocco (2005), the coefficient of friction can be a function of several quantities:

$$\mu_f = \mu_f(l, |\dot{\vec{s}}|, \Psi_1, \ldots, \Psi_N, T, H, \lambda_c, h_m, g, C_e) \tag{4.9}$$

where l is the slip path length:

$$l(t) \equiv \int_0^t |\dot{s}|(\tau)d\tau \tag{4.10}$$

$|\dot{s}|$ is modulus of the slip rate, $\Psi_1, \ldots, \Psi_N$ are state variables, T is temperature and accounts for ductility, plastic flow, rock melting and vaporization, H is humidity, λ_c is the characteristic length of the fault surface accounting for roughness and topography of asperity contacts and possibly responsible for mechanical lubrication, h_m is material hardness, g is the gouge parameter accounting for surface consumption and gouge formation during a sliding episode, and C_e is a chemical environment parameter. In general, the fault-normal traction in Eq. (4.5) should stand for a time-dependent effective normal traction accounting for a pore fluid pressure (which reduces the normal traction). Equation (4.9) coupled to evolution equations for all the variables involved in its full generality may describe a very complicated constitutive law.

According to Cocco and Bizzarri (2002) and Bizzarri and Cocco (2003), two main groups of the friction laws have been proposed – slip-dependent (e.g., Andrews 1976a,b, Barenblatt 1959, Ida 1972, Ohnaka and Yamashita 1989, Palmer and Rice 1973, Ionescu and Campillo 1999) and rate- and state-dependent (e.g., Beeler *et al*. 1994, Dieterich 1979, 1986, Okubo 1989, Okubo and Dieterich 1984, Ruina 1980, 1983). An example of a friction law that does not fit into these two groups is the time-weakening friction law proposed by Andrews (1985). Because the traction in this friction law depends only on time, this law may be used to initiate rupture propagation (for example, Andrews 1985, Bizzarri *et al*. 2001).

We may also mention the rate-and-slip-dependent laws such as Cochard and Madariaga (1994) and Ampuero and Rubin (2008). Although these have formal relationships to rate and state, their nature is different (especially because they do not have the same empirical foundation).

Here we restrict the discussion to two types of frequently used constitutive relations in earthquake source physics: the linear slip-weakening (SW) friction law as formulated by Ida (1972) and Andrews (1976a,b), and the rate- and state-dependent (R&S) friction law as formulated by Dieterich (1986). For a review of the constitutive relations for earthquake ruptures we refer to Chapter 4 in the book by Ohnaka (2013).

4.1.2.1 Linear slip-weakening friction law

The value of the coefficient of friction in the linear SW friction law decreases linearly from the value of static friction, μ_s, down to the value of dynamic (also called kinematic) friction, μ_d, over a characteristic (also called critical) distance D_c :

$$
\begin{aligned}
\mu_f &= \mu_s - \frac{\mu_s - \mu_d}{D_c}l; \quad l < D_c, \\
\mu_f &= \mu_d; \quad l \geq D_c.
\end{aligned}
\tag{4.11}
$$
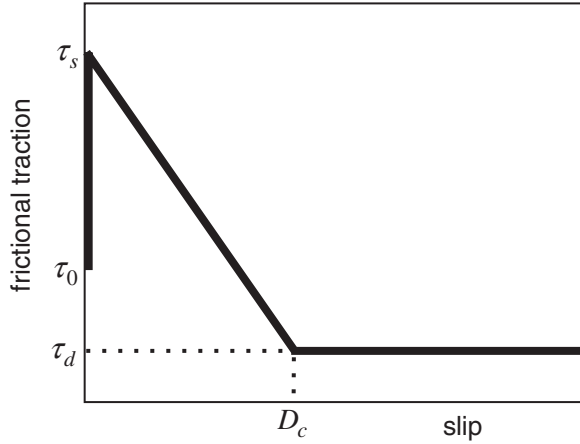
Figure 4.2 Linear slip-weakening (SW) friction law.

We can define static (yield) and dynamic (kinematic) frictional shear tractions, respectively:

$$|\vec{T}_{sh}^{s}| = \mu_s |\vec{T}_n|, \quad |\vec{T}_{sh}^{d}| = \mu_d |\vec{T}_n| \tag{4.12}$$

We will also use symbols τ_s, τ_d, τ_0 and τ_n for the static, dynamic, initial and normal tractions, respectively:

$$\tau_s \equiv |\vec{T}_{sh}^{s}|, \quad \tau_d \equiv |\vec{T}_{sh}^{d}|, \quad \tau_0 \equiv |\vec{T}_{sh}^{0}|, \quad \tau_n \equiv |\vec{T}_n| \tag{4.13}$$

The linear SW friction law is illustrated in Fig. 4.2.

Considering the SW friction law means that the evolution of the traction with slip on the fault is 'prescribed' a priori. We know the static and dynamic tractions before the rupture starts. We just do not know whether they will actually be reached. That will depend on the evolution of stress on and near the fault, and slip on the fault.

4.1.2.2 Rate- and state-dependent friction law

The value of the coefficient of friction in the R&S friction law depends on the modulus of the slip rate $|\dot{\vec{s}}_{sh}|$ and state variable Ψ :

$$\begin{aligned} \mu_f &= \mu(|\dot{\vec{s}}_{sh}|, \Psi) \\ \frac{d\Psi}{dt} &= g(|\dot{\vec{s}}_{sh}|, \Psi) \end{aligned} \tag{4.14}$$
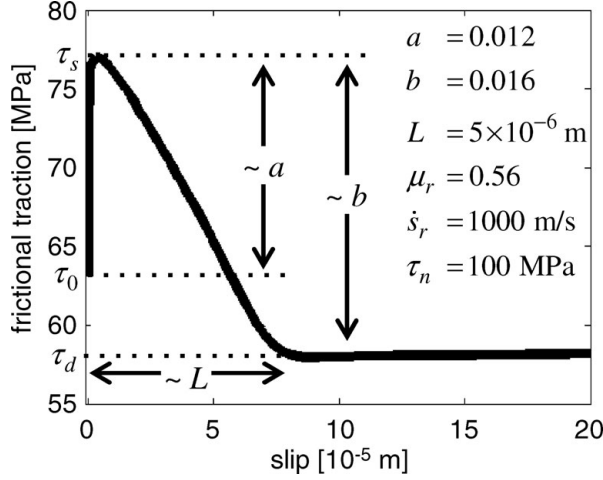
Figure 4.3 Illustration of the R&S friction law. Here, $\tau_n = |\vec{T}_n|$.

We can derive several constitutive relations from Eq. (4.14) using different functional forms for μ and g (e.g., Beeler *et al.* 1994). The R&S friction law proposed by Dieterich (1986) is

$$\mu_f = \mu_r - a \ln\left(\frac{\dot{s}_r}{|\dot{\vec{s}}_{sh}|} + 1\right) + b \ln\left(\frac{\Psi \dot{s}_r}{L} + 1\right)$$

$$\frac{d\Psi}{dt} = 1 - \frac{\Psi |\dot{\vec{s}}_{sh}|}{L}$$

(4.15)

Here a, b and L are constitutive parameters, μ_r is the reference coefficient of friction at the slip rate value $\dot{s}_r$. The second equations in (4.14) and (4.15) describe evolution of the state variable. Note that the most common version of R&S in current use does not have the $+1$ terms in Eqs. (4.15). Unlike the SW friction law, the yield and kinematic frictional tractions are not prescribed a priori, they depend on the slip rate and state variable. Therefore, it is not possible to plot the general figure of the R&S friction law. Figure 4.3 shows only an example of how traction may depend on slip for particular parameters (based on Cocco *et al.* 2004). Though the R&S friction law (4.15) does not explicitly include dependence on the slip path length, the law yields the slip-weakening, with a short slip-hardening phase, as shown by Cocco and Bizzarri (2002). Cocco and Bizzarri (2002) and Bizzarri and Cocco (2003, 2005) compared the two friction laws in detail.

4.2 Kinematic model of an earthquake source

In many applications, kinematic models are used instead of the dynamic ones. In the finite-fault kinematic model, rupture propagation is simulated using a set of point sources distributed along the fault surface. Each point source is a body-force equivalent and acts independently of other point sources. Timing of the point sources along the fault surface and

the slip time histories are determined prior to the numerical simulation itself. Consequently, in the kinematic model the point sources do not physically interact with the medium.

The corresponding theory is well explained in many textbooks and monographs, e.g., Aki and Richards (2002), Kostrov and Das (2005), Gubbins (1990), Kennett (2001), Pujol (2003). Here we restrict the discussion to a very brief review of the basic relations necessary for subsequent explanation of the implementation of the kinematic sources in the numerical methods.

4.2.1 Point source

At large distances the wavefield contains only wavelengths that are longer than the dimension of the fault because the shorter wavelengths are attenuated (e.g., Aki and Richards 2002). Therefore, if we are interested in the wavefield over a distance much larger than the dimensions of the fault itself we can use an effective point-source approximation to a true faulting surface.

The displacement at point $\vec{x}$ and time t due to the faulting surface S can be expressed by the representation theorem (Knopoff 1956, de Hoop 1958, Aki and Richards 2002):

$$u_n(\vec{x}, t) = \int_{-\infty}^{\infty} d\tau \int_S m_{pq}(\vec{\xi}, \tau) \frac{\partial G_{np}(\vec{x}, t - \tau; \vec{\xi}, 0)}{\partial \xi_q} dS \tag{4.16}$$

Here m_{pq} is the moment-density tensor:

$$m_{pq}(\vec{\xi}, t) = c_{pqrs}(\vec{\xi}) s_r(\vec{\xi}, t) n_s(\vec{\xi}) \tag{4.17}$$

where $\vec{\xi}$ specifies position on the fault surface S, c_{pqrs} is a tensor of the elastic moduli, $\vec{s}$ is the slip vector and $\vec{n}$ is the fault normal. $\frac{\partial G_{np}}{\partial \xi_q}$ is a derivative of the Green tensor. $\frac{\partial G_{np}}{\partial \xi_q}$ is physically equivalent to having a single force couple with an arm in the q-direction and forces in the p-direction at point $\vec{\xi}$ on S. The convolution, further denoted by asterisk, $m_{pq} * \frac{\partial G_{np}}{\partial \xi_q}$, represents the n-component of displacement at $\vec{x}$ due to force couples at $\vec{\xi}$; m_{pq} is the strength of the (p, q) couple.

Here we will derive the expressions for the point-source approximation. In this case we assume that surface S is eventually represented as a point and therefore we assume the Green function to be constant over the whole surface S, that is,

$$u_n(\vec{x}, t) = \left(\int_S m_{pq} dS \right) * \frac{\partial G_{np}}{\partial \xi_q} \tag{4.18}$$

In general, the moment tensor M_{pq} (the strength of the resulting (p, q) force couple at the point) is defined as

$$M_{pq} \equiv \int_S m_{pq} dS \tag{4.19}$$

Then the displacement is given by

$$u_n(\vec{x}, t) = M_{pq} * \frac{\partial G_{np}}{\partial \xi_q} \tag{4.20}$$

Let $\vec{v}$ be a unit vector in the direction of $\vec{s}$. In the case of the tangential slip, $\vec{n} \cdot \vec{v} = 0$, and an isotropic medium, the moment-density tensor takes a simple form:

$$m_{pq} = \mu(n_p s_q + n_q s_p) = \mu s(n_p v_q + n_q v_p) \tag{4.21}$$

where $s = |\vec{s}|$. The moment tensor is then

$$M_{pq} = \int_S \mu s(n_p v_q + n_q v_p) dS \tag{4.22}$$

Assuming a planar fault (fixed vector $\vec{n}$ on the fault surface), fixed slip orientation (fixed vector $\vec{v}$) and a homogeneous medium in the source region (or average μ) we obtain

$$M_{pq} = \mu(n_p v_q + n_q v_p) \int_S s(\vec{\xi}, t) dS \tag{4.23}$$

Assuming an average slip $\bar{s}(t)$ over the fault plane the integral can be approximated:

$$\int_S s(\vec{\xi}, t) dS \approx \bar{s}(t) \int_S dS = \bar{s}(t) A = \bar{s}\, s_{\text{TF}}(t) A \tag{4.24}$$

Here A is the total size of the fault surface and $s_{\text{TF}}(t)$ is the source-time function:

$$s_{\text{TF}}(t) \equiv \frac{\bar{s}(t)}{\bar{s}}, \quad \bar{s} \equiv \bar{s}(t \to \infty) \tag{4.25}$$

Then the moment tensor takes a simple form:

$$M_{pq} = \mu A \bar{s}\, s_{\text{TF}}(t)(n_p v_q + n_q v_p) \tag{4.26}$$

Using the scalar seismic moment M_0 defined as

$$M_0 \equiv \mu A \bar{s} \tag{4.27}$$

we eventually obtain the moment tensor for the tangential slip:

$$M_{pq} = M_0 (n_p v_q + n_q v_p) s_{\text{TF}}(t) \tag{4.28}$$

In the coordinate system (Fig. 4.4) with the x-axis heading north, y-axis heading east and z-axis positive downward, the components of vector $\vec{v}$ and the fault-normal vector $\vec{n}$ are

$$\begin{aligned}
v_x &= \cos\lambda \cos\Phi_S + \cos\delta \sin\lambda \sin\Phi_S \\
v_y &= \cos\lambda \sin\Phi_S - \cos\delta \sin\lambda \cos\Phi_S \\
v_z &= -\sin\lambda \sin\delta
\end{aligned} \tag{4.29}$$

$$n_x = -\sin\delta \sin\Phi_S, \quad n_y = \sin\delta \cos\Phi_S, \quad n_z = -\cos\delta \tag{4.30}$$
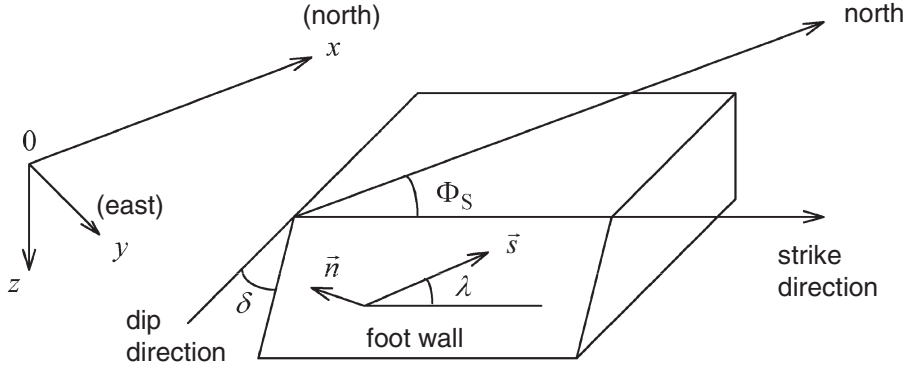
Figure 4.4 Definition of the fault-orientation parameters and the coordinate system. Φ_S – strike, δ – dip, λ – rake, $\vec{n}$ – fault normal, $\vec{s} = s\vec{v}$ is slip taken as the movement of the hanging wall relative to the foot wall.

From Eqs. (4.28)–(4.30) we obtain

$$M_{xy} = M_0 \left(\sin \delta \cos \lambda \cos 2\Phi_S + \tfrac{1}{2} \sin 2\delta \sin \lambda \sin 2\Phi_S \right) s_{\text{TF}}(t),$$

$$M_{yz} = -M_0 \left(\cos \delta \cos \lambda \sin \Phi_S - \cos 2\delta \sin \lambda \cos \Phi_S \right) s_{\text{TF}}(t),$$

$$M_{zx} = -M_0 \left(\cos \delta \cos \lambda \cos \Phi_S + \cos 2\delta \sin \lambda \sin \Phi_S \right) s_{\text{TF}}(t), \qquad (4.31)$$

$$M_{xx} = -M_0 \left(\sin \delta \cos \lambda \sin 2\Phi_S + \sin 2\delta \sin \lambda \sin^2 \Phi_S \right) s_{\text{TF}}(t),$$

$$M_{yy} = M_0 \left(\sin \delta \cos \lambda \sin 2\Phi_S - \sin 2\delta \sin \lambda \cos^2 \Phi_S \right) s_{\text{TF}}(t),$$

$$M_{zz} = M_0 \sin 2\delta \sin \lambda \, s_{\text{TF}}(t).$$

Due to the moment-tensor symmetry the remaining components are

$$M_{yx} = M_{xy}, \quad M_{zy} = M_{yz}, \quad M_{xz} = M_{zx} \qquad (4.32)$$

Sometimes it may be useful to work with the coordinate system with the x-axis heading east, y-axis heading north and z-axis positive upward (compare with the system in Fig. 4.4). The components of vector $\vec{v}$ and the fault-normal vector $\vec{n}$ are

$$v_x = \cos \lambda \sin \Phi_S - \cos \delta \sin \lambda \cos \Phi_S,$$
$$v_y = \cos \lambda \cos \Phi_S + \cos \delta \sin \lambda \sin \Phi_S, \qquad (4.33)$$
$$v_z = \sin \lambda \sin \delta,$$

$$n_x = \sin \delta \cos \Phi_S, \quad n_y = -\sin \delta \sin \Phi_S, \quad n_z = \cos \delta \qquad (4.34)$$

From Eqs. (4.28), (4.33) and (4.34) we obtain

$$M_{xy} = M_0 \left(\sin\delta \cos\lambda \cos 2\Phi_S + \tfrac{1}{2} \sin 2\delta \sin\lambda \sin 2\Phi_S \right) s_{\text{TF}}(t),$$

$$M_{yz} = M_0 \left(\cos\delta \cos\lambda \cos\Phi_S + \cos 2\delta \sin\lambda \sin\Phi_S \right) s_{\text{TF}}(t),$$

$$M_{zx} = M_0 \left(\cos\delta \cos\lambda \sin\Phi_S - \cos 2\delta \sin\lambda \cos\Phi_S \right) s_{\text{TF}}(t),$$

$$M_{xx} = M_0 \left(\sin\delta \cos\lambda \sin 2\Phi_S - \sin 2\delta \sin\lambda \cos^2\Phi_S \right) s_{\text{TF}}(t), \qquad (4.35)$$

$$M_{yy} = -M_0 \left(\sin\delta \cos\lambda \sin 2\Phi_S + \sin 2\delta \sin\lambda \sin^2\Phi_S \right) s_{\text{TF}}(t),$$

$$M_{zz} = M_0 \sin 2\delta \sin\lambda \, s_{\text{TF}}(t).$$

4.2.2 Finite-fault kinematic source

In situations when we are interested in the wavefield at distances comparable to or smaller than the size of the fault, the point-source approximation is not appropriate. In such situations we have to consider the finite-fault source. If using the dynamic source is not feasible, we may use the finite-fault kinematic source.

Recall the representation theorem (4.16),

$$u_n(\vec{x}, t) = \int_{-\infty}^{\infty} d\tau \int_S m_{pq}(\vec{\xi}, \tau) \frac{\partial G_{np}(\vec{x}, t - \tau; \vec{\xi}, 0)}{\partial \xi_q} dS \qquad (4.36)$$

Divide the fault surface S into k nonoverlapping sub-faults S_k. Then,

$$u_n(\vec{x}, t) = \sum_k \left(\int_{S_k} m_{pq} * \frac{\partial G_{np}}{\partial \xi_q} dS \right) \qquad (4.37)$$

Consider each sub-fault as a point source. Consequently, we consider one Green tensor per sub-fault. Then,

$$u_n(\vec{x}, t) = \sum_k \left(\int_{S_k} m_{pq} dS * \frac{\partial G_{np}^k}{\partial \xi_q} \right) = \sum_k \left(M_{pq}^k * \frac{\partial G_{np}^k}{\partial \xi_q} \right) \qquad (4.38)$$

Assuming only tangential slip on each sub-fault we can use Eqs. (4.21)–(4.23) to express the moment-tensor components for sub-faults:

$$M_{pq}^k = \mu_k \left(n_p^k v_q^k + n_q^k v_p^k \right) \int_{S_k} s \, dS \qquad (4.39)$$

Similarly as in the case of a point source the integral can be approximated using Eq. (4.24):

$$M_{pq}^k = \mu_k \, \bar{s}_k \, s_{\text{TF}}^k(t) A_k \left(n_p^k v_q^k + n_q^k v_p^k \right). \qquad (4.40)$$

Here A_k is size of the k-th sub-fault surface and $s_{\text{TF}}^k(t)$ is the source-time function for the k-th sub-fault:

$$s_{\text{TF}}^k(t) \equiv \frac{\bar{s}_k(t)}{\bar{s}_k}, \qquad \bar{s}_k \equiv \bar{s}_k \, (t \to \infty) \qquad (4.41)$$

Using the scalar moment we can write

$$M_{pq}^k = M_0^k \left(n_p^k \nu_q^k + n_q^k \nu_p^k \right) s_{\text{TF}}^k(t) \tag{4.42}$$

In this derivation we considered the point-source assumptions for each sub-fault. Therefore, the finite-fault kinematic source is represented by a set of point sources. Each point source is characterized by its position $\vec{x}_k$ and moment-tensor components M_{pq}^k (including the source-time functions $s_{\text{TF}}^k(t)$). We can also characterize each point source by strike Φ_S^k, dip δ^k, rake λ^k, scalar moment M_0^k and source-time function $s_{\text{TF}}^k(t)$, and use Eqs. (4.31) or (4.35) to obtain the moment-tensor components. Note that a source-time function (4.41) is defined for each point source since rupture nucleated at a hypocentre. For a single point source this is natural. In the case of finite-fault kinematic models, usually source-time function and rupture-onset time are defined for each point source. Rupture-onset time defines when rupture arrives at a particular point and after that time the time evolution is prescribed by the source-time function. In this way the rupture propagation is controlled by rupture onset time and the source-time functions are defined only for the time they are really needed.

Part II

The finite-difference method

5

Time-domain numerical methods

5.1 Introduction

A large variety of time-domain methods have been developed for modelling earthquake ground motion. They may be divided into three groups – boundary methods, domain methods and hybrid methods (note that the adjectives boundary and domain here relate to space). In general, the boundary methods are more accurate than the domain methods, but they are not computationally efficient in the case of complex (realistic) models. The reasonable balance of accuracy and computational efficiency in applications to complex models is the primary reason why the domain methods are dominant, not only in the recent modelling of earthquake motion but also in waveform inversion. Development of hybrid approaches is the consequence of a simple but important fact – no single method is the most accurate and computationally efficient for all wavefield–medium configurations. Combining two or more methods makes it possible to overcome the limitations of individual methods.

In this book we do not address the boundary methods. For an excellent overview of the boundary integral equation, boundary-element, discrete-wavenumber and Aki–Larner methods as well as of the hybrid approaches we refer to Bouchon and Sánchez-Sesma (2007).

The finite-difference method (FDM), finite-element method (FEM), Fourier pseudo-spectral method (FPSM), spectral-element method (SEM), and discontinuous Galerkin method (DGM) are the most representative domain methods for modelling rupture propagation, seismic wave propagation and earthquake ground motion. The domain methods primarily differ from each other by their approach to spatial discretization. In this book we address in detail FDM or, more precisely, FDTD (finite-difference time-domain) method, and briefly FEM and their hybrid combination. Therefore, we include in the next three sections of this chapter concise descriptions of FPSM, SEM and ADER-DGM contributed by Peter Klin, Emmanuel Chaljub, Martin Käser and Christian Pelties.

The three following sections and the subsequent chapters refer to many important articles related to the methods. Here we just mention books and chapters in books that provide introductions and overviews of the numerical domain methods: Chaljub *et al.* (2007) for SEM, de la Puente (2008) for ADER-DGM, Moczo *et al.* (2007a,b) for FDM. We may

specially mention the excellent book by Andreas Fichtner (2011) on full seismic waveform modelling and inversion. Although the primary focus of the book is waveform inversion, Fichtner briefly characterizes recent time-domain methods and concisely describes FDM and SEM. Finally, the SEG Geophysics Reprint Series No. 28 edited by Robertsson *et al*. (2012) provides both a concise introduction to numerical-modelling methods and 78 selected articles published in a variety of journals in the period 1984–2011. This volume is the follow-up to the SEG Geophysics Reprint Series No. 13 edited by Kelly and Marfurt (1990).

5.2 Fourier pseudo-spectral method

The Fourier pseudo-spectral method (FPSM) combines the simplicity of spatial discretization using a structured grid with the optimal accuracy of global spectral differential operators. The method was introduced by Kreiss and Oliger (1972) for the integration of the hyperbolic equations in dynamic meteorology and oceanography. Following the first test applications to 2D acoustic (Gazdag 1981) and 2D elastic (Kosloff *et al*. 1984) wave propagation, FPSM was considered a very promising approach in the early years of 3D seismic numerical modelling (e.g., Reshef *et al*. 1988), mainly owing to its unbeatable low spatial sampling rate and computational efficiency. Soon these advantages were counterbalanced by accuracy problems in the modelling of seismic wave propagation in media with sharp velocity contrasts (Mizutani *et al*. 2000) and free-surface boundary conditions (Xu *et al*. 1999). The main weakness of FPSM, however, was the expense of the interprocessor communication required by the parallel implementation of the algorithm. As a consequence, the use of FPSM could not benefit from early distributed-memory parallel computers as much as other methods did. As shown recently by Klin *et al*. (2010), it is possible to alleviate the mentioned accuracy problems with minor workarounds, whereas the inter-processor communication poses a much less critical problem with up-to-date high-performance computing resources. Therefore, FPSM can be qualified as concurrent with other well-established methods for the numerical simulation of earthquake ground motion. Here we describe the essential aspects of the application of FPSM to seismic wave propagation in a 3D anisotropic viscoelastic medium.

The peculiarity of FPSM consists in the evaluation of the spatial derivatives by means of multiplication in the wavenumber domain:

$$\frac{\partial \Phi}{\partial x_p} = \mathcal{F}_p^{-1}\{i k_p \mathcal{F}_p\{\Phi\}\} \tag{5.1}$$

where $\mathcal{F}_p$ denotes the spatial Fourier transform in the p-th direction (performed using the fast Fourier transform algorithm), k_p is the wavenumber in the p-th direction, and Φ may stand for a displacement-vector component. Actually, the term 'pseudo-spectral' is a little misleading because it refers only to the evaluation of the spatial derivative, whereas the

temporal evolution is usually solved using nonspectral approaches. The usual choice is the 2nd-order explicit FD scheme:

$$\vec{u}\left(\vec{x}, t + \Delta t\right) = 2\vec{u}\left(\vec{x}, t\right) - \vec{u}\left(\vec{x}, t - \Delta t\right) + (\Delta t)^2 \frac{\partial^2 \vec{u}\left(\vec{x}, t\right)}{\partial t^2} \tag{5.2}$$

where $\vec{u}$ is the displacement vector. The equation of motion for a viscoelastic anisotropic medium can be expressed as

$$\frac{\partial^2 \vec{u}\left(\vec{x}, t\right)}{\partial t^2} = \frac{1}{\rho\left(\vec{x}\right)} \nabla \cdot \left[\mathbf{C}\left(\vec{x}\right) \nabla^T \vec{u}\left(\vec{x}, t\right) + \mathbf{R}\left(\vec{x}, t\right)\right] + \vec{f}\left(\vec{x}, t\right) \tag{5.3}$$

where $\mathbf{C}$ is the 6×6 symmetric elasticity matrix (in Voigt notation), $\mathbf{R}$ is the 6-component vector that accounts for viscoelasticity, $\vec{f}$ is the source term, and ∇ is the spatial differentiation operator:

$$\nabla = \begin{pmatrix} \partial_x & 0 & 0 & 0 & \partial_z & \partial_y \\ 0 & \partial_y & 0 & \partial_z & 0 & \partial_x \\ 0 & 0 & \partial_z & \partial_y & \partial_x & 0 \end{pmatrix} \tag{5.4}$$

Viscoelasticity and attenuation correspond to the rheology of the generalized Maxwell body (GMB-EK in Chapter 3) and the term $\mathbf{R}$ includes the anelastic functions (memory variables).

The differentiation approach described in Eq. (5.1) is exact if the amplitude spectrum of the wavefield vanishes for wavenumbers larger than the Nyquist wavenumber $k_N = \pi / h$, where h is the grid spacing. Therefore FPSM allows for a relatively coarse spatial sampling (Fornberg 1987), which represents a valuable advantage in solving 3D problems. On the other hand, the nature of the global differential operators implies that numerical artefacts are spread over the whole spatial domain when a singularity arises in the wavefield (Gibb's phenomenon). This problem is significantly reduced if the differential operators are defined on staggered grids (Özdenvar and McMechan 1996) and formally expressed as

$$D_p^{\pm} \Phi = \mathcal{F}_p^{-1} \left\{ i k_p \exp\left(\pm i k_p \tfrac{1}{2} h\right) \mathcal{F}_p\left\{\Phi\right\} \right\} \tag{5.5}$$

Operators D_p^+ and D_p^- evaluate the spatial derivative of Φ in the grid (the staggered grid) which is shifted by $h/2$ in the p-th direction, forward and backward, respectively. In order to obtain the acceleration terms in the same grid, where the displacement terms are defined, the application of operators D_p^+ and D_p^- should follow an adequate inter-changing role while solving the equation of motion.

In earthquake ground motion simulations the free-surface boundary condition is typically imposed on the top of the spatial domain. The condition implies discontinuities in the periodic extension of the differentiated wavefield, which in turn appears ill-suited for the operators defined in Eq. (5.5). In order to incorporate the free-surface condition, the differentiated wavefield is first appropriately modified – it has to be made suitable for application of the differential operator. Once the operator is applied, the known effects of the employed modification are removed. The modification consists in the removal of possible discontinuities in the displacement field across points at which the free-surface condition

is imposed by means of subtraction of a linear function evaluated from the discontinuity. In order to account for the modification, a sum of constant value is applied to the obtained derivative. The free-surface condition is imposed using stress imaging (Subsection 10.1.1), but the same result can be obtained by using a sine transform instead of the ordinary fast Fourier transform to transform the stress field in the wavenumber domain and by returning with the cosine transform after the wavenumber multiplication.

FPSM is based on the heterogeneous formulation of the equation of motion. In consequence, the use of a relatively coarse regular spatial sampling exposes it particularly to numerical artefacts caused by staircase approximations of nonplanar material interfaces. The approaches based on mapping of the computational grid to the geometry of the main interfaces (e.g., Fornberg 1988b), which were proposed to mitigate these artefacts, appear impractical in the general 3D case. More workable approaches consist in honouring the discretization rules proposed by Pelties *et al*. (2010), and in adopting the volume harmonic averaging of the elastic moduli and volume arithmetic averaging of density proposed by Moczo *et al*. (2002) for the FD modelling schemes. The homogenization approach (e.g., Capdeville and Marigo 2007, 2013, Capdeville *et al*. 2010a,b, 2013) seems to be a reasonable perspective.

The rectangular spatial grid makes it easy to implement PML (Chapter 12) in order to simulate absorbing boundary conditions for the outgoing wavefield at boundaries of the spatial grid.

FPSM can be successfully applied in the numerical simulation of the seismic wavefield produced by an earthquake in large 3D crustal models (Vuan *et al*. 2011). We refer to Klin *et al*. (2010) for a more comprehensive review of FPSM and related discussions.

5.3 Spectral element method

The spectral element method (SEM) was developed in the eighties in the field of computational fluid dynamics (Patera 1984, Maday and Patera 1989) with the objective to extend the spectral method to deal with realistic 2D or 3D geometries, to capture local variations of the physical solutions and to alleviate implementation of boundary conditions.

For example, in the spectral method, complex geometries can only be handled by the so-called 'mapping and patching' strategy (Boyd 2001): a computational domain is first split into regions, or sub-domains, each of which is the image of a canonical domain (e.g., a cube in 3D) through a regular mapping. The solutions on each sub-domain are expanded on a local spectral basis (trigonometric functions or orthogonal polynomials), then patched together by enforcing the continuity of the displacement and traction vectors, usually through iterative procedures and/or overlapping strategies. For complex geometries, there is a trade-off between increasing the number of sub-domains to accurately represent the geometry of the domain and solving the resulting system of interface conditions. Moreover, this domain decomposition strategy does not change the fact that boundary conditions have to be enforced with special care and usually leads to lower accuracy near the boundaries affecting, e.g., surface waves.

As stated by Komatitsch and Vilotte (1998), SEM could have developed after the similarity between the spectral collocation methods (in which the equation of motion is exactly satisfied by the numerical solution at some well-chosen points) and variational formulations with consistent quadrature (numerical integration formula) was understood.

Thus, SEM relies on the variational formulation (weak form) of the equation of motion and in most cases its displacement formulation, in which the displacement field is forced to be globally continuous whereas the continuity of the traction vector (also at the free surface) is satisfied implicitly. We refer to Cohen and Fauqueux (2005) for the mixed velocity–stress formulation and to Festa and Vilotte (2005) for a comparative analysis of the two formulations. Here we just note that the mixed formulation makes it easier to implement PML.

SEM appears as an FEM where the solution is expanded in each element onto spectral polynomial bases of high order and where numerical integration is realized with Gauss–Jacobi quadratures. It is therefore connected to the $h - p$ version of FEM, where the accuracy of the numerical solution can be increased by decreasing the element size h or by increasing the local polynomial order p.

The first applications of SEM to acoustic and elastic wave propagation by Seriani and Priolo (1994) and Priolo *et al.* (1994) used Chebyshev polynomials together with Gauss–Lobatto–Chebyshev quadrature – as Patera (1984) did in his original article. The implementation combined the geometrical flexibility of FEM with the accuracy of the spectral methods and minimized numerical dispersion and dissipation even in challenging applications involving interface and surface waves. One drawback was that the mass matrix had to be inverted when an FD scheme was used for time evolution. This problem was circumvented independently by Faccioli *et al.* (1997) and by Komatitsch and Vilotte (1998): they used Gauss–Lobatto–Legendre quadrature together with polynomial bases built upon Legendre polynomials to derive SEM in which the mass matrix is diagonal (as in the article of Maday and Patera 1989). The implementation has become most popular in seismic applications for its computational efficiency, resulting from the use of the explicit FD time-evolution schemes, without any loss of accuracy compared to the use of Chebyshev polynomials and quadrature.

In all the above SEM implementations (Chebyshev or Legendre type), the polynomial bases are first built in one space dimension, then extrapolated by tensorization to 2D and 3D. This represents a gain in computational efficiency but also a constraint that the geometry of the elements has to be tensorized too: the elements are restricted to deformed quadrilaterals in 2D and hexahedra in 3D. The problem of finding an accurate quadrature that would possibly preserve the diagonality of the mass matrix for non-tensorized geometries is still open – as discussed by Mercerat *et al.* (2006), who implemented SEM for 2D triangular grids.

The optimal choice of the polynomial order for SEM is between $N = 4$ and $N = 8$: the lower orders do not significantly reduce numerical dispersion whereas higher orders result in a too severe Courant–Friedrichs–Lewy condition for the time step, which is not compensated by the number of grid points per wavelength needed for an acceptable level of

numerical dispersion and anisotropy (Seriani and Oliveira 2007, de Basabe and Sen 2007). An average number of five or six grid points per wavelength (i.e., about one element if $N = 4$ and half an element if $N = 8$) is used in practical applications.

Surprisingly, choosing an appropriate h can be a much more difficult task when dealing with complex heterogeneous 3D models. The main problem is how to represent variations of geometrical or mechanical properties that occur on scales smaller than the minimum propagating wavelength. A material discontinuity is a very good example. The polynomial bases used in SEM are not adapted to represent such variations – as in the original SM. The only possibility is to have the discontinuity coincide with the boundaries of elements. This approach can, however, pose a tremendous meshing task in some applications – see Chaljub *et al.* (2010). In such cases, the so-called homogenization (e.g., Capdeville and Marigo 2007, 2013, Capdeville *et al.* 2010a,b, 2013) can probably help.

For reviews presenting the numerous developments of the Legendre SEM for global or regional seismology applications we refer to Komatitsch *et al.* (2005) and Chaljub *et al.* (2007). For examples of earthquake ground motion simulations including effects of local geology we refer to Komatitsch *et al.* (2004), Lee *et al.* (2008b, 2009), Stupazzini *et al.* (2009a,b), Chaljub *et al.* (2010), Pilz *et al.* (2011). SEM has also been applied to study rupture dynamics; e.g., Madariaga *et al.* (2006), Festa and Vilotte (2006), Kaneko *et al.* (2008, 2011). Computational aspects can be found in articles by Komatitsch *et al.* (2010) and Peter *et al.* (2011).

Here, we briefly recall the key features of the Legendre SEM discretization. We recall the weak form of the equation of motion, Eq. (2.12), which can be rewritten as

$$\frac{\partial^2}{\partial t^2} \int_\Omega \rho \vec{u} \cdot \vec{w} d\Omega + \int_\Omega \sigma_{ij}(\vec{u}) \varepsilon_{ij}(\vec{w}) d\Omega = \int_\Gamma \vec{T} \cdot \vec{w} d\Gamma + \int_\Omega \vec{f} \cdot \vec{w} d\Omega \qquad (5.6)$$

where Ω is the computational domain and Γ its boundary with prescribed traction $\vec{T}$. Other quantities are the same as those in Eq. (2.12).

The spatial discretization starts with a decomposition of the computational domain Ω into K unstructured non-overlapping hexahedral elements $\Omega_k; k = 1, \ldots, K$. Each element is obtained by a regular mapping of a reference element Ω^{ref} (the unit cube in 3D). Then, virtual (also admissible) displacements are approximated by polynomials of degree N in each element and we obtain

$$\sum_{k=1}^K \frac{\partial^2}{\partial t^2} \int_{\Omega_k} \rho \vec{u}_N^j \cdot \vec{w}_N^j d\Omega + \sum_{k=1}^K \int_{\Omega_k} \sigma_{ln}\left(\vec{u}_N^j\right) \varepsilon_{ln}\left(\vec{w}_N^j\right) d\Omega$$

$$= \sum_{k=1}^K \int_{\Gamma_k} \vec{T}_N^j \cdot \vec{w}_N^j d\Gamma + \sum_{k=1}^K \int_{\Omega_k} \vec{f}_N^j \cdot \vec{w}_N^j d\Omega; \quad j = 1, \ldots, N \qquad (5.7)$$

where $\vec{u}_N^j$, $\vec{w}_N^j$, $\vec{T}_N^j$ and $\vec{f}_N^j$ are scalar j-th components of vectors approximating $\vec{u}$, $\vec{w}$, $\vec{T}$ and $\vec{f}$, respectively. The summation convention is assumed for indices j, l, n, and is not assumed for index N. Note that in Eq. (5.7) we implicitly assume that the displacements are

continuous but the material properties can be discontinuous across elements. The integrals in Eq. (5.7) are evaluated numerically by a high-order quadrature based on the Gauss–Lobatto–Legendre (GLL) points and weights (e.g., Canuto *et al.* 1988). The polynomials used for approximating the displacements are then defined as the Lagrange interpolants of the GLL points. Assembling the elementary contributions to account for the continuity of displacements, Eq. (5.7) can be written as a global system of ordinary differential equations in time:

$$\mathbf{M}\,\ddot{U}(t) + \mathbf{K}\,U(t) = \mathbf{F}(t) + \mathbf{T}(t) \tag{5.8}$$

where $\mathbf{F}(t)$ and $\mathbf{T}(t)$ are global vectors accounting for external body force and tractions, respectively, $\mathbf{M}$ and $\mathbf{K}$ are global mass and stiffness matrices, respectively, and $U(t)$ is the global vector of discrete (approximating) displacements. An important consequence of the choice of the polynomial basis is that the mass matrix is diagonal, which, as stated previously, allows for the use of a fully explicit FD scheme for the time evolution. The latter is usually done using the explicit, conditionally stable, 2nd-order leapfrog scheme (e.g., Maggio and Quarteroni 1994).

5.4 Spectral discontinuous Galerkin scheme with ADER time integration

The discontinuous Galerkin (DG) FE scheme combined with a time integration technique using Arbitrarily high order DERivatives (ADER) is a numerical method for solving the 3D equations of motion in the velocity–stress formulation. A hyperbolic system of equations may be concisely written for isotropic or anisotropic elastic, viscoelastic or poroelastic media in the form (see Eq. (2.33)),

$$\frac{\partial \tilde{Q}_p}{\partial t} + A_{pq} \frac{\partial \tilde{Q}_q}{\partial \xi} + B_{pq} \frac{\partial \tilde{Q}_q}{\partial \eta} + C_{pq} \frac{\partial \tilde{Q}_q}{\partial \zeta} = E_{pq} \tilde{Q}_q + S_p \tag{5.9}$$

Here

$$\tilde{Q} = (\sigma_{xx}, \sigma_{yy}, \sigma_{zz}, \sigma_{xy}, \sigma_{yz}, \sigma_{xz}, v_x, v_y, v_z)^T \tag{5.10}$$

The Jacobian matrices A_{pq}, B_{pq} and C_{pq} include parameters corresponding to the type of medium (Dumbser and Käser 2006, Käser *et al.* 2007, de la Puente *et al.* 2007, 2008). Matrix E_{pq} represents viscoelasticity and attenuation corresponding to the rheology of the generalized Maxwell body (GMB-EK in Chapter 3). Term S_p is an external source term representing forces of the moment-tensor sources.

In the ADER DG approach the solution is approximated inside each tetrahedral element by a linear combination of space-dependent polynomial basis functions and time-dependent degrees of freedom, as expressed through

$$(\tilde{Q}_h)_p(\xi, \eta, \zeta, t) = \hat{Q}_{pl}(t) \Phi_l(\xi, \eta, \zeta) \tag{5.11}$$

where the basis functions Φ_l form an orthogonal modal basis and are defined on the canonical reference tetrahedron such that no integration points are necessary. For a detailed

derivation of the numerical scheme we refer to articles by Käser and Dumbser (2006), and Dumbser and Käser (2006). The unique property of the ADER-DG scheme is that the temporal accuracy of the scheme is automatically coupled to the spatial accuracy determined by the degree of approximation polynomials used in Eq. (5.11). This is due to the ADER time-integration approach (Titarev and Toro 2002) that uses a Taylor series expansion in time of the solution of Eq. (5.9), replacing all temporal derivatives recursively by spatial derivatives. Thus, the Taylor series expansion only depends on spatial derivatives of the basis functions and lower-order time derivatives of the source terms. The resulting expression for the degrees of freedom can be integrated in time analytically as shown in detail by Dumbser and Käser (2006) or Käser *et al.* (2007). Therefore, the ADER-DG approach provides an arbitrarily high order approximation in space and time depending on the degree of the used basis polynomials in Eq. (5.11) and the corresponding order of the chosen Taylor series in time.

Once the high-order time-integrated degrees of freedom are computed, the evolution of the numerical solution in time is calculated via local stiffness and flux terms (Dumbser and Käser 2006). Numerical fluxes out of an element and into an element have to be calculated for each element boundary, i.e., triangular surface, for each tetrahedral element. Each flux computation requires a multiplication of two dense matrices with dimensions $(N \times N)$ and $(N \times 9)$, respectively, with N being the number of degrees of freedom and 9 the number of variables in the vector of unknowns in Eq. (5.10). The calculation of the three stiffness terms has to be carried out only once per element via a multiplication of two matrices of the same size as above; however, the $(N \times N)$ stiffness matrix is typically sparse. All operations use only local data from the element itself and its direct neighbour element sharing a common boundary. Due to this local character of the numerical scheme it is well suited for parallel computing.

With the ADER-DG approach it is possible to vary the degree of the approximation polynomials in Eq. (5.11) from one element to another. Due to the direct coupling of the temporal and spatial accuracy via the ADER approach, the scheme automatically becomes adaptive in temporal accuracy – this is the so-called p_τ-adaptation. The p_τ-adaptation allows for an adaptive choice of spatial accuracy, which enhances computational efficiency in most applications. This is because the computational domain is typically larger than the particular zone of interest where high-order accuracy is required. Even more important, the ADER-DG method can use local time stepping to reduce computational cost. Geometrically complex computational domains or requirements on spatial resolution often lead to meshes including small and large elements with significant differences in the element size. The time step for the explicit numerical schemes is restricted by the ratio of the mesh size h of the smallest element and the corresponding maximum wave speed in this element. For the global time-stepping schemes all elements are updated with this possibly strongly restrictive time step. This can lead to a large number of time levels that must be computed. With the ADER approach, time-accurate local time stepping can be used: each element can be updated with its own optimal time step. An element can be updated to the next time level if its actual time level and its local time step fulfil a certain update criterion.

The information exchange between elements across their joint boundaries works through numerical fluxes that depend on the length of the local time interval over which the flux is integrated. The local time-stepping approach can reduce the overall amount of flux calculations dramatically because only the small elements have to be updated frequently according to their small time steps. For a complete description of the p_τ-adaptation and local time stepping see the article by Dumbser *et al.* (2007).

De la Puente *et al.* (2009) and Pelties *et al.* (2012) demonstrated that the ADER-DG method is capable of numerically simulating dynamic rupture propagation on complex faults without spurious high-frequency oscillations, which pose a serious problem for other numerical grid methods. The latter aspect is important for earthquake source studies as well as for numerical simulation of earthquake ground motion. Moreover, the p_τ-adaptation and local time stepping can be advantageous in the cohesive zone of frictional sliding.

The absence of the spurious high-frequency oscillations is due to the numerical properties of the exact Riemann solver (Godunov flux). In fact, the constitutive friction law is incorporated in the solution of the so-called inverse Riemann problem at element interfaces. A mesh is constructed so that the fault everywhere coincides with the interface of two elements. The Godunov flux is an upwind scheme that is intrinsically dissipative, with the attribute that the dissipation increases steeply as a function of frequency depending on the element size and applied order of approximation. Therefore, the high-frequency content is adaptively damped without perturbing the lower, physically meaningful frequencies. Actually, this numerical property has two positive consequences: (1) no spurious high-frequency oscillations during frictional sliding, (2) mesh coarsening (*h*-adaptivity) is possible without causing artificial reflections or instabilities at the area of grid refinement due to numerical impedance.

The method has been successfully applied also to more advanced dynamic rupture problems such as bi-material faults, faults with heterogeneous stress loading, surface rupture, and fault branching (see SCEC Dynamic Rupture Code Verification Project: http://scecdata.usc.edu/cvws/). The method can accommodate both the linear slip-weakening and rate-and-state type friction laws.

The discontinuous Galerkin method is a powerful general approach that can be the basis for a variety of formulations. We refer to, e.g., de Basabe *et al.* (2008), Delcourte *et al.* (2009), Etienne *et al.* (2010), Wilcox *et al.* (2010) and Tago *et al.* (2012).

5.5 Hybrid methods

Each of the many computational and numerical methods that have been developed so far for seismic wave propagation and earthquake motion has at least one feature in which it is better or more advantageous compared to other methods – at least with respect to some specific medium–wavefield configuration. We can also say that none of the existing methods can be considered the most accurate and, at the same time, the most computationally efficient for all important medium–wavefield configurations. In many problem configurations it is

therefore reasonable to combine two or even more computational methods in order to solve the problem with a reasonable level of accuracy and computational efficiency.

It can be advantageous to solve the time dependence of a field variable using one method and the spatial dependence using some other method. For example, Alexeev and Mikhailenko (1980) combined partial separation of variables and an FD method, Mikhailenko and Korneev (1984) combined the finite integral Fourier transform and FDM.

It can be advantageous to split the computational domain into two or more parts and solve each part by the best-suited method. For example, one method may be applied in a sub-domain that includes a dynamically rupturing fault, another method may be applied in the sub-domain that includes topography of the free surface, and one method may be applied in the major part of the whole computational domain for efficient seismic wave propagation. Another example is the configuration in which we are interested in detailed modelling of earthquake ground motion in a surface local structure due to a relatively distant source. In this type of hybrid approach it is important to develop a stable and noise-free algorithm, ensuring the causal communication between neighbouring sub-domains respecting the physics of the adopted model. Several hybrid methods have been developed, most of them in 2D, in an effort to achieve reasonable computational efficiency in applications to relatively complex structural models. They include methods by Ohtsuki and Harumi (1983), Shtivelman (1984, 1985), Van den Berg (1984), Kummer *et al.* (1987), Kawase (1988), Stead and Helmberger (1988), Emmerich (1989, 1992), Gaffet and Bouchon (1989), Fäh (1992), Fäh *et al.* (1993), Bouchon and Coutant (1994), Rovelli *et al.* (1994), Robertsson *et al.* (1996), Zahradník and Moczo (1996), Moczo *et al.* (1997), Lecomte *et al.* (2004), Ma *et al.* (2004), Galis *et al.* (2008), Zhao *et al.* (2008), Liu and Sen (2010), Liu *et al.* (2011), Monteiller *et al.* (2012). Extensive references on the hybrid approaches can be found in the article by Opršal *et al.* (2009).

In Chapter 18 we describe the hybrid FD–FE method developed by Galis *et al.* (2008).

6

Brief introduction to the finite-difference method

Application of the method to a particular differential problem includes:

(a) Construction of a discrete FD model of the problem
  – coverage of the computational domain by a space–time grid,
  – FD approximations of derivatives, functions, initial and/or boundary condition at the grid points,
  – construction of a system of algebraic equations; we may call them FD equations or FD scheme.
(b) Analysis of the FD model
  – consistency and order of the approximation,
  – stability and grid dispersion,
  – convergence,
  – local error.
(c) Numerical computations.

Analysis of the FD model and numerical computations may lead to redefinition of the grid and FD approximations if the numerical behaviour of the developed FD scheme is not satisfactory.

Note that in the case of the so-called explicit FD schemes (see later), the term 'scheme' is often used in a narrower meaning for the explicit algebraic formula for updating a field variable (displacement or particle-velocity or stress-tensor component) at a spatial grid position.

6.1 Space–time grids

6.1.1 Cartesian grid

Consider a spatial Cartesian coordinate system (x, y, z) and a computational domain in the 4D space of variables (x, y, z, t) with t meaning time. A set of discrete space–time points (or positions)

$$(x_I, y_K, z_L, t_m), \quad I, K, L, m \in \{0, 1, 2, \ldots\}$$

$$x_I = x_0 + I \Delta x_I, \quad y_K = y_0 + K \Delta y_K, \quad z_L = z_0 + L \Delta z_L, \quad t_m = t_0 + m \Delta \quad (6.1)$$

defines a space–time grid. Grid coordinates x_I, y_K, z_L determine a spatial grid point (position), coordinate t_m determines a time level. The spatial increments Δx_I, Δy_K and Δz_L are usually called grid spacings, Δ is the time step. The value of a function φ at the grid point (x_I, y_K, z_L, t_m), that is $\varphi(x_I, y_K, z_L, t_m)$, may be denoted by $\varphi(I, K, L, m)$ or $\varphi_{I,K,L}^m$ or $\varphi|_{I,K,L}^m$. The exact value should be distinguished from its FD approximation, which may be denoted, e.g., by $\Phi_{I,K,L}^m$.

The Cartesian coordinate system is convenient and natural for modelling of earthquake motion in local surface structures. Systems other than Cartesian coordinate systems can also be used to define a grid. The particular choice should be problem dependent. Whereas spherical coordinates might be convenient for whole Earth models, cylindrical coordinates might be more suitable for borehole modelling. The choice of the grid determines the structure and properties of the FD approximations of derivatives, and consequently the properties of the FD scheme.

6.1.2 Uniform, nonuniform and discontinuous grids

A grid specified by Eqs. (6.1) is nonuniform in all coordinate directions – the size of the grid spacing in general varies point to point. In many applications it might be reasonable to use $\Delta x_I = \Delta y_K = \Delta z_L = h$. In such a case the grid is uniform. The use of a uniform grid usually yields the algorithmically simplest FD schemes. This, however, may contradict the computational efficiency. Therefore, in some applications it is advantageous to use a spatially discontinuous grid – part of the computational domain is covered with a uniform grid with grid spacing h_F whereas the rest of the computational domain is covered with a uniform grid with grid spacing $h_C > h_F$. The subscripts indicate coarser and finer grids, respectively. This is usually related to the heterogeneity of the medium. It is also possible to use a grid that is discontinuous in size of spatial grid spacing and/or time step.

6.1.3 Structured and unstructured grids

If at a grid point explicit information about the connection to neighbouring grid points is needed we speak about unstructured grids. If at a grid point explicit information is not needed (e.g., we can find neighbouring grid points just by using indices) we speak about structured grids. Obviously, structured grids usually yield computationally faster algorithms compared to those on unstructured grids.

6.1.4 Space–time locations of field variables

Grids and consequently FD schemes may differ in the grid positions of the displacement/particle-velocity and stress-tensor components. It is natural to think of having all of them at each space–time grid position. Clearly, such location of all field variables is ideal for imposing initial and boundary conditions in an isotropic medium and, in general, for an anisotropic medium. As will be seen later, however, having all field variables at

Typical spatial FD grid cells

displacement
conventional

$$h$$

$\square \quad u_x^m, u_y^m, u_z^m$

velocity - stress

collocated   partly-staggered   staggered

h h $h\,/2$

$\circ \quad v_x^m, v_y^m, v_z^m$

$\sigma_{xx}^m, \sigma_{yy}^m, \sigma_{zz}^m$

$\sigma_{xy}^m, \sigma_{yz}^m, \sigma_{zx}^m$

$\circ \quad v_x^{m+1/2}, v_y^{m+1/2}, v_z^{m+1/2}$

$\otimes \quad \sigma_{xx}^m, \sigma_{yy}^m, \sigma_{zz}^m$

$\sigma_{xy}^m, \sigma_{yz}^m, \sigma_{zx}^m$

$\blacksquare \quad v_x^{m+1/2}$

$\blacktriangledown \quad v_y^{m+1/2}$

$\bullet \quad v_z^{m+1/2}$

$\otimes \quad \sigma_{xx}^m, \sigma_{yy}^m, \sigma_{zz}^m$

$\square \quad \sigma_{xy}^m$

$\triangledown \quad \sigma_{yz}^m$

$\circ \quad \sigma_{zx}^m$

u ~ displacement v ~ particle velocity σ ~ stress
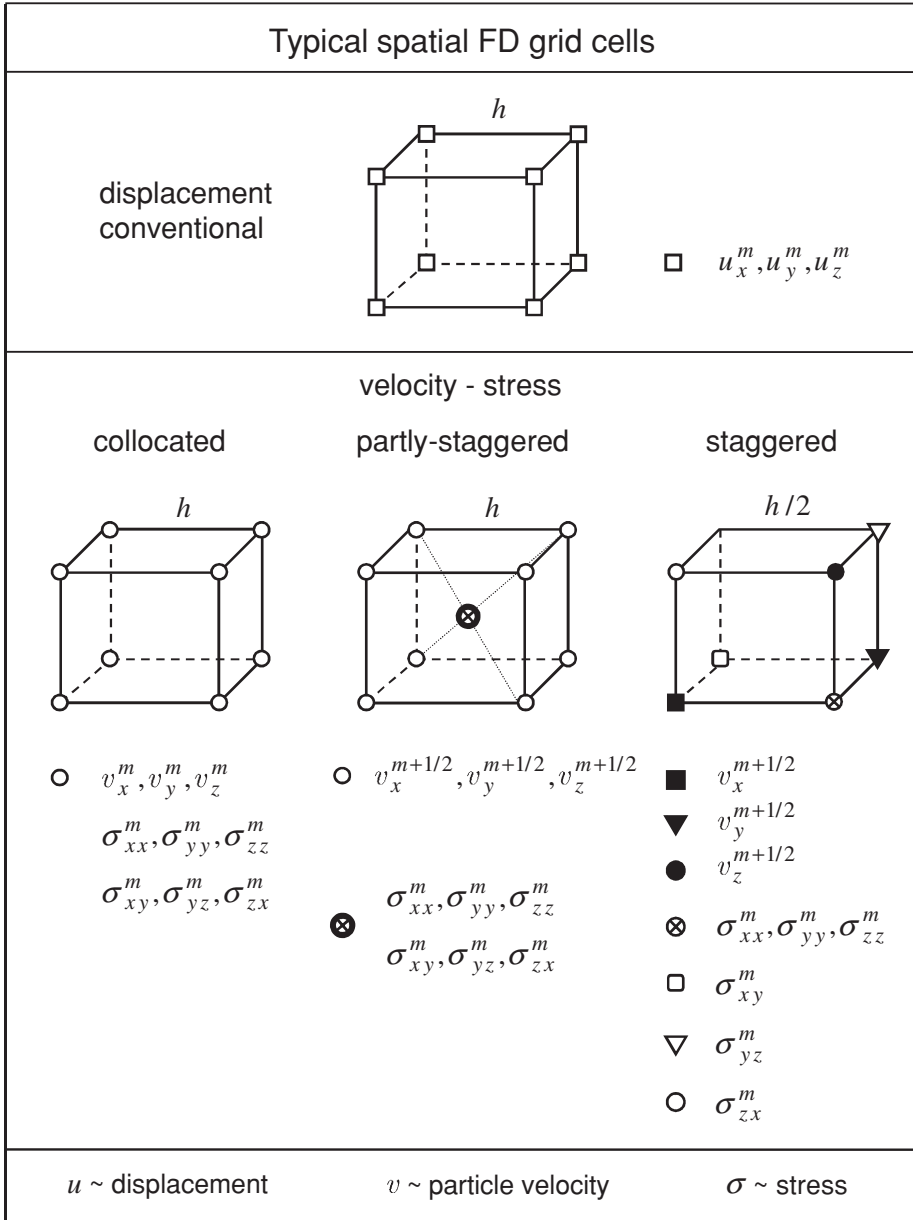
Figure 6.1 Illustration of the conventional, collocated, partly-staggered and staggered grids. The upper index *m* indicates the time level of the variable.

each grid space–time position and, at the same time, having 'easy/natural/desirable' FD approximations of derivatives is not trivial.

Figure 6.1 shows four typical FD grid cells. The first one is the conventional grid with the displacement-vector components at each grid point (position, node). It is a natural

grid for displacement schemes solving the displacement formulation of the equation of motion (the 2nd-order equation of motion). The second is the collocated grid with all the particle-velocity vectors and all the stress-tensor components at each grid position. It is a natural grid for the velocity–stress formulation with a vector of field variables consisting of all the particle-velocity and stress components. In the conventional and collocated grids all the field variables relate to the same time. The third type is the partly-staggered grid with all the particle-velocity components located at one grid position and all the stress components located at another grid position. Finally, in the staggered grid, each particle-velocity component and each shear stress component has its own grid position. The normal stress-tensor components share another grid position. In the velocity–stress formulation the temporal location of the particle-velocity vector is shifted by a half time step from the temporal location of the stress tensor in the case of the partly-staggered and staggered grids. Note, however, that in general the temporal location depends on the type of time-marching scheme. For example, use of the Runge–Kutta time-marching scheme with a spatially staggered grid leads to the same time for the particle-velocity and stress-tensor components. Use of the leapfrog time-marching scheme with a collocated grid leads to different temporal locations for the particle-velocity and stress-tensor components.

The collocated, partly-staggered and staggered grids may also be used for the displacement–stress formulation. In such a case all field variables relate to the same time.

The simplest, most natural, complementary and homogeneous is the approximation of derivatives in the velocity–stress staggered-grid schemes.

In all types of grids, an effective density (or its reciprocal value) is assigned to a grid position of each displacement or particle-velocity component, whereas an effective elastic modulus is assigned to each grid position of the stress-tensor components.

There are additional material parameters and field variables in the case of a viscoelastic or elastoplastic medium. They will be introduced later.

6.2 FD approximations based on Taylor series

6.2.1 Simple approximations

We assume sufficient smoothness of function φ and consider a Taylor series expansion of the function at point $x + h$ about point x:

$$\varphi(x + h) = \varphi(x) + h\varphi'(x) + \tfrac{1}{2}h^2\varphi''(x) + \tfrac{1}{6}h^3\varphi'''(x) + O(h^4) \qquad (6.2)$$

The equation implies

$$\varphi'(x) = \frac{1}{h}[\varphi(x + h) - \varphi(x)] - \tfrac{1}{2}h\varphi''(x) - \tfrac{1}{6}h^2\varphi'''(x) - O(h^3) \qquad (6.3)$$

We can define a forward approximation of the first derivative by

$$D_x^F \varphi(x) \equiv \frac{1}{h}[\varphi(x + h) - \varphi(x)] \qquad (6.4)$$

The accuracy of the approximation can be characterized by the truncation error. The truncation error of approximation (6.4) is

$$TrunErr\left\{D_x^F \varphi(x)\right\} \equiv TaylorExpansion\left\{D_x^F \varphi(x)\right\} - \varphi'(x)$$
$$= \tfrac{1}{2}h\varphi''(x) + \tfrac{1}{6}h^2\varphi'''(x) + O\left(h^3\right) \tag{6.5}$$

The leading term of the truncation error, $\tfrac{1}{2}h\varphi''(x)$, is proportional to increment h. Therefore, we can simply write:

$$TrunErr\left\{D_x^F \varphi(x)\right\} = O\left(h\right) \tag{6.6}$$

$$D_x^F \varphi(x) = \varphi'(x) + O\left(h\right) \tag{6.7}$$

and say that the forward approximation (6.4) of the first derivative is 1st-order accurate.

Analogously we can write for the backward approximation:

$$D_x^B \varphi(x) \equiv \frac{1}{h}\left[\varphi(x) - \varphi\left(x - h\right)\right]; \quad D_x^B \varphi(x) = \varphi'(x) + O\left(h\right) \tag{6.8}$$

1st-order accuracy is rarely sufficient. From Taylor series expansions:

$$\varphi\left(x \pm h\right) = \varphi(x) \pm h\varphi'(x) + \tfrac{1}{2}h^2\varphi''(x) \pm \tfrac{1}{6}h^3\varphi'''(x) + O(h^4) \tag{6.9}$$

we easily obtain

$$\varphi'(x) = \frac{1}{2h}\left[\varphi\left(x + h\right) - \varphi\left(x - h\right)\right] - \tfrac{1}{6}h^2\varphi'''(x) - O(h^4) \tag{6.10}$$

The leading term of the truncation error, $\tfrac{1}{6}h^2\varphi'''(x)$, is proportional to h^2. We can thus define the 2nd-order centred approximation:

$$D_x\varphi(x) \equiv \frac{1}{2h}[\varphi(x + h) - \varphi(x - h)]; \quad D_x\varphi(x) = \varphi'(x) + O(h^2) \tag{6.11}$$

Note that

$$D_x\varphi(x) = \tfrac{1}{2}\left[D_x^F \varphi(x) + D_x^B \varphi(x)\right] \tag{6.12}$$

Later we will develop various approximations. Here we show one approximation that is fundamental for many recent velocity–stress FD schemes. We derive the approximation in order to indicate how to find any desired approximation. Suppose we want to approximate the 1st derivative at x using function values at points $\{x - \tfrac{3}{2}h, x - \tfrac{1}{2}h, x + \tfrac{1}{2}h, x + \tfrac{3}{2}h\}$. Assume the approximation in the form

$$D_x^{(1-4)}\varphi(x) = \frac{1}{h}\sum_{j=1}^{2} c_j \left\{\varphi\left[x + \tfrac{1}{2}\left(2j - 1\right)h\right] - \varphi\left[x - \tfrac{1}{2}\left(2j - 1\right)h\right]\right\} \tag{6.13}$$

We want to find coefficients c_1 and c_2. Taylor expansion of the r.h.s. of Eq. (6.13) gives

$$(c_1 + 3c_2)\varphi'(x) + \tfrac{1}{24}(c_1 + 27c_2)\varphi'''(x)h^2 + \tfrac{1}{1920}(c_1 + 243c_2)\varphi^{(5)}(x)h^4 + O(h^6) \tag{6.14}$$

We require

$$c_1 + 3c_2 = 1, \quad c_1 + 27c_2 = 0 \tag{6.15}$$

Solving system of equations (6.15) we obtain $c_1 = \frac{9}{8}$, $c_2 = -\frac{1}{24}$. The desired approximation is then

$$D_x^{(1-4)}\varphi(x) = \frac{1}{h} \left\{ \frac{9}{8} \left[\varphi\left(x + \tfrac{1}{2}h\right) - \varphi\left(x - \tfrac{1}{2}h\right) \right] - \frac{1}{24} \left[\varphi\left(x + \tfrac{3}{2}h\right) - \varphi\left(x - \tfrac{3}{2}h\right) \right] \right\} \tag{6.16}$$

$$D_x^{(1-4)}\varphi(x) = \varphi'(x) + O(h^4) \tag{6.17}$$

Superscript (1–4) thus indicates the 4th-order accurate approximation of the 1st spatial derivative.

It is also easy to find forward and backward approximations of the 4th-order accuracy. Forward and backward approximations are sometimes called one-sided approximations. Consider that the x-axis is oriented positive to the right. Approximation (6.4) uses a functional value at the grid point at which we want to approximate the derivative and one grid point on the right. Approximation (6.8) uses a functional value at the grid point at which we want to approximate the derivative and one grid point on the left. In general, however, the terms forward, backward and one-sided approximation refer to approximations using values at grid points on both sides of the position at which they approximate the derivative. An approximation is called, say, forward, if it uses more points on the right and fewer points on the left. We will see such approximations in Chapter 7.

6.2.2 Combined approximations: convolution

In this subsection we show how we can obtain an approximation of a higher derivative using approximations of a lower derivative. We will use this approach in Chapter 7. Here we will indicate spatial positions using subscripts – as introduced in Subsection 6.1.1. Consider two approximations:

$$D_x^a \Phi_I \equiv \sum_k a_{k/N} \Phi_{I+k/N}, \quad D_x^b \Phi_I \equiv \sum_l b_{l/N} \Phi_{I+l/N} \tag{6.18}$$

where k, l, I, N are integers. Apply D_x^a to $D_x^b \Phi_I$:

$$D_x^a \left(D_x^b \Phi_I \right) = \sum_k a_{k/N} \sum_l b_{l/N} \Phi_{I+l/N+k/N}$$

$$= \sum_k \sum_l a_{k/N} b_{l/N} \Phi_{I+(l+k)/N} \tag{6.19}$$

Using substitution

$$j \equiv l + k \tag{6.20}$$

we obtain

$$D_x^a \left(D_x^b \Phi_I \right) = \sum_k \sum_j a_{k/N} b_{(j-k)/N} \Phi_{I+j/N} \tag{6.21}$$

Define

$$c_{j/N} \equiv \sum_k a_{k/N} b_{(j-k)/N} \tag{6.22}$$

Then,

$$D_x^{ab} \Phi_I \equiv D_x^a \left(D_x^b \Phi_I \right) = \sum_j c_{j/N} \Phi_{I+j/N} \tag{6.23}$$

Approximation $D_x^{ab} \Phi_I$ has the same form as $D_x^a \Phi_I$ and $D_x^b \Phi_I$. Its coefficients $c_{j/N}$ are given by convolution of coefficients $a_{k/N}$ and $b_{l/N}$. We may indicate the convolution by symbol $\circ$:

$$D_x^{ab} \Phi_I \equiv D_x^a \left(D_x^b \Phi_I \right) = D_x^a \circ D_x^b \Phi_I \tag{6.24}$$

Example 1. Consider the centred approximation of the first spatial derivative:

$$D_x^{(1)} \Phi_I = \frac{1}{h} \left(\Phi_{I+1/2} - \Phi_{I-1/2} \right) = \sum_k a_{k/2} \Phi_{I+k/2}$$

$$a_{\pm 1/2} = \pm \frac{1}{h}, \quad a_{k/2} = 0; \quad k \neq \pm 1 \tag{6.25}$$

Define approximation $D_x^{(2)}$:

$$D_x^{(2)} \Phi_I = D_x^{(1)} \circ D_x^{(1)} \Phi_I = \sum_j c_{j/2} \Phi_{I+j/2} \tag{6.26}$$

According to Eq. (6.22),

$$c_{j/2} = \sum_k a_{k/2} \, a_{(j-k)/2} \tag{6.27}$$

We easily obtain

$$c_{-2/2} = \frac{1}{h^2}, \quad c_{0/2} = \frac{-2}{h^2}, \quad c_{2/2} = \frac{1}{h^2}, \quad c_{j/2} = 0; \quad j \neq 0, \pm 2 \tag{6.28}$$

and

$$D_x^{(2)} \Phi_I = D_x^{(1)} \circ D_x^{(1)} \Phi_I = \frac{1}{h^2} \left(\Phi_{I-1} - 2\Phi_I + \Phi_{I+1} \right) \tag{6.29}$$

Example 2. Consider forward and backward approximations:

$$D_x^F \Phi_I = \frac{1}{h} \left(\Phi_{I+1} - \Phi_I \right), \quad D_x^B \Phi_I = \frac{1}{h} \left(\Phi_I - \Phi_{I-1} \right) \tag{6.30}$$

They may be written as

$$
\begin{aligned}
D_x^F \Phi_I &= \sum_k a_k \Phi_{I+k}; \quad a_0 = \frac{-1}{h}, \ a_1 = \frac{1}{h}, \ a_k = 0; \ k \neq 0, 1 \\
D_x^B \Phi_I &= \sum_l b_l \Phi_{I+l}; \quad b_{-1} = \frac{-1}{h}, \ b_0 = \frac{1}{h}, \ b_l = 0; \ l \neq -1, 0
\end{aligned}
\tag{6.31}
$$

Combine the two approximations:

$$
D_x^{FB} \Phi_I \equiv D_x^F D_x^B \Phi_I = D_x^F \circ D_x^B \Phi_I = \sum_j c_j \Phi_{I+j}
\tag{6.32}
$$

$$
c_j = \sum_k a_k b_{j-k}
\tag{6.33}
$$

We easily obtain

$$
c_{-1} = \frac{1}{h^2}, \quad c_0 = \frac{-2}{h^2}, \quad c_1 = \frac{1}{h^2}, \quad c_j = 0; \quad j \neq 0, \pm 1
\tag{6.34}
$$

and

$$
D_x^{FB} \Phi_I = \frac{1}{h^2} (\Phi_{I-1} - 2\Phi_I + \Phi_{I+1})
\tag{6.35}
$$

Note that the approximations (6.35) and (6.29) are the same.

6.2.3 Approximations applied to a harmonic wave

Here we develop relations that will be advantageously used in investigations of the stability of FD schemes in Chapter 7. Assume a harmonic wave:

$$
\Phi_I^m = \exp\left[i\left(\omega m \Delta - kIh\right)\right]
\tag{6.36}
$$

and apply the approximation defined by Eq. (6.25):

$$
\begin{aligned}
D_x^{(1)} \Phi_I^m &= D_x^{(1)} \{\exp\left[i\left(\omega m \Delta - kIh\right)\right]\} \\
&= \frac{1}{h} \left[\exp\left(-ik\frac{h}{2}\right) - \exp\left(ik\frac{h}{2}\right)\right] \Phi_I^m \\
&= -i\frac{2}{h} \sin\left(k\frac{h}{2}\right) \Phi_I^m
\end{aligned}
\tag{6.37}
$$

Denote

$$
\mathcal{D}_x^{(1)} \equiv -i\frac{2}{h} \sin\left(k\frac{h}{2}\right)
\tag{6.38}
$$

Then,

$$
D_x^{(1)} \Phi_I^m = D_x^{(1)} \{\exp\left[i\left(\omega m \Delta - kIh\right)\right]\} = \mathcal{D}_x^{(1)} \cdot \Phi_I^m
\tag{6.39}
$$

where we use the dot to indicate a simple multiplication of $\mathcal{D}_x^{(1)}$ and Φ_I^m.

Apply now the approximation defined by Eq. (6.29) to the harmonic wave (6.36):

$$D_x^{(2)} \Phi_I^m = D_x^{(2)} \{ \exp[i(\omega m \Delta - kIh)] \}$$

$$= \frac{1}{h^2} \left[\exp(ikh) - 2 + \exp(-ikh) \right] \Phi_I^m$$

$$= \frac{2}{h^2} \left[\cos(kh) - 1 \right] \Phi_I^m$$

$$= \left[-i\frac{2}{h} \sin\left(k\frac{h}{2} \right) \right]^2 \Phi_I^m \tag{6.40}$$

Denote

$$\mathscr{D}_x^{(2)} \equiv \left[-i\frac{2}{h} \sin\left(k\frac{h}{2} \right) \right]^2 \tag{6.41}$$

The result may be then written as

$$D_x^{(2)} \Phi_I^m = D_x^{(2)} \{ \exp[i(\omega m \Delta - kIh)] \} = \mathscr{D}_x^{(2)} \cdot \Phi_I^m \tag{6.42}$$

Compare relations (6.38) with (6.41) and also (6.39) with (6.42). We see that

$$\mathscr{D}_x^{(2)} = \mathscr{D}_x^{(1)} \cdot \mathscr{D}_x^{(1)} \tag{6.43}$$

This is understandable: it is due to the fact that approximation $D_x^{(2)}$ is defined as the convolution $D_x^{(2)} = D_x^{(1)} \circ D_x^{(1)}$, see Eqs. (6.26) and (6.29).

In general, if

$$D_x^{ab} = D_x^a \circ D_x^b \tag{6.44}$$

then

$$D_x^{ab} \{ \exp[i(\omega m \Delta - kIh)] \} = D_x^a \circ D_x^b \{ \exp[i(\omega m \Delta - kIh)] \}$$

$$= \mathscr{D}_x^a \cdot \mathscr{D}_x^b \cdot \exp[i(\omega m \Delta - kIh)] \tag{6.45}$$

We will use this important relation in deriving grid-dispersion relations in Chapter 7.

6.2.4 General note on the FD approximations

Later we will present approximations for different schemes. We will see that in searching for an appropriate approximation of the spatial derivative we can choose

- the number of spatial grid positions that are to be used,
- the number of time levels that are to be used; the spatial derivative at a time level may be then approximated by a weighted average of approximations at several time levels; this choice leads to an implicit FD scheme (see Section 6.3),
- a centred/backward/forward approximation or their combination,
- order of approximation,

- uniformity/nonuniformity of approximations in different spatial directions; later we will see how this affects properties of the schemes with respect to variation of the ratio between the P-wave and S-wave speeds.

In searching for an appropriate approximation of the temporal derivative we can choose

- the number of time levels that are to be used,
- the number of spatial grid positions that are to be used; the temporal derivative at a spatial position may be then approximated by a weighted average of approximations at several spatial positions; this choice leads to an implicit FD scheme,
- a centred or forward approximation,
- a replacement of higher-order derivatives by spatial derivatives.

We can also choose whether the order of approximation of the spatial derivative will be the same as the order of approximation of the temporal derivative.

The set of choices depends on the formulation of the equations of motion and should correspond to the desired properties of a scheme. It may be, however, far from trivial to predict the resulting properties of the scheme. Some iterations (including construction, theoretical analysis and numerical tests) might be necessary to develop a scheme appropriate for a problem.

More on the FD approximations may be found in articles by, e.g., Dablain (1986), Fornberg (1988a), Holberg (1987), Kindelan *et al.* (1990), Klimeš (1996), Tam and Webb (1993), Hixon (1997), Geller and Takeuchi (1995, 1998), Cohen (2002), JafarGandomi and Takenaka (2009), Abreu *et al.* (2013). Dablain (1986) demonstrated the properties and practical advantages (mainly significantly reduced memory requirements) of the higher-order FD approximation in application to the scalar wave equation. Fornberg (1988a) derived simple recursive formulas for calculating weights in FD approximations for any order of derivative and any order of accuracy on 1D grids with arbitrary spacing. Geller and Takeuchi (1995, 1998) approximated the spatial derivative at time t_m as an average of spatial derivatives at times t_{m-1}, t_m and t_{m+1}. Similarly, they approximated the temporal derivative at position x_I as an average of temporal derivatives at positions x_{I-1}, x_I and x_{I+1}. Holberg (1987) thought that construction of the FD approximations based on Taylor series expansion lacks physical insight. Instead of minimizing the error measured in terms of higher-order derivatives, he minimized the relative error in the components of the group velocity vector due to the grid dispersion within a specific frequency band emitted by sources. The argument for minimizing the relative error in the components of the group velocity was that the propagation of energy is governed by the group velocity. Tam and Webb (1993) minimized the error in dispersion – see Section 6.5. JafarGandomi and Takenaka (2009) developed an approximation based on the correction functions and the FD Laplacian. The correction functions are used to modify the time and space discretization steps for a design frequency and wavenumber for achieving higher phase accuracy. The FD Laplacian is introduced to reduce the grid anisotropy. Abreu *et al.* (2013) generalized the

complex-step method to develop different approximations of the 1st and 2nd derivatives of any complex analytic function.

Simple illustration of a variety of FD schemes Consider the 1st-order hyperbolic equation with a constant coefficient:

$$\frac{\partial \varphi}{\partial t} = a \frac{\partial \varphi}{\partial x} \tag{6.46}$$

Here is an example, taken from Strikwerda (2004), of five alternative approximations of the equation at the time level m and spatial position I:

- forward in time and space

$$\frac{1}{\Delta} \left(\varphi_I^{m+1} - \varphi_I^m \right) \approx a \frac{1}{h} \left(\varphi_{I+1}^m - \varphi_I^m \right) \tag{6.47}$$

- forward in time, backward in space

$$\frac{1}{\Delta} \left(\varphi_I^{m+1} - \varphi_I^m \right) \approx a \frac{1}{h} \left(\varphi_I^m - \varphi_{I-1}^m \right) \tag{6.48}$$

- forward in time, centred in space

$$\frac{1}{\Delta} \left(\varphi_I^{m+1} - \varphi_I^m \right) \approx a \frac{1}{2h} \left(\varphi_{I+1}^m - \varphi_{I-1}^m \right) \tag{6.49}$$

- centred in time and space (so-called leapfrog)

$$\frac{1}{2\Delta} \left(\varphi_I^{m+1} - \varphi_I^{m-1} \right) \approx a \frac{1}{2h} \left(\varphi_{I+1}^m - \varphi_{I-1}^m \right) \tag{6.50}$$

- Lax–Friedrichs approximation

$$\frac{1}{\Delta} \left[\varphi_I^{m+1} - \tfrac{1}{2} \left(\varphi_{I+1}^m - \varphi_{I-1}^m \right) \right] \approx a \frac{1}{2h} \left(\varphi_{I+1}^m - \varphi_{I-1}^m \right) \tag{6.51}$$

In Subsection 7.3.6 we explain the Lax–Wendroff and MacCormack approximations of Eq. (6.46)

6.3 Explicit and implicit FD schemes

In an implicit scheme, the field variable at a time level at a spatial position is calculated using values at the same time level and previous time levels. Consequently, the field variable at a time level has to be calculated simultaneously at all spatial grid points from the values of the field variables at previous time levels. Implicit schemes applied to realistic models lead to relatively large matrices. In an explicit scheme, the field variable at a spatial grid point and time level is calculated using an explicit FD formula that uses only values of field variables at previous time levels. Clearly, the explicit schemes are computationally much

simpler. Therefore, explicit FD schemes have been used in most earthquake ground motion modelling and exploration seismology studies.

An interesting example was presented by Geller and Takeuchi (1998). Their optimization of the classical 2nd-order FD displacement scheme led to an implicit FD scheme (they named it the optimally accurate scheme) because they approximated the spatial derivative as a weighted average of approximations at three time levels, and, similarly, the temporal derivative as a weighted average of approximations at three spatial positions. In order to avoid solving large systems of algebraic equations, Geller and Takeuchi applied a predictor-corrector scheme.

In compact schemes (e.g., Lele 1992) the spatial derivative at one spatial position is calculated using both spatial derivatives and values at neighbouring grid positions. As a consequence, the compact schemes are implicit.

For the implicit schemes see also, e.g., Emerman *et al*. (1982), Mufti (1985), Liu and Sen (2009).

6.4 Basic properties of FD schemes

An FD scheme should be consistent with the original problem, stable and convergent. Here we very briefly characterize these three properties. We recommend more mathematically oriented books for more detailed exposition and analysis: e.g., Isaacson and Keller (1966), Richtmyer and Morton (1967), Mitchell (1969), Marchuk (1982), Mitchell and Griffiths (1994), Morton and Mayers (1994), Thomas (1995), Shashkov (1996), Durran (1999), Cohen (2002), Forsythe and Wasow (2004), Strikwerda (2004), LeVeque (2007).

We use here the abbreviation *FDEQ* for FD equations or FD scheme, and *EQ* for a partial differential equation.

Consistency An *FDEQ* is consistent with the *EQ* if the difference between the *FDEQ* and the *EQ* (the approximation or truncation error) vanishes as the sizes of the time step Δ and spatial grid spacing h go to zero independently, that is,

$$\lim_{h \to 0, \Delta \to 0} |EQ - FDEQ| = 0 \tag{6.52}$$

In most cases no relation between h and Δ is required. If, however, condition (6.52) is true only when a certain relation is satisfied between h and Δ, the *FDEQ* is conditionally consistent.

Stability An *FDEQ* is stable if it produces a bounded solution when the exact solution is bounded, and is unstable if it produces an unbounded solution when the exact solution is bounded. If the solution of the *FDEQ* is bounded for all values of h and Δ, the *FDEQ* is unconditionally stable. If the solution of the *FDEQ* is bounded only for certain values of h and Δ, the *FDEQ* is conditionally stable. If the solution of the *FDEQ* is unbounded for all values of h and Δ, the *FDEQ* is unconditionally unstable.

The stability analysis can be performed only for a linear *EQ*. A nonlinear *EQ* must be first linearized locally. The *FDEQ* of the linearized *EQ* can be analyzed for stability. There are several methods for analyzing stability. Probably the best known is the von Neumann method. The basic idea of the von Neumann method is to represent a discrete solution at a time level and spatial grid point by a finite Fourier series, and examine stability of the individual Fourier components. In this sense the method investigates the local stability. The discrete solution is stable if and only if each Fourier component is stable.

The von Neumann method and also other methods of stability analysis are applicable to linear *FDEQ* with constant coefficients; in other words, for a homogeneous medium. Therefore, the stability condition found for the homogeneous medium has, in fact, an indicative meaning and should be checked in numerical computations for heterogeneous media.

Note that the explicit schemes can be only conditionally stable, whereas some implicit schemes can be unconditionally stable.

Convergence An *FDEQ* is convergent if the solution of the *FDEQ* approaches the exact solution of the *EQ* as the sizes of the time step and spatial grid spacing go to zero. Denoting the solutions obtained by the *EQ* and *FDEQ* as $\varphi_{I,K,L}^m$ and $\Phi_{I,K,L}^m$ respectively, the convergence means

$$\lim_{h\to 0,\Delta\to 0}\left|\Phi_{I,K,L}^m - \varphi_{I,K,L}^m\right| = 0 \tag{6.53}$$

It is important to note that the consistency is the property of the *FDEQ* because it relates the *FDEQ* to the *EQ*. On the other hand, stability and convergence are properties of the numerical solution of the *FDEQ*.

Lax equivalence theorem In general, while it is easy to analyze the consistency, proving convergence can be a very difficult mathematical problem. Therefore, it is very helpful that the convergence is related to the consistency and the stability: it follows from the Lax equivalence theorem that if the *FDEQ* is consistent and stable, it is also convergent.

Grid dispersion Because the FD solution is a discrete approximation of a true solution, the phase and group velocities in the grid in general differ from the true velocities in the medium. Grid dispersion is a very important grid phenomenon. It has a cumulative effect on wave propagation – the longer the travel distance, the larger the effect of the difference between the grid and true velocity. Therefore, grid dispersion has to be analyzed prior to the numerical calculations. Given the desired travel path, one has to choose appropriate spatial sampling of the wavelength to be propagated with a desired level of accuracy.

The grid-dispersion relation is a relation comprising frequency (real or grid), wavenumber (grid or real, respectively), grid spacing, time step and true physical speed(s) of the medium. Due to discretization, the dispersion relation in the grid differs from the dispersion relation between frequency and wavenumber in the true physical continuum. The dispersion

relation can be obtained from the stability analysis. Such analysis is feasible for many FD schemes assuming a homogeneous medium. It may be very complicated for heterogeneous media. Consequently, the effects of grid dispersion should be examined by careful numerical tests if the scheme is to be applied to heterogeneous media – which, in fact, is almost always the case.

For a detailed analysis of stability, grid dispersion and accuracy of the FD schemes in solving the equation of motion in 2D and 3D problems in homogeneous media see, e.g., articles by Marfurt (1984), Crase *et al.* (1992), Geller and Takeuchi (1995, 1998), Igel *et al.* (1995), Klimeš (1996), Mizutani *et al.* (2000), Moczo *et al.* (2000), Takeuchi and Geller (2000), Zingg (2000), Liu and Sen (2011a,b), Geller *et al.* (2012).

6.5 Approximations based on a dispersion-relation-preserving criterion

Tam and Webb (1993) presented an interesting approach for finding FD approximations. They pointed out that the quality of FD schemes (in computational fluid dynamics) is generally ranked by the order of the Taylor series expansion truncation. For example, a 4th-order scheme should be better than a 2nd-order scheme. They claim that whereas for time-independent problems such a criterion is quite sufficient, for time-dependent problems, especially acoustics problems, a consistent, stable and convergent higher-order scheme does not guarantee a good quality numerical wave solution. Their basic argument is: the propagation characteristics of the waves governed by a system of partial differential equations are encoded in the dispersion relation in the frequency and wavenumber space. Therefore, what is needed is an FD scheme that has the same or almost the same dispersion relation as the original partial differential equations.

The dispersion relation may be obtained by applying the space and time Fourier transforms to the governing equations. If the dispersion relation is to be preserved then the FD approximation should be constructed so that the Fourier transform is preserved. In other words, an FD approximation should have nearly the same Fourier transform in space or time as the original partial derivative.

Hixon (1997) used the dispersion-relation-preserving (DRP) approach of Tam and Webb (1993) and developed one-sided (forward and backward) approximations of the first derivative. Zhang and Chen (2006) and Zhang *et al.* (2012) applied a combination of the forward and backward DRP approximations developed by Hixon (1997) in their FD modelling. We will address their scheme in Chapter 7.

Tam and Webb (1993) also showed that it is possible to combine the truncated Taylor series FD approximation and the wavenumber space approximation.

7

1D problem

It is certainly very useful and instructive to introduce FD schemes in the case of the 1D problem. Many essential concepts and approaches can be explained without the unnecessary complexity of the 2D or 3D problems. Clearly, on the other hand, the 1D problem does not make it possible to introduce and distinguish important aspects of different FD schemes that emerge in 2D and 3D. One important example is the approximation of the 2nd mixed spatial derivatives in the displacement formulation. The consistency of the approximations of the 2nd mixed and nonmixed spatial derivatives is closely related to the accuracy of numerical schemes with respect to the V_P/V_S ratio.

The explanations in this chapter are essential for understanding the following chapters.

7.1 Equation of motion and the stress–strain relation

Consider a Cartesian coordinate system with spatial coordinates (x, y, z) or, interchangeably, (x_1, x_2, x_3). (Indices 1, 2, 3 and letters x, y, z can also be used interchangeably as subscripts in order to denote displacement-vector and stress-tensor components). Consider a perfectly elastic isotropic medium with density $\rho(x)$ and Lamé elastic coefficients $\mu(x)$ and $\lambda(x)$ being continuous functions of the spatial coordinate x. Let $\vec{u}(x, t)$ and $\sigma_{ij}(x, t)$ be the displacement vector and stress tensor, respectively. This defines a 1D problem along the x-axis. Table 7.1 shows wave-propagation configurations that can be described by the same form of equations. P means the longitudinal wave. If the x- and y-axes are horizontal, then SH and SV denote shear waves polarized in the horizontal and vertical directions, respectively.

Denoting the appropriate displacement-vector and stress-tensor components by u and σ, respectively, and the appropriate elastic modulus by M, the strong-form equations of motion and the stress–strain relation, i.e., Hooke's law, can be written in one of the alternative formulations (omitting the body-force term):

Displacement–stress (DS) formulation

$$\rho \frac{\partial^2 u}{\partial t^2} = \frac{\partial \sigma}{\partial x}, \quad \sigma = M \frac{\partial u}{\partial x} \tag{7.1}$$

Table 7.1 *Wave-propagation configurations described by the same form of the equation*

Direction of propagation	Displacement-vector component u	Stress-tensor component σ	Elastic modulus M	Wave	Polarization
	u_x	σ_{xx}	$\lambda + 2\mu$	P	
x	u_y	σ_{xy}	μ	SH	
	u_z	σ_{xz}	μ	SV	

Displacement (D) formulation

$$\rho\frac{\partial^2 u}{\partial t^2} = \frac{\partial}{\partial x}\left(M\frac{\partial u}{\partial x}\right) \tag{7.2}$$

Note that in the case of a homogeneous medium the equation simplifies:

$$\rho\frac{\partial^2 u}{\partial t^2} = M\frac{\partial^2 u}{\partial x^2} \tag{7.3}$$

The simplification is significant for FD approximations – the modulus is not spatially differentiated. Considering wave speed c and relation $c^2 = \frac{M}{\rho}$, Eq. (7.3) can be written as

$$\frac{\partial^2 u}{\partial t^2} = c^2\frac{\partial^2 u}{\partial x^2} \tag{7.4}$$

that is also known as the 2nd-order acoustic wave equation. It is easy to obtain the relation for even derivatives:

$$\frac{\partial^{2j} u}{\partial t^{2j}} = c^{2j}\frac{\partial^{2j} u}{\partial x^{2j}}, \quad j = 1, 2, \ldots \tag{7.5}$$

Displacement–velocity–stress (DVS) formulation

$$\rho\frac{\partial v}{\partial t} = \frac{\partial \sigma}{\partial x}, \quad v = \frac{\partial u}{\partial t}, \quad \sigma = M\frac{\partial u}{\partial x} \tag{7.6}$$

Velocity–stress (VS) formulation

$$\rho\frac{\partial v}{\partial t} = \frac{\partial \sigma}{\partial x}, \quad \frac{\partial \sigma}{\partial t} = M\frac{\partial v}{\partial x} \tag{7.7}$$

or, defining buoyancy b,

$$b = \frac{1}{\rho} \tag{7.8}$$

$$\frac{\partial v}{\partial t} = b \frac{\partial \sigma}{\partial x}, \quad \frac{\partial \sigma}{\partial t} = M \frac{\partial v}{\partial x} \tag{7.9}$$

Defining vector $\mathbf{w}$ and matrix $\mathbf{A}$,

$$\mathbf{w} \equiv (v, \sigma)^T, \quad \mathbf{A} \equiv \begin{bmatrix} 0 & b \\ M & 0 \end{bmatrix} \tag{7.10}$$

Eqs. (7.9) can be written in the form of a matrix equation:

$$\frac{\partial \mathbf{w}}{\partial t} = \mathbf{A} \frac{\partial \mathbf{w}}{\partial x} \tag{7.11}$$

Equation (7.11) is the 1D version of the matrix Eq. (2.33).

Unlike the displacement formulation, equations in the DS, DVS and VS formulations have the same form in both homogeneous and smoothly heterogeneous media.

Note the important relations between the temporal and spatial derivatives: Equations (7.9) imply

$$\frac{\partial^{2j} v}{\partial t^{2j}} = L_{xx}^j v, \quad \frac{\partial^{2j+1} v}{\partial t^{2j+1}} = L_{xx}^j \left(b \frac{\partial \sigma}{\partial x} \right), \quad j = 1, 2, \dots$$

$$L_{xx}^j = \underbrace{L_{xx} L_{xx} \dots L_{xx}}_{j}, \quad L_{xx} = b \frac{\partial}{\partial x} \left(M \frac{\partial}{\partial x} \right) \tag{7.12}$$

and an analogous relation for the temporal derivative of σ. Equation (7.11) implies

$$\frac{\partial^j \mathbf{w}}{\partial t^j} = L_x^j \mathbf{w}, \quad j = 1, 2, \dots, \quad L_x^j = \underbrace{L_x L_x \dots L_x}_{j}, \quad L_x = \mathbf{A} \frac{\partial}{\partial x} \tag{7.13}$$

7.2 A simple FD scheme: a tutorial introduction to FD schemes

This section is intended as a tutorial detailed introduction to FD modelling in the simplest case of the 1D problem in an unbounded homogeneous elastic isotropic continuum. Using the example of a simple FD scheme on a conventional space–time grid we explain the basic difference between propagation of a planar harmonic wave in a true physical continuum and in a discrete space–time grid. We analyze the properties of the scheme and grid wave in detail.

Originally we were much inspired by Chapter 2 of the book by Taflove and Hagness (2005) and also by Section 7.3 of the book by Thomas (1995). Eventually we elaborated our own version of the comprehensive analysis.

7.2.1 Plane harmonic wave in a physical continuum

Consider a plane harmonic wave with unit amplitude:

$$u(x, t) = \exp[i(\omega t - kx)] \tag{7.14}$$

which satisfies the 1D equation of motion in an unbounded homogeneous elastic isotropic medium (7.4). We call this wave a true physical wave in order to distinguish it from the wave in a grid. For a given spatial position, the behaviour of the wave is determined by the real angular frequency ω. For a given time, the behaviour of the wave is determined by the real wavenumber k. Consider time $t + \Delta t$. Clearly, at this time we can find the same value of displacement (as $u(x, t)$) at some other spatial position, say, $x + \Delta x$, at which the argument of the wave (7.14) has the same value as the argument had at time t and spatial position x. The phase $\omega(t + \Delta t) - k(x + \Delta x)$ can be equal to phase $\omega t - kx$ only if $\frac{\Delta x}{\Delta t} = \frac{\omega}{k}$. The latter equation means that the value $u(x, t)$ of displacement has moved during time Δt to the spatial position $x + \Delta x$ with the phase velocity

$$c = \frac{\omega}{k} \tag{7.15}$$

The fact that quantities ω and k are related is logical and necessary for wave (7.14) to satisfy Eq. (7.4). The relation between ω and k is called the dispersion relation. It is easy to realize that in our case the phase velocity is one and the same for any value of the angular frequency. The wave propagation can be then called dispersionless. The dispersionless propagation in our case is due to the fact that Eq. (7.4) describes wave propagation in an unbounded homogeneous elastic isotropic continuum.

In general, the dispersion relation may be written in one of three equivalent forms: $\omega = \omega(k)$, $k = k(\omega)$ or $\lambda = \lambda(f)$, where λ is the wavelength and f the frequency.

In Eq. (7.14) we assume that the amplitude is equal to 1. Clearly, because ω and k are real the amplitude does not change with time or spatial position. If the amplitude does not change with time we can say that Eq. (7.4) is nondissipative. If the amplitude does not change with spatial position we can say that Eq. (7.4) is nonattenuative. Also, these properties are due to the fact that Eq. (7.4) describes wave propagation in an unbounded homogeneous elastic isotropic continuum.

Because the dissipation and attenuation are directly related to ω and k, we can realize that relation $\omega = \omega(k)$ describes not only dispersion but, in fact, also dissipation and attenuation.

7.2.2 Plane harmonic wave in a grid

In analogy with a true physical wave (7.14), we can investigate whether a harmonic wave can propagate in a grid characterized by time step Δ and grid spacing h. In order to account for possible effects of the discrete representation we have to assume numerical (or grid)

quantities $\tilde{\omega}$ and $\tilde{k}$, which can differ from the true physical ω and k. The numerical (or grid) wave is

$$u_I^m = \exp[i(\tilde{\omega}m\Delta - \tilde{k}Ih)] \tag{7.16}$$

In general $\tilde{\omega}$ and $\tilde{k}$ can be complex:

$$\tilde{\omega} = \tilde{\omega}_{\text{real}} + i\tilde{\omega}_{\text{imag}}, \quad \tilde{k} = \tilde{k}_{\text{real}} + i\tilde{k}_{\text{imag}} \tag{7.17}$$

Then,

$$\begin{aligned} u_I^m &= \exp\left\{i\left[\left(\tilde{\omega}_{\text{real}} + i\tilde{\omega}_{\text{imag}}\right)m\Delta - \left(\tilde{k}_{\text{real}} + i\tilde{k}_{\text{imag}}\right)Ih\right]\right\} \\ &= \exp\left(-\tilde{\omega}_{\text{imag}}m\Delta + \tilde{k}_{\text{imag}}Ih\right)\exp\left[i\left(\tilde{\omega}_{\text{real}}m\Delta - \tilde{k}_{\text{real}}Ih\right)\right] \end{aligned} \tag{7.18}$$

It is clear that with nonzero imaginary parts of $\tilde{\omega}$ and/or $\tilde{k}$ the amplitude of the grid wave is not equal to 1. $\tilde{\omega}_{\text{imag}}$ and $\tilde{k}_{\text{imag}}$ determine dissipation in time and attenuation in space, respectively. The real parts $\tilde{\omega}_{\text{real}}$ and $\tilde{k}_{\text{real}}$ determine propagation in time and space, respectively. Consequently, the grid phase velocity is

$$\tilde{v} \equiv \frac{\tilde{\omega}_{\text{real}}}{\tilde{k}_{\text{real}}} \tag{7.19}$$

Obviously, with nonzero $\tilde{\omega}_{\text{imag}}$ and/or $\tilde{k}_{\text{imag}}$ the phase velocity does not mean the velocity of propagation of a particular value of displacement, as was the case for a true physical wave. Note also that even if the grid $\tilde{\omega}$ and $\tilde{k}$ are real, they are not necessarily equal to the true physical ω and k.

7.2.3 (2,2) 1D FD scheme on a conventional grid

Assume a conventional discrete space–time grid with time step Δ and grid spacing h. Use the centred 2$^{\text{nd}}$-order FD approximation to replace both the temporal and spatial 2$^{\text{nd}}$ derivatives in Eq. (7.4). Then the partial differential equation can be approximated by the FD equation:

$$\frac{1}{\Delta^2}\left(u_I^{m+1} - 2u_I^m + u_I^{m-1}\right) = c^2\frac{1}{h^2}\left(u_{I+1}^m - 2u_I^m + u_{I-1}^m\right) \tag{7.20}$$

from which we have an explicit FD scheme:

$$u_I^{m+1} = 2u_I^m - u_I^{m-1} + \left(c\frac{\Delta}{h}\right)^2\left(u_{I+1}^m - 2u_I^m + u_{I-1}^m\right) \tag{7.21}$$

Denote

$$\begin{aligned} EQ &\equiv \frac{\partial^2 u}{\partial t^2} - c^2\frac{\partial^2 u}{\partial x^2} \\ FDEQ &\equiv \frac{1}{\Delta^2}\left(u_I^{m+1} - 2u_I^m + u_I^{m-1}\right) - c^2\frac{1}{h^2}\left(u_{I+1}^m - 2u_I^m + u_{I-1}^m\right) \end{aligned} \tag{7.22}$$

Then the truncation error of the FD approximation of the partial differential equation is

$$TrunErr\,\{FDEQ\} = TaylorExpansion\,\{FDEQ\} - EQ$$

$$= \frac{1}{12}\left(\frac{\partial^4 u}{\partial t^4}\Delta^2 - c^2\frac{\partial^4 u}{\partial x^4}h^2\right) + O(\Delta^4) + O(h^4) \qquad (7.23)$$

Equation (7.23) means that the FD equation (7.20) is consistent with the differential equation (7.4) with 2nd-order accuracy both in time and space. Further, we will indicate the 2nd-order accuracy in time and space using abbreviation (2,2). Thus, in this case we can say that scheme (7.21) is a (2,2) FD scheme.

Whereas Eq. (7.4) describes wave propagation in an unbounded homogeneous elastic isotropic continuum, Eq. (7.20) describes wave propagation in a discrete representation of the continuum. Whereas a true continuum is characterized by the wave speed c, its discrete representation is characterized by the true wave speed c, time step Δ and grid spacing h. Moreover, for given c, Δ and h, the wave propagation depends also on the scheme itself – Eq. (7.20) is just one of many possible approximations that are consistent with Eq. (7.4).

We substitute displacement (7.16) for discrete displacement in Eq. (7.20). Denoting the r.h.s. of Eq. (7.16) by E, we obtain

$$u_I^m \quad = E$$
$$u_I^{m+1} = E\exp\left[i\,(\tilde{\omega}\Delta)\right] \qquad u_I^{m-1} = E\exp\left[i\,(-\tilde{\omega}\Delta)\right] \qquad (7.24)$$
$$u_{I+1}^m = E\exp[i(-\tilde{k}h)] \qquad u_{I-1}^m = E\exp[i(\tilde{k}h)]$$

and Eq. (7.20) transforms into

$$\cos(\tilde{\omega}\Delta) - 1 = \left(c\frac{\Delta}{h}\right)^2[\cos(\tilde{k}h) - 1] \qquad (7.25)$$

from which we obtain two equivalent numerical (or discrete) dispersion relations:

$$\tilde{\omega} = \frac{1}{\Delta}\arccos\left\{1 + \left(c\frac{\Delta}{h}\right)^2[\cos\left(\tilde{k}h\right) - 1]\right\} \qquad (7.26)$$

or

$$\tilde{k} = \frac{1}{h}\arccos\left\{1 + \left(\frac{h}{c\Delta}\right)^2[\cos\left(\tilde{\omega}\Delta\right) - 1]\right\} \qquad (7.27)$$

The relations are sometimes called dispersion–dissipation relations. Denoting

$$S \equiv c\frac{\Delta}{h} \qquad (7.28)$$

we have

$$\tilde{\omega} = \frac{1}{\Delta}\arccos\{1 + S^2[\cos(\tilde{k}h) - 1]\} \qquad (7.29)$$

or

$$\tilde{k} = \frac{1}{h} \arccos \left\{ 1 + \frac{1}{S^2} \left[\cos(\tilde{\omega}\Delta) - 1 \right] \right\} \tag{7.30}$$

It is obvious that the dispersion relation obtained for a planar wave propagating in the grid and governed by the FD Eq. (7.20) is fundamentally different from the dispersion relation (7.15) of the true harmonic wave in a physical continuum. We have to analyze the grid-dispersion relation in order to find the differences between the true and grid harmonic waves.

The two alternative dispersion relations (7.29) and (7.30) naturally lead us to formulate two alternative partial problems, respectively:

(a) Assume a harmonic wave with k and ω propagating in a true physical continuum without dispersion. Assume a grid wave with $\tilde{k} = k$. What will be the grid angular frequency $\tilde{\omega}$?
(b) Assume a harmonic wave with ω and k propagating in a true physical continuum without dispersion. Assume a grid wave with $\tilde{\omega} = \omega$. What will be the grid wavenumber $\tilde{k}$?

We will answer the two questions by investigating the behaviour of the grid wave with time and spatial position.

Before we proceed, note that relation (7.25) could be written as

$$\sin^2 \frac{\tilde{\omega}\Delta}{2} = S^2 \sin^2 \frac{\tilde{k}h}{2} \tag{7.31}$$

7.2.4 Analysis of grid-dispersion relations

7.2.4.1 Behaviour of a grid wave with time: grid $\tilde{\omega}$ for a wave with physical k – Part 1

The behaviour of the grid wave with time is determined by the grid angular frequency $\tilde{\omega}$. The grid wavenumber $\tilde{k}$ can be considered a parameter – real and not different from the physical k. The real $\tilde{k}$ means that the amplitude does not change with spatial position.

Assuming complex $\tilde{\omega}$ and real $\tilde{k}$, the displacement at the spatial position I and time level m can be written as

$$\begin{aligned} u_I^m &= \exp\{i[(\tilde{\omega}_{\text{real}} + i\tilde{\omega}_{\text{imag}})m\Delta - \tilde{k}Ih]\} \\ &= \exp(-\tilde{\omega}_{\text{imag}}m\Delta)\exp[i(\tilde{\omega}_{\text{real}}m\Delta - \tilde{k}Ih)] \end{aligned} \tag{7.32}$$

The value of $\tilde{\omega}_{\text{imag}}$ determines the behaviour of the amplitude with time:

$\tilde{\omega}_{\text{imag}} > 0$: the amplitude exponentially decreases with time at a given spatial position; the scheme is dissipative,

$\tilde{\omega}_{\text{imag}} = 0$: the amplitude remains constant with time at a given spatial position; the scheme is nondissipative,

$\tilde{\omega}_{\text{imag}} < 0$: the amplitude exponentially increases with time at a given spatial position; the scheme is unstable.

Before we proceed, note that even if we considered $\tilde{k}$ complex, the following analysis of the behaviour with time would not change: the imaginary part of $\tilde{k}$ would just lead to a contribution to the amplitude at a given spatial position. The contributions would be different at different spatial positions but would not change with time.

The argument of the cosine in the dispersion relation (7.29) can be expressed as

$$\tilde{k}h = kh = \frac{2\pi h}{\lambda} \tag{7.33}$$

It is reasonable to define the spatial sampling as

$$N_\lambda \equiv \frac{\lambda}{h} \tag{7.34}$$

(Note that we define N_λ here – in the investigation of the behaviour of the grid wave with time. This is an important difference compared to the definition by Taflove and Hagness, 2005. We explain this in Subsection 7.2.5.) Then,

$$\tilde{\omega} = \frac{1}{\Delta} \arccos\left\{ 1 + S^2 \left[\cos\left(\frac{2\pi}{N_\lambda}\right) - 1 \right] \right\} \tag{7.35}$$

Denoting

$$\xi = 1 + S^2 \left[\cos\left(\frac{2\pi}{N_\lambda}\right) - 1 \right] \tag{7.36}$$

and using relation

$$\arccos \xi = \frac{\pi}{2} - \arcsin \xi \tag{7.37}$$

we can write the dispersion relation (7.29) for $\tilde{\omega}$ as

$$\tilde{\omega} = \frac{1}{\Delta} \left(\frac{\pi}{2} - \arcsin \xi \right) \tag{7.38}$$

7.2.4.2 Behaviour of a grid wave with spatial position: grid $\tilde{k}$ for a wave with physical ω – Part 1

The behaviour of the grid wave with spatial position is determined by the grid wavenumber $\tilde{k}$. The grid angular frequency $\tilde{\omega}$ can be considered a parameter – real and not different from the physical ω. The real $\tilde{\omega}$ means that the amplitude of the grid wave does not change with time.

Assuming complex $\tilde{k}$ and real $\tilde{\omega}$, the displacement at spatial position I and time level m can be written as

$$u_I^m = \exp\{i[\tilde{\omega}m\Delta - (\tilde{k}_{\text{real}} + i\tilde{k}_{\text{imag}})Ih]\} = \exp(\tilde{k}_{\text{imag}}Ih)\exp[i(\tilde{\omega}m\Delta - \tilde{k}_{\text{real}}Ih)]$$

$$\tag{7.39}$$

The value of $\tilde{k}_{imag}$ determines the behaviour of the amplitude with spatial position:

$\tilde{k}_{imag} > 0$: the amplitude exponentially increases with spatial position at a given time,

$\tilde{k}_{imag} = 0$: the amplitude does not change with spatial position at a given time; the scheme is nonattenuative,

$\tilde{k}_{imag} < 0$: the amplitude exponentially decreases with spatial position at a given time; the scheme attenuates the wave in the grid.

Recall the dispersion relation for the grid wavenumber (7.30):

$$\tilde{k} = \frac{1}{h} \arccos \left\{ 1 + \frac{1}{S^2} [\cos(\tilde{\omega}\Delta) - 1] \right\}$$

Considering period T, the argument of the cosine can be written as

$$\tilde{\omega}\Delta = \omega\Delta = \frac{2\pi}{T}\Delta \tag{7.40}$$

It is reasonable to define the time sampling as

$$N_T \equiv \frac{T}{\Delta} \tag{7.41}$$

Then,

$$\tilde{k} = \frac{1}{h} \arccos \left\{ 1 + \frac{1}{S^2} \left[\cos\left(\frac{2\pi}{N_T} \right) - 1 \right] \right\} \tag{7.42}$$

Denoting

$$\zeta = 1 + \frac{1}{S^2} \left[\cos\left(\frac{2\pi}{N_T} \right) - 1 \right] \tag{7.43}$$

and using relation (7.37) for ζ the dispersion relation becomes

$$\tilde{k} = \frac{1}{h} \left(\frac{\pi}{2} - \arcsin \zeta \right) \tag{7.44}$$

7.2.4.3 Behaviour of a grid wave with time and spatial position: a joint part

Both dispersion relations (7.38) and (7.44) have the form

$$\varphi = \frac{1}{\delta} \left(\frac{\pi}{2} - \arcsin \chi \right) \tag{7.45}$$

where $\{\varphi, \delta, \chi\}$ stand for $\{\tilde{\omega}, \Delta, \xi\}$ or $\{\tilde{k}, h, \zeta\}$, respectively. Considering the definition of the function arcsin it is reasonable to investigate the case when χ is from interval $\langle -1, 1 \rangle$, and the case when χ is outside interval $\langle -1, 1 \rangle$.

The case: $-1 \leq \chi \leq 1$

It follows from $-\frac{\pi}{2} \leq \arcsin \chi \leq \frac{\pi}{2}$ and Eq. (7.45) that

$$\varphi = \frac{1}{\delta} \left(\frac{\pi}{2} - \arcsin \chi \right), \quad 0 \leq \varphi_{real} \leq \frac{\pi}{\delta}, \quad \varphi_{imag} = 0 \tag{7.46}$$

In order to consider χ outside interval $\langle -1, 1 \rangle$, use the relation (e.g., Korn and Korn 2000, p. 817)

$$\arcsin \chi = -i \ln \left(i \chi + \sqrt{1 - \chi^2} \right) \tag{7.47}$$

The case: $\chi > 1$

Rewrite relation (7.47) as follows:

$$\begin{aligned}
\arcsin \chi &= -i \ln \left(i \chi + \sqrt{1 - \chi^2} \right) \\
&= -i \ln \left(i \chi + i \sqrt{\chi^2 - 1} \right) = -i \ln \left[\exp \left(i \tfrac{\pi}{2} \right) \left(\chi + \sqrt{\chi^2 - 1} \right) \right] \\
&= -i \left\{ \ln \left[\exp \left(i \tfrac{\pi}{2} \right) \right] + \ln \left(\chi + \sqrt{\chi^2 - 1} \right) \right\} \\
&= -i \left\{ i \tfrac{\pi}{2} + \ln \left(\chi + \sqrt{\chi^2 - 1} \right) \right\} = \tfrac{\pi}{2} - i \ln \left(\chi + \sqrt{\chi^2 - 1} \right)
\end{aligned}$$

Then,

$$\varphi = i \frac{1}{\delta} \ln \left(\chi + \sqrt{\chi^2 - 1} \right), \quad \varphi_{\text{real}} = 0, \quad \varphi_{\text{imag}} = \frac{1}{\delta} \ln \left(\chi + \sqrt{\chi^2 - 1} \right) \tag{7.48}$$

The case: $\chi < -1$

Rewrite relation (7.47) as follows:

$$\begin{aligned}
\arcsin \chi &= -i \ln \left[i \left(\chi + \sqrt{\chi^2 - 1} \right) \right] = -i \ln \left[-i \left(-\chi - \sqrt{\chi^2 - 1} \right) \right] \\
&= -i \ln \left[\exp \left(-i \frac{\pi}{2} \right) \left(-\chi - \sqrt{\chi^2 - 1} \right) \right] \\
&= -i \left\{ \ln \left[\exp \left(-i \frac{\pi}{2} \right) \right] + \ln \left(-\chi - \sqrt{\chi^2 - 1} \right) \right\} \\
&= -i \left\{ -i \frac{\pi}{2} + \ln \left(-\chi - \sqrt{\chi^2 - 1} \right) \right\} = -\frac{\pi}{2} - i \ln \left(-\chi - \sqrt{\chi^2 - 1} \right)
\end{aligned}$$

Then,

$$\varphi = \frac{1}{\delta} \left[\pi + i \ln \left(-\chi - \sqrt{\chi^2 - 1} \right) \right]$$

$$\varphi_{\text{real}} = \frac{\pi}{\delta}, \quad \varphi_{\text{imag}} = \frac{1}{\delta} \ln \left(-\chi - \sqrt{\chi^2 - 1} \right) < 0 \tag{7.49}$$

The latter inequality is due to the fact that the argument of the logarithm is positive and smaller than 1.

Having obtained relations (7.46), (7.48) and (7.49) for $-1 \le \chi \le 1$, $\chi > 1$ and $\chi < -1$, respectively, we can continue with the analysis of the scheme.

7.2.4.4 Behaviour of a grid wave with time: grid $\tilde{\omega}$ for a wave with physical k – Part 2

Because $\frac{2\pi}{N_\lambda}$ is real, $-1 \le \cos \left(\frac{2\pi}{N_\lambda} \right) \le 1$. It follows from Eq. (7.36) that

$$1 - 2S^2 \le \xi \le 1 \tag{7.50}$$

Recall that $S > 0$, see Eq. (7.28). We can recognize two cases.

The case: $-1 \leq \xi \leq 1$

Investigate when $-1 \leq \xi \leq 1$. It is clear from condition (7.50) that always $\xi \leq 1$. Substituting definition (7.36) for ξ in the condition $-1 \leq \xi$ we can obtain

$$S^2 \leq \frac{2}{1 - \cos\left(\dfrac{2\pi}{N_\lambda}\right)} \tag{7.51}$$

Thus, if S satisfies condition (7.51), $-1 \leq \xi \leq 1$, and, according to (7.46),

$$\tilde{\omega} = \frac{1}{\Delta}\left(\frac{\pi}{2} - \arcsin \xi\right), \quad 0 \leq \tilde{\omega}_{\text{real}} \leq \frac{\pi}{\Delta}, \quad \tilde{\omega}_{\text{imag}} = 0 \tag{7.52}$$

Recalling Eq. (7.29),

$$\tilde{\omega} = \tilde{\omega}_{\text{real}} = \frac{1}{\Delta} \arccos\left\{1 + S^2\left[\cos\left(\frac{2\pi}{N_\lambda}\right) - 1\right]\right\} \tag{7.53}$$

Equivalently,

$$\tilde{\omega} = \tilde{\omega}_{\text{real}}$$
$$= \frac{1}{\Delta} \arccos\left\{1 + S^2\left[\cos\left(kh\right) - 1\right]\right\}$$
$$= \frac{1}{\Delta} \arccos\left\{1 + S^2\left[\cos\left(\frac{\omega\Delta}{S}\right) - 1\right]\right\} \tag{7.54}$$

Referring to Eq. (7.32) we obtain the first partial conclusion on the behaviour of the grid wave with time if S satisfies condition (7.51):

(a) Whereas a harmonic wave with k and ω can propagate in a true physical continuum without dispersion, a grid wave with $\tilde{k} = k$ can propagate with grid dispersion and its angular frequency $\tilde{\omega}$ is given by relation (7.53) or (7.54).
(b) At any spatial grid position the amplitude of a harmonic wave does not change with time. The numerical scheme is nondissipative.

The case: $\xi < -1$

Investigate now when $\xi < -1$. Substituting definition (7.36) for ξ in the latter condition we can obtain

$$S^2 > \frac{2}{1 - \cos\left(\dfrac{2\pi}{N_\lambda}\right)} \tag{7.55}$$

Thus, if S satisfies condition (7.55), $\xi < -1$, and, according to (7.49),

$$\tilde{\omega} = \frac{1}{\Delta}\left[\pi + i \ln\left(-\xi - \sqrt{\xi^2 - 1}\right)\right]$$
$$\tilde{\omega}_{\text{real}} = \frac{\pi}{\Delta}, \quad \tilde{\omega}_{\text{imag}} = \frac{1}{\Delta} \ln\left(-\xi - \sqrt{\xi^2 - 1}\right) < 0 \tag{7.56}$$

Referring again to Eq. (7.32) we obtain the second partial conclusion on the behaviour of the grid wave with time if S satisfies condition (7.55):

(c) Whereas a harmonic wave with k and ω can propagate in a true physical continuum without dispersion, a grid wave with $\tilde{k} = k$ can propagate with the grid angular frequency $\tilde{\omega}_{\text{real}} = \frac{\pi}{\Delta}$.

(d) At any spatial grid position the amplitude exponentially increases with time. The scheme is unstable.

We can quantify the exponential increase of the amplitude. Because, see (7.32) and (7.56),

$$
\begin{aligned}
u_I^m &= \exp\left(-\tilde{\omega}_{\text{imag}} m \Delta\right) \exp\left[i\left(\tilde{\omega}_{\text{real}} m \Delta - \tilde{k} I h\right)\right] \\
&= \exp\left[-m \ln\left(-\xi - \sqrt{\xi^2 - 1}\right)\right] \exp\left[i\left(m\pi - \tilde{k} I h\right)\right] \\
&= \exp\left[\ln\left(-\xi - \sqrt{\xi^2 - 1}\right)^{-m}\right] \exp\left[i\left(m\pi - \tilde{k} I h\right)\right] \\
&= \frac{1}{\left(-\xi - \sqrt{\xi^2 - 1}\right)^m} \exp\left[i\left(m\pi - \tilde{k} I h\right)\right]
\end{aligned}
$$

the amplitude amplification factor per time step is

$$
q = \frac{\left|u_I^{m+1}\right|}{\left|u_I^m\right|} = \frac{1}{-\xi - \sqrt{\xi^2 - 1}} = -\xi + \sqrt{\xi^2 - 1} > 1 \tag{7.57}
$$

The smaller ξ is, the larger is q. The amplification factor q gains its maximum value for the minimum value of ξ, that is for $\xi = 1 - 2S^2$ (see Eq. (7.50)):

$$
q_{\max} = -(1 - 2S^2) + \sqrt{(1 - 2S^2)^2 - 1} = \left(S + \sqrt{S^2 - 1}\right)^2 \tag{7.58}
$$

It follows from Eq. (7.36) that ξ gains its minimum value for $\frac{2\pi}{N_\lambda} = \pi$, that is, for $N_\lambda = 2$. Thus, the exponential increase of the amplitude is largest at wavelength

$$
\lambda_U = 2h \tag{7.59}
$$

This exponential growth originates the numerical instability. The frequency of the unstable grid wave is

$$
f_U = \frac{\tilde{\omega}_{\text{real}}}{2\pi} = \frac{1}{2\Delta} \tag{7.60}
$$

being determined only by the time step Δ.

Stability We have identified two regimes of the scheme behaviour with time. The nondissipative or stable regime is determined by condition (7.51), the unstable regime is determined by condition (7.55). The value of S, discriminating the two regimes, depends on N_λ. This is illustrated in Fig. 7.1.

In practice, however, we usually do not simulate one harmonic wave, that is, a wave with one wavelength. We have a range of wavelengths. Therefore, for a given value of grid spacing h we have a range of N_λ values – the shorter the wavelength, the smaller is N_λ. If we admit any positive value of N_λ, conditions (7.51) and (7.55) transform to

$$
S \leq 1 \tag{7.61}
$$
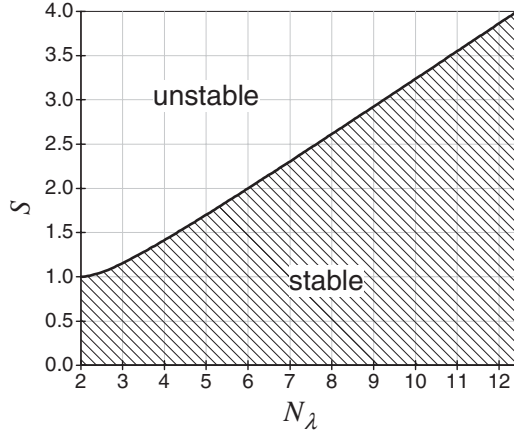
Figure 7.1 Value of factor S, discriminating the nondissipative (stable) and unstable regimes of the grid wave with physical wavelength, as a function of the spatial sampling N_λ of the physical wavelength of one harmonic wave.

and

$$S > 1 \tag{7.62}$$

respectively.

For the analyzed scheme, 1 is the maximum value of S for which the analyzed FD scheme is stable. It is reasonable to anticipate that for some other FD scheme the limiting value may be different from 1. Therefore, we denote the limiting value in general as S_M. Consequently, a general form of the stability condition for 1D schemes can be written as

$$S \leq S_M \tag{7.63}$$

From

$$S = c\frac{\Delta}{h} \leq S_M \tag{7.64}$$

we have

$$\Delta \leq \frac{h}{c}S_M \tag{7.65}$$

Define the stability ratio p as

$$p \equiv \frac{c\Delta}{hS_M} \tag{7.66}$$

Then,

$$0 < p \leq 1 \tag{7.67}$$

$$\Delta = p\frac{h}{c}S_M \tag{7.68}$$

Clearly, $\frac{h}{c}S_M$ is the maximum time step for which the scheme is stable and p quantifies the fraction of the maximum time step. Condition (7.61) for the analyzed scheme can be written as

$$S = pS_M; \quad 0 < p \le 1, \quad S_M = 1 \tag{7.69}$$

Thus, the main conclusion of the performed analysis of the scheme behaviour with time is that it is necessary to choose

$$\Delta = p\frac{h}{c}S_M; \quad 0 < p \le 1, \quad S_M = 1 \tag{7.70}$$

in order to prevent instability of the numerical solution. Factor S can be called the stability factor and relation (7.61), (7.69) or (7.70) the stability condition for the investigated numerical scheme. Factor S is also known as the Courant number. Let us note that the name reflects the fundamental article by Courant, Friedrichs and Lewy (1928 in German, 1967 in English translation) – the first article on the stability and convergence of the FD schemes solving partial differential equations. For more details see, e.g., LeVeque (2007).

Considering Eq. (7.69), relations (7.53) and (7.54) can be written as

$$\tilde{\omega} = \tilde{\omega}_{\text{real}} = \frac{1}{\Delta} \arccos\left\{1 + p^2\left[\cos\left(\frac{2\pi}{N_\lambda}\right) - 1\right]\right\}$$

$$= \frac{1}{\Delta} \arccos\left\{1 + p^2\left[\cos\left(kh\right) - 1\right]\right\}$$

$$= \frac{1}{\Delta} \arccos\left\{1 + p^2\left[\cos\left(\frac{\omega\Delta}{p}\right) - 1\right]\right\} \tag{7.71}$$

7.2.4.5 *Behaviour of a grid wave with spatial position: grid $\tilde{k}$ for a wave with physical ω – Part 2*

Clearly we can apply the results of the joint part of the analysis also in the investigation of the behaviour of the grid wave with spatial position. In the investigation, however, we have to account for the fact that we have found the stability condition (7.69) for S.

Because $\frac{2\pi}{N_T}$ is real, $-1 \le \cos\left(\frac{2\pi}{N_T}\right) \le 1$. It follows from Eq. (7.43) that

$$1 - \frac{2}{S^2} \le \zeta \le 1 \tag{7.72}$$

and, using (7.69),

$$1 - \frac{2}{p^2} \le \zeta \le 1 \tag{7.73}$$

We can recognize two cases.

The case: $-1 \leq \zeta \leq 1$

Investigate when $-1 \leq \zeta \leq 1$. It is clear from condition (7.72) that always $\zeta \leq 1$. Substituting definition (7.43) for ζ in the condition $-1 \leq \zeta$ and using (7.69) we can obtain

$$N_T \geq \frac{2\pi}{\arccos(1 - 2p^2)} \tag{7.74}$$

Relation (7.74) can be transformed into the frequency domain:

$$T = \Delta N_T \geq \frac{2\pi\,\Delta}{\arccos(1 - 2p^2)}$$

$$f = \frac{1}{T} \leq \frac{\arccos(1 - 2p^2)}{\pi} \frac{1}{2\Delta} \tag{7.75}$$

Define frequency f_{ATT}

$$f_{ATT} \equiv \frac{\arccos(1 - 2p^2)}{\pi} f_N \tag{7.76}$$

where f_N is the Nyquist frequency

$$f_N \equiv \frac{1}{2\Delta} \tag{7.77}$$

The frequency-domain equivalent of condition (7.74) can be then written as

$$f \leq f_{ATT} \tag{7.78}$$

Thus, if N_T satisfies condition (7.74) or, equivalently, f satisfies condition (7.78), according to (7.46)

$$\tilde{k} = \frac{1}{h}\left(\frac{\pi}{2} - \arcsin \zeta\right), \quad 0 < \tilde{k}_{\text{real}} \leq \frac{\pi}{h}, \quad \tilde{k}_{\text{imag}} = 0 \tag{7.79}$$

Recalling Eq. (7.42):

$$\tilde{k} = \frac{1}{h} \arccos\left\{1 + \frac{1}{p^2}\left[\cos\left(\frac{2\pi}{N_T}\right) - 1\right]\right\} \tag{7.80}$$

Equivalently,

$$\tilde{k} = \frac{1}{h} \arccos\left\{1 + \frac{1}{p^2}\left[\cos\left(\omega\Delta\right) - 1\right]\right\}$$

$$= \frac{1}{h} \arccos\left\{1 + \frac{1}{p^2}\left[\cos\left(pkh\right) - 1\right]\right\} \tag{7.81}$$

Referring to Eq. (7.39) we obtain the first partial conclusion on the behaviour of a grid wave with spatial position if N_T satisfies condition (7.74) or, equivalently, f satisfies condition (7.78):

(a) Whereas a harmonic wave with ω and k can propagate in a true physical continuum without dispersion, a grid wave with $\tilde{\omega} = \omega \leq 2\pi f_{ATT}$ can propagate with grid

dispersion and its wavenumber $\tilde{k}$ is given by either of the alternative relations (7.80) and (7.81).

(b) At any time level the amplitude does not change with spatial position. The numerical scheme is nonattenuative.

It is clear from relation (7.76) that only for $p = 1$ is the regime nonattenuative up to the Nyquist frequency f_N.

The case: $\zeta < -1$

The condition occurs if

$$N_T < \frac{2\pi}{\arccos(1 - 2p^2)} \tag{7.82}$$

or, equivalently,

$$f > f_{ATT} \tag{7.83}$$

Then, according to (7.49),

$$\tilde{k} = \frac{1}{h}\left[\pi + i \ln\left(-\zeta - \sqrt{\zeta^2 - 1}\right)\right]$$

$$\tilde{k}_{\text{real}} = \frac{\pi}{h}, \quad \tilde{k}_{\text{imag}} = \frac{1}{h}\ln\left(-\zeta - \sqrt{\zeta^2 - 1}\right) < 0 \tag{7.84}$$

Because f is upper-bounded by the Nyquist frequency f_N, we can formulate the second partial conclusion on the behaviour of a grid wave with spatial position if N_T satisfies condition (7.82):

(c) Whereas a harmonic wave with ω and k can propagate in a true physical continuum without dispersion, a grid wave with any $\tilde{\omega} = \omega \in (2\pi f_{ATT}, 2\pi f_N)$ can propagate only with the grid wavenumber $\tilde{k}_{\text{real}} = \frac{\pi}{h}$.

(d) At any time level the amplitude exponentially decreases with spatial position.

We can quantify the exponential decrease by the attenuation per grid spacing. Recall (7.39) and define

$$\exp\left(-\alpha h\right) \equiv \exp\left(\tilde{k}_{\text{imag}} h\right)$$

$$= \exp\left[\ln\left(-\zeta - \sqrt{\zeta^2 - 1}\right)\right] = -\zeta - \sqrt{\zeta^2 - 1} \tag{7.85}$$

Referring to the argument for Eq. (7.49):

$$0 < -\zeta - \sqrt{\zeta^2 - 1} < 1 \tag{7.86}$$

Relations (7.85) and (7.86) show that the amplitude is multiplied per one grid spacing by a positive number smaller than 1.
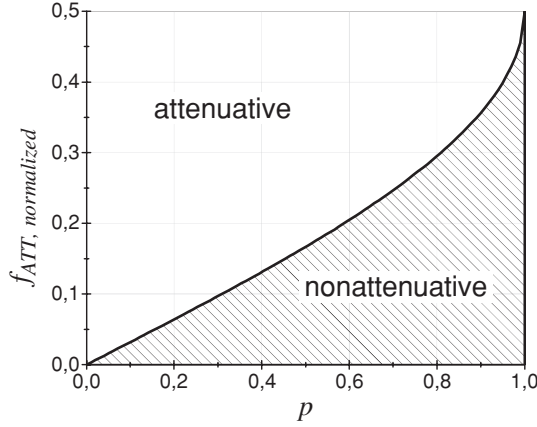
Figure 7.2 Value of the normalized frequency $f_{ATT,normalized}$, discriminating the nonattenuative and attenuative regimes of the grid wave with physical frequency, as a function of the stability ratio p for one harmonic wave.

Grid attenuation We have identified two regimes of the scheme behaviour with spatial position. The nonattenuative regime is determined by condition (7.74) or (7.78), the attenuative regime is determined by condition (7.82) or (7.83). The value of f_{ATT}, discriminating the two regimes, depends on p.

Let us illustrate the relation between f_{ATT} and p numerically. Consider normalized frequency

$$f_{normalized} \equiv f \Delta \tag{7.87}$$

Correspondingly we define

$$f_{ATT,normalized} \equiv \frac{\arccos(1 - 2p^2)}{2\pi} \tag{7.88}$$

Note that the normalized Nyquist frequency is

$$f_{N,normalized} = 0.5 \tag{7.89}$$

Figure 7.2 shows $f_{ATT,normalized}$ as a function of the stability ratio p.

We can also numerically illustrate the attenuation. Because

$$f_{normalized} = f \Delta = \frac{1}{N_T} \tag{7.90}$$

ζ defined by Eq. (7.43) and appearing in relation (7.85) can be written as

$$\zeta = 1 + \frac{1}{p^2}[\cos(2\pi f_{normalized}) - 1] \tag{7.91}$$

Considering $2 \leq N_T < \infty$, we have $0 < f_{normalized} \leq \frac{1}{2}$.

Table 7.2 *Identified partial regimes of the investigated FD scheme*

Behaviour with time continuum: k and ω grid: k and $\tilde{\omega}$	Behaviour with spatial position continuum: ω and k grid: ω and $\tilde{k}$
$0 < S \leq 1$	$N_T \geq \dfrac{2\pi}{\arccos\left(1-2S^2\right)} \qquad (f \leq f_{ATT})$
Nondissipative stable: amplitude does not change with time $$\tilde{\omega} = \tilde{\omega}_{\text{real}}$$ $$= \tfrac{1}{\Delta}\arccos\left\{1 + S^2\left\| \cos\left(kh\right) - 1 \right\| \right\}$$ $$= \tfrac{1}{\Delta}\arccos\left\{1 + S^2\left[\cos\left(\omega\Delta / S\right) - 1\right]\right\}$$ $$= \tfrac{1}{\Delta}\arccos\left\{1 + S^2\left[\cos\left(2\pi / N_\lambda\right) - 1\right]\right\}$$	Nonattenuative: amplitude does not change with spatial position $$\tilde{k} = \tilde{k}_{\text{real}}$$ $$= \tfrac{1}{h}\arccos\left\{1 + \tfrac{1}{S^2}\left[\cos\left(\omega\Delta\right) - 1\right]\right\}$$ $$= \tfrac{1}{h}\arccos\left\{1 + \tfrac{1}{S^2}\left[\cos\left(S\,kh\right) - 1\right]\right\}$$ $$= \tfrac{1}{h}\arccos\left\{1 + \tfrac{1}{S^2}\left[\cos\left(2\pi / N_T\right) - 1\right]\right\}$$
$S > 1$	$N_T < \dfrac{2\pi}{\arccos\left(1-2S^2\right)} \qquad (f_{ATT} < f \leq f_N)$
Unstable: amplitude exponentially increases with time $$\tilde{\omega}_{\text{real}} = \tfrac{\pi}{\Delta} \quad , \quad \tilde{\omega}_{\text{imag}} < 0$$	Attenuative: amplitude exponentially decreases with spatial position $$\tilde{k}_{\text{real}} = \tfrac{\pi}{h} \quad , \quad \tilde{k}_{\text{imag}} < 0$$
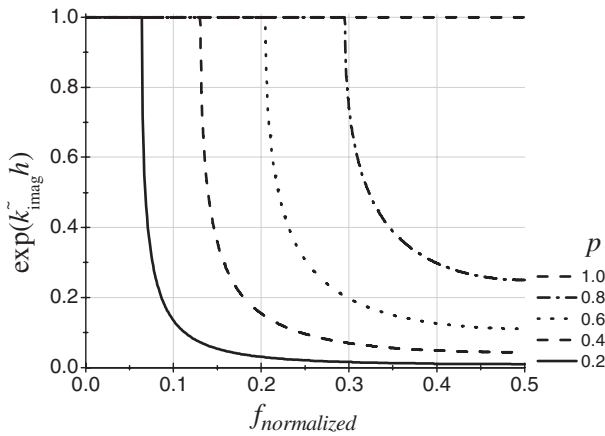
Figure 7.3 The amplitude attenuation factor of the grid wave with physical frequency as a function of the normalized frequency $f_{normalized}$. For each value of the stability ratio p the amplitude attenuation factor falls from the unit value at the normalized frequency of $f_{ATT,normalized}$.

Figure 7.3 shows the amplitude factor $\exp(\tilde{k}_{\text{imag}}h)$ as a function of $f_{normalized}$. For each value of the stability ratio p, the amplitude factor reaches its maximum value, 1, at the corresponding $f_{ATT,normalized}$. At frequencies smaller than $f_{ATT,normalized}$ the regime is nonattenuative and the amplitude factor $\exp(\tilde{k}_{\text{imag}}h)$ is equal to 1.

7.2.5 Summary of the identified partial regimes

We have identified four partial regimes of the scheme behaviour with time and spatial position. They are summarized in Table 7.2. Compare the role and meaning of the spatial

sampling N_λ and time sampling N_T. N_λ quantifies sampling of the physical wavelength, which is also the grid wavelength. N_T quantifies sampling of the physical period which is also the grid period. Note that N_λ should not be used in the analysis of the behaviour with spatial position because in that case it would quantify a wavelength that does not propagate in the grid. Similarly, N_T should not be used in the analysis of the behaviour with time because in that case it would quantify a period that does not propagate in the grid.

Obviously, for numerical simulation of wave propagation we need a conjunction of the nondissipative and nonattenuative regimes. If we choose $S \leq 1$, the simulation will be stable. It will be nonattenuative up to frequency f_{ATT}.

We have found that grid wave propagation is not dispersionless in these regimes. We should therefore quantify grid dispersion in terms of grid phase velocity.

7.2.6 Grid phase and group velocities

7.2.6.1 Grid phase velocity

The grid phase velocity is given by Eq. (7.19):

$$\tilde{v} = \frac{\tilde{\omega}_{\text{real}}}{\tilde{k}_{\text{real}}}$$

As we have found, we have two possibilities:

First possibility: Assume $\tilde{k} = k$ and use the dispersion relation for $\tilde{\omega}$.
Second possibility: Assume $\tilde{\omega} = \omega$ and use the dispersion relation for $\tilde{k}$.

The first possibility will lead to the grid phase velocity of the wave with a true physical wavelength. The second one will lead to the grid phase velocity of the wave with a true physical frequency.

Grid phase velocity of the wave with a true physical wavelength

Recalling relations (7.71) and (7.70) we obtain the following alternative relations for stable wave propagation:

$$\begin{aligned}
\tilde{v} = \frac{\tilde{\omega}_{\text{real}}}{k} &= \frac{1}{pkh} \arccos\left\{1 + p^2 \left[\cos(kh) - 1\right]\right\} c \\
&= \frac{1}{\omega\Delta} \arccos\left\{1 + p^2 \left[\cos\left(\frac{\omega\Delta}{p}\right) - 1\right]\right\} c \\
&= \frac{N_\lambda}{2\pi p} \arccos\left\{1 + p^2 \left[\cos\left(\frac{2\pi}{N_\lambda}\right) - 1\right]\right\} c
\end{aligned} \tag{7.92}$$

The grid phase velocity given by any one of the relations (7.92) is the velocity of the grid wave that has the same wavelength λ as the true physical wave. The fourth of the relations
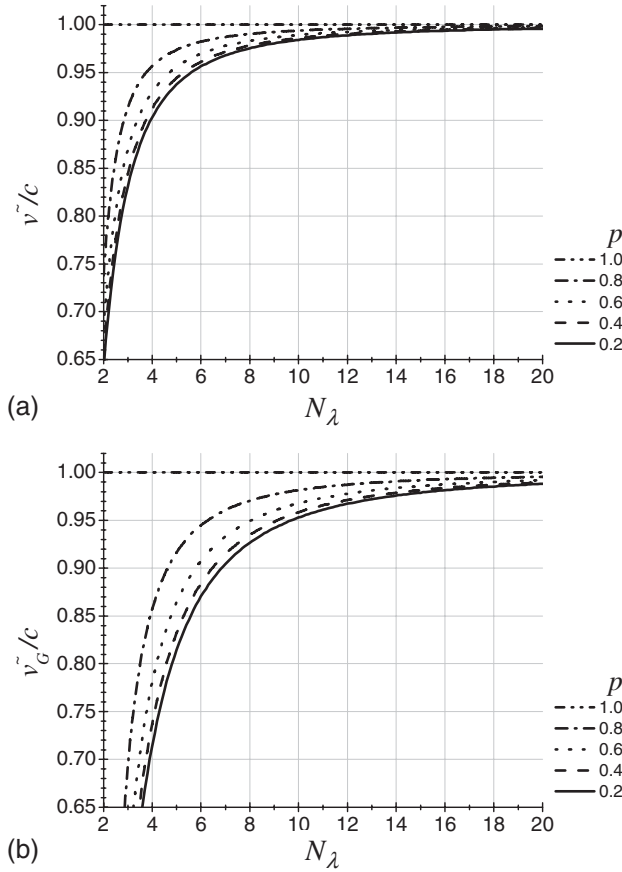
Figure 7.4 The normalized grid phase velocity (a) and normalized grid group velocity (b) of the grid wave with physical wavelength λ, as a function of the spatial sampling N_λ of the physical wavelength.

(7.92) is useful for practical simulations because, for a given value of the stability ratio p, it directly relates grid phase velocity to spatial sampling N_λ. The normalized grid phase velocities for five values of p are shown in Fig. 7.4a.

It is also interesting to look at the phase velocity of an unstable wave. Recalling relations (7.56) and (7.59), the phase velocity is

$$\tilde{v}_U = \frac{\tilde{\omega}_{\text{real}}}{k} = \frac{\pi}{\Delta} \frac{\lambda_U}{2\pi} = \frac{\pi}{\Delta} \frac{2h}{2\pi} = \frac{h}{\Delta} = \frac{c}{S} \tag{7.93}$$

The phase velocity of an unstable wave is surprisingly simply related to the stability factor S. Note that $\tilde{v}_U = \frac{h}{\Delta}$ is the maximum possible grid phase velocity. A grid wave cannot propagate a larger distance than h in one time step Δ.

Grid phase velocity of the wave with a true physical frequency

We obtain the following alternative relations for the nonattenuative regime:

$$\tilde{v} = \frac{\omega}{\tilde{k}_{real}} = \frac{\omega\Delta}{p \arccos\left\{1 + \frac{1}{p^2}\left[\cos(\omega\Delta) - 1\right]\right\}}c$$

$$= \frac{kh}{\arccos\left\{1 + \frac{1}{p^2}\left[\cos(pkh) - 1\right]\right\}}c$$

$$= \frac{2\pi}{pN_T \arccos\left\{1 + \frac{1}{p^2}\left[\cos\left(\frac{2\pi}{N_T}\right) - 1\right]\right\}}c \tag{7.94}$$

The grid phase velocity given by any one of the relations (7.94) is the velocity of the grid wave that has the same frequency as the true physical wave.

What is the phase velocity in the nondissipative (stable) but attenuative regime? Using (7.84) we obtain

$$\tilde{v} = \frac{\omega}{\tilde{k}_{real}} = \frac{h}{\pi}\frac{2\pi}{T} = \frac{2}{SN_T}c = \frac{2}{pN_T}c \tag{7.95}$$

The grid phase velocity can be numerically illustrated. In order to compare the phase velocity with attenuation, we rewrite the relations for the phase velocities (7.94) and (7.95) as functions of $f_{normalized}$:

for $f \leq f_{ATT}$

$$\tilde{v} = \frac{2\pi f_{normalized}}{p \arccos\left\{1 + \frac{1}{p^2}\left[\cos(2\pi f_{normalized}) - 1\right]\right\}}c \tag{7.96}$$

for $f_{ATT} < f \leq f_N$

$$\tilde{v} = \frac{2 f_{normalized}}{p}c \tag{7.97}$$

The upper panel of Fig. 7.5 shows the normalized grid phase velocity, the bottom panel shows the amplitude attenuation factor. Both panels clearly visualize the sudden change of the displayed quantities at f_{ATT}.

7.2.6.2 Grid group velocity

The existence of grid dispersion of the phase velocity implies the existence of the grid group velocity:

$$\tilde{v}_G \equiv \frac{\partial\tilde{\omega}}{\partial k} \tag{7.98}$$
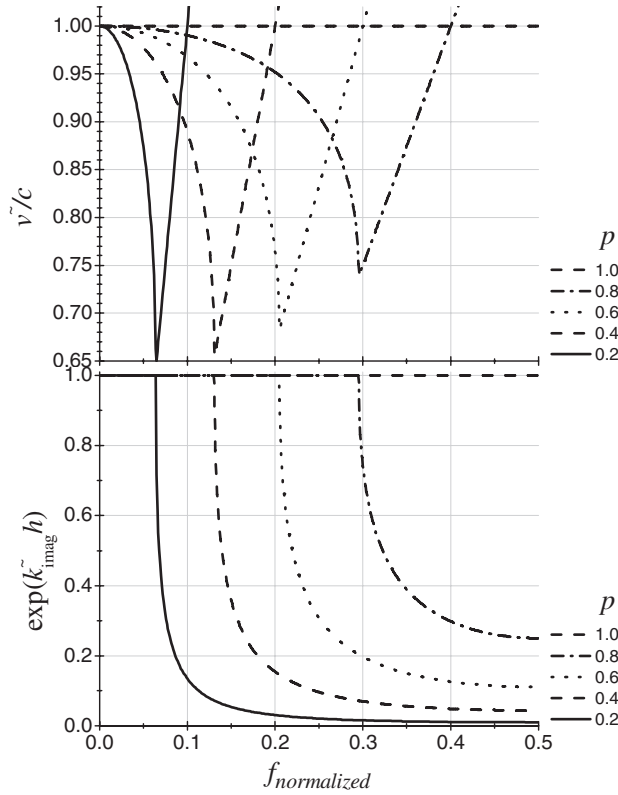
Figure 7.5 The normalized grid phase velocity (top panel) and the amplitude attenuation factor (bottom panel) of the grid wave with physical frequency ω as a function of the normalized frequency $f_{normalized}$. For each value of the stability ratio p the normalized grid phase velocity has a sharp minimum at the normalized frequency of $f_{ATT,normalized}$. For each value of p the amplitude attenuation factor falls from the unit value at $f_{ATT,normalized}$.

Recalling relations (7.53), (7.54), (7.69) and (7.70)

$$\tilde{v}_G = \frac{\partial \tilde{\omega}}{\partial k} = p \frac{\sin(kh)}{\sqrt{1 - \left\{1 + p^2 \left[\cos(kh) - 1\right]\right\}^2}} c$$

$$= p \frac{\sin\left(\dfrac{2\pi}{N_\lambda}\right)}{\sqrt{1 - \left\{1 + p^2 \left[\cos\left(\dfrac{2\pi}{N_\lambda}\right) - 1\right]\right\}^2}} c \qquad (7.99)$$

The normalized grid group velocities for five values of p are shown in Fig. 7.4b.

7.2.7 Local error

Recall scheme (7.21):

$$u_I^{m+1} = 2u_I^m - u_I^{m-1} + \left(c\frac{\Delta}{h}\right)^2 \left(u_{I+1}^m - 2u_I^m + u_{I-1}^m\right) \qquad (7.100)$$

which can be written symbolically as

$$u(I, t + \Delta) = numerical\_scheme\{u(t - \Delta), u(t)\} \qquad (7.101)$$

Define a numerical solution in one time step as

$$u^N(I, t + \Delta) \equiv numerical\_scheme\{u^E(t - \Delta), u^E(t)\} \qquad (7.102)$$

where the upper index N indicates the numerical solution, and the upper index E indicates an exact value. Because we consider

$$u(x, t) = \exp[i(\omega t - kx)] \qquad (7.103)$$

the exact displacement is complex. We can define a local error for real parts of the numerical and exact displacements as follows: a relative local error in amplitude is

$$\varepsilon_{ampl}^{Rel} \equiv \left(\frac{\Delta_{ref}}{\Delta}\right)^2 \left|\frac{A^N - A^E}{A^E}\right| = \left(\frac{\Delta_{ref}}{\Delta}\right)^2 \left|\frac{A^N}{A^E} - 1\right| \qquad (7.104)$$

where A^N is the modulus of the real part of the numerical displacement in one time step and A^E is the modulus of the real part of the exact displacement – both evaluated at time $t + \Delta$. If the local error is to be a general concept it has to be reasonably defined also for possible comparisons with other schemes. Because different numerical schemes use different time steps, we have to normalize the error for a unit time. Because the time derivative is approximated with the 2nd-order accuracy, we have to normalize the error with the square of Δ. The division gives the error a physical unit (s^{-2}) and larger value. These can be compensated, for example, by multiplication by the square of some time-step value Δ_{ref} taken as a reference.

Without loss of generality, consider for simplicity

$$x_I = 0, \quad t_m = 0 \qquad (7.105)$$

Then the errors are evaluated at

$$x_I = 0, \quad t_{m+1} = \Delta \qquad (7.106)$$

The exact real displacement at this space–time grid position is

$$\text{Re}\{u^E(0, \Delta)\} = \cos\omega\Delta \qquad (7.107)$$

and

$$A^E = |\text{Re}\{u^E(0, \Delta)\}| = |\cos\omega\Delta| \qquad (7.108)$$

The exact complex displacements entering the r.h.s. of scheme (7.100) are

$$u_I^m = 1 \qquad\qquad u_I^{m-1} = \exp(-i\omega\Delta)$$
$$u_{I+1}^m = \exp(-ikh) \quad u_{I-1}^m = \exp(+ikh) \tag{7.109}$$

The numerical complex displacement at $x_I = 0$ and $t_{m+1} = \Delta$ is

$$u^N(0,\Delta) = 2 - \exp(-i\omega\Delta) + S^2\left[\exp(-ikh) - 2 + \exp(+ikh)\right]$$
$$= 2 - \cos\omega\Delta + i\sin\omega\Delta + 2S^2\left[\cos kh - 1\right] \tag{7.110}$$

The real part of the numerical displacement is

$$\mathrm{Re}\left\{u^N(0,\Delta)\right\} = 2 - \cos\omega\Delta + 2S^2\left[\cos kh - 1\right] \tag{7.111}$$

$$A^N = \left|\mathrm{Re}\left\{u^N(0,\Delta)\right\}\right| = \left|2 - \cos\omega\Delta + 2S^2\left[\cos kh - 1\right]\right| \tag{7.112}$$

Then,

$$\varepsilon_{\mathrm{ampl}}^{\mathrm{Rel}} = \left(\frac{\Delta_{\mathrm{ref}}}{\Delta}\right)^2 \left|\frac{\left|2 - \cos\omega\Delta + 2S^2\left[\cos kh - 1\right]\right|}{|\cos\omega\Delta|} - 1\right| \tag{7.113}$$

In the previous analyses we assumed either true physical k and grid $\tilde{\omega}$ or true physical ω and grid $\tilde{k}$. Here the values entering the scheme at time levels $m-1$ and m are exact. This means that both k and ω are assumed exact at both time levels:

$$kh = \frac{2\pi h}{\lambda} = \frac{2\pi}{N_\lambda} \tag{7.114}$$

$$\omega\Delta = \frac{2\pi}{T}\Delta = \frac{2\pi}{\lambda}c\,\underbrace{p\frac{h}{c}}_{\Delta}S_M = \frac{2\pi}{N_\lambda}pS_M \tag{7.115}$$

Because $S_M = 1$,

$$\varepsilon_{\mathrm{ampl}}^{\mathrm{Rel}} = \left(\frac{\Delta_{\mathrm{ref}}}{\Delta}\right)^2 \left|\frac{\left|2 - \cos\left(\frac{2\pi}{N_\lambda}p\right) + 2p^2\left[\cos\left(\frac{2\pi}{N_\lambda}\right) - 1\right]\right|}{\left|\cos\left(\frac{2\pi}{N_\lambda}p\right)\right|} - 1\right| \tag{7.116}$$

Note that (7.115) implies

$$\left(\frac{\Delta_{\mathrm{ref}}}{\Delta}\right)^2 = \left(\frac{N_\lambda}{N_{\lambda,\mathrm{ref}}}\right)^2 \tag{7.117}$$

The local errors in amplitude for five values of p are shown in Fig. 7.6. Note that the error is zero for $p = 1$.

Note on the local error and grid dispersion It is clear that the local error in amplitude quantifies how the exact amplitude changes in one time step due to inaccuracy of the numerical scheme. In the analysis of grid dispersion we assume a constant amplitude of
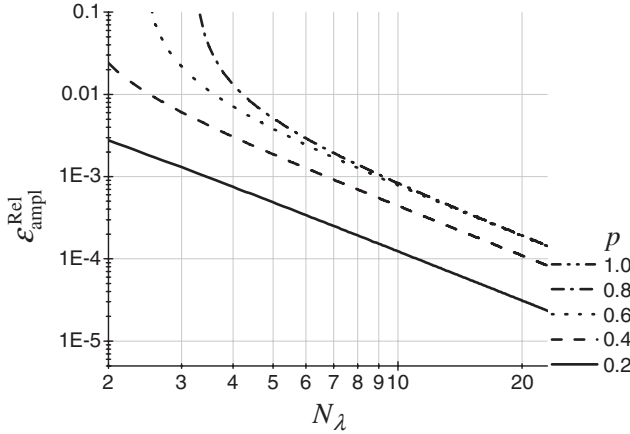
Figure 7.6 The local error in amplitude as a function of the spatial sampling N_λ of the physical wavelength. Δ_{ref} is chosen as the time step for $N_\lambda = 20$. Note that the error is zero for $p = 1$ – the corresponding line is missing.

the grid wave (wave propagating in the stable nonattenuative regime). In one analysis we assume a grid wave with grid wavenumber $\tilde{k}$ equal to the true wavenumber k and investigate how the grid frequency $\tilde{\omega}$ will be different from the true physical frequency ω. In the other analysis we assume a grid wave with frequency $\tilde{\omega}$ equal to the true frequency ω and investigate how the grid wavenumber $\tilde{k}$ will be different from the true physical wavenumber k. In both cases, the price for propagating the harmonic plane wave with constant amplitude in a discrete grid is a grid velocity that differs from the true velocity, and the difference depends on the size of the grid spacing and time step.

7.2.8 Sufficiently accurate numerical simulation

Consider an unbounded homogeneous medium characterized by the true wave speed c. Consider that a wavefield is generated in the frequency range $[f_{MIN}, f_{MAX}]$. The corresponding range of the wavelengths is $[\lambda_{MIN}, \lambda_{MAX}] = \left[\frac{c}{f_{MAX}}, \frac{c}{f_{MIN}} \right]$.

We want to numerically simulate the wavefield using the analyzed FD scheme (7.20) sufficiently accurately for the range of wavelengths $[\lambda_{MIN}, \lambda_{MAX}]$.

In order to prepare the numerical calculation we need to recall the stability condition, Eq. (7.70),

$$\Delta = p \frac{h}{c} S_M; \quad 0 < p \leq 1, \quad S_M = 1 \tag{7.118}$$

the grid dispersion of the phase velocity, Eq. (7.92) and Fig. 7.4,

$$\tilde{v} = \frac{N_\lambda}{2\pi p} \arccos \left\{ 1 + p^2 \left[\cos \left(\frac{2\pi}{N_\lambda} \right) - 1 \right] \right\} c \tag{7.119}$$

and the grid dispersion of the group velocity, Eq. (7.99) and Fig. 7.6,

$$
\tilde{v}_G = p \frac{\sin\left(\dfrac{2\pi}{N_\lambda}\right)}{\sqrt{1 - \left\{1 + p^2\left[\cos\left(\dfrac{2\pi}{N_\lambda}\right) - 1\right]\right\}^2}} c \tag{7.120}
$$

Relations (7.119) and (7.120) can be written as

$$
\tilde{v} = \Gamma\left(N_\lambda; p\right) c \tag{7.121}
$$

and

$$
\tilde{v}_G = \Gamma_G\left(N_\lambda; p\right) c \tag{7.122}
$$

with

$$
\Gamma\left(N_\lambda; p\right) = \frac{N_\lambda}{2\pi p} \arccos\left\{1 + p^2\left[\cos\left(\frac{2\pi}{N_\lambda}\right) - 1\right]\right\} > 0 \tag{7.123}
$$

and

$$
\Gamma_G\left(N_\lambda; p\right) = p \frac{\sin\left(\dfrac{2\pi}{N_\lambda}\right)}{\sqrt{1 - \left\{1 + p^2\left[\cos\left(\dfrac{2\pi}{N_\lambda}\right) - 1\right]\right\}^2}} > 0 \tag{7.124}
$$

We can proceed as follows:

(a) We choose a value of the stability ratio $0 < p \leq 1$ that is a fraction of the maximum possible time step.

(b) We require that the absolute value of the difference between the true arrival time and numerical phase arrival time at distance D be not larger than δ:

$$
\left|\frac{D}{c} - \frac{D}{\tilde{v}(p)}\right| \leq \delta \tag{7.125}
$$

Condition (7.125) transforms to

$$
\frac{D}{D + c\delta} \leq \Gamma\left(N_\lambda; p\right) \leq \frac{D}{D - c\delta} \tag{7.126}
$$

(c) We find the smallest $N_\lambda \equiv N_\lambda^{p,\delta}$ that satisfies condition (7.126).

(d) If we apply the spatial sampling $N_\lambda^{p,\delta}$ to λ_{MIN}, we obtain the value of the grid spacing:

$$
h = \frac{\lambda_{MIN}}{N_\lambda^{p,\delta}} \tag{7.127}
$$

(e) Having the grid spacing h we can determine the value of the time step:

$$
\Delta = p \frac{h}{c} S_M \tag{7.128}
$$

(f) Finally, we can check whether $f_{MAX}\Delta \leq f_{ATT,normalized}(p)$, see Eq. (7.88).
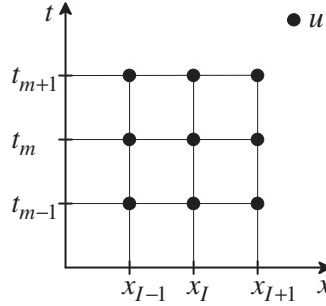
Figure 7.7 Conventional space–time grid for the 1D displacement formulation.

Steps (b)–(f) can alternatively be applied to the grid group velocity. The choice of either of the two grid velocities may be case dependent.

7.3 FD schemes for an unbounded smoothly heterogeneous medium

7.3.1 (2,2) displacement scheme on a conventional grid

Consider an unbounded smoothly heterogeneous perfectly elastic medium characterized by elastic modulus $M(x)$ and density $\rho(x)$. Recall the equation of motion in the displacement formulation (7.2):

$$\rho\frac{\partial^2 u}{\partial t^2} = \frac{\partial}{\partial x}\left(M\frac{\partial u}{\partial x}\right) \tag{7.129}$$

which can be written as

$$EQ \equiv \rho\frac{\partial^2 u}{\partial t^2} - \frac{\partial}{\partial x}\left(M\frac{\partial u}{\partial x}\right), \quad EQ = 0 \tag{7.130}$$

Consider a conventional space–time grid with time step Δ and spatial grid spacing h, see Fig. 7.7.

Approximate Eq. (7.130) at the time level m and spatial position I. Whereas the 2nd temporal derivative can be easily approximated using the 2nd-order centred FD formula, it is clear that approximating the 2nd spatial derivative is not trivial due to the presence of modulus M, which is a function of x. Defining an auxiliary function ϕ,

$$\phi \equiv M\frac{\partial u}{\partial x} \tag{7.131}$$

the 2nd spatial derivative can be approximated as

$$\frac{\partial}{\partial x}\left(M\frac{\partial u}{\partial x}\right)\bigg|_I^m = \frac{\partial \phi}{\partial x}\bigg|_I^m \doteq \frac{1}{h}\left(\phi_{I+1/2}^m - \phi_{I-1/2}^m\right) \tag{7.132}$$

Rewrite Eq. (7.131):

$$\frac{\phi}{M} = \frac{\partial u}{\partial x} \tag{7.133}$$

and integrate it:

$$\int_{x_I}^{x_{I+1}} \frac{\phi}{M} dx = \int_{x_I}^{x_{I+1}} \frac{\partial u}{\partial x} dx \tag{7.134}$$

Applying the mean-value theorem to the l.h.s. integral and approximating the mean value by $\phi_{I+1/2}^m$ we obtain

$$\phi_{I+1/2}^m \int_{x_I}^{x_{I+1}} \frac{1}{M} dx \doteq u_{I+1}^m - u_I^m \tag{7.135}$$

Define an effective grid material parameter as an integral harmonic average:

$$M_{I+1/2}^{xH} \equiv \left[\frac{1}{h} \int_{x_I}^{x_{I+1}} \frac{1}{M} dx \right]^{-1} \tag{7.136}$$

Then Eq. (7.135) gives

$$\phi_{I+1/2}^m \doteq M_{I+1/2}^{xH} \frac{1}{h} \left(u_{I+1}^m - u_I^m \right) \tag{7.137}$$

Applying approximation (7.137) to Eq. (7.132) we obtain

$$\left. \frac{\partial}{\partial x} \left(M \frac{\partial u}{\partial x} \right) \right|_I^m \doteq \frac{1}{h^2} \left[M_{I+1/2}^{xH} \left(u_{I+1}^m - u_I^m \right) - M_{I-1/2}^{xH} \left(u_I^m - u_{I-1}^m \right) \right] \tag{7.138}$$

The FD approximation of *EQ*, say *FDEQ*, is then

$$\begin{aligned} FDEQ|_I^m \equiv{} & \rho_I \frac{1}{\Delta^2} \left(u_I^{m+1} - 2u_I^m + u_I^{m-1} \right) \\ & - \frac{1}{h^2} \left[M_{I+1/2}^{xH} \left(u_{I+1}^m - u_I^m \right) - M_{I-1/2}^{xH} \left(u_I^m - u_{I-1}^m \right) \right] \end{aligned} \tag{7.139}$$

Note that the integration leading to the integral harmonic averaging of the elastic modulus was originally suggested by Tikhonov and Samarskii (see, e.g., Boore 1972b; Mitchell 1969, p. 23) as a mathematical tool to avoid differentiating the modulus.

In order to find the truncation error of the approximation, consider for simplicity that $M_{I\pm1/2}^{xH}$ are the local values of M at the grid positions $I \pm 1/2$. Then,

TrunErr {*FDEQ*} = *TaylorExpansion* {*FDEQ*} − *EQ*

$$= \frac{1}{12} \rho \frac{\partial^4 u}{\partial t^4} \Delta^2 + O(\Delta^4)$$

$$- \left(\frac{1}{24} \frac{\partial^3 M}{\partial x^3} \frac{\partial u}{\partial x} + \frac{1}{8} \frac{\partial^2 M}{\partial x^2} \frac{\partial^2 u}{\partial x^2} + \frac{1}{6} \frac{\partial M}{\partial x} \frac{\partial^3 u}{\partial x^3} + \frac{1}{12} M \frac{\partial^4 u}{\partial x^4} \right) h^2 + O(h^4)$$

$$\tag{7.140}$$

Because the leading term of the truncation error consists of a term with Δ^2 and a term with h^2, we can say that *FDEQ* is consistent with *EQ* with 2nd-order accuracy both in time and space. In the case of a homogeneous medium, *FDEQ* and its truncation error simplify:

$$FDEQ|_I^m = \rho \frac{1}{\Delta^2} \left(u_I^{m+1} - 2u_I^m + u_I^{m-1} \right) - M \frac{1}{h^2} \left(u_{I+1}^m - 2u_I^m + u_{I-1}^m \right) \quad (7.141)$$

$$TrunErr\{FDEQ\} = \frac{1}{12} \rho \frac{\partial^4 u}{\partial t^4} \Delta^2 + O(\Delta^4) - \frac{1}{12} M \frac{\partial^4 u}{\partial x^4} h^2 + O(h^4) \quad (7.142)$$

FDEQ for a homogeneous medium was investigated in detail in Section 7.2.

Approximations (7.139) and (7.141) imply the explicit FD scheme:

$$U_I^{m+1} = 2U_I^m - U_I^{m-1}$$
$$+ b_I \left(\frac{\Delta}{h} \right)^2 \left[M_{I+1/2}^{xH} \left(U_{I+1}^m - U_I^m \right) - M_{I-1/2}^{xH} \left(U_I^m - U_{I-1}^m \right) \right] \quad (7.143)$$

for a smoothly heterogeneous medium, and

$$U_I^{m+1} = 2U_I^m - U_I^{m-1} + bM \left(\frac{\Delta}{h} \right)^2 \left(U_{I+1}^m - 2U_I^m + U_{I-1}^m \right) \quad (7.144)$$

for a homogeneous medium. Using U instead of u we indicate that values in the schemes are, except for two initial time levels, approximate.

Note that Zahradník (1995b), Zahradník and Priolo (1995), Moczo *et al.* (1999) and Kristek and Moczo (2006) demonstrated that harmonic averaging (7.136) is essential for accounting for the medium heterogeneity.

7.3.2 (2,2) displacement–stress scheme on a spatially staggered grid

For the displacement–stress (DS) formulation (7.1) we define

$$EQu \equiv \rho \frac{\partial^2 u}{\partial t^2} - \frac{\partial \sigma}{\partial x}, \quad EQu = 0$$
$$EQ\sigma \equiv \sigma - M \frac{\partial u}{\partial x}, \quad EQ\sigma = 0 \quad (7.145)$$

In the DS formulation we can explicitly treat both the displacement u and stress σ. Considering a possible space–time grid we can notice an interesting feature: according to the first of Eqs. (7.145), the 2nd temporal derivative of u and the 1st spatial derivative of σ have to be approximated at the same space–time grid position. Similarly, according to the equation for $EQ\sigma$, also σ and the 1st spatial derivative of u have to share a space–time grid position. If we want to use centred approximations to both 1st spatial derivatives, we naturally come to the spatially staggered grid illustrated in Fig. 7.8.
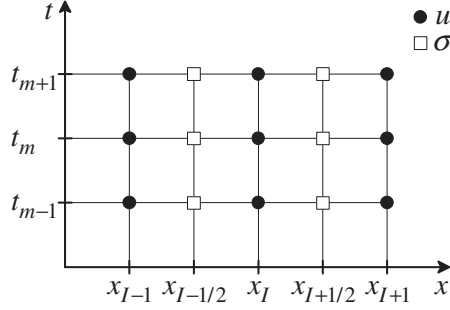
Figure 7.8 Spatially staggered space–time grid for the 1D displacement–stress formulation.

Approximate *EQu* at time level m and spatial position I:

$$FDEQu|_I^m \equiv \rho_I \frac{1}{\Delta^2} \left(u_I^{m+1} - 2u_I^m + u_I^{m-1} \right) - \frac{1}{h} \left(\sigma_{I+1/2}^m - \sigma_{I-1/2}^m \right) \qquad (7.146)$$

and $EQ\sigma$ at time level m and spatial position $I + 1/2$:

$$FDEQ\sigma|_{I+1/2}^m \equiv \sigma_{I+1/2}^m - M_{I+1/2} \frac{1}{h} \left(u_{I+1}^m - u_I^m \right) \qquad (7.147)$$

The two approximations imply the explicit DS scheme on a spatially staggered grid:

$$U_I^{m+1} = 2U_I^m - U_I^{m-1} + b_I \frac{\Delta^2}{h} \left(T_{I+1/2}^m - T_{I-1/2}^m \right) \qquad (7.148)$$

$$T_{I+1/2}^m = M_{I+1/2} \frac{1}{h} \left(U_{I+1}^m - U_I^m \right) \qquad (7.149)$$

We used symbol T to indicate approximate grid values of the stress. If we need to calculate explicitly both displacement and stress, we can use scheme (7.149) to calculate stress (having explicit variables for stress in a computer code) and then use the values of stress for updating displacement according to scheme (7.148). Note, however, that substituting $T_{I+1/2}^m$ and $T_{I-1/2}^m$ by the appropriate r.h.s. of scheme (7.149) we eliminate the stress variables and obtain

$$U_I^{m+1} = 2U_I^m - U_I^{m-1}$$
$$+ b_I \left(\frac{\Delta}{h} \right)^2 \left[M_{I+1/2} \left(U_{I+1}^m - U_I^m \right) - M_{I-1/2} \left(U_I^m - U_{I-1}^m \right) \right] \qquad (7.150)$$

which differs from the displacement scheme (7.143) only by the effective grid elastic moduli. This is just because in elaborating the DS approximation we did not face the explicit problem with the spatial derivative of the modulus and simply used $M_{I+1/2}$ and $M_{I-1/2}$. From the simple way of making the approximation, we cannot see how the effective grid values of modulus should be determined in order to properly account for the medium heterogeneity. We will address this important question later. Here, we just note that the use of the harmonic averages gives the best results (e.g., Kristek and Moczo 2006).
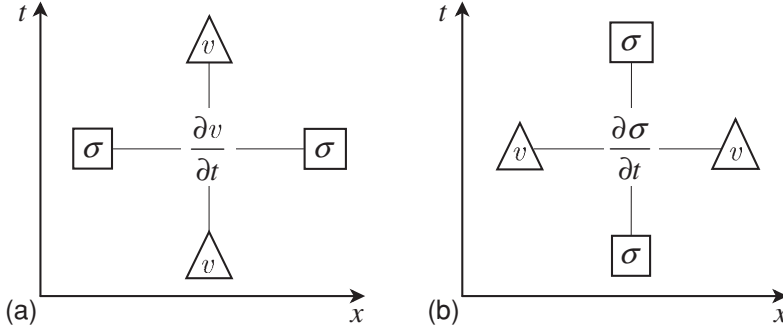
Figure 7.9 Space–time grid positions for the 2nd-order approximations of the 1st temporal and spatial derivatives in the velocity–stress formulation.

Apart from the effective grid moduli, we see that the approximation of the equation in the displacement formulation on a conventional grid and the approximations of the equations in the DS formulation on a spatially staggered grid, in both cases using the 2nd-order centred FD approximations to the temporal and spatial derivatives, led to the same explicit scheme. This is just because we deal with the 1D problem and use 2nd-order approximations.

7.3.3 (2,2) velocity–stress scheme on a staggered grid

For the velocity–stress (VS) formulation (7.9) we can define

$$
\begin{aligned}
EQv &\equiv \frac{\partial v}{\partial t} - b\frac{\partial \sigma}{\partial x}, \quad EQv = 0 \\
EQ\sigma &\equiv \frac{\partial \sigma}{\partial t} - M\frac{\partial v}{\partial x}, \quad EQ\sigma = 0
\end{aligned}
\tag{7.151}
$$

The formulation itself suggests treating both particle velocity and stress explicitly. At the same time, it is reasonable to consider replacing all the first derivatives by the centred FD approximation. In order to have both $\frac{\partial v}{\partial t}$ and $\frac{\partial \sigma}{\partial x}$ approximated by the centred FD formula at the same space–time grid position, it is reasonable to have the spatial grid position of σ displaced from that of $\frac{\partial v}{\partial t}$. Consequently, the temporal grid position of v should be shifted from that of σ – see Fig. 7.9a.

Similarly, in order to have both $\frac{\partial \sigma}{\partial t}$ and $\frac{\partial v}{\partial x}$ approximated by the centred FD formula at the same space–time grid position, it is reasonable to consider the space–time grid positions shown in Fig. 7.9b. Naturally, we come to the grid that is staggered in both time and space, Fig. 7.10.

Equations (7.151) may be approximated as

$$
\begin{aligned}
FDEQv|_I^m &\equiv \frac{1}{\Delta}\left(v_I^{m+1/2} - v_I^{m-1/2}\right) - b_I\frac{1}{h}\left(\sigma_{I+1/2}^m - \sigma_{I-1/2}^m\right) \\
FDEQ\sigma|_{I-1/2}^{m-1/2} &\equiv \frac{1}{\Delta}\left(\sigma_{I-1/2}^m - \sigma_{I-1/2}^{m-1}\right) - M_{I-1/2}\frac{1}{h}\left(v_I^{m-1/2} - v_{I-1}^{m-1/2}\right)
\end{aligned}
\tag{7.152}
$$
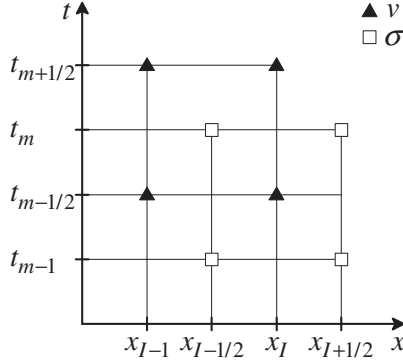
Figure 7.10 Space–time grid for the 1D velocity–stress formulation. The grid is staggered in both time and space.

The approximations are 2nd-order accurate in time and space. They imply the (2,2) VS scheme on the staggered grid:

$$
\begin{aligned}
V_I^{m+1/2} &= V_I^{m-1/2} + b_I \frac{\Delta}{h} \left(T_{I+1/2}^m - T_{I-1/2}^m \right) \\
T_{I-1/2}^m &= T_{I-1/2}^{m-1} + M_{I-1/2} \frac{\Delta}{h} \left(V_I^{m-1/2} - V_{I-1}^{m-1/2} \right)
\end{aligned}
\tag{7.153}
$$

Clearly, the second scheme can be used to update stress. Then the first scheme can be used to update particle velocity.

Substituting $T_{I+1/2}^m$ and $T_{I-1/2}^m$ in the scheme for particle velocity gives

$$
\begin{aligned}
V_I^{m+1/2} = V_I^{m-1/2} + b_I \frac{\Delta}{h} &\left[T_{I+1/2}^{m-1} + M_{I+1/2} \frac{\Delta}{h} \left(V_{I+1}^{m-1/2} - V_I^{m-1/2} \right) \right. \\
&\left. - T_{I-1/2}^{m-1} - M_{I-1/2} \frac{\Delta}{h} \left(V_I^{m-1/2} - V_{I-1}^{m-1/2} \right) \right]
\end{aligned}
\tag{7.154}
$$

The scheme for particle velocity applied to time level $m - 1$ implies

$$
b_I \frac{\Delta}{h} \left(T_{I+1/2}^{m-1} - T_{I-1/2}^{m-1} \right) = V_I^{m-1/2} - V_I^{m-3/2}
\tag{7.155}
$$

Using Eq. (7.155) in Eq. (7.154) leads to

$$
\begin{aligned}
V_I^{m+1/2} = &\, 2V_I^{m-1/2} - V_I^{m-3/2} \\
&+ b_I \left(\frac{\Delta}{h} \right)^2 \left[M_{I+1/2} \left(V_{I+1}^{m-1/2} - V_I^{m-1/2} \right) - M_{I-1/2} \left(V_I^{m-1/2} - V_{I-1}^{m-1/2} \right) \right]
\end{aligned}
\tag{7.156}
$$

Comparison of scheme (7.156) with scheme (7.143) reveals that scheme (7.156) corresponds to the equations

$$\rho \frac{\partial^2 v}{\partial t^2} = \frac{\partial}{\partial x}\left(M \frac{\partial v}{\partial x}\right) \tag{7.157}$$

or

$$\rho \frac{\partial^2 v}{\partial t^2} = \frac{\partial}{\partial x}\frac{\partial \sigma}{\partial t}, \quad \frac{\partial \sigma}{\partial t} = M \frac{\partial v}{\partial x} \tag{7.158}$$

that are obtained by temporally differentiating the displacement-formulation equation (7.2) or the DS equations (7.1), respectively. Note that once we have eliminated the explicit presence of stress we could replace temporal indices in scheme (7.156) by integer indices.

7.3.4 Optimally accurate displacement scheme on a conventional grid

Is the 2nd-order accuracy in time and space sufficient for the acceptably accurate and computationally efficient numerical modelling of seismic wave propagation? Despite the relativity of the concept the answer is no. Nor for 1D propagation over distances of several dominant wavelengths are the 2nd-order accurate schemes efficient. The question is, how to obtain an FD scheme that would be sufficiently efficient.

Here we explain a particular optimization approach by Geller and Takeuchi (1995, 1998). The concise exposition of the general criterion for the optimally accurate FD operators developed by Geller and his co-workers can be found in, e.g., Moczo *et al.* (2007a,b). Later we will explore other possibilities.

Recall the truncation error (7.142) corresponding to approximation (7.141) and scheme (7.143). In the case of a homogeneous medium it also applies to scheme (7.150), and its structure is the same as that of scheme (7.156) – apart from the particle velocity appearing instead of displacement and non-integer temporal indices. Write the error (7.142) as

$$TrunErr\{FDEQ\} = \frac{1}{12}\Delta^2 \frac{\partial^2}{\partial t^2}\left(\rho \frac{\partial^2 u}{\partial t^2}\right)\Big|_I^m + O(\Delta^4)$$
$$+ \frac{1}{12}h^2 \frac{\partial^2}{\partial x^2}\left(-M \frac{\partial^2 u}{\partial x^2}\right)\Big|_I^m + O(h^4) \tag{7.159}$$

We can think of an approximation, say *OFDEQ*, with the truncation error equal to

$$TrunErr\{OFDEQ\} = \frac{1}{12}\Delta^2 \frac{\partial^2}{\partial t^2}\left(\rho \frac{\partial^2 u}{\partial t^2} - M \frac{\partial^2 u}{\partial x^2}\right)\Big|_I^m + O(\Delta^4)$$
$$+ \frac{1}{12}h^2 \frac{\partial^2}{\partial x^2}\left(\rho \frac{\partial^2 u}{\partial t^2} - M \frac{\partial^2 u}{\partial x^2}\right)\Big|_I^m + O(h^4) \tag{7.160}$$

Why? Because the leading term of the error would be identically equal to zero in the case of normal modes in a homogeneous medium – due to the expressions in parentheses. The
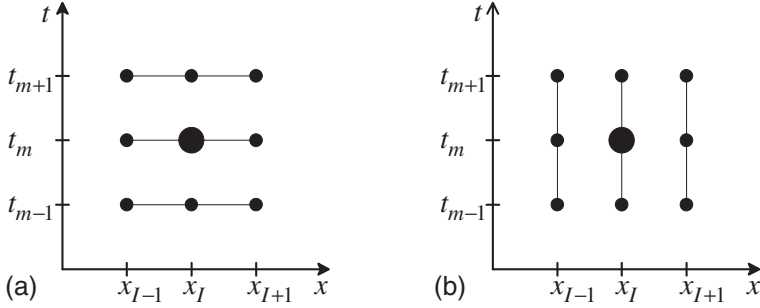
Figure 7.11 Space–time grid positions for approximating derivatives at the spatial position x_I and time t_m: (a) the 2nd spatial derivative, (b) the 2nd temporal derivative.

corresponding FD approximation, *OFDEQ*, would then be two orders more accurate in both time and space than *FDEQ* in Eq. (7.141).

We now try to find *OFDEQ*. The new term $\frac{1}{12}\Delta^2 \frac{\partial^2}{\partial t^2}\left(-M\frac{\partial^2 u}{\partial x^2}\right)\big|_I^m$ in error (7.160) can appear in the truncation error due to an approximation of the 2nd spatial derivative in Eq. (7.130). This is possible if the approximation of the spatial derivative at time t_m is some weighted average of approximations of spatial derivatives at times t_{m-1}, t_m and t_{m+1}. This is illustrated in Fig. 7.11a.

Similarly, the new term $\frac{1}{12}h^2 \frac{\partial^2}{\partial x^2}\left(\rho\frac{\partial^2 u}{\partial t^2}\right)\big|_I^m$ in Eq. (7.160) can appear due to an approximation of the 2nd temporal derivative in Eq. (7.130). This is possible if the approximation of the temporal derivative at the spatial position x_I is some weighted average of approximations of temporal derivatives at positions x_{I-1}, x_I and x_{I+1}. This is illustrated in Fig. 7.11b. Consequently, the sought approximation *OFDEQ* of Eq. (7.130) should include displacement values at nine space–time positions and could be formally written as

$$
\begin{aligned}
OFDEQ|_I^m = \rho\frac{1}{\Delta^2} \big(& a_{11}u_{I-1}^{m+1} + a_{12}u_I^{m+1} + a_{13}u_{I+1}^{m+1} \\
& + a_{21}u_{I-1}^m + a_{22}u_I^m + a_{23}u_{I+1}^m \\
& + a_{31}u_{I-1}^{m-1} + a_{32}u_I^{m-1} + a_{33}u_{I+1}^{m-1} \big) \\
- M\frac{1}{h^2} \big(& c_{11}u_{I-1}^{m+1} + c_{12}u_I^{m+1} + c_{13}u_{I+1}^{m+1} \\
& + c_{21}u_{I-1}^m + c_{22}u_I^m + c_{23}u_{I+1}^m \\
& + c_{31}u_{I-1}^{m-1} + c_{32}u_I^{m-1} + c_{33}u_{I+1}^{m-1} \big)
\end{aligned}
\tag{7.161}
$$

or, in a concise form, as

$$
OFDEQ = \left(\rho\frac{1}{\Delta^2}a_{ij} - M\frac{1}{h^2}c_{ij} \right) u_{ij}
\tag{7.162}
$$

where we assume the summation convention for indices i and j (no matrix multiplication), and u_{ij} means displacements at nine space–time positions. In matrix form they are

$$[u_{ij}] \equiv \begin{bmatrix} u_{I-1}^{m+1} & u_I^{m+1} & u_{I+1}^{m+1} \\ u_{I-1}^{m} & u_I^{m} & u_{I+1}^{m} \\ u_{I-1}^{m-1} & u_I^{m-1} & u_{I+1}^{m-1} \end{bmatrix} \tag{7.163}$$

The 18 unknown coefficients a_{ij} and c_{ij} have to be determined so that the truncation error

$$TrunErr\{OFDEQ\} = TaylorExpansion\{OFDEQ\} - \left(\rho \frac{\partial^2 u}{\partial t^2} - M \frac{\partial^2 u}{\partial x^2} \right) \tag{7.164}$$

is equal to that given by Eq. (7.160). Because *OFDEQ* uses values of displacements at nine space–time positions, only nine coefficients of the Taylor expansion of *OFDEQ* are independent. The two known terms in parentheses in Eq. (7.164) do not change the structure of independence of the Taylor expansion coefficients. Consequently, we have freedom in choosing for which coefficients we impose conditions in order to obtain the desired *TrunErr{OFDEQ}*. Denote

$$coef\, D^{(k,l)}u \equiv \text{coefficient of } (TaylorExpansion\{OFDEQ\} - EQ) \text{ at } \frac{\partial^{k+l}}{\partial t^k \partial x^l} \tag{7.165}$$

The 18 unknown coefficients a_{ij} and c_{ij} can be found from the system of equations:

$$\text{8 conditions: } coef\, D^{(k,l)}u = 0; k, l \in \{0, 1, 2\}, (k, l) \neq (2, 2), k + l \leq 3 \tag{7.166}$$

$$\text{1 condition: } coef\, D^{(2,2)}u = \frac{1}{12}(h^2 \rho - \Delta^2 M) \tag{7.167}$$

$$\text{9 conditions: } a_{ij} = c_{ji}; i, j \in \{1, 2, 3\} \tag{7.168}$$

Conditions (7.166) mean that the truncation error does not include terms with derivatives $\frac{\partial u}{\partial t}$, $\frac{\partial^2 u}{\partial t^2}$, $\frac{\partial u}{\partial x}$, $\frac{\partial^2 u}{\partial x^2}$, $\frac{\partial^2 u}{\partial t \partial x}$, $\frac{\partial^3 u}{\partial t \partial x^2}$, $\frac{\partial^3 u}{\partial t^2 \partial x}$ and u itself. Condition (7.167) requires those two additional terms in error (7.160) that are not present in error (7.159). Conditions (7.168) mean that the matrix of coefficients a_{ij} is a transpose to the matrix of coefficients c_{ij}. In other words, the temporal derivative at position x_I is calculated as an average of temporal derivatives at positions x_{I-1}, x_I and x_{I+1} in the same way as the spatial derivative at time t_m is calculated as an average of spatial derivatives at times t_{m-1}, t_m and t_{m+1}.

Note that conditions

$$coef\, D^{(4,0)}u = \frac{1}{12}\Delta^2 \rho, \quad coef\, D^{(0,4)}u = \frac{1}{12}h^2 M \tag{7.169}$$

implied by Eq. (7.160) do not need to be explicitly required because they are not independent.

Solving system (7.166)–(7.168) we obtain the following coefficients:

$$a_{ij} = \frac{1}{12} \begin{bmatrix} 1 & 10 & 1 \\ -2 & -20 & -2 \\ 1 & 10 & 1 \end{bmatrix}, \quad c_{ij} = \frac{1}{12} \begin{bmatrix} 1 & -2 & 1 \\ 10 & -20 & 10 \\ 1 & -2 & 1 \end{bmatrix} \tag{7.170}$$

Substituting them in Eq. (7.161) gives

$$\begin{aligned} OFDEQ = \rho \frac{1}{12\Delta^2} \Big[&u_{I-1}^{m+1} - 2u_{I-1}^m + u_{I-1}^{m-1} + 10 \left(u_I^{m+1} - 2u_I^m + u_I^{m-1} \right) \\ &+ u_{I+1}^{m+1} - 2u_{I+1}^m + u_{I+1}^{m-1} \Big] - M \frac{1}{12h^2} \Big[u_{I+1}^{m+1} - 2u_I^{m+1} + u_{I-1}^{m+1} \\ &+ 10 \left(u_{I+1}^m - 2u_I^m + u_{I-1}^m \right) + u_{I+1}^{m-1} - 2u_I^{m-1} + u_{I-1}^{m-1} \Big] \end{aligned} \tag{7.171}$$

Equation (7.171) is the sought optimized FD approximation, that is, the approximation with the desired truncation error (7.160). The structure of terms in the first brackets clearly visualizes how $\frac{\partial^2 u}{\partial t^2} \big|_I^m$ is approximated. It is the 1–10–1 weighted average of the standard centred 2nd-order approximations of the 2nd temporal derivatives at spatial positions x_{I-1}, x_I and x_{I+1}. Similarly, the structure of terms in the second brackets visualizes the approximation of $\frac{\partial^2 u}{\partial x^2} \big|_I^m$ by the 1–10–1 weighted average of the standard centred 2nd-order approximations of the 2nd spatial derivatives at times t_{m-1}, t_m and t_{m+1}.

Compare the standard *FDEQ*, Eq. (7.141), with the optimized *OFDEQ*, Eq. (7.171). The standard one can be written in the form of Eq. (7.171) or (7.162):

$$FDEQ = \left(\rho \frac{1}{\Delta^2} \tilde{a}_{ij} - M \frac{1}{h^2} \tilde{c}_{ij} \right) u_{ij} \tag{7.172}$$

$$\tilde{a}_{ij} = \begin{bmatrix} 0 & 1 & 0 \\ 0 & -2 & 0 \\ 0 & 1 & 0 \end{bmatrix}, \quad \tilde{c}_{ij} = \begin{bmatrix} 0 & 0 & 0 \\ 1 & -2 & 1 \\ 0 & 0 & 0 \end{bmatrix} \tag{7.173}$$

It is obvious that *OFDEQ* does not give an explicit FD scheme. This is the price for obtaining the desired truncation error by approximating the spatial derivative at time t_m by the average of approximations at times t_{m-1}, t_m and t_{m+1}, and approximating the temporal derivative at position x_I by the average of approximations at positions x_{I-1}, x_I and x_{I+1}. In this case, however, it is easy to avoid solving a large system of linear equations of the implicit scheme at each time step by using the predictor-corrector method suggested by Geller and Takeuchi (1998). The method is based on the 1st-order Born approximation.

Method for solving the implicit optimally accurate scheme Write the standard explicit and optimized implicit FD schemes in the same form:

$$\left(\rho \frac{1}{\Delta^2} \tilde{a}_{ij} - M \frac{1}{h^2} \tilde{c}_{ij} \right) \tilde{U}_{ij} = 0 \tag{7.174}$$

$$\left(\rho \frac{1}{\Delta^2} a_{ij} - M \frac{1}{h^2} c_{ij} \right) U_{ij} = 0 \tag{7.175}$$

Grid displacements $\tilde{U}_{ij}$ and U_{ij} have the same structure as u_{ij} in Eq. (7.163). It is reasonable to use an easy-to-calculate explicit scheme for obtaining the predictor value. Consider

$$\delta a_{ij} \equiv a_{ij} - \tilde{a}_{ij}, \quad \delta c_{ij} \equiv c_{ij} - \tilde{c}_{ij}, \quad \delta U_{ij} \equiv U_{ij} - \tilde{U}_{ij} \tag{7.176}$$

Substituting relations (7.176) in Eq. (7.175) and applying the 1$^{\text{st}}$-order Born approximation we obtain

$$\left(\rho \frac{1}{\Delta^2} \tilde{a}_{ij} - M \frac{1}{h^2} \tilde{c}_{ij} \right) \delta U_{ij} = - \left(\rho \frac{1}{\Delta^2} \delta a_{ij} - M \frac{1}{h^2} \delta c_{ij} \right) \tilde{U}_{ij} \tag{7.177}$$

Predictor-corrector algorithm for solving the implicit scheme (7.175)

(1) Find $\tilde{U}_I^{m+1}$ (that is $\tilde{U}_{12}$ – see Eq. (7.163)) by solving the explicit scheme (7.174). Apply to all spatial positions.
(2) Evaluate the r.h.s. of Eq. (7.177).
(3) Solve Eq. (7.177) assuming δU at time levels $m - 1$ and m equal to zero. Then it is easy to obtain δU_I^{m+1}, that is δU_{12}.
(4) $U_I^{m+1} (\equiv U_{12}) = \tilde{U}_I^{m+1} + \delta U_I^{m+1}$.
(5) The value of U_I^{m+1} is assigned to variable $\tilde{U}_I^{m+1}$.
(6) $m + 1 \rightarrow m, m \rightarrow m - 1$, continue with step 1.

Concluding remark Kristek and Moczo (2006) performed a detailed comparison of the 1D (2,2) displacement conventional-grid scheme, the optimized scheme and the (2,4) displacement–stress staggered-grid scheme (the next section) for a homogeneous space, a contact of two halfspaces and an interior layer with velocity gradient. They demonstrated superior accuracy of the optimized scheme with respect to the two other schemes.

7.3.5 (2,4) and (4,4) velocity–stress schemes on a staggered grid

We now return to the VS formulation on a staggered grid (SG) and try to find approximations more accurate than those of the (2,2) scheme. Consider the SG illustrated in Fig. 7.10 and recall Eq. (7.151) for the VS formulation:

$$EQv \equiv \frac{\partial v}{\partial t} - b \frac{\partial \sigma}{\partial x} - bf, \quad EQv = 0$$
$$EQ\sigma \equiv \frac{\partial \sigma}{\partial t} - M \frac{\partial v}{\partial x}, \quad EQ\sigma = 0 \tag{7.178}$$

Here we included the body force f for a reason that will become clear later. From the difference of Taylor expansions of $v_I^{m+1/2}$ and $v_I^{m-1/2}$ about v_I^m we obtain

$$v_I^{m+1/2} = v_I^{m-1/2} + \Delta \left. \frac{\partial v}{\partial t} \right|_I^m + \frac{1}{24} \Delta^3 \left. \frac{\partial^3 v}{\partial t^3} \right|_I^m + O(\Delta^5) \tag{7.179}$$

Similarly, from Taylor expansions of $\sigma_{I-1/2}^{m}$ and $\sigma_{I-1/2}^{m-1}$ about $\sigma_{I-1/2}^{m-1/2}$,

$$\sigma_{I-1/2}^{m} = \sigma_{I-1/2}^{m-1} + \Delta \left.\frac{\partial \sigma}{\partial t}\right|_{I-1/2}^{m-1/2} + \frac{1}{24}\Delta^3 \left.\frac{\partial^3 \sigma}{\partial t^3}\right|_{I-1/2}^{m-1/2} + O(\Delta^5) \qquad (7.180)$$

Then EQv and $EQ\sigma$ may be expressed as

$$EQv|_I^m$$

$$= \frac{1}{\Delta}\left(v_I^{m+1/2} - v_I^{m-1/2}\right) - \frac{1}{24}\Delta^2 \left.\frac{\partial^3 v}{\partial t^3}\right|_I^m + O(\Delta^4) - b\left.\frac{\partial \sigma}{\partial x}\right|_I^m - b\,f|_I^m \qquad (7.181)$$

$$EQ\sigma|_{I-1/2}^{m-1/2}$$

$$= \frac{1}{\Delta}\left(\sigma_{I-1/2}^{m} - \sigma_{I-1/2}^{m-1}\right) - \frac{1}{24}\Delta^2 \left.\frac{\partial^3 \sigma}{\partial t^3}\right|_{I-1/2}^{m-1/2} + O(\Delta^4) - M\left.\frac{\partial v}{\partial x}\right|_{I-1/2}^{m-1/2} \qquad (7.182)$$

We have two possibilities: if we drop the terms with the 3rd temporal derivative in both equations we can obtain only 2nd-order accuracy in time; if we keep the terms we can obtain 4th-order accuracy. We will explore both possibilities.

7.3.5.1 (2,4) VS SG scheme

Consider first the simpler case:

$$EQv|_I^m = \frac{1}{\Delta}\left(v_I^{m+1/2} - v_I^{m-1/2}\right) + O(\Delta^2) - b\left.\frac{\partial \sigma}{\partial x}\right|_I^m - b\,f|_I^m \qquad (7.183)$$

$$EQ\sigma|_{I-1/2}^{m-1/2} = \frac{1}{\Delta}\left(\sigma_{I-1/2}^{m} - \sigma_{I-1/2}^{m-1}\right) + O(\Delta^2) - M\left.\frac{\partial v}{\partial x}\right|_{I-1/2}^{m-1/2} \qquad (7.184)$$

The approximation of the spatial derivatives with 2nd-order accuracy (and omitting the body-force term) would give Eqs. (7.152) and eventually the (2,2) scheme (7.153). The spatial derivatives can, however, be approximated with 4th-order accuracy. Then the approximations of $EQ\sigma$ and EQv are

$$
\begin{aligned}
FDEQv|_I^m &= \frac{1}{\Delta}\left(v_I^{m+1/2} - v_I^{m-1/2}\right) \\
&\quad - b_I\frac{1}{h}\left[\frac{9}{8}\left(\sigma_{I+1/2}^{m} - \sigma_{I-1/2}^{m}\right) - \frac{1}{24}\left(\sigma_{I+3/2}^{m} - \sigma_{I-3/2}^{m}\right)\right] - b\,f|_I^m \\
FDEQ\sigma|_{I-1/2}^{m-1/2} &= \frac{1}{\Delta}\left(\sigma_{I-1/2}^{m} - \sigma_{I-1/2}^{m-1}\right) \\
&\quad - M_{I-1/2}\frac{1}{h}\left[\frac{9}{8}\left(v_I^{m-1/2} - v_{I-1}^{m-1/2}\right) - \frac{1}{24}\left(v_{I+1}^{m-1/2} - v_{I-2}^{m-1/2}\right)\right]
\end{aligned}
\qquad (7.185)
$$

The approximations lead to the explicit (2,4) VS scheme on the SG:

$$V_I^{m+1/2} = V_I^{m-1/2} + b_I \frac{\Delta}{h} \left[\tfrac{9}{8} \left(T_{I+1/2}^m - T_{I-1/2}^m \right) - \tfrac{1}{24} \left(T_{I+3/2}^m - T_{I-3/2}^m \right) \right] + \Delta b \, f|_I^m$$

$$T_{I-1/2}^m = T_{I-1/2}^{m-1} + M_{I-1/2} \frac{\Delta}{h} \left[\tfrac{9}{8} \left(V_I^{m-1/2} - V_{I-1}^{m-1/2} \right) - \tfrac{1}{24} \left(V_{I+1}^{m-1/2} - V_{I-2}^{m-1/2} \right) \right]$$

$$(7.186)$$

We compare both schemes later – after we introduce the (4,4) schemes. A simple FD code based on the scheme, with a detailed guide and numerical examples, can be found in the introductory course by Moczo *et al*. (2004b).

7.3.5.2 (4,4) VS SG schemes

If we want to have 4$^{\text{th}}$-order accuracy also in time we have to also approximate terms with the 3$^{\text{rd}}$ temporal derivative in Eqs. (7.182) and (7.181). It is clear that directly approximating the 3$^{\text{rd}}$ temporal derivative would undesirably increase the number of time levels in the scheme and thus also the requirements on computer memory. Moreover, the absolute value of the weight coefficient of the most advanced time level would be considerably smaller than those for the time levels closer to the time at which the derivative is approximated. Consequently, the corresponding explicit formula for the most advanced time level might be numerically inaccurate.

We may recall the Lax–Wendroff idea (Lax and Wendroff 1960; see Subsection 7.3.6) to replace the 1$^{\text{st}}$ temporal derivative by the 1$^{\text{st}}$ spatial derivative. In this case, however, we replace the 3$^{\text{rd}}$ temporal derivative by an adequate spatial derivative. In order to find relations between them, recall Eqs. (7.178) and write

$$\frac{\partial v}{\partial t} = b \frac{\partial \sigma}{\partial x} + bf, \quad \frac{\partial \sigma}{\partial t} = M \frac{\partial v}{\partial x} \tag{7.187}$$

We easily find

$$\frac{\partial^3 v}{\partial t^3} = b \frac{\partial}{\partial x} \left[M \frac{\partial}{\partial x} \left(b \frac{\partial \sigma}{\partial x} \right) \right] + b \frac{\partial}{\partial x} \left[M \frac{\partial}{\partial x} (bf) \right] + b \frac{\partial^2 f}{\partial t^2}$$

$$\frac{\partial^3 \sigma}{\partial t^3} = M \frac{\partial}{\partial x} \left[b \frac{\partial}{\partial x} \left(M \frac{\partial v}{\partial x} \right) \right] + M \frac{\partial}{\partial x} \left(b \frac{\partial f}{\partial t} \right)$$

$$(7.188)$$

It is obvious that the relations are considerably complicated by the body-force term. Define auxiliary functions:

$$\tilde{v} \equiv b \frac{\partial \sigma}{\partial x}, \quad \tilde{\sigma} \equiv M \frac{\partial \tilde{v}}{\partial x}, \quad \tilde{\tilde{v}} \equiv b \frac{\partial \tilde{\sigma}}{\partial x} \tag{7.189}$$

$$\tilde{\sigma} \equiv M \frac{\partial v}{\partial x}, \quad \tilde{v} \equiv b \frac{\partial \tilde{\sigma}}{\partial x}, \quad \tilde{\tilde{\sigma}} \equiv M \frac{\partial \tilde{\tilde{v}}}{\partial x} \tag{7.190}$$

The 3$^{\text{rd}}$ temporal derivatives (7.188) are then

$$
\begin{aligned}
\frac{\partial^3 v}{\partial t^3} &= \tilde{\tilde{\tilde{v}}} + b\frac{\partial}{\partial x}\left[M\frac{\partial}{\partial x}(bf) \right] + b\frac{\partial^2 f}{\partial t^2} \equiv \tilde{\tilde{\tilde{v}}} + f_v \\
\frac{\partial^3 \sigma}{\partial t^3} &= \tilde{\tilde{\tilde{\sigma}}} + M\frac{\partial}{\partial x}\left(b\frac{\partial f}{\partial t} \right) \equiv \tilde{\tilde{\tilde{\sigma}}} + f_\sigma
\end{aligned}
\tag{7.191}
$$

where we denoted terms with derivatives of the body force by f_v and f_σ. Equations (7.181) and (7.182) then become, omitting the O symbol,

$$
EQv|_I^m = \frac{1}{\Delta}\left(v_I^{m+1/2} - v_I^{m-1/2} \right) - \tfrac{1}{24}\Delta^2 \tilde{\tilde{\tilde{v}}}_I^m - \tilde{v}_I^m - \tfrac{1}{24}\Delta^2\, f_v|_I^m - b\, f|_I^m \tag{7.192}
$$

$$
EQ\sigma|_{I-1/2}^{m-1/2} = \frac{1}{\Delta}\left(\sigma_{I-1/2}^m - \sigma_{I-1/2}^{m-1} \right) - \tfrac{1}{24}\Delta^2 \tilde{\tilde{\tilde{\sigma}}}_{I-1/2}^{m-1/2} - \tilde{\sigma}_{I-1/2}^{m-1/2} - \tfrac{1}{24}\Delta^2\, f_\sigma|_{I-1/2}^{m-1/2} \tag{7.193}
$$

The 4$^{\text{th}}$-order approximation should be applied to calculate $\tilde{\sigma}$ and $\tilde{v}$:

$$
\begin{aligned}
\tilde{v}_I^m &= b_I \frac{1}{h}\left[\tfrac{9}{8}\left(\sigma_{I+1/2}^m - \sigma_{I-1/2}^m \right) - \tfrac{1}{24}\left(\sigma_{I+3/2}^m - \sigma_{I-3/2}^m \right) \right] \\
\tilde{\sigma}_{I-1/2}^{m-1/2} &= M_{I-1/2}\frac{1}{h}\left[\tfrac{9}{8}\left(v_I^{m-1/2} - v_{I-1}^{m-1/2} \right) - \tfrac{1}{24}\left(v_{I+1}^{m-1/2} - v_{I-2}^{m-1/2} \right) \right]
\end{aligned}
\tag{7.194}
$$

We can continue with one of three options to obtain $\tilde{\tilde{v}}$ and $\tilde{\tilde{\sigma}}$: (a) we consistently apply the 4$^{\text{th}}$-order approximation to calculate each of the 1$^{\text{st}}$ spatial derivatives in Eqs. (7.189) and (7.190); (b) we apply the 4$^{\text{th}}$-order approximation to calculate $\tilde{v}$ and $\tilde{\sigma}$, and then the 2$^{\text{nd}}$-order approximation to obtain the remaining quantities in Eqs. (7.189) and (7.190); (c) we consistently apply the 2$^{\text{nd}}$-order approximation to calculate each of the 1$^{\text{st}}$ spatial derivatives in Eqs. (7.189) and (7.190). The last two options are possible because terms with $\tilde{\tilde{v}}$ and $\tilde{\tilde{\sigma}}$ in Eqs. (7.192) and (7.193) are proportional to Δ^2. Correspondingly, we may refer to the three schemes as the (4,4a), (4,4b) and (4,4c) schemes. This will be clear from the truncation errors.

7.3.5.3 Comparison of the (2,2), (2,4) and (4,4) VS SG schemes

The question is, how do the (2,2), (2,4), (4,4a), (4,4b) and (4,4c) VS SG schemes compare to each other in terms of accuracy and computational efficiency? Consider for simplicity a homogeneous medium.

In the homogeneous medium and without the body-force term, Eqs. (7.192) and (7.193) considerably simplify and we obtain

$$
\frac{1}{\Delta}\left(v_I^{m+1/2} - v_I^{m-1/2} \right) = \frac{1}{24}\Delta^2 b^2 M\left.\frac{\partial^3 \sigma}{\partial x^3}\right|_I^m + b\left.\frac{\partial \sigma}{\partial x}\right|_I^m \tag{7.195}
$$

$$
\frac{1}{\Delta}\left(\sigma_{I-1/2}^m - \sigma_{I-1/2}^{m-1} \right) = \frac{1}{24}\Delta^2 b M^2\left.\frac{\partial^3 v}{\partial x^3}\right|_{I-1/2}^{m-1/2} + M\left.\frac{\partial v}{\partial x}\right|_{I-1/2}^{m-1/2} \tag{7.196}
$$

Table 7.3 *Summary of the VS SG schemes and applied approximations of the spatial derivatives*

VS SG Scheme	Approximation of $\frac{\partial \Phi}{\partial x}$	Approximation of $\frac{\partial^3 \Phi}{\partial x^3}$	The number of grid points used for approximating $\frac{\partial^3 \Phi}{\partial x^3}$ (the extent of the stencil)
(2,2)	$D_x^{(1-2)}$	not applicable	not applicable
(2,4)			
(4,4a)	$D_x^{(1-4)}$	$D_x^{(1-4)} \circ D_x^{(1-4)} \circ D_x^{(1-4)}$	10
(4,4b)		$D_x^{(1-2)} \circ D_x^{(1-2)} \circ D_x^{(1-4)}$	6
(4,4c)		$D_x^{(1-2)} \circ D_x^{(1-2)} \circ D_x^{(1-2)}$	4

Denote the 2nd-order and 4th-order approximations of the first spatial derivative:

$$D_x^{(1-2)}\Phi_I^m \equiv \frac{1}{h}\left(\Phi_{I+1/2}^m - \Phi_{I-1/2}^m\right) \tag{7.197}$$

$$D_x^{(1-4)}\Phi_I^m \equiv \frac{1}{h}\left[\frac{9}{8}\left(\Phi_{I+1/2}^m - \Phi_{I-1/2}^m\right) - \frac{1}{24}\left(\Phi_{I+3/2}^m - \Phi_{I-3/2}^m\right)\right] \tag{7.198}$$

Φ_I^m denotes either v_I^m or σ_I^m. The schemes and applied approximations are summarized in Table 7.3. Symbol $\circ$ denotes the convolution, see Subsection 6.2.2.

Truncation errors The leading terms of the truncation errors of the approximations of equations for particle velocity (*EQv*) for a homogeneous medium are

$$
\begin{array}{ll}
(2, 2) & \dfrac{1}{24}\dfrac{\partial^3 v}{\partial t^3}\Delta^2 - \dfrac{1}{24}b\dfrac{\partial^3 \sigma}{\partial x^3}h^2 \\[2mm]
(2, 4) & \dfrac{1}{24}\dfrac{\partial^3 v}{\partial t^3}\Delta^2 + \dfrac{3}{640}b\dfrac{\partial^5 \sigma}{\partial x^5}h^4 \\[2mm]
(4, 4a) & \dfrac{1}{1920}\dfrac{\partial^5 v}{\partial t^5}\Delta^4 + \dfrac{3}{640}b\dfrac{\partial^5 \sigma}{\partial x^5}h^4 \\[2mm]
(4, 4b) & \dfrac{1}{1920}\dfrac{\partial^5 v}{\partial t^5}\Delta^4 - \dfrac{1}{288}b^2 M\dfrac{\partial^5 \sigma}{\partial x^5}h^2\Delta^2 + \dfrac{3}{640}b\dfrac{\partial^5 \sigma}{\partial x^5}h^4 \\[2mm]
(4, 4c) & \dfrac{1}{1920}\dfrac{\partial^5 v}{\partial t^5}\Delta^4 - \dfrac{1}{192}b^2 M\dfrac{\partial^5 \sigma}{\partial x^5}h^2\Delta^2 + \dfrac{3}{640}b\dfrac{\partial^5 \sigma}{\partial x^5}h^4
\end{array}
\tag{7.199}
$$

The leading terms of the truncation errors for stress are analogous. Comparison of the leading terms for the (2,2) and (2,4) schemes shows the significant effect of the 4th-order approximation of the spatial derivative. Similarly, comparison for the (2,4) and (4,4) schemes shows the effect of the 4th-order approximation of the temporal derivative. The second terms in the errors for the (4,4b) and (4,4c) schemes are due to the 2nd-order approximations applied to $\tilde{\tilde{\sigma}}$ and $\tilde{v}$, and their spatial derivatives. Both schemes can be considered (4,4) schemes because Δ is proportional to h and thus product $h^2\Delta^2$ means 4th-order accuracy.

Although the leading terms of the truncation errors suggest that the (4,4a) scheme might be more accurate than the other schemes, it is necessary to check the accuracy of the schemes in terms of grid dispersion.

Grid dispersion Assume

$$\Phi_I^m = A^\Phi \exp\left[i\left(\tilde{\omega}m\Delta - \tilde{k}Ih\right)\right] \tag{7.200}$$

Then,

$$D_x^{(1-2)}\Phi_I^m = -i\frac{2}{h}\sin\left(\tfrac{1}{2}\tilde{k}h\right)\Phi_I^m \equiv \mathcal{D}_x^{(1-2)} \cdot \Phi_I^m \tag{7.201}$$

$$D_x^{(1-4)}\Phi_I^m = -i\frac{2}{h}\left[\tfrac{9}{8}\sin\left(\tfrac{1}{2}\tilde{k}h\right) - \tfrac{1}{24}\sin\left(\tfrac{3}{2}\tilde{k}h\right)\right]\Phi_I^m \equiv \mathcal{D}_x^{(1-4)} \cdot \Phi_I^m \tag{7.202}$$

With reference to Subsection 6.2.3, note that, for example, $D_x^{(1-2)}\Phi_I^m$ means the application of the $D_x^{(1-2)}$ approximation operator to quantity Φ_I^m, whereas $\mathcal{D}_x^{(1-2)} \cdot \Phi_I^m$ means a simple multiplication (indicated by a dot). It follows from Eq. (6.45) that for Φ_I^m given by Eq. (7.200)

$$D_x^{(1-4)} \circ D_x^{(1-4)} \circ D_x^{(1-4)}\Phi_I^m = \left[\mathcal{D}_x^{(1-4)}\right]^3 \cdot \Phi_I^m$$

$$D_x^{(1-2)} \circ D_x^{(1-2)} \circ D_x^{(1-4)}\Phi_I^m = \left[\mathcal{D}_x^{(1-2)}\right]^2 \mathcal{D}_x^{(1-4)} \cdot \Phi_I^m \tag{7.203}$$

$$D_x^{(1-2)} \circ D_x^{(1-2)} \circ D_x^{(1-2)}\Phi_I^m = \left[\mathcal{D}_x^{(1-2)}\right]^3 \cdot \Phi_I^m$$

It will be useful to introduce symbols S_2 and S_4,

$$S_2 = \sin\left(\tfrac{1}{2}\tilde{k}h\right), \quad S_4 = \tfrac{9}{8}\sin\left(\tfrac{1}{2}\tilde{k}h\right) - \tfrac{1}{24}\sin\left(\tfrac{3}{2}\tilde{k}h\right) \tag{7.204}$$

so that

$$\mathcal{D}_x^{(1-2)} = -i\frac{2}{h}S_2, \quad \mathcal{D}_x^{(1-4)} = -i\frac{2}{h}S_4 \tag{7.205}$$

For the l.h.s. of Eqs. (7.195) and (7.196) we obtain

$$\frac{1}{\Delta}\left(v_I^{m+1/2} - v_I^{m-1/2}\right) = i\frac{2}{\Delta}\sin\left(\tfrac{1}{2}\tilde{\omega}\Delta\right)v_I^m \tag{7.206}$$

$$\frac{1}{\Delta}\left(\sigma_{I-1/2}^m - \sigma_{I-1/2}^{m-1}\right) = i\frac{2}{\Delta}\sin\left(\tfrac{1}{2}\tilde{\omega}\Delta\right)\sigma_{I-1/2}^{m-1/2} \tag{7.207}$$

It will also be useful to introduce symbol S_ω:

$$S_\omega = \sin\left(\tfrac{1}{2}\tilde{\omega}\Delta\right) \tag{7.208}$$

We are now ready to derive grid-dispersion relations for the schemes listed in Table 7.3. Here we explicitly show only the derivation for the (4,4b) scheme because it incorporates

Table 7.4 *Dispersion relations for the
VS SG schemes*

Scheme	Dispersion relation	
(2,2)	$\sin^2\left(\frac{1}{2}\tilde{\omega}\Delta\right) =$	$S^2 S_2^2$
(2,4)		$S^2 S_4^2$
(4,4a)		$S^2 S_4^2 \left(1 - \frac{1}{6} S^2 S_4^2\right)^2$
(4,4b)		$S^2 S_4^2 \left(1 - \frac{1}{6} S^2 S_2^2\right)^2$
(4,4c)		$S^2 \left(S_4 - \frac{1}{6} S^2 S_2^3\right)^2$

both the $D_x^{(1-2)}$ and $D_x^{(1-4)}$ approximations. Equations (7.195) and (7.196) may be written as

$$i\frac{2}{\Delta} S_\omega v_I^m = \frac{1}{24}\Delta^2 b^2 M \left(-i\frac{2}{h}S_2\right)^2 \left(-i\frac{2}{h}S_4\right)\sigma_I^m + b\left(-i\frac{2}{h}S_4\right)\sigma_I^m \quad (7.209)$$

$$i\frac{2}{\Delta} S_\omega \sigma_{I-1/2}^{m-1/2} = \frac{1}{24}\Delta^2 b M^2 \left(-i\frac{2}{h}S_2\right)^2 \left(-i\frac{2}{h}S_4\right) v_{I-1/2}^{m-1/2} + M\left(-i\frac{2}{h}S_4\right) v_{I-1/2}^{m-1/2}$$
$$(7.210)$$

After rearrangement:

$$-S_\omega v_I^m = \frac{\Delta}{h} b S_4 \left(1 - \frac{1}{6}S^2 S_2^2\right)\sigma_I^m \quad (7.211)$$

$$-S_\omega \sigma_{I-1/2}^{m-1/2} = \frac{\Delta}{h} M S_4 \left(1 - \frac{1}{6}S^2 S_2^2\right) v_{I-1/2}^{m-1/2} \quad (7.212)$$

where, see Eqs. (7.28) and (7.69), S is the Courant number:

$$S = \frac{\Delta}{h}\sqrt{bM} = \frac{\Delta}{h}c \quad (7.213)$$

Substituting m and I for $m - 1/2$ and $I - 1/2$, respectively, in Eq. (7.212), we obtain

$$-S_\omega \sigma_I^m = \frac{\Delta}{h} M S_4 \left(1 - \frac{1}{6}S^2 S_2^2\right) v_I^m \quad (7.214)$$

Multiplying the l.h.s./r.h.s. of Eq. (7.211) by the l.h.s./r.h.s. of Eq. (7.214), respectively, we obtain

$$S_\omega^2 = S^2 S_4^2 \left(1 - \frac{1}{6}S^2 S_2^2\right)^2 \quad (7.215)$$

Equation (7.215) is the grid-dispersion relation for scheme (4,4b). Similarly, we obtain relations for the other schemes listed in Table 7.3. All are summarized in Table 7.4.

r.h.s. of the dispersion relation
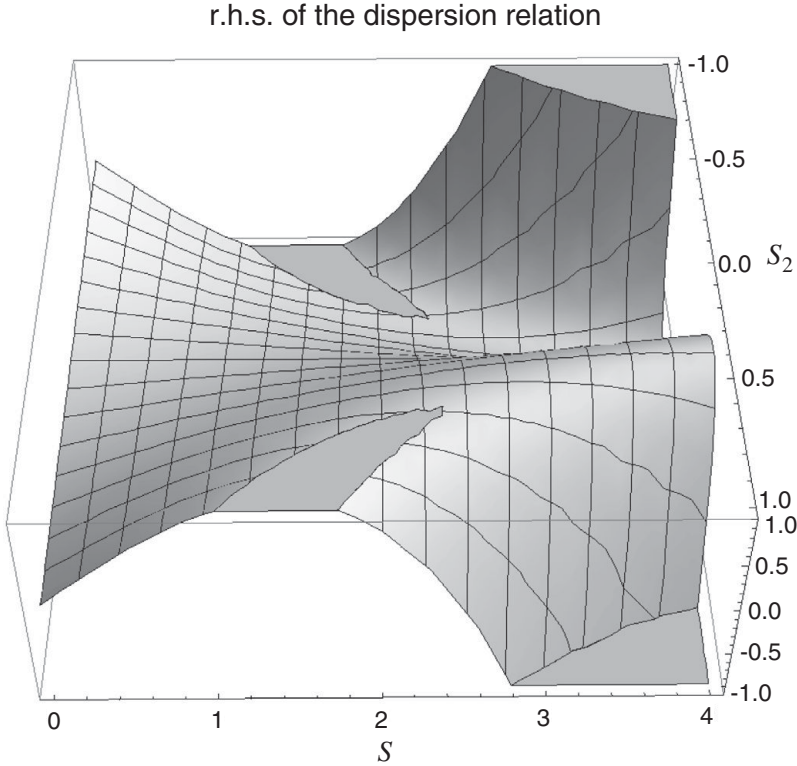
Figure 7.12 Plot of the r.h.s. of the dispersion relation Eq. (7.216) for $-1 \leq S_2 \leq 1$ and $0 \leq S \leq 4$.

Stability conditions In Subsection 7.2.4 we investigated the stability of scheme (7.21) and found the stability condition $S \leq S_M = 1$; see Eqs. (7.61)–(7.70). Here we can use the obtained dispersion relations for finding stability conditions for the investigated VS SG schemes. Consider again the (4,4b) scheme. Equation (7.215) implies, after algebraic manipulations,

$$\sin\left(\tfrac{1}{2}\tilde{\omega}\Delta\right) = \tfrac{1}{36} S S_2 \left(6 + S_2^2\right)\left(6 - S^2 S_2^2\right) \tag{7.216}$$

An important feature of Eq. (7.216) is that the sine function on the r.h.s. appears only with one argument $\tfrac{1}{2}\tilde{k}h$. Figure 7.12 shows a plot of the r.h.s. of Eq. (7.216) for $-1 \leq S_2 \leq 1$ and $0 \leq S \leq 4$. We want to find the minimum value of S above which the l.h.s. of Eq. (7.216) falls outside interval $[-1, 1]$. It is clear from Fig. 7.12 that the value sought, S_M, is obtained from Eq. (7.216) for $S_2 = 1$ or $S_2 = -1$. In both cases we obtain $S_M = 1.05018$. The conclusion for the (4,4b) scheme is that the scheme is stable if

$$S \leq S_M = 1.05018 \tag{7.217}$$

Table 7.5 *Modified dispersion relations and maximum values S_M of Courant number S for the VS SG schemes*

Scheme	Modified dispersion relation		S_M
(2,2)	$\sin\left(\frac{1}{2}\tilde{\omega}\Delta\right) =$	$S\,S_2$	1.0
(2,4)		$6^{-1}\,S\,S_2\left(6 + S_2^2\right)$	$\frac{6}{7} \approx 0.857143$
(4,4a)		$6^{-4}\,S\,S_2\left(6 + S_2^2\right)\left[6^3 - S^2 S_2^2 (6 + S_2^2)^2\right]$	2.44056
(4,4b)		$6^{-2}\,S\,S_2\left(6 + S_2^2\right)\left(6 - S^2 S_2^2\right)$	1.05018
(4,4c)		$6^{-1}\,S\,S_2\left(6 + S_2^2 - S^2 S_2^2\right)$	1.0

or, equivalently,

$$\Delta \leq \frac{h}{c} S_M = 1.05018\frac{h}{c} \tag{7.218}$$

Analogously, we can analyze the other schemes listed in Table 7.3. The modified dispersion relations and S_M values are given in Table 7.5.

The stability conditions for the (2,2) and (2,4) schemes are very well known. The S_M value for the (4,4c) scheme appears reasonable. The S_M values for the (4,4a) and (4,4b) schemes may be surprising because they are larger than 1. This is a consequence of the larger stencil – the larger number of grid points used for approximating the 3$^\text{rd}$ spatial derivative.

At this point we recommend additional reading on the analysis of stability and the Courant–Friedrichs–Lewy condition in mathematical books such as those by Strikwerda (2004) and LeVeque (2007).

Normalized grid phase velocity Any of the grid-dispersion relations in Table 7.5 may be written as

$$\sin\left(\tfrac{1}{2}\tilde{\omega}\Delta\right) = \Psi(S, \tilde{k}h) \tag{7.219}$$

from which we have

$$\tilde{\omega} = \frac{2}{\Delta}\arcsin\Psi(S, \tilde{k}h) \tag{7.220}$$

Assume $\tilde{k} = k$, that is a grid wave with a true physical wavelength. The grid phase velocity, Eq. (7.19), is

$$\tilde{v} = \frac{\tilde{\omega}_\text{real}}{k} = \frac{2}{k\Delta}\arcsin\Psi(S, kh) \tag{7.221}$$

The normalized grid phase velocity is then

$$\frac{\tilde{v}}{c} = \frac{2}{ck\Delta}\arcsin\Psi(S, kh) \tag{7.222}$$

Table 7.6 *Relations for the grid phase velocity in the VS SG schemes*

Scheme	Normalized grid phase velocity $\frac{\tilde{v}}{c}$	Ψ
(2,2)		$S\,S_2$
(2,4)		$6^{-1}\,S\,S_2\left(6+S_2^2\right)$
(4,4a)	$\dfrac{N_\lambda}{\pi p S_M}\,\arcsin\Psi$	$6^{-4}\,S\,S_2\left(6+S_2^2\right)\left[6^3-S^2S_2^2(6+S_2^2)^2\right]$
(4,4b)		$6^{-2}\,S\,S_2\left(6+S_2^2\right)\left(6-S^2S_2^2\right)$
(4,4c)		$6^{-1}\,S\,S_2\left(6+S_2^2-S^2S_2^2\right)$
$S\;=\;p\,S_M$		$S_2\;=\;\sin\left(\pi\,/\,N_\lambda\right)$

Recall Eqs. (7.63) and (7.66) for Courant number S, time step Δ and stability ratio p:

$$S \le S_M, \quad \Delta = p\frac{h}{c}S_M \tag{7.223}$$

Considering the definition of Courant number S we have

$$S = pS_M; \quad 0 < p \le 1 \tag{7.224}$$

Recall also the definition of the spatial sampling ratio N_λ, Eq. (7.34),

$$N_\lambda = \frac{\lambda}{h} \tag{7.225}$$

Then,

$$\frac{2}{ck\Delta} = \frac{2\lambda c}{c2\pi phS_M} = \frac{N_\lambda}{\pi pS_M}, \quad kh = \frac{2\pi}{\lambda}h = \frac{2\pi}{N_\lambda} \tag{7.226}$$

$$\frac{\tilde{v}}{c} = \frac{N_\lambda}{\pi pS_M}\arcsin\Psi\,(pS_M, N_\lambda) \tag{7.227}$$

Relations for the grid phase velocities are summarized in Table 7.6.

Although the stability condition found for the (4,4a) scheme formally admits values of Courant number $S \le S_M = 2.44056$, the normalized grid phase velocity for, approximately, $p > 0.4$ and $N_\lambda < 6$ falls steeply below 1. The fraction $p = 0.4$ of $S_M = 2.44056$ approximately corresponds to $S = 1$. Therefore, we further consider $S_M = 1$ for all investigated VS SG schemes except the (2,4) scheme for which $S \le S_M = 6/7 \approx 0.857143$. Figure 7.13 shows the normalized grid phase velocities for all schemes for the spatial sampling ratio $2 \le N_\lambda \le 15$ and four values of the stability ratio $p = 0.9, 0.5, 0.2, 0.1$. For $p = 0.9$ the time step is equal to 90% of its maximum value. Consider a homogeneous medium. An adequate choice then is, e.g., $p = 0.9$. It is clear from Fig. 7.13 that the grid phase velocity $\tilde{v}$ of the optimized (4,4) schemes is closer to the true physical value c than the grid velocities of the (2,2) and (2,4) schemes for, approximately, $N_\lambda > 5$. The best of the (4,4) schemes
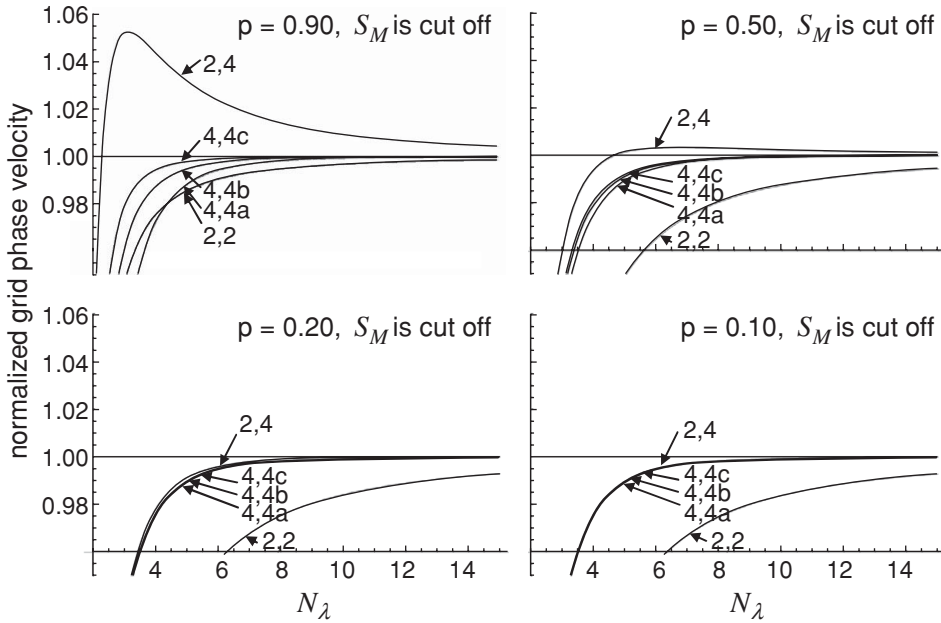
Figure 7.13 Normalized grid phase velocities $\tilde{v}/c$ for the (2,2), (2,4), (4,4a), (4,4b) and (4,4c) velocity–stress staggered-grid schemes. N_λ is the spatial sampling ratio, p is the stability ratio (fraction of the maximum possible/admitted time step). The maximum value of Courant number S is set equal to 1 except in the (2,4) scheme for which it is 6/7.

is the (4,4c) scheme. The partial conclusion is that the optimization has a positive effect – it reduces the grid dispersion compared to the schemes that are only 2nd-order accurate in time.

Consider, however, a heterogeneous medium covered with a uniform spatial grid. Assume, for instance, that the S-wave speed in the surface sediments is twice smaller than the S-wave speed beneath the sediments. For a fixed value of the grid spacing h, the maximum possible time step Δ is given by the stability condition $S \leq S_M$. The Courant number for the sediments is, however, twice smaller than the Courant number for the medium beneath the sediments. Consequently, the time step applied to sediments is twice smaller than that required by the stability condition only for sediments. This means that if $p = 0.9$ in the medium beneath sediments, $p = 0.45$ in sediments. We see that the dispersion curves of the (4,4) schemes for $p = 0.5$ are very close to each other, significantly better than the curve of the (2,2) scheme, and better than the curve of the (2,4) scheme for, approximately, $N_\lambda > 6$. In many realistic models of surface sedimentary structures, however, the maximum-to-minimum S-wave speed ratio is 5 and even more. This means that if $p = 0.9$ in the medium beneath sediments, $p \leq 0.18$ in sediments. We see that the dispersion curves for the (4,4) schemes are almost the same and very close to the

dispersion curve for the (2,4) scheme. Eventually, the dispersion curves of all schemes that are 4th-order accurate in space are practically the same for small p.

The conclusion is that in the heterogeneous models with maximum-to-minimum S-wave speed ratio larger than 2 the optimized VS SG schemes with 4th-order accuracy in both time and space do not reduce the grid dispersion compared to the (2,4) scheme.

7.3.6 (4,4) velocity–stress schemes on a collocated grid

The velocity–stress formulation can also be used for developing schemes on the collocated grid. Both the particle velocity v and stress σ are assumed at each spatial grid position. Then, instead of treating two equations of the same form, see Eq. (7.9), it is advantageous to recall the matrix formulation, Eqs. (7.10) and (7.11):

$$\mathbf{w} \equiv (v, \sigma)^T, \quad \mathbf{A} \equiv \begin{bmatrix} 0 & b \\ M & 0 \end{bmatrix}, \quad b \equiv \frac{1}{\rho} \tag{7.228}$$

$$\frac{\partial \mathbf{w}}{\partial t} = \mathbf{A} \frac{\partial \mathbf{w}}{\partial x} \tag{7.229}$$

7.3.6.1 Lax–Wendroff and MacCormack schemes

Before we continue with approximating Eq. (7.229), we briefly mention the Lax–Wendroff (1960) and MacCormack (1969, 1971) schemes. Consider for simplicity the 1st-order scalar hyperbolic equation with constant coefficient:

$$\frac{\partial u}{\partial t} = a \frac{\partial u}{\partial x} + f \tag{7.230}$$

Lax-Wendroff scheme Taylor expansion of u_I^{m+1} about u_I^m yields

$$u_I^{m+1} = u_I^m + \Delta \left. \frac{\partial u}{\partial t} \right|_I^m + \frac{1}{2} \Delta^2 \left. \frac{\partial^2 u}{\partial t^2} \right|_I^m + O(\Delta^3) \tag{7.231}$$

Equation (7.230) implies

$$\frac{\partial^2 u}{\partial t^2} = a \frac{\partial^2 u}{\partial t \partial x} + \frac{\partial f}{\partial t} = a^2 \frac{\partial^2 u}{\partial x^2} + a \frac{\partial f}{\partial x} + \frac{\partial f}{\partial t} \tag{7.232}$$

Using Eqs. (7.230) and (7.232) in Eq. (7.231) yields

$$u_I^{m+1} = u_I^m + \Delta\, a \left. \frac{\partial u}{\partial x} \right|_I^m + \frac{1}{2} \Delta^2 a^2 \left. \frac{\partial^2 u}{\partial x^2} \right|_I^m$$

$$+ \Delta\, f_I^m + \frac{1}{2} \Delta^2 a \left. \frac{\partial f}{\partial x} \right|_I^m + \frac{1}{2} \Delta^2 \left. \frac{\partial f}{\partial t} \right|_I^m + O(\Delta^3) \tag{7.233}$$

Replacing the spatial derivatives by the 2nd-order centred approximations and $\frac{\partial f}{\partial t}$ by the forward approximation we obtain the Lax–Wendroff scheme:

$$u_I^{m+1} = u_I^m + \frac{\Delta}{2h} a \left(u_{I+1}^m - u_{I-1}^m \right) + \frac{\Delta^2}{2h^2} a^2 \left(u_{I+1}^m - 2u_I^m + u_{I-1}^m \right)$$

$$+ \frac{\Delta^2}{4h} a \left(f_{I+1}^m - f_{I-1}^m \right) + \frac{\Delta}{2} \left(f_I^{m+1} + f_I^m \right) + O(\Delta^3) + O(h^2 \Delta) \quad (7.234)$$

For stability of the scheme and comparison with other schemes see, e.g., Strikwerda (2004), LeVeque (2007).

MacCormack scheme Consider now the following approximation of Eq. (7.230). First we apply forward approximations of the temporal and spatial derivatives (the latter indicated by operator D_x^F) at time level m and position I:

$$\frac{1}{\Delta} \left(\tilde{u}_I^{m+1} - u_I^m \right) \approx a D_x^F u_I^m + f_I^m \quad (7.235)$$

Because the approximations are one-sided, the value of u at the time level $m+1$ may be considered provisional and therefore denoted by a tilde. Equation (7.235) implies

$$\tilde{u}_I^{m+1} \approx u_I^m + \Delta a D_x^F u_I^m + \Delta f_I^m \quad (7.236)$$

We now approximate Eq. (7.230) in another way. Having the provisional value at $m+1$ we may apply a backward approximation at this time level. In order to obtain spatial symmetry about position I, we may apply a backward approximation at this spatial position:

$$\frac{2}{\Delta} \left(u_I^{m+1} - u_I^{m+1/2} \right) \approx a D_x^B \tilde{u}_I^{m+1} + f_I^{m+1} \quad (7.237)$$

$u_I^{m+1/2}$ may be approximated as

$$u_I^{m+1/2} \approx \tfrac{1}{2} \left(u_I^m + \tilde{u}_I^{m+1} \right) \quad (7.238)$$

Equations (7.237) and (7.238) yield

$$u_I^{m+1} \approx \tfrac{1}{2} \left(u_I^m + \tilde{u}_I^{m+1} + \Delta a D_x^B \tilde{u}_I^{m+1} + \Delta f_I^{m+1} \right) \quad (7.239)$$

Using relations (7.236) and $D_x^B D_x^F u_I^m = D_x^F D_x^B u_I^m$ in the latter equation we obtain

$$u_I^{m+1} \approx u_I^m + \tfrac{1}{2} \Delta a \left(D_x^F u_I^m + D_x^B u_I^m \right) + \tfrac{1}{2} \Delta^2 a^2 D_x^B D_x^F u_I^m$$

$$+ \tfrac{1}{2} \Delta f_I^m + \tfrac{1}{2} \Delta^2 a D_x^B f_I^m + \tfrac{1}{2} \Delta f_I^{m+1} \quad (7.240)$$

Considering

$$D_x^F u_I^m \equiv \frac{1}{h} \left(u_{I+1}^m - u_I^m \right), D_x^B u_I^m \equiv \frac{1}{h} \left(u_I^m - u_{I-1}^m \right), D_x^B f_I^m \equiv \frac{1}{h} \left(f_I^m - f_{I-1}^m \right) \quad (7.241)$$

in Eq. (7.240) we eventually obtain

$$u_I^{m+1} = u_I^m + \frac{\Delta}{2h} a \left(u_{I+1}^m - u_{I-1}^m \right) + \frac{\Delta^2}{2h^2} a^2 \left(u_{I+1}^m - 2u_I^m + u_{I-1}^m \right)$$

$$+ \frac{\Delta}{2} \left(f_I^{m+1} + f_I^m \right) + \frac{\Delta^2}{2h} a \left(f_I^m - f_{I-1}^m \right) + O(\Delta^3) + O(h^2 \Delta) \quad (7.242)$$

Relation between Lax–Wendroff and MacCormack schemes Assuming $f = 0$, relations (7.234) and (7.242) give the same (2,2) scheme.

7.3.6.2 General relations

We return now to Eq. (7.229); for the following analysis we do not include the force term. Denoting

$$EQ\mathbf{w} \equiv \frac{\partial \mathbf{w}}{\partial t} - \mathbf{A} \frac{\partial \mathbf{w}}{\partial x}, \quad EQ\mathbf{w} = 0 \quad (7.243)$$

we can express $EQ\mathbf{w}$ at time level m and spatial position I, for example, using two or three time levels. The first option is indicated by 2TL, the second one by 3TL:

$$\text{2TL}: \quad EQ\mathbf{w}|_I^m = \frac{1}{\Delta} \left(\mathbf{w}_I^{m+1} - \mathbf{w}_I^m \right)$$

$$- \frac{1}{2} \Delta \left. \frac{\partial^2 \mathbf{w}}{\partial t^2} \right|_I^m - \frac{1}{6} \Delta^2 \left. \frac{\partial^3 \mathbf{w}}{\partial t^3} \right|_I^m - \frac{1}{24} \Delta^3 \left. \frac{\partial^4 \mathbf{w}}{\partial t^4} \right|_I^m + O(\Delta^4) - \mathbf{A} \left. \frac{\partial \mathbf{w}}{\partial x} \right|_I^m$$

$$(7.244)$$

$$\text{3TL}: \quad EQ\mathbf{w}|_I^m = \frac{1}{2\Delta} \left(\mathbf{w}_I^{m+1} - \mathbf{w}_I^{m-1} \right)$$

$$- \frac{1}{6} \Delta^2 \left. \frac{\partial^3 \mathbf{w}}{\partial t^3} \right|_I^m + O(\Delta^4) - \mathbf{A} \left. \frac{\partial \mathbf{w}}{\partial x} \right|_I^m \quad (7.245)$$

Replacing the temporal derivatives by spatial derivatives, see Eq. (7.13), we obtain

$$\text{2TL}: \quad EQ\mathbf{w}|_I^m = \frac{1}{\Delta} \left(\mathbf{w}_I^{m+1} - \mathbf{w}_I^m \right)$$

$$- \frac{1}{2} \Delta \left. \mathbf{A} \frac{\partial}{\partial x} \left(\mathbf{A} \frac{\partial \mathbf{w}}{\partial x} \right) \right|_I^m - \frac{1}{6} \Delta^2 \left. \mathbf{A} \frac{\partial}{\partial x} \left[\mathbf{A} \frac{\partial}{\partial x} \left(\mathbf{A} \frac{\partial \mathbf{w}}{\partial x} \right) \right] \right|_I^m$$

$$- \frac{1}{24} \Delta^3 \left. \mathbf{A} \frac{\partial}{\partial x} \left\{ \mathbf{A} \frac{\partial}{\partial x} \left[\mathbf{A} \frac{\partial}{\partial x} \left(\mathbf{A} \frac{\partial \mathbf{w}}{\partial x} \right) \right] \right\} \right|_I^m + O(\Delta^4) - \mathbf{A} \left. \frac{\partial \mathbf{w}}{\partial x} \right|_I^m$$

$$(7.246)$$

$$\text{3TL}: \quad EQ\mathbf{w}|_I^m = \frac{1}{2\Delta} \left(\mathbf{w}_I^{m+1} - \mathbf{w}_I^{m-1} \right)$$

$$- \frac{1}{6} \Delta^2 \left. \mathbf{A} \frac{\partial}{\partial x} \left[\mathbf{A} \frac{\partial}{\partial x} \left(\mathbf{A} \frac{\partial \mathbf{w}}{\partial x} \right) \right] \right|_I^m + O(\Delta^4) - \mathbf{A} \left. \frac{\partial \mathbf{w}}{\partial x} \right|_I^m \quad (7.247)$$

We define auxiliary functions:

$$\tilde{\mathbf{w}} = \mathbf{A}\frac{\partial \mathbf{w}}{\partial x}, \quad \tilde{\tilde{\mathbf{w}}} = \mathbf{A}\frac{\partial \tilde{\mathbf{w}}}{\partial x}, \quad \tilde{\tilde{\tilde{\mathbf{w}}}} = \mathbf{A}\frac{\partial \tilde{\tilde{\mathbf{w}}}}{\partial x}, \quad \tilde{\tilde{\tilde{\tilde{\mathbf{w}}}}} = \mathbf{A}\frac{\partial \tilde{\tilde{\tilde{\mathbf{w}}}}}{\partial x} \tag{7.248}$$

Then we can rewrite Eqs. (7.246) and (7.247) as

$$2\text{TL}: \quad EQ\mathbf{w}|_I^m = \frac{1}{\Delta}\left(\mathbf{w}_I^{m+1} - \mathbf{w}_I^m\right)$$

$$-\frac{1}{2}\Delta\tilde{\tilde{\mathbf{w}}}_I^m - \frac{1}{6}\Delta^2\tilde{\tilde{\tilde{\mathbf{w}}}}_I^m - \frac{1}{24}\Delta^3\tilde{\tilde{\tilde{\tilde{\mathbf{w}}}}}_I^m + O(\Delta^4) - \tilde{\mathbf{w}}_I^m \tag{7.249}$$

$$3\text{TL}: \quad EQ\mathbf{w}|_I^m = \frac{1}{2\Delta}\left(\mathbf{w}_I^{m+1} - \mathbf{w}_I^{m-1}\right)$$

$$-\frac{1}{6}\Delta^2\tilde{\tilde{\tilde{\mathbf{w}}}}_I^m + O(\Delta^4) - \tilde{\mathbf{w}}_I^m \tag{7.250}$$

The corresponding relations for the FD schemes are then

$$2\text{TL}: \quad \mathbf{w}_I^{m+1} = \mathbf{w}_I^m + \frac{1}{2}\Delta^2\tilde{\tilde{\mathbf{w}}}_I^m + \frac{1}{6}\Delta^3\tilde{\tilde{\tilde{\mathbf{w}}}}_I^m + \frac{1}{24}\Delta^4\tilde{\tilde{\tilde{\tilde{\mathbf{w}}}}}_I^m + \Delta\tilde{\mathbf{w}}_I^m \tag{7.251}$$

$$3\text{TL}: \quad \mathbf{w}_I^{m+1} = \mathbf{w}_I^{m-1} + \frac{1}{3}\Delta^3\tilde{\tilde{\tilde{\mathbf{w}}}}_I^m + 2\Delta\tilde{\mathbf{w}}_I^m \tag{7.252}$$

7.3.6.3 Centred approximations

If we want (4,4) accuracy, we have to apply the 4th-order approximation to obtain $\tilde{\mathbf{w}}$ and $\tilde{\tilde{\mathbf{w}}}$. Then we could continue with application of the 2nd-order approximation to obtain $\tilde{\tilde{\tilde{\mathbf{w}}}}$ and $\tilde{\tilde{\tilde{\tilde{\mathbf{w}}}}}$ because terms with these auxiliary functions are proportional to Δ^2 and Δ^3, respectively. The 4th- and 2nd-order approximations are applied also to $\tilde{\tilde{\mathbf{w}}}$ and $\tilde{\tilde{\tilde{\mathbf{w}}}}$, respectively, because the centred approximations are of even order. Here we restrict the discussion to consistent application of the 4th-order approximation to each 1st spatial derivative.

The simplest available centred 4th-order approximation is

$$\mathbf{A}\frac{\partial \varphi}{\partial x}\bigg|_I^m = \mathbf{A}_I\frac{1}{h}\left[\frac{2}{3}\left(\varphi_{I+1}^m - \varphi_{I-1}^m\right) - \frac{1}{12}\left(\varphi_{I+2}^m - \varphi_{I-2}^m\right)\right] \tag{7.253}$$

where φ stands for any of the single- to triple-tilde auxiliary functions. Though easy to obtain, the resulting 2TL scheme is rather lengthy. Therefore, we show here only the 3TL scheme for the homogeneous medium:

$$v_I^{m+1} = v_I^{m-1} + \frac{864}{5184}b\frac{\Delta}{h}\left[8\left(\sigma_{I+1}^m - \sigma_{I-1}^m\right) - \left(\sigma_{I+2}^m - \sigma_{I-2}^m\right)\right]$$

$$+ \frac{1}{5184}b^2M\frac{\Delta^3}{h^3}\left[-1584\left(\sigma_{I+1}^m - \sigma_{I-1}^m\right) + 387\left(\sigma_{I+2}^m - \sigma_{I-2}^m\right) + 488\left(\sigma_{I+3}^m - \sigma_{I-3}^m\right)\right.$$

$$\left.- 192\left(\sigma_{I+4}^m - \sigma_{I-4}^m\right) + 24\left(\sigma_{I+5}^m - \sigma_{I-5}^m\right) - \left(\sigma_{I+6}^m - \sigma_{I-6}^m\right)\right] \tag{7.254}$$

$$\sigma_I^{m+1} = \sigma_I^{m-1} + \frac{864}{5184} M \frac{\Delta}{h} \left[8 \left(v_{I+1}^m - v_{I-1}^m \right) - \left(v_{I+2}^m - v_{I-2}^m \right) \right]$$

$$+ \frac{1}{5184} b M^2 \frac{\Delta^3}{h^3} \left[-1584 \left(v_{I+1}^m - v_{I-1}^m \right) + 387 \left(v_{I+2}^m - v_{I-2}^m \right) + 488 \left(v_{I+3}^m - v_{I-3}^m \right) \right.$$

$$\left. - 192 \left(v_{I+4}^m - v_{I-4}^m \right) + 24 \left(v_{I+5}^m - v_{I-5}^m \right) - \left(v_{I+6}^m - v_{I-6}^m \right) \right] \tag{7.255}$$

We can see an interesting result. v_I^{m+1} depends on v_I^{m-1} and $\sigma_{I\pm k}^m$; $k = 1, \ldots, 6$. σ_I^{m+1} depends on σ_I^{m-1} and $v_{I\pm k}^m$; $k = 1, \ldots, 6$. This means that, although we have both v_I^{m+1} and σ_I^{m+1} at the same space–time grid point, formally v_I^{m+1} does not know about σ_I^{m+1} and vice versa. Moreover, the odd-indexed and even-indexed time levels of the particle velocity are separated (decoupled). The same is true of the stresses. This is known as temporal odd–even decoupling.

In the case of the 2TL scheme, v_I^{m+1} depends on $v_{I\pm k}^m$; $k = 0, \ldots, 8$ and $\sigma_{I\pm k}^m$; $k = 1, \ldots, 6$. Similarly, σ_I^{m+1} depends on $\sigma_{I\pm k}^m$; $k = 0, \ldots, 8$ and $v_{I\pm k}^m$; $k = 1, \ldots, 6$. In other words, contrary to the 3TL scheme, v_I^{m+1} and σ_I^{m+1} are not independent.

Both schemes have, however, one more important property. Consider first the 2TL scheme. Assume the following initial conditions:

$$v_I^0 = 0, \quad \sigma_{2k+1}^0 = \sigma_{ODD}, \quad \sigma_{2k}^0 = \sigma_{EVEN}, \quad k = 0, \pm 1, \pm 2, \ldots \tag{7.256}$$

that is, zero velocity everywhere, σ_{ODD} at the odd-indexed spatial positions and σ_{EVEN} at the even-indexed spatial positions. The 2TL scheme gives

$$v_I^m = 0, \quad \sigma_{2k+1}^m = \sigma_{ODD}, \quad \sigma_{2k}^m = \sigma_{EVEN}, \quad k = 0, \pm 1, \pm 2, \ldots \tag{7.257}$$

The scheme simply reproduces the initial values.

In the case of the 3TL schemes (7.254) and (7.255), we can restrict the treatment to one of the two independent schemes. Assume the following initial conditions:

$$v_I^0 = 0, \quad \sigma_{2k+1}^1 = \sigma_{ODD}, \quad \sigma_{2k}^1 = \sigma_{EVEN}, \quad k = 0, \pm 1, \pm 2, \ldots \tag{7.258}$$

The scheme gives

$$v_I^{2m} = 0, \quad \sigma_{2k+1}^{2m+1} = \sigma_{ODD}, \quad \sigma_{2k}^{2m+1} = \sigma_{EVEN}, \quad k = 0, \pm 1, \pm 2, \ldots \tag{7.259}$$

The scheme reproduces the initial values.

The phenomenon observed in both the 2TL and 3TL schemes is known as spatial odd–even decoupling. The spatial decoupling is due to the application of the centred approximation to the first spatial derivative. Similarly, the temporal decoupling is due to the application of the centred approximation to the first temporal derivative.

The property of odd–even decoupling is general – it arises if the 1st derivatives in the 1st-order hyperbolic equations are replaced by centred approximations on the collocated grids.

7.3.6.4 Noncentred approximations

It is obvious that we can avoid temporal odd–even decoupling by using the 2TL approach, and spatial odd–even decoupling by using a noncentred approximation of the first spatial derivative.

Define the 4$^{\text{th}}$-order forward and backward operators:

$$D_x^F [\varphi_I] \equiv \frac{1}{h} \sum_{j=-1}^{3} c_j \varphi_{I+j}, \quad D_x^B [\varphi_I] \equiv \frac{1}{h} \sum_{j=-1}^{3} -c_j \varphi_{I-j} \tag{7.260}$$

with coefficients

$$c_{-1} = -\frac{1}{4}, c_0 = -\frac{5}{6}, c_1 = \frac{3}{2}, c_2 = -\frac{1}{2}, c_3 = \frac{1}{12} \tag{7.261}$$

Then,

$$\mathbf{A}\frac{\partial \varphi}{\partial x}\bigg|_I^F \approx \mathbf{A}_I D_x^F [\varphi_I], \quad \mathbf{A}\frac{\partial \varphi}{\partial x}\bigg|_I^B \approx \mathbf{A}_I D_x^B [\varphi_I] \tag{7.262}$$

Define auxiliary quantities:

$$\begin{aligned}
{}^F\tilde{\mathbf{w}}_I^m &\equiv \mathbf{A}_I D_x^F \left[\mathbf{w}_I^m\right], & {}^B\tilde{\mathbf{w}}_I^m &\equiv \mathbf{A}_I D_x^B \left[\mathbf{w}_I^m\right] \\
{}^B\tilde{\tilde{\mathbf{w}}}_I^m &\equiv \mathbf{A}_I D_x^B \left[{}^F\tilde{\mathbf{w}}_I^m\right], & {}^F\tilde{\tilde{\mathbf{w}}}_I^m &\equiv \mathbf{A}_I D_x^F \left[{}^B\tilde{\mathbf{w}}_I^m\right] \\
{}^F\tilde{\tilde{\tilde{\mathbf{w}}}}_I^m &\equiv \mathbf{A}_I D_x^F \left[{}^B\tilde{\tilde{\mathbf{w}}}_I^m\right], & {}^B\tilde{\tilde{\tilde{\mathbf{w}}}}_I^m &\equiv \mathbf{A}_I D_x^B \left[{}^F\tilde{\tilde{\mathbf{w}}}_I^m\right] \\
{}^B\tilde{\tilde{\tilde{\tilde{\mathbf{w}}}}}_I^m &\equiv \mathbf{A}_I D_x^B \left[{}^F\tilde{\tilde{\tilde{\mathbf{w}}}}_I^m\right], & {}^F\tilde{\tilde{\tilde{\tilde{\mathbf{w}}}}}_I^m &\equiv \mathbf{A}_I D_x^F \left[{}^B\tilde{\tilde{\tilde{\mathbf{w}}}}_I^m\right]
\end{aligned} \tag{7.263}$$

Equation (7.251) then can be written as

$$\mathbf{w}_I^{m+1} = \mathbf{w}_I^m + \Delta\frac{1}{2}\left({}^F\tilde{\mathbf{w}}_I^m + {}^B\tilde{\mathbf{w}}_I^m\right) + \frac{1}{2}\Delta^2\frac{1}{2}\left({}^B\tilde{\tilde{\mathbf{w}}}_I^m + {}^F\tilde{\tilde{\mathbf{w}}}_I^m\right)$$
$$+ \frac{1}{6}\Delta^3\frac{1}{2}\left({}^F\tilde{\tilde{\tilde{\mathbf{w}}}}_I^m + {}^B\tilde{\tilde{\tilde{\mathbf{w}}}}_I^m\right) + \frac{1}{24}\Delta^4\frac{1}{2}\left({}^B\tilde{\tilde{\tilde{\tilde{\mathbf{w}}}}}_I^m + {}^F\tilde{\tilde{\tilde{\tilde{\mathbf{w}}}}}_I^m\right) \tag{7.264}$$

In the homogeneous medium the resulting scheme for the particle velocity is

$$\begin{aligned}
v_I^{m+1} = v_I^m &+ \frac{1}{497664}\bigg\{6\left(-135360 bM\frac{\Delta^2}{h^2} + 60265 b^2 M^2\frac{\Delta^4}{h^4}\right)v_I^m \\
&+ b\frac{\Delta}{h}\left[435456\left(\sigma_{I+1}^m - \sigma_{I-1}^m\right) - 124416\left(\sigma_{I+2}^m - \sigma_{I-2}^m\right) + 20736\left(\sigma_{I+3}^m - \sigma_{I-3}^m\right)\right] \\
&+ bM\frac{\Delta^2}{h^2}\left[456192\left(v_{I+1}^m + v_{I-1}^m\right) - 41472\left(v_{I+2}^m + v_{I-2}^m\right) - 13824\left(v_{I+3}^m + v_{I-3}^m\right)\right. \\
&+ 5184\left(v_{I+4}^m + v_{I-4}^m\right)\bigg] + b^2 M\frac{\Delta^3}{h^3}\left[-264600\left(\sigma_{I+1}^m - \sigma_{I-1}^m\right)\right. \\
&+ 211536\left(\sigma_{I+2}^m - \sigma_{I-2}^m\right) - 62904\left(\sigma_{I+3}^m - \sigma_{I-3}^m\right) + 5760\left(\sigma_{I+4}^m - \sigma_{I-4}^m\right) \\
&+ 2088\left(\sigma_{I+5}^m - \sigma_{I-5}^m\right) - 624\left(\sigma_{I+6}^m - \sigma_{I-6}^m\right) + 72\left(\sigma_{I+7}^m - \sigma_{I-7}^m\right)\bigg] \\
&+ b^2 M^2\frac{\Delta^4}{h^4}\left[-260496\left(v_{I+1}^m + v_{I-1}^m\right) + 87888\left(v_{I+2}^m + v_{I-2}^m\right)\right. \\
&- 3568\left(v_{I+3}^m + v_{I-3}^m\right) - 6468\left(v_{I+4}^m + v_{I-4}^m\right) + 1968\left(v_{I+5}^m + v_{I-5}^m\right) \\
&- 80\left(v_{I+6}^m + v_{I-6}^m\right) - 48\left(v_{I+7}^m + v_{I-7}^m\right) + 9\left(v_{I+8}^m + v_{I-8}^m\right)\bigg]\bigg\}
\end{aligned} \tag{7.265}$$

The scheme for the stress is analogous.

Assuming the initial conditions (7.256), scheme (7.265) will reproduce the initial particle velocities. It will not, however, reproduce the initial stresses. The scheme will smooth the odd–even stress distribution by subtracting a value proportional to $|\sigma_{EVEN} - \sigma_{ODD}|$ from the larger of the two stresses and adding the same value to the smaller of the two stresses in each time step. In other words, the scheme will dissipate the initial odd–even stress distribution. Clearly, this is a substantial positive difference in behaviour compared to the 2TL scheme with the centred approximation.

7.3.6.5 Combination of MacCormack approach, DRP approximations and 4th-order Runge–Kutta time-marching scheme

Zhang and Chen (2006) and Zhang *et al.* (2012) presented an interesting scheme combining the higher-order MacCormack approach with the DRP FD operators (Tam and Webb 1993; Hixon 1996, 1997) and the 4th-order Runge–Kutta time-marching scheme. Both articles aimed to develop an FD scheme capable of including a nonplanar free surface; the first one in 2D, the second one in 3D. Here we restrict the discussion to its 1D version, solving Eq. (7.229).

The forward and backward operators are the same as those in Eqs. (7.260) except for the values of the coefficients. Coefficients $c_{-1}, \ldots, c_3$ in Eqs. (7.260) are replaced by

$$a_{-1} = -0.30874, \quad a_0 = -0.6326, \quad a_1 = 1.2330, \quad a_2 = -0.3334, \quad a_3 = 0.04168$$

$$(7.266)$$

The coefficients are obtained by minimizing the dissipation error at eight points or more per wavelength (Hixon 1997) and giving the 4th-order accuracy for the dispersion error. The update of $\mathbf{w}_I$ from time level m to time level $m + 1$ is performed in the following partial steps:

$$
\begin{aligned}
\mathbf{w}_I^{m(1)} &= \Delta\, \mathbf{A}_I D_x^F \left[\mathbf{w}_I^m \right] \\
\mathbf{w}_I^{m(2)} &= \Delta\, \mathbf{A}_I D_x^B \left[\mathbf{w}_I^m \right] + \Delta\, \mathbf{A}_I D_x^B \left[\tfrac{1}{2} \mathbf{w}_I^{m(1)} \right] \\
\mathbf{w}_I^{m(3)} &= \Delta\, \mathbf{A}_I D_x^F \left[\mathbf{w}_I^m \right] + \Delta\, \mathbf{A}_I D_x^F \left[\tfrac{1}{2} \mathbf{w}_I^{m(2)} \right] \\
\mathbf{w}_I^{m(4)} &= \Delta\, \mathbf{A}_I D_x^B \left[\mathbf{w}_I^m \right] + \Delta\, \mathbf{A}_I D_x^B \left[\mathbf{w}_I^{m(3)} \right]
\end{aligned}
\tag{7.267}
$$

$$\mathbf{w}_I^{m+1} = \mathbf{w}_I^m + \frac{1}{6}\mathbf{w}_I^{m(1)} + \frac{1}{3}\mathbf{w}_I^{m(2)} + \frac{1}{3}\mathbf{w}_I^{m(3)} + \frac{1}{6}\mathbf{w}_I^{m(4)} \tag{7.268}$$

Although the algorithm is clear and easy to perform, the overall effective (resulting) structure is not so obvious. Therefore, we substitute $\mathbf{w}_I^{m(k-1)}$ in the equation for $\mathbf{w}_I^{m(k)}$ by the r.h.s. of

the equation for $\mathbf{w}_I^{m(k-1)}$. Eventually we obtain

$$\mathbf{w}_I^{m+1} = \mathbf{w}_I^m + \Delta \left\{ \frac{1}{2} \mathbf{A}_I D_x^F \left[\mathbf{w}_I^m \right] + \frac{1}{2} \mathbf{A}_I D_x^B \left[\mathbf{w}_I^m \right] \right\}$$

$$+ \Delta^2 \frac{1}{2} \left\{ \begin{array}{l} \frac{1}{3} \mathbf{A}_I D_x^B \left[\mathbf{A}_I D_x^F \left[\mathbf{w}_I^m \right] \right] \\[4pt] + \frac{1}{3} \mathbf{A}_I D_x^F \left[\mathbf{A}_I D_x^B \left[\mathbf{w}_I^m \right] \right] \\[4pt] + \frac{1}{3} \mathbf{A}_I D_x^B \left[\mathbf{A}_I D_x^F \left[\mathbf{w}_I^m \right] \right] \end{array} \right\}$$

$$+ \Delta^3 \frac{1}{6} \left\{ \begin{array}{l} \frac{1}{2} \mathbf{A}_I D_x^F \left[\mathbf{A}_I D_x^B \left[\mathbf{A}_I D_x^F \left[\mathbf{w}_I^m \right] \right] \right] \\[4pt] + \frac{1}{2} \mathbf{A}_I D_x^B \left[\mathbf{A}_I D_x^F \left[\mathbf{A}_I D_x^B \left[\mathbf{w}_I^m \right] \right] \right] \end{array} \right\}$$

$$+ \Delta^4 \frac{1}{24} \left\{ \mathbf{A}_I D_x^B \left[\mathbf{A}_I D_x^F \left[\mathbf{A}_I D_x^B \left[\mathbf{A}_I D_x^F \left[\mathbf{w}_I^m \right] \right] \right] \right] \right\} \tag{7.269}$$

It is clear that the expressions in the four braces are approximations to

$$\mathbf{A} \frac{\partial \mathbf{w}}{\partial x}, \mathbf{A} \frac{\partial}{\partial x} \left(\mathbf{A} \frac{\partial \mathbf{w}}{\partial x} \right), \mathbf{A} \frac{\partial}{\partial x} \left[\mathbf{A} \frac{\partial}{\partial x} \left(\mathbf{A} \frac{\partial \mathbf{w}}{\partial x} \right) \right], \mathbf{A} \frac{\partial}{\partial x} \left\{ \mathbf{A} \frac{\partial}{\partial x} \left[\mathbf{A} \frac{\partial}{\partial x} \left(\mathbf{A} \frac{\partial \mathbf{w}}{\partial x} \right) \right] \right\} \tag{7.270}$$

at (I, m), respectively. Comparison with Eqs. (7.246) and (7.251) shows that scheme (7.267) and (7.268) can be obtained by the Lax–Wendroff approach applied to Eq. (7.229) and aiming to develop the (4,4) velocity–stress scheme on the collocated grid using two time levels. Consequently, the difference between scheme (7.267)–(7.268) and scheme (7.263)–(7.264) is in the method of approximating the four terms (7.270).

7.4 FD schemes for a material interface

In Section 7.2 we assumed an unbounded homogeneous medium in which both the elastic modulus and density are spatial constants. In Section 7.3 we assumed a smoothly hetero-geneous medium. Comparison of the strong-form formulations indicates why we explicitly addressed the question of determining the effective grid modulus (M_I) only in Subsection 7.3.1, where we presented the (2,2) displacement scheme on a conventional grid. We had to treat the term $\partial (M \partial u / \partial x) / \partial x$ in the displacement formulation, Eq. (7.2). We used a mathematical trick to avoid differentiating the modulus. The other strong-form formula-tions did not force us to treat the determination of the grid modulus explicitly. We simply indicated the effective grid modulus assigned to a grid spatial position by a corresponding spatial subscript. The same applies to density ρ or its reciprocal value b for all strong-form formulations.

Although the smoothness of the heterogeneous medium is a mathematically clear con-cept, it is obvious that two smooth media can differ from each other by gradient. Loosely, we can guess that local values of modulus and density at a spatial grid position might be sufficient in the case of small gradients. On the other hand, we may have some doubts

about using the local values in the case of large gradients. What is a small and what is a large value of a gradient is, of course, relative. In general, appropriate measures of spatial variability of the medium should be compared with the wavelengths or frequencies that are to be sufficiently accurately propagated in the grid. Consequently, the determination of optimal values of modulus and density at a grid position is not a trivial problem.

Probably the most important type of spatial variability of a material parameter is its discontinuous change – in other words, a material discontinuity or a material interface.

7.4.1 Simple general consideration

We start with a simple general consideration. Let $\varphi^-(x)$, $K^-(x)$ and $\psi^-(x)$ be real functions of a real argument $x < 0$. Similarly, let $\varphi^+(x)$, $K^+(x)$ and $\psi^+(x)$ be real functions of a real argument $x > 0$. Assume that the functions have their limits at $x = 0$, which we denote by $\varphi^-(0)$, $K^-(0)$, $\psi^-(0)$, $\varphi^+(0)$, $K^+(0)$ and $\psi^+(0)$, respectively. The functions satisfy equations

$$\varphi^-(x) = K^-(x)\,\psi^-(x), \quad \varphi^+(x) = K^+(x)\,\psi^+(x) \tag{7.271}$$

Moreover, functions $\varphi^\pm(x)$ satisfy the boundary (continuity) condition

$$\varphi(0) = \varphi^-(0) = \varphi^+(0) \tag{7.272}$$

Due to the boundary condition, neither of Eqs. (7.271) alone can be used as an equation for $x = 0$.

Define

$$\psi^A(0) \equiv \tfrac{1}{2}\left[\psi^-(0) + \psi^+(0)\right] \tag{7.273}$$

Then,

$$\psi^A(0) = \frac{1}{2}\left[\frac{\varphi^-(0)}{K^-(0)} + \frac{\varphi^+(0)}{K^+(0)}\right] = \frac{1}{2}\varphi(0)\left[\frac{1}{K^-(0)} + \frac{1}{K^+(0)}\right] \tag{7.274}$$

Define

$$K^H(0) \equiv \frac{2}{\left[\dfrac{1}{K^-(0)} + \dfrac{1}{K^+(0)}\right]} \tag{7.275}$$

Then,

$$\varphi(0) = K^H(0)\,\psi^A(0) \tag{7.276}$$

Equation (7.276) has two important properties: (1) it is valid directly at $x = 0$, (2) it has the same form as each of Eqs. (7.271). This is due to the arithmetic averaging of $\psi^-(0)$ and $\psi^+(0)$, and the harmonic averaging of $K^-(0)$ and $K^+(0)$. Note that the arithmetic and harmonic averages are indicated by superscripts A and H starting with Eqs. (7.273) and (7.275).

7.4.2 Hooke's law and equation of motion for a welded interface

Now we consider the contact of two homogeneous elastic halfspaces at $x = 0$. In each of the halfspaces the stress is given by Hooke's law:

$$\sigma^-(x) = M^-(x)\,\varepsilon^-(x), \quad \sigma^+(x) = M^+(x)\,\varepsilon^+(x) \tag{7.277}$$

Assuming the contact to be a welded material interface (Subsection 2.5.2), the traction continuity across the interface imposes a boundary condition for the stress:

$$\sigma^-(0) = \sigma^+(0) \tag{7.278}$$

It follows then from the above general consideration and Eqs. (7.271)–(7.276) that the stress at a welded interface can be described by

$$\sigma(0) = M^H(0)\,\varepsilon^A(0) \tag{7.279}$$

where $M^H(0)$ is the harmonic average of the elastic moduli $M^-(0)$ and $M^+(0)$, and $\varepsilon^A(0)$ is the arithmetic average of the strains:

$$M^H(0) = \frac{2}{\dfrac{1}{M^-(0)} + \dfrac{1}{M^+(0)}}, \quad \varepsilon^A(0) = \tfrac{1}{2}\left[\varepsilon^-(0) + \varepsilon^+(0)\right] \tag{7.280}$$

The equations of motion in the two halfspaces are

$$\frac{\partial^2 u^-}{\partial t^2} = b^-\frac{\partial\sigma^-}{\partial x}, \quad \frac{\partial^2 u^+}{\partial t^2} = b^+\frac{\partial\sigma^+}{\partial x} \tag{7.281}$$

Assuming continuity of displacement u and consequently continuity of acceleration $\partial^2 u/\partial t^2$ across the welded interface, the equation of motion at the interface can be written as

$$\left.\frac{\partial^2 u}{\partial t^2}\right|_{x=0} = b^H(0)\left[\frac{\partial\sigma}{\partial x}\right]^A\Bigg|_{x=0} \tag{7.282}$$

where superscripts H and A indicate the harmonic and arithmetic averages, respectively. Because b is the reciprocal of density, $b = 1/\rho$,

$$(b^H)^{-1} = \tfrac{1}{2}\left(\rho^- + \rho^+\right) = \rho^A \tag{7.283}$$

and Eq. (7.282) can also be written as

$$\rho^A(0)\left.\frac{\partial^2 u}{\partial t^2}\right|_{x=0} = \left[\frac{\partial\sigma}{\partial x}\right]^A\Bigg|_{x=0} \tag{7.284}$$

Partial summary (1) Equation (7.279) for the stress at a welded interface has the same form as Hooke's law in each of the two halfspaces. Equation (7.279) is consistent with the traction-continuity condition at a welded interface. The effective elastic modulus representing a welded interface is the harmonic average of the moduli in the homogeneous halfspaces. (2) Equation (7.282) or (7.284) for the particle acceleration at a welded interface has the

same form as the equation of motion in each of the two halfspaces. Equation (7.282) or (7.284) is consistent with the condition of continuity of displacement and particle acceleration at a welded interface. The effective density representing a welded interface is the arithmetic average of densities in the halfspaces. The statements make an important basis for developing an FD scheme for the grid point at the interface and grid points in the halfspaces.

7.4.3 Simple rheological model of a welded interface

Before we continue with an FD scheme we can recall the simple rheological model of two Hooke elements (elastic springs) connected in series, see Chapter 3. The resulting stress is equal to the stresses acting on the springs:

$$\sigma = \sigma^- = \sigma^+ \tag{7.285}$$

whereas the strains of the springs are additive:

$$\varepsilon = \varepsilon^- + \varepsilon^+ = \frac{\sigma}{M^-} + \frac{\sigma}{M^+} \tag{7.286}$$

We can think of finding an averaged Hooke spring such that the serial connection of two averaged springs would make an equivalent, in terms of the resulting stress and strain, to the considered serial connection of two different springs. We easily find the averaged spring:

$$\sigma = M^H \varepsilon^A, \quad M^H = \frac{2}{\dfrac{1}{M^-} + \dfrac{1}{M^+}}, \quad \varepsilon^A = \frac{1}{2}\left(\varepsilon^- + \varepsilon^+\right) \tag{7.287}$$

This means that the elastic modulus of the averaged spring is the harmonic average of the elastic moduli of the two springs. The serial connection of two springs can thus be considered a rheological model for traction continuity at the welded interface of two homogeneous halfspaces.

Similarly, we could consider a system of two connected particles with masses m^- and m^+. If the particles move together, the equivalent system can be made of two identical particles with mass equal to the arithmetic average of masses m^- and m^+.

7.4.4 FD schemes

Equations (7.279) and (7.284) suggest (a) harmonic averaging of the elastic moduli and arithmetic averaging of the densities at the material discontinuity, (b) averaging of the spatial derivatives of the functions at the material discontinuity.

The averaging of derivatives means averaging one-sided approximations of the derivatives of stresses and displacements (or strains). In 1D this poses a minor algorithmical problem. Having in mind the perspective of 2D or 3D simulations for a medium with nonplanar interfaces, it is clear that calculations of one-sided derivatives pose a more complicated problem. Moreover, it is not trivial to test the accuracy of such an approach.

Kristek and Moczo (2006) neglected averaging of the spatial derivatives at the interface. They defined the effective grid modulus and density as

$$M_{I+1/2}^H \equiv \left[\frac{1}{h} \int_{x_I}^{x_{I+1}} \frac{1}{M(x)} dx \right]^{-1} , \quad \rho_I^A \equiv \left[\frac{1}{h} \int_{x_{I-1/2}}^{x_{I+1/2}} \rho(x) dx \right] \qquad (7.288)$$

They applied these effective grid material parameters to three 1D schemes – (2,2) displacement scheme on the conventional grid, (2,4) displacement–stress scheme on the spatially staggered grid, and displacement optimally accurate scheme on the conventional grid. They performed detailed numerical tests of the three schemes for an unbounded homogeneous space, two halfspaces in welded contact, and for a model of an interior layer between two halfspaces. The interior layer had a large velocity gradient. The model of an unbounded homogeneous space enabled them to compare the pure effect of grid dispersion. The simulations for the model with a material interface were designed so that it was possible to separate the error due to the interface. The third model enabled them to compare the capability of the schemes to account for a dramatic change of velocity inside the layer between two identical halfspaces.

All simulations obtained with the FD schemes were compared with analytical matrix solutions. The level of accuracy of the FD solutions was quantified and characterized using envelope and phase misfits with respect to the analytical solutions.

For all three schemes and models, Kristek and Moczo (2006) demonstrated the superior accuracy of harmonic averaging of the elastic modulus compared to considering local values or arithmetic averaging of the elastic modulus. Also relevant for this chapter is the conclusion that the optimally accurate scheme is significantly more accurate than the two other schemes tested.

It is obvious that neglecting the averaging of the spatial derivatives of stress and strain decreases the order of accuracy of the scheme across the interface. Moczo *et al*. (2007a, Chapter 10) compared the conventional and optimally accurate schemes (1st-order accurate at the interface) with conventional and optimally accurate schemes treating the interface explicitly (and thus 2nd-order accurate at the interface). As might be expected, the application of the latter schemes increased accuracy at the interface.

In conclusion, all the FD schemes presented so far can be used with the effective grid parameters defined by Eqs. (7.288). The use of harmonic averaging of the elastic modulus in smoothly and discontinuously heterogeneous media makes an FD scheme capable of sufficiently accurately accounting for the medium heterogeneity. Specifically, it makes the scheme capable of sensing the position of the material interface within one grid spacing, that is, anywhere between two neighbouring spatial grid points.

7.5 FD schemes for a free surface

Two aspects make the Earth's surface a very important structural feature that has to be modelled sufficiently accurately: (a) seismic motion is often recorded at or close to the Earth's surface; (b) the Earth's surface significantly affects seismic wave propagation and

earthquake motion. In most seismological applications, the air/fluid (ocean) or air/solid (land) interface can be thought of as a free surface where a fluid or solid discontinuously terminates and air is replaced by vacuum. This means that the Earth's surface may be approximated by a surface with vanishing traction.

Consider a free surface at $x = 0$ and medium at $x \geq 0$. The traction-free condition (2.39) reduces in 1D to

$$\sigma (x = 0) = 0 \qquad (7.289)$$

No matter which FD scheme is used, it is desirable to locate the grid position of displacement or particle velocity at the free surface. We restrict our considerations here to the velocity–stress schemes, although much of the explained approaches can also be applied to the displacement–stress or displacement schemes. In the case of a staggered grid the stress is located inside the medium – a half-grid spacing away from the free surface. In the case of a collocated grid the stress is also located at the free surface.

We have two principal possibilities for calculating particle velocity at the free surface, and particle velocity and stress inside the medium near the free surface. The first approach: apply the same FD schemes as for the interior grid points assuming virtual values of stress, particle velocity and material parameters outside the medium. The second approach: apply one-sided schemes that do not need any virtual values outside the medium.

The advantage of the first approach is the use of one and the same scheme at any grid point. Its disadvantage is the need to reasonably define virtual values outside the medium. The disadvantage of the second approach is the application of different schemes for different grid positions inside the medium near the free surface – the number of grid positions depends on the scheme and the order of approximation.

The first approach leads to the so-called vacuum formalism (zero modulus outside the medium), medium taper (density taper) or imaging method. In this 1D introduction we outline only the imaging method suggested by Levander (1988). The second approach will be illustrated by the adjusted FD approximations suggested by Kristek *et al*. (2002).

7.5.1 Stress imaging

The basic idea in 1D is very simple: the antisymmetry

$$\sigma (-x) = -\sigma(x) \qquad (7.290)$$

ensures that the boundary condition given by Eq. (7.289) is satisfied. Recall the (2,4) velocity–stress staggered-grid scheme (7.186) with the spatial index $I + 1/2$ for stress:

$$V_I^{m+1/2} = V_I^{m-1/2} + b_I \frac{\Delta}{h} \left[\frac{9}{8} \left(T_{I+1/2}^m - T_{I-1/2}^m \right) - \frac{1}{24} \left(T_{I+3/2}^m - T_{I-3/2}^m \right) \right]$$

$$T_{I+1/2}^m = T_{I+1/2}^{m-1} + M_{I+1/2} \frac{\Delta}{h} \left[\frac{9}{8} \left(V_{I+1}^{m-1/2} - V_I^{m-1/2} \right) - \frac{1}{24} \left(V_{I+2}^{m-1/2} - V_{I-1}^{m-1/2} \right) \right] \qquad (7.291)$$

We assume the effective grid material parameters calculated according to (7.288).

Assume $I = 0$ corresponding to the free surface, that is, $x = 0$. For calculating $T_{1/2}^m$ we also need the value of the particle velocity outside the medium, $V_{-1}^{m-1/2}$. The simplest possibility is to set it equal to zero (Robertsson 1996). Levander (1988) considered the 2nd-order approximation of the boundary condition and imaged stress-tensor components. In 1D:

$$\frac{\partial \sigma}{\partial t}\bigg|_{-h/2}^{m-1/2} = -\frac{\partial \sigma}{\partial t}\bigg|_{h/2}^{m-1/2} \tag{7.292}$$

$$M_{-1/2}\frac{1}{h}\left(V_0^{m-1/2} - V_{-1}^{m-1/2}\right) = -M_{1/2}\frac{1}{h}\left(V_1^{m-1/2} - V_0^{m-1/2}\right) \tag{7.293}$$

Assuming

$$M_{-1/2} = M_{1/2} \tag{7.294}$$

we obtain

$$V_{-1}^{m-1/2} = V_1^{m-1/2} \tag{7.295}$$

Consistently with assumption (7.294), we can consider

$$\rho_0^A = \frac{2}{h}\int_0^{h/2} \rho(x)\,dx, \quad b_0 = \frac{1}{2\rho_0^A} \tag{7.296}$$

For calculating $V_0^{m+1/2}$ at the free surface we also need two values of stress outside the medium: $T_{-1/2}^m$ and $T_{-3/2}^m$. They are obtained from

$$T_{-1/2}^m = -T_{1/2}^m, \quad T_{-3/2}^m = -T_{3/2}^m \tag{7.297}$$

In 1D the stress imaging gives satisfactory results. In 3D this is not so. Kristek *et al.* (2002) demonstrated that in the 3D case the stress imaging in 4th-order FD modelling needs at least twice as many grid spacings per wavelength compared to what is enough inside the medium if the Rayleigh waves are to be propagated without significant grid dispersion, even in the case of a simple homogeneous halfspace. Stress imaging in 3D is presented in Subsection 10.1.1.

7.5.2 Adjusted FD approximations

Here we adapt the 3D scheme presented by Kristek *et al.* (2002) to the 1D case. Consider again the (2,4) velocity–stress staggered-grid scheme (7.186) for interior grid points. The scheme cannot be applied for calculating $V_1^{m+1/2}$, $T_{1/2}^m$ and $V_0^{m+1/2}$ if no virtual values of

stress and particle velocity outside the medium are assumed. Each of the three grid positions requires an adjusted 4th-order scheme. They are

$$T_{1/2}^m = T_{1/2}^{m-1} + M_{1/2}\frac{\Delta}{h}\left(-\tfrac{91}{72}V_0^{m-1/2} + \tfrac{11}{8}V_1^{m-1/2} - \tfrac{1}{8}V_2^{m-1/2} + \tfrac{1}{72}V_3^{m-1/2}\right)$$

$$V_1^{m+1/2} = V_1^{m-1/2} + b_1\frac{\Delta}{h}\left(-\tfrac{31}{24}T_{1/2}^m + \tfrac{29}{24}T_{3/2}^m - \tfrac{3}{40}T_{5/2}^m - \tfrac{1}{168}T_{7/2}^m\right) \qquad (7.298)$$

$$V_0^{m+1/2} = V_0^{m-1/2} + b_0\frac{\Delta}{h}\left(\tfrac{35}{8}T_{1/2}^m - \tfrac{35}{24}T_{3/2}^m + \tfrac{21}{40}T_{5/2}^m - \tfrac{5}{56}T_{7/2}^m\right)$$

where

$$b_0 = \frac{1}{\rho_0^A}; \quad \rho_0^A = \frac{2}{h}\int_0^{h/2}\rho(x)\,dx \qquad (7.299)$$

Note that in schemes for $V_1^{m+1/2}$ and $V_0^{m+1/2}$ we explicitly used the boundary condition and the consequence of the boundary condition (the spatial derivative of the particle velocity at the free surface is zero).

Kristek *et al.* (2002) developed a technique for simulating the planar free surface in the 3D case based on direct application of the boundary condition at the free surface and adjusted FD approximations of the spatial derivatives that use only values at the grid positions inside the medium. They demonstrated that with their technique it is possible to apply the same spatial sampling as inside the medium. The technique is presented in Subsection 10.1.2.

7.6 Boundaries of a spatial grid

The spatial grid has a finite number of grid points (true grid points physically addressed in the computer memory). Consequently, the grid has boundaries. In 1D there are two boundaries. Considering a rectangle in 2D, there are four boundaries, and considering a rectangular prism (rectangular parallelepiped) in 3D, there are six boundaries. In many applications a free surface makes one boundary (planar or nonplanar). Except for the free surface, the boundaries are artificial – they do not represent a surface beyond which there is no medium. Therefore, the boundaries should be designed so that they represent the true interaction of the wavefield inside the computational domain covered by the grid with the medium outside the grid. In principle, the boundary of the grid may be anything in between or including two extreme types – absolutely reflecting and absolutely transparent. In most cases we want transparent boundaries – no energy should be reflected from the boundary of the computational domain back into its interior. In some cases it may be useful to use a boundary that simulates a periodic repetition of the computational region. In other cases a condition of symmetry/antisymmetry may be reasonable.

Here we present the 1D version of only one, but so far the best, of the developed approaches – the perfectly matched layer (PML), originally introduced by Bérenger (1994) for electromagnetic wave propagation and later generalized for elastic wave propagation

by Chew and Liu (1996) and others. The name comes from the fact that the PML in a true continuum space does not reflect energy back to the computational domain. In 2D or 3D the PML makes a 'sponge' region surrounding the computational domain. Inside a PML the particle velocity and stress are attenuated in the direction perpendicular to the boundary. In 1D a PML reduces to a spatial range of grid points at the 'end' of the computational 1D domain. Here we adapt the 3D theory presented by Komatitsch and Martin (2007) and Kristek *et al.* (2009).

7.6.1 Perfectly matched layer: theory

Application of the Fourier transform to Eqs. (7.9) yields

$$i\omega v = b\frac{\partial \sigma}{\partial x}, \quad i\omega \sigma = M\frac{\partial v}{\partial x} \tag{7.300}$$

Here we use the same symbols for the quantities in the frequency and time domains. Further, we indicate the time or frequency as variables just to emphasize them. We replace the spatial differentiation with respect to x by the spatial differentiation with respect to $\tilde{x}$:

$$\frac{\partial}{\partial \tilde{x}} = \frac{1}{s}\frac{\partial}{\partial x} \tag{7.301}$$

Here s is the stretching factor (or coordinate stretching variable):

$$s = \gamma + \frac{\Omega}{\alpha + i\omega} \tag{7.302}$$

where γ, Ω and α are, in general, functions of x and define the PML medium profile. The stretching factor has to be complex if it is to attenuate. Equations (7.300) then become

$$i\omega v = \frac{1}{\gamma}b\frac{\partial \sigma}{\partial x} - \frac{d}{a + i\omega}b\frac{\partial \sigma}{\partial x}, \quad i\omega \sigma = \frac{1}{\gamma}M\frac{\partial v}{\partial x} - \frac{d}{a + i\omega}M\frac{\partial v}{\partial x} \tag{7.303}$$

with

$$a = \alpha + \Omega/\gamma, \quad d = \Omega/\gamma^2 \tag{7.304}$$

Because the second term on the r.h.s. of each of Eqs. (7.303) is a product of two complex quantities, an application of the inverse Fourier transform to the equations would give the time-domain equations with convolutory terms. In order to avoid the convolution, we define auxiliary functions:

$$\theta(\omega) = -\frac{d}{a + i\omega}b\frac{\partial \sigma}{\partial x}, \quad \zeta(\omega) = -\frac{d}{a + i\omega}M\frac{\partial v}{\partial x} \tag{7.305}$$

Equations (7.303) then become

$$i\omega v = \frac{1}{\gamma}b\frac{\partial \sigma}{\partial x} + \theta(\omega), \quad i\omega \sigma = \frac{1}{\gamma}M\frac{\partial v}{\partial x} + \zeta(\omega) \tag{7.306}$$

Application of the inverse Fourier transform to the latter equations gives

$$\frac{\partial v}{\partial t} = \frac{1}{\gamma} b \frac{\partial \sigma}{\partial x} + \theta(t), \quad \frac{\partial \sigma}{\partial t} = \frac{1}{\gamma} M \frac{\partial v}{\partial x} + \zeta(t) \tag{7.307}$$

In order to find relations for $\theta(t)$ and $\zeta(t)$, we rewrite Eqs. (7.305):

$$a\,\theta(\omega) + i\omega\,\theta(\omega) = -db \frac{\partial \sigma}{\partial x}, \quad a\,\zeta(\omega) + i\omega\,\zeta(\omega) = -dM \frac{\partial v}{\partial x} \tag{7.308}$$

and apply the inverse Fourier transform. We obtain

$$\frac{\partial}{\partial t}\theta(t) + a\,\theta(t) = -db \frac{\partial \sigma}{\partial x}, \quad \frac{\partial}{\partial t}\zeta(t) + a\,\zeta(t) = -dM \frac{\partial v}{\partial x} \tag{7.309}$$

Partial summary Whereas inside the computational region Eqs. (7.9) are to be solved, modified Eqs. (7.307) and additional Eqs. (7.309) have to be solved inside the PML. It is now clear that the auxiliary variables $\theta(t)$ and $\zeta(t)$ have the meaning of memory variables (or additional variables), and solving the additional Eqs. (7.309) replaces calculation of convolutory integrals. The selection of the PML profile, that is, parameters γ, Ω and α, is key to efficient attenuation inside the PML.

Consider for simplicity a PML starting at $x = 0$ and extending for $x > 0$, and the simplest special case of the stretching factor with $\gamma = 1$ and $\alpha = 0$:

$$s = 1 + \frac{\Omega(x)}{i\omega}; \quad \Omega(x) > 0 \tag{7.310}$$

Then,

$$\tilde{x} = x - \frac{i}{\omega} \int_0^x \Omega(\xi)\,d\xi \tag{7.311}$$

Consider a plane harmonic wave $\exp[i(\omega t - kx)]$ propagating in the positive x-direction. Replacement of x by $\tilde{x}$ introduces a multiplying factor due to the second term on the r.h.s. of Eq. (7.311). Because the multiplying factor decreases with increasing x, it attenuates the wave with increasing x.

7.6.2 Perfectly matched layer: scheme

Here we adapt the 3D scheme presented by Kristek *et al.* (2009) to the 1D case. For brevity of expressions we omit the spatial grid indexing. This should pose no problem. Clearly, θ shares a spatial position with v. Similarly, ζ shares a spatial position with σ. The parameters of the PML should be indexed if they are functions of x. Consider the following approximations at the time level m:

$$\theta^m \doteq \tfrac{1}{2}\left(\theta^{m+1/2} + \theta^{m-1/2}\right), \quad \left.\frac{\partial\theta}{\partial t}\right|^m \doteq \frac{1}{\Delta}\left(\theta^{m+1/2} - \theta^{m-1/2}\right) \tag{7.312}$$

Application of the approximations to the first of Eqs. (7.309) yields

$$\theta^{m+1/2} \doteq \frac{2 - a\Delta}{2 + a\Delta} \theta^{m-1/2} - \frac{2d\Delta}{2 + a\Delta} b \left.\frac{\partial\sigma}{\partial x}\right|^m \tag{7.313}$$

If we relate the first of Eqs. (7.307) to the time level m, we need θ^m. Using the first of Eqs. (7.312) and Eq. (7.313) we obtain

$$\theta^m \doteq \frac{2}{2 + a\Delta} \theta^{m-1/2} - \frac{d\Delta}{2 + a\Delta} b \left.\frac{\partial\sigma}{\partial x}\right|^m \tag{7.314}$$

Using Eq. (7.314) we can rewrite the first of Eqs. (7.307):

$$\left.\frac{\partial v}{\partial t}\right|^m = \left(\frac{1}{\gamma} - \frac{d\Delta}{2 + a\Delta}\right) b \left.\frac{\partial\sigma}{\partial x}\right|^m + \frac{2}{2 + a\Delta} \theta^{m-1/2} \tag{7.315}$$

Replacing a and d in Eqs. (7.313) and (7.315) using Eqs. (7.304) we obtain

$$\theta^{m+1/2} \doteq \frac{2\gamma - (\alpha\gamma + \Omega)\Delta}{A} \theta^{m-1/2} - \frac{1}{\gamma} \frac{2\Omega\Delta}{A} b \left.\frac{\partial\sigma}{\partial x}\right|^m \tag{7.316}$$

$$\left.\frac{\partial v}{\partial t}\right|^m = \frac{1}{\gamma} \left(1 - \frac{\Omega\Delta}{A}\right) b \left.\frac{\partial\sigma}{\partial x}\right|^m + \frac{2\gamma}{A} \theta^{m-1/2} \tag{7.317}$$

where

$$A = 2\gamma + (\alpha\gamma + \Omega)\Delta \tag{7.318}$$

Analogously we obtain an equation for stress and the corresponding memory variable:

$$\zeta^{m+1} \doteq \frac{2\gamma - (\alpha\gamma + \Omega)\Delta}{A} \zeta^m - \frac{1}{\gamma} \frac{2\Omega\Delta}{A} M \left.\frac{\partial v}{\partial x}\right|^{m+1/2} \tag{7.319}$$

$$\left.\frac{\partial\sigma}{\partial t}\right|^{m+1/2} = \frac{1}{\gamma} \left(1 - \frac{\Omega\Delta}{A}\right) M \left.\frac{\partial v}{\partial x}\right|^{m+1/2} + \frac{2\gamma}{A} \zeta^m \tag{7.320}$$

The temporal and spatial derivatives are approximated correspondingly to the scheme used inside the computational domain.

7.7 Wavefield excitation

In general, numerical simulation of an earthquake source and other sources of seismic waves is not a trivial problem and may considerably depend on the FD scheme. In 3D it will be addressed in detail later. Here we indicate three methods of wavefield excitation: the use of a body-force term (introduced by Aboudi 1971, Frankel 1993, Yomogida and Etgen 1993, Graves 1996), incremental stress (introduced by Virieux 1986, Coutant *et al*. 1995, Olsen *et al*. 1995a), and wavefield decomposition (introduced by Alterman and Karal 1968).

Table 7.7 *Spatial distribution of the field variables for injecting a
known source based on wavefield decomposition: the case of the
(2,2) VS SG scheme*

Field variable	Range of spatial indices of grid points where the field variable is located		
v_R	I_{MIN}	$\leq I \leq$	$I^* + 1$
v	I^*		I_{MAX}
σ_R	$I_{MIN} + 1/2$	$\leq I + 1/2 \leq$	$I^* + 1/2$
σ	$I^* + 1/2$		$I_{MAX} - 1/2$

7.7.1 Body-force term and incremental stress

Consider the velocity–stress formulation with a body-force term f:

$$\frac{\partial v}{\partial t} = b\frac{\partial \sigma}{\partial x} + bf, \quad \frac{\partial \sigma}{\partial t} = M\frac{\partial v}{\partial x} \tag{7.321}$$

Intuitively, it is most natural to make use of a body-force term in the equation of motion. In the simplest case we can prescribe function $f(t)$ at one grid position of the particle velocity.

Another possibility is to add an incremental stress $\Delta\sigma(t)$ at the grid position of the stress.

7.7.2 Wavefield injection based on wavefield decomposition

The basic idea Finally, it is also possible to inject an exact solution for the particle velocity due to a desired source. Let v_S be the particle velocity produced by a source and known from the analytical solution. The total particle velocity can be decomposed in the form

$$v(x, t) = v_S(x, t) + v_R(x, t) \tag{7.322}$$

where v_R is the particle velocity corresponding to the residual (or scattered) wavefield. However, it is not necessary to apply the decomposition everywhere.

Algorithm for the (2,2) velocity–stress staggered-grid scheme Consider a grid with the leftmost spatial index I_{MIN} and rightmost spatial index I_{MAX}. Let I^* be the spatial index of the grid point at which we want to 'inject' $v_S(x, t)$. Assume the spatial distribution of v_R, v, σ_R and σ as shown in Table 7.7. Moreover, for simplicity, assume a homogeneous medium at the spatial range $[I^* - 1, I^* + 2]$. We want the wave to propagate in the positive x-direction. Assume zero particle velocity and stress everywhere before the time level $1/2$ at which the injecting starts at I^* with $v_S(t = 0)$.

Table 7.8 *Spatial distribution of the field variables for injecting a known source based on wavefield decomposition: the case of the (2,4) VS SG scheme*

Field variable	Range of spatial indices of grid points where the field variable is located		
v_R	I_{MIN}	$\leq I \leq$	$I^* + 5$
v	I^*		I_{MAX}
σ_R	$I_{MIN} + 1/2$	$\leq I + 1/2 \leq$	$I^* + 7/2$
σ	$I^* + 3/2$		$I_{MAX} - 1/2$

The algorithm of the injection is:

(a) σ_R is updated using the scheme at $I + 1/2$; $I_{MIN} \leq I \leq I^*$
(b) σ is updated using the scheme at $I + 1/2$; $I^* \leq I \leq I_{MAX} - 1$
(c) v_R is updated using the scheme at I; $I_{MIN} \leq I \leq I^*$
(d) v is updated using the scheme at I; $I^* + 1 \leq I \leq I_{MAX}$
(e) $v(t_{m+1/2}) = v_R(t_{m+1/2}) + v_S(t_m)$ at I^*
(f) $v_R(t_{m+1/2}) = v(t_{m+1/2}) - v_S(t_m - \tau_I)$ at $I^* + 1$

Here τ_I denotes travel time of the injected wave from the spatial position I^* to the spatial position $I^* + 1$.

Algorithm for the (2,4) velocity–stress staggered-grid scheme Because the stencil of the scheme is larger, the zone where variables of the total and residual wavefield overlap is broader. The spatial distribution of v_R, v, σ_R and σ is shown in Table 7.8. A homogeneous medium is assumed at the spatial range $[I^* - 1, I^* + 6]$.

Then the algorithm of injection is as follows:

(a) σ_R is updated using the scheme at $I + 1/2$; $I_{MIN} \leq I \leq I^* + 3$
(b) σ is updated using the scheme at $I + 1/2$; $I^* + 1 \leq I \leq I_{MAX} - 1$
(c) v_R is updated using the scheme at I; $I_{MIN} \leq I \leq I^* + 2$
(d) v is updated using the scheme at I; $I^* + 3 \leq I \leq I_{MAX}$
(e) $v(t_{m+1/2}) = v_R(t_{m+1/2}) + v_S(t_m - \tau_I)$ at $I^* \leq I \leq I^* + 2$
(f) $v_R(t_{m+1/2}) = v(t_{m+1/2}) - v_S(t_m - \tau_I)$ at $I^* + 3 \leq I \leq I^* + 5$

Here τ_I denotes travel time of the injected wave from the spatial position I^* to the spatial position I.

7.8 FD scheme for the anelastic functions for a smooth medium

For simplicity, we restrict our discussion here to a smooth medium. The contact of two viscoelastic media will be addressed in Chapter 9. Recall the constitutive law in the

velocity–stress formulation for a viscoelastic continuum with GMB-EK/GZB rheology, Eqs. (3.125) and (3.118), in which we replaced the temporal derivative of strain by the spatial derivative of the particle velocity:

$$\frac{\partial}{\partial t}\sigma(t) = M_U\left[\frac{\partial v}{\partial x} - \sum_{l=1}^{n} Y_l\, \xi_l(t)\right] \tag{7.323}$$

$$\frac{\partial}{\partial t}\xi_l(t) + \omega_l\, \xi_l(t) = \omega_l \frac{\partial v}{\partial x}, \quad l = 1, \ldots, n \tag{7.324}$$

Additional to the elastic part with the unrelaxed modulus M_U in Eq. (7.323) is the anelastic part with the anelastic coefficients Y_l of simple Maxwell bodies and anelastic functions (memory variables) $\xi_l(t)$. Each of the n anelastic functions satisfies the additional equation (7.324). Recall that the summation convention does not apply to index l.

Whereas in the elastic medium we need to FD-approximate the elastic part of Eq. (7.323), in the viscoelastic medium we also need an FD scheme for updating the anelastic functions. Consider the (2,4) velocity–stress scheme in Paragraph 7.3.5.1.

The anelastic functions and their temporal derivatives can be approximated with 2$^{\text{nd}}$-order accuracy:

$$\xi_l(t_{m-1/2}) \doteq \tfrac{1}{2}[\xi_l(t_m) + \xi_l(t_{m-1})], \quad l = 1, \ldots, n \tag{7.325}$$

$$.\frac{\partial}{\partial t}\xi_l(t)|^{m-1/2} \doteq \frac{1}{\Delta}[\xi_l(t_m) - \xi_l(t_{m-1})], \quad l = 1, \ldots, n \tag{7.326}$$

Using approximations (7.325) and (7.326) in Eq. (7.324) we obtain a scheme for updating the anelastic functions:

$$\xi_l(t_m) \doteq \frac{2\omega_l\Delta}{2 + \omega_l\Delta}\left.\frac{\partial v}{\partial x}\right|^{m-1/2} + \frac{2 - \omega_l\Delta}{2 + \omega_l\Delta}\xi_l(t_{m-1}), \quad l = 1, \ldots, n \tag{7.327}$$

The value of $\xi_l(t_{m-1/2})$ needed in the stress–strain relation (7.323) can be obtained using Eq. (7.325). This means that both $\xi_l(t_m)$ and $\xi_l(t_{m-1})$ have to be kept in memory for each spatial grid position at one time. It is, however, possible (Kristek and Moczo 2003) to avoid the necessity of keeping both values in memory. Using approximation (7.325) in Eq. (7.327) it is easy to eliminate $\xi_l(t_{m-1})$ and obtain

$$\xi_l(t_{m-1/2}) \doteq -\frac{\omega_l\Delta}{2 - \omega_l\Delta}\left.\frac{\partial v}{\partial x}\right|^{m-1/2} + \frac{2}{2 - \omega_l\Delta}\xi_l(t_m), \quad l = 1, \ldots, n \tag{7.328}$$

Note that the dependence of the function at time $t_{m-1/2}$ on its value at time t_m is only apparent due to the approximation (7.325). Using relation (7.328) in (7.323) we obtain

$$\left.\frac{\partial}{\partial t}\sigma(t)\right|^{m-1/2} = \tilde{M}\left.\frac{\partial v}{\partial x}\right|^{m-1/2} - \sum_{l=1}^{n}\tilde{Y}_l^M\xi_l(t_m) \tag{7.329}$$

where

$$\tilde{M} = M_U \left(1 + \sum_{l=1}^{n} G_{1l} Y_l^M\right), \quad \tilde{Y}_l^M = G_{2l} M_U Y_l^M$$

$$G_{1l} = \frac{\omega_l \Delta}{2 - \omega_l \Delta}, \quad G_{2l} = \frac{2}{2 - \omega_l \Delta} \tag{7.330}$$

The derived relations mean that first we calculate $\xi_l(t_m)$ using relation (7.327) and then we apply the obtained values in relation (7.329). The temporal derivative of stress and spatial derivative of the particle velocity in Eq. (7.329) are approximated as in Paragraph 7.3.5.1. Then the resulting FD scheme replaces the second of Eqs. (7.186). Thus, the complete FD scheme is then

$$V_I^{m+1/2} = V_I^{m-1/2} + \Delta b \; f|_I^m$$

$$+ b_I \frac{\Delta}{h} \left[\frac{9}{8}\left(T_{I+1/2}^m - T_{I-1/2}^m\right) - \frac{1}{24}\left(T_{I+3/2}^m - T_{I-3/2}^m\right)\right] \tag{7.331}$$

$$T_{I-1/2}^m = T_{I-1/2}^{m-1} + \tilde{M}_{I-1/2} \frac{\Delta}{h} \left[\frac{9}{8}\left(V_I^{m-1/2} - V_{I-1}^{m-1/2}\right) - \frac{1}{24}\left(V_{I+1}^{m-1/2} - V_{I-2}^{m-1/2}\right)\right]$$

$$- \Delta \sum_{l=1}^{n} \tilde{Y}_{l;I-1/2}^M \xi_{l;I-1/2}^m \tag{7.332}$$

$$\xi_{l;I-1/2}^m = \frac{2 - \omega_l \Delta}{2 + \omega_l \Delta} \xi_{l;I-1/2}^{m-1}$$

$$+ \frac{2\omega_l \Delta}{2 + \omega_l \Delta} \frac{1}{h} \left[\frac{9}{8}\left(V_I^{m-1/2} - V_{I-1}^{m-1/2}\right) - \frac{1}{24}\left(V_{I+1}^{m-1/2} - V_{I-2}^{m-1/2}\right)\right] \tag{7.333}$$

8

3D finite-difference schemes

Before we address particular aspects of the FD schemes, we briefly review the development of the application and elaboration of the FDM in numerical modelling of seismic wave propagation and earthquake motion. We also refer to recent reviews of FD modelling, e.g., Moczo *et al*. (2007a,b), Fichtner (2011), Robertsson and Blanch (2011) and Robertsson *et al*. (2012). The reviews by Robertsson and his colleagues focus on exploration seismology but they are also relevant for earthquake seismology. Although related to computational electrodynamics, the extensive book by Taflove and Hagness (2005) is also a relevant reference.

8.1 Formulations and grids

8.1.1 Displacement conventional-grid schemes

The pioneering studies of applications of the FDM to seismic wave propagation were based on a strong displacement formulation and conventional grids. Representative studies include articles by Alterman and Karal (1968), Alterman and Rotenberg (1969), Alterman and Loewenthal (1970), Boore (1970, 1972a,b), Boore *et al*. (1971), Alford *et al*. (1974), Ilan *et al*. (1975), Kelly *et al*. (1976) and Marfurt (1984). Efforts to improve the displacement conventional-grid schemes (in brief, conventional schemes) continued until about the end of the 1990s; examples include schemes by Kummer *et al*. (1987), Zahradník (1995b), Zahradník and Priolo (1995) and Moczo *et al*. (1999). The last three schemes reached reasonable levels of accuracy in modelling the planar free surface and material interfaces, but they could not overcome the fundamental limitations of the conventional schemes.

Bamberger *et al*. (1980) analyzed grid dispersion and found that the ratio of the grid S-wave phase velocity to the true S-wave velocity becomes infinite inside liquids for the conventional schemes. Stephen (1983), based on numerical tests, pointed out instabilities of the heterogeneous conventional FD schemes at a liquid/solid interface. Marfurt (1984) analyzed grid dispersion and concluded that in a homogeneous elastic medium the explicit FE and FD schemes are comparable for Poisson's ratio less than 0.3; the FE scheme is superior to the FD for Poisson's ratio between 0.3 and 0.45; and none of the schemes is economically attractive for Poisson's ratio greater than 0.45. Moczo *et al*. (1999) demonstrated the decreasing accuracy of synthetics with increasing P-wave to S-wave speed ratio (V_P / V_S).

Moczo *et al.* (2010, 2011) explained why the conventional schemes have a problem with large V_P/V_S (see Section 8.3). Let us finish this very brief overview of the traditional (historical) displacement conventional-grid schemes with two important pioneering articles by Frankel and Vidale (1992) and Frankel (1993), which started the important period of 3D FD modelling of earthquake ground motion.

Being motivated by fundamental problems of the traditional (or historical) displacement conventional-grid schemes as well as by the difficulty with which the staggered-grid schemes handle complex geometries (e.g., free-surface topography), Kreiss, Petersson, Sjögreen and their collaborators have been developing a systematic novel approach for solving the 2nd-order displacement-formulation equation of motion by the FDM. For example, Nilsson *et al.* (2007) developed a (2,2) 3D displacement conventional-grid scheme based on discretization satisfying a summation-by-parts principle. The summation-by-parts discretization guarantees stability of the scheme for all V_P/V_S values. Nilsson *et al.* proved that the discrete energy is conserved by the scheme, for equations with variable coefficients on a bounded domain with traction-free or Dirichlet boundary conditions. Appelö and Petersson (2009) generalized the summation-by-parts approach to curvilinear grids, allowing the free surface boundary condition to be imposed along a realistic topography. More recently, Sjögreen and Petersson (2012) generalized the approach by Nilsson *et al.* (2007) and developed a 2D (4,4) scheme for solving the 2nd-order displacement-formulation equation of motion. Their spatial discretization satisfies the summation-by-parts principle and allows for heterogeneous materials and traction-free boundary conditions. The essential element in their generalization is the 4th-order accurate approximation of the 2nd spatial derivative with a variable coefficient, e.g., $\frac{\partial}{\partial x}\left(\mu(x)\frac{\partial u}{\partial x}\right)$, consistent with the approximation of the 2nd mixed spatial derivative, e.g., $\frac{\partial}{\partial x}\left(\mu(x)\frac{\partial u}{\partial y}\right)$, such that an energy estimate can be obtained. Compared to the previous summation-by-parts approximations, they use one virtual point outside the physical boundary. This makes it possible to enforce boundary conditions in a point-wise manner and avoid the use of projections or penalty terms. The explicit 4th-order accurate temporal discretization is energy conserving.

Kreiss and Petersson (2012) analyzed the (homogeneous medium) half-plane problem of the 2nd-order displacement-formulation equation of motion subject to the traction-free boundary condition. They developed a normal mode analysis using a modified equation approach and analyzed the influence of truncation errors in a pth-order accurate numerical approximation of the free surface boundary condition. They explained why the number of grid points per wavelength of the surface Rayleigh wave must be proportional to $(V_P/V_S)^{2/p}$ to achieve a constant phase error in the numerical solution when V_P/V_S is very large.

8.1.2 *Velocity–stress staggered-grid schemes*

Problems with instabilities and numerical dispersion produced by the mixed boundary conditions in the conventional schemes led Madariaga (1974, 1976) to introduce the velocity–stress staggered-grid (VS SG) scheme motivated by the staggered-grid scheme developed

by Yee (1966) for solving Maxwell's equations. Madariaga used the formulation for modelling rupture propagation. Virieux and Madariaga (1982) further elaborated the VS SG scheme for studying dynamic shear cracks. Virieux (1984) introduced the 2D (2,2) VS SG scheme for modelling SH waves and Virieux (1986) presented the corresponding P-SV scheme. Virieux (1986) found that the stability condition of his P-SV scheme as well as the grid P-wave phase velocity is independent of Poisson's ratio. The grid S-wave phase velocity depends on Poisson's ratio (through V_P/V_S) but is rather insensitive to V_P/V_S, and its behaviour does not degrade with increasing V_P/V_S. None of these properties is the case for the conventional schemes. The staggered-grid schemes have become the dominant type of schemes in the FD modelling of seismic wave propagation and earthquake motion. In order to decrease the number of grid points per minimum wavelength and thus increase computational efficiency, Levander (1988) introduced the 4th-order approximation in space in his 2D P-SV (2,4) VS SG scheme. Graves (1993), Olsen (1994) and Pitarka *et al*. (1997) introduced 3D (2,4) VS SG schemes, applied them to modelling of earthquake ground motion, and significantly promoted the FD modelling of earthquake ground motion. Yomogida and Etgen (1993) developed the (2,8) displacement–stress staggered-grid scheme and applied it for modelling wave propagation in the Los Angeles basin for the 1988 Whittier Narrows earthquake.

Igel *et al*. (1995) described the problems of the staggered-grid schemes in modelling seismic wave propagation in anisotropic media. Recently, Lisitsa and Vishnevskiy (2010) and Bernth and Chapman (2011) showed the generalization of the standard staggered grid to the so-called Lebedev grid, which may be considered a natural choice for an anisotropic medium.

8.1.3 Displacement–stress schemes on the grid staggered in space

In order to further reduce the memory requirements, Luo and Schuster (1990) suggested a displacement–stress 2D P-SV scheme which they called a parsimonious scheme. Because the scheme does not integrate stress in time, the stress-tensor components are only temporary quantities and the scheme is staggered only in space. The displacement–stress scheme in 3D needs only 75% of the memory needed by the velocity–stress scheme. Rodrigues (1993) and Yomogida and Etgen (1993) developed (2,8) 3D displacement–stress schemes, and Moczo *et al*. (2002) a (2,4) scheme with volume harmonic averaging of elastic moduli and volume arithmetic averaging of density.

8.1.4 Velocity–stress partly-staggered-grid schemes

For imposing the fault boundary conditions in modelling rupture dynamics, Andrews (1973) and independently Day (1977, 1982) introduced the partly-staggered grid. Magnier *et al*. (1994) elaborated the partly-staggered-grid scheme in order to incorporate anisotropy – a task not natural for staggered-grid schemes. Zhang (1997, 1999) presented his

quadrangle-grid velocity–stress scheme which is, in fact, the partly-staggered-grid scheme. Saenger and his colleagues (e.g., Saenger *et al*. 2000, Saenger and Bohlen 2004, Bohlen and Saenger 2006) elaborated and considerably promoted the application of partly-staggered-grid schemes. Saenger and his colleagues use the term 'new rotated staggered grid'. In fact, the grid in their articles was not new and the term 'rotated' reflects one feature of one particular partly-staggered-grid scheme, which is not substantial. The (2,2) displacement–stress version of the partly-staggered-grid scheme is equivalent to the (2,2) FE scheme with 1-point Gauss integration (see Section 8.2). Consequently and inherently, it may have a problem with the hourglass modes that have to be artificially suppressed.

8.1.5 Optimally accurate schemes

In the era of the staggered-grid schemes, Geller and Takeuchi (1995, 1998) and Takeuchi and Geller (2000) made an important contribution to the theory of the FD schemes and developed their optimally accurate FD schemes in application to the Galerkin-type weak form of Strang and Fix (1973) and Geller and Ohminato (1994). In their schemes displacement is the sole dependent variable, in contrast to the staggered-grid schemes. The clever idea of Geller and Takeuchi (1995) was to minimize the error of the numerical solution first of all at eigenfrequencies (or resonant frequencies), that is, at frequencies at which oscillatory motion of a linear mechanical system or finite volume of elastic continuum is naturally most amplified. Geller and Takeuchi (1995) used the 1st-order Born theory and a normal mode expansion to obtain formal estimates of the relative error of the numerical solution and a general criterion for what they named optimally accurate operators. The criterion requires that the inner product of an eigenfunction and the net error of the discretized equation of motion should be approximately equal to zero when the operand is the eigenfunction and the frequency is equal to the corresponding eigenfrequency. The criterion can be used to derive optimally accurate operators without knowing the actual values of the eigenfrequencies and eigenfunctions. Geller and Takeuchi (1995) showed that in the case of a heterogeneous medium the criterion is the logical extension of the criterion to minimize grid dispersion of phase velocity for a homogeneous medium. Geller and Takeuchi (1998) used the criterion to develop an optimally accurate 2nd-order FDTD scheme for the elastic 1D case. Takeuchi and Geller (2000) then developed optimally accurate FDTD operators for the 2D and 3D cases. Mizutani (2002) developed a scheme capable of accounting for an arbitrary position of the material discontinuity in the grid.

Whereas optimally accurate FDTD schemes require at least twice the CPU time per grid point and time step compared to 2nd-order staggered-grid FD schemes, they yield accuracy improvements on the order of 10 (for 1D), 50 (for 2D), or 100 (for 3D). From this point of view they are cost effective.

The optimization yields implicit schemes. Geller and Takeuchi (1998) applied the predictor-corrector algorithm in order to avoid solving large systems of algebraic equations. Thus, the actual computational schemes are explicit.

Kristek and Moczo (2006) numerically compared the 1D (2,2) conventional scheme, the (2,4) staggered-grid scheme and the optimally accurate scheme. The results confirmed the superior accuracy of the optimally accurate scheme with almost negligible grid dispersion.

Despite its superior accuracy, we do not apply the optimally accurate scheme for modelling earthquake motion in surface local structures. This is because the conventional scheme serves as a predictor. Consequently, the predictor is in media with large V_P / V_S so inaccurate that the corrector is not capable to 'correct' the 'predicted' values.

In media with low V_P / V_S the scheme is probably the most accurate FD scheme.

8.1.6 *Velocity–stress schemes on the collocated grid*

The 'ultimate' grid for the velocity–stress schemes should be the collocated grid (also nonstaggered or unstaggered) in which all particle-velocity and stress-tensor components share each grid position. From this point of view, the collocated grid is a natural grid not only for imposing boundary conditions (at the planar or nonplanar free surface, material interface or dynamically rupturing fault) but also for anisotropic media. It is, however, necessary to avoid the centred approximations of temporal and spatial derivatives. Their use would cause the presence of odd–even decoupling in time and space. Zhang and Chen (2006) and Zhang *et al*. (2012) therefore applied a MacCormack scheme in which the centred approximation is split into forward and backward approximations. The original (2,2) MacCormack scheme (MacCormack 1969) was extended to the (2,4) scheme by Gottlieb and Turkel (1976). Bayliss *et al*. (1986) combined the scheme with the operator splitting-time integration. Zhang and Chen (2006) and Zhang *et al*. (2012) developed a (4,4) MacCormack-type scheme in which one-sided operators are alternately applied in the multistage Runge–Kutta time integration algorithm. The applied one-sided approximations were developed by Tam and Webb (1993) and Hixon (1997).

Here we do not review the development of other aspects of FD schemes. The developments are concisely characterized in the chapters on rheological models, free surfaces, discontinuous grids, PML, earthquake source dynamics and in the following sections of this chapter.

8.2 Schemes on staggered, partly-staggered, collocated and conventional grids

In this section we assume a smoothly and weakly heterogeneous isotropic elastic unbounded medium. We briefly indicate the velocity–stress staggered-grid and partly-staggered-grid schemes as well as the displacement conventional-grid scheme. For brevity, recall just the equations for v_x and σ_{xx}:

$$
\begin{aligned}
\rho \frac{\partial v_x}{\partial t} &= \frac{\partial \sigma_{xx}}{\partial x} + \frac{\partial \sigma_{xy}}{\partial y} + \frac{\partial \sigma_{xz}}{\partial z} + f_x \\
\frac{\partial \sigma_{xx}}{\partial t} &= (\lambda + 2\mu) \frac{\partial v_x}{\partial x} + \mu \frac{\partial v_y}{\partial y} + \mu \frac{\partial v_z}{\partial z}
\end{aligned}
\tag{8.1}
$$
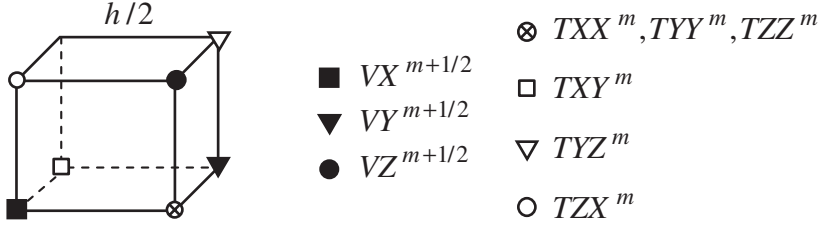
Figure 8.1 Grid cell of the staggered grid.

in the velocity–stress formulation and

$$
\rho \frac{\partial^2 u_x}{\partial t^2} = \frac{\partial}{\partial x}\left[(\lambda + 2\mu)\,\frac{\partial u_x}{\partial x}\right] + \frac{\partial}{\partial y}\left(\mu\,\frac{\partial u_x}{\partial y}\right) + \frac{\partial}{\partial z}\left(\mu\,\frac{\partial u_x}{\partial z}\right)
$$

$$
+ \frac{\partial}{\partial x}\left(\lambda\,\frac{\partial u_y}{\partial y}\right) + \frac{\partial}{\partial x}\left(\lambda\,\frac{\partial u_z}{\partial z}\right) + \frac{\partial}{\partial y}\left(\mu\,\frac{\partial u_y}{\partial x}\right) + \frac{\partial}{\partial z}\left(\mu\,\frac{\partial u_z}{\partial x}\right) + f_x \quad (8.2)
$$

in the displacement formulation. Denote the discrete grid values of the particle-velocity components v_x, v_y, v_z by VX, VY, VZ, respectively. Similarly denote the stress-tensor components σ_{xx}, σ_{xy}, σ_{zx} by TXX, TXY, TZX.

8.2.1 (2,4) velocity–stress scheme on the staggered grid

Figure 8.1 shows the grid cell. We may approximate the first of Eqs. (8.1) at the time level m and spatial grid position $I, K + 1/2, L + 1/2$. In the staggered grid we have all quantities exactly at the positions at which we need them for the most natural approximations of derivatives. The spatial distribution is unambiguous, complementary and there is no redundancy. This is the beauty of the staggered grid. The schemes for v_x and σ_{xx} are

$$
VX_{I,K+1/2,L+1/2}^{m+1/2}
$$

$$
= VX_{I,K+1/2,L+1/2}^{m-1/2} + \frac{\Delta}{\rho_{I,K+1/2,L+1/2}}\, f|_{I,K+1/2,L+1/2}^{m}
$$

$$
+ \frac{1}{\rho_{I,K+1/2,L+1/2}}\frac{\Delta}{h}\Bigg[\frac{9}{8}\left(TXX_{I+1/2,K+1/2,L+1/2}^{m} - TXX_{I-1/2,K+1/2,L+1/2}^{m}\right)
$$

$$
- \frac{1}{24}\left(TXX_{I+3/2,K+1/2,L+1/2}^{m} - TXX_{I-3/2,K+1/2,L+1/2}^{m}\right)
$$

$$
+ \frac{9}{8}\left(TXY_{I,K+1,L+1/2}^{m} - TXY_{I,K,L+1/2}^{m}\right) - \frac{1}{24}\left(TXY_{I,K+2,L+1/2}^{m} - TXY_{I,K-1,L+1/2}^{m}\right)
$$

$$
+ \frac{9}{8}\left(TZX_{I,K+1/2,L+1}^{m} - TZX_{I,K+1/2,L}^{m}\right) - \frac{1}{24}\left(TZX_{I,K+1/2,L+2}^{m} - TZX_{I,K+1/2,L-1}^{m}\right)\Bigg]
$$

$$
(8.3)
$$

Figure 8.2 Grid cell of the partly-staggered grid.

and

$$TXX^m_{I+1/2,K+1/2,L+1/2}$$

$$= TXX^{m-1}_{I+1/2,K+1/2,L+1/2}$$

$$+ \frac{\Delta}{h} \left\{ (\lambda + 2\mu)_{I+1/2,K+1/2,L+1/2} \left[\frac{9}{8} \left(VX^{m-1/2}_{I+1,K+1/2,L+1/2} - VX^{m-1/2}_{I,K+1/2,L+1/2} \right) \right. \right.$$

$$\left. - \frac{1}{24} \left(VX^{m-1/2}_{I+2,K+1/2,L+1/2} - VX^{m-1/2}_{I-1,K+1/2,L+1/2} \right) \right]$$

$$+ \lambda_{I+1/2,K+1/2,L+1/2} \left[\frac{9}{8} \left(VY^{m-1/2}_{I+1/2,K+1,L+1/2} - VY^{m-1/2}_{I+1/2,K,L+1/2} \right) \right.$$

$$\left. - \frac{1}{24} \left(VY^{m-1/2}_{I+1/2,K+2,L+1/2} - VY^{m-1/2}_{I+1/2,K-1,L+1/2} \right) \right]$$

$$+ \lambda_{I+1/2,K+1/2,L+1/2} \left[\frac{9}{8} \left(VZ^{m-1/2}_{I+1/2,K+1/2,L+1} - VZ^{m-1/2}_{I+1/2,K+1/2,L} \right) \right.$$

$$\left. \left. - \frac{1}{24} \left(VZ^{m-1/2}_{I+1/2,K+1/2,L+2} - VZ^{m-1/2}_{I+1/2,K+1/2,L-1} \right) \right] \right\} \tag{8.4}$$

On the other hand, we can immediately realize that it would be useful to have all particle-velocity components at the same grid position because this is what we have from measurements. It would also be useful to have all stress-tensor components at the same grid position because this would ease the simulation of the traction-free condition at the free surface. Finally, it would be useful to have all field variables at the same position for imposing boundary conditions at internal interfaces and, of course, for modelling wave propagation in anisotropic media. The mentioned aspects are partly addressed by schemes on the partly-staggered grid.

8.2.2 (2,4) velocity–stress scheme on the partly-staggered grid

Figure 8.2 shows the grid cell. Consider first approximating the spatial derivative of σ_{xx}:

$$\left. \frac{\partial \sigma_{xx}}{\partial x} \right|^m_I \approx \frac{9}{8} \left(TXX^m_{I+1/2} - TXX^m_{I-1/2} \right) - \frac{1}{24} \left(TXX^m_{I+3/2} - TXX^m_{I-3/2} \right) \tag{8.5}$$

Because we do not have the *TXX* values along the grid line parallel with the *x*-axis and going through the grid positions with indices (K, L), we approximate the derivative as an arithmetic average of approximations (8.5) along four grid lines parallel with the *x*-axis and going through the grid positions with indices $(K - 1/2, L - 1/2)$, $(K - 1/2, L + 1/2)$, $(K + 1/2, L - 1/2)$ and $(K + 1/2, L + 1/2)$, respectively. Similarly, we approximate all spatial derivatives. The resulting schemes are

$$
VX_{I,K,L}^{m+1/2} = VX_{I,K,L}^{m-1/2} + \frac{\Delta}{\rho_{I,K,L}} \, f|_{I,K,L}^{m} + \frac{1}{\rho_{I,K+1/2,L+1/2}}
$$

$$
\times \frac{\Delta}{4h} \left\{ \tfrac{9}{8} \left(TXX_{I+1/2,K-1/2,L-1/2}^{m} - TXX_{I-1/2,K-1/2,L-1/2}^{m} \right) \right.
$$

$$
- \tfrac{1}{24} \left(TXX_{I+3/2,K-1/2,L-1/2}^{m} - TXX_{I-3/2,K-1/2,L-1/2}^{m} \right)
$$

$$
+ \tfrac{9}{8} \left(TXX_{I+1/2,K-1/2,L+1/2}^{m} - TXX_{I-1/2,K-1/2,L+1/2}^{m} \right)
$$

$$
- \tfrac{1}{24} \left(TXX_{I+3/2,K-1/2,L+1/2}^{m} - TXX_{I-3/2,K-1/2,L+1/2}^{m} \right)
$$

$$
+ \tfrac{9}{8} \left(TXX_{I+1/2,K+1/2,L-1/2}^{m} - TXX_{I-1/2,K+1/2,L-1/2}^{m} \right)
$$

$$
- \tfrac{1}{24} \left(TXX_{I+3/2,K+1/2,L-1/2}^{m} - TXX_{I-3/2,K+1/2,L-1/2}^{m} \right)
$$

$$
+ \tfrac{9}{8} \left(TXX_{I+1/2,K+1/2,L+1/2}^{m} - TXX_{I-1/2,K+1/2,L+1/2}^{m} \right)
$$

$$
- \tfrac{1}{24} \left(TXX_{I+3/2,K+1/2,L+1/2}^{m} - TXX_{I-3/2,K+1/2,L+1/2}^{m} \right)
$$

$$
+ \tfrac{9}{8} \left(TXY_{I-1/2,K+1/2,L-1/2}^{m} - TXY_{I-1/2,K-1/2,L-1/2}^{m} \right)
$$

$$
- \tfrac{1}{24} \left(TXY_{I-1/2,K+3/2,L-1/2}^{m} - TXY_{I-1/2,K-3/2,L-1/2}^{m} \right)
$$

$$
+ \tfrac{9}{8} \left(TXY_{I-1/2,K+1/2,L+1/2}^{m} - TXY_{I-1/2,K-1/2,L+1/2}^{m} \right)
$$

$$
- \tfrac{1}{24} \left(TXY_{I-1/2,K+3/2,L+1/2}^{m} - TXY_{I-1/2,K-3/2,L+1/2}^{m} \right)
$$

$$
+ \tfrac{9}{8} \left(TXY_{I+1/2,K+1/2,L-1/2}^{m} - TXY_{I+1/2,K-1/2,L-1/2}^{m} \right)
$$

$$
- \tfrac{1}{24} \left(TXY_{I+1/2,K+3/2,L-1/2}^{m} - TXY_{I+1/2,K-3/2,L-1/2}^{m} \right)
$$

$$
+ \tfrac{9}{8} \left(TXY_{I+1/2,K+1/2,L+1/2}^{m} - TXY_{I+1/2,K-1/2,L+1/2}^{m} \right)
$$

$$
- \tfrac{1}{24} \left(TXY_{I+1/2,K+3/2,L+1/2}^{m} - TXY_{I+1/2,K-3/2,L+1/2}^{m} \right)
$$

$$
+ \tfrac{9}{8} \left(TXZ_{I-1/2,K-1/2,L+1/2}^{m} - TXZ_{I-1/2,K-1/2,L-1/2}^{m} \right)
$$

$$
- \tfrac{1}{24} \left(TXZ_{I-1/2,K-1/2,L+3/2}^{m} - TXZ_{I-1/2,K-1/2,L-3/2}^{m} \right)
$$

$$+ \tfrac{9}{8}\left(TXZ^m_{I-1/2,K+1/2,L+1/2} - TXZ^m_{I-1/2,K+1/2,L-1/2}\right)$$

$$- \tfrac{1}{24}\left(TXZ^m_{I-1/2,K+1/2,L+3/2} - TXZ^m_{I-1/2,K+1/2,L-3/2}\right)$$

$$+ \tfrac{9}{8}\left(TXZ^m_{I+1/2,K-1/2,L+1/2} - TXZ^m_{I+1/2,K-1/2,L-1/2}\right)$$

$$- \tfrac{1}{24}\left(TXZ^m_{I+1/2,K-1/2,L+3/2} - TXZ^m_{I+1/2,K-1/2,L-3/2}\right)$$

$$+ \tfrac{9}{8}\left(TXZ^m_{I+1/2,K+1/2,L+1/2} - TXZ^m_{I+1/2,K+1/2,L-1/2}\right)$$

$$- \tfrac{1}{24}\left(TXZ^m_{I+1/2,K+1/2,L+3/2} - TXZ^m_{I+1/2,K+1/2,L-3/2}\right)\Big\} \tag{8.6}$$

and

$$TXX^m_{I+1/2,K+1/2,L+1/2}$$

$$= TXX^{m-1}_{I+1/2,K+1/2,L+1/2} + \frac{\Delta}{4h}\Big\{ (\lambda + 2\mu)_{I+1/2,K+1/2,L+1/2}$$

$$\times\Big[\tfrac{9}{8}\left(VX^{m-1/2}_{I+1,K,L} - VX^{m-1/2}_{I,K,L}\right) - \tfrac{1}{24}\left(VX^{m-1/2}_{I+2,K,L} - VX^{m-1/2}_{I-1,K,L}\right)$$

$$+ \tfrac{9}{8}\left(VX^{m-1/2}_{I+1,K,L+1} - VX^{m-1/2}_{I,K,L+1}\right) - \tfrac{1}{24}\left(VX^{m-1/2}_{I+2,K,L+1} - VX^{m-1/2}_{I-1,K,L+1}\right)$$

$$+ \tfrac{9}{8}\left(VX^{m-1/2}_{I+1,K+1,L} - VX^{m-1/2}_{I,K+1,L}\right) - \tfrac{1}{24}\left(VX^{m-1/2}_{I+2,K+1,L} - VX^{m-1/2}_{I-1,K+1,L}\right)$$

$$+ \tfrac{9}{8}\left(VX^{m-1/2}_{I+1,K+1,L+1} - VX^{m-1/2}_{I,K+1,L+1}\right) - \tfrac{1}{24}\left(VX^{m-1/2}_{I+2,K+1,L+1} - VX^{m-1/2}_{I-1,K+1,L+1}\right)\Big]$$

$$+ \lambda_{I+1/2,K+1/2,L+1/2}\Big[\tfrac{9}{8}\left(VY^{m-1/2}_{I,K+1,L} - VY^{m-1/2}_{I,K,L}\right) - \tfrac{1}{24}\left(VY^{m-1/2}_{I,K+2,L} - VY^{m-1/2}_{I,K-1,L}\right)$$

$$+ \tfrac{9}{8}\left(VY^{m-1/2}_{I,K+1,L+1} - VY^{m-1/2}_{I,K,L+1}\right) - \tfrac{1}{24}\left(VY^{m-1/2}_{I,K+2,L+1} - VY^{m-1/2}_{I,K-1,L+1}\right)$$

$$+ \tfrac{9}{8}\left(VY^{m-1/2}_{I+1,K+1,L} - VY^{m-1/2}_{I+1,K,L}\right) - \tfrac{1}{24}\left(VY^{m-1/2}_{I+1,K+2,L} - VY^{m-1/2}_{I+1,K-1,L}\right)$$

$$+ \tfrac{9}{8}\left(VY^{m-1/2}_{I+1,K+1,L+1} - VY^{m-1/2}_{I+1,K,L+1}\right) - \tfrac{1}{24}\left(VY^{m-1/2}_{I+1,K+2,L+1} - VY^{m-1/2}_{I+1,K-1,L+1}\right)\Big]$$

$$+ \lambda_{I+1/2,K+1/2,L+1/2}\Big[\tfrac{9}{8}\left(VZ^{m-1/2}_{I,K,L+1} - VZ^{m-1/2}_{I,K,L}\right) - \tfrac{1}{24}\left(VZ^{m-1/2}_{I,K,L+2} - VZ^{m-1/2}_{I,K,L-1}\right)$$

$$+ \tfrac{9}{8}\left(VZ^{m-1/2}_{I,K+1,L+1} - VZ^{m-1/2}_{I,K+1,L}\right) - \tfrac{1}{24}\left(VZ^{m-1/2}_{I,K+1,L+2} - VZ^{m-1/2}_{I,K+1,L-1}\right)$$

$$+ \tfrac{9}{8}\left(VZ^{m-1/2}_{I+1,K,L+1} - VZ^{m-1/2}_{I+1,K,L}\right) - \tfrac{1}{24}\left(VZ^{m-1/2}_{I+1,K,L+2} - VZ^{m-1/2}_{I+1,K,L-1}\right)$$

$$+ \tfrac{9}{8}\left(VZ^{m-1/2}_{I+1,K+1,L+1} - VZ^{m-1/2}_{I+1,K+1,L}\right) - \tfrac{1}{24}\left(VZ^{m-1/2}_{I+1,K+1,L+2} - VZ^{m-1/2}_{I+1,K+1,L-1}\right)\Big]\Big\}$$

$$\tag{8.7}$$

Clearly, one price for having all the stress-tensor components at one grid position and all the particle-velocity components at another grid position is the more complicated scheme. Compared to the staggered-grid scheme, the stencil is no larger in the direction of the

spatial derivative but it is wider in the directions perpendicular to the direction of the spatial derivative. The other price is not obvious. It is the principal possibility of hourglass (or zero-energy) modes. These have to be suppressed, for example, by introducing artificial attenuation.

The presence of hourglass modes can be easily understood based on the equivalence of the (2,2) displacement–stress partly-staggered scheme with the standard (2,2) displacement FE scheme with Gaussian 1-point integration – see Moczo *et al.* (2010, 2011).

Recall that the partly-staggered-grid schemes are also called rotated staggered-grid schemes according to articles by Sänger and his colleagues. We prefer the term 'partly-staggered-grid schemes' because the aspect of rotation in one particular scheme is not the most substantial aspect and this type of scheme was developed earlier without any rotation.

8.2.3 (4,4) velocity–stress scheme on the collocated grid

In the velocity–stress formulation in matrix form a vector of field variables is defined that comprises all particle-velocity and stress-tensor components. The use of the collocated grid makes it possible to have all nine field variables at each grid position. Application of centred FD approximations leads to odd–even decoupling. The standard 2$^{\text{nd}}$-order and also 4$^{\text{th}}$-order approximations (based on Taylor expansions) have large truncation errors compared to the approximations on the staggered grid. Zhang and Chen (2006) and Zhang *et al.* (2012) overcome these problems using a higher-order MacCormack scheme that uses a combination of the (noncentred) one-sided approximations in the multistage Runge–Kutta time-integration algorithm. The one-sided approximations are based on minimization of the dispersion error. As we indicated in Chapter 7, the effective resulting stencil is relatively long. Because the presentation of the 3D scheme is rather lengthy we refer to the article by Zhang *et al.* (2012).

8.2.4 Displacement scheme on the conventional grid

In Subsection 7.3.1 we showed how to avoid the spatial differentiation of the elastic modulus by using a mathematical trick suggested by Tikhonov and Samarskii. We could apply the same trick also in 3D. Moczo *et al.* (1999) presented the 3D (2,2) displacement conventional grid scheme as a generalization of the 2D scheme suggested by Zahradník (1995b) and Zahradník and Priolo (1995); see also Moczo *et al.* (2007a). While reasonably accurate in a heterogeneous medium the scheme has fundamental drawbacks: (1) its accuracy rapidly decreases with increasing value of the P-wave to S-wave speed ratio; (2) it is unstable at the solid–liquid interface; (3) it is computationally inefficient due to the (2,2) order of approximation. As far as we know, a displacement scheme on the conventional grid that would overcome all three problems has not been found. In the following section we present two (2,4) displacement conventional-grid schemes, but only for the homogeneous medium.

Here, we merely point out the aspect that appears to be the key problem even in a homogeneous medium. Consider, for example, the most straightforward 2nd-order approximations:

$$
\mu \frac{\partial^2 u_x}{\partial y^2}\bigg|_{I,K,L}^m
$$
$$
= \mu \frac{1}{h}\left[\frac{1}{h}\left(UX_{I,K+1,L}^m - UX_{I,K,L}^m\right) - \frac{1}{h}\left(UX_{I,K,L}^m - UX_{I,K-1,L}^m\right)\right]
$$
$$
\mu \frac{\partial^2 u_y}{\partial y \partial x}\bigg|_{I,K,L}^m \tag{8.8}
$$
$$
= \mu \frac{1}{2h}\left[\frac{1}{2h}\left(UY_{I+1,K+1,L}^m - UY_{I+1,K-1,L}^m\right) - \frac{1}{2h}\left(UY_{I-1,K+1,L}^m - UY_{I-1,K-1,L}^m\right)\right]
$$

In the case of the 2nd nonmixed derivative we first approximate the 1st derivatives at $I, K+1/2, L$ and $I, K-1/2, L$, each over the grid spacing h, and then we approximate the derivative of the 1st derivative at I, K, L, again over h. In the case of the 2nd mixed derivative we first approximate the x-derivative at I, K, L over $2h$ and then we approximate the y-derivative of the x-derivative at I, K, L, again over $2h$. Moczo *et al.* (2010, 2011) showed that the inhomogeneity in approximating derivatives – once over h, the other time over $2h$ – is the reason for the degrading accuracy of the standard-displacement conventional grid with increasing P-wave to S-wave speed ratio. Note that in the velocity–stress (or possibly displacement–stress) schemes on the staggered, partly-staggered and collocated grids there is no inhomogeneity in approximating spatial derivatives.

In Section 8.1 we mentioned a novel approach based on the summation-by-parts principle (e.g., Nilsson *et al.* 2007, Kreiss and Petersson 2012, Sjögreen and Petersson 2012). For the recent (4,4) scheme we refer to the article by Sjögreen and Petersson (2012).

8.3 Accuracy of FD schemes with respect to P-wave to S-wave speed ratio: analysis of local errors

A P-wave to S-wave speed ratio in surface sediments as large as 5 or more often has to be accounted for in the numerical modelling of seismic motion in sedimentary basins and valleys. Five is a common value in surface sediments, mainly under the water level, and 10, though relatively large, certainly is not the maximum possible value in the unconsolidated surface water-saturated sediments.

8.3.1 Equations and FD schemes

8.3.1.1 Equations

Consider an unbounded homogeneous perfectly elastic isotropic medium. The P-wave and S-wave speeds are $V_P \equiv \alpha \equiv [(\lambda + 2\mu)/\rho]^{1/2}$ and $V_S \equiv \beta \equiv (\mu/\rho)^{1/2}$, respectively. Here

ρ is density, λ and μ are Lamé elastic moduli. Define the P-wave to S-wave speed ratio V_P/V_S or r:

$$r \equiv \alpha/\beta \tag{8.9}$$

Throughout the chapter, r and V_P/V_S, α and V_P, and β and V_S will be used interchangeably for convenience. Consider the displacement–stress (DS) formulation of the equation of motion, (2.28) and (2.23), and the displacement (D) formulation, (2.29). The latter may be written as

$$
\begin{aligned}
\frac{\partial^2 u_x}{\partial t^2} &= \alpha^2 \left(\frac{\partial^2 u_x}{\partial x^2} + \frac{\partial^2 u_y}{\partial y \partial x} + \frac{\partial^2 u_z}{\partial z \partial x} \right) + \beta^2 \left(\frac{\partial^2 u_x}{\partial y^2} - \frac{\partial^2 u_y}{\partial y \partial x} + \frac{\partial^2 u_x}{\partial z^2} - \frac{\partial^2 u_z}{\partial z \partial x} \right) \\
\frac{\partial^2 u_y}{\partial t^2} &= \alpha^2 \left(\frac{\partial^2 u_y}{\partial y^2} + \frac{\partial^2 u_z}{\partial z \partial y} + \frac{\partial^2 u_x}{\partial x \partial y} \right) + \beta^2 \left(\frac{\partial^2 u_y}{\partial z^2} - \frac{\partial^2 u_z}{\partial z \partial y} + \frac{\partial^2 u_y}{\partial x^2} - \frac{\partial^2 u_x}{\partial x \partial y} \right) \\
\frac{\partial^2 u_z}{\partial t^2} &= \alpha^2 \left(\frac{\partial^2 u_z}{\partial z^2} + \frac{\partial^2 u_x}{\partial x \partial z} + \frac{\partial^2 u_y}{\partial y \partial z} \right) + \beta^2 \left(\frac{\partial^2 u_z}{\partial x^2} - \frac{\partial^2 u_x}{\partial x \partial z} + \frac{\partial^2 u_z}{\partial y^2} - \frac{\partial^2 u_y}{\partial y \partial z} \right)
\end{aligned} \tag{8.10}
$$

8.3.1.2 FD schemes

The FD schemes differ from each other by the equation formulation, grid and order of approximation. For conciseness we will use acronyms for the analyzed schemes: D indicates the displacement formulation, DS the displacement–stress formulation; CG indicates the conventional grid, PSG the partly-staggered grid, and SG the (spatially) staggered grid. The first number in parentheses indicates the order of approximation in time, the second number the order of approximation in space. The lower-case 'a' or 'b' indicates one of two variants of the 4th-order approximation. The schemes included in the analysis are:

FD D CG (2,2) traditional FD displacement conventional grid, 2nd order in time, 2nd order in space

FD DS PSG (2,2) FD displacement–stress partly-staggered grid, 2nd order in time, 2nd order in space

FD DS SG (2,2) FD displacement–stress (spatially) staggered grid, 2nd order in time, 2nd order in space

FD D CG (2,4a) FD displacement conventional grid, 2nd order in time, 4th order in space, variant a

FD D CG (2,4b) FD displacement conventional grid, 2nd order in time, 4th order in space, variant b

FD DS SG (2,4) FD displacement–stress (spatially) staggered grid 2nd order in time, 4th order in space

FD D CG (2,2), FD D CG (2,4a), FD D CG (2,4b) FD D CG (2,2), the 2nd-order FD scheme solving the strong-form equation of motion for displacement on the conventional grid, is obtained if the derivatives in Eqs. (8.10) are replaced using standard 2nd-order centred FD formulas approximating the 2nd nonmixed and mixed derivatives.

On the conventional grid we can find several 4th-order approximations to the 2nd non-mixed and mixed spatial derivatives. Here we consider two different schemes. FD D CG (2,4a) is the scheme with the minimum possible equal coefficients of the leading terms of the truncation errors for the mixed and nonmixed derivatives. FD D CG (2,4b) has the minimum possible spatial stencil and a relatively large difference between values of coefficients of the leading terms of the truncation errors for the mixed and nonmixed derivatives.

FD DS SG (2,2), FD DS SG (2,4) FD DS SG (2,2) is obtained in the following way: The 2nd temporal derivative in Eqs. (2.28) is replaced using the standard 2nd-order centred FD formula (approximating the 2nd derivative). The 1st spatial derivatives of the stress-tensor components in Eqs. (2.28) are replaced using the standard 2nd-order centred FD formula (approximating the 1st derivative). Then all the discrete stress-tensor components on the r.h.s. of the obtained schemes are replaced by their FD approximations. The approximations are obtained from Eqs. (2.23) in which the 1st derivatives are replaced using the standard 2nd-order centred FD formula (approximating the 1st derivative). In the resulting final scheme, only displacement components appear. This is important to note, given the fact that the scheme solves the DS formulation of the equation of motion on the spatially staggered grid. Note that this type of scheme is also called the parsimonious scheme.

FD DS SG (2,4) is obtained in the same way except that 4th-order FD approximations are used to replace the 1st spatial derivatives of the stress-tensor and displacement components.

FD DS PSG (2,2) It is reasonable to compare this 2nd-order scheme solving the DS formulation of the equation of motion on the partly-staggered grid with FD D CG (2,2) and FD DS SG (2,2). The scheme is obtained in the same way as FD DS SG (2,2) except that the FD approximations are more complicated. The complication is due to the fact that the stress-tensor components are displaced from the displacement components by half-grid spacing in all three Cartesian directions (Fig. 6.1). For example, in approximating the *x*-derivative of the stress-tensor component at a grid position of the displacement component, the required values of the stress-tensor components are obtained as arithmetic averages of the values at four stress-tensor component grid positions in the corresponding *yz*-grid planes.

We do not include the velocity–stress staggered-grid (VS SG) schemes. They differ from the FD DS SG schemes only in approximating temporal derivatives. Moczo *et al.* (2010) showed that the difference between the behaviours of the corresponding 2D schemes with respect to the V_P/V_S ratio is negligible.

8.3.1.3 Unified representation of FD schemes

All schemes can be represented in a unified form. Let $U_\xi^m = U_\xi^m (I, K, L)$ be a discrete approximation to $u_\xi (Ih, Kh, Lh, m\Delta) = u_\xi (x_I, y_K, z_L, t_m)$ with $\xi \in \{x, y, z\}$, h being a

Table 8.1 *Grid positions and weight coefficients for the D_{xx} operators defined by Eq. (8.12)*

D_{xx}^{scheme}	Δ_j				$576\,w_j^{xx}$			
	$j=0$	$j=1$	$j=2$	$j=3$	$j=0$	$j=1$	$j=2$	$j=3$
$D_{xx}^{\text{FD D CG (2,2)}}$	0	1			-576	576		
$D_{xx}^{\text{FD DS SG (2,2)}}$	0	1			-576	576		
$D_{xx}^{\text{FD D CG (2,4a)}}$	0	1	2	3	-400	288	144	-32
$D_{xx}^{\text{FD D CG (2,4b)}}$	0	1	2		-720	768	-48	
$D_{xx}^{\text{FD DS SG (2,4)}}$	0	1	2	3	-730	783	-54	1

grid spacing in each of the three Cartesian directions and Δ a time step. Each numerical scheme can be then written as (compare with Eqs. (8.10))

$$U_x^{m+1} = 2U_x^m - U_x^{m-1} + \Delta^2\beta^2 \left\{ r^2 \left(D_{xx}\left[U_x^m\right] + D_{yx}\left[U_y^m\right] + D_{zx}\left[U_z^m\right] \right) \right.$$
$$\left. + D_{yy}\left[U_x^m\right] - D_{yx}\left[U_y^m\right] + D_{zz}\left[U_x^m\right] - D_{zx}\left[U_z^m\right] \right\}$$
$$U_y^{m+1} = 2U_y^m - U_y^{m-1} + \Delta^2\beta^2 \left\{ r^2 \left(D_{yy}\left[U_y^m\right] + D_{zy}\left[U_z^m\right] + D_{xy}\left[U_x^m\right] \right) \right.$$
$$\left. + D_{zz}\left[U_y^m\right] - D_{zy}\left[U_z^m\right] + D_{xx}\left[U_y^m\right] - D_{xy}\left[U_x^m\right] \right\} \qquad (8.11)$$
$$U_z^{m+1} = 2U_z^m - U_z^{m-1} + \Delta^2\beta^2 \left\{ r^2 \left(D_{zz}\left[U_z^m\right] + D_{xz}\left[U_x^m\right] + D_{yz}\left[U_y^m\right] \right) \right.$$
$$\left. + D_{xx}\left[U_z^m\right] - D_{xz}\left[U_x^m\right] + D_{yy}\left[U_z^m\right] - D_{yz}\left[U_y^m\right] \right\}$$

The schemes differ from each other by the difference operators $D_{\xi\xi}$ and $D_{\xi\eta}$; $\xi, \eta \in \{x, y, z\}$ for approximating 2$^{\text{nd}}$ nonmixed and mixed spatial derivatives. For brevity we explicitly show only D_{xx} and D_{zx} operators. The other operators are easily obtained by even permutation of the Cartesian indices.

In the set of the considered schemes we can recognize two types of nonmixed operators. The first type can be expressed as

$$D_{xx}\left[\Psi\left(I, K, L\right)\right] = \frac{1}{h^2} \sum_{j=0}^{J} w_j^{xx} \left[\Psi\left(I - \Delta_j, K, L\right) + \Psi\left(I + \Delta_j, K, L\right)\right] \quad (8.12)$$

Here Ψ represents a displacement component. According to Eq. (8.12), operators of different schemes may differ from each other by the number of grid positions at which displacement components are used for the approximation and the weight coefficients w_j^{xx} of the considered displacement component at those grid positions. The grid positions and weight coefficients are given in Table 8.1.

Table 8.2 *Grid positions and weight coefficients for the* D_{zx}
operators defined by Eq. (8.14)

D_{zx}^{scheme}	Δ_j, Δ_n		w^{zx}
	$j, n = 1$	$j, n = 2$	
$D_{zx}^{\text{FD D CG}\,(2,2)}$	1		$\dfrac{1}{4}$
$D_{zx}^{\text{FD DS SG}\,(2,2)}$	1/2		1
$D_{zx}^{\text{FD D CG}\,(2,4a)}$	1	2	$\dfrac{1}{576}\begin{bmatrix} 256 & -32 \\ -32 & 4 \end{bmatrix}$
$D_{zx}^{\text{FD D CG}\,(2,4b)}$	1	2	$\dfrac{1}{576}\begin{bmatrix} 240 & -24 \\ -24 & 0 \end{bmatrix}$
$D_{zx}^{\text{FD DS SG}\,(2,4)}$	1/2	3/2	$\dfrac{1}{576}\begin{bmatrix} 729 & -27 \\ -27 & 1 \end{bmatrix}$

The second type, for FD DS PSG (2,2), can be expressed as

$$D_{xx}\left[\Psi\left(I, K, L\right)\right] = \frac{1}{h^2} \sum_{l=L-1}^{L+1} \sum_{k=K-1}^{K+1} \alpha_{l-L+2,k-K+2}^{xx} D_{xx}^{\text{FD D CG}\,(2,2)} \Psi\left(I, k, l\right)$$

$$\alpha_{i,j}^{xx} = \frac{1}{16} \begin{bmatrix} 1 & 2 & 1 \\ 2 & 4 & 2 \\ 1 & 2 & 1 \end{bmatrix} \tag{8.13}$$

Similarly, there are two types of mixed operators. The first one is

$$D_{zx}\left[\Psi\left(I, K, L\right)\right]$$

$$= \frac{1}{h^2} \sum_{n=1}^{N} \sum_{j=1}^{N} w_{nj}^{zx} [\Psi(I + \Delta_j, K, L + \Delta_n) - \Psi(I + \Delta_j, K, L - \Delta_n)$$

$$- \Psi(I - \Delta_j, K, L + \Delta_n) + \Psi(I - \Delta_j, K, L - \Delta_n)] \tag{8.14}$$

The grid positions and weight coefficients are given in Table 8.2.

The second type, for FD DS PSG (2,2), can be expressed as

$$D_{zx}\left[\Psi\left(I, K, L\right)\right] = \frac{1}{h^2} \sum_{k=K-1}^{K+1} \alpha_{k-K+2}^{zx} D_{zx}^{\text{FD D CG}\,(2,2)} \Psi\left(I, K, L\right)$$

$$\alpha_1^{zx} = \tfrac{1}{4}, \ \alpha_2^{zx} = \tfrac{1}{2}, \ \alpha_3^{zx} = \tfrac{1}{4} \tag{8.15}$$

8.3.1.4 Truncation errors of the discrete spatial operators

Table 8.3 shows the leading and first higher terms of the truncation errors of all operators defined by Eqs. (8.12)–(8.15). We analyze them later.

Table 8.3 *The leading and 1st higher terms of the truncation errors of the nonmixed and mixed spatial operators defined by Eqs. (8.12)–(8.15). (a) 2nd-order operators, (b) 4th-order operators*

(a) Operator
truncation error $\times 20160$

$D_{xx}^{\text{FD D CG (2,2)}}$

$$1680\ \Psi^{(4,0,0)}\,h^2 \qquad\qquad + 56\ \ \Psi^{(6,0,0)}\,h^4$$

$D_{zx}^{\text{FD D CG (2,2)}}$

$$6720\ \left(\tfrac{1}{2}\Psi^{(1,0,3)} + \tfrac{1}{2}\Psi^{(3,0,1)}\right)h^2$$
$$+\ 896\ \left(\tfrac{3}{16}\Psi^{(1,0,5)} + \tfrac{10}{16}\Psi^{(3,0,3)} + \tfrac{3}{16}\Psi^{(5,0,1)}\right)h^4$$

$D_{xx}^{\text{FD DS PSG (2,2)}}$

$$11760\ \left(\tfrac{3}{7}\Psi^{(2,0,2)} + \tfrac{1}{7}\Psi^{(4,0,0)} + \tfrac{3}{7}\Psi^{(2,2,0)}\right)h^2$$
$$+\ 2996\ \left(\tfrac{1}{107}\Big(2\Psi^{(6,0,0)} + 15\Psi^{(4,2,0)} + 15\Psi^{(4,0,2)} + 15\Psi^{(2,4,0)} + 45\Psi^{(2,2,2)} + 15\Psi^{(2,0,4)}\Big)\right)h^4$$

$D_{zx}^{\text{FD DS PSG (2,2)}}$

$$11760\ \left(\tfrac{2}{7}\Psi^{(1,0,3)} + \tfrac{3}{7}\Psi^{(1,2,1)} + \tfrac{2}{7}\Psi^{(3,0,1)}\right)h^2$$
$$+\ 2996\ \left(\tfrac{1}{107}\Big(6\Psi^{(1,0,5)} + 30\Psi^{(1,2,3)} + 15\Psi^{(1,4,1)} + 20\Psi^{(3,0,3)} + 30\Psi^{(3,2,1)} + 6\Psi^{(5,0,1)}\Big)\right)h^4$$

$D_{xx}^{\text{FD DS SG (2,2)}}$

$$1680\ \Psi^{(4,0,0)}\,h^2 \qquad\qquad + 56\ \ \Psi^{(6,0,0)}\,h^4$$

$D_{zx}^{\text{FD DS SG (2,2)}}$

$$1680\ \left(\tfrac{1}{2}\Psi^{(1,0,3)} + \tfrac{1}{2}\Psi^{(3,0,1)}\right)h^2 \qquad + 56\ \ \left(\tfrac{3}{16}\Psi^{(1,0,5)} + \tfrac{10}{16}\Psi^{(3,0,3)} + \tfrac{3}{16}\Psi^{(5,0,1)}\right)h^4$$

(b) Operator
truncation error $\times 20160$

$D_{xx}^{\text{FD D CG (2,4a)}}$

$$-\ 1344\ \Psi^{(6,0,0)}\,h^4 \qquad\qquad -\ 300\ \Psi^{(8,0,0)}\,h^6$$

$D_{zx}^{\text{FD D CG (2,4a)}}$

$$-\ 1344\ \left(\tfrac{1}{2}\Psi^{(1,0,5)} + \tfrac{1}{2}\Psi^{(5,0,1)}\right)h^4 \qquad -\ 160\ \left(\tfrac{1}{2}\Psi^{(1,0,7)} + \tfrac{1}{2}\Psi^{(7,0,1)}\right)h^6$$

$D_{zx}^{\text{FD D CG (2,4b)}}$

$$-\ 224\ \Psi^{(6,0,0)}\,h^4 \qquad\qquad -\ 20\ \ \Psi^{(8,0,0)}\,h^6$$

$D_{zx}^{\text{FD D CG (2,4b)}}$

$$-1904\ \left(\tfrac{6}{17}\Psi^{(1,0,5)} + \tfrac{5}{17}\Psi^{(3,0,3)} + \tfrac{6}{17}\Psi^{(5,0,1)}\right)h^4$$
$$-\ 440\ \left(\tfrac{4}{22}\Psi^{(1,0,7)} + \tfrac{7}{22}\Psi^{(3,0,5)} + \tfrac{7}{22}\Psi^{(5,0,3)} + \tfrac{4}{22}\Psi^{(7,0,1)}\right)h^6$$

$D_{xx}^{\text{FD DS SG (2,4)}}$

$$-\ 189\ \Psi^{(6,0,0)}\,h^4 \qquad\qquad -\tfrac{45}{4}\ \ \Psi^{(8,0,0)}\,h^6$$

$D_{zx}^{\text{FD DS SG (2,4)}}$

$$-\ 189\ \left(\tfrac{1}{2}\Psi^{(1,0,5)} + \tfrac{1}{2}\Psi^{(5,0,1)}\right)h^4 \qquad -\tfrac{45}{4}\ \left(\tfrac{1}{2}\Psi^{(1,0,7)} + \tfrac{1}{2}\Psi^{(7,0,1)}\right)h^6$$

8.3.2 Local errors

With reference to Subsection 7.2.7, any one of the considered schemes may be symbolically expressed in a unified form:

$$U_\xi^{m+1}(I, K, L) = numerical\_scheme\left\{U^{m-1}, U^m\right\} \tag{8.16}$$

or, equivalently,

$$U_\xi(I, K, L, t + \Delta) = numerical\_scheme\left\{U(t - \Delta), U(t)\right\} \tag{8.17}$$

$U(t - \Delta)$ and $U(t)$ represent displacement components at relevant grid positions around (I, K, L) at times $t - \Delta$ and t, respectively, and $\xi \in \{x, y, z\}$. A numerical solution in one time step may be then expressed as

$$U_\xi^N(I, K, L, t + \Delta) = numerical\_scheme\left\{U^E(t - \Delta), U^E(t)\right\} \tag{8.18}$$

where the upper index N indicates the numerical solution, and the upper index E indicates an exact value. If we know the exact value of displacement at any time, it is possible to define a relative local error in amplitude (see Subsection 7.2.7) as

$$\varepsilon_{ampl}^{Rel} = \left(\frac{\Delta_{ref}}{\Delta}\right)^2 \left|\frac{A^N - A^E}{A^E}\right| \tag{8.19}$$

with A^N being the amplitude of the numerical solution (modulus of the displacement vector) in one time step and A^E the exact amplitude – both evaluated at time $t + \Delta$. The value of the reference time step Δ_{ref} will be specified later.

In their analysis of the 2D 2nd-order FD and FE schemes, Moczo *et al.* (2010) also defined the relative error in the direction of the displacement vector (or error in polarization or angle). The 3D problem involves three displacement-vector components and two angles. This considerably complicates the quantification of the polarization error and direct comparison of their values with the values of the error in amplitude. It is therefore reasonable to define the error in the vector difference as

$$\varepsilon_{vdiff}^{Rel} = \left(\frac{\Delta_{ref}}{\Delta}\right)^2 \frac{1}{A^E}\left[\left(U_x^N - U_x^E\right)^2 + \left(U_y^N - U_y^E\right)^2 + \left(U_z^N - U_z^E\right)^2\right]^{1/2} \tag{8.20}$$

This absolute value of the vector difference between the numerically calculated displacement vector and the exact displacement vector comprises errors in both amplitude and polarization in one reasonable value. This value can be directly compared with the error in amplitude.
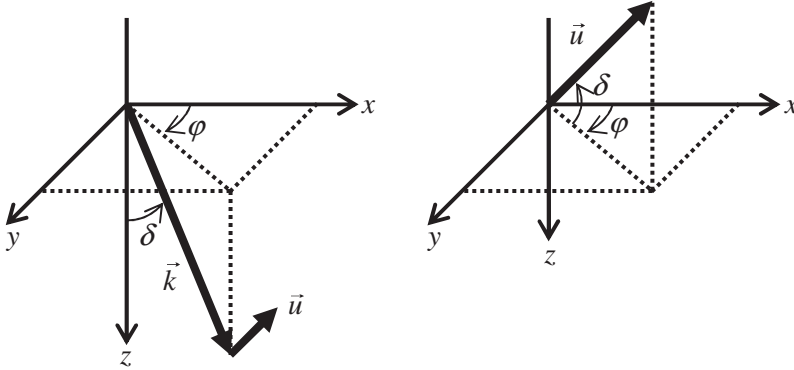
Figure 8.3 Cartesian coordinate system, angles φ and δ for defining a direction of propagation, displacement vector and displacement components of the plane S wave.

8.3.3 The exact and numerical values of displacement in a grid

Consider a harmonic plane S wave propagating in an unbounded homogeneous elastic isotropic medium as the exact solution in definitions of the local errors. Assuming a harmonic plane S wave polarized in a vertical plane determined by the z-axis and wavenumber vector $\vec{k}$, the displacement components are

$$u_\xi (x, y, z, t; \omega; \varphi, \delta) = A_\xi E^t E^x E^y E^z; \quad \xi \in \{x, y, z\} \tag{8.21}$$

where

$$
\begin{aligned}
E^t &= \exp[-i\omega t] \\
E^x &= \exp[ik_x x] & E^y &= \exp[ik_y y] & E^z &= \exp[ik_z z] \\
k_x &= k\cos\varphi\sin\delta & k_y &= k\sin\varphi\sin\delta & k_z &= k\cos\delta \\
A_x &= A\cos\varphi\cos\delta & A_y &= A\sin\varphi\cos\delta & A_z &= -A\sin\delta \\
k &= \omega/\beta, & 0 \le \delta \le \pi, & 0 \le \varphi \le 2\pi
\end{aligned} \tag{8.22}
$$

ω is the angular frequency, $k = |\vec{k}|$ is the wavenumber, δ is the angle between the positive z-axis and the wavenumber vector $\vec{k}$ (the direction of propagation), φ is the angle between the positive x-axis and the vertical plane determined by the z-axis and wavenumber vector $\vec{k}$; see Fig. 8.3. The restriction to the S wave is reasonable: numerical modelling of P-wave propagation poses a minor problem if the modelling comprises both types of waves. We will explain why this is so later. Note that the sign convention in Eqs. (8.22) is consistent with that used by Moczo *et al.* (2011).

Recalling spatial sampling $N_\lambda = \lambda/h$, Eq. (7.34), wavenumber k may be expressed as

$$k = \omega/\beta = 2\pi/(hN_\lambda) \tag{8.23}$$

and

$$k_x h = \frac{2\pi}{N_\lambda} \cos\varphi \sin\delta, \quad k_y h = \frac{2\pi}{N_\lambda} \sin\varphi \sin\delta, \quad k_z h = \frac{2\pi}{N_\lambda} \cos\delta \quad (8.24)$$

$$\omega = 2\pi\beta/(hN_\lambda) \quad (8.25)$$

Considering the stability condition for any of the numerical schemes in the form $\Delta \leq \Phi(h, \alpha, \beta)$ and the stability ratio $p = \Delta/\Phi; 0 < p \leq 1$, the time step Δ may be expressed as

$$\Delta = p\,\Phi(h, \alpha, \beta) \quad (8.26)$$

Without loss of generality, consider

$$x_I = 0, \quad y_K = 0, \quad z_L = 0, \quad t_m = 0$$

and evaluate errors at

$$x_I = 0, \quad y_K = 0, \quad z_L = 0, \quad t_{m+1} = \Delta \quad (8.27)$$

The real exact displacement at this space–time grid position is, see Eqs. (8.21) and (8.22),

$$\mathrm{Re}\left\{u_\xi(0, 0, 0, \Delta)\right\} = A_\xi \cos(\omega\Delta) \quad (8.28)$$

and the exact amplitude is

$$A^{\mathrm{E}} = \left([A_x \cos(\omega\Delta)]^2 + [A_y \cos(\omega\Delta)]^2 + [A_z \cos(\omega\Delta)]^2\right)^{1/2} = A|\cos(\omega\Delta)| \quad (8.29)$$

The exact values of (complex) displacements entering the r.h.s. of schemes (8.11) are evaluated as

$$\begin{aligned}
U_\xi^{m-1}(I, K, L) &= u_\xi(0, 0, 0, t = -\Delta; \omega; \varphi, \delta) = A_\xi \exp[+i\omega\Delta] \\
U_\xi^m(I, K, L) &= u_\xi(0, 0, 0, t = 0; \omega; \varphi, \delta) = A_\xi \\
U_\xi^m(I + \Delta_I, K + \Delta_K, L + \Delta_L) &= u_\xi(h\Delta_I, h\Delta_K, h\Delta_L, t = 0; \omega; \varphi, \delta) \\
&= A_\xi \exp[+ik_x h\Delta_I]\exp[+ik_y h\Delta_K]\exp[+ik_z h\Delta_L]
\end{aligned} \quad (8.30)$$

The grid-index increments Δ_I, Δ_K and Δ_L depend on a numerical scheme. Quantities $k_x h$, $k_y h$ and $k_z h$ are given by Eq. (8.24).

According to Eqs. (8.11)–(8.15), each scheme effectively includes the second power of quantity $(\beta/h)\,\Delta$. Quantities $\omega\Delta$, $(\beta/h)\,\Delta$ and Δ entering the numerical schemes and formulas for the errors are summarized in Table 8.4.

U_x^{m+1}, U_y^{m+1} and U_z^{m+1}, evaluated at (I, K, L), are obtained using schemes (8.11). The amplitude of the numerical solution is then

$$A^{\mathrm{N}} = \left([\mathrm{Re}\,\{U_x^{m+1}\}]^2 + [\mathrm{Re}\,\{U_y^{m+1}\}]^2 + [\mathrm{Re}\,\{U_z^{m+1}\}]^2\right)^{1/2} \quad (8.31)$$

In principle, any time step may be chosen as a reference time step Δ_{ref} appearing in formulas (7.104) and (8.20) for the errors. One reasonable choice is $\Delta_{ref} = \Delta$ for FD DS SG (2,4); $p = 0.9$, $N_\lambda = 6$, $r = 1.42$. The reason for FD DS SG (2,4) will become clear later; $N_\lambda = 6$ is the most common choice for the spatial sampling in the numerical modelling of earthquake

Table 8.4 *Quantities entering the numerical schemes and formulas for the errors*

	$\omega\Delta$	$(\beta/h)\Delta$	Δ
FD D CG (2,2)	$\dfrac{2\pi p}{N_\lambda} \dfrac{1}{\left(1+r^2\right)^{1/2}}$	$\dfrac{p}{\left(1+r^2\right)^{1/2}}$	$\dfrac{p}{N_\lambda} \dfrac{1}{\left(1+r^2\right)^{1/2}} \dfrac{\lambda}{\beta}$
FD DS PSG (2,2)	$\dfrac{2\pi p}{N_\lambda} \dfrac{1}{r}$	$\dfrac{p}{r}$	$\dfrac{p}{N_\lambda} \dfrac{1}{r} \dfrac{\lambda}{\beta}$
FD DS SG (2,2)	$\dfrac{2\pi p}{N_\lambda} \dfrac{1}{\sqrt{3}} \dfrac{1}{r}$	$\dfrac{1}{\sqrt{3}} p \dfrac{1}{r}$	$\dfrac{p}{N_\lambda} \dfrac{1}{\sqrt{3}} \dfrac{1}{r} \dfrac{\lambda}{\beta}$
FD D CG (2,4a) FD D CG (2,4b)	$\dfrac{2\pi p}{N_\lambda} 0.7 \dfrac{1}{\left(1+r^2\right)^{1/2}}$	$0.7 \dfrac{p}{\left(1+r^2\right)^{1/2}}$	$\dfrac{p}{N_\lambda} 0.7 \dfrac{1}{\left(1+r^2\right)^{1/2}} \dfrac{\lambda}{\beta}$
FD DS SG (2,4)	$\dfrac{2\pi p}{N_\lambda} \dfrac{6}{7\sqrt{3}} \dfrac{1}{r}$	$\dfrac{6}{7\sqrt{3}} p \dfrac{1}{r}$	$\dfrac{p}{N_\lambda} \dfrac{6}{7\sqrt{3}} \dfrac{1}{r} \dfrac{\lambda}{\beta}$

motion in surface sedimentary basins using the 4$^{\text{th}}$-order SG schemes, and $r = 1.42$ is taken instead of the exact minimum value $r = \sqrt{2}$.

The rightmost column in Table 8.4 includes the factor $\lambda/(\beta N_\lambda)$. It could be replaced by h/β but in both cases the time steps include explicitly the S-wave speed β in addition to the V_P/V_S ratio r. However, because the errors (7.104) and (8.20) include the ratio $\left(\Delta_{ref}/\Delta\right)^2$, the explicit presence of λ and β is removed from the errors. Consequently, apart from the absolute quantities φ and δ (angles determining the direction of propagation), errors $\varepsilon_{\text{ampl}}^{\text{Rel}}$ and $\varepsilon_{\text{vdiff}}^{\text{Rel}}$ depend only on the relative dimensionless quantities N_λ, p and r.

8.3.4 Equivalent spatial sampling for the errors in amplitude and the vector difference

Choose a reference maximum error as the maximum relative error in amplitude of FD DS SG (2,4) for $V_P/V_S = 10$ and $N_\lambda = 6$. This error is equal to 0.00112. An equivalent spatial sampling N_λ^{equiv} may be defined as a value at which the maximum relative error (a function of V_P/V_S) of a scheme is equal to the reference maximum error. The maximum relative error is determined as the maximum of errors calculated for angles $\varphi \in [0, 90]°$ and $\delta \in [0, 90]°$ with angle increment of 0.5°. Figure 8.4, left, shows the $N_\lambda^{\text{equiv}}(V_P/V_S)$ curves based on the relative error in amplitude for the stability ratio $p = 0.9$. The solid lines are used for the 4$^{\text{th}}$-order schemes, the dashed lines for the 2$^{\text{nd}}$-order schemes.

The curves for different values of the stability ratio differ from each other only negligibly. Small differences can be seen only for the lowest values of r. At first sight we realize that the equivalent spatial sampling ratios for FD DS SG (2,4), FD D CG (2,4a), FD DS SG (2,2) and FD DS PSG (2,2) depend only slightly on V_P/V_S. On the other hand, the equivalent spatial sampling ratios for FD D CG (2,4b) and FD D CG (2,2) considerably change with increasing V_P/V_S. FD D CG (2,2) is the least accurate scheme. Figure 8.4, right, shows the $N_\lambda^{\text{equiv}}(V_P/V_S)$ curves based on the relative error in the vector difference. The equivalent

Table 8.5 *The N_λ^{equiv} values for $p = 0.9$ and reference maximum error equal to 0.00112.*
Boldface: schemes for which N_λ^{equiv} based on the relative error in amplitude only
negligibly varies with V_P/V_S

V_P/V_S	**FD DS SG (2,4)**	**FD D CG (2,4a)**	**FD DS SG (2,2)**	FD D CG (2,4b)	**FD DS PSG (2,2)**	FD D CG (2,2)
	N_λ^{equiv} based on the relative error in amplitude					
1.42	**5.3**	**8.8**	**16.6**	7.8	**25.6**	15.4
5	**5.9**	**9.7**	**17.7**	14.0	**26.9**	75.4
10	**6.0**	**9.7**	**17.8**	19.7	**27.1**	153.5
	N_λ^{equiv} based on the relative error in the vector difference					
1.42	**5.3**	**8.8**	**16.6**	7.8	**25.6**	15.4
5	**8.1**	**13.1**	**33.3**	14.0	**47.5**	76.3
10	**11.5**	**18.7**	**67.3**	19.8	**97.5**	162.1
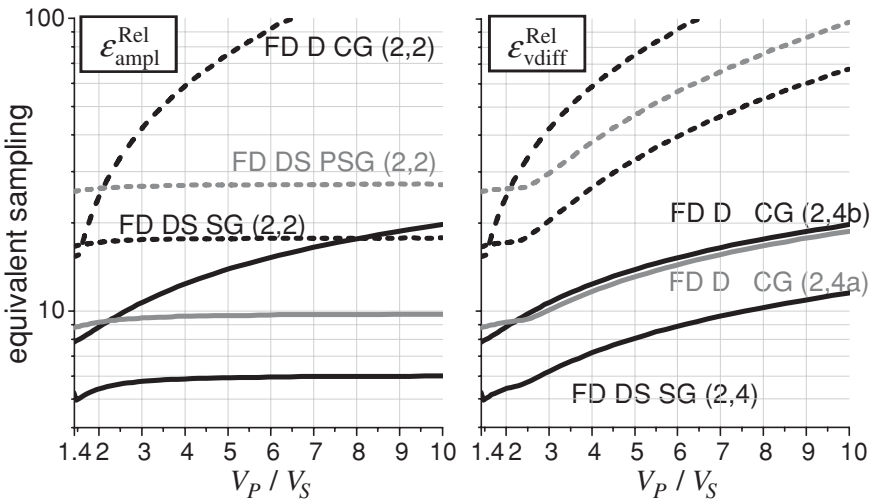
Figure 8.4 The $N_\lambda^{\text{equiv}}(V_P/V_S)$ curves. The equivalent spatial sampling N_λ^{equiv} is defined as the value at which the maximum absolute value of the relative error of a scheme is equal to the reference maximum error. The chosen reference maximum error, 0.00112, is equal to the maximum relative error in amplitude of FD DS SG (2,4) for $V_P/V_S = 10$ and $N_\lambda = 6$. The left panel shows curves for $\varepsilon_{\text{ampl}}^{\text{Rel}}$, the right panel shows curves for $\varepsilon_{\text{vdiff}}^{\text{Rel}}$.

spatial sampling ratios for each scheme increase with increasing V_P/V_S. Figure 8.4 clearly shows that, in terms of the equivalent spatial sampling, FD DS SG (2,4) is more accurate and more efficient than the other schemes. Table 8.5 lists the N_λ^{equiv} values for $p = 0.9$ and three values of V_P/V_S: 1.42, 5 and 10.

8.3.5 Essential summary based on the numerical investigation

The relative local error in amplitude of FD DS SG (2,4), FD D CG (2,4a), FD DS SG (2,2) and FD DS PSG (2,2) is almost independent of V_P/V_S. The error in the vector difference increases with increasing V_P/V_S. This can be explained only by the dependence of the polarization errors of all schemes on V_P/V_S. The dependence of the error in the vector difference on V_P/V_S has to be accounted for by a proper spatial sampling.

FD D CG (2,2) is the most sensitive to V_P/V_S and requires considerably denser spatial sampling than any other scheme if $V_P/V_S > 2$. The maximum errors in the vector difference of schemes FD DS SG (2,2) and FD DS PSG (2,2) increase with increasing V_P/V_S in the same way but FD DS PSG (2,2) requires denser spatial sampling than FD DS SG (2,2) in order to achieve the same accuracy. The maximum errors in the vector difference of all 4th-order schemes increase for $V_P/V_S > 3$ in the same way. Schemes FD D CG (2,4a) and FD D CG (2,4b) require denser spatial sampling than FD DS SG (2,4) in order to achieve the same accuracy. The 4th-order schemes are for $V_P/V_S > 3$ less sensitive to increasing V_P/V_S than the 2nd-order schemes.

8.3.6 Interpretation of the errors

8.3.6.1 The S and P waves seen by the equation of motion

The equation of motion (8.10) in concise form reads

$$\frac{\partial^2 u_i}{\partial t^2} = \alpha^2 \frac{\partial^2 u_j}{\partial x_j \partial x_i} + \beta^2 \left(\frac{\partial^2 u_i}{\partial x_j \partial x_j} - \frac{\partial^2 u_j}{\partial x_j \partial x_i} \right) \tag{8.32}$$

The S wave is solenoidal, that is, div $\vec{u} = \frac{\partial u_j}{\partial x_j} = 0$. Then, for the S wave,

$$\frac{\partial^2 u_j}{\partial x_j \partial x_i} = 0, \quad \frac{\partial^2 u_i}{\partial x_j \partial x_j} - \frac{\partial^2 u_j}{\partial x_j \partial x_i} = \frac{1}{\beta^2} \frac{\partial^2 u_i}{\partial t^2} \tag{8.33}$$

The P wave is irrotational, that is, rot $\vec{u}=0$ or $\varepsilon_{kji} \frac{\partial u_i}{\partial x_j} = 0$, where ε_{kji} is the Levi-Civita symbol. Then, for the P wave,

$$\frac{\partial^2 u_j}{\partial x_j \partial x_i} = \frac{1}{\alpha^2} \frac{\partial^2 u_i}{\partial t^2}, \quad \frac{\partial^2 u_i}{\partial x_j \partial x_j} - \frac{\partial^2 u_j}{\partial x_j \partial x_i} = 0 \tag{8.34}$$

8.3.6.2 The S and P waves seen by the FD scheme

A numerical scheme solving Eq. (8.32) can be written in the form

$$DA \left\{ \frac{\partial^2 u_i}{\partial t^2} \right\} \approx \alpha^2 DA \left\{ \frac{\partial^2 u_j}{\partial x_j \partial x_i} \right\} + \beta^2 DA \left\{ \frac{\partial^2 u_i}{\partial x_j \partial x_j} - \frac{\partial^2 u_j}{\partial x_j \partial x_i} \right\} \tag{8.35}$$

where *DA* means a discrete approximation. Equation (8.35) is, in fact, a concise symbolic form of Eqs. (8.11). With reference to Eq. (7.23), a discrete approximation to any operator

in general can be expressed as a sum of the exact differential operator and a truncation error (for which we will use symbol *TrunErr*). Equation (8.35) can be then written as

$$
\frac{\partial^2 u_i}{\partial t^2} + TrunErr\left\{\frac{\partial^2 u_i}{\partial t^2}\right\} \approx \alpha^2 \left(\frac{\partial^2 u_j}{\partial x_j \partial x_i} + TrunErr\left\{\frac{\partial^2 u_j}{\partial x_j \partial x_i}\right\}\right)
$$
$$
+ \beta^2 \left(\frac{\partial^2 u_i}{\partial x_j \partial x_j} - \frac{\partial^2 u_j}{\partial x_j \partial x_i} + TrunErr\left\{\frac{\partial^2 u_i}{\partial x_j \partial x_j} - \frac{\partial^2 u_j}{\partial x_j \partial x_i}\right\}\right)
$$

$$(8.36)$$

The harmonic plane S wave Considering the first of Eqs. (8.33), equality $\frac{\partial^2 u_i^S}{\partial t^2} = -\omega^2 u_i^S$, and the fact that each 2$^{\text{nd}}$ spatial derivative of a displacement-vector component is proportional to $-\omega^2 u_i^S/\beta^2$, Eq. (8.36) may be written as

$$
\left(1 + error_i^{tS}\right)\left(-\omega^2 u_i^S\right) \approx \alpha^2 \left(0 + error_i^{\alpha S}\right)\left(-\omega^2 u_i^S\right)\beta^{-2} + \left(1 + error_i^{\beta S}\right)\left(-\omega^2 u_i^S\right)
$$

$$(8.37)$$

and eventually

$$
u_i^S \approx \left(r^2 error_i^{\alpha S} + 1 + error_i^{\beta S} - error_i^{tS}\right) u_i^S
$$

$$(8.38)$$

The double-index summation rule does not apply to index i in Eqs. (8.37)–(8.51).

The error terms

$$
error_i^{\alpha S} = \frac{\beta^2 TrunErr\left\{\dfrac{\partial^2 u_j^S}{\partial x_j \partial x_i}\right\}}{-\omega^2 u_i^S},
$$
$$
error_i^{\beta S} = \frac{\beta^2 TrunErr\left\{\dfrac{\partial^2 u_i^S}{\partial x_j^2} - \dfrac{\partial^2 u_j^S}{\partial x_j \partial x_i}\right\}}{-\omega^2 u_i^S}
$$

$$(8.39)$$

do not depend on r, that is, V_P/V_S. However, the error term $error_i^{tS}$ does depend on r:

$$
error_i^{tS} = \frac{TrunErr\left\{\dfrac{\partial^2 u_i^S}{\partial t^2}\right\}}{-\omega^2 u_i^S} = c_1 \frac{1}{r^2} + c_2 \frac{1}{r^4} + \cdots
$$

$$(8.40)$$

Coefficients $c_l; l = 1, 2, \ldots$ do not depend on r. Note that the series in powers of $1/r^2$ is due to the 2$^{\text{nd}}$-order approximation to the 2$^{\text{nd}}$ temporal derivative. The squares of the time step, Δ^2, are expressed using $1/r^2$.

The harmonic plane P wave Considering the second of Eqs. (8.34), equality $\frac{\partial^2 u_i^P}{\partial t^2} = -\omega^2 u_i^P$, and the fact that each 2$^{\text{nd}}$ spatial derivative of a displacement-vector component is

proportional to $-\omega^2 u_i^P/\alpha^2$, Eq. (8.36) may be written as

$$\left(1 + error_i^{tP}\right)\left(-\omega^2 u_i^P\right) \approx \left(1 + error_i^{\alpha P}\right)\left(-\omega^2 u_i^P\right) + \beta^2\left(0 + error_i^{\beta P}\right)\left(-\omega^2 u_i^P\right)/\alpha^2 \tag{8.41}$$

and eventually

$$u_i^P \approx \left(1 + error_i^{\alpha P} + \frac{1}{r^2}error_i^{\beta P} - error_i^{tP}\right)u_i^P \tag{8.42}$$

Analogously to the error terms in Eqs. (8.39), $error_i^{\alpha P}$ and $error_i^{\beta P}$ do not depend on r. The dependence of $error_i^{tP}$ on r is analogous to that of $error_i^{tS}$ in Eq. (8.40).

Essential comparison of the P and S waves There is an important difference between Eq. (8.38) for the S wave and Eq. (8.42) for the P wave: whereas $r^2 error_i^{\alpha S}$ increases with increasing V_P/V_S, $\frac{1}{r^2}error_i^{\beta P}$ decreases with increasing V_P/V_S. This is why a large value of V_P/V_S does not pose a problem for the P wave.

8.3.6.3 Structure of the errors in amplitude and vector difference

Because we restrict our further discussion to the S wave, in the following section we will omit explicit indication of the S wave in the displacement-vector components and error terms. Recall Eq. (8.35). The analyzed schemes differ from each other by the approximations on the r.h.s. They share the same approximation to the 2nd time derivative:

$$DA\left\{\frac{\partial^2 u_i}{\partial t^2}\right\} \approx \frac{1}{\Delta^2}\left(u_i^{m+1} - 2u_i^m + u_i^{m-1}\right) \tag{8.43}$$

Using Eq. (8.43) in Eq. (8.35) we can get the scheme for the numerical displacement component at the time level $m+1$ in the form

$$^N u_i^{m+1} = 2u_i^m - u_i^{m-1} + \Delta^2\left(\alpha^2 DA\left\{\frac{\partial^2 u_j}{\partial x_j \partial x_i}\right\} + \beta^2 DA\left\{\frac{\partial^2 u_i}{\partial x_j \partial x_j} - \frac{\partial^2 u_j}{\partial x_j \partial x_i}\right\}\right) \tag{8.44}$$

Recalling the concept of the local error, Eqs. (8.16)–(8.20), we distinguish the numerical value, labelled N, on the l.h.s., from the exact values of the displacement components on the r.h.s. (not labelled). Subtracting u_i^{m+1} from both sides of Eq. (8.44), dividing the equation by Δ^2, and using Eq. (8.43), we obtain

$$\left(^N u_i^{m+1} - u_i^{m+1}\right)\frac{1}{\Delta^2} = -DA\left\{\frac{\partial^2 u_i}{\partial t^2}\right\} + \alpha^2 DA\left\{\frac{\partial^2 u_j}{\partial x_j \partial x_i}\right\} + \beta^2 DA\left\{\frac{\partial^2 u_i}{\partial x_j \partial x_j} - \frac{\partial^2 u_j}{\partial x_j \partial x_i}\right\} \tag{8.45}$$

Each of the discrete approximations on the r.h.s. can be replaced by the sum of the exact operator and truncation error. Then,

$$
\left({}^{\mathrm{N}}u_i^{m+1} - u_i^{m+1}\right)\frac{1}{\Delta^2} = -\frac{\partial^2 u_i}{\partial t^2} + \alpha^2 \frac{\partial^2 u_j}{\partial x_j \partial x_i} + \beta^2 \left(\frac{\partial^2 u_i}{\partial x_j \partial x_j} - \frac{\partial^2 u_j}{\partial x_j \partial x_i}\right)
$$
$$
- TrunErr\left\{\frac{\partial^2 u_i}{\partial t^2}\right\} + \alpha^2 TrunErr\left\{\frac{\partial^2 u_j}{\partial x_j \partial x_i}\right\}
$$
$$
+ \beta^2 TrunErr\left\{\frac{\partial^2 u_i}{\partial x_j \partial x_j} - \frac{\partial^2 u_j}{\partial x_j \partial x_i}\right\} \tag{8.46}
$$

The sum of the first three terms on the r.h.s. is equal to zero, see Eq. (8.32), and thus

$$
\left({}^{\mathrm{N}}u_i^{m+1} - u_i^{m+1}\right)\frac{1}{\Delta^2} = -TrunErr\left\{\frac{\partial^2 u_i}{\partial t^2}\right\} + \alpha^2 TrunErr\left\{\frac{\partial^2 u_j}{\partial x_j \partial x_i}\right\}
$$
$$
+ \beta^2 TrunErr\left\{\frac{\partial^2 u_i}{\partial x_j \partial x_j} - \frac{\partial^2 u_j}{\partial x_j \partial x_i}\right\} \tag{8.47}
$$

Considering Eqs. (8.39) and (8.40)

$$
\left({}^{\mathrm{N}}u_i^{m+1} - u_i^{m+1}\right)\frac{1}{\Delta^2} = \left(error_i^{tS} - r^2 error_i^{\alpha S} - error_i^{\beta S}\right)\omega^2 u_i \tag{8.48}
$$

Referring to definition (8.20) of the error in the vector difference and Eq. (8.29), consider an auxiliary error-component term

$$
\tilde{\varepsilon}_{i,\mathrm{vdiff}} = \frac{\left({}^{\mathrm{N}}u_i^{m+1} - u_i^{m+1}\right)}{A^{\mathrm{E}}}\frac{1}{\Delta^2} = \left(error_i^{tS} - r^2 error_i^{\alpha S} - error_i^{\beta S}\right)\frac{\omega^2 u_i}{|A \cos \omega \Delta|} \tag{8.49}
$$

Referring now to definition (8.19) of the error in amplitude and Eq. (8.29), we rearrange Eq. (8.49) and consider another auxiliary error-component term:

$$
\tilde{\varepsilon}_{i,\mathrm{ampl}} = \frac{{}^{\mathrm{N}}u_i^{m+1}}{A^{\mathrm{E}}}\frac{1}{\Delta^2} = \left(error_i^{tS} - r^2 error_i^{\alpha S} - error_i^{\beta S}\right)\frac{\omega^2 u_i}{|A \cos \omega \Delta|} + \frac{u_i^{m+1}}{|A \cos \omega \Delta|}\frac{1}{\Delta^2}
$$
$$\tag{8.50}$$

Equations (8.21) and (8.22) imply $u_i^{m+1} = u_i(t + \Delta) = \exp[-i\omega\Delta]u_i(t)$ and, consequently,

$$
\tilde{\varepsilon}_{i,\mathrm{ampl}} = \frac{{}^{\mathrm{N}}u_i^{m+1}}{A^{\mathrm{E}}}\frac{1}{\Delta^2} = \left(error_i^{tS} - r^2 error_i^{\alpha S} - error_i^{\beta S} + \frac{\exp[-i\omega\Delta]}{(\omega\Delta)^2}\right)\frac{\omega^2 u_i}{|A \cos \omega \Delta|}
$$
$$\tag{8.51}$$

Errors (7.104) and (8.20) can then be expressed as

$$
\varepsilon_{\mathrm{ampl}}^{\mathrm{Rel}} = \left(\Delta_{ref}\right)^2 \left|\left[\tilde{\varepsilon}_{x,\mathrm{ampl}}^2 + \tilde{\varepsilon}_{y,\mathrm{ampl}}^2 + \tilde{\varepsilon}_{z,\mathrm{ampl}}^2\right]^{1/2} - 1\right| \tag{8.52}
$$

$$
\varepsilon_{\mathrm{vdiff}}^{\mathrm{Rel}} = \left(\Delta_{ref}\right)^2 \left[\tilde{\varepsilon}_{x,\mathrm{vdiff}}^2 + \tilde{\varepsilon}_{y,\mathrm{vdiff}}^2 + \tilde{\varepsilon}_{z,\mathrm{vdiff}}^2\right]^{1/2} \tag{8.53}
$$

Table 8.6 *Comparison of coefficients of the leading and 1st higher terms of the truncation errors TrunErr $\{D_{xx}\}$ and TrunErr $\{D_{zx}\}$. (a) Schemes with the error in amplitude almost independent of V_P/V_S. (b) Schemes with the error in amplitude dependent on V_P/V_S*

2nd-order schemes			4th-order schemes		
operator	C_{LT}	C_{1HT}	operator	C_{LT}	C_{1HT}
(a)					
$D_{xx}^{\text{FD DS SG 2}}$		c_2	$D_{xx}^{\text{FD DS SG 4}}$		d_4
	1	c_4		1	d_6
	1	c_2		1	d_4
$D_{zx}^{\text{FD DS SG 2}}$		c_4	$D_{zx}^{\text{FD DS SG 4}}$		d_6
$D_{xx}^{\text{FD DS PSG 2}}$		$7.0\,c_2$	$D_{xx}^{\text{FD D CG 4a}}$		$7.1\,d_4$
	1	$53.5\,c_4$		1	$26.7\,d_6$
	1	$7.0\,c_2$		0.53	$7.1\,d_4$
$D_{zx}^{\text{FD DS PSG 2}}$		$53.5\,c_4$	$D_{zx}^{\text{FD D CG 4a}}$		$14.2\,d_6$
(b)					
$D_{xx}^{\text{FD D CG 2}}$		c_2	$D_{xx}^{\text{FD D CG 4b}}$		$1.2\,d_4$
	4	c_4		8.5	$1.8\,d_6$
	16	$4.0\,c_2$		22	$10.1\,d_4$
$D_{zx}^{\text{FD D CG 2}}$		$16.0\,c_4$	$D_{zx}^{\text{FD D CG 4b}}$		$39.1\,d_6$

Difference between $\varepsilon_{\text{ampl}}^{\text{Rel}}$ and $\varepsilon_{\text{vdiff}}^{\text{Rel}}$ Obviously, the auxiliary error-component terms $\tilde{\varepsilon}_{i,\text{ampl}}$ and $\tilde{\varepsilon}_{i,\text{vdiff}}$ do not quantitatively represent the entire values of $\varepsilon_{\text{ampl}}^{\text{Rel}}$ and $\varepsilon_{\text{vdiff}}^{\text{Rel}}$, respectively. They do, however, indicate where the difference between $\varepsilon_{\text{ampl}}^{\text{Rel}}$ and $\varepsilon_{\text{vdiff}}^{\text{Rel}}$ comes from. The r.h.s of Eqs. (8.49) and (8.51) differ by the 4th term in the parentheses in Eq. (8.51). The absolute value of this term is proportional to r^2, see Table 8.4. The fact that $\varepsilon_{\text{ampl}}^{\text{Rel}}$ of schemes FD DS SG (2,4), FD D CG (2,4a), FD DS SG (2,2) and FD DS PSG (2,2) is almost independent of r is likely related to the interaction of the 2nd and 4th terms because they are both proportional to r^2.

8.3.6.4 Truncation errors of the discrete approximations to the 2nd nonmixed and mixed spatial derivatives

It is interesting to look at the structure of the truncation errors of the 2nd-order and 4th-order operators for the 2nd mixed and nonmixed derivatives. The errors are shown in Table 8.3. Define ratios for each scheme:

$$
\begin{aligned}
C_{LT} &= \frac{\text{coeff. of leading term of } TrunErr\,\{D_{zx}\}}{\text{coeff. of leading term of } TrunErr\,\{D_{xx}\}} \\
C_{kHT} &= \frac{\text{coeff. of } k\text{-th higher term of } TrunErr\,\{D_{zx}\}}{\text{coeff. of } k\text{-th higher term of } TrunErr\,\{D_{xx}\}}; \quad k = 1, 2, 3, \ldots
\end{aligned}
\tag{8.54}
$$

C_{LT} and C_{1HT} are shown in Table 8.6. Table 8.6(a) includes the four schemes for which $\varepsilon_{\text{ampl}}^{\text{Rel}}$ are almost independent of V_P/V_S; Table 8.6(b) includes the other schemes. All the four schemes in Table 8.6(a) have $C_{LT} = 1$. Schemes FD DS SG (2,4), FD DS SG (2,2) and FD DS PSG (2,2) also have $C_{kHT} = 1$ (the table shows only the first one). On the other hand, neither of the two schemes in Table 8.6(b) has C_{LT} or C_{1HT} equal to 1.

We denote by c_2 and c_4 the coefficients of the leading term and 1$^{\text{st}}$ higher term of *TrunErr*$\{D_{xx}\}$ or *TrunErr*$\{D_{zx}\}$ of the 2$^{\text{nd}}$-order FD DS SG (2,2) operators. The lower index indicates the power of the grid spacing h. Similarly, denote by d_4 and d_6 the coefficients of the leading term and 1$^{\text{st}}$ higher term of *TrunErr*$\{D_{xx}\}$ or *TrunErr*$\{D_{zx}\}$ of the 4$^{\text{th}}$-order FD DS SG (2,4) operators. Table 8.6 shows the corresponding coefficients of other 2$^{\text{nd}}$-order operators as multiples of c_2 and c_4. Similarly, coefficients of the other 4$^{\text{th}}$-order operators are shown as multiples of d_4 and d_6.

In general, for the schemes of the same order (either 2$^{\text{nd}}$ or 4$^{\text{th}}$) for given C_{LT} or C_{1HT}, $\varepsilon_{\text{ampl}}^{\text{Rel}}$ and $\varepsilon_{\text{vdiff}}^{\text{Rel}}$ increase with increasing absolute values of coefficients of terms in the truncation errors. This is seen well for FD DS SG (2,2) and FD DS PSG (2,2). C_{LT} or C_{1HT} are the same but the coefficients of terms in the truncation errors are different. It is also interesting to compare FD DS SG (2,4) and FD D CG (2,4a). Although they have different C_{1HT}, the ratio of the coefficients of the leading terms, which is 7.1, well quantifies the difference in their errors (see Fig. 8.4).

8.3.7 Summary

The relative local error in amplitude, $\varepsilon_{\text{ampl}}^{\text{Rel}}$, of schemes FD DS SG (2,4), FD D CG (2,4a), FD DS SG (2,2) and FD DS PSG (2,2) is almost independent of V_P/V_S. The error in the vector difference, $\varepsilon_{\text{vdiff}}^{\text{Rel}}$, increases with increasing V_P/V_S. This can be explained by the dependence of the polarization errors of all schemes on V_P/V_S. FD D CG (2,2) is the most sensitive to increasing V_P/V_S and for $V_P/V_S > 2$ requires considerably denser spatial sampling than any other scheme. The 4$^{\text{th}}$-order schemes for $V_P/V_S > 3$ are less sensitive to increasing V_P/V_S than the 2$^{\text{nd}}$-order schemes. The maximum $\varepsilon_{\text{vdiff}}^{\text{Rel}}$ of all 4$^{\text{th}}$-order schemes increase with increasing V_P/V_S for $V_P/V_S > 3$ in the same way. FD D CG (2,4a) and FD D CG (2,4b) require denser spatial sampling than FD DS SG (2,4) in order to achieve the same accuracy.

FD DS SG (2,4), FD D CG (2,4a), FD DS SG (2,2) and FD DS PSG (2,2) with $\varepsilon_{\text{ampl}}^{\text{Rel}}$ almost independent of V_P/V_S have the same coefficients of the leading terms of the truncation errors of approximations to the 2$^{\text{nd}}$ mixed and nonmixed spatial derivatives. None of the other schemes have those coefficients equal.

The general theoretical conclusion is that the homogeneity of the approximations to the 2$^{\text{nd}}$ mixed and nonmixed spatial derivatives in terms of the coefficients of the leading terms of their truncation errors as well as the absolute values of the coefficients are key factors for the behaviour of the numerical schemes with increasing V_P/V_S. The practical conclusion for the existing schemes is that the dependence of $\varepsilon_{\text{vdiff}}^{\text{Rel}}$ on V_P/V_S should be accounted for by a proper (sufficiently dense) spatial sampling.

Comparison with the FE, spectral-element and discontinuous-Galerkin schemes can be found in the article by Moczo *et al.* (2011).

8.4 Stability and grid dispersion of the VS SG (2,4) scheme

The VS formulation of the equation of motion may be written as

$$\rho \frac{\partial v_i}{\partial t} = \frac{\partial \sigma_{ij}}{\partial x_j}, \quad \frac{\partial \sigma_{ij}}{\partial t} = \lambda \frac{\partial v_k}{\partial x_k} \delta_{ij} + \mu \left(\frac{\partial v_i}{\partial x_j} + \frac{\partial v_j}{\partial x_i} \right)$$

$$i, j, k \in \{1, 2, 3\}$$

(8.55)

Assume an unbounded homogeneous medium and

$$\Phi_{I,K,L}^m = A^\Phi \exp[i(\tilde\omega m \Delta - \tilde k_x I h - \tilde k_y K h - \tilde k_z L h)]$$

(8.56)

Here Φ denotes either v_i or σ_{ij}. For convenience we will use x_1, x_2, x_3 or x, y, z interchangeably. The 2$^{\text{nd}}$-order and 4$^{\text{th}}$-order centred approximations of the 1$^{\text{st}}$ temporal derivative and 1$^{\text{st}}$ spatial derivatives with respect to x give

$$\left. \frac{\partial \Phi}{\partial t} \right|_{I,K,L}^m \approx \frac{1}{\Delta} \left(\Phi_{I,K,L}^{m+1/2} - \Phi_{I,K,L}^{m-1/2} \right) = i \frac{2}{\Delta} S_\omega \Phi_{I,K,L}^m, \quad S_\omega = \sin\left(\tfrac{1}{2}\tilde\omega\Delta\right)$$

(8.57)

$$\left. \frac{\partial \Phi}{\partial x} \right|_{I,K,L}^m \approx \frac{1}{h} \left[\tfrac{9}{8} \left(\Phi_{I+1/2,K,L}^m - \Phi_{I-1/2,K,L}^m \right) - \tfrac{1}{24} \left(\Phi_{I+3/2,K,L}^m - \Phi_{I-3/2,K,L}^m \right) \right]$$

$$= -i \frac{2}{h} S_x \Phi_{I,K,L}^m, \quad S_x = \tfrac{9}{8} \sin\left(\tfrac{1}{2}\tilde k_x h\right) - \tfrac{1}{24} \sin\left(\tfrac{3}{2}\tilde k_x h\right)$$

(8.58)

Considering ξ for any of x, y and z,

$$\left. \frac{\partial \Phi}{\partial \xi} \right|_{I,K,L}^m \approx -i \frac{2}{h} S_\xi \Phi_{I,K,L}^m$$

$$S_\xi = \tfrac{9}{8} \sin\left(\tfrac{1}{2}\tilde k_\xi h\right) - \tfrac{1}{24} \sin\left(\tfrac{3}{2}\tilde k_\xi h\right), \quad \xi \in \{x, y, z\}$$

(8.59)

The application of approximations (8.57) and (8.59) to nine equations (8.55) yields

$$-\rho \frac{h}{\Delta} S_\omega v_x = S_x \sigma_{xx} + S_y \sigma_{xy} + S_z \sigma_{xz}$$

$$-\rho \frac{h}{\Delta} S_\omega v_y = S_y \sigma_{yy} + S_z \sigma_{yz} + S_x \sigma_{yx}$$

$$-\rho \frac{h}{\Delta} S_\omega v_z = S_z \sigma_{zz} + S_x \sigma_{zx} + S_y \sigma_{zy}$$

(8.60)

$$-\frac{h}{\Delta} S_\omega \sigma_{xx} = \lambda \left(S_x v_x + S_y v_y + S_z v_z \right) + 2\mu S_x v_x$$

$$-\frac{h}{\Delta} S_\omega \sigma_{yy} = \lambda \left(S_x v_x + S_y v_y + S_z v_z \right) + 2\mu S_y v_y$$

$$-\frac{h}{\Delta} S_\omega \sigma_{zz} = \lambda \left(S_x v_x + S_y v_y + S_z v_z \right) + 2\mu S_z v_z$$

$$-\frac{h}{\Delta} S_\omega \sigma_{xy} = \mu \left(S_y v_x + S_x v_y \right) \tag{8.61}$$

$$-\frac{h}{\Delta} S_\omega \sigma_{yz} = \mu \left(S_z v_y + S_y v_z \right)$$

$$-\frac{h}{\Delta} S_\omega \sigma_{zx} = \mu \left(S_x v_z + S_z v_x \right)$$

Substituting the stress-tensor components in Eqs. (8.60) by the stress-tensor components obtained from Eqs. (8.61) we obtain a system of three equations for three unknowns, v_x, v_y, v_z:

$$\rho \frac{h^2}{\Delta^2} S_\omega^2 v_x = \mu \left(S_x^2 + S_y^2 + S_z^2 \right) v_x + (\lambda + \mu) \left(S_x^2 v_x + S_x S_y v_y + S_x S_z v_z \right)$$

$$\rho \frac{h^2}{\Delta^2} S_\omega^2 v_y = \mu \left(S_x^2 + S_y^2 + S_z^2 \right) v_y + (\lambda + \mu) \left(S_y^2 v_y + S_y S_z v_z + S_y S_x v_x \right) \tag{8.62}$$

$$\rho \frac{h^2}{\Delta^2} S_\omega^2 v_z = \mu \left(S_x^2 + S_y^2 + S_z^2 \right) v_z + (\lambda + \mu) \left(S_z^2 v_z + S_z S_x v_x + S_z S_y v_y \right)$$

We define auxiliary quantities:

$$\Gamma \equiv \frac{h^2}{\Delta^2} S_\omega^2, \quad \Sigma \equiv S_x^2 + S_y^2 + S_z^2, \quad \beta^2 \equiv \frac{\mu}{\rho}, \quad \chi^2 \equiv \frac{\lambda + \mu}{\rho} \tag{8.63}$$

and rewrite system (8.62) in the form of a matrix equation:

$$\Gamma \begin{bmatrix} v_x \\ v_y \\ v_z \end{bmatrix} = \begin{bmatrix} \chi^2 S_x^2 + \beta^2 \Sigma & \chi^2 S_x S_y & \chi^2 S_x S_z \\ \chi^2 S_y S_x & \chi^2 S_y^2 + \beta^2 \Sigma & \chi^2 S_y S_z \\ \chi^2 S_z S_x & \chi^2 S_z S_y & \chi^2 S_z^2 + \beta^2 \Sigma \end{bmatrix} \begin{bmatrix} v_x \\ v_y \\ v_z \end{bmatrix} \tag{8.64}$$

Note that this equation is the same as that obtained by Moczo *et al.* (2000) for the 3D displacement–stress (spatially) staggered-grid (2,4) scheme. Denote the matrix in Eq. (8.64) by $\mathbf{M}$, the unit matrix by $\mathbf{1}$, and rewrite the equation:

$$[\mathbf{M} - \Gamma \mathbf{1}] \begin{bmatrix} v_x \\ v_y \\ v_z \end{bmatrix} = \begin{bmatrix} 0 \\ 0 \\ 0 \end{bmatrix} \tag{8.65}$$

The matrix on the l.h.s. may be decomposed as

$$[\mathbf{M} - \Gamma \mathbf{1}] = \chi^2 \left[\begin{bmatrix} S_x & 0 & 0 \\ 0 & S_y & 0 \\ 0 & 0 & S_z \end{bmatrix} \begin{bmatrix} 1 & 1 & 1 \\ 1 & 1 & 1 \\ 1 & 1 & 1 \end{bmatrix} \begin{bmatrix} S_x & 0 & 0 \\ 0 & S_y & 0 \\ 0 & 0 & S_z \end{bmatrix} + d\mathbf{1} \right] \tag{8.66}$$

where

$$d = \left(\beta^2 \Sigma - \Gamma\right)/\chi^2 \tag{8.67}$$

A nontrivial solution to Eq. (8.65) exists if $Det\,[\mathbf{M} - \Gamma \mathbf{1}] = 0$, which may be written as

$$\chi^6 Det \left[\begin{bmatrix} S_x & 0 & 0 \\ 0 & S_y & 0 \\ 0 & 0 & S_z \end{bmatrix} \begin{bmatrix} 1 & 1 & 1 \\ 1 & 1 & 1 \\ 1 & 1 & 1 \end{bmatrix} \begin{bmatrix} S_x & 0 & 0 \\ 0 & S_y & 0 \\ 0 & 0 & S_z \end{bmatrix} + d\mathbf{1} \right] = 0 \tag{8.68}$$

and

$$Det \begin{bmatrix} S_x^2 + d & S_x S_y & S_x S_z \\ S_x S_y & S_y^2 + d & S_y S_z \\ S_x S_z & S_y S_z & S_z^2 + d \end{bmatrix} = 0 \tag{8.69}$$

from which we obtain

$$d^2 \left(S_x^2 + S_y^2 + S_z^2\right) = 0 \tag{8.70}$$

Equation (8.70) is satisfied if

$$S_x^2 + S_y^2 + S_z^2 = 0 \quad \text{or} \quad d = 0 \tag{8.71}$$

Consequently we obtain two dispersion relations for the 3D VS SG (2,4) scheme. Considering definitions (8.67), (8.63) and (8.57), Eqs. (8.71) imply

$$\sin^2\left(\tfrac{1}{2}\tilde{\omega}\Delta\right) = \frac{\Delta^2}{h^2}\alpha^2 \left(S_x^2 + S_y^2 + S_z^2\right)$$
$$\sin^2\left(\tfrac{1}{2}\tilde{\omega}\Delta\right) = \frac{\Delta^2}{h^2}\beta^2 \left(S_x^2 + S_y^2 + S_z^2\right) \tag{8.72}$$

where $\alpha^2 = (\lambda + 2\mu)/\rho$ and $\beta^2 = \mu/\rho$ are the squares of the P-wave and S-wave speeds, respectively. Compare dispersion relations (8.72) with that in Table 7.4 for the 1D VS SG (2,4) scheme. The two relations correspond to the possibility of two independent waves – P and S waves. Similarly to the analysis in Subsection 7.3.5, we can obtain relations

$$\Delta \le \frac{6}{7\sqrt{3}}\frac{h}{\alpha}, \quad \Delta \le \frac{6}{7\sqrt{3}}\frac{h}{\beta} \tag{8.73}$$

for P and S waves. If both types of waves propagate in the grid, the condition for the P wave has to be taken as the joint stability condition because $\alpha > \beta$. Defining the stability ratio p,

$$p \equiv \frac{7\sqrt{3}}{6}\frac{\alpha}{h}\Delta \tag{8.74}$$

the condition for the time step may be written as

$$\Delta = p\frac{6}{7\sqrt{3}}\frac{h}{\alpha}; \quad 0 < p \le 1 \tag{8.75}$$

Denoting the grid P and S wave velocities by $\tilde{\alpha}$ and $\tilde{\beta}$, respectively, and assuming physical wavenumbers k_α and k_β, in analogy with Eq. (7.222) we obtain from Eqs. (8.72) relations for the normalized grid phase velocities:

$$
\begin{aligned}
\frac{\tilde{\alpha}}{\alpha} &= \frac{2}{\alpha k_\alpha \Delta} \arcsin\left[\frac{\Delta}{h}\alpha\left(S_x^2 + S_y^2 + S_z^2\right)^{1/2}\right] \\
\frac{\tilde{\beta}}{\beta} &= \frac{2}{\beta k_\beta \Delta} \arcsin\left[\frac{\Delta}{h}\beta\left(S_x^2 + S_y^2 + S_z^2\right)^{1/2}\right]
\end{aligned}
\tag{8.76}
$$

in which we consider the same time step given by (8.75). Equation (8.75) implies

$$
\frac{\Delta}{h}\alpha = p\frac{6}{7\sqrt{3}}, \quad \frac{\Delta}{h}\beta = \frac{p}{r}\frac{6}{7\sqrt{3}}; \quad r = \frac{\alpha}{\beta}
\tag{8.77}
$$

Spatial samplings for P and S waves are

$$
N_\lambda^P = \lambda_P/h, \quad N_\lambda^S = \lambda_S/h, \quad N_\lambda^P = r N_\lambda^S
\tag{8.78}
$$

If both types of waves propagate in the grid, N_λ^S has to be adopted as the joint spatial sampling because, at a given frequency, $\lambda_P > \lambda_S$. Because for both types of waves we apply the same time step (for the P wave) and the same spatial sampling (for the S wave), we obtain, in analogy with Eq. (7.226),

$$
\frac{2}{\alpha k_\alpha \Delta} = \frac{2}{\beta k_\beta \Delta} = \frac{7\sqrt{3}}{6}\frac{r N_\lambda^S}{\pi p}
\tag{8.79}
$$

Using Eqs. (8.77) and (8.79) we may rewrite relations (8.76) in the form

$$
\begin{aligned}
\frac{\tilde{\alpha}}{\alpha} &= \frac{7\sqrt{3}}{6}\frac{r N_\lambda^S}{\pi p} \arcsin\left[p\frac{6}{7\sqrt{3}}\left(S_x^2 + S_y^2 + S_z^2\right)^{1/2}\right] \\
\frac{\tilde{\beta}}{\beta} &= \frac{7\sqrt{3}}{6}\frac{r N_\lambda^S}{\pi p} \arcsin\left[\frac{p}{r}\frac{6}{7\sqrt{3}}\left(S_x^2 + S_y^2 + S_z^2\right)^{1/2}\right]
\end{aligned}
\tag{8.80}
$$

Recall that S_x, S_y, S_z are given by relation (8.59). For the P wave and the S wave we obtain, respectively,

$$
\begin{aligned}
k_x h &= \frac{2\pi}{r N_\lambda^S}\cos\varphi\sin\delta, \quad k_y h = \frac{2\pi}{r N_\lambda^S}\sin\varphi\sin\delta, \quad k_z h = \frac{2\pi}{r N_\lambda^S}\cos\delta \\
k_x h &= \frac{2\pi}{N_\lambda^S}\cos\varphi\sin\delta, \quad\quad k_y h = \frac{2\pi}{N_\lambda^S}\sin\varphi\sin\delta, \quad\quad k_z h = \frac{2\pi}{N_\lambda^S}\cos\delta
\end{aligned}
\tag{8.81}
$$

where angles φ and δ determine the direction of propagation, as shown in Fig. 8.3. Note again that the grid dispersion for the analyzed 3D VS SG (2,4) scheme is the same as the grid dispersion of the 3D displacement–stress (spatially) staggered-grid (2,4) scheme – as pointed out by Moczo *et al.* (2000), who explicitly analyzed the latter scheme.

The grid dispersion of P and S waves is illustrated in Fig. 8.5 and Fig. 8.6.

It is clear from the figures that, due to the larger wavelength of the P wave, propagation of the P wave is modelled by the FD scheme much better than propagation of the S wave. We can also see considerable grid-dispersion anisotropy of the S wave: grid dispersion is
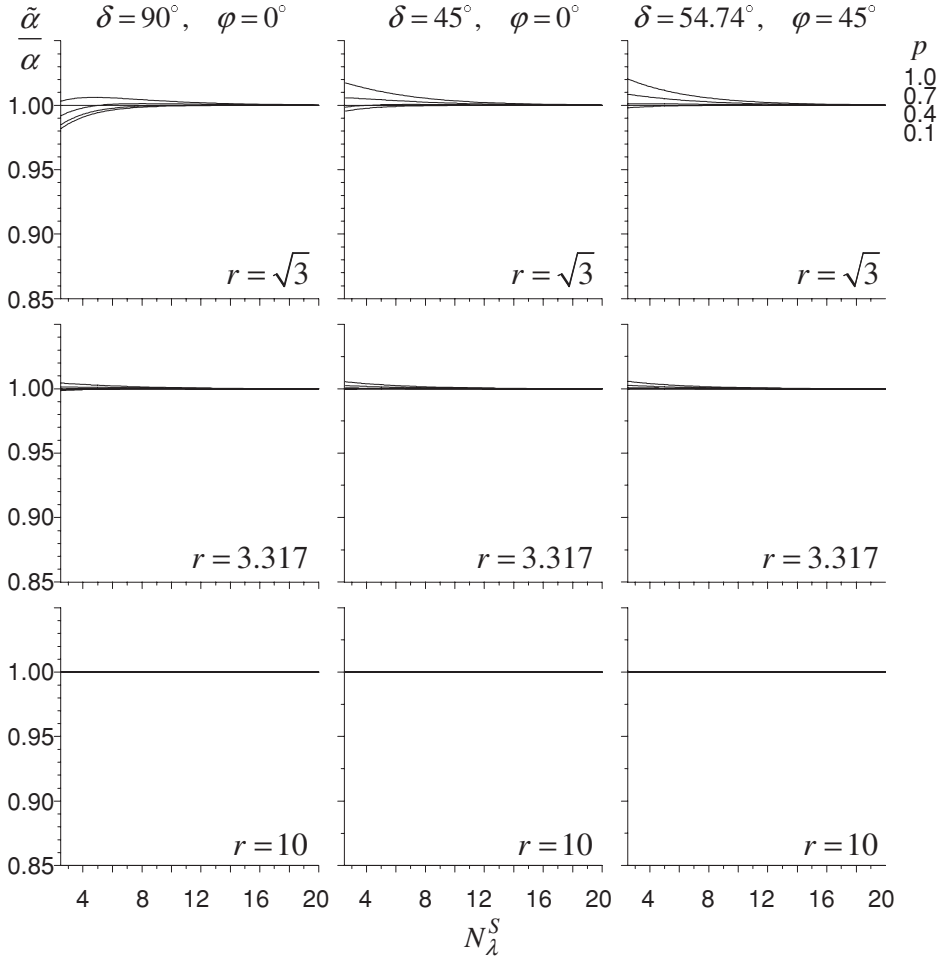
Figure 8.5 Normalized grid phase velocity of the P wave propagating in the three distinct directions: along a coordinate axis ($\delta = 90°$, $\varphi = 0°$), coordinate-plane diagonal ($\delta = 45°$, $\varphi = 0°$), and body diagonal ($\delta = 54.74°$, $\varphi = 45°$). The dispersion curves are shown for four values of the stability ratio p and three values of r: $\sqrt{3}$, 3.317, 10 corresponding to values 0.25, 0.45, 0.495 of Poisson's ratio, $\sigma = (2 - r^2)/2(1 - r^2)$.

strongest for a wave propagating along a coordinate axis and weakest for a wave propagating along a body diagonal. This is due to the effective spatial sampling of the plane wave propagating in the three directions. The densest effective sampling is just in the direction of the body diagonal.

For a given direction of propagation, the S-wave dispersion curves for all values of r are very close to each other for $p = 0.1$. This is understandable if we examine a limit of $\tilde{\beta}/\beta$ for $p \to 0$. The second of Eqs. (8.80) implies

$$\lim_{p \to 0} \frac{\tilde{\beta}}{\beta} = \frac{N_\lambda^S}{\pi} \left(S_x^2 + S_y^2 + S_z^2 \right)^{1/2} \tag{8.82}$$
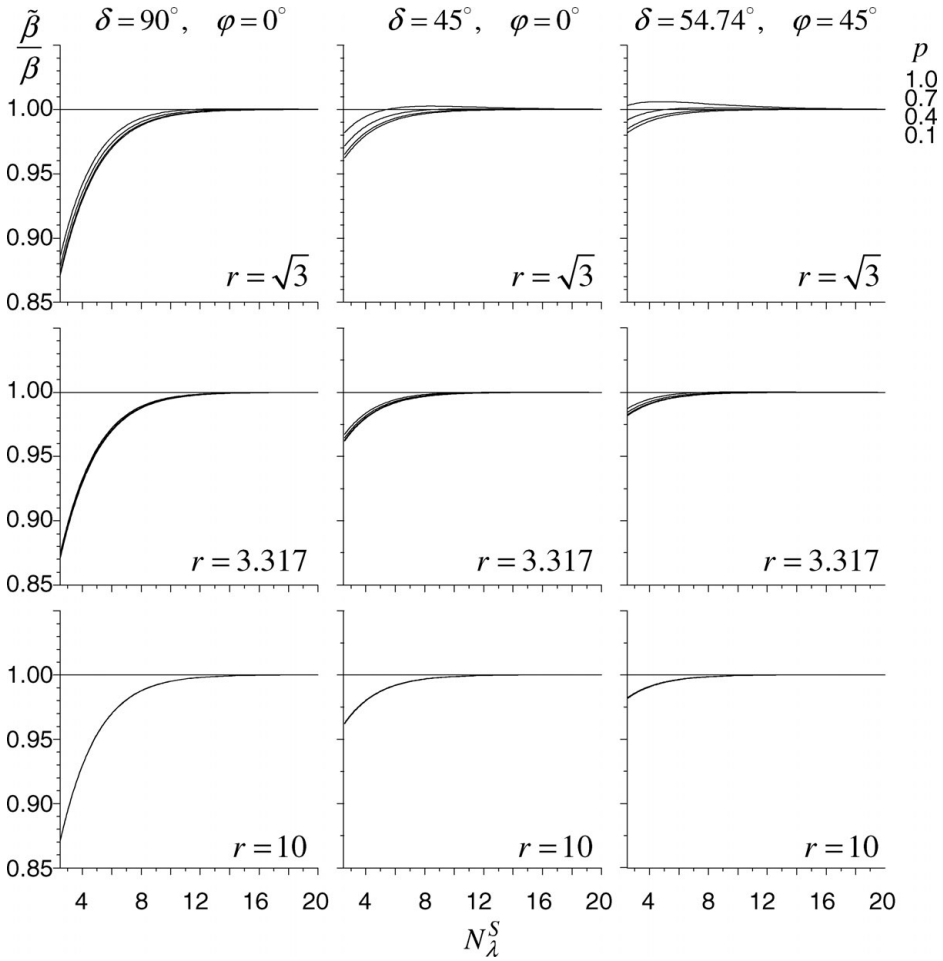
Figure 8.6 The same as Fig. 8.5 but for the S wave.

This explains why the dispersion curves (for a given direction of propagation) for p as low as 0.1 are so close to each other regardless of the value of r.

For more details, including the grid dispersion of the group velocities, comparison of the grid dispersion of the 2nd- and 4th-order schemes, as well as grid dispersion of the 3D and 2D P-SV schemes, we refer to the article by Moczo *et al.* (2000).

9

Velocity–stress staggered-grid scheme for an unbounded heterogeneous viscoelastic medium

9.1 FD modelling of a material interface

Models of the Earth's interior and surface geological structures have to include layers/blocks of different materials. Their contact, the material interface, is a material discontinuity at which material parameters change discontinuously. Assuming a welded interface, the boundary conditions are continuity of the displacement (or particle-velocity) and traction vector. An apparently natural approach to using the FDM is to apply (a) an FD scheme for the smoothly heterogeneous medium at grid points outside the discontinuity, (b) FD schemes obtained by proper incorporation of the boundary conditions at grid points at or near the interface. Such an approach has been called homogeneous. Boore (1972b) and Kelly *et al*. (1976) pointed out that a homogeneous FD scheme is specific for a particular problem. Whereas it is feasible for simple interface geometry, its application to curved material discontinuities is difficult and therefore had been considered impractical. In any case, the approach requires a stable and sufficiently accurate FD approximation of the boundary conditions, which is not a trivial problem.

In the alternative heterogeneous approach, only one FD scheme is used for all interior grid points (points not lying on the boundaries of a grid) no matter what their positions are with respect to the material interface. The presence of the interface is accounted for only by values of the effective material parameters assigned to grid positions. Therefore, the heterogeneous approach has been much more popular since the beginning of the seventies.

Clearly, a heterogeneous FD scheme should approximate solutions of the equation of motion and stress–strain relation valid for both the smoothly heterogeneous medium and the interface. In fact, the majority of the heterogeneous schemes were developed for smooth media and were only intuitively applied to media with material interfaces.

In their pioneering work, Alterman and Karal (1968) used the displacement FD scheme and homogeneous approach for models with simple geometry of the material discontinuities. They introduced the concept of fictitious grid points in order to approximate boundary conditions on material discontinuities. Difficulties in application of the homogeneous approach to curved discontinuities led Boore (1972b) to his explicit continuous stress method. Boore tried to include explicitly a stress-continuity condition on discontinuities differently from the homogeneous and heterogeneous approaches. Due to the poor

numerical properties of the method Boore (1972b) applied the heterogeneous approach in his SH modelling. In order to follow variations of the torsion modulus and, at the same time, to avoid the differentiation of the modulus, he used the mathematical trick given by Tikhonov and Samarskii (see Subsection 7.3.1) and calculated effective grid moduli as integral harmonic averages along a grid line between two neighbouring grid points. Ilan *et al*. (1975) and Ilan and Loewenthal (1976) solved the P-SV problem on the horizontal and vertical planar discontinuities with a homogeneous approach. Instead of the fictitious grid points they used Taylor expansions of displacement to couple the equation of motion with the boundary conditions. Kelly *et al*. (1976) presented their heterogeneous P-SV schemes with simple intuitive averaging of material parameters. They compared the heterogeneous and homogeneous formulations using numerical tests and showed unacceptable differences between the two approaches in the case of the corner-edge model. Kummer and Behle (1982) followed the approach of Ilan *et al*. (1975) and derived the 2nd-order SH schemes for different types of grid points lying on a step-like polygonal interface between two homogeneous blocks.

The breakthrough velocity–stress staggered-grid schemes introduced to seismic-wave propagation modelling by Virieux (1984, 1986) were significant for modelling interfaces. His 2D P-SV scheme did not suffer from stability problems caused by large V_P/V_S (or Poisson's ratio) values, which was the case for all displacement schemes on conventional grids. Although Virieux did not describe determination of the material grid parameters in his heterogeneous 2nd-order SH and P-SV velocity–stress schemes, his numerical results were sufficiently accurate at the time. Virieux also discussed the discrepancy between the homogeneous and heterogeneous formulations found by Kelly *et al*. (1976). He found it difficult to explain the features of the homogeneous solution.

Fornberg (1988b) suggested using a boundary-conforming grid in order to avoid artificial diffraction at a staircase interface. An attempt to incorporate internal boundary conditions into a displacement FD scheme was made by Sochacki *et al*. (1991), who a priori assumed validity of the equation of motion at the discontinuity and integrated it over a grid cell. Then they FD-approximated the integrated equation of motion. Cunha (1993) developed a modified staggered-grid scheme with short operators for computing derivatives of discontinuous material properties and long operators for computing derivatives of the field variables. Zahradník and Priolo (1995) explicitly pointed out the problem of justification of the heterogeneous FD schemes and a heterogeneous formulation of the equation of motion. Assuming discontinuous material parameters in the equation of motion, they obtained an expression whose dominant term is equivalent to the traction continuity condition. Graves (1996) intuitively suggested a formula for determination of effective material grid parameters in the 3D (2,4) VS SG scheme. Graves was probably the first to explicitly and clearly explain the determination of the grid parameters in his scheme. Zhang and Symes (1998) developed a 2D 4th-order full-stencil immersed interface technique to account for a curved material discontinuity. In the first step, all grid points are solved using a standard FD scheme. In the second step, each grid point whose stencil includes grid points from both sides of the discontinuity is recalculated using the previous time step's values with a special

25-point scheme determined using local boundary conditions. Lombard and Piraux (2004) presented an explicit simplified interface method for 2D velocity–stress modelling.

Equivalent medium consistent with the interface boundary conditions It seems that many developers of the heterogeneous schemes were not aware of the work by Backus (1962), Schoenberg and Muir (1989) and Muir *et al.* (1992), or they did not realize the meaning of the work for the development of the heterogeneous schemes. Backus (1962) investigated the long-wave equivalent of a finely layered medium. He showed that a homogeneous transversely isotropic medium described by five elastic coefficients is the long-wave equivalent of a stack of homogeneous isotropic layers. The coefficients of the equivalent medium are obtained by a proper averaging of the Lamé coefficients of the layers. The averaging is consistent with boundary conditions at the interfaces between layers. Backus also found the long-wave equivalent of a stack of transversely isotropic layers. Schoenberg and Muir (1989) extended the Backus approach to arbitrary anisotropic layers and showed how an equivalent, homogeneous, anisotropic medium can be constructed from the layered medium. In other words, both Backus (1962) and Schoenberg and Muir (1989) found the stress–strain relation for an averaged medium consistent with the interface boundary conditions. Neither of them explicitly mentioned FD modelling. This was done by Muir *et al.* (1992). They wrote:

How can we convert a continuous geological model into a form suitable for an FD grid? One common way is to lay the FD grid down on the continuous geological model and use whatever elastic constants happen to lie beneath each of the grid points. Unfortunately, this simple sampling scheme can cause artefacts. For example, a smooth, gently sloping interface in the geological model translates into a coarse staircase on sampling, with long horizontal runs punctuated by occasional vertical steps. These artificial steps generate unwanted diffractions. Clearly, some other representation is called for, but what works best for elastic tensors? The Schoenberg-Muir calculus (S-M) shows how to correctly average a stack of flat elastic layers of arbitrary anisotropy.

Muir *et al.* treated the contents of each cell as a stack of layers that can be averaged using the S-M calculus. Importantly, the average elastic coefficients account for the spatial distribution of the original elastic coefficients (in other words, they account also for the geometry of the contents).

Although Muir *et al.* explicitly addressed the problem of the representation of the true medium in the FD grid, apparently, until the article by Moczo *et al.* (2002), the averaged medium consistent with the interface boundary conditions did not impact the heterogeneous FD modelling of earthquake motion.

Moczo *et al.* (2002) analyzed the 1D problem in a medium consisting of two halfspaces and found a heterogeneous formulation of the equation of motion and Hooke's law. They also showed a simple rheological model of the 1D interface. They also analyzed the 3D problem and pointed out its relation to the staggered-grid schemes. Eventually, they suggested a simplified approach for the (2,4) staggered-grid schemes: an effective grid elastic modulus at the grid position of the stress-tensor component evaluated as a volume

integral harmonic average of the modulus within a volume of the grid cell centred at the grid position. Numerical tests confirmed that the scheme was more accurate than the staggered-grid schemes presented earlier.

The error at the interface in conventional, staggered-grid and optimally accurate FD modelling was numerically investigated by Kristek and Moczo (2006) and also Moczo *et al*. (2007a). For an interesting insight into FD modelling and analysis of the interface error we refer to the article by Lisitsa *et al*. (2010).

A perspective and powerful approach to effectively and efficiently represent medium heterogeneity is being developed by Capdeville and his colleagues (e.g., Capdeville and Marigo 2007, 2013; Capdeville *et al*. 2010a,b, 2013). The fundamental question in their approach, called homogenization, is how a wave at a certain frequency sees (senses) the medium heterogeneity. Capdeville and his colleagues show how to average (homogenize or simplify or smooth) the medium in order to achieve a desired level of accuracy with respect to the solution for the original, possibly small-scale heterogeneous, medium. It is likely that the approach will considerably facilitate the computational efficiency of numerical modelling.

9.2 Stress–strain relation at a material interface

Hooke's law for a smooth isotropic medium   Defining the stress vector, strain vector and elasticity matrix,

$$\vec{\sigma} \equiv \left[\sigma_{xx}, \sigma_{yy}, \sigma_{zz}, \sigma_{xy}, \sigma_{yz}, \sigma_{zx}\right]^T, \quad \vec{\varepsilon} \equiv \left[\varepsilon_{xx}, \varepsilon_{yy}, \varepsilon_{zz}, \varepsilon_{xy}, \varepsilon_{yz}, \varepsilon_{zx}\right]^T \qquad (9.1)$$

$$\mathbf{E} \equiv \begin{bmatrix} \lambda + 2\mu & \lambda & \lambda & 0 & 0 & 0 \\ \lambda & \lambda + 2\mu & \lambda & 0 & 0 & 0 \\ \lambda & \lambda & \lambda + 2\mu & 0 & 0 & 0 \\ 0 & 0 & 0 & 2\mu & 0 & 0 \\ 0 & 0 & 0 & 0 & 2\mu & 0 \\ 0 & 0 & 0 & 0 & 0 & 2\mu \end{bmatrix} \qquad (9.2)$$

the stress–strain relation may be written in the matrix form

$$\vec{\sigma} = \mathbf{E}\,\vec{\varepsilon} \qquad (9.3)$$

Boundary conditions at the welded material interface   Consider surface S with normal vector $\vec{v}$ defining the geometry of the material interface at which elastic moduli λ and μ have a discontinuity of zero order. The welded-interface boundary conditions are continuity of displacement and traction vectors across the surface at each point $\vec{\eta}$ of surface S:

$$\vec{u}^{+}\left(\vec{\eta}\right) = \vec{u}^{-}\left(\vec{\eta}\right), \quad \vec{T}^{+}\left(\vec{\eta}; \vec{v}\right) = \vec{T}^{-}\left(\vec{\eta}; \vec{v}\right) \qquad (9.4)$$

9.2.1 Planar interface parallel to a coordinate plane

Consider the simplest possible situation – a planar interface parallel to the xy-coordinate plane. The normal vector in this case is $\vec{v} = (0, 0, 1)$. Continuity of displacement implies

$$\varepsilon_{xx}^+ = \varepsilon_{xx}^-, \quad \varepsilon_{yy}^+ = \varepsilon_{yy}^-, \quad \varepsilon_{xy}^+ = \varepsilon_{xy}^- \tag{9.5}$$

and continuity of traction implies

$$\sigma_{zx}^+ = \sigma_{zx}^-, \quad \sigma_{zy}^+ = \sigma_{zy}^-, \quad \sigma_{zz}^+ = \sigma_{zz}^- \tag{9.6}$$

Components $\sigma_{xx}, \sigma_{yy}, \sigma_{xy}, \varepsilon_{zx}, \varepsilon_{zy}, \varepsilon_{zz}$ may be discontinuous across the interface.

Problem formulation If we want an FD scheme in the same form for a grid point away from the interface and a grid point at the interface, we need Hooke's law in the same form for both types of grid points. This means that we need to find the stress–strain relation for a point at the interface that would (a) be consistent with the boundary conditions, (b) have the same form as Hooke's law for a point away from the interface.

Having continuous and discontinuous stress-tensor and strain-tensor components at the interface, it will be useful to rewrite Eqs. (9.1)–(9.3) in an alternative form.

Alternative form of Hooke's law for a smooth isotropic medium Define the continuous and discontinuous stress and strain vectors:

$$\vec{\sigma}_C \equiv \left[\sigma_{zx}, \sigma_{zy}, \sigma_{zz}\right]^T, \quad \vec{\sigma}_D \equiv \left[\sigma_{xx}, \sigma_{yy}, \sigma_{xy}\right]^T \tag{9.7}$$

$$\vec{\varepsilon}_C \equiv \left[\varepsilon_{xx}, \varepsilon_{yy}, \varepsilon_{xy}\right]^T, \quad \vec{\varepsilon}_D \equiv \left[\varepsilon_{zx}, \varepsilon_{zy}, \varepsilon_{zz}\right]^T \tag{9.8}$$

Then,

$$\vec{\sigma}_C = \mathbf{R}\,\vec{\varepsilon}_D + \mathbf{P}\,\vec{\varepsilon}_C, \quad \vec{\sigma}_D = \mathbf{P}^T\vec{\varepsilon}_D + \mathbf{S}\,\vec{\varepsilon}_C \tag{9.9}$$

where

$$\mathbf{R} = \begin{bmatrix} 2\mu & 0 & 0 \\ 0 & 2\mu & 0 \\ 0 & 0 & \lambda + 2\mu \end{bmatrix}, \quad \mathbf{P} = \begin{bmatrix} 0 & 0 & 0 \\ 0 & 0 & 0 \\ \lambda & \lambda & 0 \end{bmatrix}, \quad \mathbf{S} = \begin{bmatrix} \lambda + 2\mu & \lambda & 0 \\ \lambda & \lambda + 2\mu & 0 \\ 0 & 0 & 2\mu \end{bmatrix} \tag{9.10}$$

Defining the alternative stress and strain vectors:

$$\vec{\tilde{\sigma}} = \left[\vec{\sigma}_C, \vec{\sigma}_D\right]^T, \quad \vec{\tilde{\varepsilon}} = \left[\vec{\varepsilon}_D, \vec{\varepsilon}_C\right]^T \tag{9.11}$$

and the elasticity matrix:

$$\tilde{\mathbf{E}} = \begin{bmatrix} \mathbf{R} & \mathbf{P} \\ \mathbf{P}^T & \mathbf{S} \end{bmatrix} = \begin{bmatrix} 2\mu & 0 & 0 & 0 & 0 & 0 \\ 0 & 2\mu & 0 & 0 & 0 & 0 \\ 0 & 0 & \lambda + 2\mu & \lambda & \lambda & 0 \\ 0 & 0 & \lambda & \lambda + 2\mu & \lambda & 0 \\ 0 & 0 & \lambda & \lambda & \lambda + 2\mu & 0 \\ 0 & 0 & 0 & 0 & 0 & 2\mu \end{bmatrix} \tag{9.12}$$

Hooke's law may be written in the form of Eq. (9.3):

$$\vec{\tilde{\sigma}} = \tilde{\mathbf{E}}\,\vec{\tilde{\varepsilon}} \tag{9.13}$$

Hooke's law for the interface Express discontinuous stress and strain vectors using the continuous vectors. From Eqs. (9.9) we obtain

$$\begin{aligned}
\vec{\varepsilon}_D &= -\mathbf{R}^{-1}\mathbf{P}\vec{\varepsilon}_C + \mathbf{R}^{-1}\vec{\sigma}_C \\
\vec{\sigma}_D &= \left(\mathbf{S} - \mathbf{P}^T\mathbf{R}^{-1}\mathbf{P}\right)\vec{\varepsilon}_C + \mathbf{P}^T\mathbf{R}^{-1}\vec{\sigma}_C
\end{aligned} \tag{9.14}$$

Denote

$$\begin{aligned}
\mathbf{\Phi}_1 &\equiv -\mathbf{R}^{-1}\mathbf{P}, & \mathbf{\Phi}_2 &\equiv \mathbf{R}^{-1} \\
\mathbf{\Phi}_3 &\equiv \mathbf{S} - \mathbf{P}^T\mathbf{R}^{-1}\mathbf{P}, & \mathbf{\Phi}_4 &\equiv \mathbf{P}^T\mathbf{R}^{-1}
\end{aligned} \tag{9.15}$$

Equations (9.14) then become

$$\begin{aligned}
\vec{\varepsilon}_D &= \mathbf{\Phi}_1\,\vec{\varepsilon}_C + \mathbf{\Phi}_2\,\vec{\sigma}_C \\
\vec{\sigma}_D &= \mathbf{\Phi}_3\,\vec{\varepsilon}_C + \mathbf{\Phi}_4\,\vec{\sigma}_C
\end{aligned} \tag{9.16}$$

Define an averaged function θ^A:

$$\theta^A = \tfrac{1}{2}(\theta^+ + \theta^-) \tag{9.17}$$

Consider now Eqs. (9.16) for both the $+$ and $-$ media in contact, and average the discontinuous strain and stress vectors. We obtain

$$\begin{aligned}
\vec{\varepsilon}_D^A &= \mathbf{\Phi}_1^A\vec{\varepsilon}_C + \mathbf{\Phi}_2^A\vec{\sigma}_C \\
\vec{\sigma}_D^A &= \mathbf{\Phi}_3^A\vec{\varepsilon}_C + \mathbf{\Phi}_4^A\vec{\sigma}_C
\end{aligned} \tag{9.18}$$

from which we express the stress vectors:

$$\begin{aligned}
\vec{\sigma}_C^A \equiv \vec{\sigma}_C &= \left(\mathbf{\Phi}_2^A\right)^{-1}\vec{\varepsilon}_D^A - \left(\mathbf{\Phi}_2^A\right)^{-1}\mathbf{\Phi}_1^A\vec{\varepsilon}_C \\
\vec{\sigma}_D^A &= \mathbf{\Phi}_4^A\left(\mathbf{\Phi}_2^A\right)^{-1}\vec{\varepsilon}_D^A + \left[\mathbf{\Phi}_3^A - \mathbf{\Phi}_4^A\left(\mathbf{\Phi}_2^A\right)^{-1}\mathbf{\Phi}_1^A\right]\vec{\varepsilon}_C
\end{aligned} \tag{9.19}$$

It is easy to verify that

$$\mathbf{\Phi}_4^A\left(\mathbf{\Phi}_2^A\right)^{-1} = \left[-\left(\mathbf{\Phi}_2^A\right)^{-1}\mathbf{\Phi}_1^A\right]^T \tag{9.20}$$

Define

$$\bar{\mathbf{R}} \equiv \left(\mathbf{\Phi}_2^A\right)^{-1}, \quad \bar{\mathbf{P}} \equiv -\left(\mathbf{\Phi}_2^A\right)^{-1}\mathbf{\Phi}_1^A, \quad \bar{\mathbf{S}} \equiv \mathbf{\Phi}_3^A - \mathbf{\Phi}_4^A\left(\mathbf{\Phi}_2^A\right)^{-1}\mathbf{\Phi}_1^A \tag{9.21}$$

Then Eqs. (9.19) may be written as

$$\begin{aligned}
\vec{\sigma}_C^A &= \bar{\mathbf{R}}\,\vec{\varepsilon}_D^A + \bar{\mathbf{P}}\,\vec{\varepsilon}_C \\
\vec{\sigma}_D^A &= \bar{\mathbf{P}}^T\,\vec{\varepsilon}_D^A + \bar{\mathbf{S}}\,\vec{\varepsilon}_C
\end{aligned} \tag{9.22}$$

Considering $\vec{\sigma}_C^A \equiv \vec{\sigma}_C$, $\vec{\varepsilon}_C^A \equiv \vec{\varepsilon}_C$, defining the averaged stress and strain vectors (compare with Eqs. (9.11)):

$$\vec{\tilde{\sigma}}^A = \left[\vec{\sigma}_C^A, \vec{\sigma}_D^A\right]^T, \quad \vec{\tilde{\varepsilon}}^A = \left[\vec{\varepsilon}_D^A, \vec{\varepsilon}_C^A\right]^T \tag{9.23}$$

and the elasticity matrix:

$$
\bar{\bar{\mathbf{E}}} = \begin{bmatrix} \bar{\mathbf{R}} & \bar{\mathbf{P}} \\ \bar{\mathbf{P}}^T & \bar{\mathbf{S}} \end{bmatrix} = \begin{bmatrix}
2\mu^H & 0 & 0 & 0 & 0 & 0 \\
0 & 2\mu^H & 0 & 0 & 0 & 0 \\
0 & 0 & (\lambda+2\mu)^H & \Psi & \Psi & 0 \\
0 & 0 & \Psi & \Lambda+2\mu^A & \Lambda & 0 \\
0 & 0 & \Psi & \Lambda & \Lambda+2\mu^A & 0 \\
0 & 0 & 0 & 0 & 0 & 2\mu^A
\end{bmatrix}
\tag{9.24}
$$

$$
\begin{aligned}
\Psi &= \left(\frac{\lambda}{\lambda+2\mu}\right)^A (\lambda+2\mu)^H \\
\Lambda &= \left[\left(\frac{\lambda}{\lambda+2\mu}\right)^A\right]^2 (\lambda+2\mu)^H + 2\left(\frac{\lambda}{\lambda+2\mu}\mu\right)^A
\end{aligned}
\tag{9.25}
$$

Superscripts A and H indicate the arithmetic and harmonic averages, respectively. Equations (9.22) may be written in matrix form as

$$
\vec{\sigma}^A = \bar{\bar{\mathbf{E}}} \vec{\varepsilon}^A
\tag{9.26}
$$

Equation (9.26) means nothing less than the stress–strain relation for a point at the interface. The stress–strain relation has the same form as Hooke's law (9.13) and, importantly, is consistent with the boundary conditions.

An important difference between matrices $\tilde{\mathbf{E}}$ and $\bar{\bar{\mathbf{E}}}$, or, in other words, the difference between any of the two original smooth media and the averaged medium at the interface is that matrix $\tilde{\mathbf{E}}$ for any of the two isotropic media in contact has only two independent nonzero elements, whereas matrix $\bar{\bar{\mathbf{E}}}$ has five independent nonzero elements and the averaged medium is transversely isotropic with the axis of symmetry perpendicular to the interface. This means that the exact heterogeneous formulation for a planar welded material interface parallel with a coordinate plane increases the number of the elastic coefficients necessary to describe the medium from two to five.

9.2.2 Planar interface in a general orientation

Consider now a more complicated configuration. Let the planar material interface be in a general orientation in the Cartesian coordinate system. The normal vector to the interface, $\vec{v} = (v_x, v_y, v_z)$, has all components nonzero. Find a Cartesian coordinate system $x'y'z'$ in which $\vec{v}$ is parallel to the z'-axis. Then we can find matrix $\bar{\bar{\mathbf{E}}}'$ with five independent nonzero elements. If we then transform matrix $\bar{\bar{\mathbf{E}}}'$ into the original coordinate system xyz we obtain a symmetric elasticity matrix that obviously may have all elements nonzero (though only five of them are independent). All nonzero elements of the averaged elasticity matrix mean real complications: (a) all strain-tensor components are needed to calculate each stress-tensor component at a point of the interface; (b) 21 nonzero elastic coefficients are necessary at the point.

If the geometry of the interface is defined by a nonplanar smooth surface S, the surface may locally be approximated by a planar surface tangential to surface S at a given point.

Algorithmically we have two possibilities: (1) calculate 21 nonzero elastic coefficients for each grid point and store them in memory during the entire FD time integration; (2) store only $2 + 2$ elastic coefficients (two per medium in contact) and two angles (specifying the orientation of an approximating tangential planar interface) for each grid point and calculate the elasticity matrix at each time step at each grid point.

Obviously, the incorporation of the traction-continuity condition at the material interface in the 3D problem is not a trivial task. Note that the above analysis is equivalent to the application of the Schoenberg and Muir (1989) calculus applied to the special case of one interface between two homogeneous media. See also Backus (1962) and Muir *et al.* (1992).

Still we are not finished with the complications. Note that in the staggered grid we do not have all strain-tensor components defined at each grid position of the stress-tensor components. From this point of view, the staggered grid is not really well suited for incorporation of the traction-continuity condition at the material interface.

9.2.3 Effective orthorhombic averaged medium

Rearrange matrix $\bar{\bar{\mathbf{E}}}$ into matrix $\bar{\mathbf{E}}$, which corresponds to the stress and strain vectors in their common structures given by Eqs. (9.1):

$$
\bar{\mathbf{E}} = \begin{bmatrix}
\Lambda + 2\mu^A & \Lambda & \Psi & 0 & 0 & 0 \\
\Lambda & \Lambda + 2\mu^A & \Psi & 0 & 0 & 0 \\
\Psi & \Psi & (\lambda + 2\mu)^H & 0 & 0 & 0 \\
0 & 0 & 0 & 2\mu^A & 0 & 0 \\
0 & 0 & 0 & 0 & 2\mu^H & 0 \\
0 & 0 & 0 & 0 & 0 & 2\mu^H
\end{bmatrix}
\tag{9.27}
$$

Matrix $\bar{\mathbf{E}}$ is symmetric with six diagonal and three off-diagonal elements. For the planar interface parallel to the xy-plane only five of the nine elements are independent. Consider a planar interface parallel to some other coordinate planes. The positions of the nine elements will not change – this is due to the structure of the stress and strain vectors. The positions of the five independent elements will, however, be different – due to the orientation of the interface.

In other words, for any of three canonical orientations we need at each point six values – five independent coefficients plus one index of orientation – in order to construct matrix $\bar{\mathbf{E}}$.

In general, we do not want to restrict the treatment of interfaces to one of three canonical orientations. On the other hand, the general orientation requires 21 nonzero coefficients – too many and inconsistent with the staggered distribution of the field variables. In this situation a natural compromise suggests itself: nine independent coefficients – consistent

with the above considerations on the interface orientation and consistent with the structure of the staggered grid. Moreover, a stress-tensor component is determined by the same strain-tensor components as in the isotropic medium. A medium described by nine coefficients is a medium with orthorhombic anisotropy having three axes of symmetry that are identical with the coordinate axes.

Problem formulation For a given grid point we need to find an elasticity matrix with nine independent coefficients (that is, the elasticity matrix for the orthorhombic medium) that accounts for heterogeneity of the medium inside the grid cell centred at the given grid point. We assume that the heterogeneity may be due to one or more material interfaces or a smooth variation of material parameters that can be approximated by thin layers. We may call the coefficients sought the effective material coefficients.

The sought elasticity matrix has the form

$$
\mathbf{E}^{\mathrm{ort}} \equiv
\begin{pmatrix}
\Pi_x & \lambda_{xy} & \lambda_{zx} & 0 & 0 & 0 \\
\lambda_{xy} & \Pi_y & \lambda_{yz} & 0 & 0 & 0 \\
\lambda_{zx} & \lambda_{yz} & \Pi_z & 0 & 0 & 0 \\
0 & 0 & 0 & \mu_{xy} & 0 & 0 \\
0 & 0 & 0 & 0 & \mu_{yz} & 0 \\
0 & 0 & 0 & 0 & 0 & \mu_{zx}
\end{pmatrix}
\tag{9.28}
$$

The effective coefficients sought for the cell have to satisfy the following requirement: if the cell contains only interface(s) parallel to one of the Cartesian planes, the effective coefficients must describe a transversely isotropic medium.

We split the volume of a grid cell into homogeneous isotropic subcells of a uniform size. Coefficients that satisfy all the imposed conditions are given by the following formulas:

$$
\Pi_x = \frac{1}{h} \left(\int_x \left[\mathrm{P}_{yz} \left(\lambda, \mu \right) \right]^{-1} dl \right)^{-1}, \quad
\Pi_y = \frac{1}{h} \left(\int_y \left[\mathrm{P}_{xz} \left(\lambda, \mu \right) \right]^{-1} dl \right)^{-1}
$$
$$
\Pi_z = \frac{1}{h} \left(\int_z \left[\mathrm{P}_{xy} \left(\lambda, \mu \right) \right]^{-1} dl \right)^{-1}
\tag{9.29}
$$

$$
\mu_{zx} = h \left(\iint_{zx} \left[\int_y \mu \, dl \right]^{-1} dS \right)^{-1}, \quad
\mu_{yz} = h \left(\iint_{yz} \left[\int_x \mu \, dl \right]^{-1} dS \right)^{-1}
$$
$$
\mu_{xy} = h \left(\iint_{xy} \left[\int_z \mu \, dl \right]^{-1} dS \right)^{-1}
\tag{9.30}
$$

$$
\lambda_{xz} = h^{-1} \, \Psi_{xz}(\Lambda_y(\lambda, \mu), \mathrm{P}_y(\lambda, \mu))
$$
$$
\lambda_{yz} = h^{-1} \, \Psi_{yz}(\Lambda_x(\lambda, \mu), \mathrm{P}_x(\lambda, \mu))
\tag{9.31}
$$
$$
\lambda_{xy} = h^{-1} \, \Psi_{xy}(\Lambda_z(\lambda, \mu), \mathrm{P}_z(\lambda, \mu))
$$

Here,

$$P_{\xi\zeta}(\lambda, \mu) = \left[\iint_{\xi\zeta} \frac{\lambda}{\lambda + 2\mu} dS\right]^2 \left(\iint_{\xi\zeta} \frac{1}{\lambda + 2\mu} dS\right)^{-1} + \iint_{\xi\zeta} \left(\lambda + 2\mu - \frac{\lambda^2}{\lambda + 2\mu}\right) dS$$

(9.32)

$$\Psi_{\xi\zeta}(a, b) = \iint_{\xi\zeta} \frac{a}{b} dS \left(\iint_{\xi\zeta} \frac{1}{b} dS\right)^{-1}$$

The auxiliary parameters a and b stand for an appropriate $\Lambda_\xi(\lambda, \mu)$ and $P_\xi(\lambda, \mu)$, respectively. The last two parameters are evaluated as

$$P_\xi(\lambda, \mu) = \left[\int_\xi \frac{\lambda}{\lambda + 2\mu} dl\right]^2 \left(\int_\xi \frac{1}{\lambda + 2\mu} dl\right)^{-1} + \int_\xi \left(\lambda + 2\mu - \frac{\lambda^2}{\lambda + 2\mu}\right) dl$$

(9.33)

$$\Lambda_\xi(\lambda, \mu) = P_\xi(\lambda, \mu) - 2\int_\xi \mu \, dl$$

Note that the double subscript ξ, ζ indicates averaging over the $\xi\zeta$-plane. The single subscript ξ indicates averaging along the ξ-axis.

The effective elastic coefficients (moduli) have to be determined at the grid positions of the stress-tensor components – according to the structures of vectors $\vec{\sigma}$ and $\vec{\varepsilon}$ given by Eqs. (9.1) and matrix $\mathbf{E}^{\text{ort}}$ given by Eq. (9.28). All Π_x, Π_y, Π_z and λ_{xy}, λ_{yz}, λ_{zx} have to be determined at the grid position that is shared by all the normal stress-tensor components. Coefficient μ_{xy} has to be determined at the grid position of σ_{xy}, μ_{yz} at the grid position of σ_{yz}, and μ_{zx} at the grid position of σ_{zx}.

Finally, the stress–strain relation for the orthorhombic averaged medium can be written as

$$\begin{aligned}
\sigma_{xx} &= \Pi_x \varepsilon_{xx} + \lambda_{xy} \varepsilon_{yy} + \lambda_{zx} \varepsilon_{zz} \\
\sigma_{yy} &= \lambda_{xy} \varepsilon_{xx} + \Pi_y \varepsilon_{yy} + \lambda_{yz} \varepsilon_{zz} \\
\sigma_{zz} &= \lambda_{zx} \varepsilon_{xx} + \lambda_{yz} \varepsilon_{yy} + \Pi_z \varepsilon_{zz} \\
\sigma_{xy} &= \mu_{xy} \varepsilon_{xy}, \sigma_{yz} = \mu_{yz} \varepsilon_{yz}, \sigma_{zx} = \mu_{zx} \varepsilon_{zx}
\end{aligned}$$

(9.34)

9.2.4 Effective grid density

It was shown in the analysis of the 1D problem in Section 7.4 that the effective (average) density representing the welded interface is the arithmetic average of densities in the halfspaces. In 3D, at each position of the particle-velocity component (or displacement component) an effective grid density is determined as a volume arithmetic average of density within a volume of the grid cell centred at the grid position. The averaging applies to both smoothly and discontinuously heterogeneous media. The averages are evaluated by

numerical integration. Consider, for instance, the grid position of the v_x at the grid point I, $K + 1/2$, $L + 1/2$. Then the effective density is evaluated as

$$\rho^A_{I,\text{K}+1/2,\text{L}+1/2} = \frac{1}{h^3} \int_{x_{I-1/2}}^{x_{I+1/2}} \int_{y_K}^{y_{K+1}} \int_{z_L}^{z_{L+1}} \rho \, dx \, dy \, dz \tag{9.35}$$

with superscript A indicating the arithmetic averaging.

9.2.5 Simplified approach with harmonic averaging of elastic moduli: isotropic averaged medium

The orthorhombic averaging is, as explained above, a simplification of the problem of the stress–strain relation for a point at the material interface. The orthorhombic coefficients obtained are approximately consistent with the traction-continuity condition at the material interface. Numerical tests of accuracy are presented in Chapter 19.

Moczo *et al*. (2002) implemented an even more simplified approach that was motivated by the 1D analysis, simplicity and a pragmatic desire to keep the structure, number of operations and memory requirements of the standard (2,4) staggered-grid scheme. They evaluated an effective grid elastic modulus at the grid position of the stress-tensor component as a volume integral harmonic average of the modulus within a volume of the grid cell centred at the grid position. For example, at the grid position of the normal stress-tensor components:

$$\begin{aligned}
\kappa^H_{I+1/2,\text{K}+1/2,\text{L}+1/2} &= \left[\frac{1}{h^3} \int_{x_I}^{x_{I+1}} \int_{y_K}^{y_{K+1}} \int_{z_L}^{z_{L+1}} \frac{1}{\kappa} dx \, dy \, dz \right]^{-1} \\
\mu^H_{I+1/2,\text{K}+1/2,\text{L}+1/2} &= \left[\frac{1}{h^3} \int_{x_I}^{x_{I+1}} \int_{y_K}^{y_{K+1}} \int_{z_L}^{z_{L+1}} \frac{1}{\mu} dx \, dy \, dz \right]^{-1}
\end{aligned} \tag{9.36}$$

They evaluated an effective density at each position of the particle-velocity component (or displacement component) as a volume integral arithmetic average of the density within a volume of the grid cell centred at the grid position – the averaging indicated by Eq. (9.35). The averaging applies to both smoothly and discontinuously heterogeneous media and is performed by numerical integration.

We may note that the harmonic averaging of κ and μ is formally consistent with the following assumptions: (a) continuity of a trace of the stress tensor, $\sigma_{xx} + \sigma_{yy} + \sigma_{zz} = 3\kappa \varepsilon_{kk}$, (b) continuity of deviatoric parts of the normal stress-tensor components, (c) continuity of the shear stress-tensor components across the interface.

Moczo *et al*. (2002) numerically demonstrated the accuracy of the scheme with volume harmonic averages of moduli and volume arithmetic averages of density for different wavefield–medium configurations. In one of the examples, it is shown that the scheme is capable of sensing the position of an interface within an FD cell, see Fig. 6 in their article.

Harmonic averaging and orthorhombic averaging are confronted with the exact solutions in Chapter 19.

9.3 Incorporation of realistic attenuation

9.3.1 Material interface in a viscoelastic medium

We do not have the stress–strain relation for the interface between two viscoelastic media with GMB-EK/GZB rheology. Clearly, a rigorous analysis is more complicated than the analysis for the interface between elastic media. Consequently, we have to apply an approximate approach. Here, we follow the approach suggested by Kristek and Moczo (2003), see also Moczo *et al.* (2007a), which has been shown to be numerically sufficiently accurate by comparison with the discrete wavenumber method (Bouchon 1981, Coutant 1989; code Axitra).

Consider the contact of two viscoelastic media with GMB-EK/GZB rheology. Assume one and the same set of relaxation frequencies $\omega_l; l = 1, 2, \ldots, n$ for both media. Each medium is described by a real density ρ, elastic (unrelaxed) moduli (e.g., κ and μ), and corresponding viscoelastic (complex frequency-dependent) moduli. We need to determine average (effective) density, elastic moduli and anelastic coefficients $Y_l^{\bar{M}}; l = 1, \ldots, n$ ($\bar{M}$ indicating any of the determined averaged moduli) for an averaged medium that would represent the contact of two viscoelastic media.

The average density may be evaluated in the same way as in the case of elastic media. Averaged viscoelastic moduli can be determined by numerical integration according to relations (9.29)–(9.33) or (9.36) in which complex viscoelastic moduli in the frequency domain are used instead of the real elastic moduli. The use of either (9.29)–(9.33) or (9.36) depends on the need or choice of level of accuracy. From the averaged viscoelastic moduli, the quality factors corresponding to these moduli can be determined at frequencies $\tilde{\omega}_k; k = 1, \ldots, 2n - 1$, using

$$Q_{\bar{M}}(\tilde{\omega}_k) = \frac{\bar{M}_{\text{real}}}{\bar{M}_{\text{imag}}}; \quad k = 1, 2, \ldots, 2n - 1 \tag{9.37}$$

Having values $Q_{\bar{M}}(\tilde{\omega}_k); k = 1, 2, \ldots, 2n - 1$, for each averaged modulus $\bar{M}$, we can apply the least-square method to the system of equations (3.129):

$$Q_{\bar{M}}^{-1}(\tilde{\omega}_k) = \sum_{l=1}^{n} \frac{\omega_l \tilde{\omega}_k + \omega_l^2 Q_{\bar{M}}^{-1}(\tilde{\omega}_k)}{\omega_l^2 + \tilde{\omega}_k^2} Y_l^{\bar{M}}; \quad k = 1, 2, \ldots, 2n - 1 \tag{9.38}$$

to determine anelastic coefficients for each averaged modulus $\bar{M}$.

What remains to be determined are the unrelaxed (elastic) averaged moduli. The unrelaxed modulus of any viscoelastic modulus is given by Eq. (3.20) and thus

$$\bar{M}_U = \lim_{\omega \to \infty} \bar{M}(\omega) \tag{9.39}$$

Consequently, the averaging of the viscoelastic modulus gives, in the limit, the averaging of the unrelaxed modulus. This means that the unrelaxed (elastic) modulus $\bar{M}_U$ for an averaged viscoelastic medium can be obtained in the same way as in a perfectly elastic medium, e.g., using relations (9.29)–(9.33) or (9.36).

If we do not directly know the viscoelastic moduli $\kappa(\omega)$ and $\mu(\omega)$ (or $\lambda(\omega)$ and $\mu(\omega)$) for each of the two media in contact but, instead, we know the measured or estimated $Q_\alpha(\omega)$ for the P wave and $Q_\beta(\omega)$ for the S wave, we have to proceed as follows. We assume GMB-EK/GZB rheology for each medium as well as for the averaged medium. For each of the two media we first determine Y_l^α and Y_l^β using Eqs. (3.139) and then Y_l^κ and Y_l^μ (or Y_l^λ and Y_l^μ) using Eqs. (3.140) or (3.142). Then, assuming known unrelaxed moduli for each medium, we can determine the viscoelastic moduli using Eq. (3.126) for each modulus. Then we can proceed with numerical averaging of the moduli in the frequency domain, determination of the corresponding quality factors, and determination of the anelastic coefficients as described before.

9.3.2 Scheme for the anelastic functions for an isotropic averaged medium

In Section 7.8 we presented the FD scheme for the anelastic functions for a 1D smooth medium. Here we obtain the scheme in 3D in an analogous way. Recall the constitutive law in the velocity–stress formulation for the viscoelastic continuum with GMB-EK/GZB rheology, Eqs. (3.136) and (3.137):

$$
\begin{aligned}
\frac{\partial}{\partial t}\sigma_{ij} = {} & \kappa\frac{\partial}{\partial t}\varepsilon_{kk}\delta_{ij} + 2\mu\left(\frac{\partial}{\partial t}\varepsilon_{ij} - \tfrac{1}{3}\frac{\partial}{\partial t}\varepsilon_{kk}\delta_{ij}\right) \\
& - \sum\nolimits_{l=1}^{n}\left[Y_l^\kappa\kappa\xi_l^{kk}\delta_{ij} + 2Y_l^\mu\mu\big(\xi_l^{ij} - \tfrac{1}{3}\xi_l^{kk}\delta_{ij}\big)\right]
\end{aligned}
\tag{9.40}
$$

$$
\frac{\partial}{\partial t}\xi_l^{ij}(t) + \omega_l\xi_l^{ij}(t) = \omega_l\frac{\partial}{\partial t}\varepsilon_{ij}(t), \quad l = 1,\dots,n
\tag{9.41}
$$

Except for the superscripts in the anelastic coefficients, κ and μ are the unrelaxed (elastic) moduli. Relation (9.40) can apply to either a smoothly heterogeneous viscoelastic medium or isotropic averaged medium. For simplicity we do not use an overbar to distinguish the averaged medium.

The anelastic functions and their temporal derivatives can be approximated with the 2nd-order accuracy:

$$
\xi_l^{ij}(t_{m-1/2}) \doteq \tfrac{1}{2}\big[\xi_l^{ij}(t_m) + \xi_l^{ij}(t_{m-1})\big], \quad l = 1,\dots,n
\tag{9.42}
$$

$$
\frac{\partial}{\partial t}\xi_l^{ij}(t)\bigg|^{m-1/2} \doteq \frac{1}{\Delta}\big[\xi_l^{ij}(t_m) - \xi_l^{ij}(t_{m-1})\big], \quad l = 1,\dots,n
\tag{9.43}
$$

Using approximations (9.42) and (9.43) in Eq. (9.41) we obtain a scheme for updating the anelastic functions:

$$
\xi_l^{ij}(t_m) \doteq \frac{2\omega_l\Delta}{2 + \omega_l\Delta}\frac{\partial\varepsilon_{ij}}{\partial t}\bigg|^{m-1/2} + \frac{2 - \omega_l\Delta}{2 + \omega_l\Delta}\xi_l^{ij}(t_{m-1}), \quad l = 1,\dots,n
\tag{9.44}
$$

According to Eq. (9.42), both $\xi_l^{ij}(t_m)$ and $\xi_l^{ij}(t_{m-1})$ have to be kept in memory for updating $\xi_l^{ij}(t_{m-1/2})$. To avoid this, we can use approximation (9.42) in Eq. (9.44) to eliminate $\xi_l^{ij}(t_{m-1})$ (Kristek and Moczo 2003):

$$\xi_l^{ij}(t_{m-1/2}) \doteq -\frac{\omega_l \Delta}{2 - \omega_l \Delta} \left.\frac{\partial \varepsilon_{ij}}{\partial t}\right|^{m-1/2} + \frac{2}{2 - \omega_l \Delta}\xi_l^{ij}(t_m), \quad l = 1, \dots, n \quad (9.45)$$

Using Eq. (9.45) in Eq. (9.40) for time $t_{m-1/2}$ we obtain

$$\begin{aligned}
\left.\frac{\partial \sigma_{ij}}{\partial t}\right|^{m-1/2} &= \tilde{\kappa} \left.\frac{\partial \varepsilon_{kk}}{\partial t}\right|^{m-1/2} \delta_{ij} + 2\tilde{\mu}\left(\left.\frac{\partial \varepsilon_{ij}}{\partial t}\right|^{m-1/2} - \tfrac{1}{3}\left.\frac{\partial \varepsilon_{kk}}{\partial t}\right|^{m-1/2}\delta_{ij}\right) \\
&\quad - \sum_{l=1}^{n}\left[\tilde{Y}_l^\kappa \xi_l^{kk}(t_m)\delta_{ij} + 2\tilde{Y}_l^\mu\left(\xi_l^{ij}(t_m) - \tfrac{1}{3}\xi_l^{kk}(t_m)\delta_{ij}\right)\right]
\end{aligned} \quad (9.46)$$

where

$$\begin{aligned}
\tilde{\kappa} &= \kappa\left(1 + \sum_{l=1}^{n} G_{1l}Y_l^\kappa\right), \quad \tilde{\mu} = \mu\left(1 + \sum_{l=1}^{n} G_{1l}Y_l^\mu\right) \\
\tilde{Y}_l^\kappa &= G_{2l}\kappa Y_l^\kappa, \quad \tilde{Y}_l^\mu = G_{2l}\mu Y_l^\mu \\
G_{1l} &= \frac{\omega_l \Delta}{2 - \omega_l \Delta}, \quad G_{2l} = \frac{2}{2 - \omega_l \Delta}
\end{aligned} \quad (9.47)$$

The derived relations mean that first we calculate $\xi_l^{ij}(t_m)$ using relation (9.44) and then we apply the obtained values in relation (9.46).

9.3.3 Scheme for anelastic functions for an orthorhombic averaged medium

Consider, for example, σ_{xx} for the elastic continuum given by the stress–strain relation (9.34):

$$\sigma_{xx} = \Pi_x \varepsilon_{xx} + \lambda_{xy}\varepsilon_{yy} + \lambda_{zx}\varepsilon_{zz} \quad (9.48)$$

In the velocity–stress formulation we need its temporal derivative:

$$\frac{\partial \sigma_{xx}}{\partial t} = \Pi_x\frac{\partial \varepsilon_{xx}}{\partial t} + \lambda_{xy}\frac{\partial \varepsilon_{yy}}{\partial t} + \lambda_{zx}\frac{\partial \varepsilon_{zz}}{\partial t} \quad (9.49)$$

The corresponding stress–strain relation for the viscoelastic continuum with GMB-EK/GZB rheology is

$$\begin{aligned}
\frac{\partial \sigma_{xx}}{\partial t} &= \Pi_x\frac{\partial \varepsilon_{xx}}{\partial t} + \lambda_{xy}\frac{\partial \varepsilon_{yy}}{\partial t} + \lambda_{zx}\frac{\partial \varepsilon_{zz}}{\partial t} \\
&\quad - \sum_{l=1}^{n}\left[Y_l^{\Pi_x}\Pi_x\xi_l^{xx} + Y_l^{\lambda_{xy}}\lambda_{xy}\xi_l^{yy} + Y_l^{\lambda_{zx}}\lambda_{zx}\xi_l^{zz}\right]
\end{aligned} \quad (9.50)$$

The additional ordinary differential equations for the anelastic functions ξ_l^{xx}, ξ_l^{yy} and ξ_l^{zz} satisfy Eqs. (9.41). It is easy to derive the relation for $\left.\frac{\partial \sigma_{xx}}{\partial t}\right|^{m-1/2}$ and also for the temporal derivatives of the other stress-tensor components similar to (9.46) using a procedure analogous to that explained in the previous subsection.

9.3.4 Coarse spatial distribution of anelastic functions

The GMB-EK/GZB rheology enables reasonably realistic modelling of attenuation. Its incorporation, however, considerably increases the number of operations and variables/ parameters. Therefore Zeng (1996), and independently Day (1998) and Day and Bradley (2001), introduced coarse spatial sampling of the anelastic functions and coefficients in order to significantly reduce the increased memory requirements and also computational time. In Day's (1998) approach, one anelastic function ξ_l^{ij} for one relaxation frequency ω_l is distributed with a spatial period $2h$. Then the number of relaxation frequencies is $n = 8$. Considering, for example, location of the stress-tensor component σ_{zx} at the eight vertices of a grid cube with edge h, only one of the eight anelastic functions ξ_l^{zx} is assigned to each one of the eight vertices (ξ_1^{zx} is assigned to one position, ξ_2^{zx} to another position, and so on). Then the total number of anelastic functions ξ_l^{zx}; $l = 1, 2, \ldots, 8$ in the whole grid is $\frac{1}{2}MX \cdot \frac{1}{2}MY \cdot \frac{1}{2}MZ \cdot 8 = MX \cdot MY \cdot MZ$, where MX, MY and MZ are the numbers of grid cells in the three Cartesian directions, respectively. Because there are six independent strain-tensor components, the total number of all anelastic functions in the whole grid is $MX \cdot MY \cdot MZ \cdot 6$. Since the anelastic coefficients Y_l^M may be distributed in the same coarse manner, the total number of anelastic coefficients in the grid is $MX \cdot MY \cdot MZ \cdot 9$ in the case of an orthorhombic averaged medium. In the case of harmonic averaging of the moduli, the number of anelastic coefficients is $MX \cdot MY \cdot MZ \cdot 5$ in the staggered grid or $MX \cdot MY \cdot MZ \cdot 2$ in the conventional grid. This means that the additional memory for a coarse distribution and eight relaxation frequencies is equivalent to the additional memory required by just one relaxation mechanism (that is, one relaxation frequency) without coarse sampling. Such a reduction of the memory requirements is significant. Graves and Day (2003) analyzed the stability and accuracy of the scheme with coarse spatial sampling and defined the effective modulus and quality factor necessary to achieve sufficient accuracy, especially in the case of very low Q.

In a structurally complex model there are material interfaces going through grid cells in different orientations with respect to the coordinate system. In such a case and with the originally suggested spatial sampling, it may happen that the medium from one side of the material interface is characterized over one half of the whole considered frequency range while the medium from the other side of the interface is characterized over the other half of the considered frequency range. This means that the behaviours of the two media in contact are described in two disjunctive frequency sub-intervals. Consequently, the two media cannot physically interact.

The geometry of coarse spatial sampling shown by Day (1998) and Day and Bradley (2001) is only one of several possible distributions. Keeping the same spatial periodicity of the anelastic quantities, we can choose such a distribution in which division of a grid cell into two parts characterized in two disjunctive frequency sub-intervals is always avoided. However, with any type of geometric distribution the best possible situation would be, for example, characterization of one medium in contact using relaxation frequencies $\omega_1, \omega_3, \omega_5, \omega_7$ and characterization of the other medium in contact using $\omega_2, \omega_4, \omega_6, \omega_8$.
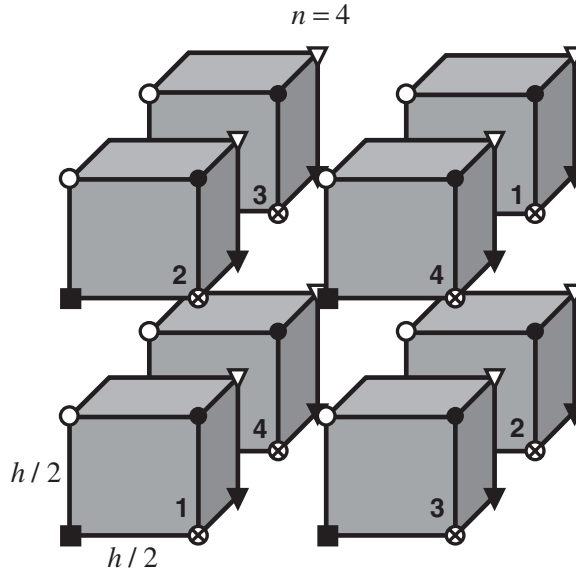
Figure 9.1 Coarse spatial distribution of grid cells and anelastic functions. The number on a cell face indicates the relaxation frequency of the anelastic functions localized in the cell. For example, grid cell 1 contains $\xi_1^{xx}, \xi_1^{yy}, \xi_1^{zz}, \xi_1^{xy}, \xi_1^{yz}, \xi_1^{zx}$. (Reproduced from Kristek and Moczo 2003)

This is much better than two disjunctive frequency sub-intervals, but still not sufficiently satisfactory.

Summation in the anelastic parts of the stress–strain relation (9.40) or (9.46) includes anelastic functions and coefficients at all relaxation frequencies ω_l; $l = 1, 2, \ldots, n$. In coarse spatial sampling, however, at any one grid position we have an anelastic function only at one relaxation frequency. Still, it is possible to account for all the anelastic functions and coefficients: the anelastic functions and coefficients from the neighbouring positions are taken with properly weighting coefficients and averaged together at the grid point where the stress-tensor component is to be evaluated.

Such averaging is possible with the material-independent anelastic functions introduced by Kristek and Moczo (2003), see Subsection 3.3.10. This is because averaging of the material-independent anelastic functions does not introduce additional unjustified averaging of the material properties. Note that this would be the case with the original material-dependent anelastic functions introduced by Day and Minster (1984), Emmerich and Korn (1987), Carcione *et al.* (1988a,b) and Robertsson *et al.* (1994).

Kristek and Moczo (2003) also suggested an alternative coarse spatial distribution of the anelastic functions that requires only $n = 4$ relaxation frequencies, keeping the same memory requirements as in the approach by Day (1998) and Day and Bradley (2001). The distribution is shown in Fig. 9.1. Kristek and Moczo (2003) numerically demonstrated the accuracy of their FD scheme with the material-independent anelastic functions and a new coarse distribution of the anelastic functions by comparison with the discrete wavenumber method (Bouchon 1981, Coutant 1989; code Axitra).

9.3.5 VS SG (2,4) scheme for a heterogeneous viscoelastic medium

For brevity we show only the scheme for the x-component of the particle velocity, the xx-component of the stress tensor, and the xx anelastic function, that is, for v_x, σ_{xx} and ξ_l^{xx}. Schemes for the other components are analogous. Denote the discrete grid values of the particle velocity components v_x, v_y, v_z by VX, VY, VZ, respectively. Similarly denote the stress-tensor components σ_{xx}, σ_{xy}, σ_{zx} by TXX, TXY, TZX. For other quantities we use the same symbols as in the corresponding equations. The schemes for v_x and σ_{xx} are then (compare with the 1D schemes (7.331)–(7.333))

$$
\begin{aligned}
VX_{I,K+1/2,L+1/2}^{m+1/2} = {}& VX_{I,K+1/2,L+1/2}^{m-1/2} + \frac{\Delta}{\bar{\rho}_{I,K+1/2,L+1/2}}\, f\,|_{I,K+1/2,L+1/2}^{m} \\
& + \frac{1}{\bar{\rho}_{I,K+1/2,L+1/2}} \frac{\Delta}{h} \Big[\tfrac{9}{8}\big(TXX_{I+1/2,K+1/2,L+1/2}^{m} - TXX_{I-1/2,K+1/2,L+1/2}^{m}\big) \\
& - \tfrac{1}{24}\big(TXX_{I+3/2,K+1/2,L+1/2}^{m} - TXX_{I-3/2,K+1/2,L+1/2}^{m}\big) \\
& + \tfrac{9}{8}\big(TXY_{I,K+1,L+1/2}^{m} - TXY_{I,K,L+1/2}^{m}\big) \\
& - \tfrac{1}{24}\big(TXY_{I,K+2,L+1/2}^{m} - TXY_{I,K-1,L+1/2}^{m}\big) \\
& + \tfrac{9}{8}\big(TZX_{I,K+1/2,L+1}^{m} - TZX_{I,K+1/2,L}^{m}\big) \\
& - \tfrac{1}{24}\big(TZX_{I,K+1/2,L+2}^{m} - TZX_{I,K+1/2,L-1}^{m}\big) \Big]
\end{aligned}
\tag{9.51}
$$

$$
\begin{aligned}
TXX&_{I+1/2,K+1/2,L+1/2}^{m} \\
={}& TXX_{I+1/2,K+1/2,L+1/2}^{m-1} \\
& + \frac{\Delta}{h} \Big\{ \tilde{M}XX_{I+1/2,K+1/2,L+1/2} \Big[\tfrac{9}{8}\big(VX_{I+1,K+1/2,L+1/2}^{m-1/2} - VX_{I,K+1/2,L+1/2}^{m-1/2}\big) \\
& - \tfrac{1}{24}\big(VX_{I+2,K+1/2,L+1/2}^{m-1/2} - VX_{I-1,K+1/2,L+1/2}^{m-1/2}\big) \Big] \\
& + \tilde{M}XY_{I+1/2,K+1/2,L+1/2} \Big[\tfrac{9}{8}\big(VY_{I+1/2,K+1,L+1/2}^{m-1/2} - VY_{I+1/2,K,L+1/2}^{m-1/2}\big) \\
& - \tfrac{1}{24}\big(VY_{I+1/2,K+2,L+1/2}^{m-1/2} - VY_{I+1/2,K-1,L+1/2}^{m-1/2}\big) \Big] \\
& + \tilde{M}ZX_{I+1/2,K+1/2,L+1/2} \Big[\tfrac{9}{8}\big(VZ_{I+1/2,K+1/2,L+1}^{m-1/2} - VZ_{I+1/2,K+1/2,L}^{m-1/2}\big) \\
& - \tfrac{1}{24}\big(VZ_{I+1/2,K+1/2,L+2}^{m-1/2} - VZ_{I+1/2,K+1/2,L-1}^{m-1/2}\big) \Big] \Big\} \\
& - \Delta \sum_{l=1}^{n} \Big(\tilde{Y}_{l;I+1/2,K+1/2,L+1/2}^{MXX}\, \xi_{l;I+1/2,K+1/2,L+1/2}^{xx;m} \\
& + \tilde{Y}_{l;I+1/2,K+1/2,L+1/2}^{MXY}\, \xi_{l;I+1/2,K+1/2,L+1/2}^{yy;m} + \tilde{Y}_{l;I+1/2,K+1/2,L+1/2}^{MZX}\, \xi_{l;I+1/2,K+1/2,L+1/2}^{zz;m} \Big)
\end{aligned}
\tag{9.52}
$$

The scheme for ξ_l^{xx} corresponding to Eq. (9.44) is

$$
\xi_{l;I+1/2,K+1/2,L+1/2}^{xx;m} = \frac{2 - \omega_l \Delta}{2 + \omega_l \Delta} \xi_{l;I+1/2,K+1/2,L+1/2}^{xx;m-1}
$$

$$
+ \frac{2\omega_l \Delta}{2 + \omega_l \Delta} \frac{1}{h} \left[\frac{9}{8} \left(VX_{I+1,K+1/2,L+1/2}^{m-1/2} - VX_{I,K+1/2,L+1/2}^{m-1/2} \right) \right.
$$

$$
\left. - \frac{1}{24} \left(VX_{I+2,K+1/2,L+1/2}^{m-1/2} - VX_{I-1,K+1/2,L+1/2}^{m-1/2} \right) \right] \qquad (9.53)
$$

Here, the effective grid density $\bar{\rho}_{I,K+1/2,L+1/2}$ is the volume arithmetic average of density given by Eq. (9.35). The effective grid material coefficients depend on the assumed type of medium.

Isotropic averaged medium

$$
\tilde{M}XX_{I+1/2,K+1/2,L+1/2} = \tilde{\kappa}_{I+1/2,K+1/2,L+1/2}^{H} + \frac{4}{3}\tilde{\mu}_{I+1/2,K+1/2,L+1/2}^{H}
$$

$$
\tilde{M}XY_{I+1/2,K+1/2,L+1/2} = \tilde{\kappa}_{I+1/2,K+1/2,L+1/2}^{H} - \frac{2}{3}\tilde{\mu}_{I+1/2,K+1/2,L+1/2}^{H} \qquad (9.54)
$$

$$
\tilde{M}ZX_{I+1/2,K+1/2,L+1/2} = \tilde{M}XY_{I+1/2,K+1/2,L+1/2}
$$

and

$$
\tilde{Y}_{l;I+1/2,K+1/2,L+1/2}^{MXX} = \tilde{Y}_{l;I+1/2,K+1/2,L+1/2}^{\kappa} + \frac{4}{3}\tilde{Y}_{l;I+1/2,K+1/2,L+1/2}^{\mu}
$$

$$
\tilde{Y}_{l;I+1/2,K+1/2,L+1/2}^{MXY} = \tilde{Y}_{l;I+1/2,K+1/2,L+1/2}^{\kappa} - \frac{2}{3}\tilde{Y}_{l;I+1/2,K+1/2,L+1/2}^{\mu} \qquad (9.55)
$$

$$
\tilde{Y}_{l;I+1/2,K+1/2,L+1/2}^{MZX} = \tilde{Y}_{l;I+1/2,K+1/2,L+1/2}^{MXY}
$$

Here $\tilde{\kappa}$, $\tilde{\mu}$, $\tilde{Y}_l^{\kappa}$, $\tilde{Y}_l^{\mu}$ are determined according to Eqs. (9.47). (Note that, for simplicity, the overbar $\bar{}$ is not used in Eqs. (9.47) to indicate that the moduli are the averaged moduli.)

Orthorhombic averaged medium

$$
\tilde{M}XX_{I+1/2,K+1/2,L+1/2} = \tilde{\Pi}_{x;I+1/2,K+1/2,L+1/2}
$$

$$
\tilde{M}XY_{I+1/2,K+1/2,L+1/2} = \tilde{\lambda}_{xy;I+1/2,K+1/2,L+1/2} \qquad (9.56)
$$

$$
\tilde{M}ZX_{I+1/2,K+1/2,L+1/2} = \tilde{\lambda}_{zx;I+1/2,K+1/2,L+1/2}
$$

and

$$
\tilde{Y}_{l;I+1/2,K+1/2,L+1/2}^{MXX} = \tilde{Y}_{l;I+1/2,K+1/2,L+1/2}^{\Pi_x}
$$

$$
\tilde{Y}_{l;I+1/2,K+1/2,L+1/2}^{MXY} = \tilde{Y}_{l;I+1/2,K+1/2,L+1/2}^{\lambda_{xy}} \qquad (9.57)
$$

$$
\tilde{Y}_{l;I+1/2,K+1/2,L+1/2}^{MZX} = \tilde{Y}_{l;I+1/2,K+1/2,L+1/2}^{\lambda_{zx}}
$$

where tilde $\tilde{}$ indicates that coefficients $\tilde{\Pi}_x$, $\tilde{\lambda}_{xy}$, $\tilde{\lambda}_{zx}$, $\tilde{Y}_l^{\Pi_x}$, $\tilde{Y}_l^{\lambda_{xy}}$, $\tilde{Y}_l^{\lambda_{zx}}$ are determined in analogy with Eqs. (9.47).

10

Schemes for a free surface

The free surface was briefly introduced in Subsection 2.5.1 and Section 7.5. The 1D FD schemes for modelling the free surface based on the stress-imaging technique and adjusted FD approximations were presented in Subsections 7.5.1 and 7.5.2, respectively. Recall the boundary conditions. Considering a free surface S with normal vector $\vec{n}$ and traction vector $\vec{T}(\vec{n})$, the traction-free condition at S, $\vec{T}(\vec{n}) = 0$, implies

$$\sigma_{ij} n_j = 0 \tag{10.1}$$

10.1 Planar free surface

If surface S is planar and perpendicular to the z-axis, $\vec{n} = (0, 0, -1)$ and Eq. (10.1) implies

$$\sigma_{iz} = 0; \quad i \in \{x, y, z\} \tag{10.2}$$

It is significantly simpler to implement the traction-free condition (10.2) than condition (10.1) in an FD scheme. This is why FD modelling of a planar free surface is reasonably feasible whereas FD modelling of free-surface topography still poses a major challenge.

As mentioned in Chapter 7, we have two principal possibilities for calculating particle velocity at and near the free surface. The first approach: apply the scheme for the interior grid points assuming virtual values of stress, particle velocity and material parameters outside the medium. The second approach: apply one-sided schemes that do not need any virtual values outside the medium. The advantage of the first approach is the use of one and the same scheme at any grid point. Its disadvantage is the need to define virtual values reasonably outside the medium. The disadvantage of the second approach is the use of different schemes for different grid positions at and near the free surface.

The first approach leads to the so-called vacuum formalism, medium taper or imaging method. The vacuum formalism applies zero moduli above the free surface. The vacuum formalism may yield a good level of accuracy in the conventional-grid displacement schemes for low values of the P-wave to S-wave speed ratio as shown by Zahradník and Priolo (1995) in 2D and Moczo *et al.* (1999) in 3D, for example. Graves (1996) and other authors did not find the vacuum formalism satisfactory in staggered-grid modelling. A density taper was used by Frankel and Leith (1992) in their displacement conventional-grid scheme.

Levander (1988) suggested using virtual values of the stress-tensor components above the free surface and applying the antisymmetry condition for the stress-tensor components about the free surface. He applied the approach to his 2D (2,4) VS SG scheme. Levander's technique may reasonably be called the stress-imaging technique. Rodrigues (1993) developed a 3D eighth-order staggered-grid displacement–stress scheme and used stress imaging with the normal stress-tensor components at the free surface. He found that it is necessary to take 10 to 15 grid points per shortest wavelength to avoid significant numerical dispersion. Therefore, he combined the stress-imaging technique with a vertically refined grid near the free surface and achieved good accuracy. Graves (1996) applied stress imaging with the normal stress-tensor components at the free surface in his 3D (2,4) VS SG modelling. Graves gave a clear explanation of the treatment of the stress-tensor and particle-velocity components at and above the free surface. Robertsson (1996) summarized three possibilities for treating the particle-velocity values at grid positions above the free surface required by the (2,4) VS SG scheme. (1) The values are calculated using the 2nd-order approximations to the boundary condition and imaged stress tensor components (e.g., Levander 1988, Graves 1996, Kristek *et al*. 2002). (2) The values are mirrored as symmetric values with respect to the free surface (e.g., Crase 1990, Rodrigues and Mora 1993). (3) Robertsson (1996) assumed zero values. Gottschämmer and Olsen (2001) compared a formulation with horizontal particle-velocity components (and normal stress-tensor components) at the free surface with a formulation with the vertical particle-velocity component at the free surface in the 3D (2,4) VS SG scheme in a homogeneous halfspace. They concluded with a recommendation to use the formulation with the vertical particle-velocity component at the free surface and to apply averaging across the free surface in order to obtain values of the horizontal components at the free surface. The comparison was performed for the common spatial sampling that was shown by Kristek *et al*. (2002) to be insufficient.

Applying the second approach, Kristek *et al*. (2002) and Moczo *et al*. (2004a) developed a 4th-order scheme with adjusted FD approximations and demonstrated its better accuracy compared to stress imaging.

10.1.1 Stress imaging in the (2,4) VS SG scheme

As mentioned before, in the staggered grid there are two obvious options for localizing the planar free surface. (a) The free surface coincides with the grid plane with positions $v_x, v_y, \sigma_{xx}, \sigma_{yy}, \sigma_{zz}, \sigma_{xy}$. Because the horizontal components of the particle velocity are at the free surface we may call this option, for brevity, the H formulation or configuration. (b) The free surface coincides with the grid plane with positions $v_z, \sigma_{yz}, \sigma_{zx}$. We indicate this formulation by letter W.

The antisymmetry

$$\sigma_{zx}(-z) = -\sigma_{zx}(z), \quad \sigma_{yz}(-z) = -\sigma_{yz}(z), \quad \sigma_{zz}(-z) = -\sigma_{zz}(z) \qquad (10.3)$$

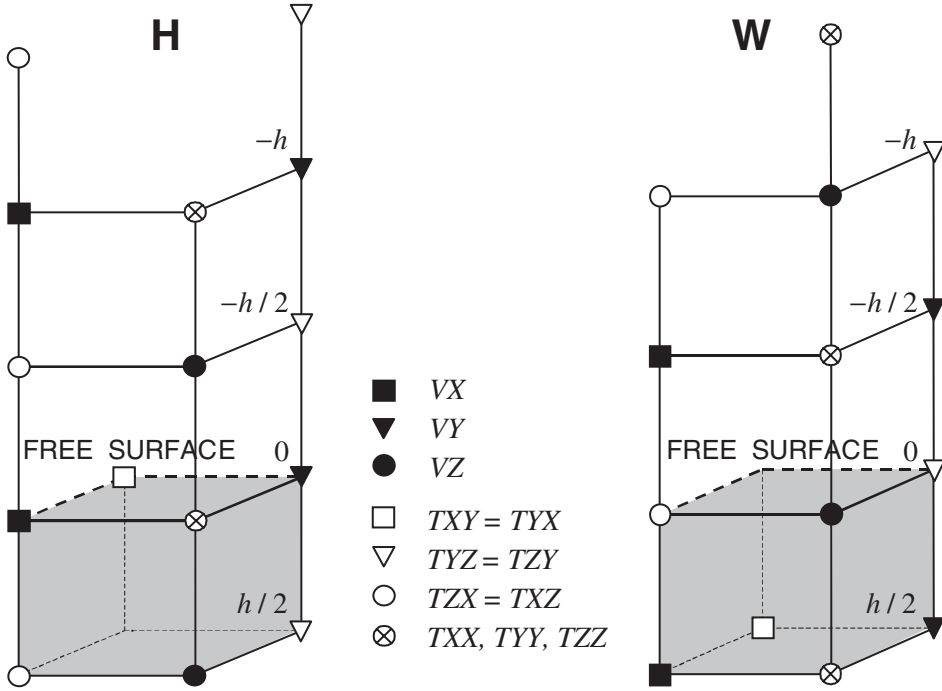ensures the free-surface condition (10.2).

Figure 10.1 Left: a surface FD grid cell, position of the free surface, and virtual field quantities above the free surface in the H formulation of the standard stress-imaging technique. Right: the same for the W formulation.

The H formulation: $v_x, v_y, \sigma_{xx}, \sigma_{yy}, \sigma_{zz}, \sigma_{xy}$ at the free surface For the discrete grid values of the particle velocity components v_x, v_y, v_z we use symbols *VX*, *VY*, *VZ*, respectively. Similarly, for the discrete grid values of the stress-tensor components $\sigma_{xx}, \sigma_{yy}, \sigma_{zz}, \sigma_{xy}, \sigma_{yz}, \sigma_{zx}$ we use symbols *TXX, TYY, TZZ, TXY, TYZ, TZX*. Figure 10.1(left) shows which quantities are needed above the free surface for the (2,4) VS SG scheme. Here, we concisely summarize the explicit application of the boundary conditions, imaged values of the stress-tensor components, and computed values of the displacement components:

> $TZZ(0) = 0$.
> $TXX(0)$ is obtained from the 4th-order approximation of the temporal derivative of the stress–strain relation for σ_{xx} in which $\frac{\partial v_z}{\partial z}$ is replaced by $\frac{\partial v_x}{\partial x}$ and $\frac{\partial v_y}{\partial y}$ according to condition $\sigma_{zz}(0) = 0$ and the temporal derivative of the stress–strain relation for σ_{zz}.
> $TYY(0)$ – analogously using the relation for σ_{yy}.
> $TZX(-h/2) = -TZX(h/2)$, $TYZ(-h/2) = -TYZ(h/2)$.
> $TZZ(-h) = -TZZ(h)$.
> $TZX(-3h/2) = -TZX(3h/2)$, $TYZ(-3h/2) = -TYZ(3h/2)$.

VX(0) is obtained from the 4$^{\text{th}}$-order approximation of the equation for v_x in which $\frac{\partial \sigma_{zx}}{\partial z}$
is obtained using imaged σ_{zx} values.

VY(0) – analogously using v_y, $\frac{\partial \sigma_{yz}}{\partial z}$ and σ_{yz}.

VZ$(-h/2)$ is obtained from the 2$^{\text{nd}}$-order approximation of condition $\sigma_{zz}(0) = 0$ and
the temporal derivative of the stress–strain relation for σ_{zz}.

VX$(-h)$ is obtained from the 2$^{\text{nd}}$-order approximation of $\sigma_{zx}(-h/2) = -\sigma_{zx}(h/2)$ and
the temporal derivative of the stress–strain relation for σ_{zx}.

VY$(-h)$ – analogously using σ_{yz}.

The treatment of the other quantities is the same as in the case of the interior grid points.

The W formulation: $v_z, \sigma_{yz}, \sigma_{zx}$ at the free surface Figure 10.1(right) shows which quantities are needed above the free surface for the (2,4) VS SG scheme. The formulation may be summarized as follows:

TZX(0) = 0, *TYZ*(0) = 0.

TZZ$(-h/2) = -TZZ(h/2)$.

TZX$(-h) = -TZX(h)$, *TYZ*$(-h) = -TYZ(h)$.

TZZ$(-3h/2) = -TZZ(3h/2)$.

VZ(0) is obtained from the 4$^{\text{th}}$-order approximation of the equation for v_z in which $\frac{\partial \sigma_{zz}}{\partial z}$
is obtained using imaged σ_{zz} values.

VX$(-h/2)$ is obtained from the 2$^{\text{nd}}$-order approximation of the condition $\sigma_{zx}(0) = 0$ and
the temporal derivative of the stress–strain relation for σ_{zx}.

VY$(-h/2)$ – analogously using $\sigma_{yz}(0) = 0$ and σ_{yz}.

VZ$(-h)$ is obtained from the 2$^{\text{nd}}$-order approximation of $\sigma_{zz}(-h/2) = -\sigma_{zz}(h/2)$ and
the temporal derivative of the stress–strain relation for σ_{zz}.

Treatment of the other quantities is the same as in the case of the interior grid points.

Comparison of the H and W formulations Although the principle is the same for both formulations, there are differences indicating possibly different numerical results. The implementation differences are summarized in Table 10.1.

Kristek *et al*. (2002) performed extensive numerical tests of both formulations against the discrete-wavenumber (DWN) method (Bouchon 1981, Coutant 1989; code Axitra). The numerical investigations showed that the W formulation is a little more accurate (indicated by the numbers in Table 10.1). However, the difference may be considered negligible with respect to the fact that both formulations need at least twice as many grid spacings per minimum wavelength compared to the scheme for the interior grid points if Rayleigh surface waves are to be propagated without significant grid dispersion.

Rodrigues (1993) used a grid that was refined only in the vertical direction and only down to a necessary depth in his eighth-order displacement–stress scheme. In his implementation,

Table 10.1 *Comparison of two formulations of the stress-imaging technique*

H formulation	W formulation
At the free surface	
1 directly prescribed stress-tensor component	2 directly prescribed stress-tensor component
2 particle-velocity components calculated using 4 imaged stress-tensor components	1 particle-velocity components calculated using 2 imaged stress-tensor components
Needed above the free surface	
5 imaged stress-tensor components	4 imaged stress-tensor components
3 particle-velocity components calculated using the 2nd-order scheme	3 particle-velocity components calculated using the 2nd-order scheme

the normal stress-tensor components are located at the free surface, which corresponds to the H formulation. Kristek *et al*. (2002) elaborated the W formulation of the Rodrigues approach and found it significantly more accurate than the original implementation of the stress-imaging technique on the uniform grid. The disadvantage of the Rodrigues approach is that it needs a three times smaller time step.

10.1.2 Adjusted FD approximations in the (2,4) VS SG scheme

The use of either at least twice finer spatial sampling or a three times smaller time step considerably degrades the efficiency of the (2,4) VS SG scheme inside the medium. Therefore Kristek *et al*. (2002) and Moczo *et al*. (2004a) developed the adjusted FD approximation (AFDA) technique.

The zero values of σ_{zz} are prescribed at the free surface in the H formulation or, alternatively, the zero values of σ_{yz} and σ_{zx} are prescribed at the free surface in the W formulation. One-sided FD approximations are used to calculate the z derivatives at the grid points at the free surface and depths of $h/2$ and h. The approximations use only values in the medium, that is, no values are assumed above the free surface.

Kristek *et al*. (2002) showed that whereas the H formulation gives slightly better phases, the W formulation gives better amplitudes. They concluded with a recommendation to use the W formulation (W-AFDA) for earthquake ground motion modelling. Therefore, we present here only W-AFDA in which the particle-velocity component v_z and the stress-tensor components σ_{zx} and σ_{yz} are located at the free surface.

The calculation of the stress-tensor and particle-velocity components in W-AFDA can be summarized as follows:

Direct application of the boundary condition:
$$TZX(0) = 0, \; TYZ(0) = 0.$$

4th-order approximations of the z derivative:

The following 4th-order approximations of the 1st derivative with respect to the z-coordinate are used in calculations of the stress-tensor and particle-velocity vector components:

$$\frac{\partial \Phi}{\partial z}(z_0) = \frac{1}{h}\left[-\frac{352}{105}\Phi(z_0) + \frac{35}{8}\Phi\left(z_0 + \frac{1}{2}h\right) - \frac{35}{24}\Phi\left(z_0 + \frac{3}{2}h\right)\right.$$
$$\left. + \frac{21}{40}\Phi\left(z_0 + \frac{5}{2}h\right) - \frac{5}{56}\Phi\left(z_0 + \frac{7}{2}h\right)\right] + O(h^4) \tag{10.4}$$

$$\frac{\partial \Phi}{\partial z}(z_0) = \frac{1}{h}\left[-\frac{11}{12}\Phi\left(z_0 - \frac{1}{2}h\right) + \frac{17}{24}\Phi\left(z_0 + \frac{1}{2}h\right) + \frac{3}{8}\Phi\left(z_0 + \frac{3}{2}h\right)\right.$$
$$\left. - \frac{5}{24}\Phi\left(z_0 + \frac{5}{2}h\right) + \frac{1}{24}\Phi\left(z_0 + \frac{7}{2}h\right)\right] + O(h^4) \tag{10.5}$$

$$\frac{\partial \Phi}{\partial z}(z_0) = \frac{1}{h}\left[-\frac{1}{12}h\Phi'(z_0 - h) - \frac{577}{528}\Phi\left(z_0 - \frac{1}{2}h\right) + \frac{201}{176}\Phi\left(z_0 + \frac{1}{2}h\right)\right.$$
$$\left. - \frac{9}{176}\Phi\left(z_0 + \frac{3}{2}h\right) + \frac{1}{528}\Phi\left(z_0 + \frac{5}{2}h\right)\right] + O(h^4) \tag{10.6}$$

$$\frac{\partial \Phi}{\partial z}(z_0) = \frac{1}{h}\left[\frac{16}{105}\Phi(z_0 - h) - \frac{31}{24}\Phi\left(z_0 - \frac{1}{2}h\right) + \frac{29}{24}\Phi\left(z_0 + \frac{1}{2}h\right)\right.$$
$$\left. - \frac{3}{40}\Phi\left(z_0 + \frac{3}{2}h\right) + \frac{1}{168}\Phi\left(z_0 + \frac{5}{2}h\right)\right] + O(h^4) \tag{10.7}$$

Depending on the particular configuration, Φ may stand for particle-velocity or stress-tensor components and z_0 for 0, $h/2$ or h.

(a) Calculation of the stress-tensor components:

   $TXX(h/2)$ is obtained from the 4th-order approximation of the temporal derivative of the stress–strain relation for σ_{xx}; $\frac{\partial v_z}{\partial z}$ is approximated using Eq. (10.5).
   $TYY(h/2)$ and $TZZ(h/2)$ – analogous to $TXX(h/2)$.
   $TZX(h)$ is obtained from the 4th-order approximation of the temporal derivative of the stress–strain relation for σ_{zx}; $\frac{\partial v_x}{\partial z}$ is approximated using Eq. (10.6) in which $\frac{\partial v_x}{\partial z}(0)$ is replaced by $\frac{\partial v_z}{\partial x}(0)$ due to condition $\sigma_{zx}(0) = 0$.
   $TYZ(h)$ is obtained from the 4th-order approximation of the temporal derivative of the stress–strain relation for σ_{yz}; $\frac{\partial v_y}{\partial z}$ is approximated using Eq. (10.6) in which $\frac{\partial v_y}{\partial z}(0)$ is replaced by $\frac{\partial v_z}{\partial y}(0)$ due to condition $\sigma_{yz}(0) = 0$.

(b) Calculation of the particle-velocity components:

   $VZ(0)$ is obtained from the 4th-order approximation of the equation for v_z; $\frac{\partial \sigma_{zz}}{\partial z}$ is approximated using Eq. (10.4) in which condition $\sigma_{zz}(0) = 0$ is used.
   $VX(h/2)$ is obtained from the 4th-order approximation of the equation for v_x; $\frac{\partial \sigma_{zx}}{\partial z}$ is approximated using Eq. (10.5).
   $VY(h/2)$ is obtained from the 4th-order approximation of the equation for v_y; $\frac{\partial \sigma_{yz}}{\partial z}$ is approximated using Eq. (10.5).
   $VZ(h)$ is obtained from the 4th-order approximation of the equation for v_z; $\frac{\partial \sigma_{zz}}{\partial z}$ is approximated using Eq. (10.7) in which condition $\sigma_{zz}(0) = 0$ is used.

The corresponding effective grid material parameters are evaluated as integral averages in the half grid-cell volumes; that is, the upper half of the volume located above the free surface is not taken into account. For example,

$$\rho_{I+1/2,K+1/2,0}^{A} = \frac{2}{h^3} \int_{x_I}^{x_{I+1}} \int_{y_K}^{y_{K+1}} \int_{z_0}^{z_{1/2}} \rho \, dx \, dy \, dz \qquad (10.8)$$

10.2 Free-surface topography

Implementation of the traction-free condition at a nonplanar surface has been one of the most difficult tasks and persisting challenges in FD modelling of seismic wave propagation and earthquake motion. The nonplanar free surface was addressed in the pioneering years of FDM in seismology by, e.g., Alterman and Rotenberg (1969), Alterman and Loewenthal (1970), Boore (1972a,b), Loewenthal and Alterman (1972), Munasinghe and Farnell (1973), Alterman and Nathaniel (1975), Ilan *et al.* (1975), Ilan and Loewenthal (1976). All the authors treated simple types of free-surface topography: e.g., one-quarter and three-quarter planes (90° and 270° vertices), a (0–180)° wedge, a vertical step discontinuity. Ilan (1977) and Jih *et al.* (1988) addressed an arbitrary polygonal free surface. The developed techniques were for 2D problems: SH (anti-plane horizontally polarized S waves in the vertical plane) or P-SV (in-plane P and vertically polarized S waves in the vertical plane). Whereas apparently the SH modelling did not pose a problem, the P-SV modelling faced problems with stability and limitations in terms of the free-surface geometry and the P-wave to S-wave speed ratio (V_P/V_S) due to conversion between the P and S waves. Mainly due to the problem in the case of large V_P/V_S, further development was mostly related to the velocity–stress or displacement–stress staggered-grid schemes, e.g., Hestholm and Ruud (1994, 1998, 2002), Pitarka and Irikura (1996), Robertsson (1996), Ohminato and Chouet (1997), Robertsson and Holliger (1997), Hestholm (1999), Hestholm *et al.* (1999), Hayashi *et al.* (2001).

A particular implementation of the traction-free condition at a nonplanar surface very much depends on the medium (e.g., elastic, viscoelastic with realistic attenuation), formulation of the equation of motion and stress–strain relation (e.g., strong-form displacement, displacement–stress or velocity–stress), grid geometry (e.g., Cartesian, curvilinear), grid type (conventional, collocated, staggered, partly-staggered), free-surface geometry (e.g., staircase, smooth), and dimensionality (2D, 3D). The mentioned aspects are reflected in a large variety of developed approaches and techniques. Correspondingly, we could follow alternative hierarchies in order to structure an overview of the recent approaches and techniques.

In the numerical modelling of seismic wave propagation and earthquake motion in surface local sedimentary structures it is important that the technique is at least stable and sufficiently accurate in sediments with the P-wave to S-wave speed ratio equal to 5 and even larger. We say 'at least' because these requirements should still go together with computational efficiency. Considering the three criteria (stability, V_P/V_S, efficiency), there

is still a need for further elaboration and development – despite significant progress in recent years.

Note that in the case of large V_P/V_S it is not just about the stability. It is also about the accuracy (see Section 8.3).

Here we restrict our discussion to a brief and simplified overview and point out the recent articles that we consider the most relevant.

We may recognize three basic strategies for treating a nonplanar free surface in FD modelling of seismic wave propagation and earthquake motion:

– FD schemes on Cartesian grids,
– FD schemes on curvilinear (conforming or boundary-conforming) grids,
– hybrid schemes combining an FD scheme with a method in which the implementation of the traction-free condition is considerably easier than in the FDM.

FD schemes on Cartesian grids Apparently, the easiest approach is based on using a staircase approximation of the true surface. Examples of the approach are the techniques developed by Pitarka and Irikura (1996), Robertsson (1996), Ohminato and Chouet (1997), Robertsson and Holliger (1997), Hayashi *et al.* (2001). We may also mention the schemes by Opršal and Zahradník (1999) and Pérez-Ruiz *et al.* (2005) but with a comment on their principal limitation for the lowest values of V_P/V_S.

Muir *et al.* (1992) demonstrated noticeable artificial diffraction generated at the grid-related steps of the internal material interfaces. Clearly, the steps of the staircase free surface can produce even stronger artificial diffraction. Artificial diffraction may be masked in the complex wavefield, which can also include true physical diffraction. Artificial step-related diffraction is considerably more visible on the differential seismograms. Artificial diffraction may be reduced within a limited frequency range by using relatively small spatial grid spacing. Numerical experience shows that with a staircase free surface it is necessary to apply a considerably finer grid compared to the grid that would be sufficient for the major part of the computational domain. Spatial oversampling of the wavefield can be circumvented by grid refinement in the vicinity of the free surface (Robertsson and Holliger 1997, Hayashi *et al.* 2001). In any case, artificial diffraction cannot be removed, it can only be reduced.

The problems with step-related artificial diffraction can be avoided using the immersed-interface (or embedded-boundary) approach, e.g., Kreiss and Petersson (2006), Lombard *et al.* (2008). Kreiss and Petersson considered the scalar 2nd-order wave equation without attenuation in 2D. Lombard and his colleagues also treated the 2D elastic problem but for the 1st-order hyperbolic system in the velocity–stress formulation, which is considerably more relevant for media with large V_P/V_S.

Lombard *et al.* (2008) considered the velocity–stress formulation on the collocated grid in which all particle-velocity and stress-tensor components share the same grid position (Lombard *et al.* used the term 'single-grid scheme'). They formulated the task as follows: treat the smooth arbitrarily shaped boundaries as simply as the straight boundaries; make the

accuracy independent of the boundary position in the grid; maintain stability for long runs. They showed that the requirements can be met by applying an explicit approach involving fictitious values of the solution in the vacuum. The calculation of the fictitious values is based on the boundary conditions and compatibility conditions satisfied by successive spatial derivatives of the solution, up to a given order depending on the spatial accuracy of the integration scheme. The traction-free conditions can be designed with arbitrary order of accuracy without numerical instabilities. Ten grid points per minimum S wavelength yields highly accurate results up to a propagation distance of 50 wavelengths. A logical but noticeable feature of the method is its capability of sub-cell resolution. Lombard *et al*. pointed out the possibility of instabilities in the case of using a staggered grid and long-time integration.

The immersed-interface method needs further elaboration in order to include heterogeneity of the medium, realistic attenuation and extension to 3D.

FD schemes on the curvilinear grids Curvilinear grids can align with the surface topography and naturally avoid artificial step-related diffraction. This idea attracted Hestholm and Ruud (1994, 1998, 2002), Hestholm (1999, 2003), Hestholm *et al*. (1999), Ruud and Hestholm (2001), Zhang and Chen (2006), Appelö and Petersson (2009), Tarrass *et al*. (2011), Lan and Zhang (2011), Zhang *et al*. (2012) and other researchers in their efforts to implement free-surface topography in seismic modelling. Appelö and Petersson (2009) considered a 2D displacement formulation (2nd-order hyperbolic equations) in a perfectly elastic medium. Lan and Zhang (2011) extended the approach by Appelö and Petersson to the 3D problem in a perfectly elastic transversally isotropic medium. Other authors considered the velocity–stress formulation. Hestholm and Ruud (2002) presented an implementation of the free-surface condition at a nonplanar surface for a viscoelastic medium in the 3D velocity–stress scheme on a staggered grid.

An interesting and innovative approach was presented by Zhang and Chen (2006) for 2D and by Zhang *et al*. (2012) for 3D free-surface topography. They used the velocity–stress formulation on the collocated grid. This is an important aspect for applying the traction-free condition. The authors transform the irregular surface in physical space into a 'flat' surface in computational space using a boundary-conforming grid. The grid is a general curvilinear grid (not the vertical stretching grid as in previous approaches by other authors). The free-surface conditions are implemented at this 'flat' surface by traction imaging. Traction imaging is logical since in the case of a nonplanar surface no single stress-tensor component is zero at the free surface. They re-write the velocity–stress equations as velocity–stress–traction equations (Eqs. 39–41 in their article) for the curvilinear grid, set the traction to zero at the surface and apply antisymmetric imaging of the traction components with respect to the free surface. In the velocity–stress–traction equations, derivatives with respect to the coordinate perpendicular to the free surface in computational space involve only tractions normal to the free surface – not the stress components. This is what the authors consider to be the main reason for the stability and accuracy of their modelling of the free surface.

Zhang *et al*. (2012) avoided the odd–even decoupling oscillations associated with centred FD approximations on the collocated grid: they applied the optimized DRP MacCormack scheme, which alternately uses forward and backward difference operators in the Runge–Kutta time stepping method (see the 1D scheme in Subsection 7.3.6). The scheme is 4th-order accurate in dispersion error. However, as pointed out by the authors, their traction imaging at a nonplanar free surface is not restricted to the particular FD scheme they used. Zhang *et al*. (2012) presented a numerical test for smooth 3D topography – the Gaussian-shaped hill.

Although numerical tests for an unbounded medium with large V_P/V_S confirmed the very good level of accuracy of the scheme (testing within the EuroseisTest Verification and Validation Project, CEA France), it is still desirable to test the accuracy with respect to V_P/V_S in the presence of the nonplanar free surface. The FD scheme developed by Zhang *et al*. (2012) should also be generalized for a viscoelastic medium with realistic attenuation.

Hybrid schemes Implementation of the traction-free condition is natural (though not necessarily more accurate) in the FEM. Moczo *et al*. (1997) combined a 2nd-order conventional FD scheme with a 2nd-order FEM for 2D viscoelastic P-SV modelling of seismic motion in near-surface sedimentary/topographic structures. Galis *et al*. (2008) developed a hybrid numerical method for a 3D viscoelastic heterogeneous medium with a nonplanar free surface. The method is based on a combination of the (2,4) VS SG FD scheme, covering a major part of the computational domain, with the (2,2) FEM, which can be applied to one or several relatively small subdomains. The FD and FE parts causally communicate at each time level in the FD–FE transition zone consisting of the FE Dirichlet boundary, FD–FE averaging zone and FD Dirichlet zone. The FE part can include the nonplanar free surface and/or a dynamically rupturing fault. The (2,2) FE method is limited in its accuracy for large V_P/V_S (see Moczo *et al*. 2010, 2011). Therefore, if the FE part were to include sediments with large V_P/V_S, the FE mesh should be sufficiently fine.

A possible hybrid combination of the FDM with other methods (e.g., meshless moving least-square method) might be explored.

11

Discontinuous spatial grid

11.1 Overview of approaches

The main advantage of a uniform grid is the algorithmical simplicity of the FD scheme. The main disadvantage of a uniform grid covering a strongly heterogeneous medium is the relatively large number of grid points and consequently the large number of algebraic operations. Typically, wave speeds in surface sediment structures are smaller than wave speeds beneath sediments, especially in a rock basement. If the minimum wave speed in the upper part of a computational model is smaller than that in the lower part of the model, it may be advantageous to use a combination of a finer grid (the grid spacing h) and a coarser grid (the grid spacing $H > h$). The finer grid may cover the upper part whereas the coarser, the lower part of the model. The total number of grid points in such a discontinuous spatial grid can be significantly smaller than that in a uniform grid. Therefore, numerical and especially FD modellers have made numerous efforts to implement discontinuous grids.

Before we introduce and explain the discontinuous grids, let us mention a simpler approach to reduce the number of grid points. Boore (1970) was the first to use a rectangular grid with varying size of grid spacings to model Love wave propagation. Mikumo and Miyatake (1987) applied varying grid spacing in the 3D case in a homogeneous medium. Moczo (1989) applied a grid with varying spacing to the 2D SH problem in a laterally heterogeneous medium. Pitarka (1999) developed 4th-order approximations of the 1st spatial derivative on the staggered grid with varying grid spacing, assuming simple functional dependence of a field variable on the spatial coordinate. His 3D velocity–stress scheme assumes variations of the grid spacings in all three coordinate directions. Grids of varying spacing do not reach the efficiency of discontinuous grids. Our limited numerical experience indicates a possible sensitivity of the simulated wavefield to variation in the size of the grid spacing, e.g., in the case of strong surface waves.

Jastram and Behle (1992) introduced a discontinuous grid with an arbitrary integer ratio of the coarser-grid spacing H to the finer-grid spacing h (that is $H/h = 2, 3, \ldots$) for their 2D acoustic, conventional-grid FD scheme. In order to calculate pressure at the missing positions in the coarser grid near the contact with the finer grid, they used trigonometric interpolation in the horizontal direction. Jastram and Tessmer (1994) generalized the concept for the 2D P-SV elastic displacement–stress staggered-grid scheme. They applied

trigonometric interpolation to the displacement and stress-tensor components. Ratio H/h could be an odd number. Wang and Schuster (1996) extended the approach by Jastram and Tessmer (1994) to 3D and an axisymmetric 4th-order scheme. Moczo *et al.* (1996) avoided interpolation of displacements at missing grid positions by using an adjusted FD approximation at the contact of the $H/h = 2$ discontinuous grid for their 2nd-order 2D SH elastic, conventional-grid scheme. Kristek *et al.* (1999) applied linear interpolation in a horizontal grid plane at the missing grid positions in the $H/h = 3$ discontinuous grid for the 3D 4th-order, viscoelastic, displacement–stress staggered-grid scheme. Aoi and Fujiwara (1999) used an $H/h = 3$ discontinuous grid for the 3D 2nd-order viscoelastic, velocity–stress staggered-grid (VS SG) scheme. They applied linear interpolation in a horizontal grid plane. Wang *et al.* (2001) developed a variable-grid method for the staggered-grid viscoelastic scheme that allows for $H/h = 2, 3$. They applied 3D interpolation in the wavenumber domain. Moczo *et al.* (2007a) used an $H/h = 3, 5, 7 \ldots$ discontinuous grid for the 3D 4th-order, viscoelastic, VS SG scheme.

Wang and Takenaka (2001) applied interpolation in the wavenumber domain in their $H/h = 2$ discontinuous grid for the 2D P-SV elastic, conventional-grid Fourier pseudo-spectral scheme. Hayashi *et al.* (2001) used an $H/h = 3$ discontinuous grid for the 2D P-SV 4th-order, viscoelastic, VS SG scheme.

The concept of a discontinuous grid was applied atypically by Robertsson and Holliger (1997) and Moczo *et al.* (1997). Robertsson and Holliger (1997) used an $H/h = 2$ discontinuous grid in order to accommodate the free-surface topography in the 3D VS SG scheme because their approach requires finer spatial discretization of the nonplanar free surface compared to the underlying interior. They applied linear interpolation in the vertical direction and sinc interpolation in the horizontal direction. Moczo *et al.* (1997) used FEs as the contact zone between the h and $2h$ FD grids for the 2D P-SV viscoelastic displacement conventional-grid scheme. A combination of fine and coarser grids was presented by Zhang (2004a,b) in his stress-grid scheme. Liu and Luan (2013) developed a mesh grading approach for high-velocity contrast media by utilizing matching unstructured fine and coarse grids. Ratio H/h can be an arbitrary odd number. The key feature of this approach is the construction of investigated lumps on the material interface. No overlapping (transition) zone is needed.

Kang and Baag (2004a) presented a combination of the spatially discontinuous grid with a locally varying time step for the 2D and 3D higher-order VS SG. Kang and Baag (2004b) further increased the computational efficiency by elaborating a discontinuous grid with a laterally localized finer grid with a locally varying time step.

It is worth mentioning the approach by Chaljub *et al.* (2003), who implemented a discontinuous spherical grid in their spectral-element modelling of elastic wave propagation in a solid–fluid sphere using the so-called mortar method. At the contact of the finer and coarser grids, two neighbouring elements do not share an entire edge or entire face. Kopriva (1989) elaborated nonmatching (i.e., spatially different) pseudo-spectral grids. His approach is close to the methodology of the nonmatching mortar spectral-element grids. Collino *et al.* (2006) used an interesting conservative space–time mesh refinement for the FDTD solution of Maxwell's equations.

All the approaches differing from each other in the H/h ratio and the method of interpolating values at the missing grid positions in the coarser grid indicate the importance of the discontinuous grid for efficient modelling.

An FD modeller could guess: the larger the grid ratio H/h, the larger the possibility of inaccuracy and, mainly, instability with an increasing number of time levels due to numerical noise generated at the contact of the grids. The noise generation and eventual instability cannot be simply correlated with the grid ratio because they may strongly depend on the material and wavefield heterogeneity. The potential complication with instability has only rarely been explicitly addressed. Among the rare exceptions, De Lilla (1997) pointed out that as the grid ratio increases the numerical inaccuracy due to the change of the grid spacing may increase. Hayashi *et al*. (2001) explicitly said that $H/h = 3$ is better for stability and accuracy compared to higher ratios. In order to reduce instability, they apply certain averaging or weighting to the replacement of the coarse-grid components within the fine grid field. Their procedure enables them to have computation stable during several thousands time steps. Wang *et al*. (2001) claimed that they have overcome a possible instability by a 3D interpolation scheme in the wavenumber domain.

Kristek *et al*. (2010) developed a stable algorithm for the discontinuous velocity–stress staggered grid with an arbitrary odd value of H/h. The algorithm is explained in detail in the following sections. Zhang *et al*. (2013b) applied and extended the concept by Kristek *et al*. (2010) for the collocated grid. Whereas Kristek *et al*. (2010) found the Lanczos filter appropriate for ensuring stability in the staggered grid, Zhang *et al*. (2013b) found the Gaussian filter better for the collocated grid.

11.2 Two basic problems and general considerations

There are two basic problems to be solved: (1) The very obvious one is that of the missing grid points – the reason for interpolation. This problem was addressed in all the published articles. (2) The other, and apparently not so obvious, problem is how to update the particle velocity and stress at those grid points of the coarser grid that coincide with the grid points of the finer grid. Kristek *et al*. (2010) showed that, in fact, this is a substantial problem.

The structure of the staggered grid (Fig. 6.1) implies that the most natural grid ratio H/h of a discontinuous grid is an odd number, $H/h = 3$ being the simplest case. Consider, for example, a grid position of σ_{xz}. For calculating it we need $\partial v_z / \partial x$. In the given grid the nearest grid positions of v_z are at distances $0.5h$ to the left and to the right from the position of σ_{xz}. If we omit these two nearest positions, the next available positions of v_z are at distances $1.5h$ to the left and to the right from the considered position of σ_{xz}. This gives a grid spacing of $H = 3h$ between two positions of v_z in the coarser grid.

Consider a hypothetical situation with a horizontal material interface between an upper medium with smaller shear-wave speed and a lower medium with larger shear-wave speed. Would a finer grid ending and a coarser grid starting just at the material interface be a good solution? No: the 4th-order interior FD formula would require interpolated values at distances of $0.5h$ and $1.5h$ from the interface in the medium with larger wave speed. Such an interpolation would lead to considerable inaccuracy. Neither would the alternative with

the 4th-order one-sided approximations (spatial extent of $3.5h$ in the vertical direction) in the upper medium be a good solution because a one-sided approximation is, in fact, an equivalent of extrapolation. A centred approximation should be better. This means placing the boundary of the finer grid in the medium with the larger wave speed. The finer and coarser grids then overlap in the medium with the larger wave speed. The finer and coarser grid should reasonably overlap even if there is no material interface and, instead, the wave speed smoothly increases.

The definition of the boundary of the finer grid and the overlapping zone depends on solving the two basic problems.

11.3 Velocity–stress discontinuous staggered grid

The vertical grid plane of the spatial VS discontinuous staggered grid is outlined in Fig. 11.1. Whereas this plane contains σ_{xx}, σ_{yy}, σ_{zz} and σ_{xz}, an analogous grid plane, displaced by $H/2$ in the y-direction, contains σ_{xy} and σ_{yz}. Clearly, there are also vertical grid planes with the finer-grid positions only. Figure 11.1 shows the simplest possible configuration with the grid ratio $H/h = 3$. Importantly, H/h can be an arbitrary odd number: $H/h = 3, 5, 7, \ldots$ Circles indicate the interior grid positions of the finer grid. The particle-velocity and stress-tensor components at these positions are updated using the interior 4th-order FD scheme for the finer grid. The boundary of the finer grid is made up of one grid row of cells indicated by grey circles. The diamonds indicate grid positions at which values have to be interpolated because these values are necessary for updating values at the grey-circle positions. Squares indicate interior grid positions of the coarser grid. The particle-velocity and stress-tensor components at these positions are updated using the interior 4th-order FD scheme for the coarser grid. Squares with inscribed circles indicate boundary positions of the coarser grid.

11.3.1 Calculation of the field variables at the boundary of the finer grid in the overlapping zone

The overlapping zone and thus also the boundary of the finer grid is placed in the medium with the larger S-wave speed. Consider some minimum wavelength in the faster medium that is to be propagated sufficiently accurately in the grid. Assume that the grid spacing h of the finer grid sufficiently oversamples this minimum wavelength. Then the updating of the field values at the finer-grid boundary (grey circles) with the interior 2nd-order scheme should be sufficiently accurate. The scheme obviously also requires the field values at the diamond positions. These values are obtained by interpolation. The bilinear interpolation (e.g., Press *et al.* 2007) is applied to v_z, σ_{xz} and σ_{yz} at one horizontal grid plane of the diamond grid positions.

Clearly, the application of the 2nd-order interior scheme to the finer-grid boundary significantly reduces the spatial extent of the interpolation – the interpolation is applied within one grid plane. The 4th-order scheme would need interpolation at three grid planes.
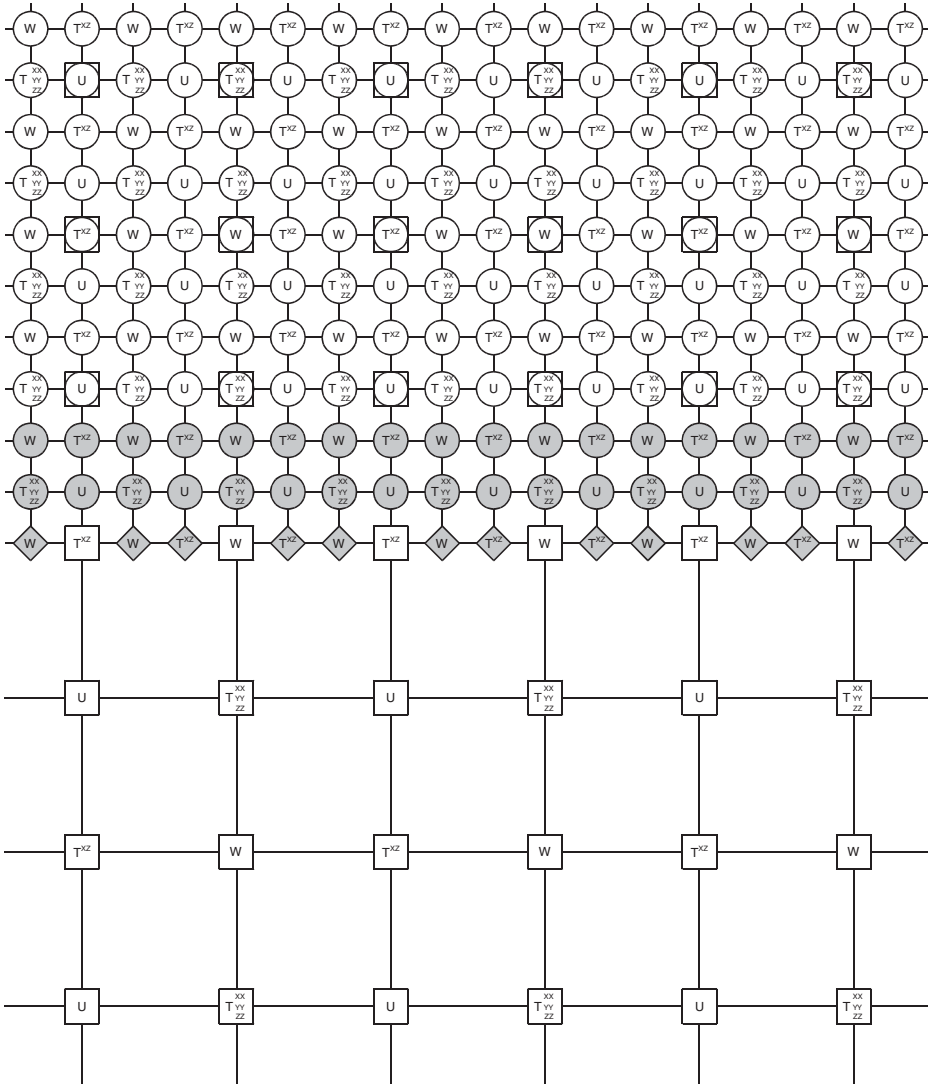
Figure 11.1 Vertical *xz*-grid plane in the simplest case of a spatially discontinuous velocity–stress staggered grid. The boundaries of the grid are not shown.

11.3.2 Calculation of the field variables at the boundary of the coarser grid in the overlapping zone

Consider the minimum wavelengths that can propagate in the overlapping zone placed in the medium with the larger wave speed. The theoretically minimum wavelength in the finer grid is $\lambda_N(h) = 2h$. The theoretically minimum wavelength in the coarser

grid is $\lambda_N(H) = 2H = (H/h)\lambda_N(h)$. Thus we have

$$0 < \lambda_N(h) < \lambda_N(H) \tag{11.1}$$

Therefore, the wavelengths larger than $\lambda_N(h)$ but smaller than $\lambda_N(H)$ present, in general, in the finer grid cannot, in principle, propagate from the finer grid into the coarser grid. In the computation, the wavefield from the finer grid enters the coarser grid through the field values at the grid positions indicated by squares with inscribed circles. Then it is clear that we cannot simply take the finer-grid field values at those grid positions for updating the field values at the internal grid positions of the coarser grid (indicated by squares). The finer-grid field values at the positions indicated by squares with inscribed circles have to be downsampled before they are used for updating the field values at the internal grid positions of the coarser grid.

Probably the best option is to apply the Lanczos downsampling filter (e.g., Duchon 1979, Turkowski and Gabriel 1990). For brevity and simplicity of the mathematical expressions we can denote the grid ratio as

$$n = H/h \tag{11.2}$$

The Lanczos filter can be expressed as

$$w_{kl}^{\mathrm{L}} = A \operatorname{sinc}\left(\pi\,\frac{k}{n}\right) \operatorname{sinc}\left(\pi\,\frac{l}{n}\right) \operatorname{sinc}\left(\pi\,\frac{\sqrt{k^2+l^2}}{2n}\right); \quad |k| \le 2n,\ |l| \le 2n \tag{11.3}$$

The scaling factor A is determined by the condition

$$\sum_{k=-2n}^{2n} \sum_{l=-2n}^{2n} w_{kl}^{\mathrm{L}} = 1 \tag{11.4}$$

Then the filtered value of a field variable Φ at the grid position (I, J) of the finer grid, $\tilde{\Phi}(I, J)$, is obtained as

$$\tilde{\Phi}(I, J) = \sum_{k=-2n}^{2n} \sum_{l=-2n}^{2n} w_{kl}^{\mathrm{L}} \Phi(I+k, J+l) \tag{11.5}$$

Because the filtered values only enter the FD approximations of the spatial derivatives in the vertical direction, the filtration is applied in a horizontal grid plane.

Thus, we work with two field values at each grid position indicated by squares with inscribed circles. One is the finer-grid value $\Phi(I, J)$. The other is $\tilde{\Phi}(I, J)$ and it is obtained by application of the Lanczos downsampling filter – using Eq. (11.5). It is this value that has to be used for updating the coarser-grid field values at the positions indicated by squares.

It is important to note that the concept of application of the Lanczos downsampling filter is general – it is in no way restricted to the VS SG formulation. We may also note that the algorithm would be exactly the same if grid positions of the particle-velocity components were positions of the displacement components.

11.3.3 Calculation of the field variables at the nonreflecting boundary

At the boundary of the grid, the overlapping zone is in contact with the nonreflecting boundary of the grid. Because in our grid we interpolate only v_z of the three particle-velocity components, v_z has to be at the leftmost/rightmost/rearmost/frontmost grid positions. In other words, the outer boundary of the grid goes through the grid positions of $\sigma_{xx}, \sigma_{yy}, \sigma_{zz}$. The bilinear interpolation (e.g., Press *et al.* 2007) requires values at certain grid positions around the interpolated position. If some of those positions are not available, which is the case near the outer boundary of the grid, it is necessary to apply an extrapolation instead of interpolation.

It follows from Eq. (11.5) that the downsampling can be applied at a grid position if the field values at n neighbouring grid positions from each side are available. Such a neighbourhood is not available for the coarser-grid positions near the grid boundary. Consequently, the finer-grid field values at those positions have to be taken for updating the field values at the internal grid positions of the coarser grid (positions indicated by squares). We have not observed the effects of those direct finer-grid field values taken from the relatively very small number of such grid positions. If the nonreflecting boundary is placed inside a perfectly matched layer, a potential effect (if any) is likely to be sufficiently eliminated.

12

Perfectly matched layer

The perfectly matched layer (PML) is probably the most efficient method to prevent reflections of seismic waves at artificial boundaries of the computational region, that is, at boundaries of the discrete spatial grid. In Section 7.6 we explained the PML in its simplest form – for 1D problems.

The PML was introduced by Bérenger (1994) for absorbing electromagnetic waves. Chew and Liu (1996), Hastings *et al*. (1996), Collino and Tsogka (2001), and Zeng *et al*. (2001) introduced the PML into modelling of elastic wave propagation. The importance of the PML for numerical modelling of seismic wave propagation was then soon recognized by Festa and Nielsen (2003), Komatitsch and Tromp (2003), Marcinkovich and Olsen (2003) and Wang and Tang (2003). The elaboration of the PML then continued intensively: e.g., Basu and Chopra (2004), Festa and Vilotte (2005), Festa *et al*. (2005), Ma and Liu (2006), Drossaert and Giannopoulos (2007a,b), Komatitsch and Martin (2007), Moczo *et al*. (2007b), Gao and Zhang (2008), Martin *et al*. (2008a,b), Meza-Fajardo and Papageorgiou (2008, 2012), Basu (2009), Martin and Komatitsch (2009), Zhang and Shen (2010) and Zhang and Gao (2011). For a comprehensive review of the development of PML theory and its applications to the numerical modelling of seismic wave propagation we refer to the articles on the convolutional PML improved at grazing incidence for elastic wave propagation and viscoelastic wave propagation by Komatitsch and Martin (2007) and Martin and Komatitsch (2009), respectively.

Zhang and Shen (2010) implemented the PML in the 4th-order velocity–stress FD scheme on the collocated grid. Zhang *et al*. (2013a) generalized the approach by Zhang and Shen (2010) by adapting it to the curvilinear collocated grid. Zhang *et al*. (2013a) also provide a concise review of PML development.

Let us also mention the nearly perfectly matched layer (NPML) introduced for electromagnetic waves by Cummer (2003). The NPML uses fewer auxiliary variables and fewer ordinary differential equations compared to the PML. We refer to articles by Chen *et al*. (2010), Chen (2011) and Chen and Zhao (2011).

Different formulations of the PML have been developed. They are termed split or unsplit and classical or convolutional. They may differ also in the form of the stretching factor. Komatitsch and Martin (2007) made a point about the limitation of the classical split in the case of grazing incidence. The convolutional PML (C-PML) technique improves the

accuracy of the discrete PML at grazing incidence. The advantage of the unsplit formulation is that it does not require the split parts of the particle-velocity vector components and stress-tensor components, and, consequently, does not increase the number of dependent variables. In the following sections we explain the basic formulations and relations between them.

12.1 Split formulation of the PML

Directional decomposition of the wavefield   Directional decompositions of the divergence of the stress tensor and of the stress tensor itself at a point are the key aspects of the split PML formulation. The equation of motion may be written as

$$
\begin{aligned}
\rho \frac{\partial^2 u_x}{\partial t^2} &= \frac{\partial \sigma_{xx}}{\partial x} + \frac{\partial \sigma_{yx}}{\partial y} + \frac{\partial \sigma_{zx}}{\partial z} = \varphi_x^x + \varphi_x^y + \varphi_x^z \\
\rho \frac{\partial^2 u_y}{\partial t^2} &= \frac{\partial \sigma_{xy}}{\partial x} + \frac{\partial \sigma_{yy}}{\partial y} + \frac{\partial \sigma_{zy}}{\partial z} = \varphi_y^x + \varphi_y^y + \varphi_y^z \\
\rho \frac{\partial^2 u_z}{\partial t^2} &= \frac{\partial \sigma_{xz}}{\partial x} + \frac{\partial \sigma_{yz}}{\partial y} + \frac{\partial \sigma_{zz}}{\partial z} = \varphi_z^x + \varphi_z^y + \varphi_z^z
\end{aligned}
\tag{12.1}
$$

Kristek *et al.* (2009) show that φ_i^j is a body force acting at a point and causing at that point a motion polarized in the i-th direction and having a tendency to propagate from that point in the j-th direction. Equations (12.1) show directional decompositions of the divergence of the stress tensor at a point. The decompositions are determined by the directions of the spatial derivatives. Hooke's law, Eq. (2.23), may be interpreted analogously: $M \frac{\partial u_i}{\partial x_j}$ (M being an appropriate modulus) means that part of the stress-tensor component at a point which has a tendency to propagate from that point in the j-th direction. Clearly, the decomposition applies also to the velocity–stress formulation.

For brevity and conciseness we indicate the spatial and temporal derivatives as

$$
\varphi_{i,j} \equiv \frac{\partial \varphi_i}{\partial x_j}, \quad \dot{\varphi}_i \equiv \frac{\partial \varphi_i}{\partial t}
\tag{12.2}
$$

Velocity–stress formulation   Consider further the velocity–stress formulation of the equation of motion (2.31) without the body-force term and with Hooke's law in the form (2.16):

$$
\rho \dot{v}_i = \sigma_{ji,j}, \quad \dot{\sigma}_{ij} = c_{ijkl} v_{k,l}
\tag{12.3}
$$

Let $p, q, r \in \{x, y, z\}$ and p denote a coordinate direction perpendicular to a planar interface between the interior region and the PML, and q, r directions perpendicular to direction p. Decomposition of the particle velocity and stress tensor,

$$
\dot{v}_i = \dot{v}_i^p + \dot{v}_i^{qr}, \quad \dot{\sigma}_{ij} = \dot{\sigma}_{ij}^p + \dot{\sigma}_{ij}^{qr}
\tag{12.4}
$$

yields the equation of motion and Hooke's law in the forms

$$
\rho \dot{v}_i^p = \sigma_{ji,j} \delta_{jp}, \quad \dot{\sigma}_{ij}^p = c_{ijkl} v_{k,l} \delta_{lp}
\tag{12.5}
$$

$$
\rho \dot{v}_i^{qr} = \sigma_{ji,j}(1 - \delta_{jp}), \quad \dot{\sigma}_{ij}^{qr} = c_{ijkl} v_{k,l}(1 - \delta_{lp})
\tag{12.6}
$$

An application of the Fourier transform to Eqs. (12.5) gives

$$i\omega\rho v_i^p = \sigma_{ji,j}\delta_{jp}, \quad i\omega\sigma_{ij}^p = c_{ijkl}v_{k,l}\delta_{lp} \tag{12.7}$$

For brevity, we use the same symbols for the quantities in the frequency and time domains. Replace the spatial differentiation with respect to x_p in Eqs. (12.7) by the spatial differentiation with respect to $\tilde{x}_p$,

$$\frac{\partial}{\partial\tilde{x}_p} = \frac{1}{s}\frac{\partial}{\partial x_p} \tag{12.8}$$

Here s is the stretching factor:

$$s = \gamma + \frac{\Omega}{\alpha + i\omega} \tag{12.9}$$

and γ, Ω and α, being in general functions of x_p, define the PML medium profile. Equations (12.7) become

$$s\, i\omega\rho v_i^p = \sigma_{ji,j}\delta_{jp}, \quad s\, i\omega\sigma_{ij}^p = c_{ijkl}v_{k,l}\delta_{lp} \tag{12.10}$$

or

$$i\omega\rho v_i^p = \frac{1}{s}\sigma_{ji,j}\delta_{jp}, \quad i\omega\sigma_{ij}^p = \frac{1}{s}c_{ijkl}v_{k,l}\delta_{lp} \tag{12.11}$$

We may recognize the L-split formulation based on Eqs. (12.10) and the R-split formulation based on Eqs. (12.11).

L-split A substitution of s in Eqs. (12.10) according to Eq. (12.9) leads to

$$\rho\left(i\omega + \frac{\Omega}{\gamma} - \frac{\Omega}{\gamma}\frac{\alpha}{\alpha + i\omega}\right)v_i^p = \frac{1}{\gamma}\sigma_{ji,j}\delta_{jp} \tag{12.12}$$

$$\left(i\omega + \frac{\Omega}{\gamma} - \frac{\Omega}{\gamma}\frac{\alpha}{\alpha + i\omega}\right)\sigma_{ij}^p = \frac{1}{\gamma}c_{ijkl}v_{k,l}\delta_{lp} \tag{12.13}$$

Define

$$\eta_i^p(\omega) = \rho\frac{\Omega}{\gamma}\frac{\alpha}{\alpha + i\omega}v_i^p, \quad \xi_{ij}^p(\omega) = \frac{\Omega}{\gamma}\frac{\alpha}{\alpha + i\omega}\sigma_{ij}^p \tag{12.14}$$

Then Eqs. (12.12) and (12.13) become

$$\rho\left(i\omega + \frac{\Omega}{\gamma}\right)v_i^p = \frac{1}{\gamma}\sigma_{ji,j}\delta_{jp} + \eta_i^p(\omega) \tag{12.15}$$

$$\left(i\omega + \frac{\Omega}{\gamma}\right)\sigma_{ij}^p = \frac{1}{\gamma}c_{ijkl}v_{k,l}\delta_{lp} + \xi_{ij}^p(\omega) \tag{12.16}$$

In order to remove the imaginary unit from the denominator in Eqs. (12.14) we rewrite them:

$$(\alpha + i\omega)\eta_i^p(\omega) = \rho\frac{\alpha\Omega}{\gamma}v_i^p, \quad (\alpha + i\omega)\xi_{ij}^p(\omega) = \frac{\alpha\Omega}{\gamma}\sigma_{ij}^p \tag{12.17}$$

An application of the inverse Fourier transform to Eqs. (12.15)–(12.17) yields

$$\rho \dot{v}_i^p + \rho \frac{\Omega}{\gamma} v_i^p = \frac{1}{\gamma} \sigma_{ji,j} \delta_{jp} + \eta_i^p \tag{12.18}$$

$$\dot{\sigma}_{ij}^p + \frac{\Omega}{\gamma} \sigma_{ij}^p = \frac{1}{\gamma} c_{ijkl} v_{k,l} \delta_{lp} + \xi_{ij}^p \tag{12.19}$$

$$\dot{\eta}_i^p + \alpha \eta_i^p = \rho \frac{\alpha \Omega}{\gamma} v_i^p, \quad \dot{\xi}_{ij}^p + \alpha \xi_{ij}^p = \frac{\alpha \Omega}{\gamma} \sigma_{ij}^p \tag{12.20}$$

Here, η_i^p and ξ_{ij}^p are functions of time. Clearly, η_i^p and ξ_{ij}^p are additional variables (memory variables) obeying ordinary differential equations (12.20). They are introduced in order to avoid a direct calculation of the convolutions that would otherwise appear in Eqs. (12.18) and (12.19). Equations (12.4), (12.6) and (12.18)–(12.20) make up the final system to be solved.

Consider the special choice of $\gamma = 1$ and $\alpha = 0$. Then the stretching factor is

$$s = 1 + \frac{\Omega}{i\omega} \tag{12.21}$$

and Eqs. (12.18)–(12.20) reduce to the well-known split PML formulation:

$$\rho \dot{v}_i^p + \rho \Omega v_i^p = \sigma_{ji,j} \delta_{jp} \tag{12.22}$$

$$\dot{\sigma}_{ij}^p + \Omega \sigma_{ij}^p = c_{ijkl} v_{k,l} \delta_{lp} \tag{12.23}$$

Note that in this special case we could, in fact, directly apply the damping terms proportional to v_i^p and σ_{ij}^p in Eqs. (12.5). An application of the Fourier transform to the modified equations would reveal that the addition of the damping terms is equivalent to replacement of the differentiation with respect to x_p by the differentiation with respect to $\tilde{x}_p$.

R-split Substituting the definition of the stretching factor s, Eq. (12.9), into Eqs. (12.11) we obtain

$$i\omega \rho v_i^p = \left(\frac{1}{\gamma} - \frac{b}{a + i\omega} \right) \sigma_{ji,j} \delta_{jp} \tag{12.24}$$

$$i\omega \sigma_{ij}^p = \left(\frac{1}{\gamma} - \frac{b}{a + i\omega} \right) c_{ijkl} v_{k,l} \delta_{lp} \tag{12.25}$$

where

$$a = \alpha + \Omega/\gamma, \quad b = \Omega/\gamma^2 \tag{12.26}$$

Define

$$\theta_i^p(\omega) = \frac{-b}{a + i\omega} \sigma_{ji,j} \delta_{jp}, \quad \zeta_{ij}^p(\omega) = \frac{-b}{a + i\omega} c_{ijkl} v_{k,l} \delta_{lp} \tag{12.27}$$

Then,

$$i\omega\rho v_i^p = \frac{1}{\gamma}\sigma_{ji,j}\delta_{jp} + \theta_i^p(\omega) \tag{12.28}$$

$$i\omega\sigma_{ij}^p = \frac{1}{\gamma}c_{ijkl}v_{k,l}\delta_{lp} + \zeta_{ij}^p(\omega) \tag{12.29}$$

In order to remove the imaginary unit from the denominator in Eqs. (12.27) we rewrite them:

$$i\omega\theta_i^p(\omega) + a\theta_i^p(\omega) = -b\sigma_{ji,j}\delta_{jp}$$
$$i\omega\zeta_{ij}^P(\omega) + a\zeta_{ij}^P(\omega) = -bc_{ijkl}v_{k,l}\delta_{lp} \tag{12.30}$$

An application of the inverse Fourier transform to Eqs. (12.28)–(12.30) yields

$$\rho\dot{v}_i^p = \frac{1}{\gamma}\sigma_{ji,j}\delta_{jp} + \theta_i^p \tag{12.31}$$

$$\dot{\sigma}_{ij}^p = \frac{1}{\gamma}c_{ijkl}v_{k,l}\delta_{lp} + \zeta_{ij}^p \tag{12.32}$$

$$\dot{\theta}_i^p + a\theta_i^p = -b\sigma_{ji,j}\delta_{jp}, \quad \dot{\zeta}_{ij}^p + a\zeta_{ij}^p = -bc_{ijkl}v_{k,l}\delta_{lp} \tag{12.33}$$

Here, θ_i^p and ζ_{ij}^p are functions of time. Similarly to the L-split case, θ_i^p and ζ_{ij}^p are additional (memory) variables.

Looking at Eqs. (12.6) and (12.31)–(12.33) we can realize that it is possible to sum the first of Eqs. (12.6) and Eq. (12.31) as well as the second of Eqs. (12.6) and Eq. (12.32). We obtain

$$\rho\dot{v}_i = \frac{1}{\gamma}\sigma_{ji,j}\,\delta_{jp} + \theta_i^p + \sigma_{ji,j}\left(1 - \delta_{jp}\right) \tag{12.34}$$

$$\dot{\sigma}_{ij} = \frac{1}{\gamma}c_{ijkl}v_{k,l}\delta_{lp} + \zeta_{ij}^p + c_{ijkl}v_{k,l}\left(1 - \delta_{lp}\right) \tag{12.35}$$

Thus, Eqs. (12.33)–(12.35) make the final system of equations to be solved.

In the special case with $\gamma = 1$ and $\alpha = 0$ both parameters a and b are equal to Ω. Note, however, that Eqs. (12.31)–(12.35) do not change. This means that the R-split formulation remains convolutional even in the case of the special form of the stretching factor.

12.2 Unsplit formulation of the PML

Here we manipulate directly with the entire equation of motion and Hooke's law for the unsplit field variables. Application of the Fourier transform to the equations yields

$$i\omega\rho v_i = \sigma_{ji,j}, \quad i\omega\sigma_{ij} = c_{ijkl}v_{k,l} \tag{12.36}$$

Replacement of the spatial differentiations with respect to x_p by differentiations with respect to $\tilde{x}_p$ yields

$$i\omega\rho v_i = \left(\frac{1}{\gamma} - \frac{b}{a + i\omega}\right)\sigma_{ji,j}\delta_{jp} + \sigma_{ji,j}(1 - \delta_{jp}) \tag{12.37}$$

$$i\omega\sigma_{ij} = \left(\frac{1}{\gamma} - \frac{b}{a + i\omega}\right)c_{ijkl}v_{k,l}\delta_{lp} + c_{ijkl}v_{k,l}\left(1 - \delta_{lp}\right) \tag{12.38}$$

Substitution of variables θ_i^p and ζ_{ij}^p, defined by Eqs. (12.27), in Eqs. (12.37) and (12.38), respectively, and a subsequent application of the inverse Fourier transform yield

$$\rho\dot{v}_i = \frac{1}{\gamma}\sigma_{ji,j}\delta_{jp} + \theta_i^p + \sigma_{ji,j}\left(1 - \delta_{jp}\right) \tag{12.39}$$

$$\dot{\sigma}_{ij} = \frac{1}{\gamma}c_{ijkl}v_{k,l}\delta_{lp} + \zeta_{ij}^p + c_{ijkl}v_{k,l}\left(1 - \delta_{lp}\right) \tag{12.40}$$

Clearly, the memory variables θ_i^p and ζ_{ij}^p satisfy differential equations (12.33). Equations (12.39) and (12.40) are the same as Eqs. (12.34) and (12.35). In other words, we see that the unsplit formulation leads to the same final equations as the R-split case of the split formulation.

Note that the presented unsplit formulation is equivalent to that introduced by Komatitsch and Martin (2007).

12.3 Summary of the formulations

Table 12.1 summarizes the formulations and their relations. For conciseness the table lists only the equations for particle velocity. It is clear that the general form of the stretching factor s given by Eq. (12.9) naturally implies the memory variables in both the split and unsplit formulations if a direct calculation of the convolutional terms is to be avoided. In the case of the L-split formulation and special choice of the stretching factor, given by Eq. (12.21), the resulting equations reduce to the well-known equations with a simple damping term – Eqs. (12.22) and (12.23). The case of the R-split formulation eventually leads to equations identical with those obtained straightforwardly in the unsplit formulation.

12.4 Time discretization of the unsplit formulation

The memory variable θ_i^p and its temporal derivative may be approximated as

$$\theta_i^{p,m} \approx \frac{1}{2}\left(\theta_i^{p,m+\frac{1}{2}} + \theta_i^{p,m-\frac{1}{2}}\right), \quad \dot{\theta}_i^{p,m} \approx \frac{1}{\Delta}\left(\theta_i^{p,m+\frac{1}{2}} - \theta_i^{p,m-\frac{1}{2}}\right) \tag{12.41}$$

Table 12.1 *PML formulations and their relations*

Formulation for velocity in the PML region perpendicular to direction $p: \ \partial \tilde{x}_p = \frac{1}{s}\partial x_p$		
Split : $\ \dot{v}_i = \dot{v}_i^{\,p} + \dot{v}_i^{\,qr}$		**Unsplit**
$\mathrm{i}\omega\rho\, v_i^{qr} = \sigma_{ji,j}\left(1-\delta_{jp}\right)$		$\mathrm{i}\omega\rho\, v_i =$ $\frac{1}{s}\sigma_{ji,j}\,\delta_{jp} + \sigma_{ji,j}\left(1-\delta_{jp}\right)$
L-split	R-split	
$s\,\mathrm{i}\omega\rho\, v_i^p = \sigma_{ji,j}\,\delta_{jp}$	$\mathrm{i}\omega\rho\, v_i^p = \frac{1}{s}\sigma_{ji,j}\,\delta_{jp}$	
general case : $\ \ s = \gamma + \Omega/(\alpha + \mathrm{i}\omega)$		
$\rho\dot{v}_i^p + \rho\dfrac{\Omega}{\gamma}\,v_i^p = \dfrac{1}{\gamma}\sigma_{ji,j}\,\delta_{jp} + \eta_i^p$ $\dot{\eta}_i^p + \alpha\eta_i^p = \rho\dfrac{\alpha\Omega}{\gamma}\,v_i^p$ $\rho\,\dot{v}_i^{qr} = \sigma_{ji,j}\left(1-\delta_{jp}\right)$	$\rho\dot{v}_i^p = \dfrac{1}{\gamma}\sigma_{ji,j}\,\delta_{jp} + \theta_i^p$ $\dot{\theta}_i^p + a\,\theta_i^p = -b\,\sigma_{ji,j}\,\delta_{jp}$ $\rho\,\dot{v}_i^{qr} = \sigma_{ji,j}\left(1-\delta_{jp}\right)$	
	leads to:	
	$\rho\,\dot{v}_i = \dfrac{1}{\gamma}\sigma_{ji,j}\,\delta_{jp} + \theta_i^p + \sigma_{ji,j}\left(1-\delta_{jp}\right)$ $\dot{\theta}_i^p + a\,\theta_i^p = -b\,\sigma_{ji,j}\,\delta_{jp}$ $a = \alpha + \Omega/\gamma, \quad b = \Omega/\gamma^2$	
special case : $\ \ s = 1 + \Omega/\mathrm{i}\omega$		
$\rho\dot{v}_i^p + \rho\Omega\, v_i^p = \sigma_{ji,j}\,\delta_{jp}$ $\rho\dot{v}_i^{qr} = \sigma_{ji,j}\left(1-\delta_{jp}\right)$	$\rho\dot{v}_i = \sigma_{ji,j}\,\delta_{jp} + \theta_i^p + \sigma_{ji,j}\left(1-\delta_{jp}\right)$ $\dot{\theta}_i^p + \Omega\,\theta_i^p = -\Omega\,\sigma_{ji,j}\,\delta_{jp}$	

Application of approximations (12.41) to Eq. (12.33) yields

$$\theta_i^{p,m+\frac{1}{2}} \approx \frac{2-a\Delta}{2+a\Delta}\theta_i^{p,m-\frac{1}{2}} - \frac{2b\Delta}{2+a\Delta}\sigma_{ji,j}^m\delta_{jp} \tag{12.42}$$

If we relate Eq. (12.39) to the time level m, we need $\theta_i^{p,m}$. Using Eqs. (12.41) and (12.42) we obtain

$$\theta_i^{p,m} \approx \frac{2}{2+a\Delta}\theta_i^{p,m-\frac{1}{2}} - \frac{b\Delta}{2+a\Delta}\sigma_{ji,j}^m\delta_{jp} \tag{12.43}$$

Using (12.43) we can rewrite Eq. (12.39) for the particle velocity:

$$\rho\dot{v}_i^m = \left(\frac{1}{\gamma} - \frac{b\Delta}{2+a\Delta}\right)\sigma_{ji,j}^m\delta_{jp} + \frac{2}{2+a\Delta}\theta_i^{p,m-\frac{1}{2}} + \sigma_{ji,j}^m(1-\delta_{jp}) \tag{12.44}$$

Substituting a and b from Eq. (12.26) in Eqs. (12.42) and (12.44), and approximating $\dot{v}_i^m$ by the central-difference formula we can obtain the final form of the equation of motion and additional equations for the memory variables:

$$v_i^{m+\frac{1}{2}} \approx v_i^{m-\frac{1}{2}} + \frac{\Delta}{\rho} \left[\frac{1}{\gamma} \left(1 - \frac{\Omega\Delta}{2\gamma + (\alpha\gamma + \Omega)\,\Delta} \right) \sigma_{ji,j}^m \delta_{jp} \right.$$

$$\left. + \frac{2\gamma}{2\gamma + (\alpha\gamma + \Omega)\,\Delta} \theta_i^{p,m-\frac{1}{2}} + \sigma_{ji,j}^m \left(1 - \delta_{jp} \right) \right] \qquad (12.45)$$

$$\theta_i^{p,m+\frac{1}{2}} \approx \frac{2\gamma - (\alpha\gamma + \Omega)\,\Delta}{2\gamma + (\alpha\gamma + \Omega)\,\Delta} \theta_i^{p,m-\frac{1}{2}}$$

$$- \frac{1}{\gamma} \frac{2\Omega\Delta}{2\gamma + (\alpha\gamma + \Omega)\,\Delta} \sigma_{ji,j}^m \delta_{jp} \qquad (12.46)$$

It is not necessary to show the analogous derivation of the time discretization for the constitutive relation (12.40). The final system of equations is

$$\sigma_{ij}^{m+1} \approx \sigma_{ij}^m + \Delta \left[\left(\frac{1}{\gamma} - \frac{\Omega\Delta}{2\gamma + (\alpha\gamma + \Omega)\,\Delta} \right) c_{ijkl} v_{k,l}^{m+\frac{1}{2}} \delta_{lp} \right.$$

$$\left. + \frac{2\gamma}{2\gamma + (\alpha\gamma + \Omega)\,\Delta} \zeta_{ij}^{p,m} + c_{ijkl} v_{k,l}^{m+\frac{1}{2}} (1 - \delta_{lp}) \right] \qquad (12.47)$$

$$\zeta_{ij}^{p,m+1} \approx \frac{2\gamma - (\alpha\gamma + \Omega)\,\Delta}{2\gamma + (\alpha\gamma + \Omega)\,\Delta} \zeta_{ij}^{p,m}$$

$$- \frac{1}{\gamma} \frac{2\Omega\Delta}{2\gamma + (\alpha\gamma + \Omega)\,\Delta} c_{ijkl} v_{k,l}^{m+\frac{1}{2}} \delta_{lp} \qquad (12.48)$$

Equations (12.45)–(12.48) represent discretization that is an alternative to that developed by Komatitsch and Martin (2007). Their discretization can be written in a form similar to Eqs. (12.45)–(12.48), see Kristek *et al.* (2009). The difference between our discretization and the discretization by Komatitsch and Martin (2007) is in the coefficients. This is due to different time integrations of Eqs. (12.33). The integration chosen by Komatitsch and Martin (2007) would be the exact integration of Eqs. (12.33) if $b = 0$. If $b \neq 0$, which is the case, both discretizations are 2nd-order accurate in time.

Kristek *et al.* (2009) numerically demonstrated the efficiency of the scheme based on Eqs. (12.45)–(12.48).

Finally, note that a rigid boundary can be prescribed at the border of PML.

13

Simulation of the kinematic sources

The basics of kinematic wavefield excitation in 1D were briefly introduced in Section 7.7.

13.1 Wavefield decomposition

Alterman and Karal (1968) introduced wavefield decomposition in order to avoid a point-source singularity. The total wavefield is decomposed into the wavefield produced by the source and the residual (or scattered) wavefield. The principle of wavefield decomposition is, in general, an efficient tool for 'injecting' an analytical source wavefield into the grid. By (a) distinguishing separate grid field variables for the source, residual and total wavefields, (b) prescribing just the source wavefield, and (c) calculating the residual and total wavefields we do not violate physical causality. In Subsection 7.7.2 we show the detailed algorithms in the cases of the 1D (2,2) and (2,4) velocity–stress staggered-grid schemes. It is clear from the algorithms that the grid field variables of the residual and total wavefields overlap only in the algorithmically minimum zone. Generalization of the algorithms to 3D is trivial.

The wavefield-decomposition technique has been applied by many modellers in a variety of FD schemes and geometrical configurations, e.g., Kelly *et al.* (1976), Vidale and Helmberger (1987), Levander (1988), Moczo (1989), Robertsson and Chapman (2000).

Wavefield decomposition has been advantageously applied in hybrid approaches combining different numerical methods, e.g., Fäh (1992), Fäh *et al.* (1993), Zahradník (1995a), Robertsson *et al.* (1996), Zahradník and Moczo (1996), Moczo *et al.* (1997).

Closely related to the Alterman and Karal (1968) approach is the generalized and sophisticated method developed by Takeuchi and Geller (2003) for implementing a source at an arbitrary location in the grid.

The general theory of wavefield decomposition, formulation of the general boundary condition and extensive references can be found in the article by Opršal *et al.* (2009).

13.2 Body-force term

The use of the body-force term was introduced by Aboudi (1971), Yomogida and Etgen (1993) and Frankel (1993) for the displacement conventional schemes, and by Graves (1996) for the velocity–stress staggered-grid schemes.
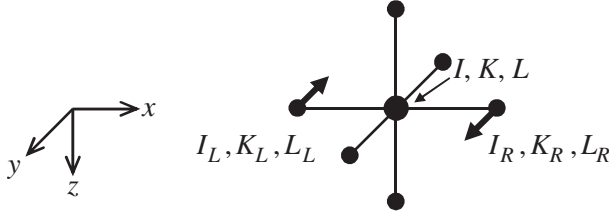
Figure 13.1 Illustration of simulation of the (y, x) couple acting at the grid point (I, K, L) of the conventional grid.

Conventional grid We want to simulate a point double-couple source using the body-force term in the equation of motion. This means simulation of a system of force couples (p, q) with strength M_{pq} acting at a grid point. Consider, for example, an (y, x) couple acting at the grid point (I, K, L); see Fig. 13.1. The body-force term in the equation of motion corresponding to this couple, that is, f_y, can be approximated as

$$f_y \approx \frac{1}{h^3}\frac{1}{2h} M_{yx}(t) \left(\delta_{II_R}\delta_{KK_R}\delta_{LL_R} - \delta_{II_L}\delta_{KK_L}\delta_{LL_L} \right) \tag{13.1}$$

where $2h$ is the arm length and $1/h^3$ normalizes the force to the unit volume, and δ_{mn} denotes the Kronecker delta.

In general, assuming the body-force couples acting at the grid point (I, K, L) in the conventional grid, we obtain for the discrete approximations to the body forces:

$$
\begin{aligned}
F^x_{I+1,K,L} &= -F^x_{I-1,K,L} = \frac{1}{2h^4} M_{xx}(t) \\[4pt]
F^y_{I+1,K,L} &= -F^y_{I-1,K,L} = \frac{1}{2h^4} M_{yx}(t) \\[4pt]
F^z_{I+1,K,L} &= -F^z_{I-1,K,L} = \frac{1}{2h^4} M_{zx}(t) \\[4pt]
F^x_{I,K+1,L} &= -F^x_{I,K-1,L} = \frac{1}{2h^4} M_{xy}(t) \\[4pt]
F^y_{I,K+1,L} &= -F^y_{I,K-1,L} = \frac{1}{2h^4} M_{yy}(t) \\[4pt]
F^z_{I,K+1,L} &= -F^z_{I,K-1,L} = \frac{1}{2h^4} M_{zy}(t) \\[4pt]
F^x_{I,K,L+1} &= -F^x_{I,K,L-1} = \frac{1}{2h^4} M_{xz}(t) \\[4pt]
F^y_{I,K,L+1} &= -F^y_{I,K,L-1} = \frac{1}{2h^4} M_{yz}(t) \\[4pt]
F^z_{I,K,L+1} &= -F^z_{I,K,L-1} = \frac{1}{2h^4} M_{zz}(t)
\end{aligned}
\tag{13.2}
$$

In the case of tangential slip the moment tensor $M_{pq}(t)$ is given by Eq. (4.31). For simplicity we do not indicate the time-level index.

Staggered grid A complication in comparison with the conventional grid is due to the different positions of the particle–velocity components in the grid. We assume a double-couple point source acting at the grid point $(I + 1/2, K + 1/2, L + 1/2)$ – the grid position of the normal stress-tensor components. We need, in the simplest approximation, 30 grid body-force terms:

$$F^x_{I+1,K+1/2,L+1/2} = -F^x_{I,K+1/2,L+1/2} = \frac{1}{h^4} M_{xx}(t)$$

$$F^x_{I+1,K+3/2,L+1/2} = -F^x_{I+1,K-1/2,L+1/2} = \frac{1}{4h^4} M_{xy}(t)$$

$$F^x_{I,K+3/2,L+1/2} = -F^x_{I,K-1/2,L+1/2} = \frac{1}{4h^4} M_{xy}(t) \qquad (13.3)$$

$$F^x_{I+1,K+1/2,L+3/2} = -F^x_{I+1,K+1/2,L-1/2} = \frac{1}{4h^4} M_{xz}(t)$$

$$F^x_{I,K+1/2,L+3/2} = -F^x_{I,K+1/2,L-1/2} = \frac{1}{4h^4} M_{xz}(t)$$

$$F^y_{I+1/2,K+1,L+1/2} = -F^y_{I+1/2,K,L+1/2} = \frac{1}{h^4} M_{yy}(t)$$

$$F^y_{I+3/2,K+1,L+1/2} = -F^y_{I-1/2,K+1,L+1/2} = \frac{1}{4h^4} M_{yx}(t)$$

$$F^y_{I+3/2,K,L+1/2} = -F^y_{I-1/2,K,L+1/2} = \frac{1}{4h^4} M_{yx}(t) \qquad (13.4)$$

$$F^y_{I+1/2,K+1,L+3/2} = -F^y_{I+1/2,K+1,L-1/2} = \frac{1}{4h^4} M_{yz}(t)$$

$$F^y_{I+1/2,K,L+3/2} = -F^y_{I+1/2,K,L-1/2} = \frac{1}{4h^4} M_{yz}(t)$$

$$F^z_{I+1/2,K+1/2,L+1} = -F^z_{I+1/2,K+1/2,L} = \frac{1}{h^4} M_{zz}(t)$$

$$F^z_{I+3/2,K+1/2,L+1} = -F^z_{I-1/2,K+1/2,L+1} = \frac{1}{4h^4} M_{zx}(t)$$

$$F^z_{I+3/2,K+1/2,L} = -F^z_{I-1/2,K+1/2,L} = \frac{1}{4h^4} M_{zx}(t) \qquad (13.5)$$

$$F^z_{I+1/2,K+3/2,L+1} = -F^z_{I+1/2,K-1/2,L+1} = \frac{1}{4h^4} M_{zy}(t)$$

$$F^z_{I+1/2,K+3/2,L} = -F^z_{I+1/2,K-1/2,L} = \frac{1}{4h^4} M_{zy}(t)$$

13.3 Incremental stress

Another possibility is to add an incremental stress $\Delta\sigma\,(t)$ at the grid position of the stress. The use of an incremental stress was introduced by Virieux (1986), Coutant *et al.* (1995), Olsen *et al.* (1995a; they used the moment tensor itself instead of the temporal derivative of the moment tensor) and later used by Pitarka (1999) and others. Compared to the direct use of the body-force term, the approach is simpler. For a double-couple point source acting at one point the corresponding assignment may be

$$TXX_{I+1/2,K+1/2,L+1/2} = TXX_{I+1/2,K+1/2,L+1/2} - \frac{\Delta}{h^3}\frac{\partial M_{xx}}{\partial t}$$

$$TYY_{I+1/2,K+1/2,L+1/2} = TYY_{I+1/2,K+1/2,L+1/2} - \frac{\Delta}{h^3}\frac{\partial M_{yy}}{\partial t}$$

$$TZZ_{I+1/2,K+1/2,L+1/2} = TZZ_{I+1/2,K+1/2,L+1/2} - \frac{\Delta}{h^3}\frac{\partial M_{zz}}{\partial t}$$

$$\qquad\qquad TXY_{I,K,L+1/2} = TXY_{I,K,L+1/2} - \frac{\Delta}{h^3}\frac{\partial M_{xy}}{\partial t}$$

$$\qquad\qquad TYZ_{I+1/2,K,L} = TYZ_{I+1/2,K,L} - \frac{\Delta}{h^3}\frac{\partial M_{yz}}{\partial t}$$

$$\qquad\qquad TZX_{I,K+1/2,L} = TZX_{I,K+1/2,L} - \frac{\Delta}{h^3}\frac{\partial M_{zx}}{\partial t}$$

$$(13.6)$$

Strictly speaking, it is clear that the point position of the point double-couple source is smeared over the grid cell with the grid position of the normal stress-tensor components at $(I + 1/2, K + 1/2, L + 1/2)$. It follows from the representation theorem that the temporal derivative of the moment tensor has to be used in the velocity–stress scheme. In the case of the displacement–stress scheme the moment tensor itself is used and the time step does not appear in the equations.

14

Simulation of dynamic rupture propagation

The discontinuity of the displacement vector and the particle-velocity vector together with the friction law poses a nontrivial boundary condition. Whereas a semi-analytical boundary-integral equation method (e.g., Das 1980, Andrews 1985, Cochard and Madariaga 1994, Aochi *et al*. 2000, Lapusta *et al*. 2000, Lapusta and Rice 2003, Day *et al*. 2005) is perhaps the most accurate method to account for the fault boundary conditions, especially on nonplanar faults (e.g., Aochi and Fukuyama 2002), its application is limited because it cannot include heterogeneity and nonlinearity (e.g., viscoplasticity) of the medium. Therefore, the fault boundary conditions have been implemented in different formulations of many numerical methods that can account for material heterogeneity, e.g., FDM (e.g., Andrews 1973, 1976a,b, 1999, Madariaga 1976, Day 1977, 1982, Miyatake 1980, Madariaga *et al*. 1998, Nielsen *et al*. 2000, Cruz-Atienza and Virieux 2004, Day *et al*. 2005, Dalguer and Day 2006, 2007, Moczo *et al*. 2007a, Rojas *et al*. 2008, 2009, Ely *et al*. 2009, Kozdon *et al*. 2011, 2013, Zhang *et al*. 2011, 2013c), FEM (e.g., Archuleta 1976, Archuleta and Frazier 1978, Oglesby *et al*. 1998, 2000, Oglesby 1999, Aagaard *et al*. 2001, Anderson *et al*. 2003, Duan and Oglesby 2006, Ma and Archuleta 2006, Ma 2008, Ma *et al*. 2008, Templeton and Rice 2008, Viesca *et al*. 2008, Barall 2009, Galis *et al*. 2010), spectral-element method (e.g., Ampuero 2002, 2008, Festa 2004, Chaljub *et al*. 2007, Kaneko *et al*. 2008), finite-volume method (e.g., Benjemaa *et al*. 2007) or discontinuous Galerkin method (e.g., de la Puente *et al*. 2009, Pelties *et al*. 2012, Tago *et al*. 2012).

A brief review of the FD implementations can be found in Moczo *et al*. (2007b). Here we just mention recent approaches. Rojas *et al*. (2008, 2009) implemented a traction-at-split-node (TSN) approach in the 2D FD scheme based on mimetic operators. They used one-sided FD operators to achieve consistent 4th-order accuracy at the grid points on the fault and grid points away from the fault. Ely *et al*. (2009) implemented the TSN method to simulate spontaneous rupture propagation on planar and nonplanar faults in a 3D medium using the generalized 2nd-order FDM of support operators. Kozdon *et al*. (2011, 2013) implemented spontaneous rupture propagation on nonplanar faults in the summation-by-parts FDM for the 2D anti-plane problem. For imposing frictional boundary conditions they used the 4th-order simultaneous approximation term (SAT). With this approach the boundary values are not directly prescribed. Instead, a penalty term is used to penalize operators for not satisfying the boundary conditions. The approach yields a strictly stable scheme and with
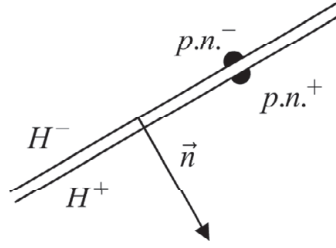
Figure 14.1 Fault surface and the normal vector $\vec{n}$.

a carefully chosen penalty parameter and a high level of accuracy. Zhang *et al.* (2011, 2013c) implemented the TSN method for spontaneous rupture propagation on nonplanar faults in the 3D curved-grid FD scheme. The FD scheme is a high-order MacCormack scheme on a collocated curved grid.

14.1 Traction-at-split-node method

Probably the most efficient method of incorporating the fault boundary conditions for simulating dynamic rupture propagation in the FD and FE methods is the traction-at-split-node (TSN) method. The TSN method was developed independently by Andrews (1973, 1976a,b, 1999) and Day (1977, 1982); see also Day *et al.* (2005).

Consider a fault as the contact of two halfspaces, H^+ and H^-. The fault is represented by the split nodes. A split node consists of two partial nodes $p.n.^+$ and $p.n.^-$, which makes it possible to represent the discontinuity in displacement and particle velocity on the fault. The partial nodes $p.n.^+$ and $p.n.^-$ belong to halfspaces H^+ and H^-, respectively (see Fig. 14.1). A partial node is characterized by quantities related to the relevant halfspace (e.g., seismic wave speeds, density, displacements, particle velocities or forces). Since the partial nodes are characterized by different displacements, the split node may experience a relative motion along the fault. A couple of the partial nodes share the fault-related quantities (e.g., slip, slip rate, coefficients of friction). Consider a normal vector $\vec{n}$ oriented from halfspace H^- to halfspace H^+ as shown in Fig. 14.1.

Due to deformation of halfspace H^- and possibly due to external forces acting in halfspace H^-, the partial node $p.n.^-$ with mass M^- is accelerated by force $\vec{F}^-$. Similarly, the partial node $p.n.^+$ is accelerated by force $\vec{F}^+$:

$$\vec{a}^- = \frac{\vec{F}^-}{M^-}, \quad \vec{a}^+ = \frac{\vec{F}^+}{M^+} \tag{14.1}$$

The acceleration of the partial nodes is affected only by the forces acting in halfspaces. Therefore Eqs. (14.1) are, in fact, describing the motion of the partial nodes as if they were at the free surfaces – there is no interaction between the partial nodes.

In order to simulate the fault, the halfspaces (and partial nodes) have to be coupled. The coupling can be accomplished by the constraint traction $\vec{T}^c$ acting at the contact of the

halfspaces. The constraint traction represents the contact force with which halfspace H^+ acts upon halfspace H^-. The constraint traction is the only traction acting at the contact or, in other words, it is the total traction (see Eq. (4.3)). We recall that the initial traction $\vec{T}^0$ represents the state of traction at the moment when rupture nucleates – it does not contribute to the acceleration. Therefore the constraint force at the partial node $p.n.^-$ is determined only by the traction variation $\Delta\vec{T}(t) \equiv \vec{T}^c(t) - \vec{T}^0$:

$$\vec{F}^{c,-}(t) = \vec{F}^c(t) = A\Delta\vec{T}(t) = A(\vec{T}^c(t) - \vec{T}^0) \tag{14.2}$$

Here A denotes the area represented by the split node. The acceleration of the partial node $p.n.^-$ is contributed by force $\vec{F}^-$ due to deformation in halfspace H^- and by the constraint force $\vec{F}^{c,-}(t)$:

$$\vec{a}^-(t) = \frac{1}{M^-}[\vec{F}^-(t) + \vec{F}^{c,-}(t)] = \frac{1}{M^-}[\vec{F}^-(t) + A(\vec{T}^c(t) - \vec{T}^0)] \tag{14.3}$$

Similarly, the constraint force acting on $p.n.^+$ and the acceleration of $p.n.^+$ are

$$\vec{F}^{c,+}(t) = -\vec{F}^c(t) = -A\Delta\vec{T}(t) = -A(\vec{T}^c(t) - \vec{T}^0) \tag{14.4}$$

$$\vec{a}^+(t) = \frac{1}{M^+}[\vec{F}^+(t) + \vec{F}^{c,+}(t)] = \frac{1}{M^+}[\vec{F}^+(t) - A(\vec{T}^c(t) - \vec{T}^0)] \tag{14.5}$$

We can approximate the time derivative by the 2nd-order central FD formula to obtain the particle velocity at partial nodes:

$$\vec{v}^-\left(t + \tfrac{1}{2}\Delta t\right) \approx \vec{v}^-\left(t - \tfrac{1}{2}\Delta t\right) + \frac{\Delta t}{M^-}[\vec{F}^-(t) + A(\vec{T}^c(t) - \vec{T}^0)]$$
$$\vec{v}^+\left(t + \tfrac{1}{2}\Delta t\right) \approx \vec{v}^+\left(t - \tfrac{1}{2}\Delta t\right) + \frac{\Delta t}{M^+}[\vec{F}^+(t) - A(\vec{T}^c(t) - \vec{T}^0)] \tag{14.6}$$

Recall the definition of the slip rate, Eq. (4.2),

$$\dot{\vec{s}} = \vec{v}^+ - \vec{v}^- \tag{14.7}$$

Using Eqs. (14.6) in (14.7) we obtain for the slip rate

$$\dot{\vec{s}}\left(t + \tfrac{1}{2}\Delta t\right) \approx \dot{\vec{s}}\left(t - \tfrac{1}{2}\Delta t\right) + \Delta t\, B\left[\frac{M^-\vec{F}^+(t) - M^+\vec{F}^-(t)}{A\,(M^- + M^+)} - (\vec{T}^c(t) - \vec{T}^0)\right] \tag{14.8}$$

where

$$B = A\frac{M^- + M^+}{M^- M^+} \tag{14.9}$$

Now find a constraint traction that ensures that a couple of the partial nodes move together. We mention two approaches – one by Andrews, the other by Day. Andrews requires zero differential acceleration. Assume an initial condition with zero slip rate. Then the requirement ensures that the partial nodes move together. For slipping nodes, however, the requirement itself is not sufficient for rupture arrest. Day requires zero slip

rate. This condition is sufficient for both the rupture onset and arrest. We explain only Day's approach.

Denote the constraint traction ensuring zero slip rate as $\vec{T}^{ct}(t)$. Note that, because $\vec{T}^{ct}(t)$ has to be evaluated at each time level at each node on the fault and compared with the frictional strength, it is called the trial traction. The question is, how to time condition $\dot{\vec{s}} = 0$. The traction is defined at time t while the slip rate is defined at $t + \Delta t/2$. If $\dot{\vec{s}}(t) = 0$ is required, the traction acts for the time interval from $t - \Delta t/2$ to $t + \Delta t/2$. If the nodes were slipping at previous times then this approach can reverse slipping. This results in the traction driving slip rather than opposing it and thus in violating the energy balance (Day 2005, personal communication). Therefore,

$$\dot{\vec{s}}\left(t + \tfrac{1}{2}\Delta t\right) = 0 \tag{14.10}$$

must be required. Applying (14.10) in (14.8) we obtain the trial traction:

$$\vec{T}^{ct}(t) \approx \vec{T}^0 + \frac{\frac{M^- M^+}{\Delta t}\dot{\vec{s}}\left(t - \tfrac{1}{2}\Delta t\right) + M^- \vec{F}^+(t) - M^+ \vec{F}^-(t)}{A\left(M^- + M^+\right)} \tag{14.11}$$

Traction $\vec{T}^{ct}(t)$ fully compensates the current forces at the contact due to deformation of halfspaces H^- and H^+ as well as due to the relative motion of the partial nodes. The current strength of the contact, $S(t)$, is determined by the friction (see Eq. (4.5)). Therefore, if the amplitude of the shear (tangential) component of $\vec{T}^{ct}(t)$ is smaller than the fault strength, $\vec{T}^{ct}(t)$ is equal to the traction acting at the contact and consequently there is no slip:

$$\left|\vec{T}^{ct}_{sh}(t)\right| \leq S(t) : \vec{T}^c(t) = \vec{T}^{ct}(t) \Rightarrow \dot{\vec{s}}\left(t + \tfrac{1}{2}\Delta t\right) = 0 \tag{14.12}$$

The contact cannot support a load larger than the current fault strength. Therefore, if $\left|\vec{T}^{ct}_{sh}(t)\right|$ is larger than the fault strength the constraint traction is determined by friction: $\vec{T}^c_{sh}(t) = \vec{T}^f_{sh}(t)$. The difference between $\vec{T}^{ct}(t)$ and $\vec{T}^f(t)$ results in a nonzero slip rate:

$$\left|\vec{T}^{ct}_{sh}(t)\right| > S(t) : \vec{T}^c(t) = \vec{T}^f(t) \Rightarrow \dot{\vec{s}}\left(t + \tfrac{1}{2}\Delta t\right) \neq 0 \tag{14.13}$$

Because we assume no opening of the contact or penetration of the material at the contact (see Eq. (4.6)), the normal component of $\vec{T}^f(t)$ is determined by $\vec{T}^{ct}(t)$:

$$\vec{T}^f_n(t) = \vec{T}^{ct}_n(t) \tag{14.14}$$

Consequently, the normal component of the slip-rate remains zero.

In principle we can use Eq. (14.8) to obtain the slip rate, but it is advantageous to express $\dot{\vec{s}}(t + \Delta t/2)$ using $\vec{T}^{ct}(t)$. First, assume $\dot{\vec{s}}\left(t + \Delta t/2\right) \neq 0$ for $\vec{T}^c_{sh}(t) = \vec{T}^f_{sh}(t)$ in Eq. (14.8). Then assume $\dot{\vec{s}}\left(t + \Delta t/2\right) = 0$ for $\vec{T}^c_{sh}(t) = \vec{T}^{ct}_{sh}(t)$ in Eq. (14.8):

$$\dot{\vec{s}}_{sh}\left(t + \tfrac{1}{2}\Delta t\right) \approx \dot{\vec{s}}_{sh}\left(t - \tfrac{1}{2}\Delta t\right) + \Delta t\, B\left[\frac{M^- \vec{F}^+_{sh}(t) - M^+ \vec{F}^-_{sh}(t)}{A(M^- + M^+)} - \left(\vec{T}^f_{sh}(t) - \vec{T}^0_{sh}\right)\right]$$

$$0 \approx \dot{\vec{s}}_{sh}\left(t - \tfrac{1}{2}\Delta t\right) + \Delta t\, B\left[\frac{M^- \vec{F}^+_{sh}(t) - M^+ \vec{F}^-_{sh}(t)}{A(M^- + M^+)} - \left(\vec{T}^{ct}_{sh}(t) - \vec{T}^0_{sh}\right)\right] \tag{14.15}$$

By subtracting the second equation from the first we obtain the formula for the slip rate:

$$\dot{\vec{s}}_{sh}\left(t + \tfrac{1}{2}\Delta t\right) \approx \Delta t\, B\big[\vec{T}^{ct}_{sh}(t) - \vec{T}^{f}_{sh}(t)\big] \qquad (14.16)$$

We can express the frictional traction $\vec{T}^{f}_{sh}(t)$ as

$$\vec{T}^{f}_{sh}(t) = S(t)\vec{\Upsilon}(t) \qquad (14.17)$$

Vector $\vec{\Upsilon}(t)$ has to be obtained from the requirement that friction opposes slipping. Recall the colinearity condition (4.8) and its explanation in relation to the slip-rate direction. We may write

$$\vec{T}^{f}_{sh}(t) = S(t)\frac{\dot{\vec{s}}_{sh}(t)}{\left|\dot{\vec{s}}_{sh}(t)\right|} \qquad (14.18)$$

According to Day (2005, personal communication) the procedure of finding the trial traction $\vec{T}^{ct}(t)$ using condition (14.10) and the direction of the frictional traction $\vec{T}^{f}_{sh}(t)$ using $\dot{\vec{s}}_{sh}(t)$ can cause, in some rare cases, large oscillations of the rake direction just around the time of rupture arrest. Day avoids the problem by modifying the colinearity condition:

$$\vec{T}^{f}_{sh}(t) = S(t)\frac{\dot{\vec{s}}_{sh}\left(t + \tfrac{1}{2}\Delta t\right)}{\left|\dot{\vec{s}}_{sh}\left(t + \tfrac{1}{2}\Delta t\right)\right|} \qquad (14.19)$$

Using Eq. (14.16) in (14.19) we obtain

$$\vec{T}^{f}_{sh}(t) = \frac{S(t)}{S(t) + \left|\vec{T}^{ct}_{sh}(t) - \vec{T}^{f}_{sh}(t)\right|}\vec{T}^{ct}_{sh}(t) \qquad (14.20)$$

This means that the shear component of the frictional traction $\vec{T}^{f}_{sh}(t)$ has the same direction as the shear component of the trial traction $\vec{T}^{ct}_{sh}(t)$. Therefore, see Eq. (14.17),

$$\vec{\Upsilon}(t) = \frac{\vec{T}^{ct}_{sh}(t)}{\left|\vec{T}^{ct}_{sh}(t)\right|} \qquad (14.21)$$

Now we can rewrite relations (14.13) in more detail:

$$\left|\vec{T}^{ct}_{sh}(t)\right| > S(t): \quad \vec{T}^{c}_{n}(t) = \vec{T}^{ct}_{n}(t) \Rightarrow \dot{\vec{s}}_{n}\left(t + \tfrac{1}{2}\Delta t\right) = 0$$

$$\vec{T}^{c}_{sh}(t) = S(t)\frac{\vec{T}^{ct}_{sh}(t)}{\left|\vec{T}^{ct}_{sh}(t)\right|} \Rightarrow \dot{\vec{s}}_{sh}\left(t + \tfrac{1}{2}\Delta t\right) = \Delta t\, B\big[\vec{T}^{ct}_{sh}(t) - \vec{T}^{f}_{sh}(t)\big]$$

$$(14.22)$$

The TSN method explained here may be used if the time-stepping algorithm is explicit and the force applied to one node accelerates only that node during one time iteration. Note that Tago *et al.* (2012) developed a TSN method for the discontinuous Galerkin method which is more general in that velocity and traction changes at nodes of the interface elements are coupled, and the coupled TSN equations are solved numerically by the predictor-corrector method.

The accuracy of the TSN method depends heavily on the accuracy of the calculation of the body forces $\vec{F}^+$ and $\vec{F}^-$. These forces are computed for each time level assuming zero tangential traction.

Note on discretization of rupture-dynamics problems For accurate and reliable results of numerical simulations of rupture propagation, proper discretization of the problem is necessary. Spatial sampling obtained from sampling criteria for wave propagation problems is not sufficient for correctly resolving rupture propagation. We have to properly resolve the breakdown zone as well as characteristic length scales on the fault (characterizing topography of the fault and heterogeneities).

Day *et al.* (2005) derived two estimates of breakdown-zone width assuming linear slip-weakening: an approximation at zero speed, Λ_0, and an approximation at large propagation distance, Λ. For correct resolution, Λ_0 for mode III (anti-plane mode) is more important because it is always smaller than Λ_0 for mode II (in-plane mode):

$$\Lambda_0^{\text{III}} = \frac{9\pi}{32} \mu \frac{D_c}{\tau_s - \tau_d} \tag{14.23}$$

The breakdown zone shrinks as the rupture propagates. It is possible to find an analytical form of the estimate of breakdown-zone width at distance L only for mode III:

$$\Lambda^{\text{III}}(L) = \Lambda_0^{\text{III}} \frac{2L_0/L}{1 + (L_0/L)^2}, L_0 = \frac{1}{\pi} \mu D_c \frac{\tau_s - \tau_d}{(\tau_0 - \tau_d)^2} \tag{14.24}$$

At the same distance Λ^{III} will be smaller than Λ^{II}. However, the rupture may propagate to a larger distance in the in-plane direction and therefore, eventually, the breakdown-zone width near the end of the fault may be smaller in the in-plane direction than at the end of the fault in the anti-plane direction. An analytical solution for Λ^{II} is not available (see Day *et al.* 2005 for the procedure to obtain a numerical solution).

According to Day *et al.* (2005), Λ_0^{III} has to be resolved by more than one spatial sampling. Otherwise it is likely that the solution will be too oscillatory and consequently it may lead to rupture arrest. Of course, better resolution is necessary to achieve reasonable accuracy. Day *et al.* (2005) found that their DFM (2$^{\text{nd}}$-order in space and time) achieved stability of the solution when the minimum breakdown-zone width in the in-plane direction was resolved by 3.3 grid spacings, and the median of the breakdown-zone width was resolved by 4.4 grid spacings. Although the estimates were derived assuming homogeneous conditions and, moreover, the spatial sampling is method dependent, the estimates may serve as a good starting point.

Let us note (Day 2013, personal communication) that, in addition to resolution of the breakdown zone, it is necessary that the grid spacing h be small enough to resolve any length scales λ related to the fault (e.g., length scales of heterogeneities or geometry of the fault), that is,

$$h < \lambda \tag{14.25}$$

Moreover, the solution can be considered reliable if the slip is smaller than the length scales on the fault, that is,

$$|\vec{s}| < \lambda \qquad (14.26)$$

If this condition is not satisfied, then slip will juxtapose misfitting geometrical and material features. Note that the method will provide a solution even if condition Eq. (14.26) is not satisfied. However, such a solution cannot be considered a valid solution for obvious reasons.

14.2 Implementation of TSN in the staggered-grid scheme

The TSN method for simulation of rupture propagation on an earthquake fault was explained in Section 14.1. As mentioned there, the method was developed independently by Andrews (1973, 1976a,b, 1999) and Day (1977, 1982). Andrews implemented his TSN formulation in an FD scheme in which spatial differentiation is equivalent to the FEM. Day implemented his slightly different formulation of the TSN method in the 2nd-order partly-staggered FD scheme. Both Andrews and Day applied the TSN method to investigate the dynamics of earthquake rupture propagation.

Day *et al.* (2005) compared the TSN method with the boundary-integral method and found a very good level of agreement. Dalguer and Day (2006) compared the TSN method with the thick-fault method of Madariaga *et al.* (1998) and the stress-glut method presented by Andrews (1999). Using extensive numerical tests they demonstrated the superior accuracy of the TSN method compared to the thick-fault and stress-glut methods.

Dalguer and Day (2007) implemented the TSN method in the (2,4) VS SG FD scheme. The fault plane is represented by the grid plane of the split nodes for the normal stress-tensor components, the corresponding shear stress-tensor component (σ_{xy}), and two fault-parallel components of the particle velocity (v_x and v_y). Dalguer and Day applied the 4th-order centred approximation to spatial derivatives at grid points at distances $3h/2$ and more from the fault plane. At grid points at distances h and $h/2$ from the fault plane they applied the 2nd-order centred approximation. Finally, at grid points on the fault plane, Dalguer and Day applied the 1st-order one-sided approximation for spatial derivatives in the direction perpendicular to the fault plane and the 2nd-order centred approximation for derivatives in the directions parallel to the fault plane.

Dalguer and Day performed numerical tests of their implementation (they termed it SGSN – staggered-grid split node) against a partly-staggered implementation of the TSN method (Day 1977, 1982) and a boundary-integral method, and found it satisfactorily accurate, with convergence rates similar to those of the two latter methods.

Kristek *et al.* (2006) and Moczo *et al.* (2007a) presented three different implementations of the TSN method in the VS SG scheme. In the first one they applied the 4th-order approximation to the spatial derivatives away from the fault plane, and the 2nd-order approximations at grid positions close to and on the fault plane. In the second implementation they applied the 4th-order approximation to the spatial derivatives away from the fault, 2nd-order approximations at grid positions close to the fault, and 4th-order approximations on the
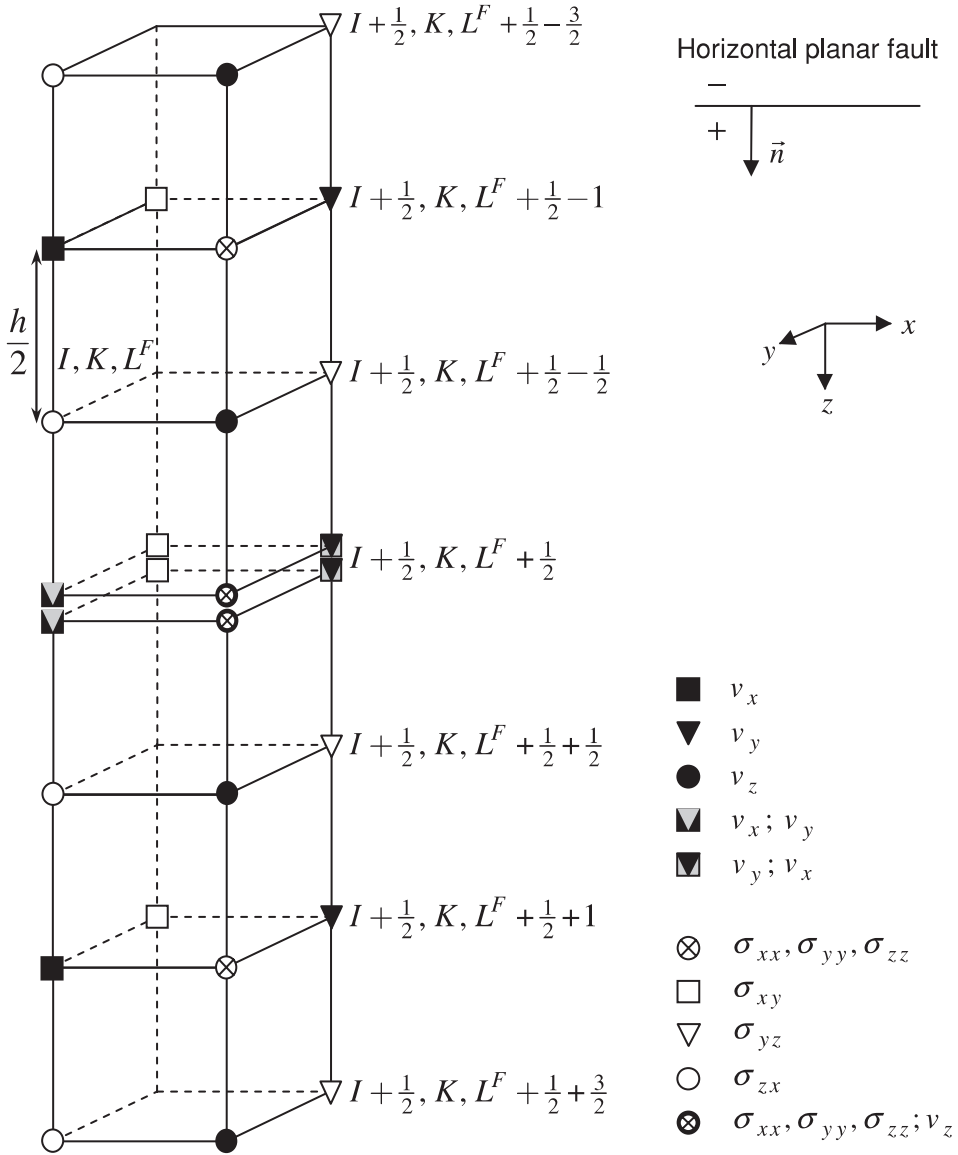
Figure 14.2 Configuration of the fault plane in the staggered grid. The fault is represented by a horizontal grid plane of split nodes.

fault plane. In the third implementation they applied the 4th-order approximations to the spatial derivatives everywhere.

Here we describe the first implementation. The geometrical configuration of the horizontal fault plane and spatially staggered grid is shown in Fig. 14.2. Because the fault plane is represented as a contact of the '−' and '+' fault surfaces, the corresponding horizontal grid

plane with spatial index $L^F + 1/2$ is split into two grid planes. Assuming shear faulting, we have to distinguish the '−' and '+' values of the horizontal components of the particle velocity, $v_x^\pm$ and $v_y^\pm$, two normal stress-tensor components, $\sigma_{xx}^\pm$ and $\sigma_{yy}^\pm$, and one shear stress-tensor component, $\sigma_{xy}^\pm$, which become discontinuous when slip on the fault occurs. For conciseness, in the following we will partly or fully omit grid indices if the omission will not cause misunderstanding. Basically, we will show or comment only those parts of the algorithm that are modified or different compared to the (2,4) VS SG scheme for interior grid points for a medium without a faulting surface. The notation is relatively close to that of Dalguer and Day (2007).

Grid points at distances $3h/2$ from the fault plane Spatial derivatives at $L = L^F + 1/2 \pm 3/2$ in the z-direction (fault-normal) are approximated using the standard 4th-order formula in which the '−' or '+' values on the fault are taken:

$$\frac{\partial \varphi}{\partial z} \approx D_z^{(1-4)}\varphi = \frac{1}{h}\left[\tfrac{9}{8}(\varphi_{L+1/2} - \varphi_{L-1/2}) - \tfrac{1}{24}(\varphi_{L+3/2}^- - \varphi_{L-3/2}^+)\right] \qquad (14.27)$$

Here, $\varphi \in \{v_x, v_y, \sigma_{zz}\}$ and $+/-$ applies in correspondence to $+/-$ in the grid index L, that is,

if $L = L^F + 1/2 - 3/2$, the rightmost term is $(\varphi_{L^F+1/2}^- - \varphi_{L^F+1/2-6/2})$
if $L = L^F + 1/2 + 3/2$, the rightmost term is $(\varphi_{L^F+1/2+6/2} - \varphi_{L^F+1/2}^+)$

Equation (14.27) also defines the spatial operator $D_z^{(1-4)}$. Later we will also use symbol $D_z^{(1-2)}$ for the 2nd-order centred approximation; see Eqs. (7.197) and (7.198).

Grid points at distances h from the fault plane All spatial derivatives at grid points at $L = L^F + 1/2 \pm 1$ are approximated by the 2nd-order centred FD formula.

Grid points at distances $h/2$ from the fault plane All spatial derivatives at grid points at $L = L^F + 1/2 \pm 1/2$ are approximated by the 2nd-order centred FD formula. For derivatives in the z-direction appropriate values are taken:

$$\frac{\partial \varphi}{\partial z} \approx D_z^{(1-2)}\varphi = \frac{1}{h}(\varphi_{L+1/2}^- - \varphi_{L-1/2}^+) \qquad (14.28)$$

with $+/-$ applied in correspondence to $+/-$ in the grid index L.

Split nodes on the fault plane The grid index in the z-direction for the split nodes is $L = L^F + 1/2$. The centred 2nd-order approximation is used for the spatial derivatives of the $+/-$ functions in the x- and y-directions. An adjusted 2nd-order approximation is used for the spatial derivative of the shear stress-tensor components σ_{zx} and σ_{zy} in the z-direction:

$$\left(\frac{\partial \sigma_{z\gamma}}{\partial z}\right)^\pm \approx \frac{1}{h}\left[\mp \tfrac{8}{3}\left(T_\gamma - T_\gamma^0\right) \pm 3\sigma_{z\gamma, L\pm1/2} \mp \tfrac{1}{3}\sigma_{z\gamma, L\pm3/2}\right] \qquad (14.29)$$

T_γ and T_γ^0 are the components of the constraint and initial tractions on the fault and $\gamma \in \{x, y\}$. Then approximations of the equations of motion for $v_x^\pm$ and $v_y^\pm$ are

$$\rho^\pm \frac{1}{\Delta t}\left[v_\gamma^{\pm,m+1/2} - v_\gamma^{\pm,m-1/2}\right] = \left[D_x^{(1-2)}\sigma_{x\gamma}^{\pm,m} + D_y^{(1-2)}\sigma_{y\gamma}^{\pm,m}\right] + \left(\frac{\partial \sigma_{z\gamma}}{\partial z}\right)^{\pm,m} \quad (14.30)$$

Here $(\frac{\partial \sigma_{z\gamma}}{\partial z})^\pm$ is defined by Eq. (14.29). The slip rate at time level $m + 1/2$ is

$$\dot{s}_\gamma^{m+1/2} = v_\gamma^{+,m+1/2} - v_\gamma^{-,m+1/2} \quad (14.31)$$

Then slip is obtained from

$$s_\gamma^{m+1} = s_\gamma^m + \Delta t \dot{s}_\gamma^{m+1/2} \quad (14.32)$$

A value of the constraint traction $\vec{T}^c$ on the fault obtained under the condition of $\dot{\vec{s}}^{m+1/2} = 0$ defines the trial traction. For simplicity of notation here, let $\vec{T}^{ct}$ denote the shear component of the trial traction, see Eqs. (14.12) and (14.22). The boundary conditions on the fault are enforced by

$$T_\gamma^c = T_\gamma^{ct}; |T^{ct}| \leq S$$

$$T_\gamma^c = \frac{\vec{T}^{ct}}{|\vec{T}^{ct}|}S; |\vec{T}^{ct}| > S \quad (14.33)$$

In evaluation of the trial traction at grid positions of the particle-velocity components, the missing components of the trial traction are obtained by interpolation:

$$\left|\vec{T}_{I,K+1/2}^{ct}\right|^2 = \left[T_{x,I,K+1/2}^{ct}\right]^2 + \left[\tfrac{1}{4}\left(T_{y,I+1/2,K}^{ct} + T_{y,I-1/2,K}^{ct} + T_{y,I+1/2,K+1}^{ct} + T_{y,I-1/2,K+1}^{ct}\right)\right]^2 \quad (14.34)$$

and

$$\left|\vec{T}_{I+1/2,K}^{ct}\right|^2 = \left[\tfrac{1}{4}\left(T_{x,I,K+1/2}^{ct} + T_{x,I+1,K+1/2}^{ct} + T_{x,I,K-1/2}^{ct} + T_{x,I+1,K-1/2}^{ct}\right)\right]^2$$
$$+ \left[T_{y,I+1/2,K}^{ct}\right]^2 \quad (14.35)$$

The missing components of the slip rate in the evaluation of the slip-path length are interpolated analogously.

Finally, the approximations for the temporal derivatives of the stress-tensor components are

$$\dot{\sigma}_{xy}^\pm \approx \mu \left(D_y^{(1-2)}v_x^\pm + D_x^{(1-2)}v_y^\pm\right) \quad (14.36)$$

$$\dot{\sigma}_{\gamma\gamma}^\pm \approx \lambda^\pm \left[D_x^{(1-2)}v_x^\pm + D_y^{(1-2)}v_y^\pm + \left(\frac{\partial v_z}{\partial z}\right)^\pm\right] + 2\mu^\pm D_\gamma^{(1-2)}v_\gamma^\pm \quad (14.37)$$

and

$$\dot{\sigma}_{zz}^{\pm} \approx \lambda^{\pm} \left[D_x^{(1-2)} v_x^{\pm} + D_y^{(1-2)} v_y^{\pm} + \left(\frac{\partial v_z}{\partial z} \right)^{\pm} \right] + 2\mu^{\pm} \left(\frac{\partial v_z}{\partial z} \right)^{\pm} \qquad (14.38)$$

where the adjusted 2nd-order approximation is used for the z-derivative:

$$\left(\frac{\partial v_z}{\partial z} \right)^{\pm} \approx \frac{1}{h} \left[\mp \tfrac{8}{3} v_z \pm 3 v_{z,L\pm1/2} \mp \tfrac{1}{3} v_{z,L\pm3/2} \right] \qquad (14.39)$$

Values of the continuous z-component of the particle velocity on the fault,

$$v_z = v_{z,I+1/2,K+1/2,L^F+1/2} \qquad (14.40)$$

are determined from the 2nd-order approximation to the boundary condition:

$$\left(\dot{\sigma}_{zz}^{+} = \dot{\sigma}_{zz}^{-} \right)_{L^F+1/2} \qquad (14.41)$$

The algorithms of the second and third implementations are relatively more complicated and we will not detail them here. For a numerical comparison of the three implementations see Moczo *et al*. (2007a), Section 11.3.

We did not introduce any artificial damping in the FD schemes. Dalguer and Day (2007) introduced viscous damping into the equations of motion in order to suppress short-wavelength oscillations arising from the numerical dispersion characteristic for a low-order FD approximation. Alternatively, the oscillations can be reduced using the adaptive smoothing algorithm, see Section 17.3.

14.3 Initiation of spontaneous rupture propagation

Numerical simulations of rupture propagation under the linear slip-weakening friction law require artificial procedures to initiate spontaneous rupture propagation. A frequently used technique is based on imposing stress asperity. The effects of this artificial initiation depend on the geometry and size of the asperity, the spatial distribution of the stress in and around the asperity, and a maximum overstress value. It is necessary to understand and minimize the effects of artificial initiation on the subsequent spontaneous rupture propagation.

Numerical and analytical studies show that the size of the asperity should be chosen as small as possible. If an initiation zone is too small, rupture will not propagate or will terminate spontaneously at a finite distance from the nucleation region. On the other hand, if the initiation zone is too large it may strongly affect rupture propagation. Criteria for estimating the minimum size have been proposed for 2D in-plane and anti-plane rupture modes (Andrews 1976a,b, Campillo and Ionescu 1997, Favreau *et al*. 1999, Uenishi and Rice 2003) and for 3D (Day 1982, Uenishi and Rice 2004). Other studies (e.g., Galis *et al*. 2010, Bizzarri 2010) suggest that these estimates do not provide general rules for designing 3D simulations.

A variety of geometries/shapes of the initiation zone have been used for 3D dynamic rupture simulations. A square initiation patch has frequently been chosen (e.g., Harris *et al*.

2009). Uenishi and Rice (2004), Dunham (2007), Galis *et al.* (2010) and Bizzarri (2010) suggested an elliptical initiation zone, while Ripperger *et al.* (2007) tested arbitrarily shaped initiation regions.

Within the stress asperity the initial stress is chosen larger than the static stress. The overstress (difference between the initial stress and static stress) inside the asperity is assumed small, usually not larger than 1% over the static stress. Note that quantifying of the overstress by a percentage of the static stress does not lead to proper scaling of the overstress with the stress drop and strength excess. For example, two configurations with equal stress drops and strength excesses but with different initial stresses should provide the same results. Consider overstress quantified as a percentage of the static stress. Assumption of the same percentage in both configurations then leads to different overstresses in MPa (because initial stress and consequently also static stress are different in the configurations) which eventually leads to different results. Therefore, it is reasonable to quantify the overstress independently of the initial stress – by percentage of the stress drop, strength excess or difference between the static and dynamic stresses.

Most published studies that use stress-asperity parameterization for rupture initiation assume a stress discontinuity at the asperity edge: the asperity stress suddenly drops to the level of the initial background stress. Two recent studies applied a smooth spatial distribution of stress in and around the asperity (Galis *et al.* 2010, Bizzarri 2010).

Recently, Bizzarri (2010) tested different rupture initiation techniques, and showed that (a) forced rupture propagation with a proper rupture velocity leads to a gradual transition from imposed initiation to spontaneous rupture propagation, (b) an elliptical stress asperity with smooth stress is a valid alternative to forced rupture-propagation initiation. Bizzarri (2010) did not address the size of the initiation zone or overstress value.

Galis *et al.* (2014) performed extensive numerical simulations of 3D rupture propagation governed by the linear slip-weakening friction law (see Subsection 4.1.2). They considered square, elliptical and circular shapes of the initiation zone with constant overstress, 0.5% of $\tau_s - \tau_0$, and values of the strength parameter $S = (\tau_s - \tau_0)/(\tau_0 - \tau_d)$ from 0.1 to 2.0. They found that the area of the initiation zone, for given values of S and overstress, determines whether the rupture will spontaneously propagate or not regardless of the particular shape of the initiation zone; see Fig. 14.3. The transition between propagating and non-propagating ruptures can be approximated by the curve

$$A_{init} = 1.75 S^{2.81} + 3.82 \tag{14.42}$$

Here $A_{init} = A/L_{fric}^2$ is the dimensionless area of the initiation zone determined by area A of the initiation zone in metres and parameter $L_{fric} = \mu D_c/(\tau_s - \tau_d)$ proposed by Dunham (2007).

Galis *et al.* (2014) also presented the analytical formula derived using theoretical arguments:

$$A'_{init} = \frac{(3\pi)^3}{2^{11}} \frac{\tau_0 - \tau_d}{\tau_i - \tau_0} \frac{(\tau_s - \tau_d)^2}{(\tau_0 - \tau_d)^4} \mu^2 D_c^2 \tag{14.43}$$
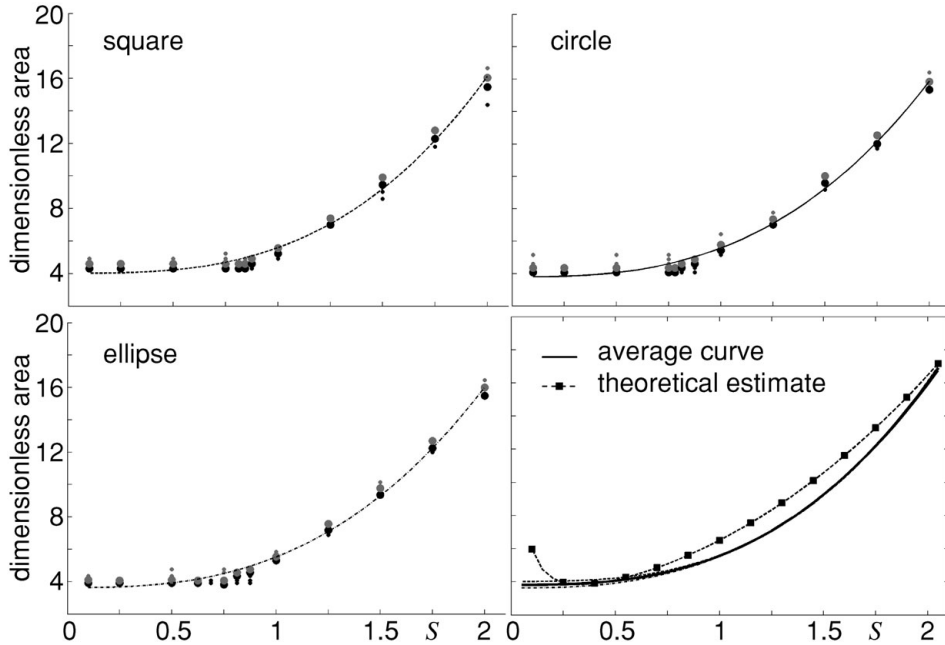
Figure 14.3 Search for the minimal size of the initiation zone that generates spontaneous rupture propagation. Each dot represents one numerical simulation. Black dots: simulations when rupture did not propagate spontaneously. Grey dots: simulations when rupture propagated spontaneously. Large dots were used for approximating the delimiting boundary by curve. Right bottom panel shows comparison of approximation of the numerical results, (14.42), with the theoretical estimate, (14.43). Simulations were performed using the FEM (Chapter 16) with $h = 50$ m.

Here τ_i is the initial traction inside the initiation zone. This theoretical estimate is in very good agreement with numerical results (see Fig. 14.3) for values $S > {\sim}0.25$. The assumptions/approximations used for the derivation are not valid for very low values of S. This is a reason for the worse agreement between numerical results and theoretical estimates for values of $S < {\sim}0.25$. They also found theoretical estimates which are in excellent agreement with the numerical results. See Galis *et al.* (2014) for more details.

Galis *et al.* (2014) also investigated the effects of the overstress value. First they considered a fixed size of the initiation zone. They found indications that the use of overstress values much larger than the minimum overstress leading to spontaneous propagation strongly affects rupture propagation, particularly in the case with large values of S. They also searched for the minimal overstress that ensures spontaneous rupture propagation for different sizes of the initiation zone. They observed that the adjusted overstress value is a good way to minimize the size of the initiation zone without introducing numerical artefacts.

15

Preparation of computations and a computational algorithm

(1) Input data
- spatial distribution of
  - P-wave and S-wave speeds
  - density
  - quality factors Q_P and Q_S (or Q_κ and Q_μ)
- source and receiver positions
- type of source, source-time function

(2) Determination of computational parameters
- grid spacing from the maximum frequency up to which the simulation should be accurate at a desired level (the size of the computational domain relates to the minimum frequency)
- time step from stability condition
- number of time levels
- parameters of PML

(3) Building computational model
- coverage of the computational domain with a discontinuous grid
- calculation of effective material grid parameters

(4) Algorithm of the computer code
- reading input control parameters
- reading computational model (grid model)
- reading source-time function and source parameters
- time loop (for determined number of time levels)
  - calculation of strain rates from particle velocities
    - inside model
    - in PML
    - near and at the free surface
  - update of anelastic functions from strain rates
  - update of stresses from strain rates and anelastic functions

- update of particle velocities
  - inside model
  - in PML
  - near and at the free surface
- application of source
- storing seismograms and/or snapshots

(5) Post-processing of the simulated motion (for example, low-pass or band-pass filtration)

It is necessary to perform numerical simulations for at least two different discretizations, e.g., for two sizes of the spatial grid spacing, in order to check the sensitivity of the simulated motion with respect to the computational parameters.

Part III

Finite-element method and hybrid
finite-difference–finite-element method

16

Finite-element method

Detailed expositions of the FEM and its application to a variety of problems can be found in books such as those by Strang and Fix (1988), Zienkiewicz and Taylor (1989), Ottosen and Petersson (1992), Belytschko *et al.* (2000), Hughes (2000), Felippa (2005) and Reddy (2006).

The purpose of this chapter is to briefly introduce the basics of the FEM and explain our efficient implementation based on the global restoring-force vector with significantly lower memory requirements as compared to the requirements of the global stiffness matrix. We also use so-called e-invariants for efficient computation of the restoring-force vector. The chapter will provide a basis for later expositions of FE modelling of rupture propagation and the hybrid FD–FE method.

Unlike most chapters on the FDM, here we indicate the spatial and temporal derivatives, respectively, as

$$\varphi_{i,j} \equiv \frac{\partial \varphi_i}{\partial x_j}, \quad \dot{\varphi}_i \equiv \frac{\partial \varphi_i}{\partial t} \tag{16.1}$$

We choose this notation in order to have the equations in a concise form.

16.1 Weak form of the equation of motion

Consider a domain $\bar{\Omega} = \Omega \cup \Gamma$, where Ω is an interior and Γ its boundary. We assume that boundary Γ can be decomposed into two parts, Γ_D and Γ_N, without overlapping, that is, $\Gamma_D \cap \Gamma_N = \emptyset$ (see Fig. 16.1). We assume a prescribed displacement vector at boundary Γ_D and prescribed traction at boundary Γ_N. Recall the strong-form equation of motion (2.7):

$$\rho \ddot{u}_i = \sigma_{ij,j} + f_i \tag{16.2}$$

and boundary condition (2.8) at Γ_N:

$$\sigma_{ij}(\vec{x}) \, n_j(\vec{x}) = h_i; \quad \vec{x} \in \Gamma_N \tag{16.3}$$

where $\vec{n}(\vec{x})$ is an outer normal. Here we also consider the boundary condition at Γ_D:

$$u_i(\vec{x}, t) = g_i(\vec{x}, t); \quad \vec{x} \in \Gamma_D \tag{16.4}$$
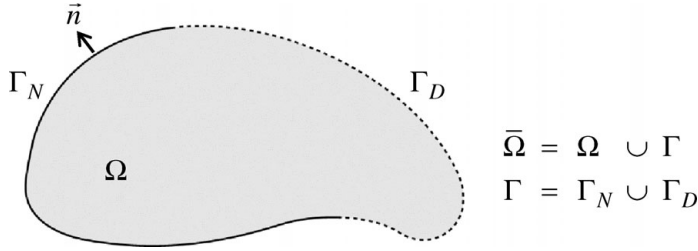
Figure 16.1 Domain $\bar{\Omega}$ is formed by the interior Ω and the boundary Γ. The Dirichlet boundary condition is considered on the part Γ_D and the Neumann boundary condition is considered on the part Γ_N; $\vec{n}$ is outer normal at boundary Γ_N.

In Chapter 2 we showed the weak-form equation of motion. We did not, however, consider boundary conditions. Here we use an alternative approach that is more suitable for deriving the FEM.

Consider a weighting function w – an arbitrary function satisfying two conditions:

$$w(\vec{x}) = 0; \quad \vec{x} \in \Gamma_D \tag{16.5}$$

$$\int_\Omega (w,_x)^2 \, dx < \infty \tag{16.6}$$

The first condition for w is due to the boundary condition (16.4). The second one will be explained later. We can multiply Eqs. (16.2) and (16.3) by the weighting function w, integrate them over domain Ω and its boundary Γ_N, respectively, and then sum them up. We obtain

$$\int_\Omega w(\rho \ddot{u}_i - f_i)d\Omega - \int_\Omega w\sigma_{ij,j}d\Omega + \int_{\Gamma_N} w(\sigma_{ij}n_j - h_i)d\Gamma = 0 \tag{16.7}$$

Note that the integral of the boundary condition (16.4) multiplied by weighting function w is zero due to condition (16.5).

Rewrite the second term in Eq. (16.7):

$$w\sigma_{ij,j} = (w\sigma_{ij}),_j - w,_j \sigma_{ij} \tag{16.8}$$

Rearrange and integrate Eq. (16.8) over the domain Ω:

$$\int_\Omega (w\sigma_{ij}),_j \, d\Omega = \int_\Omega w,_j \sigma_{ij}d\Omega + \int_\Omega w\sigma_{ij,j}d\Omega \tag{16.9}$$

Using Gauss's divergence theorem we convert the integral on the l.h.s. of Eq. (16.9) to a surface integral:

$$\int_\Omega (w\sigma_{ij}),_j \, d\Omega = \int_\Gamma w\sigma_{ij}n_j d\Gamma = \int_{\Gamma_N} w\sigma_{ij}n_j d\Gamma \tag{16.10}$$

where we used the property (16.5) of the weighting function w. Now we can use Eqs. (16.9) and (16.10) to express the second term of Eq. (16.7):

$$\int_\Omega w\sigma_{ij,j}d\Omega = \int_{\Gamma_N} w\sigma_{ij}n_j d\Gamma - \int_\Omega w_{,j}\,\sigma_{ij}d\Omega \qquad (16.11)$$

Eventually, using Eq. (16.11) we rewrite Eq. (16.7):

$$\int_\Omega w\left(\rho\ddot{u}_i - f_i\right)d\Omega + \int_\Omega w_{,j}\,\sigma_{ij}d\Omega - \int_{\Gamma_N} wh_i d\Gamma = 0 \qquad (16.12)$$

For the equation to be meaningful the integrals must be well defined. That imposes conditions on solution u_i. Moreover, the solution u_i has to satisfy the boundary condition (16.4). The conditions on solution u_i of Eq. (16.12) are weaker than of the strong-form Eq. (16.2). For example, the weak form allows solutions u_i to be piece-wise linear functions. The piece-wise linear functions cannot be solutions of the strong-form equation because the derivatives are not well defined. Therefore Eq. (16.12) is called the weak form of the equation of motion. Note that Eq. (16.12) has to be satisfied for an arbitrary weighting function w. Consequently, Eq. (16.12) represents, in fact, three infinite sets of equations (one set for each component of solution). To solve Eq. (16.12) in practical applications we have to consider only a finite set of weighting functions.

16.2 Discrete weak form of the equation of motion for an element

We can imagine an element as a domain with a simple geometric shape with nodes in the vertices, e.g., tetrahedron, hexahedron or pyramid. In the next section we define the element using shape functions. Assume an element with n nodes. Assign numbers or indices to nodes so that each node can be referred to by a number from a set $\nu \equiv \{1, \ldots, n\}$. Then we can define a set $\nu_D \subset \nu$ as a set of indices of nodes on boundary Γ_D at which the displacement vector is prescribed. Similarly, we can define a complementary set $\nu\setminus\nu_D$ as a set of the free nodes at which the displacement vector is not prescribed. Correspondingly, n_D denotes the number of the nodes with prescribed displacement and $n - n_D$ denotes the number of the free nodes.

Now recall the weak form of the equation of motion (16.12). Further, we assume one and the same set of weighting functions for all three components of displacement.

We can define a finite set of the weighting functions $\tilde{S}^w$ as

$$\tilde{S}^w \equiv \{s_l | l \in \nu\setminus\nu_D\} \qquad (16.13)$$

This means that the weighting functions are from a finite set of $n - n_D$ functions, s_l, defined only for nodes not lying on boundary Γ_D. No weighting functions are defined for nodes on boundary Γ_D. Note that functions from $\tilde{S}^w$ are zero on Γ_D – in accordance with (16.5).

In general, we can consider the solution approximated by a linear combination of shape functions, which may be different from weighting functions. Here, we limit the discussion

to the Bubnov–Galerkin approach only. Following the Bubnov–Galerkin approach, the shape functions are chosen to be the same as the weighting functions whenever possible. Therefore, we use the terms weighting and shape functions interchangeably. Then the most straightforward choice for approximating the solution would be a linear combination of the functions from $\tilde{S}^w$:

$$u_i\,(\vec{x}, t) \approx \sum_{k \in \nu \setminus \nu_D} s_k(\vec{x})\, U_{ik}^I(t) \tag{16.14}$$

Here $U_{ik}^I(t)$ are time-dependent coefficients of the linear interpolation. However, the approximate solution in this form does not satisfy the boundary condition (16.4) because the shape functions, introduced in (16.13), are zero at Γ_D. Therefore, we have to add a new term to the solution, which will ensure the satisfaction of the boundary condition. Define a new set of functions

$$\tilde{S} \equiv \{s_l | l \in \nu_D\} \tag{16.15}$$

which are nonzero at Γ_D. Using these new functions and new coefficients $G_{ik}(t)$ we can modify the form of the approximate solution,

$$u_i\,(\vec{x}, t) \approx \sum_{k \in \nu \setminus \nu_D} s_k(\vec{x}) U_{ik}^I(t) + \sum_{k \in \nu_D} s_k(\vec{x}) G_{ik}(t) \tag{16.16}$$

where

$$s_k \begin{cases} \in \tilde{S}^w & \text{if} \quad k \in \nu \setminus \nu_D \\ \in \tilde{S} & \text{if} \quad k \in \nu_D \end{cases} \tag{16.17}$$

and

$$U_{ik}^I(\vec{x}) = 0; \quad \vec{x} \in \Gamma_D, \qquad G_{ik}(\vec{x}) = 0; \quad \vec{x} \notin \Gamma_D \tag{16.18}$$

At the boundary, the first term of (16.16) vanishes and only the second one remains. Therefore we can write

$$u_i(\vec{x}, t) = g_i(\vec{x}, t) \approx \sum_{k \in \nu_D} s_k(\vec{x})\, G_{ik}(t); \quad \vec{x} \in \Gamma_D \tag{16.19}$$

We see that the added shape functions ensure the (approximate) satisfaction of the boundary condition.

We can simplify Eq. (16.16) by introducing a set of shape functions S that include additional functions:

$$S \equiv \tilde{S}^w \cup \tilde{S} = \{s_l | l \in \nu\} \tag{16.20}$$

Then we can introduce coefficients U_{ik} as

$$U_{ik} \equiv U_{ik}^I + G_{ik} \tag{16.21}$$

and rewrite (16.16):

$$u_i(\vec{x}, t) \approx \sum_{k \in \nu} s_k(\vec{x})\, U_{ik}(t); \quad s_k \in S \tag{16.22}$$

We can also extend the set of weighting functions. The extended set of weighting functions S^w includes zero functions for nodes on boundary Γ_D and shape functions for all other nodes. Let

$$\hat{s}_l \begin{cases} \equiv s_l, & l \in \nu \setminus \nu_D \\ \equiv 0, & l \in \nu_D \end{cases} \tag{16.23}$$

Then,

$$S^w \equiv \{\hat{s}_l | l \in \nu\} \tag{16.24}$$

We illustrate function sets $\tilde{S}^w$, S^w, $\tilde{S}$ and S using a simple example. Consider the 2D quadrilateral element with four nodes in the vertices. Denote them 1, 2, 3 and 4. Assume a prescribed displacement at node 3. Then set $\tilde{S}^w$, defined by (16.13), will be $\tilde{S}^w = \{s_1, s_2, s_4\}$. The s_3 is missing. Set $\tilde{S}$, defined by Eq. (16.15), will be $\tilde{S} = \{s_3\}$. Then, according to (16.20) and (16.24), $S = \{s_1, s_2, s_3, s_4\}$ and $S^w = \{s_1, s_2, 0, s_4\}$, respectively.

Assuming the finite set of weighting functions (16.24) and assuming the approximate solution (16.22), we can rewrite the weak-form equation (16.12):

$$\int_\Omega w_k \left(\rho s_l \ddot{U}_{il} - f_i \right) d\Omega + \int_\Omega w_{k,j} \sigma_{ij} d\Omega - \int_{\Gamma_N} w_k h_i d\Gamma = 0 \tag{16.25}$$

Here $k, l \in \nu$, $w_k \in S^w$ and $s_l \in S$. We obtain three finite sets of $n - n_D$ equations for $n - n_D$ unknown coefficients U_{il} (the l.h.s. will be zero for $k \in \nu_D$). This is a discrete or Galerkin weak form. Note that the Galerkin form includes the boundary conditions at Γ_D. Note also that the stress tensor σ_{ij} implicitly depends on the spatial derivatives of displacement and consequently on the spatial derivatives of the shape functions. Condition (16.6) thus guarantees the existence of the second integral on the l.h.s. of (16.25).

Before we continue with the derivation of a matrix form of Eq. (16.25) we define the shape functions.

16.3 Shape functions

The properties of a final FE scheme very much depend on the choice of shape functions. To obtain the converging scheme the shape functions must be smooth inside an element, continuous at boundaries between elements, and complete. The first two conditions guarantee that the integrals in the discrete weak form, Eq. (16.25), are well defined. The second condition may be physically interpreted as the requirement of displacement continuity across elements. According to the third condition, the shape functions must be able to exactly represent linear polynomials inside the element. This may be physically interpreted as the requirement of exact representation of the constant-strain state inside an element.

So far we have considered only one element. Next we consider the whole domain Ω covered by elements without holes and overlapping.

In general, the shape functions may be defined in the whole domain. In the case of a large number of elements and nodes this approach is very expensive because it leads to functions
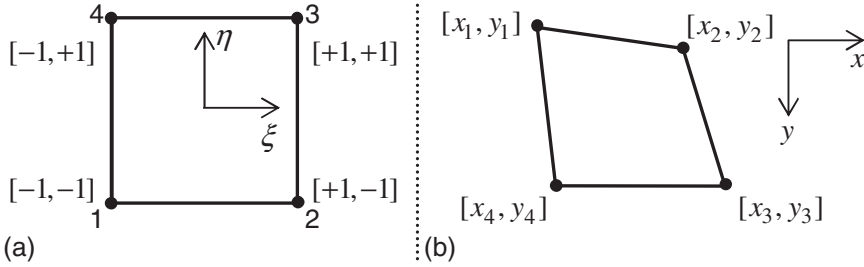
Figure 16.2 Transformation from the local to the physical coordinates in 2D. Left: a reference element Ω^{ref} in the local coordinates (ξ, η). Right: an element in the physical coordinates (x, y).

of very high order. It is better to use shape functions defined per element. In this case we can use low-order functions and still have a reasonable approximation of the solution in the whole domain. For simplicity, consider a 1D example. Consider linear shape functions per element. In such a case the solution in one element will be approximated by a linear function (see Eq. (16.22)). If we cover the whole domain with more elements, the solution in the domain will be approximated by a piece-wise linear function.

In addition to the local shape functions, it may be useful to transform elements from the physical coordinates (x, y, z) into the local coordinates (ξ, η, ζ), and define the shape functions in the local coordinates. Consequently, the shape functions for all elements will have the same form in the local coordinates. This means that for a given type of element we have to derive the shape functions only once. For simplicity, we first derive and present the shape functions for a quadrilateral element in 2D and then for a hexahedral element in 3D.

Assume a reference element Ω^{ref} as a square element in the local coordinate system (ξ, η) as shown in Fig. 16.2. The nodes are at positions

$$\vec{\xi} \equiv (-1, 1, 1, -1), \quad \vec{\eta} \equiv (-1, -1, 1, 1) \tag{16.26}$$

We need to define four shape functions for set S. These functions are used to approximate the solution $u_i(\vec{x}, t)$. We can find them by solving the system of equations

$$s_k(\xi_l, \eta_l) = \delta_{kl}; \quad k, l = 1, 2, 3, 4 \tag{16.27}$$

where δ_{kl} is the Kronecker delta. The system consists of four equations for each shape function. Therefore, to make system (16.27) uniquely solvable, the shape functions must have four parameters. We will consider shape functions in the form

$$s_k(\xi, \eta) = a_k\xi + b_k\eta + c_k\xi\eta + d_k, \quad k = 1, 2, 3, 4 \tag{16.28}$$

After solving the system (16.27) for shape functions in the form (16.28) the shape functions can be written as

$$\begin{aligned}
s_1(\xi, \eta) &= \tfrac{1}{4}(1 - \xi)(1 - \eta), \quad s_2(\xi, \eta) = \tfrac{1}{4}(1 + \xi)(1 - \eta) \\
s_3(\xi, \eta) &= \tfrac{1}{4}(1 + \xi)(1 + \eta), \quad s_4(\xi, \eta) = \tfrac{1}{4}(1 - \xi)(1 + \eta)
\end{aligned} \tag{16.29}$$

These functions are called bilinear because for fixed η we obtain a linear function of ξ, and vice versa, for fixed ξ we obtain a linear function of η. Note that the consequence of using shape functions satisfying the system of equations (16.27) is that coefficient U_{il} represents the i-th component of displacement at node l.

The formation of the function set S^w is also straightforward. This set contains only those shape functions from set S that are not associated with nodes on boundary Γ_D. The functions from S associated with nodes at Γ_D are replaced with zeros, as indicated by Eq. (16.23). Moreover, the functions from S^w have to be zero at Γ_D. This condition is implicitly satisfied for the shape functions in S^w as a consequence of Eq. (16.27).

For practical use of the shape functions in the local coordinates we need a transformation from the local to the physical coordinates. In general, if a function is given at the nodes of an element, we can use shape functions to interpolate the function in the element. We can use this approach to express the transformation from the local to the physical coordinates as

$$x = x_k s_k(\xi, \eta), \quad y = y_k s_k(\xi, \eta) \tag{16.30}$$

where x_k and y_k are the x- and y-positions of the nodes in the physical coordinates. We can use the local coordinates if the transformation is unique for the element. The transformation (16.30) exists and is unique if the element in the physical coordinates has the shape of a convex quadrilateral, that is, if each of the inner angles is smaller than 180°, and the way of numbering the nodes in the global and local coordinates is the same. Figure 16.3a shows an element in the local coordinates with the nodes numbered counterclockwise. Figure 16.3b shows the case of a well-shaped element with correct numbering and, consequently, with a unique transformation. Figure 16.3c illustrates a nonunique transformation due to a different numbering order in the local and physical coordinates. The nonunique transformation in Fig. 16.3d is due to an element with the inner angle at node 4 larger than 180°.

Earlier we mentioned conditions for the shape functions. We now check whether the shape functions (16.29) satisfy all conditions. The shape functions (16.29) are obviously smooth and continuous inside an element. Is the solution approximated using the shape functions (16.29) continuous across two elements? Consider the situation in Fig. 16.4. A solution in two quadrilateral elements is approximated by bilinear functions in each element. The solution is defined at nodes regardless of which element we are looking at. Therefore, we have to check only the behaviour of the shape functions at the contact of the elements, between nodes 2 and 5. Due to bilinearity, the solution on the edge of the element is a linear function uniquely defined by solution at nodes 2 and 5. Consequently, the linear function at the contact of two elements is the same for both elements and the solution is continuous across the elements. This is true for any two quadrilateral elements with bilinear shape functions. The last of the requirements was exact representation of the constant strain or, in other words, exact representation of linear polynomials. Consider the
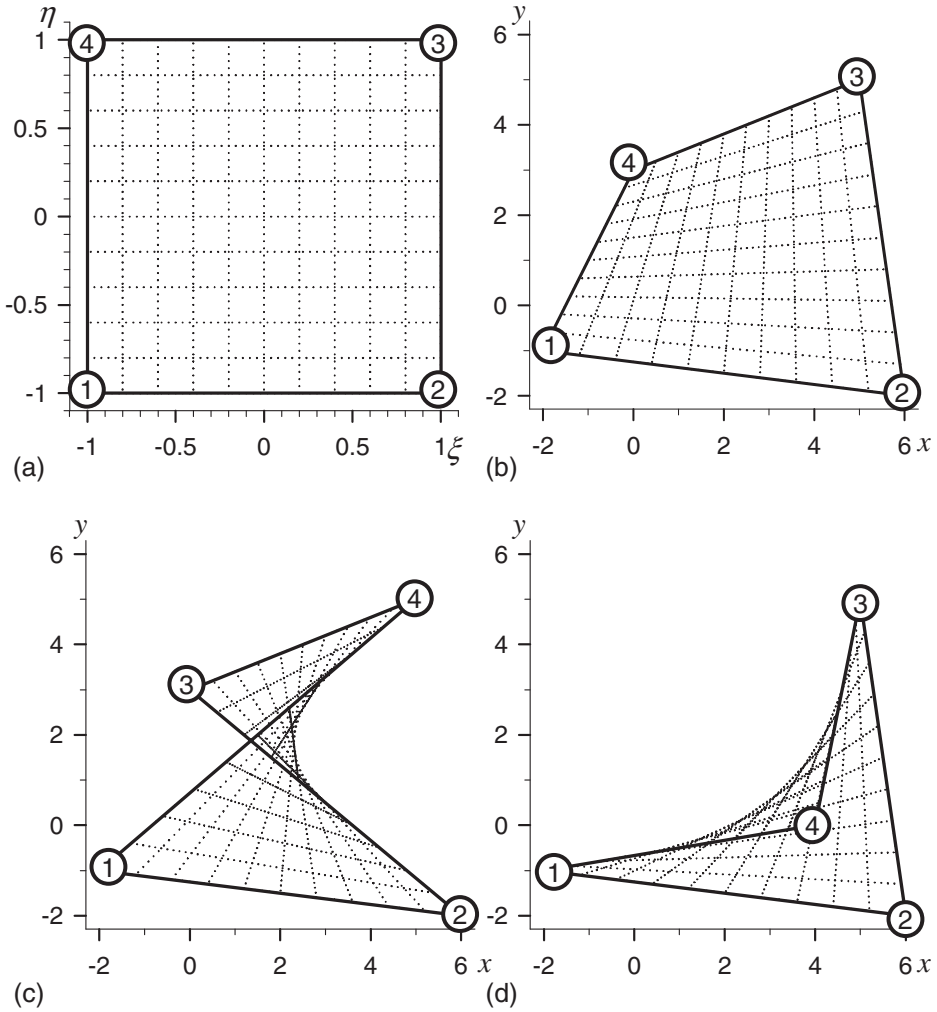
Figure 16.3 Example of transformations from the local to the physical coordinates in 2D: (a) reference element in the local coordinates, (b) unique transformation to a convex quadrilateral, (c) nonunique transformation caused by wrong node numbering, (d) nonunique transformation to a nonconvex quadrilateral.

linear function $f(x, y) = ax + by + c$. The values of this function at nodes of the element will be

$$
\begin{aligned}
F_1 &= ax_1 + by_1 + c, & F_2 &= ax_2 + by_2 + c \\
F_3 &= ax_3 + by_3 + c, & F_4 &= ax_4 + by_4 + c
\end{aligned}
\tag{16.31}
$$

We use shape functions (16.29) to approximate function $f(x, y)$ in one element:

$$
f(x, y) \approx s_1 F_1 + s_2 F_2 + s_3 F_3 + s_4 F_4
\tag{16.32}
$$
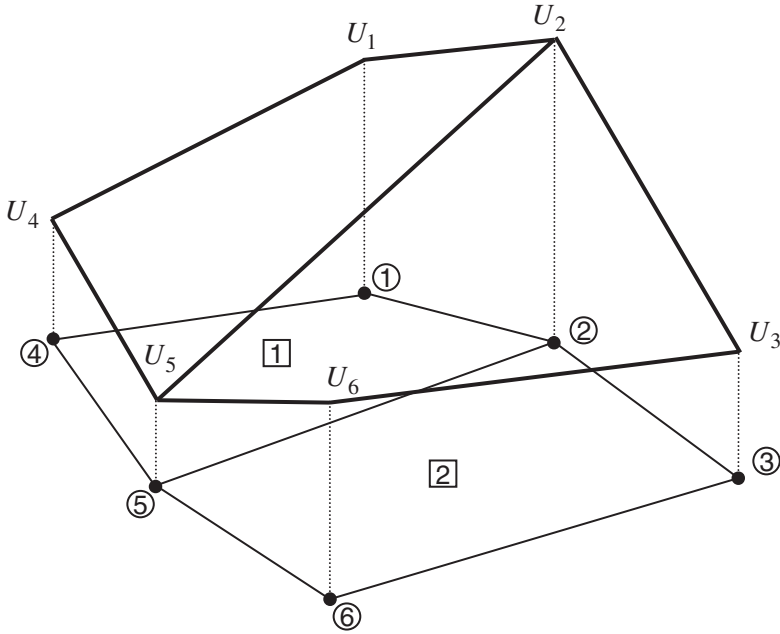
Figure 16.4 Proof of the continuity of the displacement on the contact of two quadrilateral elements with bilinear shape functions.

After using (16.31) in (16.32), and rearranging terms on the r.h.s. with respect to coefficients a, b and c we obtain

$$f(x, y) \approx a \sum_{k=1}^{4} s_k x_k + b \sum_{k=1}^{4} s_k y_k + c \sum_{k=1}^{4} s_k \qquad (16.33)$$

Considering (16.30), the first sum is equal to x and the second sum is equal to y. It remains to be shown that the last sum equals 1. This is straightforward if we use the definition of the shape functions (16.29). We can rewrite Eq. (16.33) as

$$f(x, y) \approx ax + by + c \qquad (16.34)$$

and we see that the linear function $f(x, y)$ is exactly represented by the shape functions.

Now we can easily extend the 2D quadrilateral element into a 3D hexahedral element. We assume a reference element, Ω^{ref}, as a cube in the local coordinates (ξ, η, ζ), Fig. 16.5. The nodes are at positions

$$\vec{\xi} \equiv (-1, 1, 1, -1, -1, 1, 1, -1)$$
$$\vec{\eta} \equiv (-1, -1, 1, 1, -1, -1, 1, 1) \qquad (16.35)$$
$$\vec{\zeta} \equiv (-1, -1, -1, -1, 1, 1, 1, 1)$$
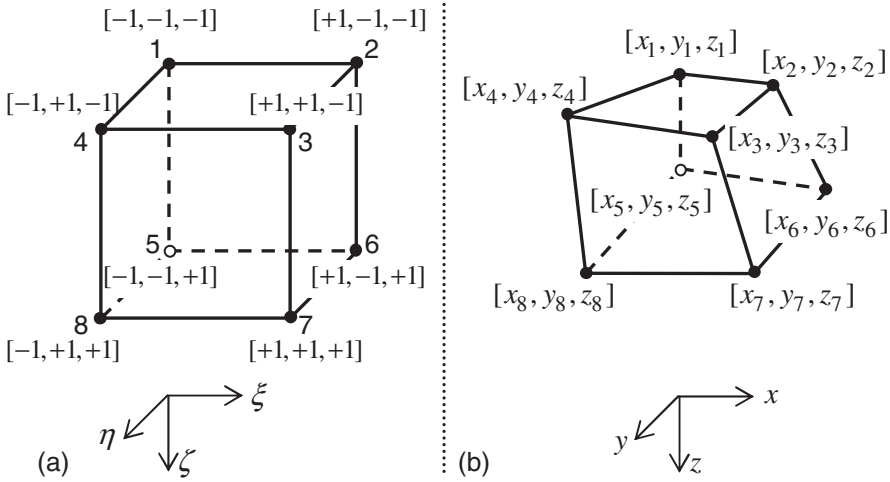
Figure 16.5 Transformation from the local to the physical coordinates in 3D. Left: a reference element Ω^{ref} in the local coordinates (ξ, η, ζ). Right: an element in the physical coordinates (x, y, z).

Consider trilinear functions:

$$s_k(\xi, \eta, \zeta) = a_k\xi + b_k\eta + c_k\zeta + d_k\xi\eta + e_k\eta\zeta + f_k\xi\zeta + g_k\xi\eta\zeta + h_k \quad (16.36)$$

A linear function for ξ can be obtained from the trilinear function by fixing two remaining variables η and ζ. Solving system (16.27) for $k, l = 1, 2, \ldots, 8$ gives eight shape functions, which can be written as

$$s_k(\xi, \eta, \zeta) = \tfrac{1}{8}(1 + \xi_k\xi)(1 + \eta_k\eta)(1 + \zeta_k\zeta); \quad k = 1, 2, \ldots, 8 \quad (16.37)$$

where ξ_k, η_k and ζ_k are components of vectors $\vec{\xi}$, $\vec{\eta}$ and $\vec{\zeta}$ defined in Eq. (16.35). The transformation of the physical coordinates can be defined analogously with (16.30):

$$x = x_k s_k(\xi, \eta, \zeta), \quad y = y_k s_k(\xi, \eta, \zeta), \quad z = z_k s_k(\xi, \eta, \zeta) \quad (16.38)$$

Similarly to the 2D case, the element in the local coordinates may be used only if transformation (16.38) exists and is unique. This means that the element has to have the shape of a convex hexahedron and the nodes in the physical and local coordinates must be numbered in the same way.

We do not address the satisfaction of the requirements in the 3D case as it is just a simple and straightforward extension of what we have shown in 2D.

In the following sections we will use the abbreviation HEX8 to denote the hexahedral element with eight nodes and trilinear shape functions.

16.4 FE scheme for an element using the local restoring-force vector

In the previous section we discussed the shape functions and decided to use local shape functions in the local coordinates (ξ, η, ζ). Incorporating the transformation of coordinates and integration over the reference element Ω^{ref}, we can rewrite Eq. (16.25):

$$\int_{\Omega^{\text{ref}}} w_k \rho s_l \ddot{U}_{il} \det \mathbf{J} \, d\Omega - \int_{\Omega^{\text{ref}}} w_k f_i \det \mathbf{J} \, d\Omega$$

$$+ \int_{\Omega^{\text{ref}}} w_{k,j} \sigma_{ij} \det \mathbf{J} \, d\Omega - \int_{\Gamma_N^{\text{ref}}} w_k h_i \det \mathbf{J} \, d\Gamma = 0; \quad k, l \in \nu \qquad (16.39)$$

Here $\mathbf{J}$ is Jacobian of the transformation from local to physical coordinates:

$$\mathbf{J} = \begin{pmatrix} x_{,\xi} & x_{,\eta} & x_{,\zeta} \\ y_{,\xi} & y_{,\eta} & y_{,\zeta} \\ z_{,\xi} & z_{,\eta} & z_{,\zeta} \end{pmatrix} \qquad (16.40)$$

where x, y and z are determined by Eq. (16.38). The set of Eqs. (16.39) may be written in a more readable and concise matrix form. For this we modify terms in Eq. (16.39) separately.

Vectors of the shape functions Define the vector of the shape functions $\mathbf{s}$,

$$\mathbf{s} \equiv (s_1, s_2, \ldots, s_n)^T \qquad (16.41)$$

with $s_1, s_2, \ldots, s_n$ given by Eq. (16.37). Recall that n denotes the number of nodes in the element. Similarly to S^w, vector $\mathbf{s}^w$ can be defined by replacing the shape functions in $\mathbf{s}$ related to the nodes on boundary Γ_D with zeros.

Local load-force vector Using vector $\mathbf{s}^w$ we can rewrite the second term in Eq. (16.39):

$$\mathbf{f}_i \equiv \int_{\Omega^{\text{ref}}} \mathbf{s}^w f_i \det \mathbf{J} \, d\Omega \qquad (16.42)$$

Each of vectors $\mathbf{f}_i$ has n components. The f_{ik} component (the k-component of vector $\mathbf{f}_i$) represents the i-component of force acting at node k. Then we can define the local load-force vector $\mathbf{f}^e$:

$$\mathbf{f}^e \equiv \left(\mathbf{f}_x^T, \mathbf{f}_y^T, \mathbf{f}_z^T \right)^T \qquad (16.43)$$

The vector $\mathbf{f}^e$ has $3n$ components. Note that here we used the adjective 'local' because the vector is defined for the element, not because it is expressed in the local coordinates.

Local boundary-condition vector Using vector $\mathbf{s}^w$ we can rewrite the fourth term in Eq. (16.39):

$$\mathbf{b}_i \equiv \int_{\Gamma_N^{\text{ref}}} \mathbf{s}^w h_i \det \mathbf{J} \, d\Gamma \qquad (16.44)$$

Each of the $\mathbf{b}_i$ vectors has n components. The b_{ik} component (the k-component of vector $\mathbf{b}_i$) represents the i-component of force acting at node k due to traction h_i acting at Γ_N^{ref}. Then we can define the local boundary-condition vector $\mathbf{b}^e$:

$$\mathbf{b}^e \equiv (\mathbf{b}_x^T, \mathbf{b}_y^T, \mathbf{b}_z^T)^T \tag{16.45}$$

The vector $\mathbf{b}^e$ has $3n$ components.

Local mass matrix Now we focus on the first term in Eq. (16.39). Recall that $\ddot{U}_{il}$ is constant in space (being a function of time) and therefore we can rewrite the term:

$$\int_{\Omega^{ref}} w_k \rho s_l \ddot{U}_{il} \det \mathbf{J} \, d\Omega = \int_{\Omega^{ref}} w_k \rho s_l \det \mathbf{J} \, d\Omega \ddot{U}_{il} \tag{16.46}$$

Define a local mass matrix $\mathbf{m}^e$ as

$$\mathbf{m}^e \equiv \begin{pmatrix} \tilde{\mathbf{m}}^e & \mathbf{0} & \mathbf{0} \\ \mathbf{0} & \tilde{\mathbf{m}}^e & \mathbf{0} \\ \mathbf{0} & \mathbf{0} & \tilde{\mathbf{m}}^e \end{pmatrix} \tag{16.47}$$

with matrices $\tilde{\mathbf{m}}^e$ defined as

$$\tilde{\mathbf{m}}^e \equiv \int_{\Omega^{ref}} \mathbf{s}^w \rho \mathbf{s}^T \det \mathbf{J} \, d\Omega \tag{16.48}$$

The dimensions of $\tilde{\mathbf{m}}^e$ and the local mass matrix $\mathbf{m}^e$ are $n \times n$ and $3n \times 3n$, respectively. We define also a local vector of discrete displacements $\mathbf{u}^e$ as

$$\mathbf{u}^e \equiv \left[\left(\mathbf{u}_x^e\right)^T, \left(\mathbf{u}_y^e\right)^T, \left(\mathbf{u}_z^e\right)^T \right]^T \tag{16.49}$$

where

$$\mathbf{u}_i^e \equiv (U_{i1}, U_{i2}, \dots, U_{in})^T \tag{16.50}$$

As mentioned before, U_{il} represents the i-component of displacement at node l. The dimensions of vectors $\mathbf{u}_i^e$ are $n \times 1$, dimensions of the local discrete-displacement vector are $3n \times 1$. Using the local mass matrix and discrete-displacement vector we can rewrite terms in (16.46) in matrix-vector notation:

$$\int_{\Omega^{ref}} w_k \rho s_l \det \mathbf{J} \, d\Omega \ddot{U}_{il} \rightarrow \mathbf{m}^e \ddot{\mathbf{u}}^e \tag{16.51}$$

Local restoring-force vector for an elastic isotropic medium The FE formulation with the concept of restoring forces at nodes considerably reduces memory requirements compared to the FE formulation with the global stiffness matrix. Our formulation and implementation is based on the outline of the formulation presented by Archuleta (1976, and personal communication) who refers to Frazier and Petersen (1974).

Consider the third term in Eq. (16.39):

$$\int_{\Omega^{\text{ref}}} w_{k,j} \sigma_{ij} \det \mathbf{J} \, d\Omega \tag{16.52}$$

For $i = x$ we can rewrite the integral as

$$\int_{\Omega^{\text{ref}}} w_{k,j} \sigma_{ij} \det \mathbf{J} \, d\Omega \stackrel{i=x}{=} \int_{\Omega^{\text{ref}}} (w_{k,x} \sigma_{xx} + w_{k,y} \sigma_{xy} + w_{k,z} \sigma_{xz}) \det \mathbf{J} \, d\Omega \tag{16.53}$$

and using the vector of shape functions $\mathbf{s}^w$ as

$$\mathbf{r}_x \equiv \int_{\Omega^{\text{ref}}} \left(\mathbf{s}^w{}_{,x} \, \sigma_{xx} + \mathbf{s}^w{}_{,y} \, \sigma_{xy} + \mathbf{s}^w{}_{,z} \, \sigma_{xz} \right) \det \mathbf{J} \, d\Omega \tag{16.54}$$

The dimension of vector $\mathbf{r}_x$ is $n \times 1$.

Analogously we can proceed with $i = y$ and $i = z$ and define vectors $\mathbf{r}_y$ and $\mathbf{r}_z$, respectively,

$$\mathbf{r}_y \equiv \int_{\Omega^{\text{ref}}} \left(\mathbf{s}^w{}_{,x} \, \sigma_{yx} + \mathbf{s}^w{}_{,y} \, \sigma_{yy} + \mathbf{s}^w{}_{,z} \, \sigma_{yz} \right) \det \mathbf{J} \, d\Omega \tag{16.55}$$

$$\mathbf{r}_z \equiv \int_{\Omega^{\text{ref}}} \left(\mathbf{s}^w{}_{,x} \, \sigma_{zx} + \mathbf{s}^w{}_{,y} \, \sigma_{zy} + \mathbf{s}^w{}_{,z} \, \sigma_{zz} \right) \det \mathbf{J} \, d\Omega \tag{16.56}$$

Then the local restoring-force vector is

$$\mathbf{r}^e \equiv \left(\mathbf{r}_x^T, \mathbf{r}_y^T, \mathbf{r}_z^T \right)^T \tag{16.57}$$

The dimension of vector $\mathbf{r}^e$ is $3n \times 1$. The r_{ik}^e component of the vector represents the i-component of force acting at node k as a consequence of the elastic forces acting in the element. The elastic forces are a reaction to the current deformation of the element. They try to get the element back into a state of equilibrium or, in other words, they try to restore the element.

We need to express the stress-tensor components in Eqs. (16.54)–(16.56). For the elastic isotropic medium they are given by Hooke's law, Eq. (2.23):

$$\sigma_{ij} = \lambda u_{k,k} \delta_{ij} + \mu(u_{i,j} + u_{j,i}) \tag{16.58}$$

For Hooke's law we need derivatives of the approximate solution. Using vectors of the shape functions $\mathbf{s}$ and discrete displacements $\mathbf{u}_i$ we rewrite Eq. (16.22):

$$u_i(\vec{x}, t) \approx \sum_{k \in \nu} s_k(\vec{x}) \, U_{ik}(t) = \mathbf{s}^T \cdot \mathbf{u}_i^e \tag{16.59}$$

Spatial derivatives apply only to $\mathbf{s}$ because vectors $\mathbf{u}_i^e$ are only functions of time. In general, we can write the derivatives of displacement as

$$u_{i,j} = \mathbf{s},_j^T \cdot \mathbf{u}_i^e \tag{16.60}$$

Here we need derivatives with respect to the physical coordinates (x, y, z) but our shape functions are defined for the local coordinates (ξ, η, ζ). Applying the chain rule leads to

$$
\begin{aligned}
\mathbf{s},_x &= \mathbf{s},_\xi \, \xi,_x + \mathbf{s},_\eta \, \eta,_x + \mathbf{s},_\zeta \, \zeta,_x \\
\mathbf{s},_y &= \mathbf{s},_\xi \, \xi,_y + \mathbf{s},_\eta \, \eta,_y + \mathbf{s},_\zeta \, \zeta,_y \\
\mathbf{s},_z &= \mathbf{s},_\xi \, \xi,_z + \mathbf{s},_\eta \, \eta,_z + \mathbf{s},_\zeta \, \zeta,_z
\end{aligned}
\tag{16.61}
$$

The inverse Jacobian of transformation (16.38) is

$$
\mathbf{J}^{-1} =
\begin{pmatrix}
\xi,_x & \xi,_y & \xi,_z \\
\eta,_x & \eta,_y & \eta,_z \\
\zeta,_x & \zeta,_y & \eta,_z
\end{pmatrix}
\tag{16.62}
$$

By comparing Eqs. (16.62) and (16.61) we see that we can use the corresponding components of the inverse Jacobian to express derivatives of the local coordinates (ξ, η, ζ) with respect to the physical coordinates (x, y, z) needed in Eq. (16.61).

Note on computation of integrals To construct the local quantities we have to compute volume or surface integrals. For example, in the case of the local restoring-force vector we have to compute integrals (16.54)–(16.56). In general, numerical integration is used for the HEX8 elements. To choose the correct order of numerical integration, one must analyze the functions that are to be integrated. Gaussian integration is the most efficient integration in terms of the lowest number of integration points needed to achieve the desired precision. Therefore, 8-point (2 points in each direction) Gaussian integration is usually used for the HEX8 elements. This integration is exact for up to cubic polynomials and therefore it is considered an exact integration for the undeformed elements ('exact' here means that the error is caused only by a discrete representation of numbers). In the case of the deformed elements we may need to increase the order of integration due to the more complicated form of det $\mathbf{J}$. However, in general, the more deformed the element we use, the larger will be the systematic error.

Sometimes it is reasonable to use integration with lower accuracy than what is required for the exact integration. This may be due to higher efficiency (lower accuracy of integration may mean fewer integration points and consequently fewer operations) or due to different properties of the final scheme. For better efficiency, 1-point Gaussian integration is often used with the HEX8 elements (e.g., Ma and Liu 2006). However, note that the scheme based on the 1-point Gaussian integration has to be used with algorithms for reducing hourglass modes. Otherwise it will provide unusable results. See Chapter 17 for an example of the reduced integration.

Local restoring-force vector for an isotropic medium with realistic attenuation Here we will address the implementation of realistic attenuation based on the rheology of GMB-EK/GZB into the FEM. The general procedure is the same as for the elastic case, the difference is only in the type of stress–strain relation adopted.

In Chapter 3 we derived stress–strain relations for a 3D viscoelastic continuum using the GMB-EK/GZB. Recall the stress–strain relation, Eq. (3.134):

$$\sigma_{ij} = \kappa \varepsilon_{kk} \delta_{ij} + 2\mu \left(\varepsilon_{ij} - \tfrac{1}{3} \varepsilon_{kk} \delta_{ij} \right) - \sum_{l=1}^{n_l} \left[Y_l^\kappa \kappa \zeta_l^{kk} \delta_{ij} + 2 Y_l^\mu \mu \left(\zeta_l^{ij} - \tfrac{1}{3} \zeta_l^{kk} \delta_{ij} \right) \right]$$

(16.63)

where κ and μ are the unrelaxed bulk and shear modulus, respectively, Y_l^κ and Y_l^μ are corresponding anelastic coefficients, defined by Eqs. (3.140), and ζ_l^{ij} are anelastic functions defined by the differential equation, see Eq. (3.135):

$$\dot{\zeta}_l^{ij} + \omega_l \zeta_l^{ij} = \omega_l \varepsilon_{ij}$$

(16.64)

Recall that indices i, j and k are spatial indices and therefore $i, j, k \in \{1, 2, 3\}$. Index l is related to the relaxation frequencies and therefore $l \in \{1, 2, \ldots, n_l\}$. The summation convention does not apply to index l. We can rewrite the stress–strain relation (16.63) in a form more suitable for implementation in the FEM:

$$\sigma_{ij} = \sigma_{ij}^E - \sum_{l=1}^{n_l} \sigma_{ij}^{Al}$$

(16.65)

Here σ_{ij}^E and σ_{ij}^{Al} denote the elastic and anelastic parts, respectively. The anelastic parts may be defined by

$$\begin{aligned}
\sigma_{xx}^{Al} &= Y^+ \zeta_l^{xx} + Y^- \zeta_l^{yy} + Y^- \zeta_l^{zz} \\
\sigma_{yy}^{Al} &= Y^- \zeta_l^{xx} + Y^+ \zeta_l^{yy} + Y^- \zeta_l^{zz} \\
\sigma_{zz}^{Al} &= Y^- \zeta_l^{xx} + Y^- \zeta_l^{yy} + Y^+ \zeta_l^{zz} \\
\sigma_{xy}^{Al} &= 2\mu Y_l^\mu \zeta_l^{xy} \\
\sigma_{yz}^{Al} &= 2\mu Y_l^\mu \zeta_l^{yz} \\
\sigma_{xz}^{Al} &= 2\mu Y_l^\mu \zeta_l^{xz}
\end{aligned}$$

(16.66)

where $Y^+ = \kappa Y_l^\kappa + \tfrac{4}{3}\mu Y_l^\mu$ and $Y^- = \kappa Y_l^\kappa - \tfrac{2}{3}\mu Y_l^\mu$. The anelastic functions are obtained from Eq. (16.64) as follows (Kristek and Moczo 2003). The temporal derivative of $\zeta_l^{ij}(t)$ is approximated by the 2nd-order central difference formula. Function $\zeta_l^{ij}(t)$ itself is approximated as the arithmetic average:

$$\zeta_l^{ij}(t) = \tfrac{1}{2} \left[\zeta_l^{ij}(t - \tfrac{1}{2}\Delta t) + \zeta_l^{ij}\left(t + \tfrac{1}{2}\Delta t\right) \right]$$

(16.67)

Finally, we obtain the recurrent formula:

$$\zeta_l^{ij}\left(t + \tfrac{1}{2}\Delta t\right) = \frac{2\omega_l \Delta t \varepsilon_{ij}(t) + (2 - \omega_l \Delta t)\, \zeta_l^{ij}\left(t - \tfrac{1}{2}\Delta t\right)}{2 + \omega_l \Delta t}$$

(16.68)

We use (16.68) to obtain $\zeta_l^{ij}\left(t + \frac{1}{2}\Delta t\right)$ and then (16.67) to obtain $\zeta_l^{ij}(t)$. (Compare with the algorithm for the velocity–stress staggered-grid scheme in Section 7.8.)

As we have already discussed, numerical integration is used to compute the local restoring-force vector. This implies that anelastic functions are required at all integration points. Moreover, the recurrent formula (16.68) implies that the anelastic functions have to be stored in computer memory. That would cause drastic memory requirements and consequently the computations for a viscoelastic medium would be impossible for many realistic problems. To reduce the memory requirements down to a feasible level we evaluate the anelastic functions only at the centre of the element. This can be interpreted as considering the constant strain in an element for calculating the anelastic functions using Eq. (16.68).

Matrix form of the discrete weak-form equation of motion for an element Using the local load-force vector $\mathbf{f}^e$, Eq. (16.43), local boundary-condition vector $\mathbf{b}^e$, Eq. (16.45), local mass matrix $\mathbf{m}^e$, Eq. (16.47), discrete-displacement vector $\mathbf{u}^e$, Eq. (16.49), and local restoring-force vector $\mathbf{r}^e$, Eq. (16.57), we can rewrite Eqs. (16.39) in a matrix form:

$$\mathbf{m}^e \ddot{\mathbf{u}}^e = \mathbf{r}^e + \mathbf{b}^e + \mathbf{f}^e \tag{16.69}$$

16.5 FE scheme for the whole domain using the global restoring-force vector

Now we have derived equations for the element, we can look again at the whole domain Ω. The whole domain must be covered by elements without holes and overlapping. Naturally, most of the nodes will be shared between two or more elements. In general, the elements may have different shapes and/or different numbers of nodes as long as the requirement of displacement continuity across elements is satisfied.

Global and local indexing of nodes, and indexing of the elements Each node in an element is indexed locally (within the element) by a number from 1 to n. Because the local numbering is not unique in the whole mesh of elements covering the domain, a unique global indexing of nodes is necessary. In the global indexing, each node in the mesh is assigned a unique number from 1 to N. Similarly, each element is assigned a unique number from 1 to N^e. Moreover, the local node index and the element index uniquely determine the global node index. Note, however, that we cannot uniquely determine a local index from the global one if the node is shared by two or more elements. Figure 16.6 illustrates the local and global indexing in an example of the 1D elements.

Global mass matrix, global restoring-force vector and global load-force vector We define the global restoring-force vector with the same structure as the local restoring-force vector:

$$\mathbf{R} = \left(\mathbf{R}_x^T, \mathbf{R}_y^T, \mathbf{R}_z^T\right)^T \tag{16.70}$$
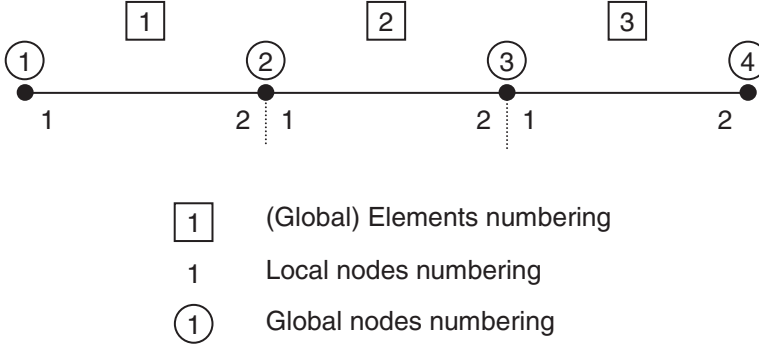
Figure 16.6 Example in 1D of the local and global numbering of nodes as well as the numbering of elements. Here we assume three elements: $N^e = 3$, with two nodes per element; $n = 2$, which is four nodes in total; and $N = 4$.

Here, vectors $\mathbf{R}_x$, $\mathbf{R}_y$ and $\mathbf{R}_z$ have N components, and vector $\mathbf{R}$ has $3N$ components. Denote the i-component of the restoring force acting at the node with the global number J as R_{iJ}. This component is a sum of all restoring-force contributions at node J from all elements sharing node J. Assume a node with the global number J that belongs to elements e_1, e_2, e_3 and e_4. Node J has local numbers n_1, n_2, n_3 and n_4, respectively. Then the corresponding component of $\mathbf{R}$ is

$$R_{iJ} = r_{in_1}^{e_1} + r_{in_2}^{e_2} + r_{in_3}^{e_3} + r_{in_4}^{e_4} \tag{16.71}$$

The same approach is used to construct the global load-force vector

$$\mathbf{F} = \left(\mathbf{F}_x^T, \mathbf{F}_y^T, \mathbf{F}_z^T\right)^T \tag{16.72}$$

and the global boundary-condition vector:

$$\mathbf{B} = \left(\mathbf{B}_x^T, \mathbf{B}_y^T, \mathbf{B}_z^T\right)^T \tag{16.73}$$

In the case of the global vector $\mathbf{B}$ we also apply the requirement of traction continuity across elements. Then the force contributions between elements cancel out and only contributions from the traction vector h_i acting at boundary Γ_N of the domain remain.

The global mass matrix is created considering the inertial forces. Due to the matrix structure, the process is formally more complicated than for vectors. We define the global discrete-displacement vector:

$$\mathbf{U} \equiv \left(\mathbf{U}_x^T, \mathbf{U}_y^T, \mathbf{U}_z^T\right)^T \tag{16.74}$$

Each node is assigned one displacement – no matter how many elements share the node. We need to create auxiliary matrices $\mathbf{M}^e$. We start with the local mass matrix $\mathbf{m}^e$; we add zero columns and rows to it until matrix $\mathbf{M}^e$ has elements of $\mathbf{m}^e$ only in columns and rows corresponding to the global indices of nodes in element e. This way we create N^e matrices,

one for each element. Each matrix $\mathbf{M}^e$ has dimensions $3N \times 3N$ (that is, dimensions of the global mass matrix). Now we can define the global inertial force:

$$\tilde{\mathbf{F}} \equiv \sum_{e=1}^{N^e} \mathbf{M}^e \mathbf{U} \tag{16.75}$$

Because the global vector of displacements does not change between elements, we can take it out of the sum and eventually define the global mass matrix:

$$\mathbf{M} \equiv \sum_{e=1}^{N^e} \mathbf{M}^e \tag{16.76}$$

Due to the blocky structure of the local mass matrices, the global mass matrix also has blocky structure:

$$\mathbf{M} = \begin{pmatrix} \tilde{\mathbf{M}} & \mathbf{0} & \mathbf{0} \\ \mathbf{0} & \tilde{\mathbf{M}} & \mathbf{0} \\ \mathbf{0} & \mathbf{0} & \tilde{\mathbf{M}} \end{pmatrix} \tag{16.77}$$

with sub-matrices having dimensions $N \times N$. Element $\tilde{M}_{IJ}$ of sub-matrix $\tilde{\mathbf{M}}$ is a sum of all contributions from the local mass sub-matrices $\tilde{\mathbf{m}}^e$ corresponding to nodes I and J. Only one element is considered from one sub-matrix – the one from the row corresponding to the global node I and column corresponding to the global node J. Of course, in practical applications, the construction of the auxiliary matrices $\mathbf{M}^e$ is useless and we can directly create the global mass matrix using the relations explained in this paragraph.

Using the global quantities we can write the global system of equations as

$$\mathbf{M}\ddot{\mathbf{U}} = \mathbf{R} + \mathbf{B} + \mathbf{F} \tag{16.78}$$

In general it is a system of $3N$ equations. If there is no Dirichlet boundary (Γ_D), the system is well defined and is solvable – we have $3N$ equations for $3N$ unknowns. Assume, however, boundary Γ_D with N_D nodes (displacements prescribed at these nodes). Recall the definition of the components of vector $\mathbf{U}$, Eqs. (16.18) and (16.21). Due to the prescribed displacements the number of unknowns is $3(N - N_D)$. The vector of the shape functions $\mathbf{s}^w$ was defined so that the components corresponding to the nodes at Γ_D are zero. Consequently, there are zero rows in the global mass matrix as well as zeros in the corresponding row in the global-force vector and boundary-condition vector. This means that the number of independent equations is only $3(N - N_D)$ – the same as the number of unknowns. Thus, system (16.78) is uniquely solvable also in the case of nodes at the boundary Γ_D.

Time integration System (16.78) is a system of partial differential equations. To solve the system we approximate the 2nd time derivative by the central FD formula:

$$\ddot{\mathbf{U}}(t) \approx \frac{\mathbf{U}(t - \Delta t) - 2\mathbf{U}(t) + \mathbf{U}(t + \Delta t)}{(\Delta t)^2} \tag{16.79}$$

Using Eqs. (16.79) and (16.78) we obtain the explicit scheme

$$\mathbf{U}^{(m+1)} = (\Delta t)^2 \, \mathbf{M}^{-1} \left(\mathbf{R}^{(m)} + \mathbf{F}^{(m)} + \mathbf{B}^{(m)} \right) + 2\mathbf{U}^{(m)} - \mathbf{U}^{(m-1)} \qquad (16.80)$$

where m indicates the time level; the time level m corresponds to time $t^m = t_0 + m \Delta t$. For simulating seismic wave propagation we can assume the initial conditions

$$\mathbf{U}^{(-1)} = \mathbf{0}, \quad \mathbf{U}^{(0)} = \mathbf{0} \qquad (16.81)$$

Scheme (16.80) is conditionally stable. The stability condition for an undeformed, that is cubic, element is (e.g., Serón *et al.* 1989)

$$\Delta t \le \frac{h}{\alpha_{\max}} \qquad (16.82)$$

where h is the element edge length and $\alpha_{\max}$ is the maximum P-wave speed. Note that if the mesh contains elements with different sizes, the stability condition has to be evaluated locally. For that we can modify the stability condition as

$$\Delta t \le \min \left\{ \frac{h_1}{\alpha_1}, \frac{h_2}{\alpha_2}, \ldots, \frac{h_{N^e}}{\alpha_{N^e}} \right\} \qquad (16.83)$$

where $h_1, h_2, \ldots, h_{N^e}$ are the minimum edge lengths of elements and $\alpha_1, \alpha_2, \ldots, \alpha_{N^e}$ are maximum P-wave speeds inside each element.

Lumped mass matrix To solve the system of Eqs. (16.80) we need the inverse of the mass matrix, $\mathbf{M}^{-1}$. The mass matrix $\mathbf{M}$ is sparse; for example, in the case of the HEX8 elements the mass matrix has $N \times N$ elements (taking into account that for the x, y and z displacement components the mass matrix has the same values) but only approximately $27 \times N$ nonzero elements. Unfortunately, the inverse mass matrix is no longer sparse and we would need to store the whole mass matrix. This would mean very large memory requirements as well as a large number of operations to actually find the inverse of such a large matrix. The situation is much easier with a diagonal mass matrix. The inverse of the diagonal mass matrix is also diagonal. Therefore, the mass matrix $\mathbf{M}$ is usually replaced or approximated by the diagonal lumped mass matrix $\mathbf{M}^L$. The elements of $\mathbf{M}^L$ are defined as

$$\mathbf{M}_{II}^L \equiv \sum_{J=1}^{N} \mathbf{M}_{IJ}, \quad \mathbf{M}_{IJ}^L \equiv 0 \quad \text{if} \quad I \ne J \qquad (16.84)$$

From the physical point of view, the approximation means that the mass of an element is concentrated at the nodes. For example, assume a lumped mass matrix and a force acting at one node. At this node we would see a change in displacement after the first time update but displacements at the other nodes would remain unchanged. They will sense the acting force only through deformation of the element caused by the displacement at the first node. Consequently, displacements at the other nodes would change after two updates. Consider now the same example but with a full mass matrix. In this case the nonzero nondiagonal elements of the mass matrix would be responsible for the reaction of the other nodes in the element during the first update.

Even though the lumped mass matrix seems to change the physics dramatically, in many practical applications the approach usually works well. However, there are situations when it is not so – see Chapter 17 for an example.

16.6 Efficient computation of the restoring-force vector

To minimize the computational requirements one can use special coordinates for updating the restoring-force vector proposed by Balažovjech and Halada (2006) and Moczo *et al.* (2007a) for a 2D quadrilateral element. The description of an element in the standard coordinates (local or physical) also contains information about the position/location of the element. But the position/location is not needed for computation of the restoring force, because the restoring force depends only on the deformation of the element. Therefore Balažovjech and Halada proposed parameterizing the element using new local coordinates. They called them e-invariants. The benefit of using e-invariants comes from the fact that the shape functions expressed in these local coordinates have a very simple form. Consequently, the number of operations required to update the restoring force is significantly lower than in the case of the standard shape functions.

Here we show and briefly comment on the final expressions of the approach for the restoring-force computation in 3D (Balažovjech, personal communication). Recall the definition of the local restoring-force vector, Eq. (16.54). Consider only the element without nodes at boundary Γ_D. In such a case $\mathbf{s}^w = \mathbf{s}$ and we can write

$$\mathbf{r}_x \equiv \int_{\Omega^m} \left(\mathbf{s}_{,x}\, \sigma_{xx} + \mathbf{s}_{,y}\, \sigma_{xy} + \mathbf{s}_{,z}\, \sigma_{xz} \right) \det \mathbf{J}\, d\Omega \tag{16.85}$$

We can do so analogously also for the *y*- and *z*-components.

Define a transformation matrix:

$$\mathbf{T} \equiv \begin{pmatrix} 1 & 1 & 1 & 1 & 1 & 1 & 1 & 1 \\ -1 & 1 & 1 & -1 & -1 & 1 & 1 & -1 \\ -1 & -1 & 1 & 1 & -1 & -1 & 1 & 1 \\ -1 & -1 & -1 & -1 & 1 & 1 & 1 & 1 \\ 1 & -1 & 1 & -1 & 1 & -1 & 1 & -1 \\ 1 & 1 & -1 & -1 & -1 & -1 & 1 & 1 \\ 1 & -1 & -1 & 1 & -1 & 1 & 1 & -1 \\ -1 & 1 & -1 & 1 & 1 & -1 & 1 & -1 \end{pmatrix} \tag{16.86}$$

The shape functions for the reference element can be then expressed using matrix $\mathbf{T}$:

$$\mathbf{s}^{(inv)} \equiv \mathbf{T}\,\mathbf{s} = (1, \xi, \eta, \zeta, \xi\eta, \eta\zeta, \xi\zeta, \xi\eta\zeta)^T \tag{16.87}$$

(compare with the standard shape functions defined by Eq. (16.37)). Matrix $\mathbf{T}$ has the property

$$\mathbf{I} = \tfrac{1}{8}\mathbf{T}^T\mathbf{T} \tag{16.88}$$

where $\mathbf{I}$ is the unit matrix.

To compute the stresses needed in Eq. (16.85) we need to know the spatial derivatives of displacement. Using (16.88) we express the spatial derivatives of displacement:

$$\mathbf{u}_i^e,_j = \mathbf{s},_j^T \cdot \mathbf{u}_i^e = \mathbf{s},_j^T \cdot \left(\tfrac{1}{8}\mathbf{T}^T\mathbf{T}\right) \cdot \mathbf{u}_i^e = \tfrac{1}{8}\mathbf{s},_j^{(inv)T} \cdot \mathbf{u}_i^{(inv)} \tag{16.89}$$

Using (16.88) we can rewrite the restoring force (16.85) in this form:

$$\mathbf{r}_x \equiv \tfrac{1}{8}\mathbf{T}^T\int_{\Omega^m}\left(\mathbf{s}^{(inv)},_x\,\sigma_{xx} + \mathbf{s}^{(inv)},_y\,\sigma_{xy} + \mathbf{s}^{(inv)},_z\,\sigma_{xz}\right)\det\mathbf{J}d\Omega \tag{16.90}$$

We can obtain the Jacobian for Eq. (16.90) from definition (16.40). We just have to replace the expressions for coordinates x, y, z. We can express the physical coordinates from Eq. (16.38) using the approach indicated in Eq. (16.89). We obtain

$$x = \tfrac{1}{8}\mathbf{s}^{(inv)T}\mathbf{x}^{(inv)}, \quad y = \tfrac{1}{8}\mathbf{s}^{(inv)T}\mathbf{y}^{(inv)}, \quad z = \tfrac{1}{8}\mathbf{s}^{(inv)T}\mathbf{z}^{(inv)} \tag{16.91}$$

where

$$\mathbf{x}^{(inv)} = \mathbf{T}\begin{pmatrix} x_1 \\ x_2 \\ \vdots \\ x_n \end{pmatrix}, \quad \mathbf{y}^{(inv)} = \mathbf{T}\begin{pmatrix} y_1 \\ y_2 \\ \vdots \\ y_n \end{pmatrix}, \quad \mathbf{z}^{(inv)} = \mathbf{T}\begin{pmatrix} z_1 \\ z_2 \\ \vdots \\ z_n \end{pmatrix} \tag{16.92}$$

16.7 Comparison of formulations with the restoring force and stiffness matrix

Compare the formulation with the restoring force (the one we use) with a common formulation based on the stiffness matrix $\mathbf{K}$. The relation between the stiffness matrix and the restoring force may be written as

$$\mathbf{R} = -\mathbf{K}\mathbf{U} \tag{16.93}$$

Matrix $\mathbf{K}$ is very sparse. Consider a mesh of the HEX8 elements. The total number of elements in the matrix $\mathbf{K}$ is $3N \times 3N$ whereas the number of the nonzero elements is approximately $3N \times 81$. Storing only the nonzero elements clearly is more feasible than storing all elements. However, considering the tens of millions of nodes in relatively modest 3D numerical modelling, we easily realize that even the latter number of nonzero elements poses a serious problem. The restoring-force vector has only $3N$ elements – we need to store 81 times fewer elements compared to storing the nonzero elements in the stiffness matrix.

On the other hand, the stiffness matrix does not change with time – it is enough to calculate it once at the beginning of simulation. The restoring force has to be updated

at each time level. This means that the restoring force reduces memory requirements but increases the number of algebraic operations.

Note that the stiffness matrix is time independent only if material parameters are time independent. Nonlinear (e.g., elastoplastic) behaviour of a medium implies a time-dependent stiffness matrix. The matrix has to be updated at each time level and the stiffness-matrix formulation means both large memory and computational time requirements.

16.8 Essential summary of the FEM implementation

Use of the restoring-force concept significantly reduces the memory requirements compared to the commonly used global stiffness matrix. The need to calculate the restoring forces at each time level, however, increases the number of operations and thus the computational time. This increase can be significantly reduced by the use of e-invariants. Consequently, the combination of the restoring forces and e-invariants represents a memory-efficient implementation of the FEM.

17

Traction-at-split-node modelling of dynamic rupture propagation

This chapter is devoted to implementation of the TSN method for modelling dynamic rupture propagation in the FE algorithm. There are different implementations of dynamic models in the FEM. Archuleta (1976) and Archuleta and Frazier (1978) published one of the first implementations. Their rupture propagation was not spontaneous because the rupture speed was prescribed but the evolution of traction was calculated. Day (1977) implemented his version of the TSN in the standard FE algorithm. Later Andrews (1999) implemented his version of the TSN in the FD algorithm with spatial differentiation equivalent to the FEM. The method was, however, limited to a homogeneous medium and 'brick' elements. Oglesby (1999) implemented an algorithm for spontaneous rupture propagation into Dyna2D (Whirley *et al.* 1992) and Dyna3D (Whirley and Engelmann 1993) codes. Because of the nature of the codes, Oglesby's approach was based on elastic and frictional forces. But, in fact, it was equivalent to Andrews' version of the TSN.

17.1 Implementation of TSN in the FEM

Here we explain the TSN implementation in the FEM described in Chapter 16. We recall that the TSN explained in Chapter 14 may be used with numerical methods with an explicit time-stepping algorithm and if the force applied at one node accelerates only that node during one time iteration. These requirements are satisfied with the explicit scheme (16.80) with the lumped mass matrix (16.84). As we explained in Chapter 16, we use the lumped mass matrix for practical reasons.

In a TSN the fault surface is covered by split nodes whereas the rest of the domain is covered by normal nodes. Recall that a split node consists of two partial nodes – $p.n.^+$ and $p.n.^-$. The partial node $p.n.^+$ belongs only to halfspace H^+ whereas $p.n.^-$ belongs only to halfspace H^-. A partial node is characterized by quantities related to the relevant halfspace (e.g., seismic wave speeds, density, displacements, particle velocities or forces). A couple of the partial nodes share the fault-related quantities (e.g., slip, slip rate, coefficients of friction). This imposes additional constraints in creating the global system of the FE equations from the local ones. We have to ensure that the restoring force at the partial node $p.n.^-$ is only due to deformation in halfspace H^- and, similarly, the restoring force at the partial node $p.n.^+$ is only due to deformation of the halfspace H^+. Analogously, we have

to ensure that mass M^- is only due to the density distribution in halfspace H^- and mass M^+ is only due to the density distribution in halfspace H^+. In other words, if there is no interaction between the partial nodes $p.n.^+$ and $p.n.^-$, the partial nodes should behave as nodes at a free surface.

The first step in the TSN algorithm is to compute the trial traction $\vec{T}^{ct}$. Recall Eq. (14.11):

$$\vec{T}^{ct}(t) \approx \vec{T}^0 + \frac{\dfrac{M^- M^+}{\Delta t}\dot{\vec{s}}\left(t - \dfrac{\Delta t}{2}\right) + M^- \vec{F}^+(t) - M^+ \vec{F}^-(t)}{A(M^- + M^+)} \tag{17.1}$$

Forces $\vec{F}^+$ and $\vec{F}^-$ are components of the global restoring-force vector corresponding to the partial nodes $p.n.^+$ and $p.n.^-$, respectively.

Vector $\vec{T}^{ct}$ can be decomposed into the normal and shear (tangential) components:

$$\begin{aligned}
\vec{T}_n^{ct}(t) &= [\vec{T}^{ct}(t) \cdot \vec{n}]\vec{n} \\
\vec{T}_{sh}^{ct}(t) &= \vec{T}^{ct}(t) - \vec{T}_n^{ct}(t)
\end{aligned} \tag{17.2}$$

To evaluate the fault strength $S(t)$ according to the linear slip-weakening friction law (4.11), we need the slip path l defined by (4.10). The slip path at time t can be approximated:

$$l(t) \approx l(t - \Delta t) + \Delta t |\dot{\vec{s}}(t - \Delta t/2)| \tag{17.3}$$

The total traction on the fault, $\vec{T}^c(t)$, and the slip rate are determined by Eqs. (14.12), (14.22) and (14.16):

$$\left|\vec{T}_{sh}^{ct}(t)\right| \leq S(t): \vec{T}^c(t) = \vec{T}^{ct}(t) \qquad \Rightarrow \dot{\vec{s}}\left(t + \tfrac{1}{2}\Delta t\right) = 0$$

$$\left|\vec{T}_{sh}^{ct}(t)\right| > S(t): \vec{T}_n^c(t) = \vec{T}_n^{ct}(t) \qquad \Rightarrow \dot{\vec{s}}_n\left(t + \tfrac{1}{2}\Delta t\right) = 0 \tag{17.4}$$

$$\vec{T}_{sh}^c(t) = S(t)\frac{\vec{T}_{sh}^{ct}(t)}{\left|\vec{T}_{sh}^{ct}(t)\right|} \Rightarrow \dot{\vec{s}}_{sh}\left(t + \tfrac{1}{2}\Delta t\right) \approx \Delta t\, B\big[\vec{T}_{sh}^{ct}(t) - \vec{T}_{sh}^f(t)\big]$$

The updated slip-rate value is then used to obtain the displacements at the partial nodes $p.n.^+$ and $p.n.^-$. The velocity of the centroid of two partial nodes is

$$\vec{v}_{cent}\left(t + \tfrac{1}{2}\Delta t\right) = \vec{v}_{cent}\left(t - \tfrac{1}{2}\Delta t\right) + \Delta t\,\frac{\vec{F}^+(t) + \vec{F}^-(t)}{M^+ + M^-} \tag{17.5}$$

The slip rate, that is, the differential velocity between two partial nodes, is distributed between the partial nodes according to their masses:

$$\vec{v}^-\left(t + \tfrac{1}{2}\Delta t\right) = \vec{v}_{cent}\left(t + \tfrac{1}{2}\Delta t\right) - \Delta t\,\frac{M^+ \dot{\vec{s}}\left(t + \tfrac{1}{2}\Delta t\right)}{M^+ + M^-} \tag{17.6}$$

$$\vec{v}^+\left(t + \tfrac{1}{2}\Delta t\right) = \vec{v}_{cent}\left(t + \tfrac{1}{2}\Delta t\right) + \Delta t\,\frac{M^- \dot{\vec{s}}\left(t + \tfrac{1}{2}\Delta t\right)}{M^+ + M^-} \tag{17.7}$$

The displacements at the partial nodes are then

$$\vec{u}^-(t + \Delta t) = \vec{u}^-(t) + \Delta t \ \vec{v}^-(t + \tfrac{1}{2}\Delta t) \tag{17.8}$$

$$\vec{u}^+(t + \Delta t) = \vec{u}^+(t) + \Delta t \ \vec{v}^+(t + \tfrac{1}{2}\Delta t) \tag{17.9}$$

The problem with integration: why the 8-point Gaussian integration does not work
As we explained in Chapter 16, numerical integration is used to compute the restoring-force vector or mass matrix. Because of its accuracy and efficiency, the 8-point Gaussian integration is usually used with the HEX8 element with trilinear shape functions. We also recall that for practical reasons the lumped mass matrix, Eq. (16.84), is usually used instead of the fully integrated mass matrix. However, our numerical tests showed that 8-point Gaussian integration does not produce the correct solution for rupture propagation with the TSN implementation. To explain this behaviour we have to look at the integration in detail.

A nondiagonal mass matrix is a consequence of the properties of the shape functions and locations of integration points. The integration points for 8-point Gaussian integration are located inside an element where all shape functions are nonzero. Therefore, matrix $\tilde{\mathbf{m}}^e$, Eq. (16.48), consists of only nonzero elements and consequently the mass matrix is nondiagonal.

As we briefly mentioned in Chapter 16, we can use other integration schemes. For some applications it may be advantageous to use schemes with lower-order accuracy than what is required, also known as reduced integration. Sometimes, however, reduced integration may lead to solutions polluted by oscillations (also known as hourglass modes, zero-energy modes or spurious zero-energy modes). If the solution is not affected by the oscillations, it may be considered a reasonable solution (e.g., Ottosen and Petersson 1992, Zienkiewicz and Taylor 1989).

We can use, for example, the 8-point Lobatto integration. This integration is accurate only for linear functions (compare with the accuracy of 8-point Gaussian integration). The integration points for 8-point Lobatto integration are located at nodes, where always one shape function equals 1 and all others equal 0. Therefore, the mass matrix computed by 8-point Lobatto integration is naturally diagonal. Moreover, it can be shown that it is the same as the lumped mass matrix. Our numerical tests showed that 8-point Lobatto integration produces a solution close to the reference solution also for rupture propagation with the TSN implementation.

The use of 8-point Gauss integration with the lumped mass matrix is the equivalent of using 8-point Lobatto integration to compute the mass matrix and using 8-point Gaussian integration to compute the restoring force. Therefore, we conjecture that the combination of different integration schemes used for integrating the mass matrix and restoring force is the reason why 8-point Gaussian integration does not produce the correct solution with the TSN implementation.

Intuitively we can expect that the integration scheme may affect the stability of the final scheme. The stability of the HEX8 elements with reduced integration was analyzed by Hughes (2000), who refers to Flanagan and Belytschko (1981). For a 'brick' element

with size h_x in the x-direction, h_y in the y-direction and h_z in the z-direction the stability condition is

$$\Delta t \leq \left(\alpha_{\max} \sqrt{h_x^{-2} + h_y^{-2} + h_z^{-2}} \right)^{-1} \tag{17.10}$$

For a cube element with $h = h_x = h_y = h_z$ the condition simplifies:

$$\Delta t \leq \frac{h}{\sqrt{3}\alpha_{max}} \tag{17.11}$$

Comparing Eqs. (17.11) and (16.82) we see that the time step is smaller if reduced integration is applied.

For completeness, we should explain why 8-point Gaussian integration with the lumped mass matrix works for kinematic sources. In our approach, the kinematic point source is implemented using body forces. Our numerical tests showed that 8-point Gaussian integration with the lumped mass matrix produces large errors and opposite polarization of displacements at the nodes next to nodes at which the force is applied. This error is spatially very localized and strongly vanishes with distance. Moreover, the kinematic sources have time evolution prescribed a priori and therefore this localized error does not affect the source. In the case of the dynamic model the error appears in the neighbourhood of the partial node and reaches its maximum value at nodes next to the partial node. Therefore, the deformation of halfspaces and consequently also computation of forces $\vec{F}^+$ and $\vec{F}^-$ is affected. In the case of the dynamic model the interaction between the radiated wavefield and rupture propagation is crucial. Therefore, the error affects the evolution of the rupture. Consequently, the radiated wavefield is also affected and the error is no longer local.

17.2 Spurious high-frequency oscillations of the slip rate

Despite the superior properties of the TSN method, the slip-rate time histories obtained using the TSN very often contain spurious high-frequency oscillations. We briefly summarize possible reasons leading to these oscillations following Galis *et al.* (2010).

For a given initial stress and material parameters on a fault, it is the friction law that controls initiation, propagation and healing of rupture. First, consider Coulomb friction; that is, a very simple friction law with an instantaneous change of traction from the static to the dynamic value (Fig. 17.1a). The stress is discontinuous at the crack tip. This implies an infinitely large slip rate at the crack tip. The slip-rate value then rapidly decreases with time. The narrow pulse of the slip rate with infinite peak value implies an infinitely broad spectrum and thus also very high frequencies.

Next, consider a linear slip-weakening friction law (Fig. 17.1b). The gradual decrease of stress (during finite time and slip) removes the infinite value of the slip rate at the crack tip. Naturally, the steeper is the decrease of the stress in the friction law, the steeper is the increase of the slip rate and, consequently, the broader is the spectrum of the shear-stress and slip-rate variations generated by the slipping point. The spectrum of the slip rate is
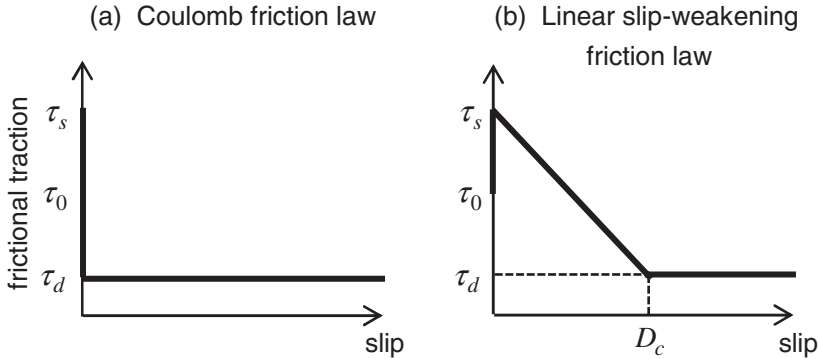
Figure 17.1 Coulomb friction law (a) and linear slip-weakening friction law (b). Here τ_0 is initial traction, τ_s static traction and τ_d dynamic traction.

also discussed by Kaneko *et al.* (2008) and de la Puente *et al.* (2009). Note that in the limiting case of an infinite slope the slip-weakening friction law becomes the Coulomb friction law.

The gradual decrease of the stress at a slipping point implies the existence of a breakdown zone – the spatial zone on the fault plane behind the crack tip where the shear stress decreases from its static to its dynamic value.

Thus, a possibly broad-spectrum slip-rate and stress variations generated by each slipping point as well as the spatial breakdown zone have to be properly discretized in a numerical method in order to avoid the effect of numerical grid dispersion at higher frequencies and to properly capture the stress changes in the breakdown zone.

The wave propagation problems are linear. Therefore, it is relatively easy to correctly treat high frequencies in the discrete model. The effect of numerical grid dispersion may become considerable/visible for wavelengths sampled by less than a certain number of samples. Therefore, the size of the spatial grid spacing determines how accurately high frequencies are propagated by a grid. Moreover, because of the linear character of the wave propagation problem, it is possible to apply a-posteriori filtration to remove the high frequencies as long as the high-frequency content did not affect (due to the accuracy of number representation or not-a-number values) the content at lower frequencies.

In the rupture propagation problems, the effect of numerical grid dispersion may become more dramatic due to nonlinear coupling between the shear stress and slip rate. In the TSN method a slip-rate increment at each time level is calculated from the difference between the trial traction $\vec{T}^{ct}$ and frictional traction at a point of the fault, Eq. (17.4). Whereas the frictional traction itself does not suffer from oscillations (because it is determined by the friction law), $\vec{T}^{ct}$ is not smooth in time, reflecting the presence of high-frequency stress variations inaccurately propagated by the grid. The inaccurately determined slip-rate increment is used in calculation of the slip rate in the next time level – thus causing oscillations of the slip rate, which in turn affects the value of the trial traction.

Thus, for a given friction law (for a given steepness of the stress decrease) and order of approximation in the applied numerical method, it is the size of the spatial grid spacing that determines how accurately high frequencies are propagated by the grid and how large are the high-frequency oscillations of the slip rate. In most practical applications the spatial sampling will probably not be fine enough to prevent visible spurious oscillations in the low-order approximation numerical method.

If the high-frequency content does not affect the development and propagation of rupture, it is possible to apply a-posteriori filtration to remove the oscillations. However, because of the nonlinear character of rupture propagation we cannot, in general, a-priori assume that the high-frequency content would not change the development and propagation of rupture. Therefore, a-posteriori filtration cannot serve as a systematic tool for reducing the oscillations. If the high frequencies affect rupture propagation, then the only possibility is to utilize run-time methods to suppress the high-frequency oscillations. In the next section we discuss three different methods to suppress the oscillations, including a-posteriori filtration.

17.3 Approaches to suppress high-frequency oscillations

17.3.1 Adaptive smoothing

In this section we present an adaptive smoothing algorithm for suppressing/reducing spurious high-frequency oscillations of the slip-rate time histories in the FE–TSN modelling of dynamic rupture with slip-dependent friction laws proposed by Galis *et al.* (2010).

As outlined in Section 17.2, in the TSN method a slip-rate increment at each time level is calculated from the difference between the trial traction $\vec{T}^{ct}$ and frictional traction. The trial traction is not smooth due to the high-frequency stress variations inaccurately propagated by the grid. To suppress or reduce these oscillations we can spatially smooth $\vec{T}^{ct}$. There are different ways to spatially smooth $\vec{T}^{ct}$. In the algorithm proposed by Galis *et al.* (2010) it is possible to control when and how to apply smoothing.

If the smoothing is applied to the entire fault it removes high frequencies also from the rupture front. Consequently, it affects rupture propagation. Therefore, we should apply the smoothing only behind the rupture front. Then the question is, how to identify the rupture front. The best results were obtained with the so-called 9-point threshold criterion, that is, the smoothing is applied when the slip rate is larger than 0 m/s simultaneously at a node and at eight neighboring nodes (assuming a regular mesh of the HEX8 elements).

Once the threshold criterion for the application of smoothing is satisfied, we apply the smoothing. The smoothing is defined as a weighted average of the original $\vec{T}^{ct}$ and Gaussian-filtered $\vec{T}^{ct}$. Let p be the averaging parameter and $0 \leq p \leq 1$. Assume a regular mesh of nodes on the fault plane such that we can refer to the nodes on the fault plane using indices (i, j). Then the smoothed traction at point (i, j) can be defined as

$$\overline{\vec{T}^{ct}}(i, j) \equiv \sum_{k=i-1}^{i+1} \sum_{l=j-1}^{j+1} w_{kl} \vec{T}^{ct}(k, l) \qquad (17.12)$$
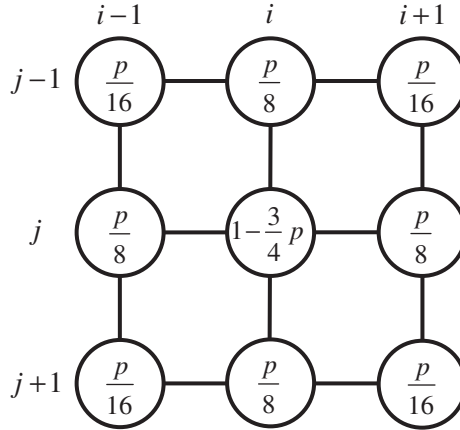
Figure 17.2 Scheme of the effective weighting coefficients in the adaptive smoothing algorithm for calculation of the trial traction at grid position (i, j) on the fault plane. The averaging parameter $p \in \langle 0, 1 \rangle$ and may vary with time. (Modified from Galis *et al.* 2010)

where

$$w \equiv \begin{pmatrix} p/16 & p/8 & p/16 \\ p/8 & 1 - 3p/4 & p/8 \\ p/16 & p/8 & p/16 \end{pmatrix} \tag{17.13}$$

Note that for $p = 0$ and $p = 1$ the matrix of the weight coefficients w becomes

$$w^0 = \begin{pmatrix} 0 & 0 & 0 \\ 0 & 1 & 0 \\ 0 & 0 & 0 \end{pmatrix}, \quad w^1 = \begin{pmatrix} 1/16 & 1/8 & 1/16 \\ 1/8 & 1/4 & 1/8 \\ 1/16 & 1/8 & 1/16 \end{pmatrix} \tag{17.14}$$

respectively. Also note that w^1 is identical to the coefficients of the Gaussian filter. The coefficients are illustrated in Fig. 17.2.

The values of the parameters were calibrated using extensive numerical tests. One of the key requirements was the minimal impact of the smoothing on rupture propagation speed. The other key requirement was, naturally, the efficiency in suppressing high-frequency oscillations. The numerical tests showed that better results were obtained when smoothing was applied gradually behind the rupture front. In looking for the smoothing algorithm and values of parameters we chose a configuration with sub-Rayleigh rupture speed and one discretization. Afterwards, we tested the best algorithm and parameters also for other discretizations and a configuration with super-shear rupture propagation speeds.

Based on the performed numerical tests, we define adaptive smoothing as follows: p varies linearly from 0 for no slip to $p_{\text{max}} = 0.4$ when slip reaches the critical distance. For larger slip p remains constant. The numerical tests demonstrated that adaptive smoothing is capable of significantly reducing high-frequency oscillations without affecting rupture propagation speed. Efficiency of the adaptive smoothing is illustrated in Fig. 17.3.

$$\frac{\tau_s - \tau_0}{\tau_0 - \tau_d} = 1.62$$

$$\frac{\tau_s - \tau_0}{\tau_0 - \tau_d} = 0.5$$
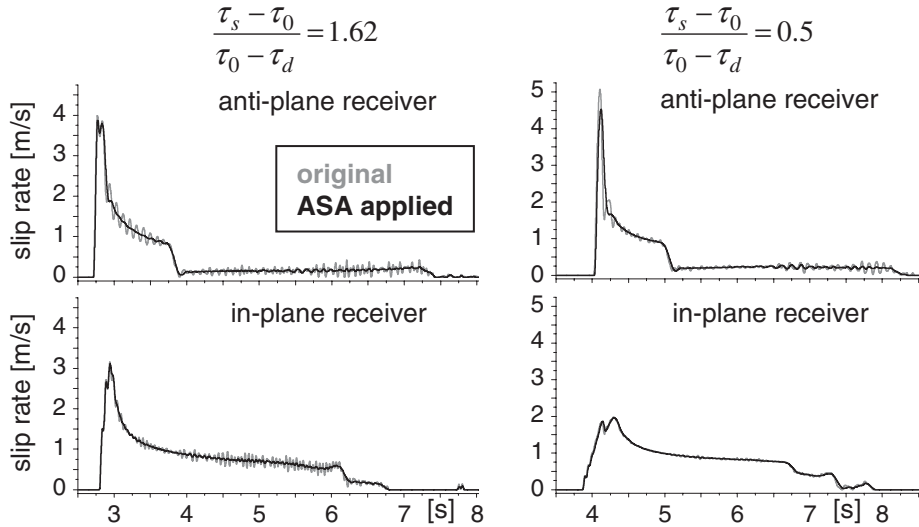
Figure 17.3 Illustration of the efficiency of the adaptive smoothing algorithm (ASA) in suppression of high-frequency oscillations. Here τ_0 is initial traction, τ_s static traction and τ_d dynamic traction. (Modified from Galis *et al*. 2010)

Note that the smoothing is applied only behind the rupture front and gradually in order to minimize the impact on rupture propagation speed. Therefore, the efficiency of suppressing high-frequency oscillations is lower near the rupture front, that is, at the beginning of the slip-rate curves.

Importantly, the adaptive smoothing algorithm is general in the sense that it enables tuning options – modified values of the smoothing parameters. Other values may prove more efficient for some particular configurations. This has to be numerically tested. Other parameter values would be found if the smoothness of the slip-rate curve were a more important criterion than the rupture propagation speed.

Galis *et al*. (2010) assumed a uniform grid on the fault. This allowed using the same weighting coefficients in the averaging formula at all grid points. In principle it should not be a problem to determine weighting coefficients for a nonuniform grid.

17.3.2 Kelvin–Voigt damping

Day (1982), Day and Ely (2002), Day *et al*. (2005) and Dalguer and Day (2007) applied an added artificial Kelvin–Voigt viscosity in their implementations of the TSN method to regularize the numerical solution and suppress the spurious oscillations. Kelvin–Voigt damping may be considered artificial in the sense that it is not intended to simulate realistic attenuation. It is used because it suppresses the high frequencies of the solution that cannot

be accurately computed by the grid. For implementing Kelvin–Voigt damping, Day and his colleagues considered the stress–strain relation in the form

$$\sigma_{ij} = \lambda \frac{\partial u_k}{\partial x_k}\delta_{ij} + \mu \left(\frac{\partial u_i}{\partial x_j} + \frac{\partial u_j}{\partial x_i} \right) + \bar{\eta}\Delta t \left[\lambda \frac{\partial \dot{u}_k}{\partial x_k}\delta_{ij} + \mu \left(\frac{\partial \dot{u}_i}{\partial x_j} + \frac{\partial \dot{u}_j}{\partial x_i} \right) \right] \quad (17.15)$$

where $\bar{\eta}$ is a damping parameter and $\dot{u}$ is the particle velocity. Day (1982), Day and Ely (2002) and Day *et al.* (2005) applied Kelvin–Voigt damping in the DFM (discrete fault model) implementation of TSN, that is, in their FD scheme on the partly-staggered grid. This scheme suffers from the so-called hourglass modes (zero-energy modes). Kelvin–Voigt damping helps in suppressing these modes. Therefore, the damping was applied in the whole grid. For this approach a preferred value of damping is $\bar{\eta} \sim 0.1$ (Day *et al.* 2005). Dalguer and Day (2007) applied Kelvin–Voigt damping in their SGSN method (staggered-grid split-node FD implementation of TSN). The staggered-grid FD scheme does not suffer from hourglass modes. Therefore, artificial damping was applied only to the fault surface to suppress spurious high-frequency oscillations. The corresponding damping parameter $\bar{\eta}_s$ is therefore not equivalent to parameter $\bar{\eta}$. Dalguer and Day numerically examined the sensitivity of the solution with respect to $\bar{\eta}_s$. They found that although their method converges even with no artificial damping applied, the application of damping with proper values of $\bar{\eta}_s$ greatly accelerates the convergence. Artificial damping reduces the rupture time error and spurious oscillations in the slip-rate time histories if a proper value of the damping parameter is used. However, the peak slip-rate misfit increases with damping (having a minimum if no damping is applied). They concluded that the preferred value of the damping parameter is $\bar{\eta}_s \sim 0.3$, but the optimal value is likely problem dependent.

17.3.3 A-posteriori filtration

If spurious high-frequency oscillations appeared in numerical simulations of rupture propagation, were not sufficiently reduced or suppressed by artificial damping or adaptive smoothing, and did not unphysically affect development and propagation of rupture, it is possible and reasonable to apply a-posteriori filtration to the simulated slip-rate time histories. Kristekova *et al.* (2012) quantitatively compared three methods of a-posteriori filtration – low-pass filtering, discrete-wavelet denoising, empirical-mode-decomposition denoising – and adaptive smoothing. They used a set of slip-rate time histories simulated by the 3D FEM–TSN on a planar fault. The simulated slip-rate histories were obtained with a cubic mesh and four discretizations (25 m, 50 m, 100 m and 150 m); see Galis *et al.* (2010). The smooth reference slip-rate time history was obtained by a careful iterative and adjusted denoising of the slip-rate simulated using the finest (technically possible) discretization (25 m). The efficiency of the smoothing methods was evaluated using time–frequency analysis and time–frequency misfit criteria (Kristekova *et al.* 2006, 2009) based on the continuous wavelet transform. The time–frequency tools were capable of clearly indicating distortions caused by spurious oscillations and/or by a-posteriori filtration.

The main conclusion of the investigation by Kristekova *et al.* (2012) is that the safest way to reduce/suppress the oscillations is to apply a method that reduces the oscillations during numerical simulation of rupture propagation, e.g., adaptive smoothing. The adaptive smoothing algorithm does not distort the slip-rate and considerably reduces oscillations. Slight oscillations can remain in the tail. They can be safely removed a posteriori if necessary.

The result of application of low-pass filtering is very sensitive to the choice of corner frequency. Determination of the optimal corner frequency can be problematic even using the Fourier spectrum of the slip-rate time history. It is considerably better to determine it using the time–frequency representation of the slip-rate history. A proper filter should be selected for each slip-rate history separately, taking into account the character of both the slip-rate history and oscillations. Application of the same filter to many different slip-rate time histories can lead to considerable distortions of some of them. Considering all the mentioned aspects, low-pass filtering can give good results but only with carefully determined parameters of the filter.

Discrete-wavelet denoising (e.g., Donoho 1995) can reduce spurious high-frequency oscillations, but if the oscillations overlap with the main slip-rate peak the discrete-wavelet denoising is not as efficient as other methods in the vicinity of the peak and behind it.

Empirical-mode-decomposition denoising (e.g., Flandrin *et al.* 2004) is efficient and sufficiently accurate in the vicinity of the slip-rate peak. Some small oscillations can remain in the tail; if necessary it is easy to suppress them by additional filtering. The main advantage of empirical-mode-decomposition denoising is that it is an adaptive data-driven method and therefore it can be applied automatically (in the simplest version even without determining parameters of denoising). This property makes the method suitable for processing large data sets of different slip-rate time histories.

18

Hybrid finite-difference–finite-element method

The FEM more easily incorporates boundary conditions at the free surface compared to the FDM. This is true for a planar free surface as well as for free-surface topography. Therefore, the FEM is better suited for simulating the traction-free condition and rupture propagation than the FDM. On the other hand, an FD scheme can computationally be considerably more efficient for modelling seismic wave propagation, for instance, if the seismic waves produced by a dynamically rupturing fault are to be propagated away from the fault. It is therefore natural to think of a hybrid combination of the two methods if we want to include both a dynamic earthquake source and wave propagation in a complex heterogeneous medium. Moczo *et al.* (1997) combined the (2,2) conventional displacement FD scheme with the (2,2) standard FE scheme for 2D viscoelastic P-SV modelling of seismic motion in near-surface sedimentary/topographic structures. Ma *et al.* (2004) combined the (2,4) velocity–stress staggered-grid (VS SG) scheme with the (2,2) standard FE scheme for 2D elastic P-SV modelling.

In this chapter we explain the hybrid method developed by Galis *et al.* (2008). This hybrid method combines the (2,2) standard FE scheme with the (2,4) VS SG scheme for 3D viscoelastic modelling.

18.1 Computational domain

As already pointed out, the main idea of the hybrid combination of the two methods is to achieve efficient numerical simulations for important realistic problem configurations. Such configurations may include free-surface topography and material heterogeneity as well as a dynamically rupturing fault. Correspondingly, a computational domain of the hybrid FD–FE method may include one or more FE regions that would cover those parts of the model where the free-surface topography or fault has to be considered. To achieve better efficiency, the FE regions should be as small as possible compared to the FD region, which should cover a major part of the whole computational domain. The computational domain is schematically illustrated in Fig. 18.1. It is crucial that the FE regions causally communicate at each time level with the FD region. The FD–FE communication is explained in detail in the following sections.
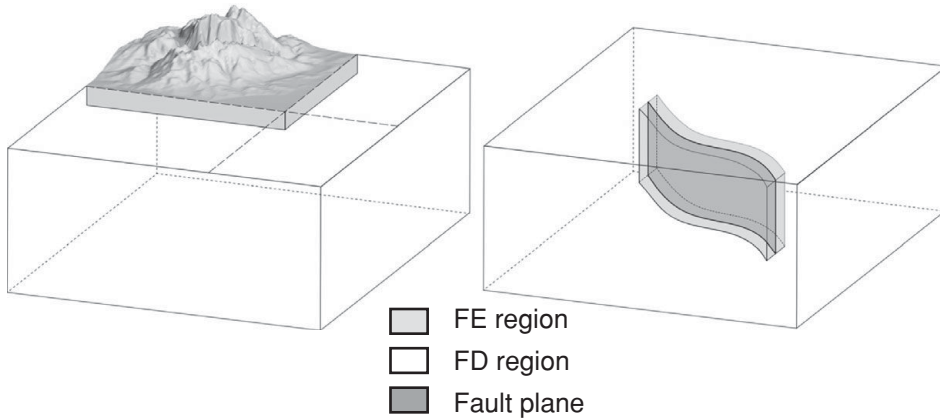
Figure 18.1 Illustration of the computational domain. The FE region can cover the part of the model with free-surface topography (left) or a dynamically rupturing surface (right). The rest of the domain is covered with the FD grid. One computational domain can, in principle, include several FE regions.

18.2 Principle of the FD–FE causal communication

At each time level: (1) the wavefields in the FE region(s) and FD regions are updated independently by the FE and FD schemes, respectively; (2) the FE region(s) and FD region causally communicate (exchange appropriate values) within the FD–FE transition zone. Given the structures of both schemes, the transition zone has to consist of several grid (mesh) surfaces at which the FD and FE regions overlap.

In the FD–FE transition zone the size of the grid spacing in the FE grid is twice as small as that in the FD grid. Away from the transition zone the size of an element can, in principle, vary. The twice-smaller FE grid spacing is algorithmically the most natural option because any other ratio between the FD and FE grid spacings would make the schemes for updating in the transition zone much more complicated and it is likely that it would produce more numerical noise. Intuitively, at a rough estimate, such a choice seems reasonable given the 2nd- and 4th-order approximations of spatial derivatives in the FE and FD schemes, respectively. Strictly speaking, however, the spatial sampling does not simply scale with the approximation order. For example, an increase in the approximation order by two does not mean that a twice-larger grid spacing can be used. This is additionally and independently supported by results obtained by Kristek and Moczo (2006). They indicated by their numerical investigations for the 1D problem that the 4th-order staggered-grid scheme requires denser spatial sampling than that usually used by many users, who consider it approximately twice as coarse as that in the 2nd-order conventional schemes. This indicates that if we apply proper sampling in the FD region, the FE region should be over-sampled. But in many applications this will cause no problems, because the modelling of the free-surface topography or dynamic rupture propagation requires denser spatial sampling compared to that usually used for wave propagation.
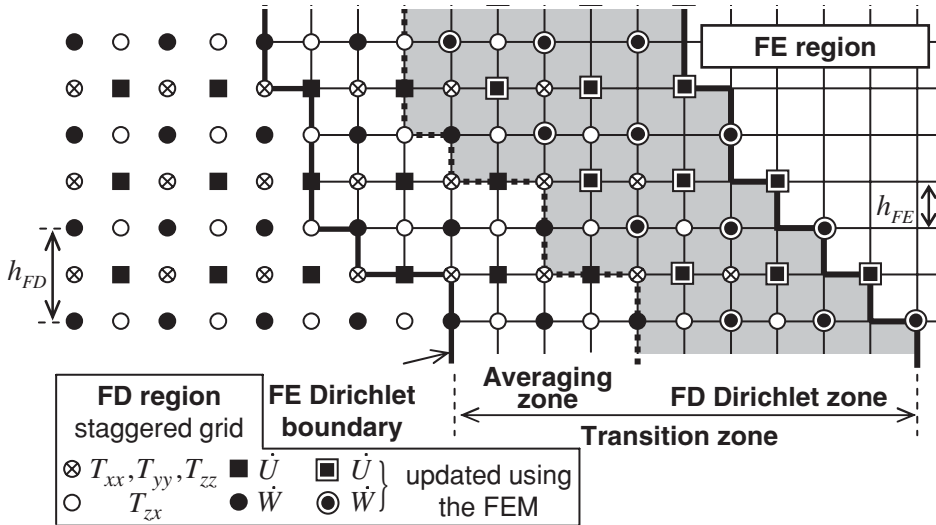
Figure 18.2 Illustration of the FD–FE transition zone used in hybrid modelling for causal FD–FE communication at each time level. For simplicity, only one vertical grid plane is shown. h_{FD} is the spatial grid spacing in the FD grid. h_{FE} is the spatial grid spacing in the uniform part of the FE grid in and near the transition zone; the rest of the FE grid can be nonuniform. Note that no special symbol is used to indicate the positions of the displacement vector in the FE grid. Each intersection of the grid lines in the FE region is a position of all the components of the displacement vector.

18.3 Smooth transition zone with FD–FE averaging

The shape and size of the transition zone are basically determined by the FD schemes for updating the particle-velocity and stress-tensor components. The transition zone is illustrated in Fig. 18.2. The figure shows an example of a vertical cross-section of a particular transition zone. The zone consists of the FE Dirichlet boundary, the FD–FE averaging zone, and the FD Dirichlet zone. It is clear that the FE Dirichlet boundary for the 2nd-order displacement FE scheme consists of a single staircase grid surface that has to go through the grid points of the FD staggered grid. At the same time, a finite-thickness Dirichlet zone is necessary for the 4th-order velocity–stress staggered-grid FD scheme.

Note that causal FD–FE communication is formally possible even without the averaging zone. However, our numerical tests (Galis *et al*. 2008) clearly show that the averaging zone significantly improves results – even a one-grid-spacing thick averaging zone makes a significant difference in the numerical behaviour of the transition zone.

The local thickness and staircase shape of the FD Dirichlet zone are determined by the following requirement: the particle velocity at the FD grid points located at the grid interface between the averaging zone and the FD Dirichlet zone should be calculated using the 4th-order velocity–stress staggered-grid FD scheme for an interior grid point. This is possible if relevant stress-tensor components are available. The FD Dirichlet zone has to include those stress-tensor components. In principle, those stress-tensor components could

be calculated using the FE scheme, but a special algorithm would be necessary because the stresses are not defined at the FE nodes. Therefore, it is algorithmically more efficient to update those stress-tensor components from the particle velocities using the FD scheme. This widens the width of the FD Dirichlet zone.

The algorithm of the FD–FE hybrid method can be summarized in the following steps. For brevity we use U for any displacement component, $\dot{U}$ for any particle-velocity component, and T for any stress-tensor component. Subscripts FD and FE refer to the corresponding grids. The lower-case m denotes a time level.

(1) Displacements $U_{\text{FE}}(m+1)$ are updated at the grid points of the interior FE region (the FE grid points excluding the FE Dirichlet boundary).

(2) Stress-tensor components $T(m)$ are updated at the grid points of the FD region including the stress-tensor grid positions inside the FD Dirichlet zone.

(3) Particle velocities $\dot{U}_{\text{FD}}(m+\frac{1}{2})$ are updated at the grid points of the interior FD region including the dashed line (Fig. 18.2) between the averaging zone and FD Dirichlet zone.

(4) Particle velocities $\dot{U}_{\text{FD}}(m+\frac{1}{2})$ within the FD Dirichlet zone (at the grid points indicated by the double squares and circles in Fig. 18.2) are updated using the FE displacement values at the same grid points:

$$\dot{U}_{\text{FD}}\left(m+\tfrac{1}{2}\right) = \frac{U_{\text{FE}}(m+1) - U_{\text{FE}}(m)}{\Delta t} \tag{18.1}$$

(5) Particle velocities $\dot{U}_{\text{FD}}\left(m+\frac{1}{2}\right)$ in the averaging zone, including the dashed line between the averaging and FD Dirichlet zones, are replaced by values obtained by weighted averaging of the FE particle velocities and $\dot{U}_{\text{FD}}\left(m+\frac{1}{2}\right)$:

$$\dot{U}_{\text{FD}}^{w}\left(m+\tfrac{1}{2}\right) = w\frac{U_{\text{FE}}(m+1) - U_{\text{FE}}(m)}{\Delta t} + (1-w)\,\dot{U}_{\text{FD}}\left(m+\tfrac{1}{2}\right) \tag{18.2}$$

where $w = 1$ at the dashed line between the averaging and FD Dirichlet zones, and $w = 0$ at the FE Dirichlet boundary. The weighting coefficient linearly changes between the two values over the averaging zone.

(6) Displacements $U_{\text{FE}}(m+1)$ in the averaging zone, including the dashed line between the averaging and FD Dirichlet zones, are replaced by averaged values $U_{\text{FE}}^{w}(m+1)$:

$$\begin{aligned}
\dot{U}_{\text{FE}}^{w}\left(m+\tfrac{1}{2}\right) &= w\,\dot{U}_{\text{FE}}\left(m+\tfrac{1}{2}\right) + (1-w)\,\dot{U}_{\text{FD}}\left(m+\tfrac{1}{2}\right) \\
U_{\text{FE}}^{w}(m+1) &= U_{\text{FE}}(m) + \Delta t\,\dot{U}_{\text{FE}}\left(m+\tfrac{1}{2}\right)
\end{aligned} \tag{18.3}$$

(7) Displacements $U_{\text{FE}}(m+1)$ are updated at the FE Dirichlet boundary using the FE displacements and FD particle velocities at the same grid points:

$$U_{\text{FE}}(m+1) = U_{\text{FE}}(m) + \Delta t\,\dot{U}_{\text{FD}}\left(m+\tfrac{1}{2}\right) \tag{18.4}$$

Recall that the FE Dirichlet boundary consists of a single staircase grid surface that goes through the grid points of the FD staggered grid. A grid position of the FD staggered grid is the position of either just one particle-velocity component or one shear stress-tensor component or three normal stress-tensor components or no field variable. The symbolic Eqs. (18.3) and (18.4) require all the particle-velocity components at a given grid position. Consequently, an interpolation of the missing particle-velocity components is necessary. We refer to Fig. 4 and Eqs. (33)–(41) in the article by Galis *et al.* (2008) for the possible spatial configurations of the grid positions at which interpolations are necessary and the interpolation formulas.

Galis *et al.* (2008) performed extensive numerical tests of the behaviour of the FD–FE transition zone. They found no evidence of instabilities in practically sufficiently long time windows. The averaging zone is crucial for accuracy. The FD–FE transition zone without the averaging zone produces slight but evident numerical noise.

They also found that simulating dynamic rupture needs a sufficient distance (at least nine FE grid spacings) between the FD–FE transition zone and the fault. For smaller distances the FD–FE transition zone slightly affects the rupture propagation. The FD–FE transition zone is stable and provides sufficiently accurate results also in the case of a material interface intersecting the transition zone.

Based on extensive numerical tests, Galis *et al.* (2008) concluded that the hybrid FD–FE method is stable, converging and sufficiently accurate.

18.4 Illustrative numerical simulations using hybrid FD–FE method

Galis *et al.* (2008) illustrated the hybrid FD–FE method by simulating two hypothetical earthquakes near Grenoble, France. One was the thrust event beneath Grenoble, the other was a strike-slip event in the Belledonne Massif. They were inspired by a previous study by Cotton *et al.* (1998), who considered point sources. Galis *et al.* (2008) used finite sources with dynamic rupture propagation with a linear-slip weakening friction law. A continuous increase of the static and dynamic coefficients of friction was used to restrict rupture to an area approximately 4 km × 2 km in order to produce an $M_w = 5.3$ event. The parameters inside this area were constant, except in the initiation zone. Even though both faults were planar, application of the hybrid method was advantageous due to the higher accuracy of the FEM for dynamic rupture propagation.

The structure of the sediment–bedrock interface together with the positions of the faults for both events is shown in Fig. 18.3. The horizontal fault is located at a depth of 5 km. The top of the vertical fault is at a depth of approximately 1.5 km and the ruptured area reaches a depth of approximately 3.5 km. The fault is located in the FE box and the rest of the computational domain is covered by the FD grid. Because the FE box is relatively small in comparison to the size of the whole domain, the hybrid FD–FE simulations are significantly more efficient compared to simulations in which only the FE modelling is applied to the whole domain. The simulations are accurate up to approximately 7.6 Hz in the bedrock and up to approximately 0.7 Hz near the free surface in the sediments.
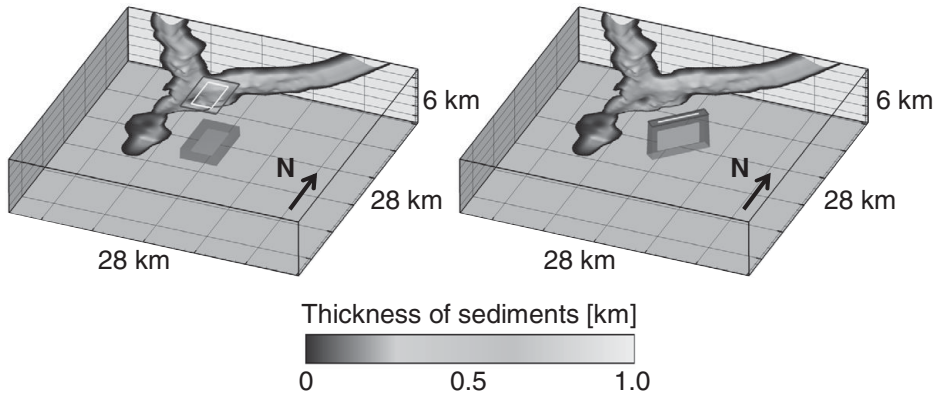
Figure 18.3 The structure of the sediment–bedrock interface together with the positions of the faults (light grey rectangles) for both considered events. The greyscale indicates the sediment thickness. For both events the fault is located in the FE box (dark grey box) and the rest of the computational domain is covered by the FD grid. Projections of the fault and FE box onto the free surface are also indicated. (Modified from Galis *et al*. 2008)

The results of the simulations of the two events are illustrated in Fig. 18.4 and Fig. 18.5. Snapshots indicate complex wavefields inside the sediments due to the geometrically complicated sediment–bedrock interface. At the same time, the space–time variation of the motion in the valley due to the thrust event considerably differs from that due to the strike-slip event. Clearly, this is a consequence of different geometrical configurations of the valley structure and the rupturing fault. To better illustrate the possibility of the hybrid method, Galis *et al*. (2008) also simulated a strike-slip event with a fault dipping 85° NE. The small change in the dipping angle was chosen because such a small change would be a major problem for the staggered-grid FD scheme on a uniform Cartesian grid. Figure 18.6 illustrates the differences in the maxima of the absolute values of the vertical component of the particle acceleration at the free surface.

18.5 Potential improvement of the hybrid FD–FE method

Galis *et al*. (2008) used hexahedral elements in the whole FE mesh. Compared to tetrahedral elements, usually a smaller number of hexahedral elements is needed to cover the same volume. Therefore, the hexahedral elements are usually considered as more efficient than the tetrahedral elements. On the other hand, it is much more complicated to generate a mesh from hexahedral than tetrahedral elements for complex configurations. Therefore, from a practical point of view, the choice of tetrahedral elements in the FE mesh may be more appropriate for structurally complex configurations.

Moczo *et al*. (1997) used triangular elements inside the FE mesh and square elements inside the overlapping FD–FE zone to obtain stable and accurate results in their 2D hybrid FD–FE method. We may expect similar limitations in the 3D case as well – cubic elements
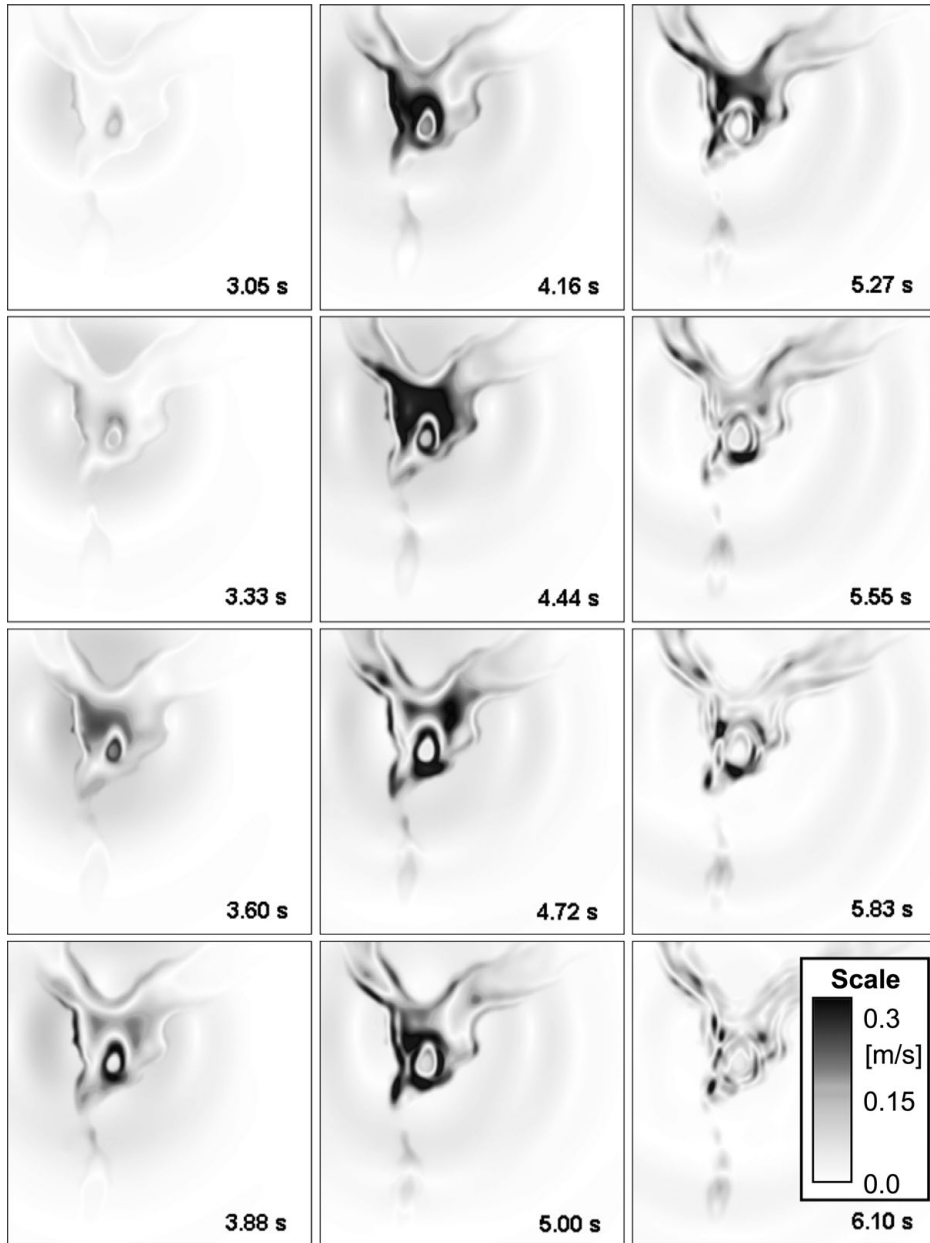
Figure 18.4 Sequence of snapshots of the absolute value of the horizontal component of particle velocity at the free surface for a simulated thrust earthquake beneath the Grenoble valley. (Modified from Galis *et al*. 2008)
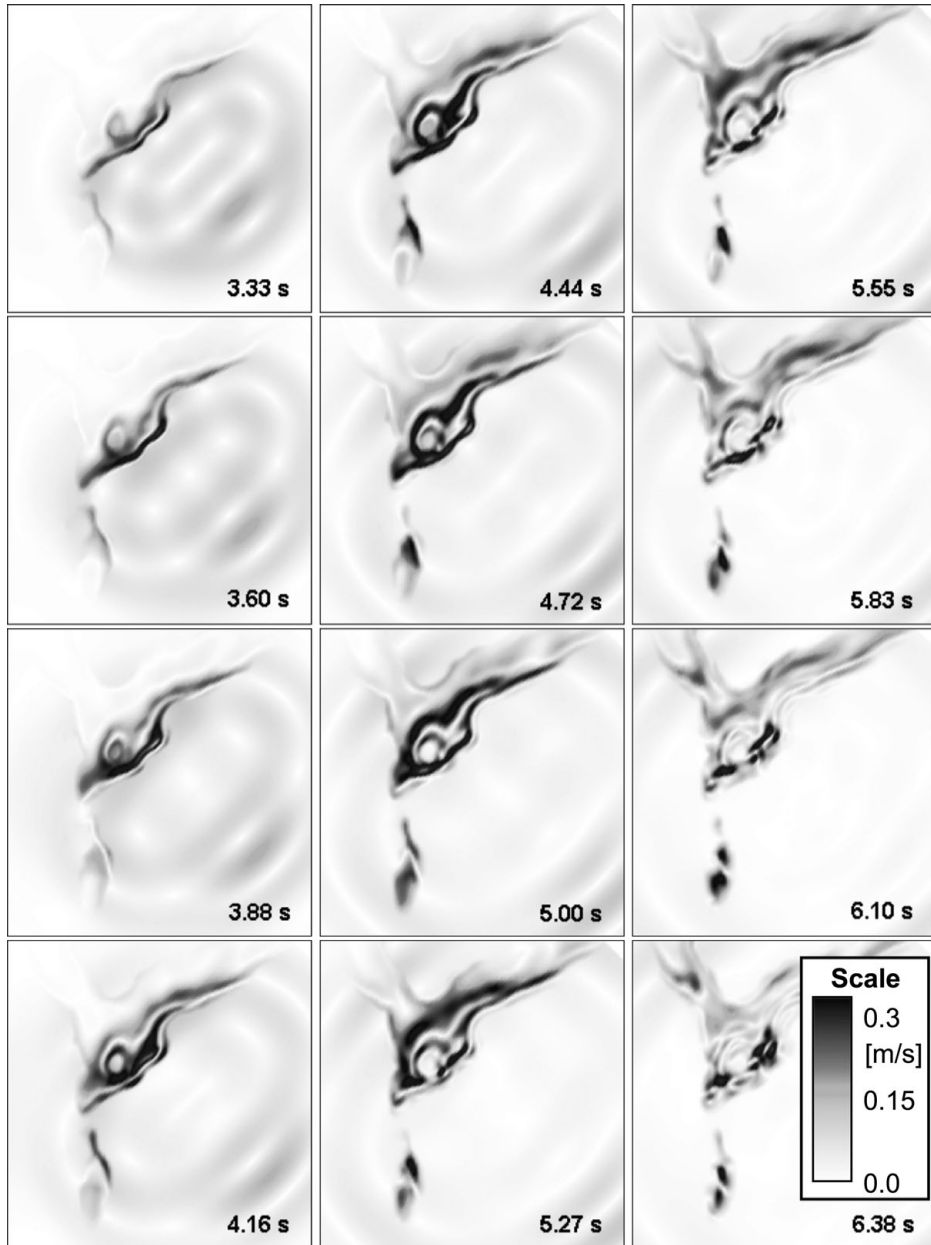
Figure 18.5 Sequence of snapshots of the absolute value of the horizontal component of particle velocity at the free surface for a simulated strike-slip earthquake near the Grenoble valley. (Modified from Galis *et al*. 2008)
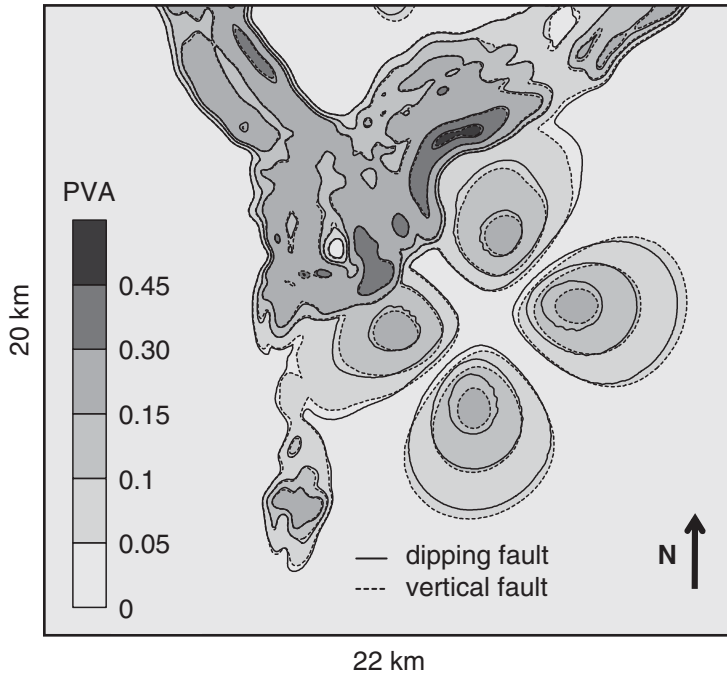
Figure 18.6 Spatial distribution of the maximum of the absolute value of the vertical component of acceleration (PVA) at the free surface for vertical- and dipping-fault events. (Modified from Galis *et al.* 2008)

might be necessary inside the FD–FE transition zone in order to get stable and accurate results. In contrast with 2D, in 3D it is not possible to directly connect the tetrahedral and hexahedral elements due to the requirement of continuity of displacement across elements. A widely used approach in FE modelling in engineering and physics is the use of a transition layer of pyramidal elements between the hexahedral elements in the transition zone and the tetrahedral elements inside the FE region (e.g., Zgainski *et al.* 1996, Owen and Saigal 2001, Bluck and Walker 2008). Because the FD–FE transition zone remains the same as in the case of a purely hexahedral mesh, the inclusion of a transition layer of pyramidal elements should not affect the numerical behaviour of the FD–FE transition zone itself. Careful tests would be necessary to check the behaviour of the transition from hexahedral to tetrahedral elements in applications to seismic wave propagation.

Although tetrahedral elements are considered less efficient than hexahedral elements, the use of tetrahedral elements inside the FE region may yield a more efficient FD–FE hybrid method because the FE region covered by tetrahedral elements may be smaller for complex configurations than in the case of a purely hexahedral mesh.

Part IV

Finite-difference modelling of seismic motion
at real sites

19

Modelling of earthquake motion: Mygdonian basin

19.1 Modelling of earthquake motion and real earthquakes by the FDM

Methodological simplicity, easy implementation, computational efficiency and sufficient accuracy are the primary reasons why the FDM has been applied in numerical modelling of real earthquakes and for earthquake motion prediction. Each of the four named aspects or characteristics of FD modelling is, in fact, a very relative concept and should be classified with sufficient care, especially the aspect of accuracy, which certainly is not a default property of any FD scheme. The historic truth, however, is that the four aspects led seismologists to apply FD modelling in relatively complex structure–wavefield configurations. The FDM has probably been the dominant numerical method in earthquake ground motion modelling. We believe that it has the potential to be one of the key methods also in the future.

Let us mention first the pioneering 2D numerical-modelling studies of earthquake ground motion using the FDM – Boore *et al*. (1971) and Boore (1972a). The significance of the method for 3D modelling of earthquakes, earthquake ground motion and site effects is documented by numerous studies and articles: e.g., Frankel and Vidale (1992), Frankel (1993), Graves (1993, 1998), Yomogida and Etgen (1993), Olsen (1994, 2000), Olsen *et al*. (1995a,b, 1997, 2003, 2006, 2008), Olsen and Archuleta (1996), Pitarka *et al*. (1997, 1998, 2004), Graves *et al*. (1998, 2008), Sato *et al*. (1998, 1999), Wald and Graves (1998), Shapiro *et al*. (2000), Peyrat *et al*. (2001), Harris *et al*. (2002), Aochi and Madariaga (2003), Liu *et al*. (2006), Aagaard *et al*. (2008a,b), Harmsen *et al*. (2008), Lee *et al*. (2008a), Frankel *et al*. (2009), Fukuyama *et al*. (2009), Pulido and Dalguer (2009), Wang *et al*. (2009), Bielak *et al*. (2010), Chaljub *et al*. (2010), Chavez *et al*. (2010, 2011), Ely *et al*. (2010), Graves and Pitarka (2010), Hartzell *et al*. (2010), Iwaki and Iwata (2010), Kim *et al*. (2010), Macpherson *et al*. (2010), Mai *et al*. (2010), Mena *et al*. (2010), Peyrat and Favreau (2010), Skarlatoudis *et al*. (2010), Aochi *et al*. (2011), Graves and Aagaard (2011), Roten *et al*. (2011), Day *et al*. (2012), Nakamura *et al*. (2012), Imperatori and Mai (2013), Maeda *et al*. (2013).

Some of the listed 3D FD studies had a major impact on earthquake ground motion analysis and modelling. As this book is mainly about the methodology of FD modelling, it is fair to say that not all the applied schemes and codes had state-of-the-art methodology for reaching maximum possible accuracy implemented at the time of application. Moreover,

not all FD schemes had been sufficiently verified and analyzed for accuracy before they were applied.

Verification In general, the verification of a numerical method may be defined as the demonstration of the consistency of the numerical method with the original mathematical-physical problem defined by the controlling equation, constitutive law, and initial and boundary conditions. Quantitative analysis of accuracy should be part of the verification. Once the method has been verified and analyzed for accuracy it should be confronted with observations – it should be validated.

Validation In general, the validation may be defined as the demonstration of the capability of the theoretical model (i.e., the mathematical-physical model and its numerical approximation) to predict/reproduce observations.

Strictly speaking, the verification is easier than the validation. The verification itself, however, is not as easy as many would expect. This is clear from the SCEC (Southern California Earthquake Center) code comparative exercise (Day *et al.* 2003 and also Bielak *et al.* 2010) as well as from the E2VP (Euroseistest Verification and Validation Project).

If in validation 'the observations' mean seismic records (or full seismic waveforms) in the finite-frequency range up to several Hz, then the validation is still a major challenge for the future. Having in mind deterministic and probabilistic seismic hazard analysis, the goal and meaning of the validation can be defined in a (relatively) narrower, weaker sense in order to validate the tested methods for practical application.

19.2 Mygdonian basin near Thessaloniki, Greece

19.2.1 Why the Mygdonian basin? – the E2VP

The first numerical simulations of site effects appeared in the late sixties (1D) and seventies (2D: e.g., FE, FD, boundary-element, Aki-Larner methods), together with the first instrumental estimates through site-to-reference spectral ratios. This immediately initiated a debate on whether (a) numerical simulations were reliable and (b) site effects were robust enough (i.e., repeatable within an acceptable variability range) from one event to the other. In order to answer these questions, the first 'blind test' was organized in the late eighties for two sites, Turkey Flat (Parkfield area, central California) and the Ashigara valley (Kanagawa Prefecture, south-west of Tokyo, Japan) to investigate the ability of numerical simulations to predict the actually observed characteristics of ground motion amplification. The conjunction of several factors, i.e., significant local and regional earthquake activity, a typical sedimentary basin, the occurrence of the destructive Stivos earthquake (M_w 6.5, June 20, 1978, 23:03 local time; the largest earthquake near Thessaloniki since 1932), and the feedback from the Turkey Flat and Ashigara valley experiments, caused a number of Greek and European scientists led by Kyriazis Pitilakis and Pierre-Yves Bard to promote

the idea of establishing a test site in the Mygdonian basin for experimental and theoretical investigations of site effects. Their efforts were finally successful and, since starting in 1994, the Mygdonian basin has become the object of focused research in many international and Greek projects (e.g., EUROSEIS-TEST, EUROSEIS-MOD, EUROSEIS-RISK, ISMOD, ITSAK-GR, among many others; see http://euroseisdb.civil.auth.gr). In 2008, a new project funded by CEA (Commissariat à l'énergie atomique et aux énergies alternatives, Cadarache, France) and ILL (Institut Laue Langevin, Grenoble, France) was launched under the super-vision of Fabrice Hollender, in close cooperation with ISTerre (Institut des Sciences de la Terre, Joseph Fourier University, Grenoble, France; Pierre-Yves Bard and Emmanuel Chaljub), AUTH (Aristotle University of Thessaloniki, Greece; Kyriazis Pitilakis and Maria Manakou) and ITSAK (Institute of Engineering Seismology and Earthquake Engineering, Thessaloniki, Greece; Nikolaos Theodoulidis and Alexandros Savvaidis). The objective of this Euroseistest Verification and Validation Project (E2VP) was to evaluate the accuracy and reliability of the existing methods for numerical modelling/prediction of earthquake ground motion at real sites. A major effort was focused on 3D linear viscoelastic modelling, another on 2D nonlinear modelling. The 3D linear viscoelastic modelling included both verification and validation components. Numerical teams from Europe, the USA, Japan and China were invited to participate. From the original 18 teams intending to participate, eight teams contributed to the 3D modelling over the whole duration and four teams were able to reach a very satisfactory level of agreement for the most complex 3D viscoelastic models (one team applied its FD scheme; one team, a Fourier pseudo-spectral scheme; and two teams, independent implementations of the spectral-element method). Surprisingly, the balance between the original intentions and competitive results is very similar to that of the ESG (Effects of Surface Geology) 2006 Grenoble valley comparative exercise (Chaljub *et al.* 2010). Note that in E2VP one team using the discontinuous Galerkin method was able to reach very good agreement with the four teams in the purely elastic case. Another team, using an arbitrary high order derivative–discontinuous Galerkin method, and capable of joining the four teams, retired for a non-scientific reason.

19.2.2 The realistic model and implied challenges

The Mygdonian basin, an elongated tectonic graben located approximately 30 km ENE of the city of Thessaloniki (Fig. 19.1), is one of the major threats for the city, as witnessed by the 1978 Stivos earthquake, which occurred on one of the fault branches shaping the graben. A realistic 3D seismic model of the Mygdonian sedimentary basin has been developed with more than a decade of focused seismological, geophysical and geotechnical investigations by Greek seismologists and their international collaborators (e.g., Raptakis *et al.* 1998, 2000, 2005; Pitilakis *et al.* 1999, 2011, 2013; Chávez-García *et al.* 2000, Makra *et al.* 2001, 2005; Manakou 2007; Manakou *et al.* 2007, 2010). Two variant 3D viscoelastic models were adopted for E2VP (Hollender *et al.* 2010). The geometry of the basin is indicated in Fig. 19.2, the material parameters in Table 19.1.
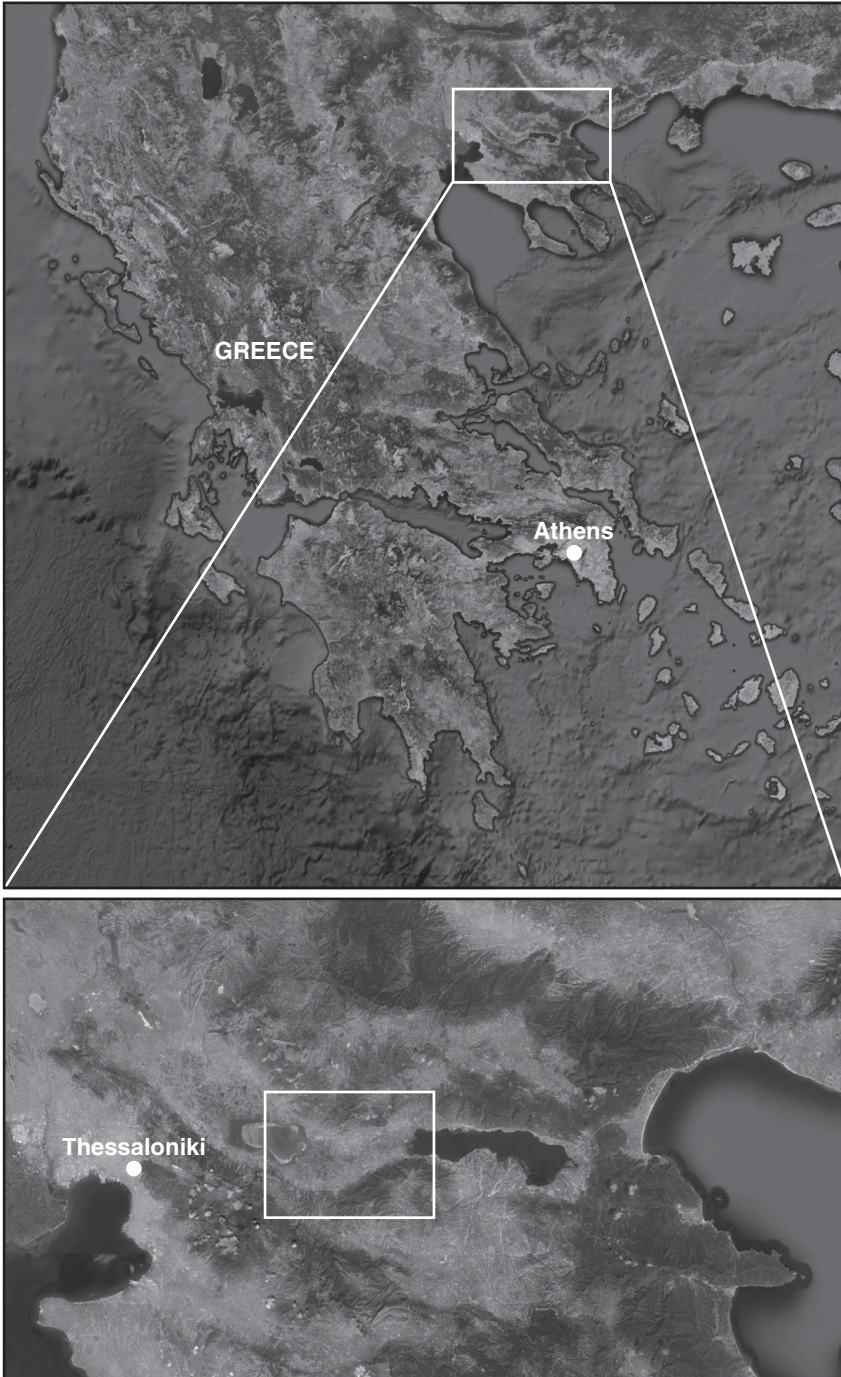
Figure 19.1 Location of the Mygdonian basin near the city of Thessaloniki, Greece.

Table 19.1 *Material parameters of two variants of the Mygdonian basin model in E2VP*

Layer	3D model with homogeneous layers				3D model with constant-gradient layers				Q_κ
	V_S	V_P	ρ	Q_S	V_S	V_P	ρ	Q_S	
	(m/s)	(m/s)	(kg/m^3)		(m/s)	(m/s)	(kg/m^3)		
1	200	1500	2100	20	200-250	1500-1600	2100	20-25	∞
2	350	1800	2200	35	250-500	1600-2200	2100-2130	25-50	∞
3	650	2500	2200	65	500-900	2200-2800	2130-2250	50-90	∞
Bedrock	2600	4500	2600	260	2600	4500	2600	260	∞
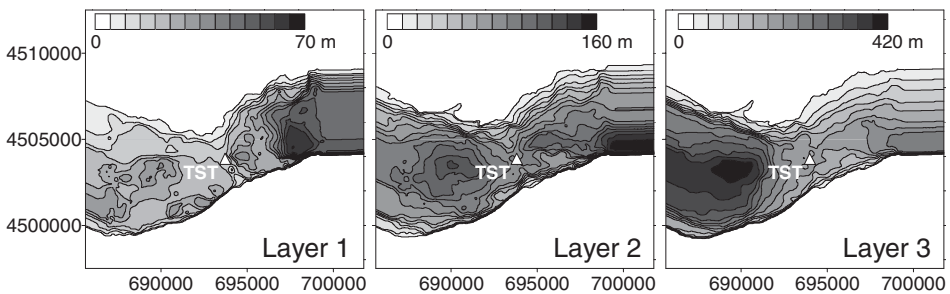
Figure 19.2 Geometry of a 3D model of the Mygdonian basin. Left: interface between the uppermost and middle sedimentary layers; middle: interface between the middle and bottom sedimentary layers; right: interface between the bottom sedimentary layer and bedrock. TST is the abbreviation for the location of a local seismic station.

The model with homogeneous sediment layers can be characterized by

- complicated geometry of the internal interfaces in sediments and the sediment–bedrock interface,
- relatively low V_S in layer 1,
- large V_S contrast between sediments and bedrock ranging from 4 to 13,
- large V_P / V_S in layer 1 (7.5) and layer 2 (>5).

These characteristics indicate that the numerical modelling of seismic motion is far from trivial, especially as modelling was considered for frequencies up to 4 Hz. The model with constant-gradient layers is free of (zero-order) discontinuities of material parameters themselves inside the sediments – only the first spatial derivatives of the material parameters are discontinuous at the interfaces between layers. The absence of zero-order discontinuities makes the gradient model easier for numerical modelling of wave propagation. Because exact solutions for the two variant models do not exist, it is reasonable to verify the capability of a numerical-modelling method using simplified (canonical) models – prior

Table 19.2 *Parameters of the elastic models Can2 and Can3. H denotes thickness.*

	Can2			Can3		
H	V_S	V_P	ρ	V_S	V_P	ρ
(m)	(m/s)	(m/s)	(kg/m³)	(m/s)	(m/s)	(kg/m³)
17.3	200	1500	2100	200-250	1500-1600	2100
72.5	350	1800	2200	250-500	1600-2200	2100-2130
115.6	650	2500	2200	500-900	2200-2800	2130-2250
inf.	2600	4500	2600	2600	4500	2600
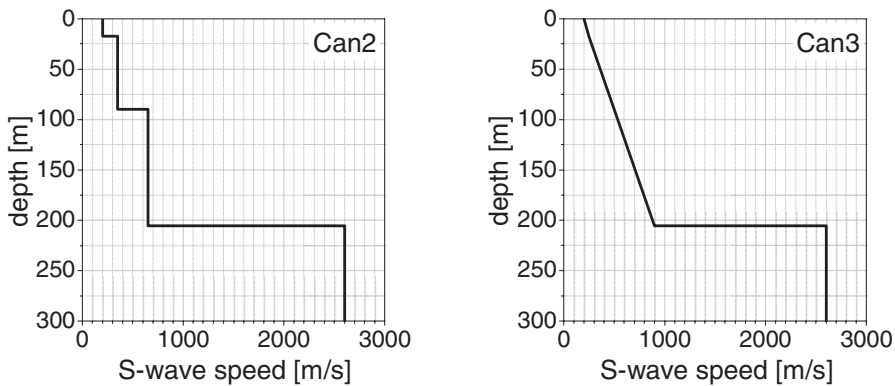
Figure 19.3 S-wave speed as a function of depth. Left: model Can2; right: model Can3.

to the numerical simulation for the available realistic complex models. The canonical models should enable testing of the method for crucial aspects associated with the realistic models.

19.2.3 Comparative modelling for stringent canonical models

Six canonical models, Can0 – Can5, were designed for testing in E2VP, which can also be used for testing new numerical schemes in difficult conditions. Complete descriptions are available at www.sismowine.org. Here we focus on Can2 – Can4.

Can2 – 1D structure consisting of three horizontal homogeneous elastic isotropic layers over a halfspace, 3D wavefield generated by a single vertical force at the free surface and a point double-couple source at 3 km depth in the halfspace. The model represents the vertical profile beneath the TST seismic station in the Mygdonian basin. Table 19.2 shows the parameters of the model, the V_S profile is illustrated in Fig. 19.3 (left). The numerical simulations are performed for frequencies up to 4 Hz.

The right-handed Cartesian coordinate system is considered with x positive north, y positive east, z positive downward. The single vertical force $\vec{f} = (0, 0, s)$ (positive downward) at the free surface is at the origin of the coordinate system $(0, 0, 0)$. The force time history is $s(t) = 5 \cdot 10^{11} \, D(t)$ where $D(t)$ is a band-pass filtered Dirac delta function. The point double-couple (DC) acts at $(0, 0, 3000)$ m, strike is $22.5°$, dip $90°$, rake $0°$, scalar seismic moment 10^{18} N m, and the moment time history is the time integral of $D(t)$.

Figure 19.4 shows the vertical component of the particle velocity at a receiver (2828.4, 2828.4, 0) m at the free surface at the xy grid diagonal at a distance of 4000 m. Note that the wavelengths at 1 and 4 Hz in the uppermost layer with $V_S = 200$ m/s are 200 and 50 m, respectively. Given the vertical point force at the surface, strong surface Rayleigh waves (consisting mainly of the fundamental and first higher modes) are developed along the xy grid diagonal. In the four panels we show four different FD solutions obtained by the (2,4) velocity–stress staggered-grid scheme using grid spacing $h = 5$ m. The solutions differ from each other by the effective grid elastic moduli and density (see Section 9.1), that is, by discrete material representation:

LOC – local (point) values of the elastic moduli and density,

ARI – volume arithmetic averages of the elastic moduli and volume arithmetic averages of the density evaluated using numerical integration over a grid cell centred at the grid position of the elastic modulus or density,

HAR – volume harmonic averages of the elastic moduli and volume arithmetic averages of density evaluated using numerical integration over a grid cell centred at the grid position of the elastic modulus or density; see Subsection 9.2.5,

ORT – volume effective coefficients corresponding to the orthorhombic averaged medium; see Subsection 9.2.3.

The **LOC**, **ARI** and **HAR** types of material representation are isotropic whereas the **ORT** type is anisotropic. Note a very important aspect of the FD modelling: the material interfaces do not coincide with a grid plane in the two applied grids. In other words, the material interfaces go through the interior of the grid cells. The geometry of the interfaces is accounted for solely by evaluating effective grid material parameters.

The FD seismogram in each panel is shown together with the reference solution obtained by Emmanuel Chaljub using the DWN codes – Axitra (Bouchon 1981, Coutant 1989) for the deep DC source and a code developed by Yoshiaki Hisada (Hisada 1994, 1995) for the surface force. The level of agreement between the FD and DWN seismograms in phase and amplitude is quantified using the time–frequency phase and envelope goodness-of-fit (GOF) criteria, respectively; see Appendix. We use here the positive-valued goodness-of-fit instead of the time–frequency misfit criteria due to restriction to the greyscale figure.

As expected (based on our numerical experience), the **LOC** material representation yields the worst result – the smallest GOF values, especially for Rayleigh waves. The **ARI** representation yields a very good result. This is because the material interfaces are horizontal and the dominant wave group, the Rayleigh waves, propagates in the horizontal direction. A more detailed examination of the body-wave group (in the time window
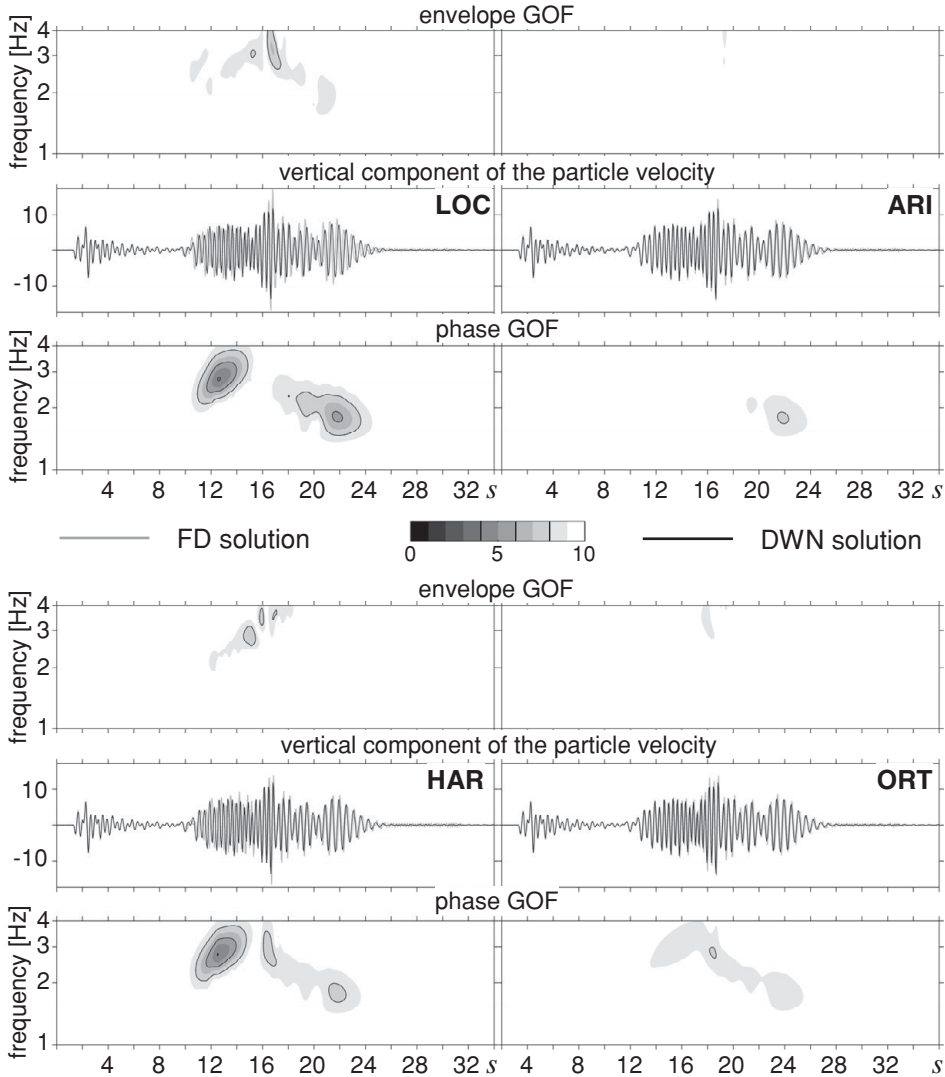
Figure 19.4 FD (grey) and DWN (black) seismograms for Can2. The FD seismograms are obtained for $h = 5$ m using four different material representations – **LOC**, **ARI**, **HAR** and **ORT**. The level of agreement between the FD and DWN seismograms in phase and amplitude is quantified using the time–frequency phase and envelope goodness-of-fit criteria, respectively. Phase and envelope GOF = 10 mean that the compared seismograms are the same.

of 1–9 s) using the locally normalized time–frequency misfit would show that **ARI** is worse than **HAR** and **ORT**. This is because the body-wave group is generated by the deep DC source in the halfspace. Note that the **ARI** representation yields considerably worse results (compared to **HAR** and **ORT**) as soon as waves do not propagate along an interface. Let
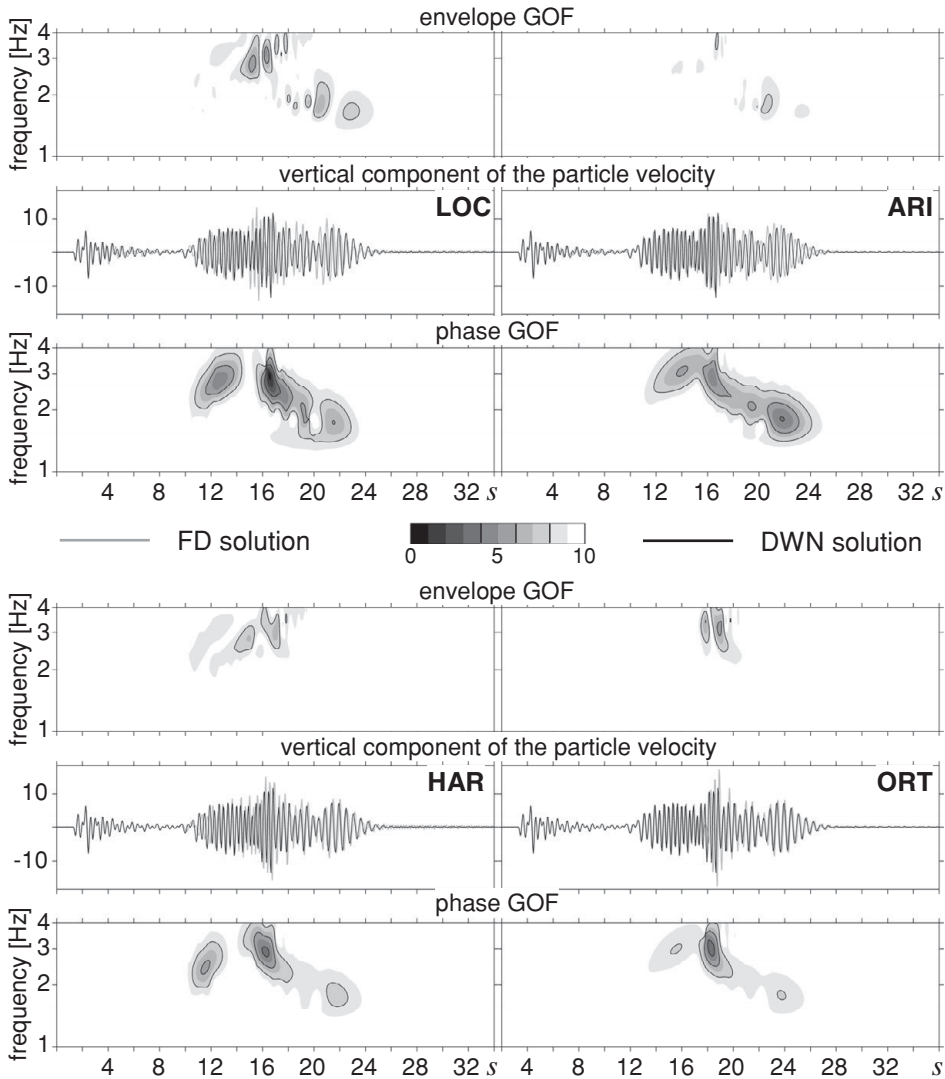
Figure 19.5 The same as Fig. 19.4 but for $h = 10$ m.

us also note that in the case of a model consisting of horizontal planar layers one can use, for instance, the very accurate DWN method instead of the FD method. The **ORT** representation yields better results than the **HAR** does.

Figure 19.5 is analogous to Fig. 19.4. It shows FD solutions obtained with the coarser spatial grid, $h = 10$ m. The level of agreement between the FD and DWN seismograms is considerably smaller due to coarse spatial discretization, especially at higher frequencies. Note that $h = 10$ m corresponds to five grid spacings per wavelength at 4 Hz in a medium
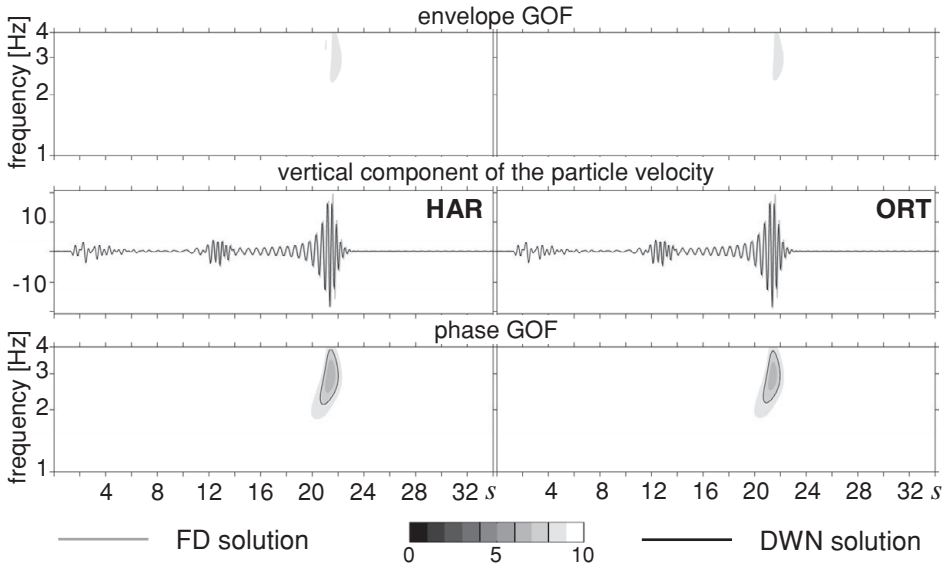
Figure 19.6 Seismograms and GOFs for Can3: as for Fig. 19.4 but only for the **HAR** and **ORT** representations.

with an S-wave speed of 200 m. The results for $h = 5$ m and $h = 10$ m strongly indicate that it is necessary to perform numerical simulations for at least two different discretizations, for example, for two sizes of the spatial grid spacing, in order to assess the sensitivity of the simulated motion with respect to the computational parameters.

Can3 – modification of Can2: vertical constant gradients of material parameters in the layers. Table 19.2 shows parameters of the model, the V_S profile is illustrated in Fig. 19.3 (right). The numerical simulations are performed for frequencies up to 4 Hz. Figure 19.6 shows a simple comparison of the FD solutions for $h = 5$ m and the material representations **HAR** and **ORT** with the DWN solution obtained by Emmanuel Chaljub. It is clear that the difference between the **HAR** and **ORT** representations is smaller than in Can2. This is because Can3 does not have zero-order material interfaces in the sediments.

Can4 – 2D structure representing a simplified NS profile of the Mygdonian basin going through the TST seismic station; 3D wavefield generated by the point double-couple source (as in Can2 and Can3) at a depth of 3000 m, halfway between the northern and southern margins of the basin. The geometry of the structure is shown in Fig. 19.7, the material parameters are the same as in Can2. The wedge-type northern margin of the basin makes the modelling very difficult. It is not obvious how to determine what is a sufficient discretization and how to effectively represent the complex heterogeneity at the basin edge. Because there is no exact solution for the model, Florent De Martin developed a spectral-element mesh that follows all material interfaces, and

North | 1.5 km | 3.5 km | South

72.5 m ⊢17.3 m

115.6 m

simplified geometry
of the basin edge

$z = H \cdot Min \left\{ 1, \dfrac{2.5 - x}{1.5} \right\}$

$x \in \left[-2.5, 2.5 \right]$

the layering is the
same as in the Can2
and Can3 models
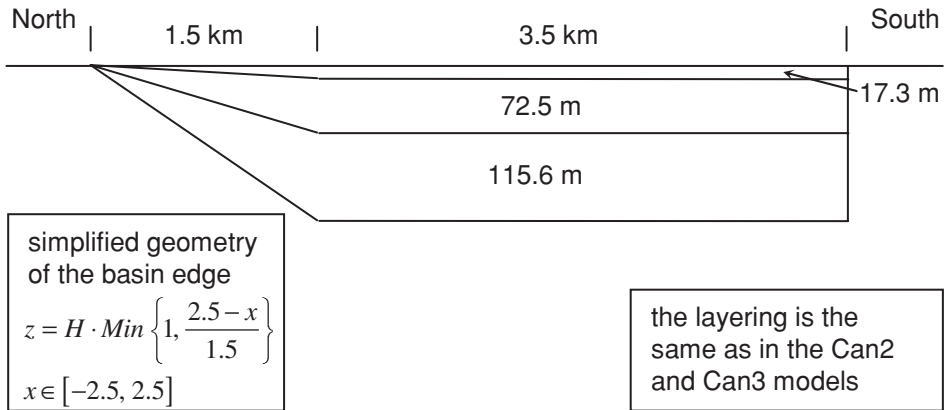
Figure 19.7 Geometry of the 2D structure in the Can4 problem.

the minimum size of the element at the northern edge is only 0.5 m. Such a fine discretization is necessary for SEM in order to reach sufficient accuracy in the wedge-type northern margin. This is because one has to 'follow' the discontinuities in an SEM in order to get sufficient accuracy. The spectral-element (SE) simulation performed by the code written by De Martin took 40 days on a 128 core cluster. Though only relative and indicative, in practice all this means that the obtained solution can be considered a sufficiently accurate reference for our FD solutions that use a uniform grid in which the material interfaces go through the interiors of the grid cells. Recall that the geometry of the interfaces is accounted for solely by evaluating effective grid material parameters. Figure 19.8 compares our FD solutions at one receiver close to the northern edge and one receiver close to the southern edge of the basin (both receivers and the point source are in one vertical plane) with the reference SE solution obtained by Florent De Martin. Three FD solutions are obtained with $h = 5$ m, using the **ARI**, **HAR** and **ORT** representations.

The conclusions for the three representations are:

- The **ORT** representation yields FD seismograms that are in excellent agreement with the SE reference solutions at both receivers.
- The **HAR** representation yields FD seismograms that are in excellent agreement with the SE reference solution at receiver R1. The motion at R2 is dominated by surface waves generated at both the northern and southern edges and propagating along the horizontal interfaces. The latter fact likely causes the difference between the FD and SE seismograms at receiver R2 after 16 s.
- The **ARI** representation yields results worse than those obtained with the **HAR** and **ORT** representations at receiver R1. At receiver R2 the **ARI** representation yields results no worse than those obtained with the **HAR** representation.

(a)
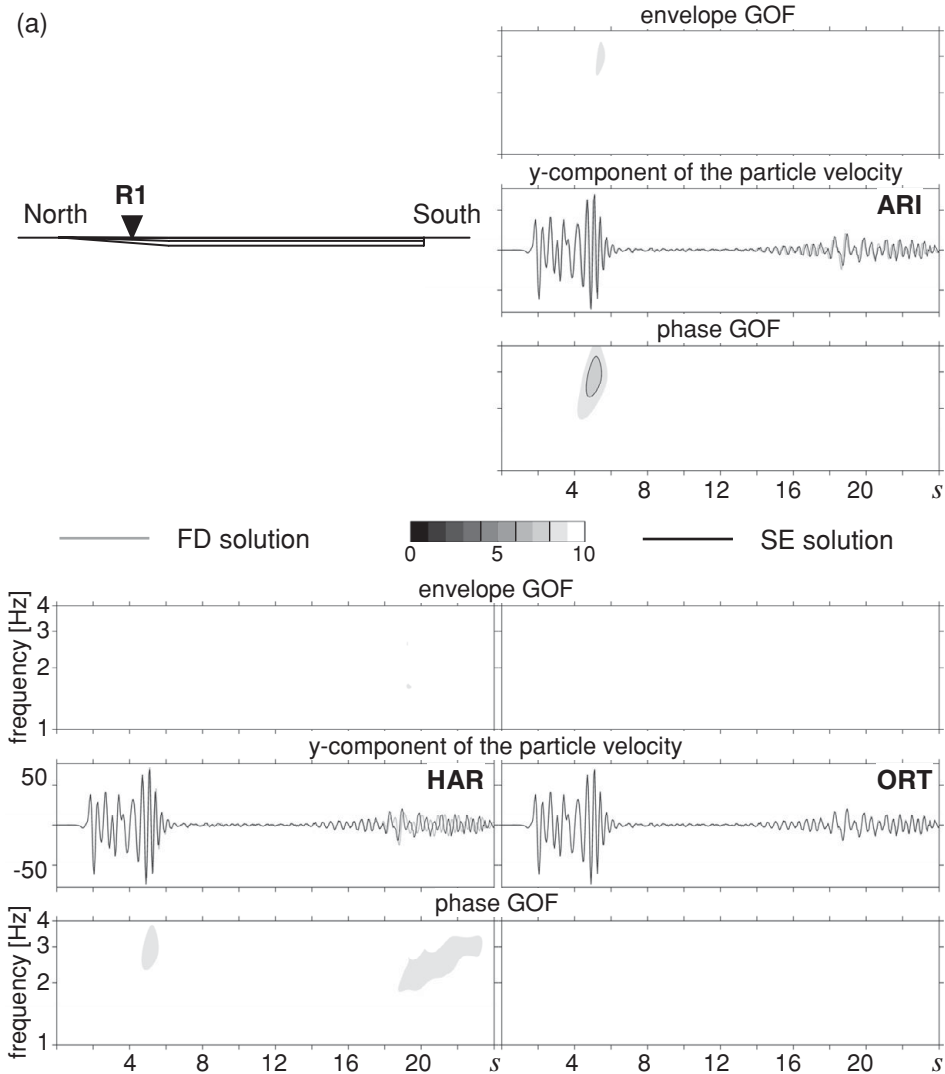
Figure 19.8 (a) FD (grey) and SE (black) seismograms for Can4. The FD seismograms are obtained for $h = 5$ m using three different material representations – **ARI**, **HAR** and **ORT**. (b), (c) and (d) differ from (a) by the receiver or the component of the particle velocity – as indicated directly in the figure.

Each of the three FD simulations took approximately 28 hours on 256 cores. This is an example of the computational efficiency of FD modelling with proper material parameterization.

The main conclusion is: The **ORT** representation gives excellent results for both R1 and R2 configurations. The **HAR** representation gives comparable results if the wavefield is not

(b)

envelope GOF

North **R1** ▼ South

vertical component of the particle velocity
ARI

phase GOF

4   8   12   16   20   *s*

—— FD solution   0   5   10   —— SE solution

frequency [Hz] 4 3 2 1

envelope GOF

vertical component of the particle velocity

20

HAR

ORT

-20

frequency [Hz] 4 3 2 1

phase GOF

4   8   12   16   20   *s*   4   8   12   16   20   *s*
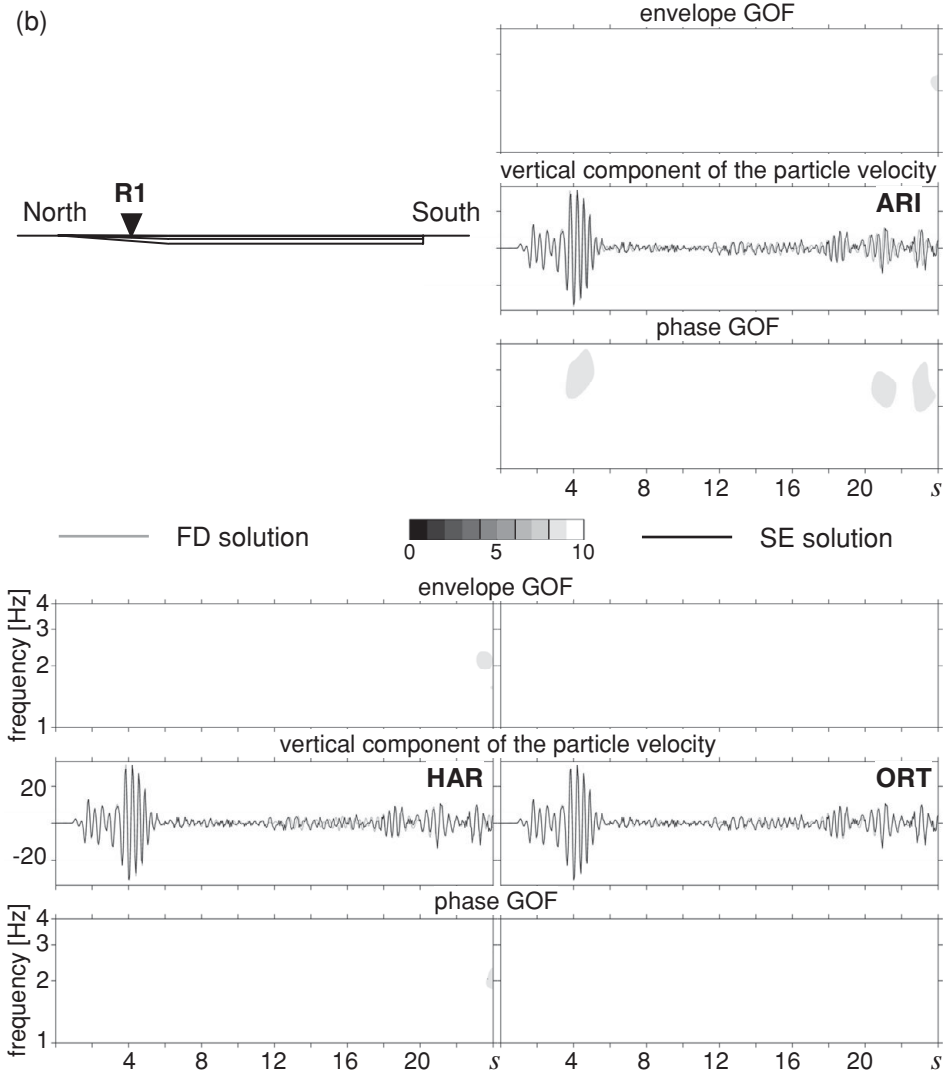
Figure 19.8 (*continued*)

dominated by surface waves propagating along horizontal material interfaces. There is no reason to use the **ARI** representation.

Complete comparison of simulations by the (2,4) velocity–stress staggered-grid scheme (Kristek and Moczo), (4,4) velocity–stress collocated-grid scheme (Z. Zhang, W. Zhang and Chen), spectral-element method (Chaljub and De Martin), and Fourier pseudo-spectral method (Klin and Priolo) is the subject of a journal article.

(c)

North   **R2**   South

envelope GOF

y-component of the particle velocity   **ARI**

phase GOF

4   8   12   16   20   *s*

―――― FD solution   0   5   10   ―――― SE solution

envelope GOF

frequency [Hz] 4 3 2 1

y-component of the particle velocity   **HAR**   **ORT**

50

-50

phase GOF

frequency [Hz] 4 3 2 1

4   8   12   16   20   *s*   4   8   12   16   20   *s*
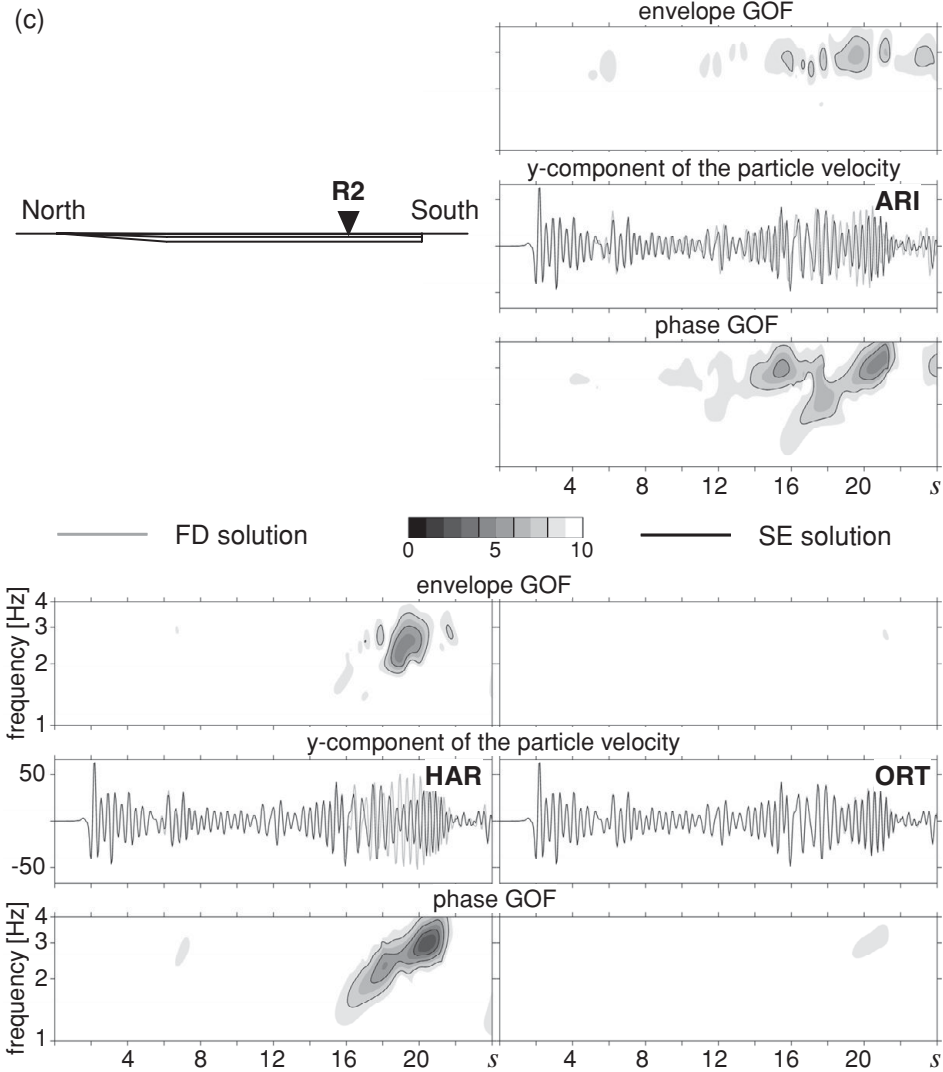
Figure 19.8 (*continued*)

19.2.4 Modelling for the realistic three-layered viscoelastic model

Here we illustratively compare the FD **ORT** simulation ($h = 5$ m) with the SE simulation obtained by Emmanuel Chaljub using the SPECFEM3D code developed by Dimitri Komatitsch and Jeroen Tromp (e.g., Komatitsch and Tromp 1999, Tromp *et al.* 2008, Peter *et al.* 2011).

The model was described in Subsection 19.2.2. The wavefield is generated by a double-couple source beneath TST at a depth of 3 km.
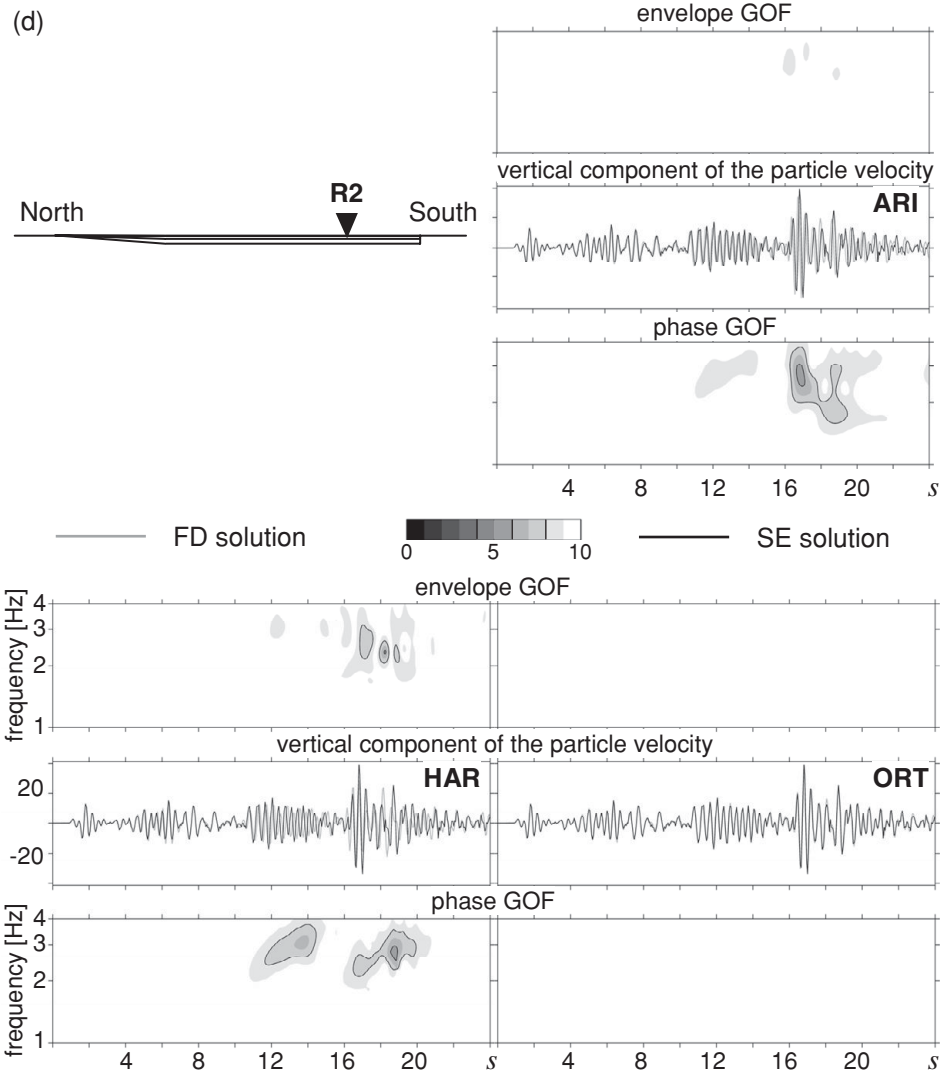
Figure 19.8 (*continued*)

The model for the SE simulation is discretized with a conforming, unstructured mesh of elements: the surface elements are 50 m in horizontal size at the surface and are coarsened twice with depth to reach 200 m. The vertical sizes of the elements are chosen following two simple rules: to respect a minimum number of gridpoints per local wavelength and to follow the interfaces in sediments as much as possible. The latter constraint is critical for accuracy in modelling surface waves. The mesh is built on a simple layer-cake strategy: the basin interfaces are extended to flat interfaces when one gets close to the basin edge and
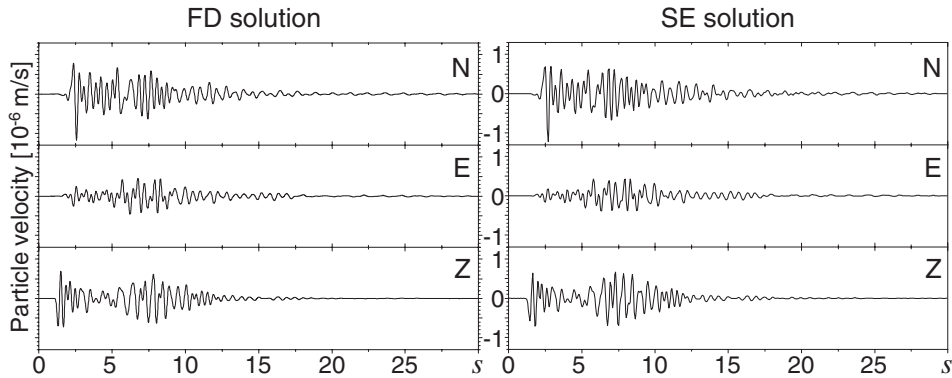
Figure 19.9 The FD **ORT** and SE seismograms for the realistic 3D viscoelastic model, TST station.

each modified layer is filled with the same number of elements in the vertical direction. The resulting numerical representation of the interfaces is not uniform: it is optimized within the central part of the basin but not close to the edges. The smallest (vertical) element size is found in the first layer of the model and equals 2.5 m.

The SE simulation does not serve as a reference solution at the same level of accuracy as the SE solution for Can4, and the visual comparison of the FD **ORT** and SE seismograms in Fig. 19.9 is illustrative.

Recall that all the numerical solutions presented and mentioned in this chapter together with detailed descriptions of the computational models are available at www.sismowine. org.

Finally, let us note that we do not present simulations for real local earthquakes. At the time of preparation of the book, the numerical simulations in E2VP had not reached a satisfactory level of agreement with records. Additional investigations strongly indicated the possibility that the available structural model should be improved.

19.2.5 Lessons learned from ESG 2006 and E2VP

The ESG 2006 comparative exercise (Chaljub *et al.* 2010) and numerous detailed comparative analyses performed in E2VP lead to conclusions important for the practical application of numerical methods in predicting earthquake ground motion at a site of interest:

Methodological – general
- There is no single numerical-modelling method that can be considered the best – in terms of accuracy and computational efficiency – for all structure–wavefield configurations important for predicting earthquake ground motion in surface local structures.
- Apparently and intuitively 'small' or 'insignificant' differences in the discrete representation of spatial variations in material parameters can cause considerable

inaccuracies and consequently discrepancies in predictions obtained by different methods.

- Sufficiently accurate and computationally efficient methods for implementing continuous and discontinuous material heterogeneity (consistent with the interface boundary condition), realistic attenuation (no simpler than that corresponding to the GZB/GMB-EK rheology), a nonreflecting boundary (no less efficient than PML) and free-surface conditions prove to be the key elements of a reasonably accurate numerical simulation.

Methodological – FD method

- The commonly used name of 'finite-difference method' in numerical modelling of earthquake ground motion may represent one of a large variety of FD schemes and codes. Surprisingly, not all FD schemes used for simulations and publications are at the state-of-the-art level: the available methods and techniques for representing spatial material heterogeneity, realistic attenuation, large V_P/V_S, free surface and nonreflecting boundaries of the grid are not implemented in some frequently applied codes.

Practical

- The numerical-simulation methods and the corresponding computer codes are not yet in a 'press-button' mode; the codes should never be applied as black-box tools, that is, without sufficient methodological knowledge of the method and the code.
- At least two different but comparably accurate, verified and state-of-the-art methods should be applied in order to obtain reliable numerical prediction of earthquake ground motion at a site of interest.
- Material interfaces should not be artificially introduced in the computational model; their presence can have a strong impact on the locally induced surface waves.
- It is necessary to perform numerical simulations for at least two different discretizations, e.g., for two sizes of the spatial grid spacing or element, in order to assess the sensitivity of the simulated motion with respect to the computational parameters.

Concluding remarks: search for the best scheme

We have mentioned several times that no single numerical-modelling method developed so far is better than other methods for all important configurations of the medium and wavefield. Being better for a particular problem configuration means:

– either being more accurate at some level of computational efficiency (quantified in terms of requirements on computer time and memory)
– or being more computationally efficient at an optional level of accuracy.

A method or scheme applicable to a wider class of medium–wavefield configurations is not necessarily the most efficient method for some important configurations to which other (possibly less universal) methods are applicable. In fact, the less universal method might be considerably more efficient for some configurations at the same level of accuracy. The importance of computational efficiency increases with complexity of the model and maximum frequency up to which the numerical modelling should be sufficiently accurate.

In view of what we have just said about the numerical methods in general, can one particular FD scheme be better than other schemes for all important problem configurations? It is not easy to answer in a rigorous and comprehensive manner – especially at the present state of development and elaboration of the FD schemes, which certainly is far from what is in principle possible. It is, however, very likely that what we said about all numerical-modelling methods is also true about all possible FD schemes.

We may, however, think of properties of a hypothetical best FD scheme for a certain class of important problems. The best scheme should be consistent with the mathematical-physical problem with an optional level of accuracy (e.g., with an optional and the same order of accuracy in space and time), stable, and computationally efficient.

Particular properties of the best FD scheme for modelling earthquake motions should include:

– stability at a
  • free surface (planar and nonplanar),
  • contact of the free surface with internal material interface,
  • contact of the free surface with the PML,

- contact of the internal material interface and the PML
- liquid–solid interface (if a water layer is an important part of model),
- optional level of accuracy
  - for any value of the P-wave to S-wave speed ratio, that is $V_P / V_S \in (\sqrt{2}, \infty)$, or, equivalently, for any value of Poisson's ratio, that is $\sigma \in (0, 0.5)$,
  - in a medium with strong gradient of material parameters,
  - in a medium with strong contrast of material parameters at an internal interface,
  - in a medium with material interfaces not coinciding with grid planes or grid lines,
  - at and near the free surface (planar and nonplanar),
  - in an attenuative medium,
  - at and near a rupturing fault (planar and nonplanar),
  - of implementation of a kinematic source,
- computational efficiency in terms of
  - relatively low memory,
  - relatively short computational time.

Can all particle-velocity and stress-tensor components at each grid position of a curvilinear grid, relatively small stencils for approximating derivatives, and a proper effective grid representation of material properties or some other ingredients make it possible to achieve better schemes? Recent intensive effort to develop new, more accurate and more efficient schemes indicates several strategies. The future will show which of them will make it possible to apply the FD method further and better than before in earthquake ground motion modelling and prediction.

Appendix A

Time–frequency misfit and goodness-of-fit criteria for quantitative comparison of time signals

In the process of development and verification of a numerical method for calculation of seismic wave propagation it is necessary to quantitatively compare a numerically simulated signal with a reference or exact solution. In the process of validation of the numerical method it is necessary to quantitatively compare a numerically simulated signal with a seismic record. Comparison of two recorded signals significantly helps in the analysis and interpretation of the process under investigation. The quantitative misfit and goodness-of-fit criteria introduced by Kristekova *et al.* (2006, 2009) are summarized and explained in this appendix.

A.1 Characterization of a signal

Here we restrict our discussion to basic concepts and relations for characterizing a signal necessary in the further exposition.

A.1.1 Simplest characteristics

Consider the simplest case of a monochromatic signal:

$$s_m(t) = A\cos(2\pi f t + \phi) \tag{A.1}$$

where t is time, A is amplitude, ϕ is phase and f is frequency. Signal characteristics A, ϕ and f are unambiguously defined and very easy to interpret. If a signal is more complicated, the notion of amplitude, phase and frequency may be not so obvious. For example, when $A = A(t)$, and $f = f(t)$ and $\phi = \phi(t)$ in the argument of the cosine function, the amplitude and phase are ambiguous.

The analytical signal (e.g., Flandrin 1999) enables us to develop proper unambiguous characteristics. The analytical signal $\tilde{s}(t)$ with respect to signal $s(t)$ is

$$\tilde{s}(t) = s(t) + iH\{s(t)\} \tag{A.2}$$

where $H\{s(t)\}$ is the Hilbert transform of signal $s(t)$. Relations

$$A(t) = |\tilde{s}(t)|, \quad \phi(t) = \text{Arg}[\tilde{s}(t)] \tag{A.3}$$

and

$$f(t) = \frac{1}{2\pi}\frac{d\,\text{Arg}[\tilde{s}(t)]}{dt} \tag{A.4}$$

define the envelope, phase and (so-called instantaneous) frequency of the signal at time t. Although these quantities are unambiguous, in fact they represent just averaged values. For example, Qian (2002) suggests using the term 'mean instantaneous frequency' instead of the instantaneous frequency. The narrower is the spectral content at time t, the better is the estimate of the dominant amplitude, phase and frequency by Eqs. (A.3) and (A.4).

Clearly, the analytical signal cannot be used for determining the three basic characteristics of a signal if its spectral content is complicated and changes with time.

A.1.2 Time–frequency decomposition

The instantaneous spectral content or time evolution at any frequency of a signal, and hence the time evolution of the spectral content of the signal, can be obtained using the time–frequency (TF) representation of the signal. The TF representation can be calculated using, for example, the continuous wavelet transform (CWT). The CWT of signal $s(t)$ is defined by

$$CWT_{(a,b)}\{s(t)\} = \frac{1}{\sqrt{|a|}} \int_{-\infty}^{\infty} s(t)\psi^* \left(\frac{t-b}{a} \right) dt \qquad (A.5)$$

with a being the scale parameter, b the translational parameter, and ψ the analyzing wavelet. The asterisk denotes the complex conjugate function. The scale parameter a is inversely proportional to frequency f. Consider an analyzing wavelet with a spectrum that has zero amplitudes at negative frequencies. Such a wavelet is an analytical signal and is called the progressive wavelet. A Morlet wavelet

$$\psi(t) = \pi^{-1/4} \exp(i\omega_0 t) \exp(-t^2/2) \qquad (A.6)$$

with $\omega_0 = 6s^{-1}$, is a proper choice for a wide class of signals and problems, and can be considered as a progressive wavelet. The TF representation of signal $s(t)$ based on the CWT, $W(t, f)$, can be then defined by choosing a relation between the scale parameter a and frequency f. Assume

$$a = \omega_0/2\pi f \qquad (A.7)$$

Then,

$$W(t, f) \equiv CWT_{(a,b)}\{s(t)\} = \sqrt{\frac{2\pi|f|}{\omega_0}} \int_{-\infty}^{\infty} s(\tau)\psi^* \left(2\pi f \frac{\tau - t}{\omega_0} \right) d\tau \qquad (A.8)$$

$W^2(t, f)$ represents the energy distribution (energy density) of the signal in the TF plane. See, for example, the monographs by Daubechies (1992) and Holschneider (1995) for comprehensive expositions of the CWT and Morlet wavelet. The useful properties of the CWT for the TF analysis of complicated seismic records have been demonstrated by, for example, Kristekova *et al.* (2008) and others. Their analysis of seismic records led to identification of a sequence of relatively weak explosions.

Having determined the TF representation, an envelope $A(t, f)$ and phase $\phi(t, f)$ at a given point of the TF plane can be defined:

$$A(t, f) = |W(t, f)|, \qquad \phi(t, f) = \text{Arg}[W(t, f)] \qquad (A.9)$$

Holschneider (1995) showed that if $W(t, f)$ is defined using the CWT with the progressive wavelet, envelope $A(t, f)$ and phase $\phi(t, f)$ are consistent with those defined using the analytical signal.

Note that the TF representation obtained using the CWT is more suitable for the analysis of complicated nonstationary signals than the TF representation obtained using the windowed Fourier transform. This is because the CWT is not limited by the fixed TF resolution as it is in the case of the windowed Fourier transform.

A.2 Comparison of signals

A.2.1 TF envelope and phase differences

Consider a signal $s(t)$ and a reference signal $sr(t)$. Given Eqs. (A.8) and (A.9) it is clear that

$$\Delta A(t, f) = A(t, f) - Ar(t, f) = |W(t, f)| - |Wr(t, f)| \tag{A.10}$$

defines the difference between the envelopes of signals $s(t)$ and $sr(t)$ at each (t, f) point. Similarly,

$$\Delta\phi(t, f) = \phi(t, f) - \phi r(t, f) = \text{Arg}[W(t, f)] - \text{Arg}[Wr(t, f)] \tag{A.11}$$

defines the difference between two phases at each (t, f) point.

The envelope difference $\Delta A(t, f)$ is a local difference that can attain any value. The local phase difference needs some explanation. A little complication comes from the fact that $\text{Arg}[\xi]$ always gives the phase of the complex variable ξ in the range of $(-\pi, \pi]$. If, say, two phases are $170\pi/180$ and $-160\pi/180$, Eq. (A.11) formally gives $330\pi/180$ instead of the correct value $-30\pi/180$. It is clear that definition (A.11) would need an additional condition to treat similar situations. Instead, however, we can avoid the additional condition by using the following equivalent definition:

$$\Delta\phi(t, f) = \text{Arg}\left[\frac{W(t, f)}{Wr(t, f)}\right] \tag{A.12}$$

Relation (A.12) always gives the local phase difference in the range of $(-\pi, \pi]$.

A.2.2 Locally normalized and globally normalized criteria

Having the local envelope and phase differences at the (t, f) point, we can define a variety of TF misfit criteria to quantitatively compare the entire signals, their important parts or characteristics of the signals.

Locally normalized criteria In some problems it is important to investigate relatively small parts of the signal – no matter how large the amplitudes of those parts are with respect to the maximum amplitude of the entire signal. In other cases one may be interested in a detailed TF anatomy of the disagreement between two entire signals including small-amplitude parts. For comparing two signals in such situations we need to define local misfit criteria – criteria whose values for one (t, f) point would depend only on the characteristics at that (t, f) point.

Consider how to define a local TF misfit criterion for the envelope. It is clear that such a criterion should quantify the relative difference between two envelopes at the (t, f) point.

Consequently, $\Delta A(t, f)$ given by Eq. (A.10) should be normalized by $Ar(t, f)$. At the same time, due to its nature, the phase difference (A.12) itself provides the proper quantification for the local TF phase misfit criterion. We can choose, however, the range $(-1, 1]$ instead of $(-\pi, \pi]$: we can divide the phase difference (A.12) by π.

The preceding considerations can be taken as arguments and a basis for defining the locally normalized TF misfit criteria:

$$TFEM_{LOC}(t, f) = \frac{\Delta A(t, f)}{Ar(t, f)} \qquad (A.13)$$

and

$$TFPM_{LOC}(t, f) = \frac{\Delta\phi(t, f)}{\pi} \qquad (A.14)$$

$TFEM_{LOC}$ is the locally normalized TF envelope misfit criterion, $TFPM_{LOC}$ is the locally normalized TF phase misfit criterion.

Globally normalized criteria In another class of problems it may be reasonable to give the largest weights to local envelope/phase differences for those parts of the signals in which the envelope of the reference signal reaches the largest values. For example, it may be reasonable to require that the envelope misfit be equal to the local envelope difference $\Delta A(t, f)$ just at that (t, f) point at which envelope $Ar(t, f)$ of the reference signal reaches its maximum, $\max_{t, f}\{Ar(t, f)\}$. At the other (t, f) points with the envelope smaller than $\max_{t, f}\{Ar(t, f)\}$ such a misfit could be proportional to the ratio between $Ar(t, f)$ and $\max_{t, f}\{Ar(t, f)\}$. Consequently, we can define the globally normalized criteria by

$$TFEM_{GLOB}(t, f) = \frac{Ar(t, f)}{\max_{t, f}\{Ar(t, f)\}} TFEM_{LOC}(t, f)$$

$$= \frac{\Delta A(t, f)}{\max_{t, f}\{Ar(t, f)\}} \qquad (A.15)$$

$$TFPM_{GLOB}(t, f) = \frac{Ar(t, f)}{\max_{t, f}\{Ar(t, f)\}} TFPM_{LOC}(t, f)$$

$$= \frac{Ar(t, f)}{\max_{t, f}\{Ar(t, f)\}} \frac{\Delta\phi(t, f)}{\pi} \qquad (A.16)$$

Note that it is the normalization by $\max_{t, f}\{Ar(t, f)\}$ at each (t, f) point that makes the criteria globally normalized.

Clearly, the values of the globally normalized TF misfit criteria account for both the envelope/phase difference at a (t, f) point and the significance of the envelope at that point with respect to the maximum envelope of the reference signal. In this sense they quantify an overall level of disagreement between two signals. We apply global normalization in the definition of TF misfits when we are not much interested in the detailed anatomy of the signals and misfits in those parts of the signal where its amplitudes are too small compared to the maximum amplitude of the reference signal.

A.3 Comparison of three-component signals

The above considerations on the locally and globally normalized misfit criteria for one-component signals can be extended also to the misfits for three-component signals.

A.3.1 TF misfit criteria

The case: one signal being a reference If the amplitudes of one component of the reference signal are significantly smaller than the amplitudes of two other components (e.g., a common situation with polarized particle motion), the only reasonable choice for global normalization is to take the maximum TF envelope value from all three components of the reference signal. This choice naturally quantifies the misfits with respect to meaningful values of the three-component reference signal. It also prevents obtaining too large misfits due to possible division by very small envelope values corresponding to insignificant amplitudes of the signal components. Clearly, this choice is reasonable also if the amplitudes of all three components are comparable.

A formal definition of one local normalization factor for all three components would clearly contradict the local character of a misfit criterion. Therefore, each component has to be treated as a 'one-component' signal if one is interested in the detailed anatomy of the TF misfit.

Now we can define a set of misfit criteria for the three-component signals when one of them can be considered a reference. The locally normalized and globally normalized TF envelope misfits $TFEM_{LOC,i}^{REF}(t, f)$ and $TFEM_{GLOB,i}^{REF}(t, f)$ characterize how the envelopes of two signals differ at each (t, f) point. Similarly, $TFPM_{LOC,i}^{REF}(t, f)$ and $TFPM_{GLOB,i}^{REF}(t, f)$ characterize how the phases of two signals differ at each (t, f) point.

Projections of the TF misfits onto the time domain give the time-dependent envelope and phase misfits $TEM_{LOC,i}^{REF}(t)$, $TEM_{GLOB,i}^{REF}(t)$, $TPM_{LOC,i}^{REF}(t)$ and $TPM_{GLOB,i}^{REF}(t)$. Projections of the TF misfits onto the frequency domain give the frequency-dependent envelope and phase misfits $FEM_{LOC,i}^{REF}(f)$, $FEM_{GLOB,i}^{REF}(f)$, $FPM_{LOC,i}^{REF}(f)$ and $FPM_{GLOB,i}^{REF}(f)$.

Finally, it is often very useful to have single-valued envelope and phase misfits $EM_{LOC,i}^{REF}$, $EM_{GLOB,i}^{REF}$, $PM_{LOC,i}^{REF}$ and $PM_{GLOB,i}^{REF}$. All the misfits are summarized in Table A.1. The envelope and phase misfits can attain any value in the range $(-\infty, \infty)$ and $(-1, 1)$, respectively.

The case: no signal being a reference The misfit criteria for this case can be defined, in fact, formally in the same way as criteria in the case with a reference signal. The only question is, which of the two signals should be formally taken as a reference? The reasonable way is to find a maximum envelope for each of the two signals. Then the signal with the smaller maximum can be chosen as a reference signal. In the case of the globally normalized criteria for the three-component signals the maximum is taken from all components. In the case of the locally normalized criteria the reference signal should be chosen separately for each component.

Note that the evaluation of the TF misfits themselves does not give us a reason to prefer the smaller of the two maxima. Our choice comes from the possible link to the goodness-of-fit criteria developed by Anderson (2004). We take the smaller maximum consistently with the Anderson criteria.

A.3.2 TF goodness-of-fit criteria

The envelope TF misfits quantify and characterize how much two envelopes differ from each other. Correspondingly, the envelope misfit can attain any value within the range of $(-\infty, \infty)$, with 0 meaning the agreement. While formally applicable to any level of disagreement, clearly, the envelope misfits are most useful for comparing relatively close envelopes.

Table A.1 *TF misfit criteria for three-component signals assuming one of them as a reference signal*

$s_i(t)$, $sr_i(t)$; $i = 1, 2, 3$	a 3-component signal and a 3-component reference signal
$W_i = W_i(t, f)$, $Wr_i = Wr_i(t, f)$	TF representation of signals $s_i(t)$ and $sr_i(t)$

time-frequency envelope and phase misfits

locally normalized TF envelope misfit

$$TFEM_{LOC,i}^{REF}(t, f) = \frac{|W_i| - |Wr_i|}{|Wr_i|}$$

locally normalized TF phase misfit

$$TFPM_{LOC,i}^{REF}(t, f) = \frac{1}{\pi}\text{Arg}[\frac{W_i}{Wr_i}]$$

globally normalized TF $\begin{Bmatrix} \text{envelope} \\ \text{phase} \end{Bmatrix}$ misfit

$$\begin{Bmatrix} TFEM_{GLOB,i}^{REF}(t, f) \\ TFPM_{GLOB,i}^{REF}(t, f) \end{Bmatrix} = \frac{|Wr_i|}{\max_{i;\,t,f}(|Wr_i|)} \begin{Bmatrix} TFEM_{LOC,i}^{REF}(t, f) \\ TFPM_{LOC,i}^{REF}(t, f) \end{Bmatrix}$$

time-dependent envelope and phase misfits

locally normalized

$$\begin{Bmatrix} TEM_{LOC,i}^{REF}(t) \\ TPM_{LOC,i}^{REF}(t) \end{Bmatrix} = \frac{\sum_f |Wr_i| \begin{Bmatrix} TFEM_{LOC,i}^{REF}(t, f) \\ TFPM_{LOC,i}^{REF}(t, f) \end{Bmatrix}}{\sum_f |Wr_i|}$$

globally normalized

$$\begin{Bmatrix} TEM_{GLOB,i}^{REF}(t) \\ TPM_{GLOB,i}^{REF}(t) \end{Bmatrix} = \frac{\sum_f |Wr_i| \begin{Bmatrix} TFEM_{LOC,i}^{REF}(t, f) \\ TFPM_{LOC,i}^{REF}(t, f) \end{Bmatrix}}{\max_{i;\,t}\left(\sum_f |Wr_i|\right)}$$

frequency-dependent envelope and phase misfits

locally normalized

$$\begin{Bmatrix} FEM_{LOC,i}^{REF}(f) \\ FPM_{LOC,i}^{REF}(f) \end{Bmatrix} = \frac{\sum_t |Wr_i| \begin{Bmatrix} TFEM_{LOC,i}^{REF}(t, f) \\ TFPM_{LOC,i}^{REF}(t, f) \end{Bmatrix}}{\sum_t |Wr_i|}$$

globally normalized

$$\begin{Bmatrix} FEM_{GLOB,i}^{REF}(f) \\ FPM_{GLOB,i}^{REF}(f) \end{Bmatrix} = \frac{\sum_t |Wr_i| \begin{Bmatrix} TFEM_{LOC,i}^{REF}(t, f) \\ TFPM_{LOC,i}^{REF}(t, f) \end{Bmatrix}}{\max_{i;\,f}\left(\sum_t |Wr_i|\right)}$$

single-valued envelope and phase misfits

locally normalized

$$\begin{Bmatrix} EM_{LOC,i}^{REF} \\ PM_{LOC,i}^{REF} \end{Bmatrix} = \sqrt{\frac{\sum_f \sum_t |Wr_i|^2 \begin{Bmatrix} |TFEM_{LOC,i}^{REF}(t, f)| \\ |TFPM_{LOC,i}^{REF}(t, f)| \end{Bmatrix}^2}{\sum_f \sum_t |Wr_i|^2}}$$

globally normalized

$$\begin{Bmatrix} EM_{GLOB,i}^{REF} \\ PM_{GLOB,i}^{REF} \end{Bmatrix} = \sqrt{\frac{\sum_f \sum_t |Wr_i|^2 \begin{Bmatrix} |TFEM_{LOC,i}^{REF}(t, f)| \\ |TFPM_{LOC,i}^{REF}(t, f)| \end{Bmatrix}^2}{\max_i\left(\sum_f \sum_t |Wr_i|^2\right)}}$$

However, in practice it is often necessary to compare signals whose envelopes differ considerably. Comparison of real records with synthetics in some problems can be a good example. In such a case it is reasonable to look for the level of agreement rather than details of disagreement. The goodness-of-fit criteria provide a suitable tool for this.

The goodness-of-fit criteria approach a zero value with an increasing level of disagreement. On the other hand, some finite value is chosen to quantify the agreement.

The TF envelope goodness-of-fit criteria can be introduced on the basis of the TF envelope misfits:

$$\begin{aligned} TFEG(t, f) &= A\exp\{-|TFEM(t, f)|^k\} \\ TEG(t) &= A\exp\{-|TEM(t)|^k\} \\ FEG(f) &= A\exp\{-|FEM(f)|^k\} \\ EG &= A\exp\{-|EM|^k\} \\ A &> 0, \quad k > 0 \end{aligned} \tag{A.17}$$

Table A.2 *Locally and globally normalized TF misfit criteria for three-component signals, **none being a reference***

$s1_i(t)$, $s2_i(t)$; $i=1,2,3$	two 3-component signals
$W1_i = W1_i(t,f)$, $W2_i = W2_i(t,f)$	*TF* representations of signals $s1_i(t)$ and $s2_i(t)$

$$Wr_i \quad \begin{aligned} &= W1_i \quad \text{if} \quad \max_{i;\,t,f}\left(|W1_i|\right) < \max_{i;\,t,f}\left(|W2_i|\right) \\ &= W2_i \quad \text{if} \quad \max_{i;\,t,f}\left(|W1_i|\right) \geq \max_{i;\,t,f}\left(|W2_i|\right) \end{aligned}$$

time-frequency envelope and phase misfits

locally normalized TF envelope misfit
$$TFEM_{LOC,i}(t,f) = \frac{|W1_i| - |W2_i|}{|Wr_i|}$$

locally normalized TF phase misfit
$$TFPM_{LOC,i}(t,f) = \frac{1}{\pi}\text{Arg}[\frac{W1_i}{W2_i}]$$

globally normalized TF $\left\{\begin{array}{l}\textbf{envelope}\\\textbf{phase}\end{array}\right\}$ **misfit**
$$\left\{\begin{array}{l}TFEM_{GLOB,i}(t,f)\\TFPM_{GLOB,i}(t,f)\end{array}\right\} = \frac{|Wr_i|}{\max_{i;\,t,f}\left(|Wr_i|\right)}\left\{\begin{array}{l}TFEM_{LOC,i}(t,f)\\TFPM_{LOC,i}(t,f)\end{array}\right\}$$

time-dependent envelope and phase misfits

locally normalized

$$\left\{\begin{array}{l}TEM_{LOC,i}(t)\\TPM_{LOC,i}(t)\end{array}\right\} = \frac{\sum_f |Wr_i|\left\{\begin{array}{l}TFEM_{LOC,i}(t,f)\\TFPM_{LOC,i}(t,f)\end{array}\right\}}{\sum_f |Wr_i|}$$

globally normalized

$$\left\{\begin{array}{l}TEM_{GLOB,i}(t)\\TPM_{GLOB,i}(t)\end{array}\right\} = \frac{\sum_f |Wr_i|\left\{\begin{array}{l}TFEM_{LOC,i}(t,f)\\TFPM_{LOC,i}(t,f)\end{array}\right\}}{\max_{i;\,t}\left(\sum_f |Wr_i|\right)}$$

frequency-dependent envelope and phase misfits

locally normalized

$$\left\{\begin{array}{l}FEM_{LOC,i}(f)\\FPM_{LOC,i}(f)\end{array}\right\} = \frac{\sum_t |Wr_i|\left\{\begin{array}{l}TFEM_{LOC,i}(t,f)\\TFPM_{LOC,i}(t,f)\end{array}\right\}}{\sum_t |Wr_i|}$$

globally normalized

$$\left\{\begin{array}{l}FEM_{GLOB,i}(f)\\FPM_{GLOB,i}(f)\end{array}\right\} = \frac{\sum_t |Wr_i|\left\{\begin{array}{l}TFEM_{LOC,i}(t,f)\\TFPM_{LOC,i}(t,f)\end{array}\right\}}{\max_{i;\,f}\left(\sum_t |Wr_i|\right)}$$

single-valued envelope and phase misfits

locally normalized

$$\left\{\begin{array}{l}EM_{LOC,i}\\PM_{LOC,i}\end{array}\right\} = \sqrt{\frac{\sum_f \sum_t |Wr_i|^2\left|\left\{\begin{array}{l}TFEM_{LOC,i}(t,f)\\TFPM_{LOC,i}(t,f)\end{array}\right\}\right|^2}{\sum_t \sum_f |Wr_i|^2}}$$

globally normalized

$$\left\{\begin{array}{l}EM_{GLOB,i}\\PM_{GLOB,i}\end{array}\right\} = \sqrt{\frac{\sum_f \sum_t |Wr_i|^2\left|\left\{\begin{array}{l}TFEM_{LOC,i}(t,f)\\TFPM_{LOC,i}(t,f)\end{array}\right\}\right|^2}{\max_i\left(\sum_t \sum_f |Wr_i|^2\right)}}$$

Here, factor A quantifies the agreement between two envelopes in terms of the chosen envelope misfit: The envelope goodness-of-fit criterion is equal to A if the envelope misfit is equal to 0. Choice of the exponent k determines sensitivity of the goodness-of-fit value with respect to the misfit value.

Similarly, we can define the TF phase goodness-of-fit criteria as the goodness-of-fit equivalents to the TF phase misfit criteria (Table A.2):

$$\begin{aligned} TFPG(t,f) &= A(1 - |TFPM(t,f)|^k)\\ TPG(t) &= A(1 - |TPM(t)|^k)\\ FPG(f) &= A(1 - |FPM(f)|^k)\\ PG &= A(1 - |PM|^k) \end{aligned} \tag{A.18}$$

Table A.3 *Discrete goodness-of-fit values against the misfit values*

Misfit	Misfit	Goodness-of-Fit	
Envelope	Phase	Numerical value	Verbal value
± 0.00	± 0.0	10	
± 0.11	± 0.1	9	excellent
± 0.22	± 0.2	8	
± 0.36	± 0.3	7	good
± 0.51	± 0.4	6	
± 0.69	± 0.5	5	fair
± 0.92	± 0.6	4	
± 1.20	± 0.7	3	
± 1.61	± 0.8	2	poor
± 2.30	± 0.9	1	
± ∞	± 1.0	0	

Table A.3 shows the discrete goodness-of-fit values against the misfit values for $A = 10$ and $k = 1$ that we consider a practically reasonable choice for a wide class of problems. Consistently with Anderson (2004), the fourth column of the table assigns possible verbal levels to the goodness-of-fit numerical values.

The TF goodness-of-fits and verbal levels given in Table A.3 can be reasonably applied to an analysis of the level of agreement between earthquake records and simulations, and possibly also to some other problems. Note, however, that the mapping between the TF misfits and TF goodness-of-fits, and eventually also the choice of the verbal classification, may be easily adjusted for a specific comparative analysis by modifying the range of the goodness-of-fit criteria $[0, A]$, exponent k, and the verbal classification.

The concept of TF misfits is general and makes it possible to define properly tuned criteria for comparing time signals.

References

Aagaard, B. T., T. M. Brocher, D. Dolenc, D. S. Dreger, R. W. Graves, S. C. Harmsen, S. H. Hartzell, S. Larsen, M. L. Zoback 2008a. Ground-motion modeling of the 1906 San Francisco earthquake, Part I: Validation using the 1989 Loma Prieta Earthquake. *Bull. Seism. Soc. Am*. 98, 989–1011.

Aagaard, B. T., T. M. Brocher, D. Dolenc, D. S. Dreger, R. W. Graves, S. C. Harmsen, S. H. Hartzell, S. Larsen, K. McCandless, S. Nilsson, N. A. Petersson, A. Rodgers, B. Sjögreen, M. L. Zoback 2008b. Ground-motion modeling of the 1906 San Francisco earthquake, Part II: Ground-motion estimates for the 1906 earthquake and scenario events. *Bull. Seism. Soc. Am*. 98, 1012–1046.

Aagaard, B. T., T. H. Heaton, J. F. Hall 2001. Dynamic earthquake ruptures in the presence of lithostatic normal stresses: Implications for friction models and heat production. *Bull. Seism. Soc. Am*. 91, 1765–1796.

Aboudi, J. 1971. Numerical simulation of seismic sources. *Geophysics* 36, 810–821.

Abreu, R., D. Stich, J. Morales 2013. On the generalization of the complex step method. *J. Comput. Appl. Math*. 241, 84–102.

Aki, K., P. G. Richards 2002. *Quantitative Seismology*, 2nd edn. University Science Books.

Alexeev, A. S., B. G. Mikhailenko 1980. The solution of dynamic problems of elastic wave propagation in inhomogeneous media by a combination of partial separation of variables and finite-difference methods. *J. Geophys*. 48, 161–172.

Alford, R. M., K. R. Kelly, D. M. Boore 1974. Accuracy of finite-difference modeling of the acoustic wave equation. *Geophysics* 39, 834–842.

Alterman, Z. S., F. C. Karal 1968. Propagation of elastic waves in layered media by finite difference methods. *Bull. Seism. Soc. Am*. 58, 367–398.

Alterman, Z., D. Loewenthal 1970. Seismic waves in a quarter and three-quarter plane. *Geophys. J. R. Astr. Soc*. 20, 101–126.

Alterman, Z. S., R. Nathaniel 1975. Seismic waves in a wedge. *Bull. Seism. Soc. Am*. 65, 1697–1719.

Alterman, Z. S., A. Rotenberg 1969. Seismic waves in a quarter plane. *Bull. Seism. Soc. Am*. 59, 347–368.

Ampuero, J.-P. 2002. Etude physique et numérique de la nucléation des séismes. PhD Thesis. Université Paris 7, Denis Diderot.

Ampuero, J.-P. 2008. SEM2DPACK: A spectral element method for 2D wave propagation and earthquake source dynamics, version 2.3.3, available at http://sourceforge.net/projects/sem2d/.

Ampuero, J.-P., Y. Ben-Zion 2008. Cracks, pulses and macroscopic asymmetry of dynamic rupture on a bimaterial interface with velocity-weakening friction. *Geophys. J. Int.* 173, 674–692.

Ampuero, J.-P., J. Ripperger, P. M. Mai 2006. Properties of dynamic earthquake ruptures with heterogeneous stress drop. In R. Abercrombie *et al.* (eds.), *Earthquakes: Radiated Energy and the Physics of Faulting*, 255–261, Washington, D.C.: American Geophysical Union.

Ampuero, J.-P., A. M. Rubin 2008. Earthquake nucleation on rate-and-state faults: Aging and slip laws. *J. Geophys. Res.* 113, B01302.

Anderson, J. G. 2004. Quantitative measure of the goodness-of-fit of synthetic seismograms. In *13th World Conference on Earthquake Engineering Conference Proceedings*, Vancouver, Canada, Paper 243.

Anderson, J. G., B. Aagaard, K. Hudnut 2003. Fault interactions and large complex earthquakes in the Los Angeles area. *Science* 302, 1946–1949.

Andrews, D. J. 1973. A numerical study of tectonic stress release by underground explosions. *Bull. Seism. Soc. Am.* 63, 1375–1391.

Andrews, D. J. 1976a. Rupture propagation with finite stress in antiplane strain. *J. Geophys. Res.* 81, 3575–3582.

Andrews, D. J. 1976b. Rupture velocity of plane strain shear cracks. *J. Geophys. Res.* 81, 5679–5687.

Andrews, D. J. 1985. Dynamic plane-strain shear rupture with a slip-weakening friction law calculated by a boundary integral method. *Bull. Seism. Soc. Am.* 75, 1–21.

Andrews, D. J. 1999. Test of two methods for faulting in finite-difference calculations. *Bull. Seism. Soc. Am.* 89, 931–937.

Andrews, D. J., Y. Ben-Zion 1997. Wrinkle-like slip pulse on a fault between different materials. *J. Geophys. Res.* 102, 553–571.

Aochi, H., V. Durand, J. Douglas 2011. Influence of super-shear earthquake rupture models on simulated near-source ground motion from the 1999 Izmit, Turkey, earthquake. *Bull. Seism. Soc. Am.* 101, 726–741.

Aochi, H., E. Fukuyama 2002. Three-dimensional nonplanar simulation of the 1992 Landers earthquake. *J. Geophys. Res.* 107, 2035.

Aochi, H., E. Fukuyama, M. Matsu'ura 2000. Selectivity of spontaneous rupture propagation on a branched fault. *Geophys. Res. Lett.* 27, 3635–3638.

Aochi, H., R. Madariaga 2003. The 1999 Izmit, Turkey, earthquake: Nonplanar fault structure, dynamic rupture process, and strong ground motion. *Bull. Seism. Soc. Am.* 93, 1249–1266.

Aoi, S., H. Fujiwara 1999. 3D finite-difference method using discontinuous grids. *Bull. Seism. Soc. Am.* 89, 918–930.

Appelö, D., N. A. Petersson 2009. A stable finite difference method for the elastic wave equation on complex geometries with free surfaces. *Commun. Comput. Phys.* 5, 84–107.

Archuleta, R. J. 1976. Experimental and numerical three-dimensional simulations of strike-slip earthquakes. PhD Thesis. University of California, San Diego.

Archuleta, R. J., G. A. Frazier 1978. Three-dimensional numerical simulations of dynamic faulting in a half-space. *Bull. Seism. Soc. Am.* 68, 541–572.

Assimaki, D., W. Li, J. Steidl, J. Schmedes 2008. Quantifying nonlinearity susceptibility via site-response modeling uncertainty at three sites in the Los Angeles basin. *Bull. Seism. Soc. Am.* 98, 2364–2390.

Backus, G. E. 1962. Long-wave elastic anisotropy produced by horizontal layering. *J. Geophys. Res*. 67, 4427–4440.

Balažovjech, M., L. Halada 2006. Effective computation of restoring force vector in FEM. *Kybernetika* 43, 767–776.

Bamberger, A., G. Chavent, P. Lailly 1980. Etude de schémas numériques pour les équations de l'élastodynamique linéaire. Technical Report 41, INRIA.

Barall, M. 2009. A grid-doubling finite-element technique for calculating dynamic three-dimensional spontaneous rupture on an earthquake fault. *Geophys. J. Int*. 178, 845–859.

Barenblatt, G. I. 1959. Concerning equilibrium crack forming during brittle fracture. The stability of isolated cracks. Relationship with energetic theories. *Appl. Math. Mech.* 23, 1273–1282.

Basu, U. 2009. Explicit finite element perfectly matched layer for transient three-dimensional elastic waves. *Int. J. Num. Methods Eng*. 77, 151–176.

Basu, U., A. K. Chopra 2004. Perfectly matched layers for transient elastodynamics of unbounded domains. *Int. J. Num. Methods Eng*. 61, 156–157.

Bayliss, A., K. E. Jordan, B. J. LeMesurier, E. Turkel 1986. A fourth-order accurate finite-difference scheme for the computation of elastic waves. *Bull. Seism. Soc. Am*. 76, 1115–1132.

Beeler, N. M., T. E. Tullis, J. D. Weeks 1994. The roles of time and displacement in the evolution effect in rock friction. *Geophys. Res. Lett*. 21, 1987–1990.

Belytschko, T., W. K. Liu, B. Moran 2000. *Nonlinear finite elements for continua and structures*. New York: John Wiley & Sons.

Benjemaa, M., N. Glinsky-Olivier, V. M. Cruz-Atienza, J. Virieux, S. Piperno 2007. Dynamic non-planar crack rupture by a finite volume method. *Geophys. J. Int*. 171, 271–285.

Ben-Menahem, A., S. J. Singh 2000. *Seismic Waves and Sources*, 2nd edn. Mineola, New York: Dover Publications.

Ben-Zion, Y., D. J. Andrews 1998. Properties and implications of dynamic rupture along a material interface. *Bull. Seism. Soc. Am*. 88, 1085–1094.

Bérenger, J. P. 1994. A perfectly matched layer for the absorption of electromagnetic waves. *J. Comp. Phys*. 114, 185–200.

Bernth, H., C. H. Chapman 2011. A comparison of the dispersion relations for anisotropic elastodynamic finite-difference grids. *Geophysics* 76, WA43–WA50.

Beroza, G., H. Kanamori 2009. Comprehensive overview. In H. Kanamori (ed.), *Earthquake Seismology*, 1–58, Treatise on Geophysics, Vol. 4, Amsterdam: Elsevier.

Bielak, J., R. W. Graves, K. B. Olsen, R. Taborda, L. Ramírez-Guzmán, S. M. Day, G. P. Ely, D. Roten, T. H. Jordan, P. J. Maechling, J. Urbanic, Y. Cui, G. Juve 2010. The ShakeOut earthquake scenario: Verification of three simulation sets. *Geophys. J. Int*. 180, 375–404.

Bizzarri, A. 2010. How to promote earthquake ruptures: Different nucleation strategies in a dynamic model with slip-weakening friction. *Bull. Seism. Soc. Am*. 100, 923–940.

Bizzarri, A., M. Cocco 2003. Slip-weakening behavior during the propagation of dynamic ruptures obeying rate- and state-dependent friction laws. *J. Geophys. Res*. 108, 2373–2373.

Bizzarri, A., M. Cocco 2005. 3D dynamic simulations of spontaneous rupture propagation governed by different constitutive laws with rake rotation allowed. *Annals of Geophysics* 48, 279–299.

Bizzarri, A., M. Cocco, D. J. Andrews, E. Boschi 2001. Solving the dynamic rupture problem with different numerical approaches and constitutive laws. *Geophys. J. Int.* 144, 656–678.

Blanch, J. O., J. O. A. Robertsson 1997. A modified Lax-Wendroff correction for wave propagation in media described by Zener elements. *Geophys. J. Int.* 131, 381–386.

Blanch, J. O., J. O. A. Robertsson, W. W. Symes 1995. Modeling of a constant Q: Methodology and algorithm for an efficient and optimally inexpensive viscoelastic technique. *Geophysics* 60, 176–184.

Bluck, M. J., S. P. Walker 2008. Polynomial basis functions on pyramidal elements. *Commun. Numer. Mech. Eng.* 24, 1827–1837.

Bohlen, T., E. H. Saenger 2006. Accuracy of heterogeneous staggered-grid finite-difference modeling of Rayleigh waves. *Geophysics* 71, T109–T115.

Boore, D. M. 1970. Love waves in nonuniform wave guides: Finite difference calculations. *J. Geophys. Res.* 75, 1512–1527.

Boore, D. M. 1972a. A note on the effect of simple topography on seismic SH waves. *Bull. Seism. Soc. Am.* 62, 275–284.

Boore, D. M. 1972b. Finite difference method for seismic wave propagation in heterogeneous materials. In B. A. Bolt (ed.), *Seismology: Surface Waves and Earth Oscillations*, 1–37, Methods in Computational Physics, Vol. 11, New York: Academic Press.

Boore, D. M., K. Larner, K. Aki 1971. A comparison of two independent methods for the solution of wave-scattering problems: Theoretical response of a sedimentary basin to vertically incident SH waves. *J. Geophys. Res.* 76, 588–569.

Bouchon, M. 1981. A simple method to calculate Green's functions for elastic layered media. *Bull. Seism. Soc. Am.* 71, 959–971.

Bouchon, M., F. J. Sánchez-Sesma 2007. Boundary integral equations and boundary elements methods in elastodynamics. In R.-S. Wu, V. Maupin, R. Dmowska (eds.), *Advances in Wave Propagation in Heterogeneous Earth*, 157–189, Advances in Geophysics, Vol. 48, London: Elsevier–Academic Press.

Bouchon, M., O. Coutant 1994. Calculation of synthetic seismograms in a laterally varying medium by the boundary element–discrete wavenumber method. *Bull. Seism. Soc. Am.* 84, 1869–1881.

Boyd, J. P. 2001. *Chebyshev and Fourier Spectral Methods*, 2nd edn., Mineola, New York: Dover Publications.

Campillo, M., I. R. Ionescu 1997. Initiation of antiplane shear instability under slip dependent friction. *J. Geophys. Res.* 102, 20363–20371.

Canuto, C., M. Y. Hussaini, A. Quarteroni, T. A. Zhang 1988. *Spectral Methods in Fluid Dynamics*. New York: Springer-Verlag.

Capdeville, Y., L. Guillot, J.-J. Marigo 2010a. 1-D non-periodic homogenization for the seismic wave equation. *Geophys. J. Int.* 181, 897–910.

Capdeville, Y., L. Guillot, J.-J. Marigo 2010b. 2-D non-periodic homogenization to upscale elastic media for P-SV waves. *Geophys. J. Int.* 182, 903–922.

Capdeville, Y., J.-J. Marigo 2007. Second order homogenization of the elastic wave equation for non-periodic layered media. *Geophys. J. Int.* 170, 823–838.

Capdeville, Y., J.-J. Marigo 2013. A non-periodic two scale asymptotic method to take account of rough topographies for 2-D elastic wave propagation. *Geophys. J. Int.* 192, 163–189.

Capdeville, Y., E. Stutzmann, N. Wang, J. P. Montagner 2013. Residual homogenization for seismic forward and inverse problems in layered media. *Geophys. J. Int.* 194, 470–487.

Carcione, J. M. 2001. *Wave Fields in Real Media: Wave Propagation in Anisotropic, Anelastic and Porous Media*. Oxford: Pergamon.

Carcione, J. M. 2007. *Wave Fields in Real Media: Wave Propagation in Anisotropic, Anelastic, Porous and Electromagnetic Media*. Amsterdam: Elsevier.

Carcione, J. M., D. D. Kosloff, R. Kosloff 1988a. Viscoacoustic wave propagation simulation in the earth. *Geophys. J*. 53, 769–777.

Carcione, J. M., D. D. Kosloff, R. Kosloff 1988b. Wave-propagation simulation in a linear viscoelastic medium. *Geophys. J*. 95, 597–611.

Chaljub, E., Y. Capdeville, J. P. Vilotte 2003. Solving elastodynamics in a fluid–solid heterogeneous sphere: A parallel spectral element approximation on non-conforming grids. *J. Comp. Phys*. 187, 457–491.

Chaljub, E., D. Komatitsch, J.-P. Vilotte, Y. Capdeville, B. Valette, G. Festa 2007. Spectral-element analysis in seismology. In R.-S. Wu, V. Maupin, R. Dmowska (eds.), *Advances in Wave Propagation in Heterogeneous Earth*, 365–420, Advances in Geophysics Vol. 48, London: Elsevier–Academic Press.

Chaljub, E., P. Moczo, S. Tsuno, P.-Y. Bard, J. Kristek, M. Käser, M. Stupazzini, M. Kristekova 2010. Quantitative comparison of four numerical predictions of 3D ground motion in the Grenoble Valley, France. *Bull. Seism. Soc. Am*. 100, 1427–1455.

Chavez, M., E. Cabrera, R. Madariaga, H. Chen, N. Perea, D. Emerson, A. Salazar, M. Ashworth, C. Moulinec, X. Li, M. Wu, G. Zhao 2010. Low-frequency 3D wave propagation modeling of the 12 May 2008 Mw 7.9 Wenchuan earthquake. *Bull. Seism. Soc. Am*. 100, 2561–2573.

Chavez, M., K. B. Olsen, E. Cabrera, N. Perea 2011. Observations and modeling of strong ground motions for the 9 October 1995 Mw 8 Colima-Jalisco, Mexico, earthquake. *Bull. Seism. Soc. Am*. 101, 1979–2000.

Chávez-García, F. J., D. Raptakis, K. Makra, K. Pitilakis 2000. Site effects at Euroseistest -II. Results from 2D numerical modeling and comparison with observations. *Soil Dyn. Earthq. Eng*. 19, 23–39.

Chen, J. 2011. Application of the nearly perfectly matched layer for seismic wave propagation in 2D homogeneous isotropic media. *Geophys. Prosp*. 59, 662–672.

Chen, J., C. Zhang, R. P. Bording 2010. Comparison between the nearly perfectly matched layer and unsplit convolutional perfectly matched layer methods using acoustic wave modeling. *J. Seism. Explor*. 19, 173–185.

Chen, J., J. Zhao 2011. Application of the nearly perfectly matched layer to seismic-wave propagation modeling in elastic anisotropic media. *Bull. Seism. Soc. Am*. 101, 2866–2871.

Chew, W. C., Q. H. Liu 1996. Perfectly matched layers for elastodynamics: A new absorbing boundary condition. *J. Comp. Acoustics* 4, 341–359.

Cocco, M., A. Bizzarri 2002. On the slip-weakening behavior of rate- and state-dependent constitutive laws. *Geophys. Res. Lett*. 29, 1–4.

Cocco, M., A. Bizzarri, E. Tinti 2004. Physical interpretation of the breakdown process using a rate- and state-dependent friction law. *Tectonophysics* 378, 241–262.

Cochard, A., R. Madariaga 1994. Dynamic faulting under rate-dependent friction. *PAGEOPH* 142, 419–445.

Cohen, G. C. 2002. *Higher-Order Numerical Methods for Transient Wave Equations*. Berlin: Springer.

Cohen, G., S. Fauqueux 2005. Mixed spectral finite elements for the linear elasticity system in unbounded domains. *SIAM J. Sci. Comput*. 26, 864–884.

Collino, F., T. Fouquet, P. Joly 2006. Conservative space-time mesh refinement methods for the FDTD solution of Maxwell's equations. *J. Comp. Phys*. 211, 9–35.

Collino, F., C. Tsogka 2001. Application of the perfectly matched absorbing layer model to the linear elastodynamic problem in anisotropic heterogeneous media. *Geophysics* 66, 294–307.

Cotton, F., C. Berge, F. Lemeille, A. Pitarka, B. Pitarka, M. Vallon 1998. Three-dimensional simulation of earthquakes in the Grenoble's basin. In K. Irikura *et al*. (eds.), *The Effects of Surface Geology on Seismic Motion*, Vol. 2, 873–878, Rotterdam: Balkema.

Courant, R., K. O. Friedrichs, H. Lewy 1928. Über die partiellen Differenzen-gleichungen der mathematischen Physik. *Mathematische Annalen* 100, 32–74.

Coutant, O. 1989. Program of numerical simulation Axitra. Research Report LGIT (in French), Université Joseph Fourier, Grenoble.

Coutant, O., J. Virieux, A. Zollo 1995. Numerical source implementation in a 2D finite difference scheme for wave propagation. *Bull. Seism. Soc. Am*. 85, 1507–1512.

Crase, E. 1990. High-order (space and time) finite-difference modeling of the elastic wave equation. *Annual International Meeting, Society of Exploration Geophysicists*, Expanded Abstracts, 987–991.

Crase, E., C. Wideman, M. Noble, A. Tarantola 1992. Nonlinear elastic wave-form inversion of land seismic-reflection data. *J. Geophys. Res*. 97, 4685–4703.

Cruz-Atienza, V. M., J. Virieux 2004. Dynamic rupture simulation of non-planar faults with a finite-difference approach. *Geophys. J. Int*. 158, 939–954.

Cummer, S. A. 2003. A simple, nearly perfectly matched layer for general electromagnetic media. *IEEE Microw. Wirel. Compon. Lett*. 13, 128–130.

Cunha, C. A. 1993. Elastic modeling in discontinuous media. *Geophysics* 59, 1840–1851.

Dablain, M. A. 1986. The application of high-order differencing to the scalar wave equation. *Geophysics* 51, 54–66.

Dahlen, F. A., J. Tromp 1998. *Theoretical Global Seismology*. Princeton, New Jersey: Princeton University Press.

Dalguer, L. A., S. M. Day 2006. Comparison of fault representation methods in finite difference simulations of dynamic rupture. *Bull. Seism. Soc. Am.* 96, 1764–1778.

Dalguer, L. A., S. M. Day 2007. Staggered-grid split-node method for spontaneous rupture simulation. *J. Geophys. Res.* 112, B02302.

Das, S. 1980. A numerical method for determination of source time functions for general three-dimensional rupture propagation. *Geophys. J. R. Astr. Soc.* 62, 591–604.

Daubechies, I. 1992. *Ten Lectures on Wavelets*. Philadelphia: SIAM.

Day, S. M. 1977. Finite element analysis of seismic scattering problems. PhD Dissertation. University of California, San Diego.

Day, S. M. 1982. Three-dimensional simulation of spontaneous rupture: The effect of nonuniform prestress. *Bull. Seism. Soc. Am.* 72, 1881–1902.

Day, S. M. 1998. Efficient simulation of constant Q using coarse-grained memory variables. *Bull. Seism. Soc. Am.* 88, 1051–1062.

Day, S. M., J. Bielak, D. S. Dreger, R. W. Graves, S. Larsen, K. B. Olsen, A. Pitarka 2003. Tests of 3D elastodynamic codes: Final report for Lifelines Project 1A02. Pacific Earthquake Engineering Research Center.

Day, S. M., C. R. Bradley 2001. Memory-efficient simulation of anelastic wave propagation. *Bull. Seism. Soc. Am.* 91, 520–531.

Day, S. M., L. A. Dalguer, N. Lapusta, Y. Liu 2005. Comparison of finite difference and boundary integral solutions to three-dimensional spontaneous rupture. *J. Geophys. Res.* 110, B12307.

Day, S. M., G. P. Ely 2002. Effect of a shallow weak zone on fault rupture: Numerical simulation of scale-model experiments. *Bull. Seism. Soc. Am.* 92, 3022–3041.

Day, S. M., J. B. Minster 1984. Numerical simulation of wavefields using a Padé approximant method. *Geophys. J. R. Astr. Soc.* 78, 105–118.

Day, S. M., D. Roten, K. B. Olsen 2012. Adjoint analysis of the source and path sensitivities of basin-guided waves. *Geophys. J. Int.* 189, 1103–1124.

de Basabe, J. D., M. K. Sen 2007. Grid dispersion and stability criteria of some common finite-element methods for acoustic and elastic wave equations. *Geophysics* 72, T81–T95.

de Basabe, J. D., M. K. Sen, M. F. Wheeler 2008. The interior penalty discontinuous Galerkin method for elastic wave propagation: Grid dispersion. *Geophys. J. Int.* 175, 83–93.

de Hoop, A. T. 1958. Representation theorems for the displacement in an elastic solid and their applications to elastodynamic diffraction theory. DSc Thesis. Technische Hogeschool, Delft.

de la Puente, J. 2008. *Seismic Wave Propagation for Complex Rheologies: Discontinuous Galerkin Methods for the Simulation of Earthquakes.* Saarbrücken: VDM Verlag Dr. Müller.

de la Puente, J., J.-P. Ampuero, M. Käser 2009. Dynamic rupture modeling on unstructured meshes using a discontinuous Galerkin method. *J. Geophys. Res.* 114, B10302.

de la Puente, J., M. Dumbser, M. Käser, H. Igel 2008. Discontinuous Galerkin methods for wave propagation in poroelastic media. *Geophysics* 73, T77–T97.

de la Puente, J., M. Käser, M. Dumbser, H. Igel 2007. An arbitrary high-order discontinuous Galerkin method for elastic waves on unstructured meshes – IV. Anisotropy. *Geophys. J. Int.* 169, 1210–1228.

Delcourte, S., L. Fezoui, N. Glinsky-Olivier 2009. A high-order discontinuous Galerkin method for the seismic wave propagation. *ESAIM Proc.* 27, 70–89.

De Lilla, A. 1997. Finite difference seismic wave propagation using discontinuous grid sizes. MSc Thesis. Massachusetts Institute of Technology, Massachusetts.

Di Carli, S., C. Francois-Holden, S. Peyrat, R. Madariaga 2010. Dynamic inversion of the 2000 Tottori earthquake based on elliptical subfault approximations. *J. Geophys. Res.* 115, B12328.

Dieterich, J. H. 1979. Modeling of rock friction – 1. Experimental results and constitutive equations. *J. Geophys. Res.* 84, 2161–2168.

Dieterich, J. H. 1986. A model for the nucleation of earthquake slip. In S. Das *et al.* (eds.), *Earthquake Source Mechanics*, 37–47, Geophysical Monograph 37, Maurice Ewing Series 6, Washington, D.C.: American Geophysical Union.

Donoho, D. L. 1995. De-noising by soft-thresholding. *IEEE Trans. Inf. Theory* 42, 613–627.

Drossaert, F. H., A. Giannopoulos 2007a. A nonsplit complex frequency-shifted PML based on recursive integration for FDTD modeling of elastic waves. *Geophysics* 72, T9–T17.

Drossaert, F. H., A. Giannopoulos 2007b. Complex frequency shifted convolution PML for FDTD modelling of elastic waves. *Wave Motion* 44, 593–604.

Duan, B., D. D. Oglesby 2006. Heterogeneous fault stresses from previous earthquakes and the effect on dynamics of parallel strike-slip faults. *J. Geophys. Res.* 111, B05309.

Duchon, C. E. 1979. Lanczos filtering in one and two dimensions. *J. Appl. Meteorol.* 18, 1016–1022.

Dumbser, M., M. Käser 2006. An arbitrary high-order discontinuous Galerkin method for elastic waves on unstructured meshes – II. The three-dimensional isotropic case. *Geophys. J. Int.* 167, 319–336.

Dumbser, M., M. Käser, E. F. Toro 2007. An arbitrary high-order discontinuous Galerkin method for elastic waves on unstructured meshes – V. Local time stepping and p-adaptivity. *Geophys. J. Int.* 171, 695–717.

Dunham, E. M. 2007. Conditions governing the occurrence of supershear ruptures under slip-weakening friction. *J. Geophys. Res.* 112, B07302.

Dunham, E. M., D. Belanger, L. Cong, J. E. Kozdon 2011. Earthquake ruptures with strongly rate-weakening friction and off-fault plasticity, Part 1: Planar faults. *Bull. Seism. Soc. Am.* 101, 2296–2307.

Durran, D. R. 1999. *Numerical Methods for Wave Equations in Geophysical Fluid Dynamics*. New York: Springer.

Dziewonski, A. M., T. A. Chou, J. H. Woodhouse 1981. Determination of earthquake source parameter from waveform data for studies of regional and global seismicity. *J. Geophys. Res.* 86, 2825–2852.

Dziewonski, A., B. Romanowicz 2009. Overview. In B. Romanowicz, A. Dziewonski (eds.), *Seismology and Structure of the Earth*, 1–29, Treatise on Geophysics, Vol. 1, Amsterdam: Elsevier.

Ely, G. P., S. M. Day, J.-B. Minster 2009. A support-operator method for 3-D rupture dynamics. *Geophys. J. Int.* 177, 1140–1150.

Ely, G. P., S. M. Day, J.-B. Minster 2010. Dynamic rupture models for the southern San Andreas Fault. *Bull. Seism. Soc. Am.* 100, 131–150.

Emerman, S. H., W. Schmidt, R. A. Stephen 1982. An implicit finite-difference formulation of the elastic wave equation. *Geophysics* 47, 1521–1526.

Emmerich, H. 1989. 2-D wave propagation by a hybrid method. *Geophys. J. Int.* 99, 307–319.

Emmerich, H. 1992. PSV-wave propagation in a medium with local heterogeneities: A hybrid formulation and its application. *Geophys. J. Int.* 109, 54–64.

Emmerich, H., M. Korn 1987. Incorporation of attenuation into time-domain computations of seismic wave fields. *Geophysics* 52, 1252–1264.

Etienne, V., E. Chaljub, J. Virieux, N. Glinsky 2010. An hp-adaptive discontinuous Galerkin finite-element method for 3-D elastic wave modelling. *Geophys. J. Int.* 183, 941–962.

Faccioli, E., F. Maggio, R. Paolucci, A. Quarteroni 1997. 2D and 3D elastic wave propagation by a pseudo-spectral domain decomposition method. *J. Seismology* 1, 237–251.

Favreau, P., M. Campillo, I. R. Ionescu 1999. Initiation of in-plane shear instability under slip-dependent friction. *Bull. Seism. Soc. Am.* 89, 1280–1295.

Fäh, D. 1992. A hybrid technique for the estimation of strong ground motion in sedimentary basins. Dissertation ETH 9767. Swiss Federal Institute of Technology, Zürich.

Fäh, D., P. Suhadolc, G. F. Panza 1993. Variability of seismic ground motion in complex media: The case of a sedimentary basin in the Friuli (Italy) area. *J. Appl. Geophys.* 30, 131–148.

Felippa, C. A. 2005. Introduction to finite element methods (ASEN 5007). Lecture notes. University of Colorado, Boulder.

Festa, G. 2004. Slip imaging by isochron back projection and source dynamics with spectral element methods. Tesi di Dottorato in Geofisica, Universita degli studi di Bologna.

Festa, G., E. Delavaud, J. P. Vilotte 2005. Interaction between surface waves and absorbing boundaries for wave propagation in geological basins: 2D numerical simulations. *Geophys. Res. Lett.* 32, L20306.

Festa, G., S. B. Nielsen 2003. PML absorbing boundaries. *Bull. Seism. Soc. Am.* 93, 891–903.

Festa, G., J. P. Vilotte 2005. The Newmark scheme as velocity–stress time-staggering: An efficient PML implementation for spectral element simulations of elastodynamics. *Geophys. J. Int.* 161, 789–812.

Festa, G., J.-P. Vilotte 2006. Influence of rupture initiation on the intersonic transition: Crack-like versus pulse-like modes. *Geophys. Res. Lett.* 33, L15320.

Festa, G., A. Zollo 2012. From data to source parameters: Kinematic modeling. In A. Bizzarri, H. S. Bhat (eds.), *The Mechanics of Faulting: From Laboratory to Real Earthquakes*, 5–62, Kerala, India: Research Signpost.

Fichtner, A. 2011. *Full Seismic Waveform Modelling and Inversion*. Heidelberg: Springer.

Flanagan, D. P., T. Belytschko 1981. A uniform strain hexahedron and quadrilateral with orthogonal hourglass control. *Int. J. Num. Methods Eng.* 17, 679–706.

Flandrin, P. 1999. *Time-Frequency/Time-Scale Analysis*. San Diego: Academic Press.

Flandrin, P., P. Goncalves, G. Rilling 2004. Detrending and denoising with Empirical Mode Decompositions. *EUSIPCO-04* 1581–1584.

Fornberg, B. 1987. The pseudospectral method: Comparisons with finite differences for the elastic wave equation. *Geophysics* 52, 483–501.

Fornberg, B. 1988a. Generation of finite difference formulas on arbitrarily spaced grids. *Math. Computation* 51, 699–706.

Fornberg, B. 1988b. The pseudospectral method: Accurate representation of interfaces in elastic wave calculations. *Geophysics* 53, 625–637.

Forsythe, G. E., W. R. Wasow 2004. *Finite-Difference Methods for Partial Differential Equations*. Mineola, New York: Dover Publications.

Frankel, A. 1993. Three-dimensional simulations of ground motions in the San Bernardino Valley, California, for hypothetical earthquakes on the San Andreas fault. *Bull. Seism. Soc. Am.* 83, 1020–1041.

Frankel, A., W. Leith 1992. Evaluation of topographic effects on P-waves and S-waves of explosions at the Northern Novaya-Zemlya test site using 3-D numerical simulations. *Geophys. Res. Lett.* 19, 1887–1890.

Frankel, A., W. R. Stephenson, D. Carver 2009. Sedimentary basin effects in Seattle, Washington: Ground-motion observations and 3D simulations. *Bull. Seism. Soc. Am.* 99, 1579–1611.

Frankel, A., J. E. Vidale 1992. A three-dimensional simulation of seismic waves in the Santa Clara Valley, California, from a Loma Prieta aftershock. *Bull. Seism. Soc. Am.* 82, 2031–2045.

Frazier, G. A., C. M. Petersen 1974. 3-D stress wave code for the Illiac IV. Systems, Science and Software Report, SSS-R-74–2103.

Fukuyama, E., R. Ando, C. Hashimoto, S. Aoi, M. Matsu'ura 2009. A physics-based simulation of the 2003 Tokachi-oki, Japan, earthquake to predict strong ground motions. *Bull. Seism. Soc. Am.* 99, 3150–3171.

Gaffet, S., M. Bouchon 1989. Effects of two-dimensional topographies using the discrete wavenumber-boundary integral equation method in P-SV cases. *J. Acoust. Soc. Am.* 85, 2277–2283.

Galis, M., P. Moczo, J. Kristek 2008. A 3-D hybrid finite-difference–finite-element viscoelastic modelling of seismic wave motion. *Geophys. J. Int.* 175, 153–184.

Galis, M., P. Moczo, J. Kristek, M. Kristeková 2010. An adaptive smoothing algorithm in the TSN modelling of rupture propagation with the linear slip-weakening friction law. *Geophys. J. Int.* 180, 418–432.

Galis, M., C. Pelties, J. Kristek, P. Moczo, J.-P. Ampuero, P. M. Mai 2014. On initiation of dynamic rupture propagation with linear slip-weakening friction. *Geophys. J. Int*., submitted.

Gao, H., J. Zhang 2008. Implementation of perfectly matched layers in an arbitrary geometrical boundary for elastic wave modelling. *Geophys. J. Int.* 174, 1029–1036.

Gazdag, J. 1981. Modeling of the acoustic wave equation with transform methods. *Geophysics* 46, 854–859.

Gélis, C., L. F. Bonilla 2012. 2-D P–SV numerical study of soil–source interaction in a non-linear basin. *Geophys. J. Int.* 191, 1374–1390.

Geller, R. J., H. Mizutani, N. Hirabayashi 2012. Existence of a second island of stability of predictor-corrector schemes for calculating synthetic seismograms. *Geophys. J. Int.* 188, 253–262.

Geller, R. J., T. Ohminato 1994. Computation of synthetic seismograms and their partial derivatives for heterogeneous media with arbitrary natural boundary conditions using the direct solution method. *Geophys. J. Int.* 116, 421–446.

Geller, R. J., N. Takeuchi 1995. A new method for computing highly accurate DSM synthetic seismograms. *Geophys. J. Int.* 123, 449–470.

Geller, R. J., N. Takeuchi 1998. Optimally accurate second-order time-domain finite difference scheme for the elastic equation of motion: One-dimensional case. *Geophys. J. Int.* 135, 48–62.

Gottlieb, D., E. Turkel 1976. Dissipative two-four methods for time-dependent problems. *Math. Comp.* 30, 703–723.

Gottschämmer, E., K. B. Olsen 2001. Accuracy of the explicit planar free-surface boundary condition implemented in a fourth-order staggered-grid velocity–stress finite-difference scheme. *Bull. Seism. Soc. Am.* 91, 617–623.

Graves, R. W. 1993. Modeling three-dimensional site response effects in the Marina District Basin, San Francisco, California. *Bull. Seism. Soc. Am.* 83, 1042–1063.

Graves, R. W. 1996. Simulating seismic wave propagation in 3D elastic media using staggered-grid finite differences. *Bull. Seism. Soc. Am.* 86, 1091–1106.

Graves, R. W. 1998. Three-dimensional finite-difference modeling of the San Andreas fault: Source parameterization and ground-motion levels. *Bull. Seism. Soc. Am.* 88, 881–897.

Graves, R. W., B. T. Aagaard 2011. Testing long-period ground-motion simulations of scenario earthquakes using the Mw 7.2 El Mayor-Cucapah mainshock: Evaluation of finite-fault rupture characterization and 3D seismic velocity models. *Bull. Seism. Soc. Am.* 101, 895–907.

Graves, R. W., B. Aagaard, K. Hudnut, L. Star, J. Stewart, T. H. Jordan 2008. Broadband simulations for Mw 7.8 southern San Andreas earthquakes: ground motion sensitivity to rupture speed. *Geophys. Res. Lett.* 35, L22302.

Graves, R. W., S. M. Day 2003. Stability and accuracy analysis of coarse-grain viscoelastic simulations. *Bull. Seism. Soc. Am.* 93, 283–300.

Graves, R. W., A. Pitarka 2010. Broadband ground-motion simulation using a hybrid approach. *Bull. Seism. Soc. Am.* 100, 2095–2123.

Graves, R. W., A. Pitarka, P. G. Somerville 1998. Ground-motion amplification in the Santa Monica area: Effects of shallow basin-edge structure *Bull. Seism. Soc. Am.* 88, 1224–1242.

Guatteri, M., P. Spudich 2000. What can strong-motion data tell us about slip-weakening fault-friction laws? *Bull. Seism. Soc. Am.* 90, 98–116.

Gubbins, D. 1990. *Seismology and Plate Tectonics*. Cambridge: Cambridge University Press.

Harmsen, S. C., S. H. Hartzell, P. Liu 2008. Simulated ground motion in Santa Clara Valley, California, and vicinity from M ≥ 6.7 scenario earthquakes. *Bull. Seism. Soc. Am.* 98, 1243–1271.

Harris, R. A., M. Barall, R. J. Archuleta, E. M. Dunham, B. T. Aagaard, J.-P. Ampuero, H. S. Bhat, V. M. Cruz-Atienza, L. A. Dalguer, P. Dawson, S. M. Day, B. Duan, G. P. Ely, Y. Kaneko, Y. Kase, N. Lapusta, Y. Liu, S. Ma, D. D. Oglesby, K. B. Olsen, A. Pitarka, S. Song, E. Templeton 2009. The SCEC/USGS dynamic earthquake rupture code verification exercise. *Seismol. Res. Lett.* 80, 119–126.

Harris, R. A., S. M. Day 1997. Effects of a low-velocity zone on a dynamic rupture. *Bull. Seism. Soc. Am.* 87, 1267–1280.

Harris, R. A., J. F. Dolan, R. Hartleb, S. M. Day 2002. The 1999 Izmit, Turkey, earthquake: A 3D dynamic stress transfer model of intraearthquake triggering. *Bull. Seism. Soc. Am.* 92, 245–255.

Hartzell, S. H., S. C. Harmsen, A. Frankel 2010. Effects of 3D random correlated velocity perturbations on predicted ground motions. *Bull. Seism. Soc. Am.* 100, 1415–1426.

Hartzell, S. H., T. H. Heaton 1983. Inversion of strong ground motion and teleseismic waveform data for the fault rupture history of the 1979 Imperial Valley, California, earthquake. *Bull. Seism. Soc. Am.* 73, 1553–1583.

Hastings, F. D., J. B. Schneider, S. L. Broschat 1996. Application of the perfectly matched layer (PML) absorbing boundary condition to elastic wave propagation. *J. Acoust. Soc. Am.* 100, 3061–3069.

Hayashi, K., D. R. Burns, M. N. Toksöz 2001. Discontinuous-grid finite-difference seismic modeling including surface topography. *Bull. Seism. Soc. Am.* 91, 1750–1764.

Helbig, K. 1984. Anisotropy and dispersion in periodically layered media. *Geophysics* 49, 364–373.

Hestholm, S. O. 1999. Three-dimensional finite difference viscoelastic wave modelling including surface topography. *Geophys. J. Int.* 139, 852–878.

Hestholm, S. O. 2003. Elastic wave modeling with free surfaces: Stability of long simulations. *Geophysics* 68, 314–321.

Hestholm, S. O., B. O. Ruud 1994. 2D finite-difference elastic wave modelling including surface topography. *Geophys. Prosp.* 42, 371–390.

Hestholm, S. O., B. O. Ruud 1998. 3-D finite-difference elastic wave modeling including surface topography. *Geophysics* 63, 613–622.

Hestholm, S. O., B. O. Ruud 2002. 3D free-boundary conditions for coordinate-transform finite-difference seismic modelling. *Geophys. Prosp.* 50, 463–474.

Hestholm, S. O., B. O. Ruud, E. S. Husebye 1999. 3-D versus 2-D finite-difference seismic synthetics including real surface topography. *Phys. Earth Planet. Int.* 113, 339–354.

Hisada, Y. 1994. An efficient method for computing Green's functions for a layered half-space with sources and receivers at close depths. *Bull. Seism. Soc. Am.* 84, 1456–1472.

Hisada, Y. 1995. An efficient method for computing Green's functions for a layered half-space with sources and receivers at close depths (Part 2). *Bull. Seism. Soc. Am.* 85, 1080–1093.

Hixon, R. 1996. On increasing the accuracy of MacCormack schemes for aeroacoustic applications. NASAContractor Report 202311 ICOMP-96–11.

Hixon, R. 1997. Evaluation of a high-accuracy MacCormack-type scheme using benchmark problems. *J. Comp. Acoustics* 6, 291–305.

Holberg, O. 1987. Computational aspects of the choice of operator and sampling interval for large-scale simulation of wave phenomena. *Geophys. Prosp.* 35, 629–655.

Hollender F., M. Manakou, P.-Y. Bard, E. Chaljub, D. Raptakis, K. Pitilakis, S. Tsuno 2010. Euroseistest verification and validation project: An international effort to evaluate ground motion numerical simulation relevance. *Seismol. Res. Lett.* 81, 322.

Holschneider, M. 1995. *Wavelets: An Analysis Tool*. Oxford: Clarendon Press.

Hughes, T. J. R. 2000. The finite element method: Linear static and dynamic finite element method analysis. Mineola, New York: Dover Publications.

Ida, Y. 1972. Cohesive force across the tip of a longitudinal-shear crack and Griffith's specific surface energy. *J. Geophys. Res.* 77, 3796–3805.

Ide, S. 2009. Slip inversion. In H. Kanamori (ed.), *Earthquake Seismology*, 193–223, Treatise on Geophysics, Vol. 4, Amsterdam: Elsevier.

Igel, H., P. Mora, B. Riollet 1995. Anisotropic wave propagation through finite-difference grids. *Geophysics* 60, 1203–1216.

Ilan, A. 1977. Finite-difference modeling for P-pulse propagation in elastic media with arbitrary polygonal surface. *J. Geophys. Res.* 43, 41–58.

Ilan, A., D. Loewenthal 1976. Instability of finite difference schemes due to boundary conditions in elastic media. *Geophys. Prosp.* 24, 431–453.

Ilan, A., A. Ungar, Z. S. Alterman 1975. An improved representation of boundary conditions in finite difference schemes for seismological problems. *Geophys. J. R. Astr. Soc.* 43, 727–745.

Imperatori, W., P. M. Mai 2013. Broad-band near-field ground motion simulations in 3-dimensional scattering media. *Geophys. J. Int.* 192, 725–744.

Ionescu, I. R., M. Campillo 1999. Influence of the shape of the friction law and fault finiteness on the duration of initiation. *J. Geophys. Res.* 104, 3013–3024.

Isaacson, E., H. B. Keller 1966. *Analysis of Numerical Methods*. New York: J. Wiley & Sons.

Iwaki, A., T. Iwata 2010. Simulation of long-period ground motion in the Osaka sedimentary basin: Performance estimation and the basin structure effects. *Geophys. J. Int.* 181, 1062–1076.

Iwan, W. D. 1967. On a class of models for the yielding behavior of continuous and composite systems. *J. Appl. Mech.* 34, 612–617.

JafarGandomi, A., H. Takenaka 2009. Non-standard FDTD for elastic wave simulation: Two-dimensional P-SV case. *Geophys. J. Int.* 178, 282–302.

Jastram, C., A. Behle 1992. Acoustic modeling on a grid of vertically varying spacing. *Geophys. Prosp.* 40, 157–169.

Jastram, C., E. Tessmer 1994. Elastic modeling on a grid of vertically varying spacing. *Geophys. Prosp.* 42, 357–370.

Jih, R.-S., K. L. McLaughlin, Z. A. Der 1988. Free-boundary conditions of arbitrary polygonal topography in a two-dimensional explicit elastic finite-difference scheme. *Geophysics* 53, 1045–1055.

Joyner, W. B., A. T. F. Chen 1975. Calculation of nonlinear ground response in earthquakes. *Bull. Seism. Soc. Am.* 65, 1315–1336.

Kaneko, Y., J.-P. Ampuero, N. Lapusta 2011. Spectral-element simulations of long-term fault slip: Effect of low-rigidity layers on earthquake-cycle dynamics. *J. Geophys. Res.* 116, B10313.

Kaneko, Y., N. Lapusta, J.-P. Ampuero 2008. Spectral-element modeling of spontaneous earthquake rupture on rate and state faults: Effect of velocity-strengthening friction at shallow depths. *J. Geophys. Res.* 113, B09317.

Kang, T.-S., C.-E. Baag 2004a. An efficient finite-difference method for simulating 3D seismic response of localized basin structures. *Bull. Seism. Soc. Am.* 94, 1690–1705.

Kang, T.-S., C.-E. Baag 2004b. Finite-difference seismic simulation combining discontinuous grids with locally variable timesteps. *Bull. Seism. Soc. Am.* 94, 207–219.

Käser, M., M. Dumbser 2006. An arbitrary high-order discontinuous Galerkin method for elastic waves on unstructured meshes – I. The two-dimensional isotropic case with external source terms. *Geophys. J. Int.* 166, 855–877.

Käser, M., M. Dumbser, J. de la Puente, H. Igel 2007. An arbitrary high-order discontinuous Galerkin method for elastic waves on unstructured meshes – III. Viscoelastic attenuation. *Geophys. J. Int.* 168, 224–242.

Kausel, E., D. Assimaki 2002. Seismic simulation of inelastic soils via frequency-dependent moduli and damping. *J. Engrg. Mech.* 128, 34–47.

Kawase, H. 1988. Time-domain response of a semi-circular canyon for incident SV, P, and Rayleigh waves calculated by the discrete wavenumber boundary element method. *Bull. Seism. Soc. Am.* 78, 1415–1437.

Kelly, K. R., K. J. Marfurt (eds.) 1990. *Numerical Modeling of Seismic Wave Propagation*. Geophysical Reprint Series No. 13. Tulsa, Oklahoma: Society of Exploration Geophysicists.

Kelly, K. R., R. W. Ward, S. Treitel, R. M. Alford 1976. Synthetic seismograms: A finite-difference approach. *Geophysics* 41, 2–27.

Kennett, B. L. N. 2001. *The Seismic Wavefield. Vol. I: Introduction and Theoretical Development*. Cambridge: Cambridge University Press.

Kim, A., D. S. Dreger, S. Larsen 2010. Moderate earthquake ground-motion validation in the San Francisco Bay Area. *Bull. Seism. Soc. Am.* 100, 819–825.

Kindelan, M., A. Kamel, P. Sguazzero 1990. On the construction and efficiency of staggered numerical differentiators for the wave equation. *Geophysics* 55, 107–110.

Klimeš, L. 1996. Accuracy of elastic finite differences in smooth media. *PAGEOPH* 148, 39–76.

Klin, P., E. Priolo, G. Seriani 2010. Numerical simulation of seismic wave propagation in realistic 3-D geo-models with a Fourier pseudo-spectral method. *Geophys. J. Int.* 183, 905–922.

Knopoff, L. 1956. Diffraction of elastic waves. *J. Acoust. Soc. Am.* 28, 217–229.

Komatitsch, D., G. Erlebacher, D. Goeddeke, D. Michea 2010. High-order finite-element seismic wave propagation modeling with MPI on a large GPU cluster. *J. Comp. Phys.* 229, 7692–7714.

Komatitsch, D., Q. Liu, J. Tromp, P. Suss, C. Stidham, J. H. Shaw 2004. Simulations of ground motion in the Los Angeles basin based upon the spectral-element method. *Bull. Seism. Soc. Am.* 94, 187–206.

Komatitsch, D., R. Martin 2007. An unsplit convolutional perfectly matched layer improved at grazing incidence for the seismic wave equation. *Geophysics* 72, SM155–SM167.

Komatitsch, D., J. Tromp 1999. Introduction to the spectral-element method for 3-D seismic wave propagation. *Geophys. J. Int.* 139, 806–822.

Komatitsch, D., J. Tromp 2003. A perfectly matched layer absorbing boundary condition for the second-order seismic wave equation. *Geophys. J. Int.* 154, 146–153.

Komatitsch, D., S. Tsuboi, J. Tromp 2005. The spectral-element method in seismology. In A. Levander, G. Nolet (eds.), *Seismic Earth: Array Analysis of Broadband Seismograms*, 205–227. Washington, D.C.: American Geophysical Union.

Komatitsch, D., J.-P. Vilotte 1998. The spectral element method: An efficient tool to simulate the seismic response of 2D and 3D geological structures. *Bull. Seism. Soc. Am.* 88, 368–392.

Kopriva, D. A. 1989. Domain decomposition with both spectral and finite-difference methods for the accurate computation of flows with shocks. *Appl. Numer. Math.* 6, 141–151.

Korn, G. A., T. M. Korn 2000. *Mathematical Handbook for Scientists and Engineers*. Mineola, New York: Dover Publications.

Kosloff, D. D., M. Reshef, D. Loewenthal 1984. Elastic wave calculations by the Fourier method. *Bull. Seism. Soc. Am.* 74, 875–891.

Kostrov, B. V., S. Das 2005. *Principles of Earthquake Source Mechanics*. Cambridge: Cambridge University Press.

Kozdon, J. E., E. M. Dunham, J. Nordström 2011. Interaction of waves with frictional interfaces using summation-by-parts difference operators: Weak enforcement of nonlinear boundary conditions. *J. Sci. Comput.* 50, 341–367.

Kozdon, J. E., E. M. Dunham, J. Nordström 2013. Simulation of dynamic earthquake ruptures in complex geometries using high-order finite-difference methods. *J. Sci. Comput.* 55, 92–124.

Kramer, S. L. 1996. *Geotechnical Earthquake Engineering*. New Jersey: Prentice Hall.

Kreiss, H. O., J. Oliger 1972. Comparison of accurate methods for the integration of hyperbolic equations. *Tellus* 24, 199–215.

Kreiss, H. O., N. A. Petersson 2006. A second order accurate embedded boundary method for the wave equation with Dirichlet data. *SIAM J. Sci. Comp.* 27, 1141–1167.

Kreiss, H.-O., N. A. Petersson 2012. Boundary estimates for the elastic wave equation in almost incompressible materials. *SIAM J. Numer. Anal.* 50, 1556–1580.

Kristek, J., P. Moczo 2003. Seismic-wave propagation in viscoelastic media with material discontinuities: A 3D fourth-order staggered-grid finite-difference modeling. *Bull. Seism. Soc. Am.* 93, 2273–2280.

Kristek, J., P. Moczo 2006. On the accuracy of the finite-difference schemes: The 1D elastic problem. *Bull. Seism. Soc. Am.* 96, 2398–2414.

Kristek, J., P. Moczo, R. J. Archuleta 2002. Efficient methods to simulate planar free surface in the 3D 4th-order staggered-grid finite-difference schemes. *Studia Geoph. Geod.* 46, 355–381.

Kristek, J., P. Moczo, M. Galis 2006. Comparison of the 2nd-order and 4th-order staggered-grid finite-difference. Implementations of the TSN method for rupture propagation. *EoS Trans. AGU*, 87(52), Fall Meeting Supplement, Abstract S41C–1341.

Kristek, J., P. Moczo, M. Galis 2009. A brief summary of some PML formulations and discretizations for the velocity–stress equation of seismic motion. *Studia Geoph. Geod.* 53, 459–474.

Kristek, J., P. Moczo, M. Galis 2010. Stable discontinuous staggered grid in the finite-difference modelling of seismic motion. *Geophys. J. Int.* 183, 1401–1407.

Kristek, J., P. Moczo, K. Irikura, T. Iwata, H. Sekiguchi 1999. The 1995 Kobe mainshock simulated by the 3D finite differences. In K. Irikura *et al.* (eds.), *The Effects of Surface Geology on Seismic Motion 3*, 1361–1368, Rotterdam: Balkema.

Kristekova, M., M. Galis, P. Moczo, J. Kristek 2012. Quantitative evaluation of efficiency of the methods for a posteriori filtration of the slip-rate time histories. *Geophys. Res. Abstracts* 14, EGU2012–6997.

Kristekova, M., J. Kristek, P. Moczo 2009. Time-frequency misfit and goodness-of-fit criteria for quantitative comparison of time signals. *Geophys. J. Int.* 178, 813–825.

Kristekova, M., J. Kristek, P. Moczo, S. M. Day 2006. Misfit criteria for quantitative comparison of seismograms. *Bull. Seism. Soc. Am.* 96, 1836–1850.

Kristekova, M., P. Moczo, P. Labák, A. Cipciar, L. Fojtikova, J. Madaras, J. Kristek 2008. Time-frequency analysis of explosions in the ammunition factory in Novaky, Slovakia. *Bull. Seism. Soc. Am.* 98, 2507–2516.

Kummer, B., A. Behle 1982. Second-order finite-difference modeling of SH-wave propagation in laterally inhomogeneous media. *Bull. Seism. Soc. Am.* 72, 793–808.

Kummer, B., A. Behle, F. Dorau 1987. Hybrid modeling of elastic-wave propagation in two-dimensional laterally inhomogeneous media. *Geophysics* 52, 765–771.

Lan, H., Z. Zhang 2011. Three-dimensional wave-field simulation in heterogeneous transversely isotropic medium with irregular free surface. *Bull. Seism. Soc. Am.* 101, 1354–1370.

Langston, C. A., J. S. Barker, G. B. Pavlin 1982. Point-source inversion techniques. *Phys. Earth Planet. Int.* 30, 228–241.

Lapusta, N., J. R. Rice 2003. Nucleation and early seismic propagation of small and large events in a crustal earthquake model. *J. Geophys. Res.* 108, 2205.

Lapusta, N., J. R. Rice, Y. Ben-Zion, G. T. Zheng 2000. Elastodynamic analysis for slow tectonic loading with spontaneous rupture episodes on faults with rate- and state-dependent friction. *J. Geophys. Res.* 105, 23765–23789.

Lax, P. D., B. Wendroff 1960. Systems of conservation laws. *Comm. Pure Appl. Math.* 13, 217–237.

Lay, T., T. C. Wallace 1995. *Modern Global Seismology*. San Diego: Academic Press.

Lecomte, I., H. Gjøystdal, F. Maaø, R. Bakke, A. Drottning, T. A. Johansen 2004. Efficient and flexible seismic modelling of reservoirs: The HybriSeis concept. *The Leading Edge* 23, 432–437.

Lee, S.-J., Y.-C. Chan, D. Komatitsch, B.-S. Huang, J. Tromp 2009. Effects of realistic surface topography on seismic ground motion in the Yangminshan region of Taiwan based upon the spectral-element method and LiDAR DTM. *Bull. Seism. Soc. Am.* 99, 681–693.

Lee, S.-J., H.-W. Chen, B.-S. Huang 2008a. Simulations of strong ground motion and 3D amplification effect in the Taipei Basin by using a composite grid finite-difference method. *Bull. Seism. Soc. Am.* 98, 1229–1242.

Lee, S.-J., H.-W. Chen, Q. Liu, D. Komatitsch, B.-S. Huang, J. Tromp 2008b. Three-dimensional simulations of seismic-wave propagation in the Taipei basin with realistic topography based upon the spectral-element method. *Bull. Seism. Soc. Am.* 98, 253–264.

Lele, S. K. 1992. Compact finite difference schemes with spectral-like resolution. *J. Comp. Phys.* 103, 16–42.

Levander, A. R. 1988. Fourth-order finite-difference P-SV seismograms. *Geophysics* 53, 1425–1436.

LeVeque, R. J. 2007. *Finite Difference Methods for Ordinary and Partial Differential Equations: Steady-State and Time-Dependent Problems*. Philadelphia: SIAM.

Lisitsa, V., O. Podgornova, V. Tcheverda 2010. On the interface error analysis for finite difference wave simulation. *Comput. Geosci.* 14, 769–778.

Lisitsa, V., D. Vishnevskiy 2010. Lebedev scheme for the numerical simulation of wave propagation in 3D anisotropic elasticity. *Geophys. Prosp.* 58, 619–635.

Liu, H.-P., D. L. Anderson, H. Kanamori 1976. Velocity dispersion due to anelasticity: Implications for seismology and mantle composition. *Geophys. J. R. Astr. Soc.* 47, 41–58.

Liu, P. C., R. J. Archuleta 2004. A new nonlinear finite fault inversion with three-dimensional Green's functions: Application to the 1989 Loma Prieta, California, earthquake. *J. Geophys. Res.* 109, B02318.

Liu, P., R. J. Archuleta 2006. Efficient modeling of Q for 3D numerical simulation of wave propagation. *Bull. Seism. Soc. Am.* 96, 1352–1358.

Liu, P., R. J. Archuleta, S. H. Hartzell 2006. Prediction of broadband ground-motion time histories: Hybrid low/high-frequency method with correlated random source parameters. *Bull. Seism. Soc. Am.* 96, 2118–2130.

Liu, T., T. Hu, M. K. Sen, J. Yang, R. Wang, J. Wei, S. Wang 2011. A hybrid scheme for seismic modelling based on Galerkin method. *Geophys. J. Int.* 186, 1165–1178.

Liu, T., Y. Luan 2013. Mesh grading approach for wave propagation in high velocity-contrast media. *Soil. Dyn. Earthq. Eng.* 50, 182–191.

Liu, Y., N. Lapusta 2008. Transition of mode II cracks from sub-Rayleigh to inter-sonic speeds in the presence of favorable heterogeneity. *J. Mech. Phys. Solids* 56, 25–50.

Liu, Y., M. K. Sen 2009. An implicit staggered-grid finite-difference method for seismic modelling. *Geophys. J. Int.* 179, 459–474.

Liu, Y., M. K. Sen 2010. A hybrid scheme for absorbing edge reflections in numerical modeling of wave propagation. *Geophysics* 75, A1–A6.

Liu, Y., M. K. Sen 2011a. Finite-difference modeling with adaptive variable-length spatial operators. *Geophysics* 76, T79–T89.

Liu, Y., M. K. Sen 2011b. Scalar wave equation modeling with time-space domain dispersion-relation-based staggered-grid finite-difference schemes. *Bull. Seism. Soc. Am.* 101, 141–159.

Loewenthal, D., Z. S. Alterman 1972. Theoretical seismograms for the two welded quarter-planes. *Bull. Seism. Soc. Am.* 62, 619–630.

Lombard, B., J. Piraux 2004. Numerical treatment of two-dimensional interfaces for acoustic and elastic waves. *J. Comp. Phys.* 195, 90–116.

Lombard, B., J. Piraux, C. Gélis, J. Virieux 2008. Free and smooth boundaries in 2-D finite-difference schemes for transient elastic waves. *Geophys. J. Int.* 172, 252–261.

Luo, Y., G. Schuster 1990. Parsimonious staggered grid finite-differencing of the wave equation. *Geophys. Res. Lett.* 17, 155–158.

Ma, S. 2008. A physical model for widespread near-surface and fault zone damage induced by earthquakes. *Geochem. Geophy. Geos.* 9, 1–9.

Ma, S., R. J. Archuleta 2006. Radiated seismic energy based on dynamic rupture models of faulting. *J. Geophys. Res.* 111, B05315.

Ma, S., R. J. Archuleta, P. Liu 2004. Hybrid modeling of elastic P-SV wave motion: A combined finite-element and staggered-grid finite-difference approach. *Bull. Seism. Soc. Am.* 94, 1557–1563.

Ma, S., S. Custódio, R. J. Archuleta, P. Liu 2008. Dynamic modeling of the 2004 Mw 6.0 Parkfield, California, earthquake. *J. Geophys. Res.* 113, B02301.

Ma, S., P. Liu 2006. Modeling of the perfectly matched layer absorbing boundaries and intrinsic attenuation in explicit finite-element methods. *Bull. Seism. Soc. Am.* 96, 1779–1794.

MacCormack, R. W. 1969. The effect of viscosity in hypervelocity impact cratering. AIAA Paper 69-354.

MacCormack, R. W. 1971. Numerical solution of the interaction of a shock wave with a laminar boundary layer. In M. Holt (ed.), *Proceedings of the Second International*

Conference on Numerical Methods in Fluid Dynamics, 151–163, Lecture Notes in Physics, New York: Springer-Verlag.

Macpherson, K. A., E. W. Woolery, Z. Wang, P. Liu 2010. Three-dimensional long-period ground-motion simulations in the Upper Mississippi Embayment. *Seismol. Res. Lett.* 81, 391–405.

Madariaga, R. 1974. Seismic radiation from dynamic frictional faulting models. *EOS Trans. AGU* 56, 1147.

Madariaga, R. 1976. Dynamics of an expanding circular fault. *Bull. Seism. Soc. Am.* 66, 639–666.

Madariaga, R., J.-P. Ampuero, M. Adda-Bedia 2006. Seismic radiation from simple models of earthquakes. In R. Abercrombie *et al.* (eds.), *Earthquakes: Radiated Energy and the Physics of Faulting*, 223–236, Washington, D.C.: American Geophysical Union.

Madariaga, R., K. B. Olsen, R. J. Archuleta 1998. Modeling dynamic rupture in a 3D earthquake fault model. *Bull. Seism. Soc. Am.* 88, 1182–1197.

Maday, Y., A. T. Patera 1989. Spectral element methods for the incompressible Navier–Stokes equations. In A. K. Noor, J. T. Oden (eds.), *State of the Art Survey in Computational Mechanics*, 71–143, New York: ASME.

Maeda, T., T. Furumura, S. Noguchi, S. Takemura, S. Sakai, M. Shinohara, K. Iwai, S.-J. Lee 2013. Seismic- and tsunami-wave propagation of the 2011 off the Pacific coast of Tohoku earthquake as inferred from the tsunami-coupled finite-difference simulation. *Bull. Seism. Soc. Am.* 103, 1456–1472.

Maggio, F., A. Quarteroni 1994. Acoustic wave propagation by spectral methods. *East-West J. Numer. Math.* 2, 129–150.

Magnier, S.-A., P. Mora, A. Tarantola 1994. Finite differences on minimal grids. *Geophysics* 59, 1435–1443.

Mai, P. M., W. Imperatori, K. B. Olsen 2010. Hybrid broadband ground-motion simulations: Combining long-period deterministic synthetics with high-frequency multiple S-to-S backscattering. *Bull. Seism. Soc. Am.* 100, 2124–2142.

Makra, K., F. J. Chávez-García, D. Raptakis, K. Pitilakis 2005. Parametric analysis of the seismic response of a 2D sedimentary valley: Implications for code implementations of complex site effects. *Soil Dyn. Earthq. Eng.* 25, 303–315.

Makra, K., D. Raptakis, F. J. Chávez-García, K. Pitilakis 2001. Site effects and design provisions: The case of Euroseistest. *PAGEOPH* 158, 2349–2367.

Manakou, M. 2007. Contribution of the determination of a 3D soil model for the site response study. Application to the sedimentary Mygdonian basin. PhD Thesis (in Greek, with English summary). Department of Civil Engineering, Aristotle University of Thessaloniki.

Manakou, M., F. J. Chávez-García, K. Pitilakis 2007. The 3D geological structure of the Mygdonian sedimentary basin (Greece). 4th International Conference on Earthquake Geotechnical Engineering, June 25–28, 2007, Paper No. 1686.

Manakou, M. V., D. G. Raptakis, F. J. Chávez-García, P. I. Apostolidis, K. D. Pitilakis 2010. 3D soil structure of the Mygdonian basin for site response analysis. *Soil Dyn. Earthq. Eng.* 30, 1198–1211.

Marcinkovich, C., K. B. Olsen 2003. On the implementation of perfectly matched layers in a three-dimensional fourth-order velocity–stress finite difference scheme. *J. Geophys. Res.* 108, 2276–2276.

Marchuk, G. I. 1982. *Methods of Numerical Mathematics*. Berlin, Heidelberg: Springer.

Marfurt, K. J. 1984. Accuracy of finite-difference and finite-element modeling of the scalar and elastic wave equations. *Geophysics* 49, 533–549.

Martin, R., D. Komatitsch 2009. An unsplit convolutional perfectly matched layer technique improved at grazing incidence for the viscoelastic wave equation. *Geophys. J. Int.* 179, 333–344.

Martin, R., D. Komatitsch, A. Ezziani 2008a. An unsplit convolutional perfectly matched layer improved at grazing incidence for seismic wave propagation in poroelastic media. *Geophysics* 73, T51–T61.

Martin, R., D. Komatitsch, S. D. Gedney 2008b. A variational formulation of a stabilized unsplit convolutional perfectly matched layer for the isotropic or anisotropic seismic wave equation. *Comput. Model. Eng. Sci.* 37, 274–304.

Masing, G. 1926. Eigenspannungen und verfertigung beim messing. In *Proceedings 2nd International Congress of Applied Mechanics*, Zürich, Switzerland, 332–335.

McDonal, F. J., F. A. Angona, L. R. Mills, R. L. Sengbush, R. G. van Nostrand, J. E. White 1958. Attenuation of shear and compressional waves in Pierre shale. *Geophysics* 23, 421–439.

Mena, B., P. M. Mai, K. B. Olsen, M. D. Purvance, J. N. Brune 2010. Hybrid broadband ground-motion simulation using scattering Green's functions: Application to large-magnitude events. *Bull. Seism. Soc. Am.* 100, 2143–2162.

Mercerat, E. D., J.-P. Vilotte, F. J. Sánchez-Sesma 2006. Triangular spectral element simulation of two-dimensional elastic wave propagation using unstructured triangular grids. *Geophys. J. Int.* 166, 679–698.

Meza-Fajardo, K. C., A. S. Papageorgiou 2008. A nonconvolutional, split-field, perfectly matched layer for wave propagation in isotropic and anisotropic elastic media: Stability analysis. *Bull. Seism. Soc. Am.* 98, 1811–1836.

Meza-Fajardo, K. C., A. S. Papageorgiou 2012. Study of the accuracy of the multiaxial perfectly matched layer for the elastic-wave equation. *Bull. Seism. Soc. Am.* 102, 2458–2467.

Mikhailenko, B. G., V. I. Korneev 1984. Calculation of synthetic seismograms for complex subsurface geometries by a combination of finite integral Fourier transform and finite-difference techniques. *J. Geophys.* 54, 195–206.

Mikumo, T., T. Miyatake 1987. Numerical modeling of realistic fault rupture processes. In B. A. Bolt (ed.), *Seismic Strong Motion Synthetics*, 91–151, Orlando, Florida: Academic Press.

Mitchell, A. R. 1969. *Computational Methods in Partial Differential Equations*. London: J. Wiley & Sons.

Mitchell, A. R., D. F. Griffiths 1994. *The Finite Difference Method in Partial Differential Equations*. New York: J. Wiley & Sons.

Miyatake, T. 1980. Numerical simulations of earthquake source process by a three-dimensional crack model. Part I. Rupture process. *J. Phys. Earth* 28, 565–598.

Mizutani, H. 2002. Accurate and efficient methods for calculating synthetic seismograms when elastic discontinuities do not coincide with the numerical grid. PhD Thesis. The University of Tokyo.

Mizutani, H., R. J. Geller, N. Takeuchi 2000. Comparison of accuracy and efficiency of time-domain schemes for calculating synthetic seismograms. *Phys. Earth Planet. Int.* 119, 75–97.

Moczo, P. 1989. Finite-difference technique for SH-waves in 2-D media using irregular grids: application to the seismic response problem. *Geophys. J. Int.* 99, 321–329.

Moczo, P., P.-Y. Bard 1993. Wave diffraction, amplification and differential motion near strong lateral discontinuities. *Bull. Seism. Soc. Am.* 83, 85–106.

Moczo, P., E. Bystrický, J. Kristek, J. M. Carcione, M. Bouchon 1997. Hybrid modeling of P-SV seismic motion at inhomogeneous viscoelastic topographic structures. *Bull. Seism. Soc. Am.* 87, 1305–1323.

Moczo, P., J. Kristek 2005. On the rheological models used for time-domain methods of seismic wave propagation. *Geophys. Res. Lett.* 32, L01306.

Moczo, P., J. Kristek, M. Galis 2004a. Simulation of the planar free surface with near-surface lateral discontinuities in the finite-difference modeling of seismic motion. *Bull. Seism. Soc. Am.* 94, 760–768.

Moczo, P., J. Kristek, M. Galis, E. Chaljub, V. Etienne 2011. 3-D finite-difference, finite-element, discontinuous-Galerkin and spectral-element schemes analysed for their accuracy with respect to P-wave to S-wave speed ratio. *Geophys. J. Int.* 187, 1645–1667.

Moczo, P., J. Kristek, M. Galis, P. Pažák 2010. On accuracy of the finite-difference and finite-element schemes with respect to P-wave to S-wave speed ratio. *Geophys. J. Int.* 182, 493–510.

Moczo, P., J. Kristek, M. Galis, P. Pažák, M. Balažovjech 2007a. The finite-difference and finite-element modeling of seismic wave propagation and earthquake motion. *Acta Physica Slovaca* 57, 177–406.

Moczo, P., J. Kristek, L. Halada 2000. 3D fourth-order staggered-grid finite-difference schemes: Stability and grid dispersion. *Bull. Seism. Soc. Am.* 90, 587–603.

Moczo, P., J. Kristek, L. Halada 2004b. *The Finite-Difference Method for Seismologists: An Introduction*. Bratislava: Comenius University.

Moczo, P., J. Kristek, V. Vavryčuk, R. J. Archuleta, L. Halada 2002. 3D heterogeneous staggered-grid finite-difference modeling of seismic motion with volume harmonic and arithmetic averaging of elastic moduli and densities. *Bull. Seism. Soc. Am.* 92, 3042–3066.

Moczo, P., P. Labák, J. Kristek, F. Hron 1996. Amplification and differential motion due to an antiplane 2D resonance in the sediment valleys embedded in a layer over the half-space. *Bull. Seism. Soc. Am.* 86, 1434–1446.

Moczo, P., M. Lucká, J. Kristek, M. Kristekova 1999. 3D displacement finite differences and a combined memory optimization. *Bull. Seism. Soc. Am.* 89, 69–79.

Moczo, P., J. O. A. Robertsson, L. Eisner 2007b. The finite-difference time-domain method for modeling of seismic wave propagation. In R.-S. Wu, V. Maupin (eds.), *Advances in Wave Propagation in Heterogeneous Earth*, 421–516. Advances in Geophysics Vol. 48, London: Elsevier–Academic Press.

Monelli, D., P. M. Mai, S. Jonsson, D. Giardini 2009. Bayesian imaging of the 2000 Western Tottori (Japan) earthquake through fitting of strong motion and GPS data. *Geophys. J. Int.* 176, 135–150.

Monteiller, V., S. Chevrot, D. Komatitsch, N. Fuji 2012. A hybrid method to compute short-period synthetic seismograms of teleseismic body waves in a 3-D regional model. *Geophys. J. Int.* 192, 230–247.

Morton, K. W., D. F. Mayers 1994. *Numerical Solution of Partial Differential Equations*. Cambridge: Cambridge University Press.

Mufti, I. R. 1985. Seismic modeling in the implicit mode. *Geophys. Prosp.* 33, 619–656.

Muir, F., J. Dellinger, J. T. Etgen, D. Nichols 1992. Modeling elastic fields across irregular boundaries. *Geophysics* 57, 1189–1193.

Munasinghe, M., G. W. Farnell 1973. Finite-difference analysis of Rayleigh wave scattering at vertical discontinuities. *J. Geophys. Res.* 78, 2454–2466.

Murphy, W. F. I. 1982. Effects of partial saturation on attenuation in Massilon sandstone and Vycor porous glass. *J. Acoust. Soc. Am.* 71, 1458–1468.

Muravskii, G. 2005. On description of hysteretic behavior of materials. *Int. J. Solids Struct.* 42, 2625–2644.

Nakamura, T., H. Takenaka, T. Okamoto, Y. Kaneda 2012. FDM simulation of seismic-wave propagation for an aftershock of the 2009 Suruga bay earthquake: Effects of ocean-bottom topography and seawater layer. *Bull. Seism. Soc. Am.* 102, 2420–2435.

Nielsen, S. B., J. M. Carlson, K. B. Olsen 2000. Influence of friction and fault geometry on earthquake rupture. *J. Geophys. Res.* 105, 6069–6088.

Nilsson, S., N. A. Petersson, B. Sjögreen, H.-O. Kreiss 2007. Stable difference approximations for the elastic wave equation in second order formulation. *SIAM J. Numer. Anal.* 45, 1902–1936.

O'Connell, R. J., B. Budiansky 1978. Measures of dissipation in viscoelastic media. *Geophys. Res. Lett.* 5, 5–8.

Oglesby, D. D. 1999. Earthquake dynamics on dip-slip faults. PhD Thesis. University of California, Santa Barbara.

Oglesby, D. D., R. J. Archuleta, S. B. Nielsen 1998. Earthquakes on dipping faults: The effects of broken symmetry. *Science* 280, 1055–1059.

Oglesby, D. D., R. J. Archuleta, S. B. Nielsen 2000. Dynamics of dip-slip faulting: Explorations in two dimensions. *J. Geophys. Res.* 105, 13643–13653.

Oglesby, D. D., S. M. Day 2001. Fault geometry and the dynamics of the 1999 Chi-Chi (Taiwan) earthquake. *Bull. Seism. Soc. Am.* 91, 1099–1111.

Oglesby, D. D., P. M. Mai 2012. Fault geometry, rupture dynamics and ground motion from potential earthquakes on the North Anatolian Fault under the Sea of Marmara. *Geophys. J. Int.* 188, 1071–1087.

Oglesby, D. D., P. M. Mai, K. Atakan, S. Pucci 2008. Dynamic models of earthquakes on the North Anatolian fault zone under the Sea of Marmara: Effect of hypocenter location. *Geophys. Res. Lett.* 35, L18302.

Ohminato, T., B. A. Chouet 1997. A free-surface boundary condition for including 3D topography in the finite-difference method. *Bull. Seism. Soc. Am.* 87, 494–515.

Ohnaka, M. 2013. *The Physics of Rock Failure and Earthquakes*. Cambridge: Cambridge University Press.

Ohnaka, M., T. Yamashita 1989. A cohesive zone model for dynamic shear faulting based on experimentally inferred constitutive relation and strong motion source parameters. *J. Geophys. Res.* 94, 4089–4104.

Ohtsuki, A., K. Harumi 1983. Effects of topography and subsurface inhomogeneities on seismic SV waves. *Earthq. Eng. Struct. Dyn.* 11, 441–462.

Okubo, P. G. 1989. Dynamic rupture modeling with laboratory-derived constitutive relation. *J. Geophys. Res.* 94, 12321–12335.

Okubo, P. G., J. H. Dieterich 1984. Effects of physical fault properties on frictional instabilities produced on simulated faults. *J. Geophys. Res.* 89, 5817–5827.

Olsen, K. B. 1994. Simulation of three-dimensional wave propagation in the Salt Lake basin. PhD Thesis. University of Utah, USA.

Olsen, K. B. 2000. Site amplification in the Los Angeles basin from three-dimensional modeling of ground motion. *Bull. Seism. Soc. Am.* 90, S77–S94.

Olsen, K. B., R. J. Archuleta 1996. Three-dimensional simulation of earthquakes on the Los Angeles fault system. *Bull. Seism. Soc. Am.* 86, 575–596.

Olsen, K. B., R. J. Archuleta, J. R. Matarese 1995a. Three-dimensional simulation of a magnitude 7.75 earthquake on the San Andreas fault. *Science* 270, 1628–1632.

Olsen, K. B., S. M. Day, C. R. Bradley 2003. Estimation of Q for long-period (> 2 sec) waves in the Los Angeles basin. *Bull. Seism. Soc. Am.* 93, 627–638.

Olsen, K. B., S. M. Day, J. B. Minster, Y. Cui, A. Chourasia, M. Faerman, R. Moore, P. Maechling, T. Jordan 2006. Strong shaking in Los Angeles expected from southern San Andreas earthquake. *Geophys. Res. Lett.* 33, L07305.

Olsen, K. B., S. M. Day, J.-B. Minster, Y. Cui, A. Chourasia, D. Okaya, P. J. Maechling, T. H. Jordan 2008. TeraShake2: Spontaneous rupture simulations of Mw 7.7 earthquakes on the southern San Andreas Fault. *Bull. Seism. Soc. Am.* 98, 1162–1185.

Olsen, K. B., R. Madariaga, R. J. Archuleta 1997. Three dimensional dynamic simulation of the 1992 Landers earthquake. *Science* 278, 834–838.

Olsen, K. B., J. C. Pechmann, G. T. Schuster 1995b. Simulation of 3D elastic wave propagation in the Salt Lake Basin. *Bull. Seism. Soc. Am.* 85, 1688–1710.

Olson, A., R. Apsel 1982. Finite faults and inverse theory with applications to the 1979 Imperial Valley earthquake. *Bull. Seism. Soc. Am.* 72, 1969–2001.

Opršal, I., C. Matyska, K. Irikura 2009. The source-box wave propagation hybrid methods: General formulation and implementation. *Geophys. J. Int.* 176, 555–564.

Opršal, I., J. Zahradník 1999. Elastic finite-difference method for irregular grids. *Geophysics* 64, 240–250.

Ottosen, N. S., H. Petersson 1992. *Introduction to the Finite Element Method*. Harlow: Prentice Hall.

Owen, S. J., S. Saigal 2001. Formation of pyramid elements for hexahedra to tetrahedra transitions. *Comput. Methods Appl. Mech. Eng.* 190, 4505–4518.

Özdenvar, T., G. A. McMechan 1996. Causes and reduction of numerical artifacts in pseudo-spectral wavefield extrapolation. *Geophys. J. Int.* 126, 819–828.

Palmer, A. C., J. R. Rice 1973. The growth of slip surfaces in the progressive failure of overconsolidated clay. *Proc. R. Soc. London* A332, 527–548.

Patera, A. T. 1984. A spectral element method for fluid dynamics: Laminar flow in a channel expansion. *J. Comp. Phys.* 54, 468–488.

Pelties, C., J. de la Puente, J.-P. Ampuero, G. B. Brietzke, M. Käser 2012. Three-dimensional dynamic rupture simulation with a high-order discontinuous Galerkin method on unstructured tetrahedral meshes. *J. Geophys. Res.* 117, B02309.

Pelties, C., M. Käser, V. Hermann, C. E. Castro 2010. Regular versus irregular meshing for complicated models and their effect on synthetic seismograms. *Geophys. J. Int.* 183, 1031–1051.

Pérez-Ruiz, J. A., F. Luzón, A. García-Jerez 2005. Simulation of an irregular free surface with a displacement finite-difference scheme. *Bull. Seism. Soc. Am.* 95, 2216–2231.

Peter, D., D. Komatitsch, Y. Luo, R. Martin, N. Le Goff, E. Casarotti, P. Le Loher, F. Magnoni, Q. Liu, C. Blitz, T. Nissen-Meyer, P. Basini, J. Tromp 2011. Forward and adjoint simulations of seismic wave propagation on fully unstructured hexahedral meshes. *Geophys. J. Int.* 186, 721–739.

Peyrat, S., P. Favreau 2010. Kinematic and spontaneous rupture models of the 2005 Tarapacá intermediate depth earthquake. *Geophys. J. Int.* 181, 369–381.

Peyrat, S., K. Olsen, R. Madariaga 2001. Dynamic modeling of the 1992 Landers earthquake. *J. Geophys. Res.* 106, 26467–26482.

Pilz, M., S. Parolai, M. Stupazzini, R. Paolucci, J. Zschau 2011. Modelling basin effects on earthquake ground motion in the Santiago de Chile basin by a spectral element code. *Geophys. J. Int.* 187, 929–945.

Pitarka, A. 1999. 3D elastic finite-difference modeling of seismic motion using staggered grids with nonuniform spacing. *Bull. Seism. Soc. Am.* 89, 54–68.

Pitarka, A., R. W. Graves, P. G. Somerville 2004. Validation of a 3D velocity model of the Puget Sound region based on modeling ground motion from the 28 February 2001 Nisqually earthquake. *Bull. Seism. Soc. Am.* 94, 1670–1689.

Pitarka, A., K. Irikura 1996. Modeling 3D surface topography by finite-difference method: Kobe-JMA station site, Japan, case study. *Geophys. Res. Lett.* 23, 2729–2732.

Pitarka, A., K. Irikura, T. Iwata 1997. Modelling of ground motion in the Higashinada (Kobe) area for an aftershock of the 1995 January 17 Hyogo-ken Nanbu, Japan, earthquake. *Geophys. J. Int.* 131, 231–239.

Pitarka, A., K. Irikura, T. Iwata, H. Sekiguchi 1998. Three-dimensional simulation of the near-fault ground motion for the 1995 Hyogo-Ken Nanbu (Kobe), Japan, earthquake. *Bull. Seism. Soc. Am.* 88, 428–440.

Pitilakis, K., D. Raptakis, K. Lontzetidis, Th. Tika-Vassilikou 1999. Geotechnical and geophysical description of Euro-seistest, using field, laboratory tests and moderate strong motion recordings. *J. Earthq. Eng.* 3, 381–409.

Pitilakis, K., D. Raptakis, K. Makra, M. Manakou, F. J. Chávez-García 2011. Euroseistest 3D array for the study of complex site effects. In S. Akkar, P. Gülkan, T. van Eck (eds.), *Earthquake Data in Engineering Seismology*, 145–166. Geotechnical Geological and Earthquake Engineering, Vol. 14, Dordrecht: Springer.

Pitilakis, K., Z. Roumelioti, D. Raptakis, M. Manakou, K. Liakakis, A. Anastasiadis, D. Pitilakis 2013. The EUROSEISTEST strong ground motion database and web portal. *Seism. Res. Lett.* 84, 796–804.

Press, W. H., S. A. Teukolsky, W. T. Vetterling, B. P. Flannery 2007. *Numerical Recipes*. Cambridge: Cambridge University Press.

Priolo, E., J. M. Carcione, G. Seriani 1994. Numerical-simulation of interface waves by high-order spectral modeling techniques. *J. Acoust. Soc. Am.* 95, 681–693.

Pujol, J. 2003. *Elastic Wave Propagation and Generation in Seismology*. Cambridge, Cambridge University Press.

Pulido, N., L. A. Dalguer 2009. Estimation of the high-frequency radiation of the 2000 Tottori (Japan) earthquake based on a dynamic model of fault rupture: Application to the strong ground motion simulation. *Bull. Seism. Soc. Am.* 99, 2305–2322.

Qian, S. 2002. *Introduction to Time-Frequency and Wavelet Transforms*. New Jersey: Prentice Hall.

Ranjith, K., J. R. Rice 2001. Slip dynamics at an interface between dissimilar materials. *J. Mech. Phys. Solids* 49, 341–361.

Raptakis, D., F. J. Chávez-García, K. Makra, K. Pitilakis 2000. Site effects at Euroseistest – I. Determination of the valley structure and confrontation of observations with 1D analysis. *Soil Dyn. Earthq. Eng.* 19, 1–22.

Raptakis, D., M. Manakou, F. J. Chávez-García, K. Makra, K. Pitilakis 2005. 3D configuration of Mygdonian basin and preliminary estimate of its site response. *Soil Dyn. Earthq. Eng.* 25, 871–887.

Raptakis, D., N. P. Theodulidis, K. Pitilakis 1998. Data analysis of the Euroseistest strong motion array in Volvi (Greece): Standard and horizontal-to-vertical spectral ratio techniques. *Earthquake Spectra* 14, 203–223.

Reddy, J. N. 2006. *An Introduction to the Finite Element Method*. New York: McGraw-Hill.

Reshef, M., D. D. Kosloff, M. Edwards, C. Hsiung 1988. Three-dimensional elastic modeling by the Fourier method. *Geophysics* 53, 1184–1193.

Richtmyer, R. D., K. W. Morton 1967. *Difference Methods for Initial Value Problems*. New York: J. Wiley & Sons.

Ripperger, J., J.-P. Ampuero, P. M. Mai, D. Giardini 2007. Earthquake source characteristics from dynamic rupture with constrained stochastic fault stress. *J. Geophys. Res.* 112, B04311.

Robertsson, J. O. A. 1996. A numerical free-surface condition for elastic/viscoelastic finite-difference modeling in the presence of topography. *Geophysics* 61, 1921–1934.

Robertsson, J. O. A., J. O. Blanch 2011. Numerical methods, finite difference. In H. Gupta (ed.), *Encyclopaedia of Solid Earth Geophysics*, 2nd edn., Dordrecht: Springer.

Robertsson, J. O. A., J. O. Blanch, K. Nihei, J. Tromp (eds.) 2012. *Numerical Modeling of Seismic Wave Propagation: Gridded Two-Way Wave-Equation Methods*. Geophysical Reprint Series No. 28. Tulsa, Oklahoma: Society of Exploration Geophysicists.

Robertsson, J. O. A., J. O. Blanch, W. W. Symes 1994. Viscoelastic finite-difference modeling. *Geophysics* 59, 1444–1456.

Robertsson, J. O. A., C. H. Chapman 2000. An efficient method for calculating finite-difference seismograms after model alterations. *Geophysics* 65, 907–918.

Robertsson, J. O. A., K. Holliger 1997. Modeling of seismic wave propagation near the earth's surface. *Phys. Earth Planet. Int.* 104, 193–211.

Robertsson, J. O. A., A. Levander, K. Holliger 1996. A hybrid wave propagation simulation technique for ocean acoustic problems. *J. Geophys. Res.* 101, 11225–11241.

Rodrigues, D. 1993. Large scale modelling of seismic wave propagation. PhD Thesis. École Centrale Paris.

Rodrigues, D., P. Mora 1993. An efficient implementation of the free-surface boundary condition in 2-D and 3-D elastic cases. *63rd Annual International Meeting, Society of Exploration Geophysicists*, Expanded Abstracts 215–217.

Rojas, O., S. M. Day, J. E. Castillo, L. A. Dalguer 2008. Modelling of rupture propagation using high-order mimetic finite differences. *Geophys. J. Int.* 172, 631–650.

Rojas, O., E. M. Dunham, S. M. Day, L. A. Dalguer, J. E. Castillo 2009. Finite difference modelling of rupture propagation with strong velocity-weakening friction. *Geophys. J. Int.* 179, 1831–1858.

Roten, D., K. B. Olsen, J. C. Pechmann, V. M. Cruz-Atienza, H. Magistrale 2011. 3D simulations of M 7 earthquakes on the Wasatch Fault, Utah, Part I: Long-period (0–1 Hz) ground motion. *Bull. Seism. Soc. Am.* 101, 2045–2063.

Rovelli, A., A. Caserta, L. Malagnini, F. Marra 1994. Assessment of potential strong ground motions in the city of Rome. *Annali di Geofisica* 37, 1745–1769.

Rubin, A. M., J.-P. Ampuero 2007. Aftershock asymmetry on a bimaterial interface. *J. Geophys. Res.* 112, B05307.

Ruina, A. L. 1980. Friction laws and instabilities: A quasistatic analysis of some dry frictional behavior. PhD Thesis. Brown University, Providence.

Ruina, A. L. 1983. Slip instability and state variable friction laws. *J. Geophys. Res.* 88, 10359–10370.

Ruud, B. O., S. O. Hestholm 2001. 2D surface topography boundary conditions in seismic wave modelling. *Geophys. Prosp.* 49, 445–460.

Saenger, E. H., T. Bohlen 2004. Finite-difference modeling of viscoelastic and anisotropic wave propagation using the rotated staggered grid. *Geophysics* 69, 583–591.

Saenger, E. H., N. Gold, S. A. Shapiro 2000. Modeling the propagation of elastic waves using a modified finite-difference grid. *Wave Motion* 31, 77–92.

Sato, T., R. W. Graves, P. G. Somerville 1999. Three-dimensional finite-difference simulations of long-period strong motions in the Tokyo metropolitan area during the 1990 Odawara earthquake (MJ 5.1) and the great 1923 Kanto earthquake (MS 8.2). *Bull. Seism. Soc. Am.* 89, 579–607.

Sato, T., R. W. Graves, P. G. Somerville, S. Kataoka 1998. Estimates of regional and local strong motions during the great 1923 Kanto, Japan, earthquake (Ms 8.2), Part 2: Forward simulation of seismograms using variable-slip rupture models and estimation of near-fault long-period ground motions. *Bull. Seism. Soc. Am.* 88, 206–227.

Semblat, J.-F., A. Pecker 2009. *Waves and Vibrations in Soils: Earthquakes, Traffic, Shocks, Construction Works*. Pavia, Italy: IUSS Press.

Seriani, G., S. P. Oliveira 2007. Optimal blended spectral-element operators for acoustic wave modeling. *Geophysics* 72, SM95–SM106.

Seriani, G., E. Priolo 1994. Spectral element method for acoustic wave simulation in heterogeneous media. *Finite Elem. Anal. Des.* 16, 337–348.

Serón, F. J., F. J. Sanz, M. Kindelán 1989. Elastic wave propagation with the finite element method. IBM, European Center for Science and Engineering Computing.

Shapiro, N. M., K. B. Olsen, S. K. Singh 2000. Wave-guide effects in subduction zones: Evidence from three-dimensional modeling. *Geophys. Res. Lett.* 27, 433–436.

Shashkov, M. 1996. *Conservative Finite-Difference Methods on General Grids*. Roca Raton, Florida: CRC Press.

Shearer, P. 2009. *Introduction to Seismology*, 2nd edn. Cambridge: Cambridge University Press.

Shtivelman, V. 1984. A hybrid method for wave field computation. *Geophys. Prosp.* 32, 236–257.

Shtivelman, V. 1985. Two-dimensional acoustic modelling by a hybrid method. *Geophysics* 50, 1273–1284.

Schoenberg, M., F. Muir 1989. A calculus for finely layered anisotropic media. *Geophysics* 54, 581–589.

Scholz, C. 2002. *The Mechanics of Earthquakes and Faulting*, 2nd edn. Cambridge: Cambridge University Press.

Sipkin, S. A. 1982. Estimation of earthquake source parameters by the inversion of waveform data: Synthetic waveforms. *Phys. Earth Planet. Int.* 30, 242–259.

Sjögreen, B., N. A. Petersson 2012. A fourth order accurate finite difference scheme for the elastic wave equation in second order formulation. *J. Sci. Comput.* 45, 17–48.

Skarlatoudis, A. A., C. B. Papazachos, N. P. Theodulidis, J. Kristek, P. Moczo 2010. Local site-effects for the city of Thessaloniki (N. Greece) using a 3-D finite-difference method: A case of complex dependence on source and model parameters. *Geophys. J. Int.* 182, 279–298.

Sochacki, J., J. H. George, R. E. Ewing, S. B. Smithson 1991. Interface conditions for acoustic and elastic wave propagation. *Geophysics* 56, 168–181.

Spencer, J. W. J. 1981. Stress relaxation at low frequencies in fluid-saturated rocks. *J. Geophys. Res.* 86, 1803–1812.

Stead, R. J., D. V. Helmberger 1988. Numerical-analytical interfacing in two dimensions with applications to modeling NTS seismograms. Birkhauser, Basel, Switzerland.

Stein, S., M. Wysession 2003. *An Introduction to Seismology, Earthquakes, and Earth Structure*. Oxford: Blackwell Publishing.

Stephen, R. A. 1983. A comparison of finite difference and reflectivity seismograms for marine models. *Geophys. J. R. Astr. Soc.* 72, 39–57.

Strang, G., G. J. Fix 1973. *An Analysis of the Finite Element Method*. Englewood Cliffs, New Jersey: Prentice Hall.

Strang, G., G. J. Fix 1988. *An Analysis of the Finite Element Method*. Wellesley, Massachusetts: Wellesley-Cambridge Press.

Strikwerda, J. C. 2004. *Finite Difference Schemes and Partial Differential Equations*. Philadelphia: SIAM.

Stupazzini, M., J. de la Puente, C. Smerzini, M. Käser, H. Igel, A. Castellani 2009a. Study of rotational ground motion in the near-field region. *Bull. Seism. Soc. Am.* 99, 1271–1286.

Stupazzini, M., R. Paolucci, H. Igel 2009b. Near-fault earthquake ground-motion simulation in the Grenoble Valley by a high-performance spectral element code. *Bull. Seism. Soc. Am.* 99, 286–301.

Taflove, A., S. C. Hagness 2005. *Computational Electrodynamics: The Finite-Difference Time-Domain Method*. Boston: Artech House.

Tago, J., V. M. Cruz-Atienza, J. Virieux, V. Etienne, F. J. Sánchez-Sesma 2012. A 3D hp-adaptive discontinuous Galerkin method for modeling earthquake dynamics. *J. Geophys. Res.* 117, B09312.

Takeuchi, N., R. J. Geller 2000. Optimally accurate second order time-domain finite difference scheme for computing synthetic seismograms in 2-D and 3-D media. *Phys. Earth Planet. Int.* 119, 99–131.

Takeuchi, N., R. J. Geller 2003. Accurate numerical methods for solving the elastic equation of motion for arbitrary source locations. *Geophys. J. Int.* 154, 852–866.

Tam, C. K. W., J. C. Webb 1993. Dispersion-relation-preserving finite difference schemes for computational acoustics. *J. Comp. Phys.* 107, 262–281.

Tarrass, I., L. Giraud, P. Thore 2011. New curvilinear scheme for elastic wave propagation in presence of curved topography. *Geophys. Prosp.* 59, 889–906.

Templeton, E. L., J. R. Rice 2008. Off-fault plasticity and earthquake rupture dynamics: 1. Dry materials or neglect of fluid pressure changes *J. Geophys. Res.* 113, B09306.

Thomas, J. W. 1995. *Numerical Partial Differential Equations: Finite Difference Methods*. New York: Springer.

Tinti, E., A. Bizzarri, M. Cocco 2005. Modeling the dynamic rupture propagation on heterogeneous faults with rate- and state-dependent friction. *Ann. Geophys.* 48, 327–345.

Tinti E., M. Cocco, E. Fukuyama, A. Piatanesi 2009. Dependence of slip weakening distance (Dc) on final slip during dynamic rupture of earthquakes. *Geophys. J. Int.* 177, 1205–1220.

Titarev, V. A., E. F. Toro 2002. ADER: Arbitrary high order Godunov approach. *J. Sci. Comput.* 17, 609–618.

Tromp, J., D. Komatitsch, Q. Liu 2008. Spectral-element and adjoint methods in seismology. *Commun. Comput. Phys.* 3, 1–32.

Turkowski, K., S. Gabriel 1990. Filters for common resampling tasks. In A. S. Glassner (ed.), *Graphics Gems I*, 147–165, San Diego: Academic Press.

Uenishi, K., J. R. Rice 2003. Universal nucleation length for slip-weakening rupture instability under nonuniform fault loading. *J. Geophys. Res.* 108, 2042.

Uenishi, K., J. R. Rice 2004. Three-dimensional rupture instability of a slip-weakening fault under heterogeneous loading. *Eos Trans. AGU*, 85(46), Fall Meeting Supplement, Abstract S13E–04.

Van den Berg, A. 1984. A hybrid solution for wave propagation problems in regular media with bounded irregular inclusions. *Geophys. J. R. Astr. Soc.* 79, 3–10.

Vidale, J. E., D. V. Helmberger 1987. Path effects in strong motion seismology. In B. A. Bolt (ed.), *Seismic Strong Motion Synthetics*, 267–319, Orlando, Florida: Academic Press.

Viesca, R. C., E. L. Templeton, J. R. Rice 2008. Off-fault plasticity and earthquake rupture dynamics: 2. Effects of fluid saturation. *J. Geophys. Res.* 113, B09307.

Virieux, J. 1984. SH-wave propagation in heterogeneous media: Velocity–stress finite-difference method. *Geophysics* 49, 1933–1957.

Virieux, J. 1986. P-SV wave propagation in heterogeneous media; velocity–stress finite-difference method. *Geophysics* 51, 889–901.

Virieux, J., R. Madariaga 1982. Dynamic faulting studied by a finite difference method. *Bull. Seism. Soc. Am.* 72, 345–369.

Vuan, A., P. Klin, G. Laurenzano, E. Priolo 2011. Far-source long-period displacement response spectra in the Po and Venetian Plains (Italy) from 3D wavefield simulations. *Bull. Seism. Soc. Am.* 101, 1055–1072.

Wald, D. J., R. W. Graves 1998. The seismic response of the Los Angeles basin, California. *Bull. Seism. Soc. Am.* 88, 337–356.

Wang, H., H. Igel, F. Gallovič, A. Cochard 2009. Source and basin effects on rotational ground motions: Comparison with translations. *Bull. Seism. Soc. Am.* 99, 1162–1173.

Wang, Y., G. T. Schuster 1996. Finite-difference variable grid scheme for acoustic and elastic wave equation modeling. In *Proceedings of the 66th Annual International Meeting, Society of Exploration Geophysicists*, Expanded Abstracts, 674–677. Denver, Colorado.

Wang, Y., H. Takenaka 2001. A multidomain approach of the Fourier pseudospectral method using discontinuous grid for elastic wave modeling. *Earth Planets Space* 53, 149–158.

Wang, T., X. Tang 2003. Finite-difference modeling of elastic wave propagation: A non-splitting perfectly matched layer approach. *Geophysics* 68, 1749–1755.

Wang, Y., J. Xu, G. T. Schuster 2001. Viscoelastic wave simulation in basins by a variable-grid finite-difference method. *Bull. Seism. Soc. Am.* 91, 1741–1749.

Whirley, R. G., B. E. Engelmann 1993. DYNA3D: A nonlinear, explicit, three-dimensional finite element code for solid and structural mechanics – User manual. University of California, Lawrence Livermore National Laboratory.

Whirley, R. G., B. E. Engelmann, J. O. Hallquist 1992. DYNA2D: A nonlinear, explicit, two-dimensional finite element code for solid and structural mechanics – User manual. University of California, Lawrence Livermore National Laboratory.

White, J. 1965. *Seismic Waves*. New York: McGraw-Hill.

Wilcox, L. C., G. Stadler, C. Burstedde, O. Ghattas 2010. A high-order discontinuous Galerkin method for wave propagation through coupled elastic–acoustic media. *J. Comp. Phys.* 229, 9373–9396.

Xu, H., S. M. Day, J.-B. Minster 1999. Two dimensional linear and nonlinear wave propagation in a half-space. *Bull. Seism. Soc. Am.* 89, 903–917.

Xu, T., G. A. McMechan 1995. Composite memory variables for viscoelastic synthetic seismograms. *Geophys. J. Int.* 121, 634–639.

Xu, T., G. A. McMechan 1998. Efficient 3-D viscoelastic modeling with application to near-surface land seismic data. *Geophysics* 63, 601–612.

Yee, K. 1966. Numerical solution of initial boundary value problems involving Maxwell's equations in isotropic media. *IEEE Trans. Antennas Propagat.* 14, 302–307.

Yomogida, K., J. T. Etgen 1993. 3-D wave propagation in the Los Angeles basin for the Whittier-Narrows earthquake. *Bull. Seism. Soc. Am.* 83, 1325–1344.

Zahradník, J. 1995a. Comment on 'A hybrid method for estimation of ground motion in sedimentary basins: Quantitative modeling for Mexico City' by D. Fäh, P. Suhadolc, St. Mueller and G.F. Panza *Bull. Seism. Soc. Am.* 85, 1268–1270.

Zahradník, J. 1995b. Simple elastic finite-difference scheme. *Bull. Seism. Soc. Am.* 85, 1879–1887.

Zahradník, J., P. Moczo 1996. Hybrid seismic modeling based on discrete-wave number and finite-difference methods. *PAGEOPH* 148, 21–38.

Zahradník, J., E. Priolo 1995. Heterogeneous formulation of elastodynamic equations and finite-difference schemes. *Geophys. J. Int.* 120, 663–676.

Zeng, X. 1996. Finite difference modeling of viscoelastic wave propagation in a generally heterogeneous medium in the time domain, and a dissection method in the frequency domain. PhD Thesis. University of Toronto.

Zeng, Y. Q., J. Q. He, Q. H. Liu 2001. The application of the perfectly matched layer in numerical modeling of wave propagation in poroelastic media. *Geophysics* 66, 1258–1266.

Zgainski, F.-X., J.-L. Coulomb, Y. Maréchal, F. Claeyssen, X. Brunotte 1996. A new family of finite elements: The pyramidal elements. *IEEE Trans. Magnetics* 32(3), 1393–1396.

Zhang, C., W. W. Symes 1998. Fourth order, full-stencil immersed interface method for elastic waves with discontinuous coefficients. *68th Annual International Meeting, Society of Exploration Geophysicists*, Expanded Abstracts, 1929–1932.

Zhang, J. 1997. Quadrangle-grid velocity–stress finite-difference method for elastic-wave-propagation simulation. *Geophys. J. Int.* 131, 127–134.

Zhang, J. 1999. Quadrangle-grid velocity–stress finite difference method for poroelastic wave equations. *Geophys. J. Int.* 139, 171–182.

Zhang, J. 2004a. Elastic wave modelling in heterogeneous media with high velocity contrasts. *Geophys. J. Int.* 159, 223–239.

Zhang, J. 2004b. Wave propagation across fluid–solid interfaces: A grid method approach. *Geophys. J. Int.* 159, 240–252.

Zhang, J., H. Gao 2011. Irregular perfectly matched layers for 3D elastic wave modeling *Geophysics* 76, T27–T36.

Zhang, W., X. Chen 2006. Traction image method for irregular free surface boundaries in finite difference seismic wave simulation. *Geophys. J. Int.* 167, 337–353.

Zhang, W., X. Chen, Z. Zhang 2012. Three-dimensional elastic wave numerical modelling in the presence of surface topography by a collocated-grid finite-difference method on curvilinear grid. *Geophys. J. Int.* 190, 358–378.

Zhang, W., Y. Shen 2010. Unsplit complex frequency-shifted PML implementation using auxiliary differential equations for seismic wave modeling. *Geophysics* 75, T141–T154.

Zhang, Z., W. Zhang, X. Chen 2013a. Complex frequency-shifted perfectly matched layer with auxiliary differential equations on curved grid finite-difference method. *Geophys. J. Int*. submitted.

Zhang, Z., W. Zhang, H. Li, X. Chen 2013b. Stable discontinuous grid implementation for collocated-grid finite-difference seismic wave modelling. *Geophys. J. Int.* 192, 1179–1188.

Zhang, Z., W. Zhang, X. Chen 2013c. Three dimensional curved grid finite-difference method for non-planar rupture dynamics. *J. Geophys. Res*. submitted.

Zhang, Z., G. Zhu, X. Chen 2011. Rupture dynamics simulation for non-planar fault by a curved grid finite difference method. *American Geophysical Union, Fall Meeting 2011*, Abstract #S43C–2269.

Zhao, L., L. Wen, L. Chen, T. Zheng 2008. A two-dimensional hybrid method for modeling seismic wave propagation in anisotropic media. *J. Geophys. Res.* 113, B12307.

Zienkiewicz, O. C., R. L. Taylor 1989. *The Finite Element Method*, 4th edn., Vol. 1. McGraw-Hill.

Zingg, D. W. 2000. Comparison of high-accuracy finite-difference methods for linear wave propagation. *SIAM J. Sci. Comput.* 22, 476502.

Index